CONF-811203--Vol 1

I-3862

MASTER

CONF-811203-- Vol. 1

DE82 016600

HOT ELECTRON RING PHYSICS

of the 2nd workshop

proceedings

VOLUME 1

DECEMBER 1-3, 1981

SAN DIEGO, CALIFORNIA

SPONSORED BY

FUSION ENERGY DIVISION

OAK RIDGE NATIONAL LABORATORY

Oak Ridge, Tennessee

Operated by Union Carbide Corporation under contract W-7405-eng-26

with the Office of Fusion Energy, U.S. Department of Energy

and

JAYCOR

San Diego, California

DISTRIBUTION OF THIS DOCUMENT IS UNLIMITED

PREFACE

The Second Workshop on Hot Electron Ring Physics was held at San Diego, California, on December 1-3, 1981, under the sponsorship of the Oak Ridge National Laboratory (ORNL) and JAYCOR. About 70 participants representing both the United States and Japan attended the workshop. The first workshop in this series was held at Oak Ridge, Tennessee, December 3-5, 1979 (see *EBT Ring Physics: Proceedings of the Workshop*, CONF-791228, Oak Ridge, Tennessee).

The workshop organizing committee members were:

N. A. Uckan, Chairman, ORNL

N. A. Krall, Chairman, JAYCOR

Diane Miller, Arrangements/Finance, JAYCOR

DeLena Akers, Proceedings, ORNL

The purposes of the workshop were (1) to evaluate and review the progress made in the experimental and theoretical understanding of the hot electron ring properties since the first workshop; (2) to assess various techniques used in the analyses of ring equilibrium, stability, heating, scaling, etc.; and (3) to identify the processes that influence the operating regimes of present and future experiments.

Technical coverage in the workshop was very broad and included the presentation of 43 papers (11 experimental and 32 theoretical), followed by open forum discussions of topics selected by the workshop participants.

These proceedings include (1) workshop summaries prepared by the session chairmen and (2) full-length manuscripts that were submitted to the workshop and presented at the following workshop sessions: Overview (2 invited papers); Stability (12 papers); Ring Properties and Scaling (10 papers); Ring Heating (9 papers); Synchrotron Emission (5 papers); and Ions, Tandems, Equilibria, and Power Balance (5 papers). Open-forum discussions are partially reported at the end of the proceedings. An Author Index, the Attendance List, and the Agenda conclude the proceedings. (Because of the need for the camera-ready publication, variations in style and format were inevitable.)

The local host for the workshop was JAYCOR, and a special acknowledgment is due to Nick Krall and Diane Miller for the excellent arrangements and warm hospitality at San Diego. The efforts of session chairmen provided an enthusiastic forum for discussion of the papers that contributed largely to the success of the workshop. The assistance of DeLena Akers in the preparation and coordination of these proceedings is gratefully acknowledged. Thanks are also due to Caila Cox and to the staff of the ORNL FED Reports Office for handling many details of the publication.

The organizing committee wishes to express its appreciation to McDonnell Douglas Astronautics Company; Science Applications, Inc.; and TRW, Inc.; for co-hosting the workshop reception.

N. A. Uckan
Oak Ridge, Tennessee
January 1982

CONTENTS — VOLUME I

1. SUMMARY OF THE WORKSHOP 1

2. OVERVIEW..... 21

HOT ELECTRON RINGS: DIAGNOSTIC REVIEW AND SUMMARY OF MEASUREMENTS — G. R. Haste 23

A PERSPECTIVE ON EBT ELECTRON RING THEORY — N. A. Krall 45

3. STABILITY 81

CURVATURE DRIVEN INSTABILITIES IN A HOT ELECTRON PLASMA: RADIAL ANALYSIS — H. L. Berk, J. W. Van Dam, M. N. Rosenbluth, D. A. Spong 83

RADIAL STRUCTURE OF INSTABILITY MODES IN THE EBT HOT ELECTRON ANNULUS — D. A. Spong, H. L. Berk, J. W. Van Dam, and M. N. Rosenbluth 93

STABILITY OF LOW FREQUENCY MODES IN A HOT ELECTRON BUMPY TORUS — K. T. Tsang and P. J. Catto 117

KINETIC THEORY OF EBT STABILITY — C. Z. Cheng 143

STABILIZATION OF THE HIGH-BETA PLASMA INSTABILITY WITH ECH HOT ELECTRON ANNULUS IN THE SYMMETRIC MIRROR — S. Hiroe, T. Kunibe, H. Akiyama, and M. Inutake 145

EXPERIMENTAL HOT-TO-WARM ELECTRON DENSITY RATIO FOR INSTABILITY THERSHOLD IN THE ELMO BUMPY TORUS — S. Hiroe, L. A. Berry, R. J. Colchin, J. C. Glowienda, G. R. Haste, D. L. Hillis, and T. Uckan 167

STABILIZATION OF THE FLUTE INSTABILITY BY A D.C. ELECTRIC FIELD IN TOROIDAL PLASMAS — I. Alexeff 181

NECESSARY AND SUFFICIENT CRITERIA FOR THE STABILITY OF A HOT PARTICLE RING - PLASMA SYSTEM — T. M. Antonsen, Jr. and Y. C. Lee 191

SIMULATION STUDIES ON STABILITY AND β LIMITS OF EBT — Y. Ohsawa and J. M. Dawson 213

PARAMETRIC DECAY INSTABILITIES IN ECR HEATED PLASMAS — M. Porkolab 237

THE WHISTLER INSTABILITY AT RELATIVISTIC ENERGIES — N. T. Gladd 247

HIGH-FREQUENCY MICROINSTABILITIES IN HOT-ELECTRON PLASMAS — Y-J. Chen, W. M. Nevins, and G. R. Smith 279

STABILITY OF ANISOTROPIC RELATIVISTIC HOT ELECTRON PLASMA IN THE ELMO BUMPY TORUS — K. T. Nguyen, T. Kammash, and R. J. Kashuba 289

4. RING PROPERTIES AND SCALING 315

HARD X-RAY MEASUREMENTS OF THE HOT ELECTRON RINGS IN EBT-S — D. L. Hillis 317

INTERACTION OF MICROWAVE WITH HOT ELECTRON RING IN NAGOYA BUMPY TORUS — M. Tanaka, M. Hosokawa, M. Fujiwara, and H. Ikegami 339

RING TEMPERATURE SCALING — N. A. Uckan 361

PARAMETRIC STUDY OF THE RELATIVISTIC ELECTRON RING — S. Hamasaki, N. A. Krall, and J. L. Sperling 373

PROSPECTS FOR CONTROL OF ELMO RINGS — G. E. Guest and R. A. Dandl 393

NONADIABATICITY AND HIGH ENERGY PARTICLE ORBITS IN EBT — L. W. Owen, L. E. Deleanu, and C. L. Hedrick 409

THE NONADIABATIC MOTION OF HOT ANNULUS ELECTRONS IN EBT-I AND EBT-P — R. E. Juhala, M. A. Prelas, and C. B. Wallace 425

HEATING OF ENERGETIC ELECTRONS AND ELMO RING FORMATION IN SYMMETRIC MIRROR FACILITY — B. H. Quon, R. A. Dandl, N. H. Lazar, and R. F. Wuerker 441

SPATIAL STRUCTURE OF THE SM-1 SYMMETRIC MIRROR HOT ELECTRON RING USING DIAMAGNETIC MEASUREMENTS — L. L. Lao, B. H. Quon, R. A. Dandl, and N. H. Lazar 463

BUMPY TORUS ANNULUS STARTUP — J. L. Sperling, S. Hamasaki, and N. A. Krall 471

CONTENTS — VOLUME II

5. RING HEATING 485

RAY TRACING STUDIES OF MICROWAVE HEATING OF THE ANNULUS IN EBT DEVICES — D. B. Batchelor, R. C. Goldfinger, and H. Weitzner 487

FOKKER-PLANCK CALCULATIONS OF ELECTRON CYCLOTRON RESONANT HEATING (ECRH) IN MIRROR GEOMETRY — B. W. Stallard, Y. Matsuda, and W. M. Nevins 505

MULTIPLE FREQUENCY ECH (MFECH) IN SM-1 AND STM-1 — N. Lazar, J. Barter, R. Dandl, W. DiVergilio, B. Quon, and R. Wuerker 519

SIMULATION OF ELECTRON CYCLOTRON RESONANCE HEATING WITH MULTIPLE FREQUENCIES IN MIRROR GEOMETRY — T. K. Samec, B. I. Hauss, and G. Guest 531

SIMULATION OF MULTI-FREQUENCY ECRH — T. D. Rognlien 545

THEORY OF MULTIFREQUENCY ECRH — J. E. Howard, M. A. Lieberman, A. J. Lichtenberg, and R. H. Cohen 561

DOPPLER-SHIFTED RESONANCE ABSORPTION BY HOT ELECTRONS — J. W. Shearer 583

ENHANCEMENT OF EBT RING PARAMETERS DURING ION CYCLOTRON HEATING — F. W. Baity, J. C. Glowienka, D. L. Hillis, and T. L. Owens 597

NONSTANDARD HEATING EXPERIMENTS IN EBT — J. C. Glowienka, W. A. Davis, D. L. Hillis, T. Uckan, F. M. Bieniosek, and L. Solensten 609

6. SYNCHROTRON EMISSION 633

SYNCHROTRON EMISSION MEASUREMENTS FROM THE HOT ELECTRON RINGS IN EBT — J. Wilgen and T. Uckan 635

SYNCHROTRON EMISSION FROM THE RING ELECTRONS IN EBT — T. Uckan and N. A. Uckan 657

ELECTROMAGNETIC INTERACTIONS OF NON-MAXWELLIAN PLASMAS — S. Tamor 689

ANALYTIC EXPRESSIONS FOR SYNCHROTRON RADIATION FROM EBT — D. Winske, D. A. Boyd, and G. D. Tsakiris 701

ELECTRON SYNCHROTRON EMISSION FROM THE EBT RING PLASMA — C. M. Celata 717

7. IONS, TANDEMS, EQUILIBRIA, AND POWER BALANCE 719

ION RING SCALING STUDIES FOR AN EBT REACTOR — M. R. Gordinier and R. J. Kashuba 721

RING POWER BALANCE OBSERVING PLASMA STABILITY CONSTRAINTS — R. B. Campbell and B. G. Logan 739

NUMERICAL STUDY OF VLASOV EQUILIBRIUM FOR BUMPY CYLINDER PLASMA WITH HOT ELECTRON RINGS — T. Watanabe, K. Hamamatsu, J. W. Van Dam, and K. Nishikawa 761

SENSITIVITY OF HEAVY ION BEAM PROBE TO HOT ELECTRONS IN EBT — F. M. Bieniosek and K. A. Conner 793

THE "NEGATIVE" TANDEM MIRROR — P. Poulsen, S. L. Allen, T. A. Casper, D. P. Grubb, R. A. Jong, W. E. Nexsen, G. D. Porter, and T. C. Simonen 815

8. OPEN FORUM 827

MHD STABILITY OF TANDEM MIRRORS — P. Poulsen, A. Molvig, J. Shearer 829

AUTHOR INDEX 833

ATTENDANCE LIST 835

AGENDA 839

1. SUMMARY OF THE WORKSHOP

N. A. Uckan, N. A. Krall, W. B. Ard, D. B. Batchelor, H. L. Berk, L. A. Berry, M. Fujiwara, N. T. Gladd, G. R. Haste, C. L. Hedrick, R. J. Kashuba, J. B. McBride, B. H. Quon, J. L. Sperling, D. A. Spong, K. T. Tsang, and T. Watanabe

0. INTRODUCTION

The second workshop on Hot Electron Ring Physics was held at San Diego, California, December 1-3, 1981. Attending were approximately 70 scientists from the United States and Japan. The first workshop in this series was held at Oak Ridge, Tennessee, December 3-5, 1979 (see EBT Ring Physics, Proceedings of the Workshop, CONF-791228, Oak Ridge, Tennessee).

The purposes of the workshop were (1) to evaluate and review the progress made in the experimental and theoretical understanding of the hot electron ring properties since the first workshop; (2) to assess various existing methods (and/or techniques) used in the analyses of ring equilibrium, stability, heating, scaling, etc.; and (3) to identify the processes that influence the operating regimes of present and future experiments.

The first part of the workshop (two and one-half days) was devoted to presentations of 43 papers (11 experimental, 32 theoretical) in the following workshop sessions: Overview (2 invited papers); Stability (12 papers); Ring Properties and Scaling (10 papers); Ring Heating (9 papers); Synchrotron Emission (5 papers); and Ions, Tandems, Equilibria, and Power Balance (5 papers). The second part of the workshop (one-half day) was devoted to open-forum discussions of topics selected by the workshop participants. It is convenient to review the workshop under the subject categories chosen for the sessions.

1. OVERVIEW

(Chairman: N. A. Uckan, ORNL)

In recent years, high beta hot electron plasmas (rings or discs) have become of great interest because of the key role they play in the ELMO Bumpy Torus (EBT) concept and in thermal barriers for mirror machines. The hot electron population is a ubiquitous feature of plasmas created by electron cyclotron heating (ECH), and production of these plasmas has been amply demonstrated in open and closed geometries, in more than a dozen experiments, during the last two decades. The overview session included two invited papers, one that

described background information on diagnostic capabilities to measure various properties of hot electrons and summarized these measurements (G. R. Haste, ORNL) and one that dealt with theoretical aspects of hot electron rings (N. A. Krall, Jaycor).

The hot electron population in ECH plasmas has been studied with an array of diagnostics that measure various properties such as the magnetic field produced, the radiation emitted, the ionization produced, etc. Haste presented a survey of these diagnostics, which were placed in one of the three categories: (1) diamagnetic effects, (2) electromagnetic radiation, and (3) ionization and excitation. Haste's review focused on the capabilities of each of the state-of-the-art systems and discussed their spatial and temporal resolution, along with factors that affect the evaluation and interpretation of the measurements.

Diamagnetic effects were determined either from global measurements with diamagnetic loops, which give total stored energy, or from local measurements of the diamagnetic field with Hall probes, which provide detailed information about the ring structure. It was pointed out that the magnetic measurements were valid in a frequency range that was limited by the magnetic diffusion time.

The rings are capable of emission over an extremely broad frequency range (from low frequencies to hard x-rays). Measurements with rf loops were made to determine frequency spectra of fluctuations; however, interpretation of the results in some cases was difficult because of the contributions from other plasma components. Measurement of microwave noise was used to indicate the presence of hot electrons and, when it is used in conjunction with skimmer probes, to obtain the radial dimensions of the hot electron rings. Synchrotron emission measurements were useful for investigating radiation spectra and the time response of the hot electrons; however, difficulties existed in their interpretation due to optical transparency of the plasma and wall reflections. Energetic electrons can radiate a significant fraction of their kinetic energy as bremsstrahlung radiation. The measurement of thin-target bremsstrahlung was one of the most productive methods for determining the hot electron (ring) parameters (density and

temperature). The thick-target bremsstrahlung, on the other hand, provided information on radiation level (enclosure radiation) and hot electron scattering losses.

Several diagnostics have made use of ionization and excitation, which take place in the vicinity of the hot electron rings, either by the hot electrons or by the background plasma there. One of the principal means for investigating fluctuations has been spatially resolved measurement of the visible emission (the light emitted by the plasma), which was mainly H_α radiation in the case of EBT. Heavy ion beam probes were also used for determining spatial profiles of plasma potentials and the spatial location and extent of the hot electrons.

Examples of data obtained from these diagnostics were presented, and a subset of these data was used to demonstrate the experimental determination of the ring power losses in EBT experiments. There was an agreement within a factor of 2-4 between measured and calculated values (which were obtained from classical processes: scattering, drag, and synchrotron radiation) for the ring power losses. (Measured values were higher than the calculated ones.) It was pointed out by Haste that this discrepancy could be taken as evidence for an additional loss process; however, the confidence limits in the experiment and in the calculations were not sufficient to support this conclusion. It was noted that within the present range of uncertainty the power loss appeared to be classical; however, additional loss processes, on the order of classical contributions, cannot be excluded.

The properties of hot electron ECH plasmas have been analyzed by a variety of theoretical approaches and techniques. Most aspects of EBT ring theory were either reported in the past or covered in the summaries of the other sessions to follow and are not reported here. Theories in increasing levels of sophistication have been developed to address questions of equilibria, heating, stability, and loss mechanisms. A review by Krall considered the capabilities and uncertainties of theory in addressing these various topics, and a perspective was given for organizing them into a structure relevant to the experiments. It was pointed out that the equilibrium studies have taken increasing account of geometry and adiabaticity, the heating

studies have gone from nonrelativistic to relativistic, the stability work has begun to recognize the interactive nature of the ring-core problem, and loss/power balance studies have included classical, single-particle, and collective processes.

In order to assess the results of theoretical ideas and to identify the processes that are important in influencing the operating regimes of experiments, Krall concentrated on the loss versus gain processes and tried to evaluate the physics to the extent that it influences loss and/or gain. Examples were given from modeling studies for present EBT-I/S experiments as well as for the future EBT-P. The questions concerned the existence of a stable operating point or window for the hot electron plasma, a favorable power balance, and efficient heating and startup scenarios. It was shown that the results obtained were consistent with present experimental operating window and power needs and that results for EBT-P were within the design limits.

2. STABILITY

(Chairmen: H. L. Berk, IFS, Texas;
R. J. Kashuba, McDonnell Douglas Company; J. B. McBride, SAI;
J. L. Sperling, Jaycor; D. A. Spong, ORNL; K. T. Tsang, SAI)

There was a significant interest in the stability properties of hot electron rings as evidenced by the 12 papers presented (despite the fact that there was a stability workshop in May 1981 where 15 papers were presented by many of the same authors; see EBT Stability Theory, Proceedings of the Workshop, CONF-810512, Oak Ridge, Tennessee). The work can roughly be divided into low ($\omega < \omega_{ci}$), intermediate ($\omega \gtrsim \omega_{ci}$), and high ($\omega \approx \omega_{ce}$) frequency modes. The low and intermediate frequency modes are expected to play a role in determining the operating boundaries of the experiment, whereas the high frequency modes tend to impact the ring and core energy balances through enhanced scattering and losses. The core interchange mode is typical of the low frequency range; the hot electron interchange and core compressional Alfven wave

are characteristic of the intermediate range; and the Whistler, upper hybrid loss-cone, and parametric decay instabilities fall into the high frequency group.

In the low and intermediate frequency ranges, work was reported by H. L. Berk et al. (analytical) and D. A. Spong et al. (numerical) on radially dependent solutions of the eigenmode equations (a Z-pinch model), and various stability requirements were discussed for unfavorable curvature-driven instabilities. Various modes were observed that establish a stable operating window with upper and lower limits on the core density (to stabilize the compressional and hot electron interchange modes), upper limits on the core beta (interacting core interchange), and lower limits on hot electron beta (core interchange). A wider stability window at high m values (azimuthal mode number) was obtained from numerical calculations than that from the analytic estimates.

A somewhat different approach was taken in the paper by K. T. Tsang and P. J. Catto (SAI) in which low frequency modes in tandem mirrors and EBTs were considered. A gyrokinetic description was used, and perturbed quantities were represented in eikonal form. In appropriate limits, equations reduce to the ones obtained previously for tandem mirrors (the ballooning interchange mode in the limit that compressibility is unimportant) and for EBT (the interchange mode in the local limit with $k_{\parallel} = 0$). It was shown that the stability of the magnetic trapped particle mode (originally developed by Rosenbluth) is significantly changed by its finite frequency and coupling to the interchange.

In addition, work is presently under way to take into account ballooning effects (i.e., finite $k_{\parallel}$). Formulation of the problem was discussed both by Tsang and Catto and by C. A. Cheng (IFS/PPPL); however, not many results have been obtained in this area as yet. In an extension of previous EBT stability work, K. T. Nguyen and T. Kammash (U. Michigan) considered relativistic effects that indicate enhanced stability of the core interchange mode.

In a paper by S. Hiroe et al. (IPP, Nagoya U./ORNL), experimental results of relatively low frequency waves ($\lesssim$100 kHz) were reported from

the axisymmetric mirror machine ASMIC-1, in which the high beta plasma was injected along a magnetic field line. Plasma disruption was observed and instabilities were attributed to drift wave and resistive instabilities. However, with hot electron rings, instability was strongly affected (i.e., stabilized).

The absence of flute instability in EBT was investigated by classical incompressible MHD in a paper by I. Alexeff (U. Tenn.), which was submitted but not presented at the workshop. It was shown that shear (which comes about from the assumption that the electric field is not constant along the field line) reduces the flute growth rate.

In a paper by Y. Ohsawa (IPP, Nagoya U.) and J. M. Dawson (UCLA), a particle simulation of EBT was presented. The model was electromagnetic, and a destabilizing external magnetic field was imposed by internal noninteracting currents. The remaining interaction is self-consistent, and it was shown that hot electron rings strongly improve stability of the configuration.

A paper by T. M. Antonsen and Y. C. Lee (U. Maryland) proves that a necessary and sufficient energy principle applies to the EBT. In the formulation the plasma was treated in the guiding center limit and the magnetic field geometry was arbitrary. When the effects of dissipation were included, the principal can be applied when $\partial F/\partial \varepsilon|_J < 0$. If dissipation was neglected, stable negative energy modes can be present even when $\Delta W < 0$.

With respect to the high frequency range, a variety of unstable modes was identified. The possibility of parametric instabilities during ECH at $\omega \approx \omega_{ce}$ and $\omega \approx 2\omega_{ce}$ was discussed in a paper by M. Porkolab (LLNL/MIT). The findings were that the excitation of the Bernstein wave at $2\omega_{ce}$ may be of some importance but that more detailed study was required to determine its role, if any, in EBT ring heating and power balance.

The role of Whistler instabilities in ring power balance was investigated by N. T. Gladd (Jaycor). Results of detailed numerical calculations indicated that while the relativistic effects reduce the Whistler growth rates, they do not completely stabilize these modes.

It was pointed out that since even a small level of Whistler turbulence can lead to a significant increase in the electron scattering rates, this was thought to play a role in ring power balance.

A paper by Y-J. Chen et al. (LLNL) was also on high frequency instabilities. A progress report was given on the development and application of a code that solves the electromagnetic dispersion relation for a nonrelativistic, infinite, homogeneous plasma for application to thermal barriers in tandem mirrors. Examples were given for both Whistler and upper hybrid loss-cone modes driven by the hot electrons. A Fokker-Planck code with ECH was used to calculate the electron distribution function.

3. RING PROPERTIES AND SCALING

(*Chairmen:* W. B. Ard, McDonnell Douglas Company; M. Fujiwara, IPP, Nagoya U.; N. T. Gladd, Jaycor; B. H. Quon, TRW)

A thorough understanding of hot electron rings is essential to the bumpy torus concept and to the thermal barriers in tandem mirror. Detailed experimental investigations were made in the EBT-I/S, NBT, and symmetric mirror (SM-1) experiments, and results were reported by D. L. Hillis (ORNL), M. Fujiwara et al. (IPP, Nagoya U.), and B. H. Quon et al. (TRW), respectively. All three (the EBT, NBT, and SM-1) groups found that under almost all conditions the rings formed at a given temperature (i.e., $T_{ring} \approx 190$-230 keV for EBT-I, ≈ 450-550 keV for EBT-S, ≈ 80-100 keV for NBT, and ≈ 300-350 keV for SM-1), which remained essentially constant with increasing heating power. However, the ring density and hence the beta increase roughly linearly with heating power. Ring power losses were found to scale classically in both EBT and NBT; that is, the losses scale with classical collision rates on background electrons and the energy losses were the same order (within a factor of 2-4) as the calculated value.

The NBT results on the location of the rings at different magnetic field strengths were somewhat different from the EBT results. In NBT the ring radius does not exactly coincide with the second or first harmonic resonance zone, as it does in EBT. Fujiwara and co-workers suggested that the actual ring location depends on the product of the heating efficiency and the confinement efficiency at a given radius. When both of these efficiencies peaked at the same radius the rings were well defined in radius.

Most of the experiments in EBT and NBT were carried out with single-frequency ECH; however, second or third frequencies (which were largely separated in frequency) were also used. A unique feature of the SM-1 device was the use of closely spaced multiple-frequency ECH. This resulted in rings with greater stored energy and higher beta (especially when the frequency separation was comparable to the bounce frequency of the warm electrons) than usual single-frequency heating experiments. The ring temperature, on the other hand, did not change. Quon presented results of detailed measurements of magnetic field and ring structure, which were made with arrays of Hall probes. A noteworthy result was the large axial extent of the rings in SM-1 and the radial thickening of the rings with an increase in ring beta as more heating frequencies were added. The spatial structure of the rings in SM-1 was deduced, as described by L. L. Lao et al. (TRW), by correlating the diamagnetic measurements with predictions obtained from anisotropic multifluid equilibrium models. It was shown that the model developed could be very closely fitted to the SM-1 data.

The scaling of the ring temperature in present and future experiments is important because it affects both the stability and the power balance. A paper by N. A. Uckan (ORNL) pointed out that the ring temperature limit was found in all ring experiments. Compilation of data from all ECH hot electron plasma experiments showed that in all cases the limiting hot electron temperature scaled such that the ratio of the hot electron gyroradius to the magnetic field scale length ρ_e/L was a constant (≈ 0.05). The results obtained were from a dozen or so experiments and covered a factor of 2 on device dimensions and an order of magnitude in operating magnetic field strength. The observed

scaling law suggested that nonadiabatic effects play an important role in determining the ring temperature.

The adiabatic invariant μ begins to break down at a value that roughly coincides with $\rho/L \simeq 0.05$. Numerical analyses of the nonadiabaticity of ring electron motion were carried out by C. L. Hedrick et al. (ORNL) and R. E. Juhala et al. (McDonnell Douglas Company). The work by Hedrick et al. focused on identifying the different ways in which particle motion becomes nonadiabatic in a bumpy torus geometry. It was found that although μ fluctuations play a strong role in determining the behavior of the hot electron rings, the energy losses due to μ fluctuations alone (especially for $\rho/L \lesssim 0.05$) were not clearly dominant. Only for particle energies of about five times the measured ring temperature ($\rho/L \gtrsim 0.1$) do rapid direct losses start to become important. Also developed in the paper was a Fokker-Planck calculation with phenomenological coefficients corresponding to nonadiabatic processes. This was found to be useful in determining the role that various boundary conditions play in determining the ring distribution and its slope (ring temperature), in that the temperature was found to be determined by the ratio of scattering in energy and pitch angle. The model was a simplified one and indicated the necessity for developing the new Fokker-Planck coefficients that take into account μ fluctuations.

A paper by Juhala et al. considered an axisymmetric mirror geometry and focused on the difference in $\Delta\mu/\mu$ levels between a vacuum field geometry and a field geometry distorted by the high beta hot electron ring. Preliminary results indicated that the onset of nonadiabatic behavior occurred at about the measured ring temperature and that an energy cutoff was roughly an order of magnitude higher. A comparison was made with and without the ring field present and no appreciable change in energy cutoff was observed, although broadening of the loss cone was noted.

A parametric model of ring behavior that was developed in a paper by S. Hamasaki et al. (Jaycor) included various gain (microwave heating) and loss (collisions, radiation, adiabaticity, microinstabilities) processes. It was reported that a temperature scaling ($\rho/L \approx$ constant) consistent with the experiments cannot be obtained based on the classical losses (collisions and radiation) only. This was also true if the nonadiabatic effects were included, unless a mechanism was present for relaxing the ring anisotropy. This relaxation was thought to be due to Whistlers, and Hamasaki reported that inclusion of Whistler instability along with all the other losses provides a better comparison with present experiments.

The amount of microwave energy required to start up the rings in bumpy tori is important, and a scaling law for this process was derived in a paper by J. L. Sperling et al. (Jaycor). This scaling was based on a balancing of first harmonic heating and collisional drag, and resulting power estimates were found to be consistent with the available microwave power in present bumpy tori experiments. When extrapolated to future (larger and denser) experiments, this scaling was pessimistic in terms of required startup power and suggested that additional preheating processes or startup procedures (such as low density) may be needed.

A paper by G. E. Guest and R. A. Dandl (AMPC, Inc.) suggested a framework in which many of the details discussed in the previous papers can be combined to indicate how one can control the final distribution of hot electrons and what kind of controls would be useful. The nature of the heating processes in the different electron energy regimes was discussed. It was pointed out that the process of heating electrons from the collisional to the noncollisional regime was the most complicated phase, and since so much power was expended in this phase, understanding this phase offers good prospects for control of the rings.

4. RING HEATING

(Chairmen: D. B. Batchelor and C. L. Hedrick, ORNL;
T. Watanabe, Hiroshima U.)

This session clearly indicated the expanded interest in the physics of the formation of hot electron plasmas by ECH. Papers presented dealt with several topics: (1) theoretical and/or experimental results of single- or multiple-frequency ECH in bumpy tori (EBT-I/S, etc.) and mirrors (SM-1, etc.); (2) projections for ECH in tandem mirrors (TMX-Upgrade, MFTF-B, STM-1, etc.); and (3) effects of ion cyclotron heating (ICH) on ring parameters in EBT.

D. B. Batchelor et al. (ORNL) summarized the models used to describe the present EBT-I/S experiments and to project future experiments (e.g., EBT-P). Calculations of power absorbed by the rings in EBT-I were larger by a factor of 4-6 than the recent experimental estimates of ring losses. An unexpected aspect was that in this model the ring plasma in EBT-P might be underpowered relative to the core plasma at the assumed operating point. This was surprising because experiments to date have indicated the opposite ratio of the ring/core power deposition. It was pointed out that the absorption is sensitive to the assumed form of the ring and core distribution functions and that the 28-GHz power planned for EBT-P was omitted from these calculations.

A paper by B. W. Stallard et al. (LLNL) described theoretical (Fokker-Planck) calculations of the expected hot electron distribution in TMX-Upgrade. In TMX the desired hot electron energy ($\sim$50 keV) is much less than would be expected on the basis of previous ECH experiments. It was proposed to limit the temperature by using antennas (rather than simple wave guides) to direct the microwave power to specific high absorption regions of the plasma (resonant zones). Calculations indicated that if the power is absorbed at localized regions of phase space, then the hot electron distribution can be limited to 50 keV and that by varying the magnetic field design (e.g., mirror ratio) certain optimizations can be carried out.

A paper by N. H. Lazar et al. (TRW) summarized the results from SM-1 and the plans for a five-cell axisymmetric tandem mirror, STM-1. The principal feature of these experiments was that the ring stored energy ($W_\perp \sim \beta$) per unit power can be substantially increased if several (with a maximum of four available) closely spaced ECH frequencies were used instead of a single frequency. The explanation given for this significant improvement in the power efficiency was that the heating of electrons from low temperatures (e.g., tens or hundreds of eV) to higher energy (hundreds of keV) was modified in the intermediate energy range by multiple-frequency ECH (MFECH). Single-particle and Monte Carlo calculations were presented by T. K. Samec et al. (TRW) for the intermediate energies that may bear on this issue. The heating and energy diffusion rates calculated from a Monte Carlo test particle simulation were drastically different from (higher than) the appropriate quasi-linear values and were found to be sensitive to the input microwave spectrum even for small frequency separations. Additional observations from SM-1 with MFECH were that for a given power the operating window was much wider and that an increase in W by as much as a factor of 10 was possible (with four frequencies). The temperature of the hot electrons ($T \sim 350$ keV) was independent of operating conditions and MFECH, and the increase in $W_\perp$ ($\sim\beta$) was due to an increase in the density of energetic electrons. In STM-1 further investigations will be made of heating and control processes of hot electron plasmas (rings and/or discs).

The phenomenon observed in SM-1 with MFECH was discussed from the standpoint of superadiabatic limits on linear heating in two separate papers by T. D. Rognlien (LLNL) and by J. E. Howard et al. (UC Berkeley). Rognlien reported results from a Monte Carlo simulation showing a superadiabatic cutoff in the velocity diffusion coefficient ($E_{cutoff} \sim 10$ keV), which moves to higher energy when multiple heating frequencies having the proper frequency separations were used. Howard et al. addressed the same problem by investigating the resonance overlap properties of an idealized area-preserving map. Superadiabatic heating limits (KAM surfaces) were also found that moved to higher energy when the frequency separation (~bounce frequency) was correct.

These results and the favorable agreement between predicted optimal frequency separation and the experimental results seem very promising. It was pointed out that moving the adiabatic limit from ~10 to ~20 keV for fundamental heating increases the number of electrons which can be effectively heated to high energies by the second harmonic resonance. However, a more detailed calculation is required to determine the quantative effect on the density of the high energy electrons and to assess whether the multi-frequencies directly affect the second harmonic heating.

J. W. Shearer (LLNL) discussed the importance of the large deviations in spatial location of the Doppler shifted resonance point for energetic electrons. When the absorption was strong, as was the case for fundamental heating in parallel stratified geometries, the high parallel velocity electrons tended to absorb most of the wave energy, thereby shielding the bulk of the electron distribution from the incident waves. Examples were presented for MFTF-B that showed that these effects need to be included in heating models.

A side effect of ICH on EBT-S, an increase of the hot electron ring temperature and density, was discussed by F. W. Baity et al. (ORNL). The magnitude of the ring enhancement and the toroidal extent of the effect (a single ICH antenna was used) were found to depend on the ICH wave propagation and loading. In a predominantly deuterium plasma (~98% deuterium, 2% hydrogen), the ring stored energy more than doubled (40% increase in ring temperature and a factor of ~2 increase in ring density) with less than 10 kW of ICH (at 30 MHz) input to the plasma. Although the mechanism responsible for the ring enhancement was not understood, this effect may have important implications for ring heating and power balance in future EBT devices.

A paper by J. C. Glowienka et al. (ORNL) described results of nonstandard heating experiments on EBT-S. In these experiments, an attempt was made to form the rings under different resonance conditions (fundamental or second harmonic resonance) as well as to separate the ring and core plasma heating. The feature of most interest was that formation of either a potential well or a positive potential hill was possible when the core and ring heatings were separated.

5. SYNCHROTRON EMISSION

(Chairman: G. R. Haste, ORNL)

Measurements of the synchrotron emission spectrum emitted by the relativistic hot electrons can be a useful diagnostic method in determining the ring properties. In this session there were one experimental and four theoretical papers.

A paper by J. B. Wilgen and T. Uckan (ORNL) reviewed the synchrotron measurements carried out on EBT-I/S. In these experiments a swept superheterodyne system was used in the frequency range 80-110 GHz and the viewing angle was 90°. The system calibration and the effect of reflections resulted in a factor of 4 uncertainty in the measured signal strengths. A comparison of the known ring temperature (obtained from hard x-ray measurements) with the measured antenna temperature yielded an inferred wall reflection coefficient of 95%. Many of the measurements compared EBT-I (using 18 GHz) with EBT-S (using 28 GHz). The spectra for both were quite flat, but the slope was greater for EBT-I than for EBT-S, which is consistent with the lower ring temperature for EBT-I. The intensities of the two spectra, calculated on the basis of temperature and density parameters derived from x-ray measurements, had a ratio of 8. The measured ratio was 6, or 25% lower. Detailed comparisons of the radiation signal with the sorted energy indicated that the emission was increasing with stored energy but was not strictly proportional. The ring temperature and density behavior were deduced from correlation of the emission and the stored energy. Relatively small variations in ring temperature with operating conditions (i.e., power, neutral pressure) were determined that were qualitatively similar to the variations seen in the x-ray determination of the ring temperature.

There were a number of common features in the theoretical papers presented by T. Uckan and N. A. Uckan (ORNL), S. Tamor (SAI), C. Celata (Dartmouth College), and D. Winske et al. (U. Maryland). Plasma dispersion and absorption were neglected, and the effects of anisotropy on the ordinary and extraordinary emission were calculated.

In a paper by the Uckans, the expressions for the emission spectrum were calculated using the Schott-Trubnikov formula for single-particle emission, and only the results for a 90° viewing angle were reported. At about 100 GHz, it was shown that the emission increased by roughly one order of magnitude in progressing from EBT-I to EBT-S, and there was a similar increase in proceeding to EBT-P. Anisotropy effects were examined through the use of several distribution functions. It was concluded that with increasing temperature and anisotropy, the total emission increases, the slope of the spectrum decreases, and the peak of the spectrum moves to a higher frequency. The ratio of the extraordinary to the ordinary mode was shown to decrease with temperature and increase with anisotropy.

A paper by Tamor emphasized the potential of synchrotron emission as a tool for studying anisotropy. The emission at various observation angles was calculated for loss-cone distributions at various loss-cone angles. In agreement with the Uckan results, it was found that the emission at 90° increased as the loss-cone angle increased. When the viewing angle was approximately equal to the loss-cone angle, the polarization as well as the total emission began to change. Tamor concluded that the angular distribution of radiation at high harmonics was a promising candidate for a ring diagnostic but that if one was restricted to a single viewing angle, an angle less than 90° would be desirable. An extension of emission studies was presented in which the same formalism was used to calculate the absorption as a function of frequency and loss-cone angle. Some small regions of negative absorption were observed that seemed to be real. Celata pointed out that Bekefi had also found negative absorption for some non-Maxwellian distribution functions.

Celata reinforced the points made in the earlier talks. In addition, a comparison of the exact emission, integrated over the solid angle, with the Trubnikov approximate solution was given. An agreement was found for ring temperatures less than 500 keV; however, for temperatures greater than 1 MeV the exact value was significantly higher. Also presented was the dependence of the total power emitted on the ring parameters and anisotropy.

The results presented in the previous papers were obtained from numerical calculations. A paper by Winske et al. concentrated on the use of analytic expressions, partly derived and partly obtained by curve fitting, to plan for the synchrotron diagnostic on EBT by the University of Maryland group. The analytic expressions were shown to be in good agreement with the numerical results. The advantage given to the analytic approach was that it was easier to investigate small parameter ranges; thus, the effects of errors in the experimental determinations were made more apparent. Calculations of the polarization at two fixed frequencies to be measured (80 and 140 GHz) were presented. Winske indicated that by this method it is possible to determine the ring temperature and loss-cone angle (provided the loss-cone angle exceeds 45°).

6. IONS, TANDEMS, EQUILIBRIA, AND POWER BALANCE

(Chairman: L. A. Berry, ORNL)

The power required to sustain the hot electron rings (for EBTs) or discs (for tandem mirror reactors with thermal barriers) is a critical issue affecting the desirability of both concepts. The power requirements for a tandem mirror reactor were estimated within the constraints of present stability theory in a paper by R. B. Campbell (TRW) and B. G. Logan (LLNL). Within the constraints, the power balance was acceptable. The sensitivity to various stability parameters was assessed, and it was found that if refined theory or experiments lead to a factor of 2 relaxation in the constraints, the power required to sustain the hot electron plasma can be significantly reduced.

Correspondingly, increased restrictions could pose serious problems. One possibility for the EBT is the use of energetic ions to form high beta rings. The losses due to charge exchange were analyzed in a paper by M. R. Gordinier and R. J. Kashuba (McDonnell Douglas Company) and found to be small, thus providing latitude in choosing the

optimum ring thickness. In contrast, less reliance on an energetic ion population is needed in the negative tandem mirror, as described in a paper by P. Poulsen et al. (LLNL). It was pointed out that running a tandem mirror with the central cell negative with respect to ground produces the same performance obtained in the positive configuration as employed on TMX. A sloshing ion distribution in the end plugs is not needed for negative potential operation.

The configurations discussed in the previous papers rely heavily on the experimental ECH database. One quantity that is difficult to measure directly is the spatial location and extent of the hot electrons. A paper by F. M. Bieniosek and K. A. Connor (RPI) suggested that the hot electron ring is located near the second harmoic resonance ($\omega \sim 2\omega_{ce}$) surface and has a thickness of a few centimeters (a few Larmor radii). The technique is based on the relative sensitivity of one- and two-electron ionization events to energetic electrons and uses a heavy ion beam probe.

The equilibrium calculations utilized for evaluating either the tandem mirror or the EBT configurations assume that the ambipolar potential does not significantly perturb equilibrium quantities. This constraint was relaxed in a paper by T. Watanabe et al. (Hiroshima U.). The calculations suggest that in the absence of a background plasma, large electric fields could develop and perturb the equilibrium. When the rings were immersed in a dense background plasma, these effects were minimized.

ACKNOWLEDGMENTS

This workshop was sponsored by the Oak Ridge National Laboratory (supported by the Office of Fusion Energy, U.S. Department of Energy, under contract W-7405-eng-26 with the Union Carbide Corporation) and Jaycor (supported by the Office of Fusion Energy, U.S. Department of Energy). Financial contributions were also made by the following corporations: McDonnell Douglas Astronautics Company, Science Applications, Inc., and TRW, Inc.

2. OVERVIEW

HOT ELECTRON RINGS: DIAGNOSTIC REVIEW AND SUMMARY OF MEASUREMENTS*

G. R. Haste
Oak Ridge National Laboratory
Oak Ridge, Tennessee 37830

1. ABSTRACT

The hot electron population is a ubiquitous feature of plasmas created by electron cyclotron heating (ECH). This distinctive and unique feature has been studied with an array of diagnostics which have measured various properties. Some of these diagnostics will be reviewed, then the data from a sub-set of them will be used to illustrate the present status of the agreement between the measured and calculated ring power losses.

2. HOT ELECTRON DIAGNOSTICS

The hot electron population shares with other plasma components the ability to ionize atoms and ions, to emit radiation and to alter the vacuum magnetic field by it's diamagnetism. This population behaves differently in that these effects are modified due to the high energies of the hot electrons - energies which can be well into the MeV range. The diagnostics which measure these properties will be placed in one of the three categories:

*Research sponsored by the Office of Fusion Energy, U.S. Department of Energy, under contract W7405-eng-26 with the Union Carbide Corporation

1) Diagmagnetic effects
2) Electromagnetic Radiation
3) Ionization and Excitation.

The distinctions between these are arbitrary. Though arbitrary, this classification serves as a useful framework for discussing the various diagnostics.

2.1 Diamagnetic Effects

As is well known, a particle's magnetic moment is given by $\mu = W_\perp/B$, where $W_\perp$ is the perpendicular component of the energy at the point where the magnetic field strength is B. The spatial variation of the diamagnetic field will depend on the geometry of the hot electron component. A general approach has been to adopt a model for the hot electron geometry, then to use the measured quantities to determine the model parameters. In order of sophistication these models have included: a single composite dipole, a set of current sheets, and MHD pressure equilibria.

The quantities which are measured depend on the total magnetic field, with the vacuum plus diamagnetic contributions. Two techniques have been used to distinguish the two: the vacuum contribution can be subtracted electronically; or measurements can be made of the diamagnetic field components normal to the vacuum field. In the latter case the vacuum contribution is identically zero. Particular care must be taken to eliminate the vacuum contributions because these vary in time, e.g. due to generator fluctuations.

These magnetic measurements are valid in a frequency range which is limited by the magnetic diffusion time. In EBT, for example, the time for diffusion through the one-inch aluminum vacuum vessel walls is of the order of 50 msec, so that frequencies above about 200 Hz are very difficult to observe.

These diamagnetic measurements fall into two classes: global measurements with loops surrounding the plasma (diamagnetic loops) and detailed local measurements of the diamagnetic field, with Hall probes or magnetometers.

2.1.1 Diamagnetic loops[1]

Because the diamagnetic loops are larger than the hot electron rings they are not sensitive to the spatial distributions. This insensitivity to the geometry is an advantage in determining the total stored energy. This trait is emphasized on EBT, where the diamagnetic loops are arranged as Helmholtz pairs on each cavity. As is well known, the field due to Helmholtz pairs is uniform near the center. Conversely the coupling between the Helmholtz pair and a current distribution near the center is not very sensitive to the location of that distribution.

The effects of rings in adjacent cavities must be taken into account. This has been done in two ways on EBT. The coupling can be calculated, or it can be measured by turning off the rings in one or more cavities. The two approaches agree: about 25% of the signal is due to the nearest neighboring cavities, about 4% to the next cavities, and the remaining cavities do not produce a noticeable effect.

2.1.2 Local Measurements

Hall probes have been used on the SM[2] and NBT[3] devices. A Hall probe was mounted off the midplane on NBT which was sensitive to the component normal to the vacuum field. The variations of the signals from this probe were interpreted to show that the ring axial extent increased with total ring stored energy.

An array of Hall probes, on axis as well as outside the rings, has been used in SM [2]. By carefully comparing the observed signals with the predictions from an MHD equilibrium code, the parameters of the MHD equilibrium were determined. This has led to some of the most detailed information about the ring structure yet available.

A magnetometer which uses NMR techniques has been used on EBT. This technique measures the total field, not the components of the field vector. Since the frequency can be measured very precisely the potential exists for very precise field measurements. However, the method for compensating for vacuum field variations has so far prevented precision beyond about 0.1 gauss, which is less than the field variations due to plasma fluctuations. These measurements have corroborated the data from the diamagnetic loops.

2.2 ELECTROMAGNETIC EMISSION

The rings are capable of emission over an extremely broad frequency range. The range extends from low frequencies in the RF range to high frequencies observed as microwave radiation, and on beyond to the extremely high frequencies of x-rays. The frequency of these emissions are dependent on the characteristics of the plasma or rings. However, the intensity depends not only on these characteristics, but on the boundary conditions as well.

2.2.1 RF Loops

Antennas have been inserted in several devices. In EBT, for example, they have shown that the frequency spectra for B and $B_{\parallel}$ differ. The problems with interpreting these signals is the effect of the other plasma components. The core plasma components could just as easily produce these emissions, so it is difficult to separate the core and ring contributions. Also, both the core and surface plasmas can act to shield the antenna from the source.

2.2.2 Microwave Emission

From the earliest days of PTF[4], up to present devices, microwave noise has been used to indicate the presence of hot electrons. In NBT[3], for example, the microwave noise has been measured in conjunction with skimmer probes to give the radial dimensions of the hot electron ring.

Synchrotron emission measurements in EBT have proven to be a very useful diagnostic for investigating the time response of the rings, and for corroborating the temperature measurements from X-rays. A great deal of analysis is necessary in order to interpret the synchrotron results. For example, the analysis must be a relativistic treatment, and the details of the pitch angle and energy distributions are very important. An experimental difficulty is due to the optical transparency of the rings. Since the back wall can be readily seen, reflections contribute to the signal, which tends to increase the amount of radiation detected.

2.2.3 X-Ray Emission

Energetic electrons, as they encounter scattering centers, are able to radiate significant fractions of their kinetic energy as bremsstrahlung radiation. This bremsstrahlung may be either thin-target, in which the scattering centers are within the plasma, or thick-target, created when the electrons strike a solid surface. Because the first process depends on the hot electron density, and the second depends on the hot electron current to the surface, and because the spectral shapes and intensities differ, it is important to separate the processes in the measurement. The boundary conditions referred to above mean that the experiment must be collimated such that the proper process is viewed.

2.2.3.1 Thin-Target

One of the most productive methods for determining the ring parameters is the measurement of the bremsstrahlung spectrum from thin-target radiation. Collimation such that no electrons strike solid surfaces along the line-of-sight, as well as shielding the detector from other radiation sources, such as scattered radiation, ensures that the only radiation comes from the rings themselves. Relating the observations to the ring parameters requires extensive analysis, in which relativistic effects and angular distributions are important.

The most important ring parameters determined from this technique are the ring temperature and density.

2.2.3.2 Thick-Target

In most ECH experiments the dominant contribution to the x-ray levels comes from the thick-target bremsstrahlung as the energetic electrons strike the solid surfaces. A possible exception may occur for high temperature rings with high impurity levels. For this case the thin-target contribution may be comparable. The radiation level, which has been as high as 3000 R/hr in EBT, is typically measured with unsophisticated radiation monitors, such as ionization meters.

The usual source for the thick-target radiation is the current of energetic electrons which have been scattered from the rings. The magnitude of the radiation can be calculated with a number of assumptions, such as classical scattering and a simplified model for the bremsstrahlung produced. The observed radiation can then be compared with that calculated, with fairly good agreement.

Although radiation monitors are adequate for measuring the gross radiation level, they are not a sensitive measure of spatial distributions or of rapid time variations. For these more detailed measurements, special detectors can be used. For example, in EBT a scannable array of PIN diodes has been installed to view the mirror throat, where the principal radiation source is located. Fluctuations have been observed with this system, which are certainly due to fluctuations in the current of hot electrons to the wall. It cannot be determined whether these fluctuations are due to density fluctuations of the ring or of the scattering centers (background plasma).

Thick-target radiation can also be induced by introducing probes into the plasma. Some of the clearest evidence for flute instabilities in a hot electron plasma was obtained by introducing a probe into the periphery of the PTF plasma, then observing the time variation of the x-rays produced at the tip. Also, the skimmer probes, which have been used on ELMO, and are now in use on EBT and NBT, have radiation measurement devices (ionization chambers or PIN diodes) in the tips so the radiation can be measured as a function of probe position.

2.3 IONIZATION AND EXCITATION

Several diagnostics have made use of the ionization and excitation which takes place in the vincinity of the hot electron rings, either by the hot electrons or by the background plasma there.

2.3.1 Visible Emission

One of the principal means for investigating fluctuations has been spatially resolved measurements of the light emitted by the plasma. In the case of EBT this light is mainly H_α radiation. Since the rate coefficient is greater at 100 eV than at 100 keV, and since the background density is greater than the ring density, most of the excitation is due to the background plasma. The rings are important in these experiments since they form a boundary, inside of which the fluctuation level is lower than outside in the surface plasma region.

2.3.2 Heavy Ion Beam Probe[5]

Ionization of a heavy ion beam probe has been an extremely useful diagnostic, both on EBT and NBT. The principal objective has been to determine the potential distribution, including the ring region. Since the ionization rate depends on the density multiplied by the rate coefficient, the radial dependence of this product can be determined simultaneously with the potential profile. Since the rings and the background plasma each contribute to this signal the measurement gives a combination of their effects. Their separate contributions can be evaluated in one of two ways: The rings can be turned off in the cavity being investigated, thereby removing that contribution, so the separation is effected by a simple subtraction. Another technique is to utilize ionization to higher charge states. Since more energy is required to remove multiple electrons, the reaction rate for multiple ionization depends on the electron temperature. The rings become, relative to the background plasma, more effective in ionizing the beam particles for multiple ionization.

3. POWER BALANCE

An example of the use of some of the diagnostics discussed above will be directed toward the experimental determination of the ring power balance. It should be emphasized that there are at least two types of power balance which could be considered: one could ask whether the input power to the ring is equal to the power lost by the ring, or one could ask whether the power lost from the ring experimentally agrees with that expected theoretically. In this section the first question will not be addressed because there is no measure of the input power to the rings at present. Instead the second question will be at issue. The various terms in the power loss will be compared with the theoretical expectations.

The various components of the power loss are shown in the set of equations[6] below. The terms are listed in order of increasing importance for EBT-S. MKS units are used, except for the ring temperature T, which is in keV.

TABLE I

RING POWER LOSS EQUATIONS

$$P_{ring} = P_{brems} + P_{synch} + P_{scatt} + P_{drag}$$

$$P_{brems} = 5.35 \times 10^{-37}\, n_r\, n_p\, T^{1/2}\, V$$

$$P_{synch} = 6.2 \times 10^{-17}\, B_r^{\,2}\, n_r\, T\left(1 + \frac{T}{204}\right) V$$

$$P_{scatt} = 1.1 \times 10^{-32} \ln \Lambda\, \frac{n_r\, n_p}{T^{1/2}}\, V$$

$$P_{drag} = 4 \times 10^{-32} \frac{\gamma}{(\gamma^2 - 1)^{1/2}}\, n_r\, n_p\, V$$

The first term, bremsstrahlung, is very important as a diagnostic tool, but it is insignificant as a power loss mechanism. Synchrotron radiation is not important for EBT-S, but it's contribution varies

as the square of the magnetic field and it becomes more important as the temperature increases. The scattering loss is due to the power lost from the ring as the particles are scattered out. The last term, the cooling by the core plasma, is the dominant term.

3.1 EXPERIMENTAL PARAMETERS

The various factors in the expressions above are experimentally determined and are subject to experimental error. For example, the ring volume, which enters each of the terms linearly, is determined indirectly. The total stored energy is determined by the diamagnetic loops. The energy density is determined by bremsstrahlung, which gives separately the density and temperature. The ratio of the total stored energy to the energy density gives the ring volume. The experimental values of the volume, determined in this indirect manner, are shown in fig. 1, for a range of conditions. The average value is 2.1 l, with a standard deviation of ± 15%.

3.2 SYNCHROTRON RADIATION

Synchrotron radiation losses have been measured in the frequency range between 80 and 110 GHz. This has been done for EBT-1, operating at 18 GHz, and for EBT-S, with 28 GHz. The spectra for the two cases are shown in fig. 2. The two curves at the top, with bumps and wiggles, are the measured spectra. For comparison the spectra which are expected are shown by the smooth curves. As can be seen, the spectra are expected to be quite flat over this frequency range and that agrees with the observation. Regarding the magnitude of the signals, the signal strength for EBT-S is expected to be higher than that for EBT-1 by a factor of 8. The observed ratio is 6, or 25% less than expected. The relative values have been mentioned because the absolute strengths have some uncertainity. The receiving system is calibrated with a noise source, but the uncertainty is about a factor of 2. There is an additional factor of 2 uncertainty

due to the effect of wall reflections. Other portions of the plasma can, through multiple reflections, contribute to the observed signal. The uncertainity due to this cause leads to an overall factor of 4 uncertainity in the absolute signal strengths. However, within this factor of 4, the observed strength agrees with that which is expected.

3.3 SCATTERING

The next term in the power loss expression, the scattering loss, is determined indirectly. The power in the energetic particles as they strike the chamber walls is not directly measured, but the bremsstrahlung they produce <u>is</u> measured. The bremsstrahlung can be related to the scattered power by considering the conversion process from particle energy to radiation. A plausibility argument for this relation is indicated in the equation below.

SCATTERING LOSS RELATION TO BREMSSTRAHLUNG

$$P_{brems} \;\alpha\; \underbrace{\frac{n_r\, n_p}{T^{3/2}}}_{\text{particle loss rate}} \times \underbrace{(T)}_{\text{energy per particle}} \times \underbrace{(Z_{wall}\, T)}_{\text{conversion efficiency to x-rays}} \times \underbrace{(V)}_{\text{ring volume}}$$

thus

$$P_{brems} \;\alpha\; Z_w\, n_r\, n_p\, T^{1/2}\, V$$

The <u>particle</u> loss rate is proportional to the product of the ring and core densities, divided by the 3/2 power of the ring temperature. To convert this particle loss rate to a power loss it must be multiplied by the energy per particle, which is, on the average, just equal to the temperature. The conversion efficiency into bremsstrahlung is proportional to the Z of the wall material and the

electron energy, which again, has an average value of T. The final term is just the ring volume, V. The result of this combination of factors is that the bremsstrahlung radiation should be proportional to the product of ring and core densities, to the square root of the temperature, and to the ring volume.

The experimental variation of the bremsstrahlung radiation level is shown in fig. 3. The product of the ring and core densities times the square root of the ring temperature is plotted vertically and the observed radiation level in the enclosure is plotted horizontally. There is a linear relation between the two, which is valid for more than an order of magnitude variation in the variables. Thus, the radiation level observed is consistent with that expected from classical scattering. However, the uncertainities in relating the observations to that calculated are such that additional processes cannot be excluded. None the less, the linear relationship imposes a constraint that any additional losses should scale as classical Coulomb losses.

3.4 TOTAL RING POWER

The largest term in the power loss equation is that for drag cooling. Unfortunately, there is no measurement of this loss process, either direct or indirect. There is, however, a technique for measuring the total power loss from the ring, and that is to monitor the ring after the power to a single cavity is turned off. This is possible only for EBT-1, operated with 18 GHz, because in that configuration the power to each cavity can be controlled. When operating with either 10.6 GHz or 28 GHz that control is not possible.

A number of parameters can be observed during the decay of the ring, including diamagnetism, synchrotron radiation, and bremsstrahlung. Figure 4 shows the decay of the synchrotron radiation and of the diamagnetic signals. The slower decay of the synchrotron radiation is consistent with the fact that the lower energy ring particles are lost more rapidly, leaving behind the higher energy particles which decay more slowly. Since the radiation intensity varies as T^2 for EBT-1 parameters the higher energy particles are more

efficient in producing synchrotron radiation, and the observed difference between the synchrotron and diamagnetic signals is consistent with that expected.

It is apparent from the discussion above that there are several characteristic times for the ring. In addition to those already mentioned, the thin target bremsstrahlung is also measured. These characteristic times have been measured as a function of power and pressure. The variation of the synchrotron radiation, which has the longest characteristic time, and of the bremsstrahlung signal, which has the shortest, are shown in fig. 5. The corresponding stored energy values are shown in fig. 6.

The total ring power loss is just equal to the stored energy divided by the decay time for the ring energy. However, as has been demonstrated above, there are several characteristic times which might be taken for the ring decay time, which differ by nearly a factor of 4. In making the comparison with the theoretical estimates the time which will be chosen is the 'build-up' time for the bremsstrahlung signal. There are several reasons for making this choice:

1) The problems of interpretation are less than with other signals. The decay times are comparable with the skin times of the vacuum vessel, so the diamagnetic signals are modified by this effect. The synchrotron signals are sensitive to the evolution of the energy distribution, and so may not be representative of the ring as a whole.

2) The build-up takes place when the microwave power is on, so any microwave driven losses in steady-state are also present in build-up.

3) The bremsstrahlung build-up time is the shortest of the characteristic times, and so maximizes the determination of the power loss.

Figure 7 shows the variation of the ring power loss with neutral pressure. For this figure the measured power is obtained by dividing the stored energy by the bremsstrahlung build-up time of 100 msec. The calculated power is the sum of the various components in the power loss equation.

3.5 DISCUSSION

There is a factor of about 4 between the measured and calculated values for the ring power loss. This discrepancy could be taken as evidence for additional loss processes, but the uncertainties in the experiment and in the calculations do not permit this conclusion to be supported with confidence. The discussion above has pointed to the fact that the total power loss may be overestimated by nearly a factor of 4. The same level of uncertainty holds for the synchrotron and scattering determinations. Less apparent are the uncertainties in the calculated values. For example, scattering by core electrons has been left out of these estimates. Other, similar considerations suggest that the calculations may be under estimated. The uncertainty in the measurement, which probably leads to an over estimate is indicated by the error bars. The error bars on the calculated curve indicate the calculations probably under estimate the ring power loss. In any case, the conclusions from these comparisons are:

1) Within the present range of uncertainty the power loss appears to be classical.

2) Additional loss processes, of the order of the classical contributions, cannot be excluded.

REFERENCES

1. K. H. Carpenter, EBT Ring Physics, Proc. of the Workshop, Dec. 3-5, 1979, Conf-791228, 143 (1980).

2. B. H. Quon et al., Bull. Am. Phys. Soc. 25, 994,
   L. N. Lao et al., Bull. Am. Phys. Soc. 26, 928.
   B. H. Quon et al., 2nd EBT Ring Physics Workshop (These proceedings).
   l. N. Lao et al., 2nd EBT Ring Physics Workshop (These proceedings)

3. M. Fujiwara et al., EBT Ring Physics, Proc. of the Workshop December 3-5, 1979, Conf-791228, 123 (1980).
   M. Tanaka, et al., 2nd EBT Ring Physics Workshop (These Proceedings).

4. R. A. Dandl et al., Thermonuclear Div. Semi Ann. Prog. Rep., Period Ending January 31, 1961, ORNL 3104, 29.

5. F. M. Bieniosek and K. A. Conner, 2nd EBT Ring Physics Workshop (These proceedings).

6. S. K. Borowski et al., Nucl. Fusion 19 (1980) 177.

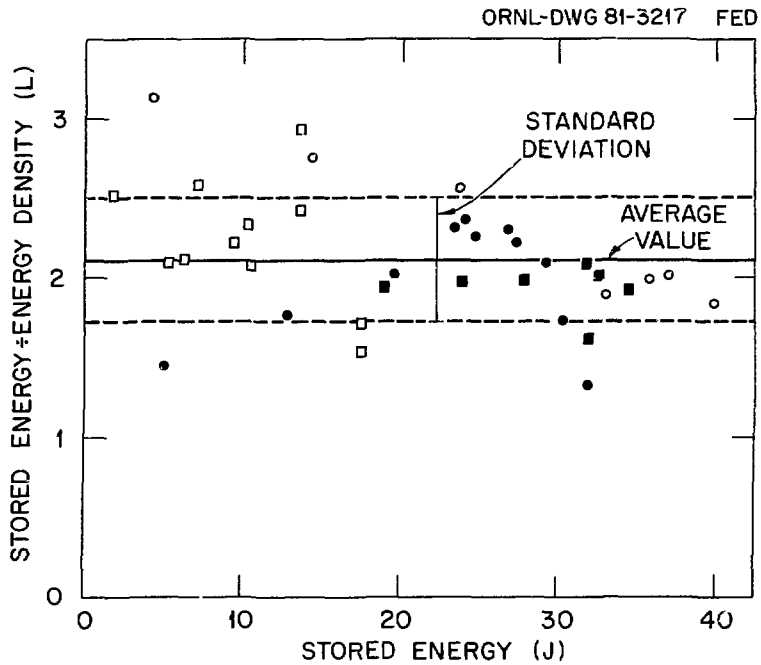

Figure 1. Ring volume determination for EBT-S. The volume is defined as the ratio of the total stored energy, determined by diamagnetic loops, to the energy density, determined by bremsstrahlung measurements. Numerous values of neutral pressure and microwave power are represented in the figure. The average and standard deviation values are shown.

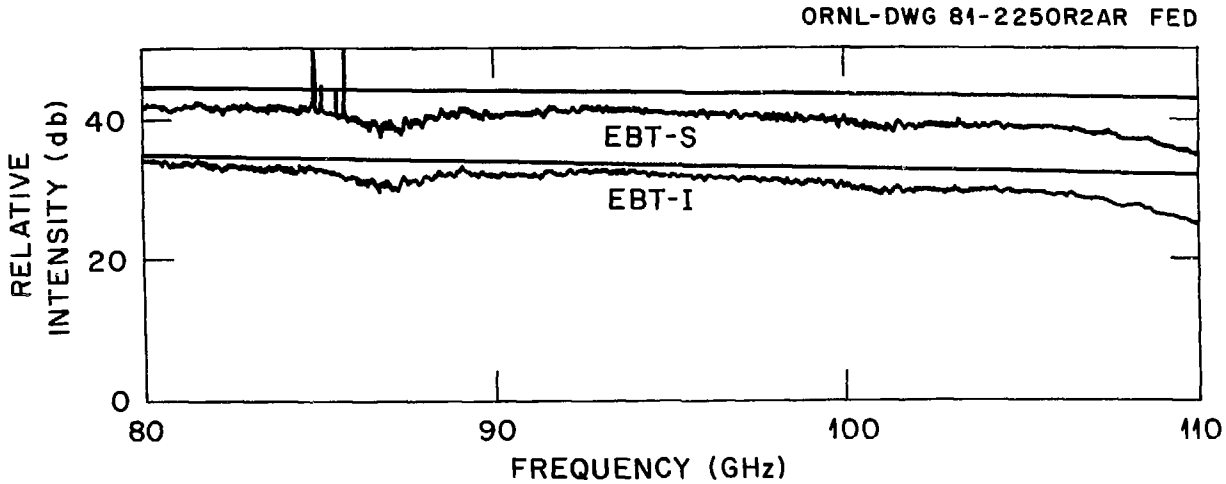

$$\frac{I_\omega^x\,(\text{EBT-S})}{I_\omega^x\,(\text{EBT-I})} \simeq \begin{cases} 8\ (\text{theory}) \\ 5\text{-}10\ (\text{experiment}) \end{cases}$$

POWER 42 kW

PRESSURE 6×10^{-6} torr

Figure 2. Synchrotron radiation spectra for EBT-1 and EBT-S. The signal with no input from the horn antenna is labelled noise level. The experimental spectra for 18 GHz and 28 GHz are labelled EBT-1 and EBT-S respectively. The spectra expected theoretically are the straight lines above the EBT-1 and EBT-S curves.

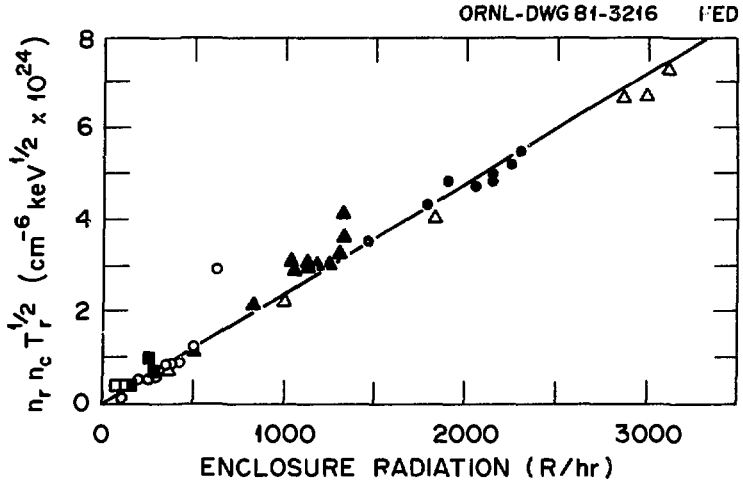

Figure 3. Variation of observed radiation level vs that expected from classical scattering losses.

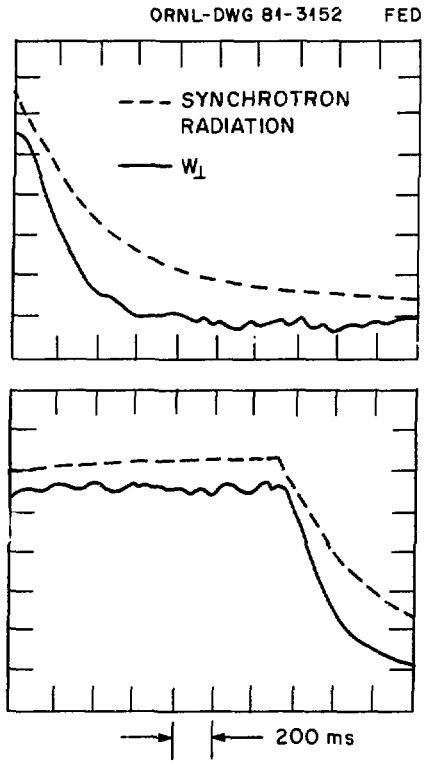

SAME WAVEFORMS DISPLAYED USING A DIFFERENT TRIGGER TIME - SHOWS SIGNAL LEVELS JUST PRIOR TO TURN OFF OF POWER TO CAVITY S1.

Figure 4. Decay curves for synchrotron radiation and for stored energy. The total power to the torus is 40 kW at 18 GHz. The power to a single sector is pulsed off for this measurement. The delay in the decay of the stored energy is related to the magnetic diffusion time in the vacuum chamber wall.

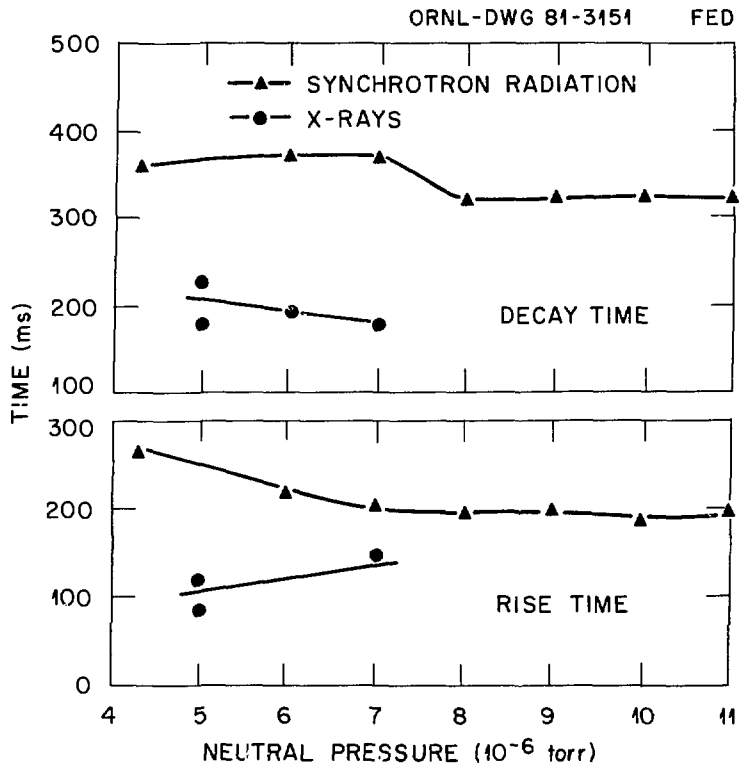

Figure 5. Variation of characteristics ring times with neutral pressure. Rise and decay times are shown for synchrotron radiation and for free-free bremsstrahlung.

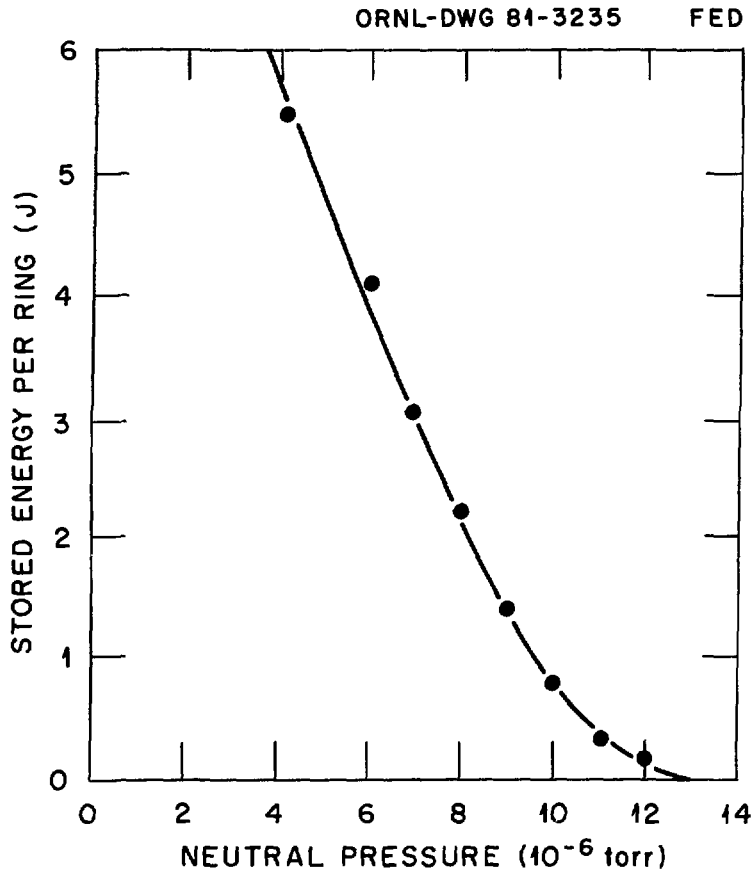

Figure 6. Variation of stored energy per cavity vs neutral pressure. These measurements were made by pulsing the power (at 18 GHz) to a single cavity, while keeping the other cavities constant.

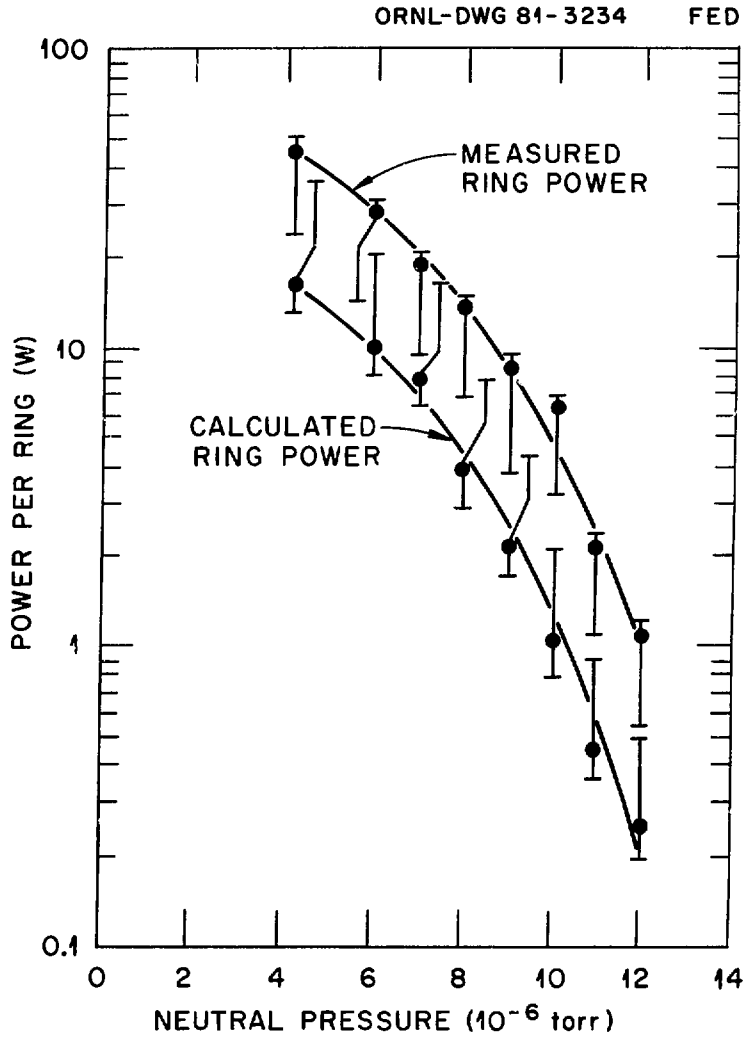

Figure 7. Variation of ring power with neutral pressure, the experimental values represent the ratio of the stored energy (figure 6) to the shortest of the characteristic ring times (figure 5).

A PERSPECTIVE ON EBT ELECTRON RING THEORY*

Nicholas A. Krall

JAYCOR
San Diego, California 92138

The hot electron population in ECH plasmas has been analyzed by a wide array of theoretical approaches and techniques. Topics considered have included heating, equilibria, stability, and loss mechanisms, with the degree of sophistication increasing year-by-year. The heating studies have gone from non-relativistic to relativistic, the equilibrium studies have taken increasing account of geometry and adiabaticity, the stability work has begun to recognize the interactive nature of the ring-core problem, and loss studies have included both classical, single particle, and collective processes. A survey of these theoretical topics will review the capabilities and uncertainties of theory in addressing these various topics, including limitations imposed by computing capability, existing analytic theory, and geometry complications and uncertainties. The results of existing theory will be combined to give a conceptual picture of the formation and behavior of the hot electron system in present devices, as well as the changes expected as larger and more reactor-like experiments are brought into operation.

*Research sponsored by the Office of Fusion Energy, U.S. Department of Energy.

1. INTRODUCTION

In contrast with the extensive diagnostics and experiments just reviewed by Glenn Haste,[1] most aspects of EBT theory have been fairly widely reported in the past, and scarcely need a review. What I will do instead is to give my own perspective for organizing the various aspects of the EBT theory into a structure relevant to experiment. If successful, then you will understand the framework in which I at least listen to the talks that are presented during this week.

Ring theory is complex; not only does it have a lot of different aspects, but you cannot always judge by the work that is going on how broad the problem really is. Recently, for example, there has been a tremendous amount of work carried out to determine the stability boundaries within which you can have an operating EBT. This is clearly very important because if you want a reasonable beta, and therefore a favorable power balance, there has to be an operating window in which nature will allow you to exist. But there is much more to EBT rings than stability; I am going to more or less ignore stability in my talk on the grounds that it is going to be discussed in depth in the talks during the rest of the week.

Now, one straightforward way of looking at a plasma device is shown in Figure 1: you recognize that there are equilibrium questions; you worry about instability limits, i.e., in the case of EBT, questions having to do with anisotropy which gives rise to electromagnetic modes and questions of curvature which lead us to think about interchange modes; microwave heating is an essential aspect of EBT, and therefore you think about microwave scattering, parametric processes and so on; orbit effects are generally device specific, and in the EBT the question of loss cones, drift surfaces, and drift cones clearly impacts the plasma loss rates; in addition, we have wave heating physics, effects produced by interaction of rings with the background, and a lot of questions of geometry. Furthermore, there are several devices,

EBT-1, S, R, P, and NBT, and so on, the differences in the way these devices are laid out have specific effects on many aspects of the physics. Now, in a leisurely program, what you do is turn the researchers loose on all of these problems, people like me slog away at these different aspects for some number of years, and eventually you build a big picture of what describes the phenomena in an EBT-type device over a wide parameter range.

In the real world, however, we do not have any leisure at all. Program results and needs are determined by energy timetables rather than by an optimum schedule for basic research. So you begin to look for ways to organize the research program and results in a different way, trying to isolate the problems that are most important and trying quickly and effectively to establish what kinds of effects you can expect from the different phenomena that are listed. In this second way of describing EBT ring theory, we directly think about loss versus gain processes and you try to evaluate the physics by the extent it really influences loss, and by the extent it really influences gain. The questions you are trying to answer are twofold: 1) what is the nature of the operating point, that is, can you afford to run the device in the allowed operating windows, and 2) what are the startup conditions: can you be sure that a device designed to operate in a favorable window will have enough power, adequate geometry, adequate density control, and so on, to allow the device to be started up.

Under the category of "gain" we place physics associated with wave properties. There are a number of issues in that category:

- Ordinary modes, extraordinary modes, and mode conversion
- Propagation and absorption of these different electromagnetic modes
- Locations of resonances, particularly with respect to material walls and magnets

- Accessibility of these resonance surfaces both to waves and to particles
- Broadening of these resonances as the temperature increases
- Parametric processes to allow other than straightforward ECH heating when you pump with the microwaves
- The level of the electric fuel fluctuations produced by microwave processes.

Concerning the last item on the list, there is no wave heating calculation I know of that does not require some statement as to the level of E^2, the amplitude of the ECH mode, and this in general is a function of radius and time. What is done in practice ordinarily is to simply take E^2 as constant, and to treat this constant as a parameter. This is a fairly important aspect of the theory and you are reduced to simply estimating E^2 by power flow and seeing if the resulting numbers are reasonable. It would be nice if experiment could measure this sort of thing. I did not think to ask the previous speaker if there was any chance of Stark broadening to measure E^2.

A similar list contains physics of loss:

- Cooling by interaction with the background, including energy dependence
- Dependence of drag cooling on the distribution function of the ring
- The energetics of startup, because the competition between heating and cooling is going to be different at the cold temperature of the startup than at the operating point
- The properties of the background, since drag as well as the absorption of radiation is a function of local properties and in the vicinity of the ring things are not particularly well known

- Radiation is a loss mechanism, more important at higher temperature, and affected by the magnetic field geometry, the distribution function of the ring volume, and so on
- The scattering of particles is a loss-physics problem that ties together with other phenomena, for example, scattering inside the ring produces loss to the extent that the geometry is considered
- Outer field lines intercept walls and magnets; particles on these lines scatter into parallel velocity and are immediately lost (loss-cone effect)
- A different effect is scattering into a drift cone with particles, thus diffusing radially
- Scattering by drift instabilities which eventually fills any loss cone
- Adiabaticity, which has been more and more appreciated as the ring temperatures increase, since particles then see a rapidly changing magnetic field instead of a slowly changing magnetic field, altering their orbits
- Scattering by the microwave fields, producing not only heating but possible changes in pitch angle
- Stability losses, including both interchange instability because a beta limit is reached, and diffusive losses due to instabilities
- Instability loss by both cross field diffusion and, if there is a loss cone, scattering into these cones; both whistlers and drift waves are possible candidates for these modes.

2. EQUILIBRIUM AND STABILITY QUESTIONS

As an example of using loss and gain to determine what should be studied, consider things like equilibrium. Equilibria have been studied in one, two, and three dimensions. Double adiabatic theory is most usually used in the analytic studies of ring equilibria, and what one finds is very simply that there is one. J. B. Taylor wrote down, many years ago, analytic equilibria appropriate in mirror and cusp geometries:[2]

$$B \leq B_M \begin{cases} p_{\parallel} = KB(B_M - B)^m \\ p_{\perp} = p_{\parallel} - \dfrac{B\,dp_{\parallel}}{dB} = KmB^2(B_M - B)^{m-1} \end{cases}$$

$$B \geq B_M \quad \{ \; p_{\perp} = p_{\parallel} = 0 \tag{1}$$

In these equilibria, B_M determines the axial length of the ring and m is related to the shape. There are limits on these equilibria which limit the temperature anisotropy:

$$1 + \frac{p_{\perp} - p_{\parallel}}{B^2} \geq 0 \qquad \text{(Firehose)} \tag{2}$$

$$1 + \frac{1}{B}\,\frac{\partial P_{\perp}}{\partial B} \geq 0 \qquad \text{(Mirror)} \tag{3}$$

This is not really any surprise, because the ring exists; so is there any real point to studying the equilibria in depth? Well, in fact there are; as you will see, aspects of the loss process in which the ring size, the ring shape, and the ring distribution are both affected by and affect the loss process; these quantities must satisfy equilibrium

constraints. In the Taylor equilibria, for example, the parallel and perpendicular pressure are related to the magnetic field and the maximum field. The parameter m influences the gradients, determining whether the ring is flat and broad with edges, sharp or smooth; and the combination of B_M and m determines the anisotropy.

$$\frac{dp_{\parallel}}{dB} = K(B_M - B)^{m-1} [B_M - (m + 1)B] \tag{4}$$

$$\frac{dp_{\perp}}{dB} = 2mKB(B_M - B)^{m-2} [B_M - (m + 1)B/2] \tag{5}$$

Equilibrium studies are particularly important when you realize that whistler instabilities involve anisotropy, classical diffusion involves shape, and drift waves involve gradients; all these effect loss and change the plasma, and you have to still satisfy the equilibria conditions. This self-consistent picture is seldom drawn, which makes it a bit of a waste to study equilibria. One question is does the transport evolve the plasma to a state where the equilibria no longer exist? So, in other words, equilibrium studies are valuable if they are seen in the context of the whole system.

Stability calculations should also be evaluated in context. Remember, the stability of this device has been considered for a long time. It is instructive to contrast a couple of early calculations with what is being done now. In the early days, the question was why is the ring stable? It's sitting in a mirror geometry, so it should obviously be unstable; yet it obviously exists. Why? One of the first ideas was that it is stable because it digs its own well, and is thus stabilized by minimum B. That idea, of course, is nonsense. Don Pearlstein and I showed, almost 15 years ago, that you cannot stabilize a system by a self dug well.[3] The "well" translates right along with the plasma, like an air bubble underwater. The mechanism

is an electromagnetic component to the interchange mode due to finite-β. The next suggestion was stabilization by the cold plasma background, and that sounds fairly plausible. This idea was originally (as far as I know) conceived by Harold Furth who mentioned it repeatedly in 1964/65 before we finally got around to calculating it in 1966.[4,5] The point is that it was a fairly torturous procedure to come up with plausible, theoretical statements as to why the ring, which is obviously stable, is not unstable. If we did not have the experiment to look at, we would have gone through these arguments and produced quite a different picture of the ring than exists in the laboratory. The existence of the ring defied the early theoretical predictions. Well, this early work was fairly primitive compared to the work being done now,[6,7] in which the stability of the core and of the ring are considered together, because this presumably will tell us that although a 40 percent beta ring will stabilize the core, it will not stabilize a 40 percent beta core. Clearly, at some beta the system is unstable because of interactive instabilities of ring and core. But while everybody works on this, and there are lots of papers at this workshop on this very important topic, remember what little success we had in producing absolutely rigid quantitative numbers for what the ring should be doing even when we knew what it was doing.

In addition to interchange modes, there are microinstabilities in the system, for instance whistlers; there have been ideas over the years as to profile heating and such that would increase the parallel temperature and stabilize such modes. I will comment on that later, but note that increasing $T_{\parallel}$ can increase loss rates as well.

3. RING MODELING AS A GUIDE TO THEORY

If you want to know what the effect of various bits of physics will be, you have to string them together in some sort of model of the system, and there have been at least two basic approaches to doing this. A really good idea is to solve Fokker-Planck type equations,

$$\frac{\partial f}{\partial t} + v_{Dy} \sin\theta \frac{\partial f}{\partial r} + \left(\Omega_o - \frac{Ec}{BR_T} \cos\theta\right) \frac{\partial f}{\partial \theta}$$

$$+ \left(\frac{v_{Dy}}{r} \cos\theta + \frac{eEv_{Dy}\sin\theta}{mv^2}\right) \frac{\partial f}{\partial \theta} = a(f) \frac{\partial^2 f}{\partial v^2}$$

$$+ b(f) \frac{\partial f}{\partial v} + c(f)f + S(f) \quad . \qquad (6)$$

The solution to this equation gives the distribution function including the curvature drifts, the ambient fields, as well as collision-operator effects such as radiation, collisions, diffusion, and so on. It's difficult to solve Eq. (6) in realistic conditions because the ring is relativistic, the problem is a multi-time problem, bounce times are very different from drift times, drift times are different from absorption times, radiation times are different from both, loss cones involve electron transit times, and so on. Nonetheless, this kind of approach is the most satisfying, if you can do it, because this distribution is not Maxwellian. ECH gives a hot tail on a cool background distribution. There has been work in this direction, some of it presented at the last workshop on EBT rings by Tolliver, Jaeger, and Hedrick.

Figure 2 and Figure 3 show a typical result of a Fokker-Planck treatment. By actually solving the mesh in radius and velocity, one gets distribution functions as functions of energy at each radial point. This demonstrates clearly the coexistence of cold electrons

and hot electrons, with no clear distinction between a ring and background. The trouble with this approach has been its inability to approach experimental conditions. The velocity grid, for example, involves a maximum velocity. Keeping a reasonable mesh size limits V_{max}. Relativistic effects are ignored, and radiation losses cannot be treated properly. Thus, Figure 2 gives ring temperatures of about 1/50 of T_{exp}, and sizes much larger than in the experiment.

The result is that these nice looking distributions in radius and energy give a feeling for what really goes on, but do not give quantitative numbers within even one or two orders magnitude, because of the necessary approximations. Remember, however, that this really promising work was done over two years ago; there are no papers at this meeting following up this work, incorporating the advances in computation that have developed. Considering the flood of stability papers, I think it's too bad. There has been some progress on this line with a simpler fluid-like approach. This approach ignores a different set of aspects of the problem, for example the radial dependence, and solves quasilinear type equations for evolution of distribution functions in terms of heating, drag, scattering, particle production, and so on.

$$\frac{\partial f}{\partial t}(p_{\perp o}, p_{\parallel o}) = Q(p_\perp, p_\parallel) + C + S + P(p_\perp, p_\parallel) \qquad (7)$$

Even Eq. (7) is intractable as it stands, and is solved by taking moments.

It is assumed that the distribution function has a particular form. If an especially complex form is chosen, it has many parameters, e.g., density, temperatures, parallel and perpendicular to magnetic fields, skewness, etc. One can take as many moments as there are parameters, and in principle can build up a complete kinetic description of the problem. As an example, following Hamasaki, et al.,[8] consider a distribution function,

$$f(p_\perp, p_\parallel, 0) = \frac{n_o}{A} \exp\left[-\frac{(P_\parallel^2/T_\parallel + P_\perp^2/T_\perp)}{m_o(\gamma + 1)}\right]$$

$$\cdot\, H(a_o p_\perp^2 - p_\parallel^2) \tag{8}$$

$$f(p_\perp, p_\parallel, z) = f(p_{\perp o}, p_{\parallel o}, 0)$$

$$p_{\perp o}^2 = p_\perp^2\, B_o/B(z)$$

$$p_{\parallel o}^2 = p_\parallel^2 + p_\perp^2 - p_{\perp o}^2 \tag{9}$$

This distribution is specified by three parameters, n, $T_\perp$, $T_\parallel$, and H is the Heavyside function to describe a loss cone if the ring lies on open field lines

$$a_o = \sqrt{(B_z/B_o) - 1} \tag{10}$$

Taking moments of the kinetic equation gives a description for how the temperatures evolve with time in response to all the phenomena included in the RHS of Eq. (7). A lot can be included, because doing it in the fluid way removes the multi-time aspects. For example, the loss cone is determined by the kinetic geometry and making f proportional to H simply requires instantaneously that the distribution function has a loss-cone shape. That way you do not have to watch the particles travel a field line and get lost out the end at some particular rate which is a very time-consuming problem on the computer.

Doing the problem in a fluid-like way by characterizing the distribution by a few parameters makes a lot of progress because one can fold in all kinds of effects.

$$\int dp$$

$$\int p_{\perp o}^{2}/(\gamma + 1)\ dp$$

$$\int p_{\parallel o}^{2}/(\gamma + 1)\ dp \qquad (11)$$

In this case, three moments are taken describing particle conservation, and two components of momentum conservation. So this tells how $T_\perp$ evolves with time, how $T_\parallel$ evolves with time, and so on, in response to microwave heating, Q, collisions, C, radiation loss, S, adiabatic effects, loss cone effects, H, stability effects, and so on. These can be folded in one after the other, with appropriate bounce averages in the magnetic field, to give some feeling for which physics is important, how important it is, how big an instability has to be before it impacts power balance, how much a departure from adiabaticity it takes before the operating point changes, to what extent these results change if you have field lines intersecting a magnet in the mirror throat, what change occurs if the magnet gets skinny as opposed to fat, and so on. So in an organizational way, this seems to be a fairly useful approach; it lacks a lot in that it does not have the radial dependence, the curvature drift, and so on, but these can presumably be built in as the models develop. The advantage of this approach is that we can solve it.

Now what I am going to do for the rest of the talk is focus on some of these effects and how they influence the bumpy torus within the framework of a fluid model, to give us an organizational way to see what we should be considering in understanding the ring. Let us start with Q, the heating terms.

A. RESONANCE AND RELATIVITY

Some of this work is due to S. Hamasaki and J. B. McBride, who originated a lot of this work 2-3 years ago. Two questions that immediately arise with respect to wave heating are the location and shape of the resonances and the accessibility of these resonances to waves launched exterior to the plasma. All these depend on B, which for each field line is a function of axial position. Figure 4 shows the importance of keeping relativity in the problem. What is shown are heating rates as a function of axial position through the mirror, for the n = 2 mode, at two different temperatures. The solid line is relatively cold plasma of 100 keV, the dotted line is for 500 keV; in the colder situation, the heating is still fairly well localized, even at 100 keV, whereas as the temperature increases, the heating distributes itself more and more along the axis of the device. Distributing the heating changes the accessibility problem as well as changing the energy deposited. When loss cones are considered, the particles can be increasingly localized and may not sample a local resonance. Relativistic effects remove this problem because the heating is distributed throughout the axis of the device. So relativity does make a difference and it is strongly a function of temperature. Figure 4 is for the second harmonic; similar curves for other harmonics and polarizations will be shown later in the workshop.

B. ACCESSIBILITY AND STARTUP

Another question is whether the waves will reach the resonant surfaces. Figure 5 shows the first harmonic resonant surface and the first harmonic cutoff; an extraordinary wave propagating from the outside would encounter a cutoff before it sees a first harmonic resonant surface. Ordinary modes do not have this cutoff, and would propagate clear on through. The problem is that if you compare ordinary mode heating with extraordinary mode heating, you find that extraordinary, first harmonic, heats much more than the ordinary mode, as seen in Figure 6. What is plotted is the heating rate, which is a

function of harmonic number. So extraordinary modes heat very well but they do not propagate, ordinary modes do not heat very well (at least when the plasma is relatively cool), but they propagate very nicely. This introduces the idea of mode conversion, a technique by which an ordinary mode propagating through the system reflects off the wall and in large part comes back as an extraordinary mode and thereby heats. This is necessary because if you look at the heating as a function of temperature (Figure 7) and compare it with loss processes, there is clearly a tremendous startup problem without first harmonic heating in the extraordinary mode. The loss in Figure 7 includes synchrotron, bremmstrahlung, and collisional drag. Ordinary mode heating falls well below the line of loss. Extraordinary mode heating can work, although it looks like there may be a problem at very cold T_e. There are operating points which are plausible and have hundreds of keV for ring energy, where heating = loss.

What about second harmonic heating? Second harmonic heating is virtually a relativistic effect, so it does not help very much in the startup phase. It helps quite a bit at higher T. The same physics which helps determine what the operating points are, at which heating balances drag, and so on, may not be at all the physics which determines the ability to start the ring up. If the machine is designed to properly take into account the energy needs at the operating points, it might still have too little energy to reach that point.

C. FIELD AMPLITUDES

When you do calculations like those just described, there is unfortunately a problem which I have mentioned earlier, namely that the heating rates are a function of the microwave field amplitudes in the system. Curves like Figure 7 look very nice and are not that hard to obtain using quasilinear theories, but there is an assumption as to the amplitude of the ECH. This particular calculation assumed E to be 100 V per cm, which gives a consistent value for the input power and plasma density. But there is no measurement of E; the theory

uses what is plausible. For example, since the heating rate is proportional to E^2, if all the input energy is absorbed by the plasma (perfectly reflecting walls), then $\langle\gamma\rangle E^2$ will be given by the input power. That is, if the waves are only weakly damped, the amplitude simply builds up until you are absorbing energy at the same rate you are putting it in. So there is no reason, really, in problems of this sort to assume that the electric field is independent of temperature or independent of the damping rate. I presume that if the walls are really sufficiently reflecting, even a weakly damped mode will be adequate because the electric field will simply build up until E^2 is large. We do not know how to calculate really detailed profiles of E^2, particularly in a plasma bounded by walls of a certain composition.

D. LOSS CONES

Loss cones represent another important energy sink. Figure 8a shows the ring location in NBT and Figure 8b in EBT-1. The dotted area is the ring, showing that the ring particles sit on field lines which intersect walls. If some or all of the ring sits on field lines that intersect the wall, the distribution must be loss cone. Particles that are scattered do not have to diffuse neoclassically, they simply stream along the field line and hit the magnets. It is obvious, of course, that a loss cone increases the losses, but other changes created by a loss cone are more subtle and they impact on many other physics ideas, including both heating and other loss calculations. Figure 9 shows some results from fluid models in which a loss cone is introduced for a case in which $T_\perp = 2T_\parallel$. The density along the axis goes to zero at some location (Figure 9a); without the loss cone, the density would decrease to some modest value and rise in the next bump. The effect of the density cutoff is to make the energy absorption more and more dependent on the details of midplane heating, because more particles stay in the midplane. This gives less $n = 1$ heating than would be true if n = const. along a field line. Perpendicular heating tends to be greater than parallel heating for all

harmonics since, because of the loss cone, when $T_{\parallel}$ increases above $T_{\perp}$, the large $T_{\parallel}$ particles are lost out the device. There is less synchrotron radiation from a loss cone distribution because the plasma tends to sit in regions of lower magnetic field. $T_{\perp}$ is greater than $T_{\parallel}$ no matter what the parallel mode number is, as shown in Figure 9b, where $T_{\perp}$ vs. $T_{\parallel}$ is shown as a function of $k_{\parallel}$, the mode number along the magnetic field. Without a loss cone, as $k_{\parallel}$ goes to zero, most of the heating goes into perpendicular energy. As $k_{\parallel}$ increases, $T_{\parallel}/T_{\perp}$ also increases; but with the loss cone, T drops as $k_{\parallel}$ increases, with $T_{\perp}$ still bigger than $T_{\parallel}$. Naturally, equilibrium temperatures are lower because of the loss cone, but less obviously, the geometric location of the loss cone makes a difference, as shown in Figure 9c, where a_0 is the extent along B of the absorber or magnet. Figure 9c shows $T_{\perp}$ versus $T_{\parallel}$ at various locations of the loss cone compared with the mirror throat. As the location of the metal that is causing the loss cone goes nearer the mirror throat, the temperature of the system increases. These are effects which are over and above the obvious cooling of the plasma by the loss cone, and they affect the kinds of heating calculations to be done, the kinds of radiation calculations to be done, the question of mode structure in the system, and so on. So loss cones make a difference in more ways than one.

E. STABILITY LOSS

What about stability losses? The example I will give in detail is loss due to whistler modes. Hedrick and others looked at this instability a long time ago; it appeared at that time that because of relativistic broadening of the resonances, whistlers would become less important. Gladd has worked this out in more detail to determine whether the instability really goes away. The answer is that it does not. It goes down, but not out. Knowing that there is going to be a whistler instability, even without knowing the saturation level, it is possible to determine what a given level of turbulence will do to the system. Will it actually effect the predictions of energy balance

and operating point? Whistler turbulence has been included in the fluid model by calculating the real frequency, wave number, and growth rate of the maximum growing mode, taking a constant fluctuating wave amplitude as a parameter, and using quasilinear techniques to get diffusion.

$$\omega_r = \frac{eB_o}{m_o c} \frac{(1 - T_\parallel/T_\perp)}{\Gamma}$$

$$\Gamma = \left[1 + 3 \frac{T_\perp + T_\parallel}{m_o c^2}\right] \qquad \Rightarrow \quad k_\parallel > \frac{1}{L}$$

The diffusion can be into a loss cone or across the magnetic field, with very different results. Rather than show the effect of whistlers by themselves, consider at the same time another effect, namely, loss of adiabaticity.

F. ADIABATICITY

Many people have discussed this in the last year or so; the basic idea is that as the energy of the electron increases, the bounce time decreases, and the magnetic field changes significantly over a cyclotron period;

$$\varepsilon \equiv \frac{1}{B} \frac{dB}{dt} \frac{1}{\omega_c} \sim \frac{v_\parallel}{L\omega_c} \gtrsim 1 \quad ,$$

the orbits then cease to be adiabatic. It is well known that these effects are not power law effects, they come in as $\exp(-\frac{1}{\varepsilon})$, and so loss of adiabaticity has a very sharp onset. When you think about the fact that heating times in these devices are milliseconds, while the bounce times are nanoseconds, it clearly requires pretty good

adiabaticity in order not to have losses exceeding collisional drag. This loss has been included in the fluid model using results by Bernstein, Howard, Cohen, and others, using a diffusion coefficient in velocity space due to the loss of adiabaticity.

$$N(\mu,T)f = \frac{\partial}{\partial\mu}\left(\frac{\langle\Delta\mu^2\rangle}{2\Delta t}\ \frac{\partial f}{\partial\mu}\right)$$

$$\frac{\langle\Delta\mu^2\rangle}{\mu^2} = A\ \frac{V^2}{V_{\perp o}^{\ 2}}\ \exp\left(-\ 2\ \frac{KL}{\rho}\ \frac{V^2}{V_{\perp o}^{\ 2}}\right) \qquad (12)$$

where ρ is the electron gyroradius, L is the bounce length, and K is a function of pitch angle. This shows again the advantage of the fluid-like calculation: you can include new effects quickly and find out what they will do.

G. MODELING RESULTS

Figure 10 shows the result of both whistlers and nonadiabaticity. What is done is to run this fluid type model including the loss cone (which is required to get numbers anything like the experiment), and include loss of adiabaticity and then ask what is the effect of a low level of whistler turbulence. $E_\omega^{\ 2} = 0$ gives the equilibrium temperature in the absence of whistlers but including the other effects I have mentioned, and Figure 10 shows the dependence of the operating point as a function of the (assumed) level of whistler turbulence $E_\omega^{\ 2}$. The dependence on $E_\omega^{\ 2}$ is quite pronounced. The ring temperature goes from almost 1 MeV for EBT-S down to maybe 500, 400, 300, 200 keV as the whistler amplitude is increased. How much turbulence does it take to change T? The scale in Figure 10 is 10^{-4} ergs/cm^3. The energy density of the ring is of order 10^4 ergs/cm^3, which means that a fluctuation energy about 8 orders of magnitude down from thermal energy still gives a visible effect in the framework of the fluid model. So,

to say that instability goes down but not out makes a difference, because it takes so little to have a noticeable effect.

The calculation shown in Figure 10 includes nonadiabaticity, collisional drag, synchrotron radiation, scattering into the loss cone, whistler loss, and ionization. The calculation also includes relativistic broadening of the resonances and field line averaging of the heating terms. The fluid model does a lot of things realistically, by giving up on the total kinetic approach and using the distribution function of a specified form.

Well, do you need all this detail? Yes. There are a lot of EBT devices and both absolute numbers and scaling from device to device are important. It is usually possible to get one device right by adjusting the electric field level. Once a plausible level for one device is chosen, it isn't easy to fit four or five experiments with the same model. Actually, we believe it is impossible without the introduction of these nonclassical processes--loss cones, whistlers, nonadiabaticity. With these effects, it is possible to get a scenario in which one model gives points that fall somewhere near the existing data points for four or five devices. This will all be presented elsewhere in the workshop, but an example of the competition between the various processes is given, from a typical run of this sort, in Figure 11. The synchrotron radiation limit is not reached in these experiments, NBT, EBT-1, -S, but loss-cone effects are large. The loss contribution is largely due to nonadiabaticity with comparable losses from whistlers and drag. The whistler amplitude was taken to be about 10^{-4} ergs/cm^3. The beauty of doing simplified physics is that you can keep at least the lowest order term of an awful lot of effects. And it makes a difference--leaving one out makes a substantial difference in results.

What about collisional drag alone, if you forget about all of this nonclassical stuff? Typically, if nothing is included but classical effects, the temperature is too large, its dependence on the

microwave power level is too strong, and the scaling is wrong. The predicted ring temperature in EBT-1 is comparable or bigger than EBT-S, contrary to the experiment. So collisions alone have trouble with scaling, they have trouble with magnitude, and they have trouble with dependence of the temperature on the microwave field. And this is what leads us to work hard to look for nonclassical effects: they are sure to be there.

So what about EBT-P? Basically, three questions that you ask in EBT ring physics are: is there an operating point which is microscopically stable, that is, will not disrupt? within those operating points, will the power balance be favorable? and, if you try to reach such an operating point with favorable power balance, will the startup power be comparable to the power designed for the device? Having discussed the first two points, let me at least write down the results of exercising the model I've just talked about through the startup mode as well as through the operating point mode. This calculation was done by Sperling who concluded (Figure 12) that based on the models described, noting that at startup the plasma is cold and one needn't worry about whistlers and so on, typically the model as described gives about 10 kilowatts of power required for startup with background densities of less than 10^{12}. Another question is whether EBT-P is being designed with the adequate startup power. Having established that the model can reproduce present experimental power needs, we exercise the code to predict that it takes of order a megawatt at a density of 10^{13} cm^{-3} to startup EBT-P. This is comparable to the power being designed for the device. Reactor calculations are pretty speculative, but a calculation with a 10^{14} cm^{-3} density predicts hundreds of megawatts to startup the reactor, indicating a need for density ramping or some other cleverness.

In conclusion, this talk gave a perspective in which to assess the results of theoretical ideas. It emphasized that even if there is a stable operating window, it must be determined whether there is any sense in looking out that window, and what physics is required to answer that question.

REFERENCES

1. G. R. Haste, 2nd EBT Ring Physics Workshop, San Diego, California (December 1-3, 1981).
2. J. B. Taylor, Phys. Fluids 6, 1529 (1963).
3. L. D. Pearlstein and N. A. Krall, Phys. Fluids 9, 2231 (1966).
4. H. Furth, private communication (1964).
5. N. A. Krall, Phys. Fluids 9, 820 (1966).
6. D. B. Nelson and C. L. Hedrick, Nucl. Fusion 19, 283 (1979).
7. J. W. Van Dam and Y. C. Lee, 1979 EBT Ring Physics Workshop, Oak Ridge, Tennessee, p. 471 (1979).
8. S. Hamasaki, N. A. Krall, and J. L. Sperling, "The Classical Theory of the Bumpy Torus Relativistic Annulus," JAYCOR Report No. J510-81-048 (1981).

MHD Equilibria

Instability Limits

- Anisotropy - Whistlers
- Curvature - Interchange
- Wave Heating - Parametric Processes
- Etc.

Orbit Effects

- Loss Cones
- Drift Surfaces/Cones
- Adiabatic Effects
- Microwave Scattering
- Etc.

Wave Heating Physics

- Resonant Surfaces
- Cutoffs
- Relativistic Effects

Interaction with Background

- Collisional Drag
- Synchrotron Radiation
- Scattering
- Interactive Instabilities

Geometry

- EBT-1, S, R, P, ...

Figure 1. Standard elements of ring physics.

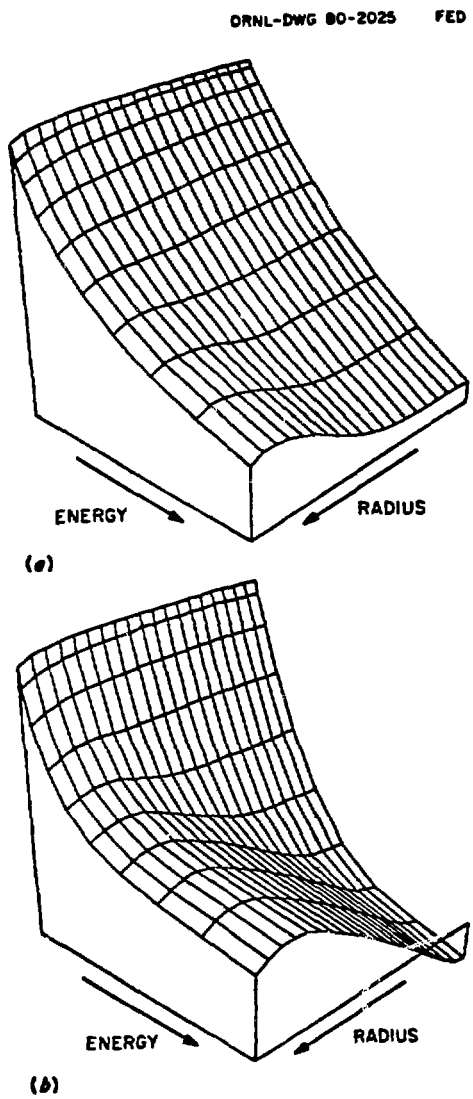

Figure 2. Plot of $\ln f_0$ vs energy and radius for an edge neutral density of $n_0 = 3 \times 10^{10}$ cm^{-3} (a) with first-harmonic microwave heating only and (b) with first- and second-harmonic microwave heating.

ORNL-DWG 76-18487R

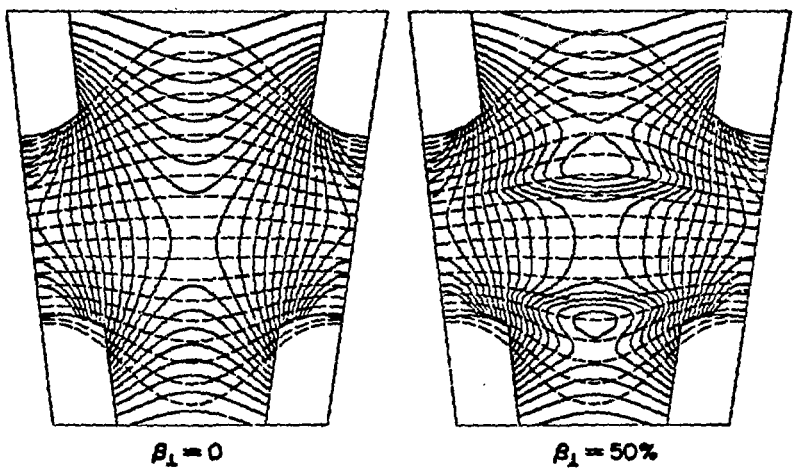

Figure 3. 3-D bumpy torus equilibrium without and with a $\beta = 0.5$ annulus region. Magnetic field lines are indicated by dashed lines and $|\beta|$ contours by solid lines.

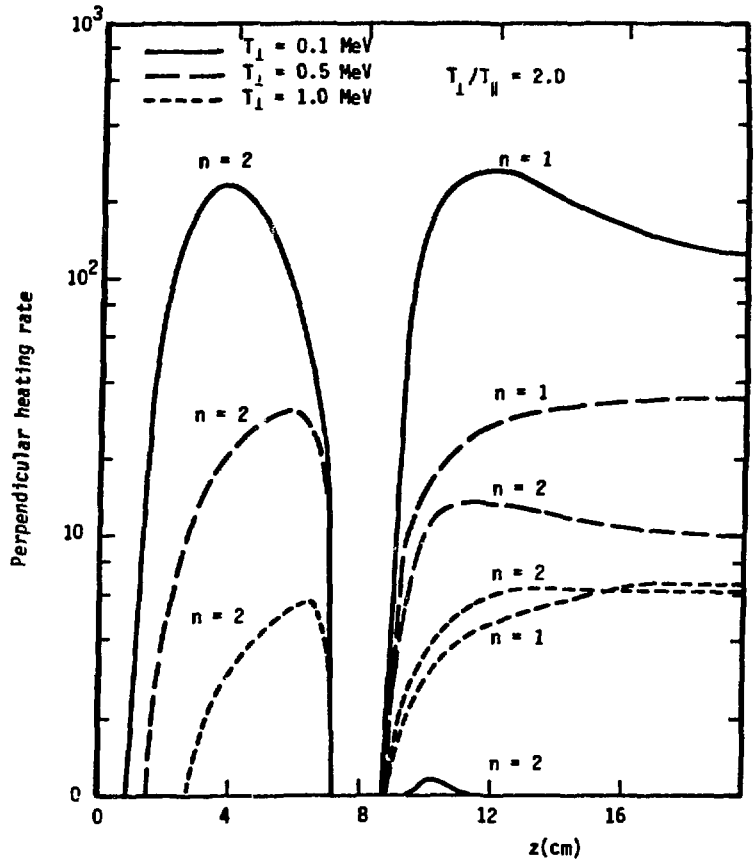

Figure 4. Heating rates at various locations along the magnetic axis, for two temperatures, due to second harmonic absorption.

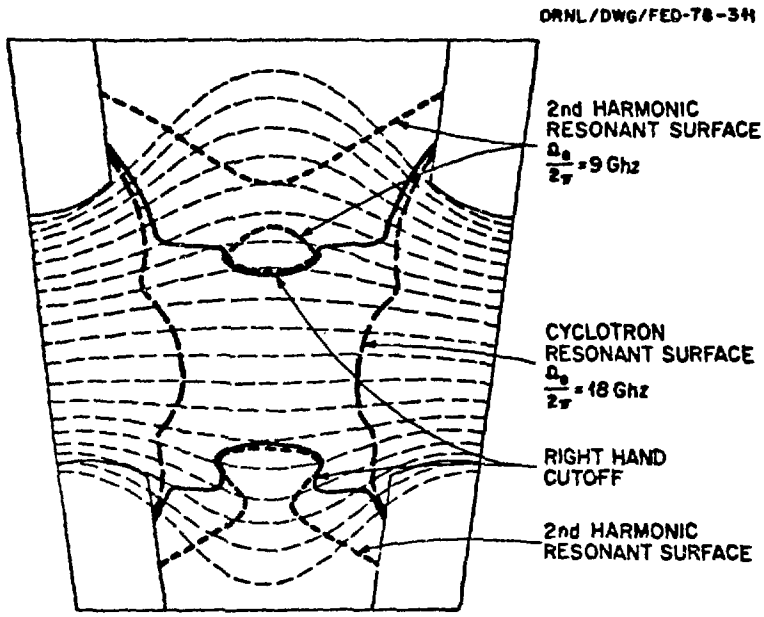

Figure 5. Resonant surfaces and cutoffs (for x-0 mode).

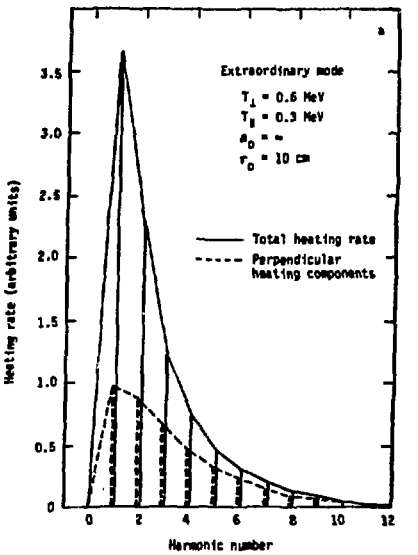

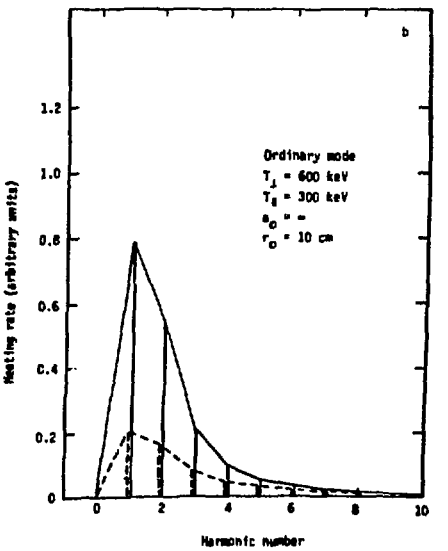

Figure 6. Heating of ordinary and extraordinary modes at various harmonic numbers.

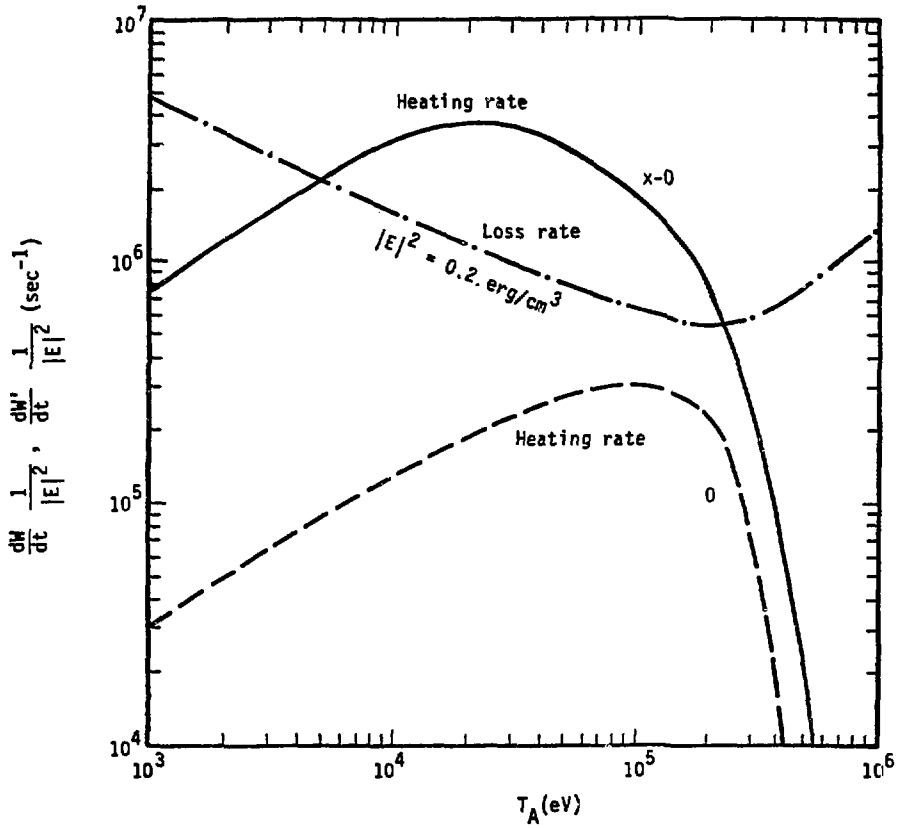

Figure 7. x-O and O mode heating compared with classical loss processes.

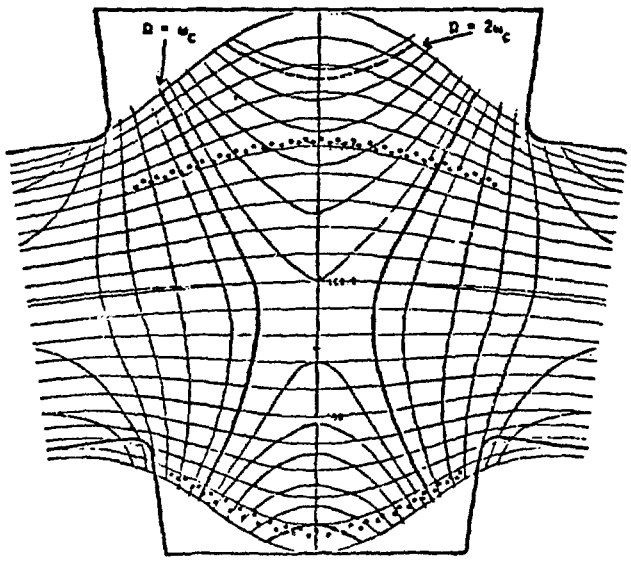

Figure 8a. Section of NBT in the horizontal midplane. Dotted lines show location of the ring.

ORNL-DWG 74-2066A-R2

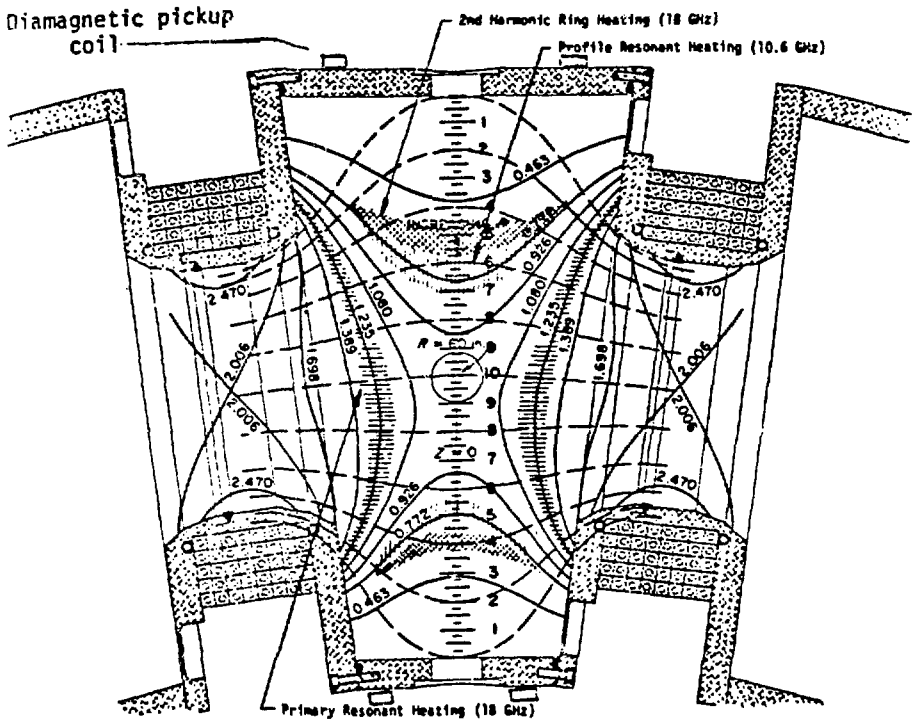

Figure 8b. Section through EBT-1 in the horizontal midplane. Solid lines indicate surfaces of constant B, and dotted lines indicate flux lines. Shaded areas are regions of cyclotron resonance for electrons when B_0 = 4.55 kG.

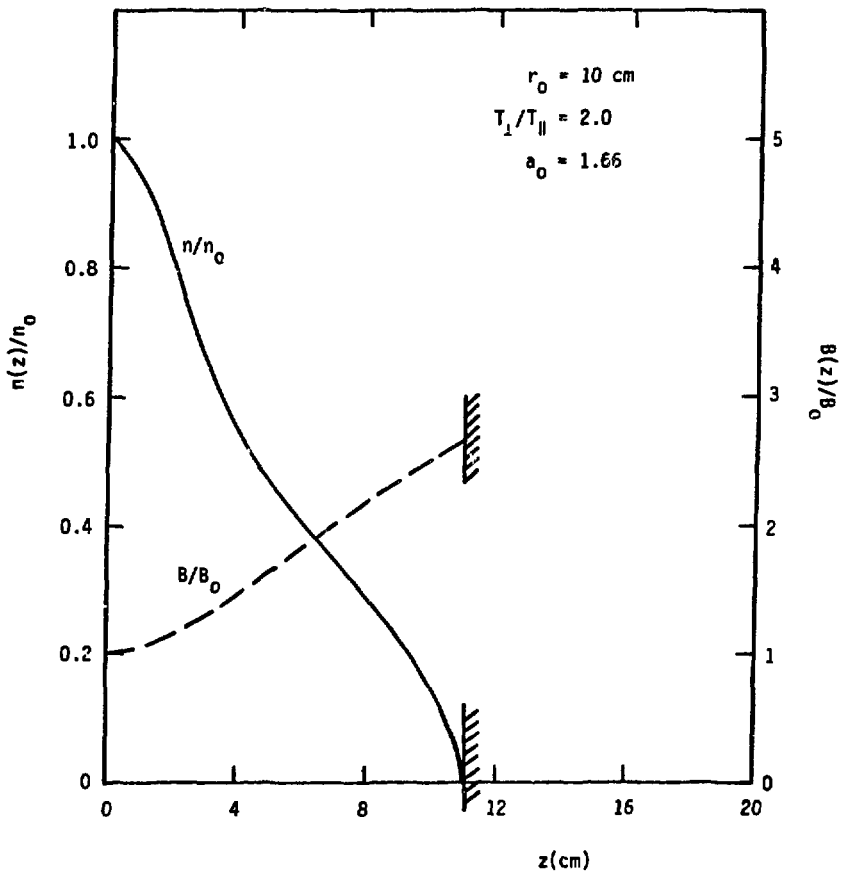

Figure 9a. Loss-cone effect on density profile.

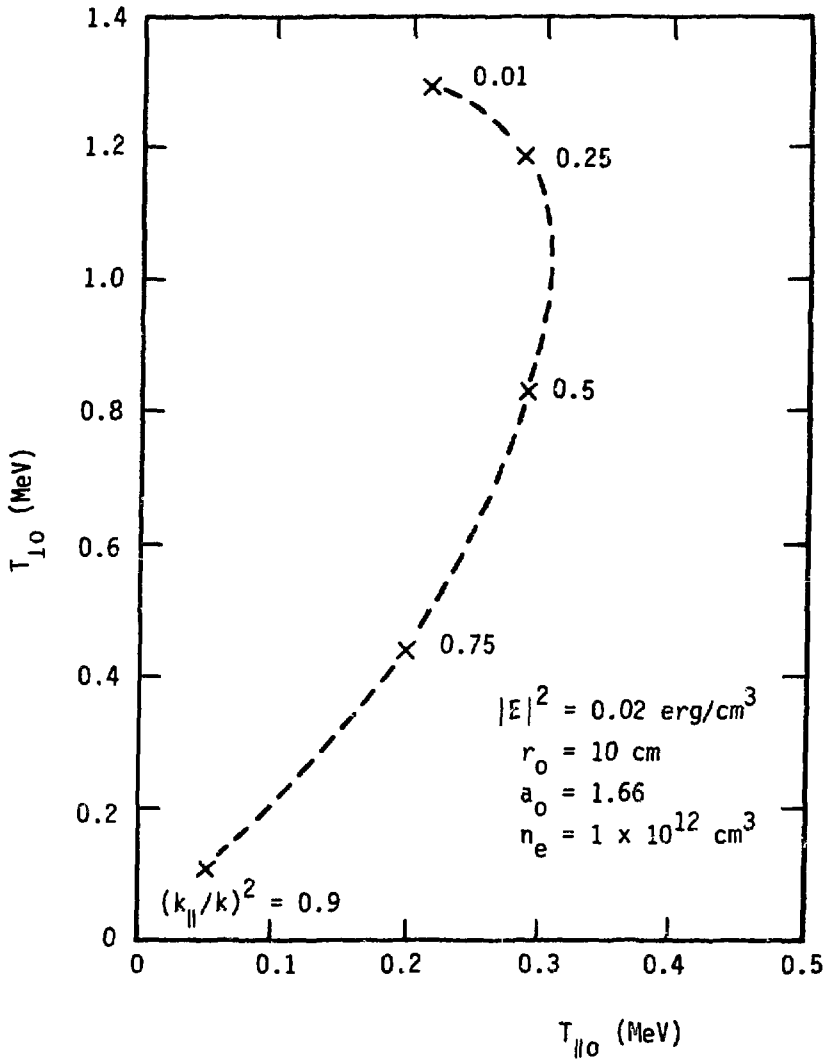

Figure 9b. Loss-cone effects on anisotropy for various wave numbers.

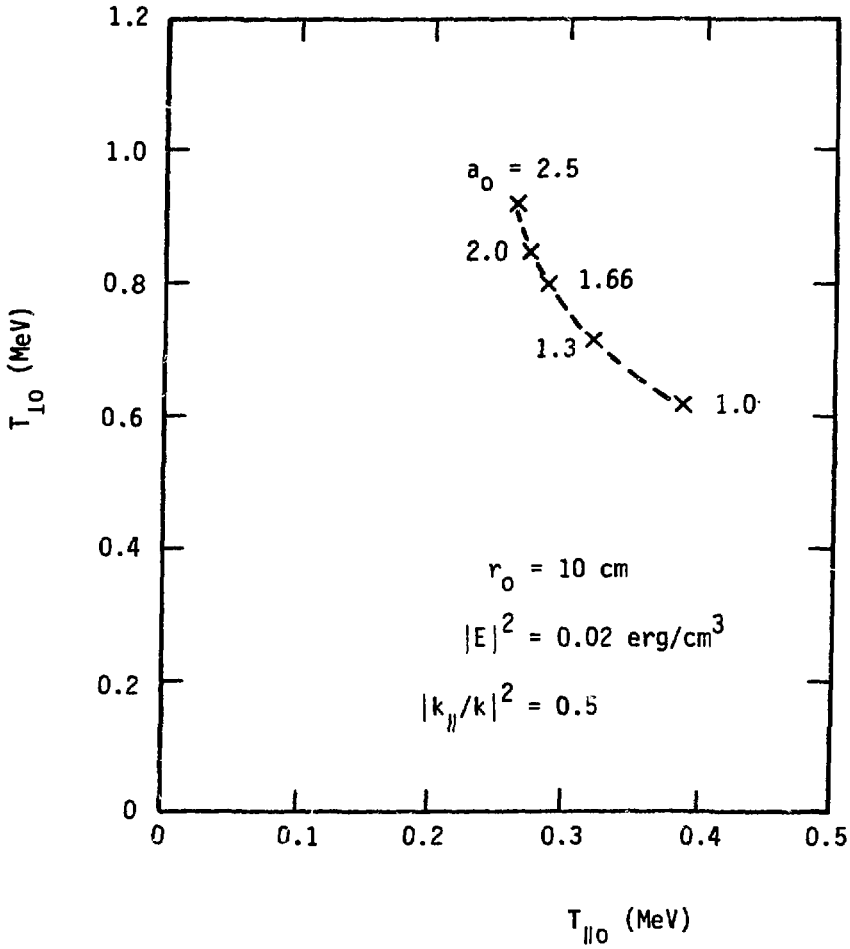

Figure 9c. Loss-cone effects on anisotropy for various location of the loss cone.

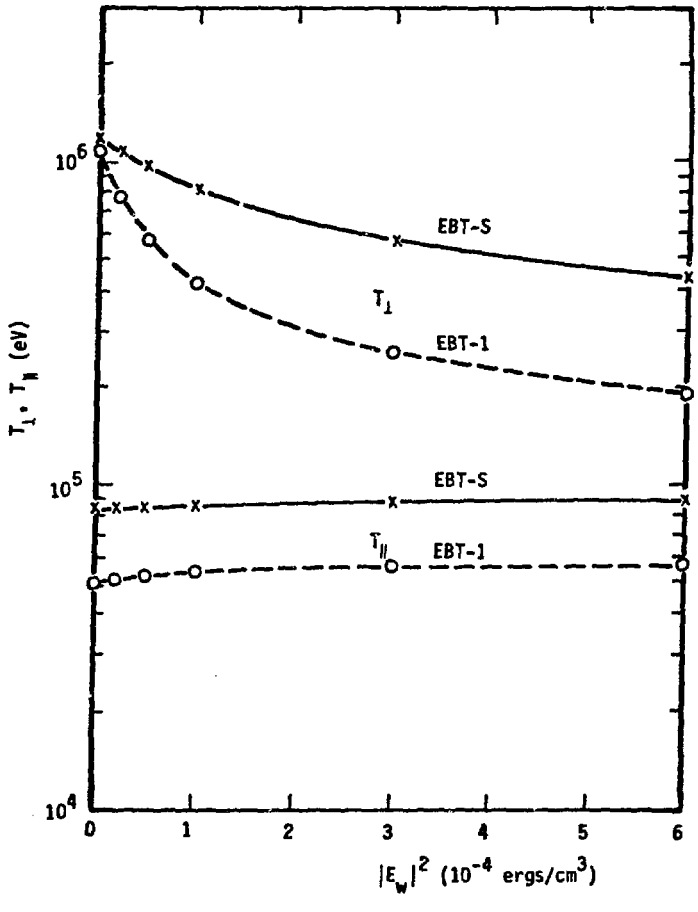

Figure 10. Effect of whistler turbulence on the ring temperature. The baseline result, $E_\omega^2 = 0$, includes loss due to non-adiabaticity.

Collisions	Synchrotron Radiation	Loss Cone		
		Classical	Whistler	Nonadiabaticity
15%	.1%	1%	20%	63.9%

Figure 11. Relative loss rates through various channels for a typical EBT-S run.

Device	Startup Power	Density
EBT-N/1/S	10 kW	10^{12} cm^{-3}
EBT-P	1 MW	10^{13} cm^{-3}
EBT-R	200 MW	10^{14} cm^{-3}

Figure 12. Estimated startup requirements for various devices.

3. STABILITY

CURVATURE-DRIVEN INSTABILITIES IN A HOT ELECTRON PLASMA: RADIAL ANALYSIS

H. L. Berk
J. W. Van Dam
M. N. Rosenbluth

Institute for Fusion Studies
The University of Texas at Austin
Austin, Texas 78712

D. A. Spong

Oak Ridge National Laboratory
Oak Ridge, Tennessee 37830

Abstract

The theory of unfavorable curvature-driven instabilities is developed for a plasma interacting with a hot electron ring whose drift frequencies are larger than the growth rates predicted from conventional magnetohydrodynamic theory. A z-pinch model is used to emphasize the radial structure of the problem. Stability criteria are obtained for the five possible modes of instability: The conventional hot electron interchange, a high-frequency hot electron interchange, (at frequencies larger than the ion-cyclotron frequency), a compressional instability, a background pressure-driven interchange, and an interacting pressure-driven interchange.

Summary of Results

We have developed a self-consistent theory for the curvature-driven instabilities of a hot electron plasma in a z-pinch model. One can apply the results of this theory to a bumpy torus if one associates (a) the radius of the annulus in our z-pinch model with the average radius of curvature of the magnetic field sampled by the hot electrons and (b) the wavenumber k in the z-direction of symmetry by the poloidal wavenumber m/r_p, where m is an integer and r_p is the experimentally measured minor radial position of the hot electrons with respect to the magnetic axis.

The stability picture that emerges is as follows.

If the dynamics of the hot electrons can decouple from those of the background plasma, and if the hot electron beta, β_h, is sufficiently large so that

$$\beta_h > \frac{4\Delta}{R} - 2\beta_c \, , \tag{1}$$

where Δ is the hot electron annulus half-width, R the radius of curvature, and β_c the background plasma beta, then the hot electrons create a diamagnetic well that stably confines the background plasma. Generally, the conditions for the decoupling of the hot electron dynamics are that:

(1) The background ion density , n_c , be sufficiently high so that ideal the MHD growth rate for the low-frequency hot electron interchange is sufficiently less than the curvature drift frequency (calculated using the perpendicular energy) and also that the high-frequency hot electron interchange mode not be excited;

(2) The background density be sufficiently low so that, roughly, the curvature drift frequency is less than the compressional Alfvén frequency; and

(3) The background plasma beta, β_c, be sufficiently low, namely, $\beta_c \lesssim 2\Delta/R$.

Conditions (1) and (2) indicate that a window in the values of the background plasma density for stable operation may be present. Condition (3) sets a limit on the background plasma beta that can be contained. These conditions need to be studied carefully when a complete survey of parameters is considered, particularly the finite ion cyclotron frequency. There then arises a range of parameters where the stability window can disappear. To improve on the stability picture at these parameters, it will be necessary both to solve our radial eigenmode equation more accurately and to introduce additional physics, such as the axial variation of equilibrium quantities and the effects of finite Larmor radius.

To be more quantitative, we note that we have found two types of modes: (a) short wavelength WKB-like modes where a substantial fraction of a radial wavelength, $2\pi/k_r$, fits across the outer edge of the hot electron annulus of half-thickness Δ (somewhat arbitrarily we have chosen $k_r\Delta = 2$, which is the longest wavelength for one particular model); and (b) layer modes whose radial wavelengths are long compared to the annulus thickness.

For the short wavelength modes, even when $\beta_h > 4\Delta/R - 2\beta_c$, four other types of curvature-driven instabilities were found:

(1) A low-frequency ($\omega < \omega_{ci}$) hot electron instability. This instability is driven by the hot electron pressure and is predictable from MHD theory.[1,2] It is stabilized if the hot electron to background ion density fraction satisfies

$$\frac{n_h}{n_c} < \frac{k_\perp^2\Delta^2}{4} q_o \left(1 - \frac{\beta_c R}{2\Delta}\right)^2 , \qquad (2)$$

where R is the radius of curvature, $k_\perp^2 = k_r^2 + k^2$, $q_o = V_{cv\perp}/\omega_{ci}\Delta = (\gamma^2 - 1)c^2/(2\gamma\omega_{ce}\omega_{ci}R\Delta)$, $\gamma m_e c^2$ is the mean relativistic energy of the electrons, β_c the background plasma beta, and $\omega_{ce,i}$ the electron and ion cyclotron frequencies (in units of radians/sec). Since $q_o > 1$ in present EBT experiments, this criterion is readily satisfied. For reactor-like devices this criterion is significant.

(2) A high-frequency hot electron instability that is driven by the hot electron pressure when frequencies are comparable or greater than the ion cyclotron frequency.[3] To excite this instability one generally needs

$$q \equiv \frac{k^2}{k_\perp^2} q_o > \frac{1}{4} \quad . \tag{3}$$

Stabilization is achieved if

$$\frac{n_h}{n_c} < \left[1 - \left(\frac{1}{q} + \frac{\beta_c R}{2\Delta}\right)^{1/2}\right]^2 \quad . \tag{4}$$

This is not a stringent criterion as long as $q \neq 1/(1 - \beta_c R/2\Delta)$. However, when $q \simeq 1/(1 - \beta_c R/2\Delta)$, the above condition goes to zero, indicating that there is no stable value for n_h/n_c . However, this result probably depends on our idealization of the mathematical model. A calculation incorporating more realistic physical effects is needed.

(3) A compressional Alfvén instability[4,5,6] is excited if the background plasma ion density , n_c , is too large. The stability condition requires

$$\frac{n_h}{n_c} > \frac{2\beta_h \Delta q}{R} \frac{\left(\frac{R\beta}{2\Delta} - 1\right)\left(1 - \frac{\beta_c R}{2\Delta}\right)}{\left[1 - q\left(1 - \frac{\beta_c R}{2\Delta}\right)\right]^2} \quad , \tag{5}$$

where β_h is the hot electron beta. This condition gives a reasonable upper density limit if $q \neq 1/(1 - \beta_c R/2\Delta)$. However, when $q \approx 1/(1 - \beta_c R/2\Delta)$, the above condition has no stable operating region. In fact, when $q \approx 1/(1 - \beta_c R/2\Delta)$, the compressional Alfvén and high-frequency hot electron modes coalesce, and analysis then shows that there is no stable operating regime (assuming $\beta_c R/2\Delta \ll 1$) when

$$\left(1 - \frac{1}{q}\right)^4 < 32 \frac{\beta_h \Delta}{R} \left(\frac{R\beta}{2\Delta} - 1\right) . \qquad (6)$$

[Eq. (6) requires $\beta_h < .25$ for its validity.] We note that if $q_o < 1$, we can avoid this unstable region. If $q_o \gg 1$, only a relatively narrow band of parameters is resonant, and the introduction of additional effects may yield reasonable stability properties. However, if $q_o \approx 1$, we conjecture that even more realistic modeling will have difficulty in finding stable operation.

A mode involving the interaction of the hot electron pressure with the background pressure arises when $\beta_c R/2\Delta > 1$, which yields the basic background beta limit discussed by Van Dam and Lee[7] and Nelson.[8] At fixed background temperature, this condition also limits the background density. In order that this background beta limit be the governing limit for stability, rather than the density limit of the compressional Alfvén mode, we require

$$\frac{T_c}{T_h} > \left(\frac{4\Delta}{R}\right) \beta_h q_o \qquad \text{for } q_o \ll 1 \tag{7}$$

If, for $q_o \gg 1$, we assume that a more realistic theory will spread the denominator of Eq. (5) so that it has a minimum value of order unity, then the condition of Eq. (7) is altered to

$$\frac{T_c}{T_h} > T\, \beta_h \left(1 - \frac{2\Delta}{R\beta_h}\right) \frac{\Delta}{R} \qquad \text{for } q_o \gg 1 , \tag{8}$$

where T is a number of order unity.

For the long wavelength layer modes, we do not find the hot electron pressure-driven interchange modes, since the hot electron pressure has no net change across the annulus layer. We still find background density limits due to the compressional Alfvén-type mode. If $k\Delta q_o \ll 1$, the stability limit for this mode is similar to Eq. (5) with $q = q_o$, viz.,

$$\frac{n_h}{n_c} > \frac{\beta_h^2}{2} q_o \quad , \tag{9}$$

where we have assumed $R\beta/2\Delta \gg 1$ and $\beta_c R/2\Delta \ll 1$. For $k\Delta q_o \gg 1$, the stability condition becomes

$$\frac{n_h}{n_c} > \frac{\beta_h^2}{q_o (k\Delta)^2} \quad . \tag{10}$$

However for $k\Delta q_o \to 1$, we find that there is no stability region. Here too, more realistic calculations are needed. In particular, the condition for justifying the layer approach breaks down near $\omega_{ci} = kv_{cvl}$.

We find that the long wavelength background pressure-driven interchange layer mode is also limited by the condition $\beta_c < 2\Delta/R$. However, for some parameters the background beta limit can be substantially less. For example, we have

$$\beta_c < \beta_{crit} \equiv \frac{2\Delta}{R} \text{Min} \left[1, \frac{4k\Delta q_o}{27\left(1 - \frac{2\Delta}{R\beta_h}\right)\frac{n_h}{n_c}} \right]$$

$$\simeq \frac{2\Delta}{R} \text{Min} \left[1, \frac{4k\Delta}{21\left(1 - \frac{2\Delta}{R\beta_h}\right)\beta_h^2} \right] , \qquad (11)$$

where we have bounded n_h/n_c by Eq. (5) and assumed $q_o << 1$. Thus, since $k\Delta$ can be as small as Δ/r, the critical β_c limit can be reduced below $2\Delta/R$, when β_h increases to moderate values that are still less than unity.

Acknowledgements

The authors have benefited from fruitful discussions with A. El Nadi.

This work was supported by the United States Department of Energy under contract no. DE-FG05-80ET-53088 and under contract J-7405-eng-26 with the Union Carbide Corporation and the University of Texas Program Development Fund.

References

1. N. A. Krall, Phys. Fluids 9, 820 (1966).

2. H. L. Berk, Phys. Fluids 19, 1255 (1976).

3. R. R. Dominguez and H. L. Berk, Phys. Fluids 21, 827 (1978).

4. A. M. El Nadi, to be published in Phys. Fluids.

5. H. L. Berk, M. N. Rosenbluth, and J. W. Van Dam, in Proc. U. S.-Japan Workshop on Non-Axisymmetric Confinement Systems, Institute for Fusion Studies, IFSR 5 (1980).

6. M. N. Rosenbluth, Phys. Rev. Lett. 46 1525 (1981).

7. J. W. Van Dam and Y. C. Lee, in Proc. EBT Ring Physics Workshop (ORNL, Oak Ridge, 1979), Conf. -791228, p. 471.

8. D. B. Nelson, Phys. Fluids 23, 1850 (1980).

RADIAL STRUCTURE OF INSTABILITY MODES IN THE EBT HOT ELECTRON ANNULUS*

D. A. Spong
Oak Ridge National Laboratory
Oak Ridge, Tennessee 37830

H. L. Berk, J. W. Van Dam, and M. N. Rosenbluth
Institute for Fusion Studies
University of Texas at Austin
Austin, Texas 78712

In the ELMO Bumpy Torus (EBT) device, a hot electron annulus is present near the outside edge of a warm core plasma. Although this provides a localized minimum in B and stabilizes low beta interchange modes of the core plasma, a number of instabilities may still persist in such a configuration. These are: the hot electron interchange mode, the coupling of the ring with compressional Alfven waves of the core plasma, core plasma pressure-driven modes, and instabilities present in the cold surface plasma region outside the ring. The radial structure of such modes is of interest because both instabilities localized to the ring region and those extending into the core plasma can be present in the appropriate parameter regions. Also, studies of the radial structure are useful in assessing the importance of effects such as finite $k_\perp \rho_i$ and $k_\perp \rho_H$ that are not included in the present theory. Radially resolved calculations have been done for a z-pinch model which corresponds to a bumpless, azimuthally symmetric version of EBT. A shooting method is employed that matches derivatives of the eigenfunction near the center of the annulus. Relativistic effects are included and a variety of boundary conditions and core and hot electron models have been considered. Results are discussed for the various modes that are present.

*Research sponsored by the Office of Fusion Energy, U.S. Department of Energy, under contract W-7405-eng-26 with the Union Carbide Corporation.

1. INTRODUCTION

Recently, there has been substantial interest[1-3] in the stability properties of a hot electron annulus immersed in a warm background core plasma, such as is present in the EBT device. A variety of couplings between ring and core plasma modes may exist in such a configuration, leading to instabilities that limit plasma parameters and/or enhance losses. Since the hot electron rings in an EBT device are localized to the region of the electron cyclotron resonances, the radial structure of the instability eigenmodes tends to be most significant near the rings, on the outside edge of the plasma. Slab model calculations that use simple, analytically tractable plasma profiles have indicated the importance of the radial wave number[4] on the hot electron interchange and compressional Alfvén modes. To more accurately examine such effects, we have developed a method for numerically solving the full radial eigenmode equation for realistic plasma and hot electron models. In this paper we discuss results obtained using a hot electron distribution that is a delta function in $p_{\parallel}$ (parallel momentum) and μ (magnetic moment).

This model allows us to retain the full frequency response of the hot electron perturbed pressure. Previous radially dependent results have been discussed[4] for this eigenmode equation that assumed $\Delta_B/R_c \ll 1$ in calculating the hot electron perturbed pressure and thus neglected the mode frequency, ω, and hot electron curvature drift, ω_{cvl}, in comparison with the hot electron grad-B drift, ω_{dB}. Also, in the present calculations, we have retained relativistic effects.

2. BASIC EQUATIONS

2.1 RADIAL EIGENMODE EQUATION

As discussed elsewhere, a radial eigenmode equation may be derived for curvature-driven instabilities in a plasma-hot electron ring configuration by using the momentum balance equation with ion inertial effects included, supplemented by the drift kinetic equation for the perturbed hot electron pressure. This is a second-order equation and

is given below; here it has been written in terms of the displacement ξ:

$$\xi = i\frac{\underline{E} \times \hat{b}}{\omega B} \exp(-i\omega t + ikz) \quad , \tag{1}$$

$$\frac{d}{dr}\left(rp\frac{d\xi_r}{dr}\right) - Q\xi_r = 0 \quad , \tag{2}$$

where

$$P = \frac{\lambda B^2(1 + G_1)}{DV_A^2} \quad ,$$

$$Q = \frac{rB^2}{V_A^2}\left[\frac{k^2\lambda(1 + G_1)}{D} - \frac{\omega^2\lambda}{V_A^2 D} - \frac{k^2V_A^2}{rB^2}\frac{d}{dr}(p_\parallel + p_\perp)\right.$$

$$\left. - \frac{k^2V_A^2}{r^2}(\sigma + G_2) + \frac{2\lambda\omega k(1 - G_2)}{r\omega_{ci}D} + \frac{k^2V_A^2(1 - G_2)^2}{r^2D} + \frac{V_A^2}{rB^2}\frac{d}{dr}\left(\frac{r\lambda B^2S}{V_A^2D}\right)\right] \quad ,$$

$$S = \frac{1 - G_2}{r} + \frac{\omega k(1 + G_1)}{\omega_{ci}} \quad ,$$

$$D = 1 + G_1 - \frac{\lambda}{k^2V_A^2} \quad ,$$

$$\lambda = \frac{\omega^2\omega_{ci}^2}{\omega_{ci}^2 - \omega^2} \quad ,$$

where

k = wave number along the axis of the z-pinch (corresponds to the poloidal direction in the torus),

V_A = core plasma Alfvén velocity,

p , $p_\perp$ = total (core plus hot electron ring) pressures, and

ω_{ci} = ion cyclotron frequency.

The functions G_1, G_2, and G_3 are kinetic integrals involving the distribution function:

$$G_1 = -B\sum_j \int \frac{dp_\parallel d\mu\ \mu^2}{\gamma m_j} \left[\frac{1}{B}\frac{\partial F_j}{\partial \mu} + \frac{\left(\frac{k}{m_j q_j B}\frac{\partial F_j}{\partial r} + \frac{\gamma\omega_{cv}}{p_\parallel}\frac{\partial F_j}{\partial p_\parallel}\right)}{\gamma(\omega - \omega_{DB} - \omega_{cv})} \right] \tag{3}$$

$$G_2 = -\sum_j \int \frac{dp_\parallel d\mu\ \mu}{\gamma m_j} p_\parallel^2 \left[\frac{1}{B}\frac{\partial F_j}{\partial \mu} + \frac{\left(\frac{k}{m_j q_j B}\frac{\partial F_j}{\partial r} + \frac{\gamma\omega_{cv}}{p_\parallel}\frac{\partial F_j}{\partial p_\parallel}\right)}{\gamma(\omega - \omega_{DB} - \omega_{cv})} \right] \tag{4}$$

$$G_3 = -\sum_j \int \frac{1}{B}\frac{dp_\parallel d\mu p_\parallel^4}{\gamma m_j} \left[\frac{1}{p_\parallel}\frac{\partial F_j}{\partial p_\parallel} + \frac{\left(\frac{k}{m_j q_j B}\frac{\partial F_j}{\partial r} + \frac{\gamma\omega_{cv}}{p_\parallel}\frac{\partial F_j}{\partial p_\parallel}\right)}{\gamma(\omega - \omega_{DB} - \omega_{cv})} \right] \tag{5}$$

where

$$\omega_{DB} = \frac{k\mu}{q_j m_j B\gamma}\frac{dB}{dr} ,$$

$$\omega_{cv} = -\frac{kp_\parallel^2}{q_j m_j B\gamma r} ,$$

$$c^2 p_\parallel^2 = H^2 - 2\mu Bc^2 - m_j^2 c^4 ,$$

H = the relativistic energy ,

$\mu = p_\perp^2/2B$, and

$\gamma = (1 - V^2/c^2)^{-1/2}$.

For the results to be discussed here, these integrals have been evaluated using a delta function distribution for the hot electrons,

$$F_{Hot} = \frac{\gamma_0 p_{\perp H}}{\mu_0 B^2} \delta(p_\parallel)\delta(\mu - \mu_0) , \tag{6}$$

resulting in the following:

$$G_1 = (\omega - \omega_{DB})^{-1} \{\omega[1 + \beta_\perp - \beta_{\perp H} \frac{\mu_0 B}{\gamma_0^2 m_e^2 c^2}]$$

$$- \omega_{cv\perp}[1 + r \frac{d}{dr} (\frac{p_\perp c}{B^2})]\} - 1,$$

$$G_2 = \beta_\parallel c/2 , \tag{7}$$

$$G_3 = 3\beta_\parallel c/2 ,$$

where

$$\omega_{cv\perp} = - \frac{k\mu_0}{em_e\gamma_0 r} ,$$

$$\omega_{DB} = \frac{k\mu_0}{em_e\gamma_0 B} \frac{dB}{dr} .$$

These integrals have been evaluated for other models, such as a Maxwellian, but only the above case is considered here.

2.2 EQUILIBRIUM MODEL

The equilibrium quantities that enter directly into Eq. (2) are the hot electron perpendicular pressure, $p_{\perp H}$; the core electron pressure, p_c; the core electron temperature, T_c; the core ion density, n_i; and the magnetic field, B. Since the magnetic moment is a fixed value for the distribution function under consideration, the radial profile of the hot electron relativistic energy is determined completely by specifying its value at one point (taken here to be at the plasma edge) and the equilibrium magnetic field.

The hot electron and core electron pressure profiles are

$$p_{\perp H} = p_{\perp H_0} \begin{cases} 0 & x < -x_0 \\ \dfrac{(x - x_0)^4 (x + x_0)^4}{x_0^8} & -x_0 < x < x_0 \\ 0 & x > x_0 \end{cases} , \qquad (8)$$

$$p_c = p_{co} \begin{cases} 1 & x < 0 \\ (1-S) \dfrac{(x - x_0)^4 (x + x_0)^4}{x_0^8} + S & 0 < x < x_0 \\ S & x > x_0 \end{cases} , \qquad (9)$$

where

$$x = \frac{r - r_0}{\Delta} ,$$

Δ = hot electron annulus half-width,

X_0 = extent of the pressure profiles,

(measured in units of Δ), and

S = density shelf factor.

Such forms for the profiles have been chosen because they have gradients exactly equal to zero on the inside and outside of the ring. Also, these profiles have continuous first and second derivatives, which are required in evaluating the final term in the coefficient Q of Eq. (2). The core electron temperature profile is chosen to be a constant, T_{co}. The core ion density is given by:

$$n_i = n_e + n_{Hot} \quad , \tag{10}$$

where

$$n_e = \frac{p_c}{T_{co}}$$

and

$$n_{Hot} = \frac{2\gamma_0 p_{\perp H}}{e m_0 c^2 (\gamma_0^2 - 1)}$$

Examples of the core ion density and hot electron beta profiles are presented in Fig. 1.

It is noted that this choice of profiles will exclude certain instability modes. These are core plasma pressure-driven-gradient modes, driven by gradients on the inside half of the hot electron ring, and instabilities driven by gradients in the cold surface plasma region outside the rings.

The magnetic field profile has been obtained here by using an equilibrium equation appropriate to the z-pinch model, i.e., with the magnetic field line radius of curvature taken to be the radial variable, r. This equation is then written as follows

$$\frac{1}{r^2}\frac{d}{dr}\left(r^2\frac{B^2}{2\mu_0}\right) = -\frac{dp_\perp}{dr} - \frac{p_{\perp H}}{r} \quad , \tag{11}$$

where μ_0 = vacuum magnetic permeability = $4\pi \times 10^{-7}$.
The solution for B may be expressed in terms of integrals over the core and hot electron pressure profiles,

$$B = \frac{1}{r}\left[r_i^2 B_i^2 - 2r^2\mu_0(p_{\perp H} + p_{\perp c}) + 2\mu_0\int_{r_i}^{r} r'dr'(p_{\perp H} + 2p_{\perp c})\right]^{1/2} \quad , \tag{12}$$

where B_i is the magnetic field specified at some fixed radial location r_i (here taken to be on the outside of the hot electron ring). The first and second derivatives of B are then given as

$$\Delta_B^{-1} = \frac{1}{B}\frac{dB}{dr} = -\frac{1}{r} - \frac{\mu_0}{B^2}\frac{dp_\perp}{dr} - \frac{\mu_0 p_{\perp H}}{rB^2} \quad , \tag{13}$$

$$\frac{1}{B}\frac{d^2B}{dr^2} = \frac{1}{r^2} + \frac{1}{\Delta_B^2} + \frac{2\mu_0}{B^2\Delta_B}\left(\frac{dp_\perp}{dr} + \frac{p_{\perp H}}{r}\right)m + \frac{\mu_0}{B^2}\left(\frac{p_{\perp H}}{r^2} - \frac{d^2p_\perp}{dr^2} - \frac{1}{r}\frac{dp_{\perp H}}{dr}\right) \quad . \tag{14}$$

Typical profiles of B and Δ_B^{-1} are plotted in Fig. 1 for several different values of β_{Hot}.

2.3 NUMERICAL METHOD AND BOUNDARY CONDITIONS

The numerical procedure for solving Eq. (2) is based on the SUPORT[5] code. This solves linear two-point boundary value problems; the method of superposition coupled with orthonormalization of the homogeneous equation basis functions (when linear dependence becomes present) is employed. In using SUPORT, Eq. (2) is broken into the two parts:

$$\frac{dy_1}{dr} = \frac{y_2}{rP} \quad ,$$

$$\frac{dy_2}{dr} = Qy_1 \quad , \tag{15}$$

where $y_1 = \xi$ and $y_2 = P\frac{d\xi}{dr}$. When y_1 and y_2 are separated into real and imaginary parts, a system of four coupled first-order equations results, which is the form actually solved by the code. This system is then solved on the intervals r_{min} to r_0 and r_0 to r_{max}. The condition which determines the eigenvalue is matching of the derivative of y_1 at $r = r_0$ (center of the hot electron ring). This results in a dispersion relation of the form

$$D(\omega) = \frac{dy_1}{dr}\Big|_{r=r_0^+} - \frac{dy_1}{dr}\Big|_{r=r_0^-} = 0 \quad . \tag{16}$$

This equation has been solved by using a first-order Newton's method to obtain ω. In obtaining marginal stability boundaries, a somewhat different procedure is used in order to avoid a lengthy following of the unstable roots. This method uses the fact that at marginal stability ω is purely real and thus $D(\omega)$ is real (in the case in which the waves are evanescent outside the ring region). Marginal stability is then given by setting $D_r(\omega,p)$ and $\partial D/\partial\omega$ equal to zero and solving for the real part of ω and the parameter p (e.g., core density) which

determines the nearness to marginal stability. In practice, a two-step computational cycle may be used:

$$p_1 = \frac{D(p_0,\omega_0)p_{-1} - D(p_{-1},\omega_0)p_0}{D(p_0,\omega_0) - D(p_{-1},\omega_0)} , \tag{17}$$

$$\omega_1 = \frac{D_\omega(p_1,\omega_0)\omega_{-1} - D_\omega(p_1,\omega_{-1})\omega_0}{D_\omega(p_1,\omega_0) - D_\omega(p_1,\omega_{-1})} , \tag{18}$$

where the -1, 0, and 1 subscripts refer to the initial guess, intermediate point, and updated guess, respectively. The derivatives D_ω are calculated numerically using centered differences.

The boundary conditions on the eigenfunction ξ at r_{min} and r_{max} are derived from the differential equation by assuming outgoing plane waves. Since the coefficients are nearly constant outside the annulus region [if terms of $O(1/r)$ and higher may be neglected], solutions of the form $\xi \sim \exp(ik_x x)$ may be used. k_x is then given as

$$k_x = \pm i\Delta\sqrt{\frac{Q}{rP}} . \tag{19}$$

In order to pick the appropriate sign here, two conditions have been used. If k_x is largely real, then an outgoing energy condition is used. This is obtained by calculating $\partial\omega/\partial k_x$ using Eq. (19). Since $\partial\omega/\partial k_x$ scales as k_x, picking one of the signs in (19) will result in outgoing energy. On the other hand, if k_x is mostly imaginary, then the waves are required to be evanescent at the boundary, i.e., $Im(k_x) < 0$ for $x < 0$ and $Im(k_x) > 0$ for $x > 0$. In general, unstable and marginally stable roots will fall into the latter category (evansecent boundary conditions). Once k_x is picked, then y_1 is required to satisfy a derivative boundary condition $\frac{1}{y_1}\frac{dy_1}{dx} = ik_x$ at $r = r_{min}$ and $r = r_{max}$.

3. RESULTS

Solutions of Eq. (2) are discussed here for two types of instability: the hot electron interchange and the compressional Alfvén mode. In addition, other modes have been found, such as the Nelson-Van Dam-Lee interchange mode. However, there has not been time to sufficiently map out the stability boundaries for this mode yet, so it is not discussed here. The hot electron interchange and compressional Alfvén modes are relatively insensitive to the core temperature, so low core temperatures have been assumed in most of these calculations in order to exclude the Nelson-Van Dam-Lee mode at the higher core densities.

An example of the dependence of the real and imaginary parts of the eigenfrequency on core density is shown in Fig. 2. This is for an azimuthal mode number m = 10 (azimuthal here refers to the direction the small way around the torus — or along the axis of the z-pinch) and $n_{Hot} = 5 \times 10^{11}$ cm^{-3}, $T_{Hot} = 500$ keV. Other parameters are taken as typical of EBT-S. As may be seen, there is a mode that is stabilized by increasing core density (identified as the hot electron interchange mode) and a second mode that is stabilized by decreasing the core density (identified as the compressional Alfvén mode). Between the marginal stability points of these modes, there is a stable window where both modes are stable. A second example of the dependence of these two modes on core density is shown in Fig. 3 for m = 5. Here it may be seen that the marginal stability points for both modes have intersected, resulting in a loss of the stable window. Such a deterioration of the window has also been observed in analytic calculations[4] that assume a fixed radial eigenfunction based on an approximation to the differential Eq. (2); this eigenfunction had an effective radial wave number of $k_r = 2/\Delta$. Results from such calculations for EBT-S are shown in Fig. 4 for mode numbers m = 1, 3, 6, 8, 12, and 20, taking a fixed core electron and ring temperature and varying the core and hot electron densities.

In order to make comparisons between the stability boundaries of Fig. 4 and those predicted from the radial shooting code, it is desirable to lower the number of free parameters used in Fig. 4. This can be accomplished by considering only a few values of hot electron density (since the boundaries are not strongly dependent on this variable) and plotting the core density vs the azimuthal mode number (on which the stability boundaries do have a strong dependence). Such a plot for the analytic local stability boundaries is shown in Fig. 5 for $n_{Hot} = 3 \times 10^{11}$ cm^{-3} and 5×10^{11} cm^{-3}.

As discussed in Sect. 2.3, the marginal stability boundaries can be followed with the shooting calculation by starting out at known marginal points, such as those given in Figs. 2 and 3, and then gradually changing parameters and following the roots. In doing this, the imaginary part of ω must be set to some fixed small value. Here $\omega_{imag}/\omega_{ci} = 0.1$ has been assumed, which is generally less than one-tenth of the real part of ω at the marginal boundaries. Smaller values can be used; however, setting ω_i exactly equal to zero at the marginal boundaries can result in numerical difficulties due to the singularities (i.e., at $D = 0$ and $1 + G_1 = 0$) that can be present in Eq. (2) when ω is purely real. The resulting nonlocal stability boundaries are shown in Fig. 6 for $n_{Hot} = 3 \times 10^{11}$ cm^{-3} and 5×10^{11} cm^{-3}. Comparing these with the boundaries of Fig. 5 indicates that at high m values ($m > 5$) the nonlocal boundaries give a larger stability window than the local results. However, at low m values ($m < 5$) the nonlocal calculations do not give any window such as that present in the results of Fig. 5. The reasons behind this have to do with the form taken by the eigenfunctions as m changes. In Figs. 7 and 8 eigenfunctions are plotted as a function of position within the annulus and azimuthal mode number ($m = 1, 3, 5, 10$) for the hot electron interchange and compressional Alfvén modes, respectively. As may be seen, for both cases the eigenfunctions become significantly flatter as m is lowered. It is then not surprising that the nonlocal and local calculations (which assume a fixed value of $k_r = 2/\Delta$, independent of m) disagree at low values of m. At $m < 5$ the eigenfunctions are similar in form to that assumed in the layer modes, which have been examined analytically in another paper in this proceedings.[6] These modes are

generally predicted to be unstable at low m for the parameters used in Fig. 6. It should be noted that the boundary conditions used in the nonlocal calculation would be expected to break down for the low m numbers, particularly at m = 1. If the eigenfunction were followed further into the core plasma, it is expected that it would extend progressively further into the center as m is decreased. Such a result was reported recently[1,7] where Eq. (2) was solved all the way into r = 0. Matching onto a plane wave solution as assumed in the outgoing energy/evanescent boundary conditions then becomes a poor approximation at low m, since the cylindrical geometry will begin to have an important influence on the wave structure. Such considerations probably limit the validity of the present calculation to $m \geq 3$.

Other factors that make the present calculation inapplicable to low m numbers are coupling to the shear Alfvén wave and the fact that variation of the equilibrium quantities along the field lines has not been taken into account. In order to include these factors, the appropriate parallel wavelength for the shear Alfvén wave will have to be determined. If the periodicity length is once around the torus, $\lambda_{\parallel} = 2\pi R_0$, then $k_{\parallel} \ll k$ and the shear Alfvén wave coupling may not have much influence. However, if the parallel wavelength is of the order of the mirror sector length or the annulus length, then $k_{\parallel}$ is greater than k for a finite range of the lower m numbers ($m < 3$ for sector length and $m < 7$ for ring length), and coupling to the shear Alfvén wave could significantly modify the stability results presented here.

ACKNOWLEDGMENTS

The authors would like to gratefully acknowledge assistance from John Whitson of UCC-ND Computer Sciences at Oak Ridge National Laboratory in the use of the SUPORT code and the Newton's root solver. We also have benefited from useful discussions with Adel El-Nadi.

The work of D. A. Spong was supported by the U.S. Department of Energy under contract W-7405-eng-26 with the Union Carbide Corporation. The work of J. W. Van Dam, H. L. Berk, and M. N. Rosenbluth was supported by the U.S. Department of Energy under contract DE-FG-80-ET-53088 with the University of Texas.

REFERENCES

1. A. M. El Nadi and K. T. Tsang, "The Radial EBT Stability Problem," paper presented at the Annual Controlled Fusion Theory Conference, April 8-10, 1981, Austin, Texas (Abstract 1B3); also, see A. M. El Nadi, "The Compressional Alfvén Mode for Realistic EBT Plasmas," Bull. Am. Phys. Soc. 26, Abstract 6U18 (1981).

2. H. L. Berk, "EBT Stability Theory," paper presented at the U.S.-Japan Workshop on the Theory of Non-Axisymmetric Confinement Systems, Austin, Texas, December 8-11, 1980.

3. K. T. Tsang and C. Z. Cheng, "Stability of Hot Electron Plasma in the ELMO Bumpy Torus," in the EBT Stability Theory: Proc. of the Workshop, Oak Ridge National Laboratory Report CONF-810512 (September 1981).

4. J. W. Van Dam, H. L. Berk, M. N. Rosenbluth, and D. A. Spong, "Radially Dependent Stability Theory for EBT," in EBT Stability Theory: Proc. of the Workshop, Oak Ridge National Laboratory Report CONF-810512 (September 1981); also, in the same proceedings, D. A. Spong, J. W. Van Dam, H. L. Berk, and M. N. Rosenbluth, "Numerical Solutions of the EBT Radial Eigenmode Problem."

5. M. R. Scott and H. A. Watts, SIAM J. Numer. Anal. 14, 40 (1977).

6. H. L. Berk, M. N. Rosenbluth, J. W. Van Dam, and D. A. Spong, "Curvature Induced Modes in a Hot Electron Plasma," paper presented at the Second EBT Ring Physics Workshop, December 1-3, 1981, Oak Ridge, Tennessee.

7. D. A. Spong, J. W. Van Dam, H. L. Berk, and M. N. Rosenbluth, "Numerical Solutions of the EBT Radial Eigenmode Problem," Bull. Am. Phys. Soc. 26, Abstract 6U16 (1981).

FIGURE CAPTIONS

Fig. 1. Profiles of core plasma density, hot electron beta, magnetic field, and magnetic gradient for parameters typical of EBT-S.

Fig. 2. Real and imaginary parts of the eigenfrequency ω as a function of core plasma density for $m = 10$, $n_{Hot} = 5 \times 10^{11}$ cm^{-3}, $T_{Hot} = 500$ keV.

Fig. 3. Real and imaginary parts of the eigenfrequency ω as a function of core plasma density for $m = 5$, $n_{Hot} = 5 \times 10^{11}$ cm^{-3}, $T_{Hot} = 500$ keV.

Fig. 4. Localized EBT-S stability boundaries as a function of β_{core} and β_{Hot} for $m = 1, 3, 6, 8, 12, 20$ with $T_{core} = 200$ eV, $T_{Hot} = 500$ keV.

Fig. 5. Localized EBT-S stability boundaries as a function of azimuthal mode number for $n_{Hot} = 3 \times 10^{11}$ cm^{-3} and 5×10^{11} cm^{-3}.

Fig. 6. Nonlocal EBT-S stability boundaries as a function of azimuthal mode number for $n_{Hot} = 3 \times 10^{11}$ cm^{-3} and 5×10^{11} cm^{-3}.

Fig. 7. Radial eigenfunctions for the hot electron interchange mode as a function of azimuthal mode number for $n_{Hot} = 5 \times 10^{11}$ cm^{-3}, $n_{core} = 1 \times 10^{12}$ cm^{-3}, $T_{Hot} = 500$ keV, $T_{core} = 1$ eV.

Fig. 8. Radial eigenfunctions for the compressional Alfvén mode as a function of azimuthal mode number for $n_{Hot} = 5 \times 10^{11}$ cm^{-3}, $n_{core} = 6 \times 10^{13}$ cm^{-3}, $T_{Hot} = 500$ keV, $T_{core} = 1$ eV.

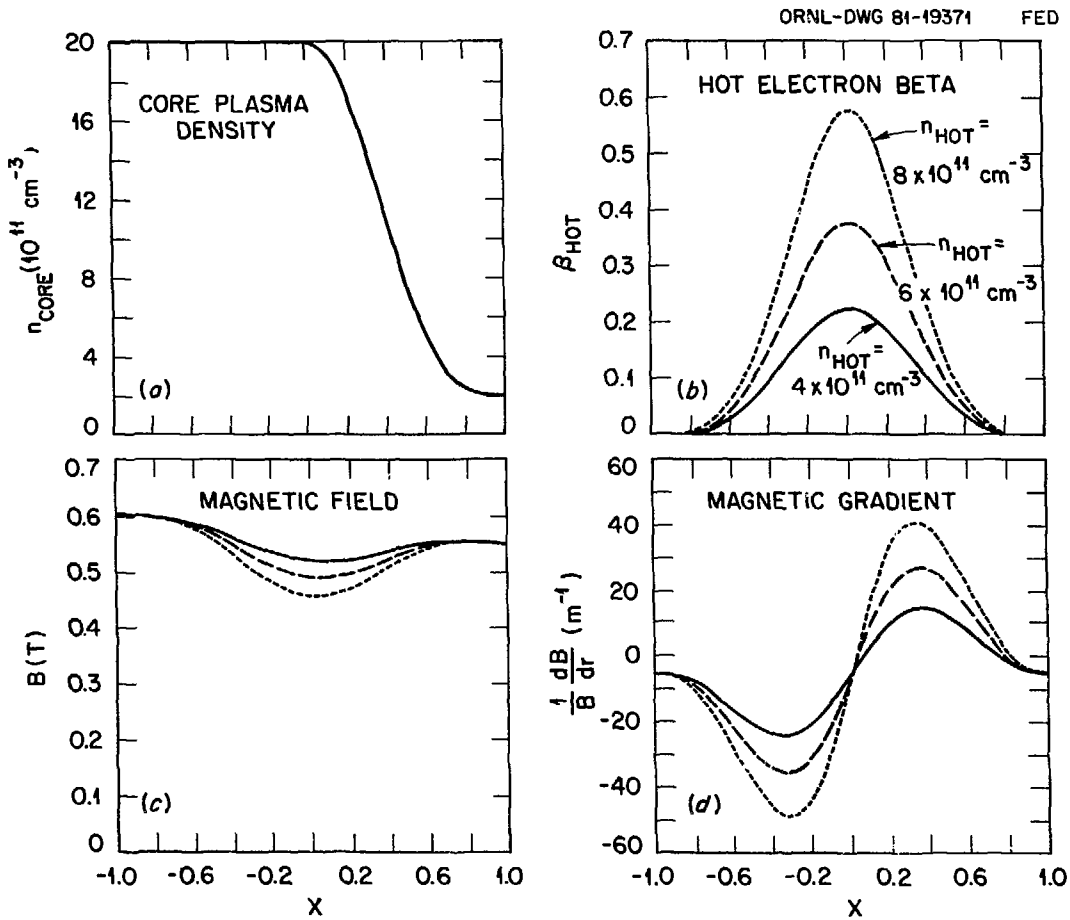
ORNL-DWG 81-19371 FED
CORE PLASMA DENSITY
$n_{CORE}(10^{11}\ cm^{-3})$
(a)
HOT ELECTRON BETA
β_{HOT}
$n_{HOT} = 8 \times 10^{11}\ cm^{-3}$
$n_{HOT} = 6 \times 10^{11}\ cm^{-3}$
$n_{HOT} = 4 \times 10^{11}\ cm^{-3}$
(b)
MAGNETIC FIELD
B (T)
(c)
MAGNETIC GRADIENT
$\frac{1}{B}\frac{dB}{dr}\ (m^{-1})$
(d)
X
X

Fig. 1

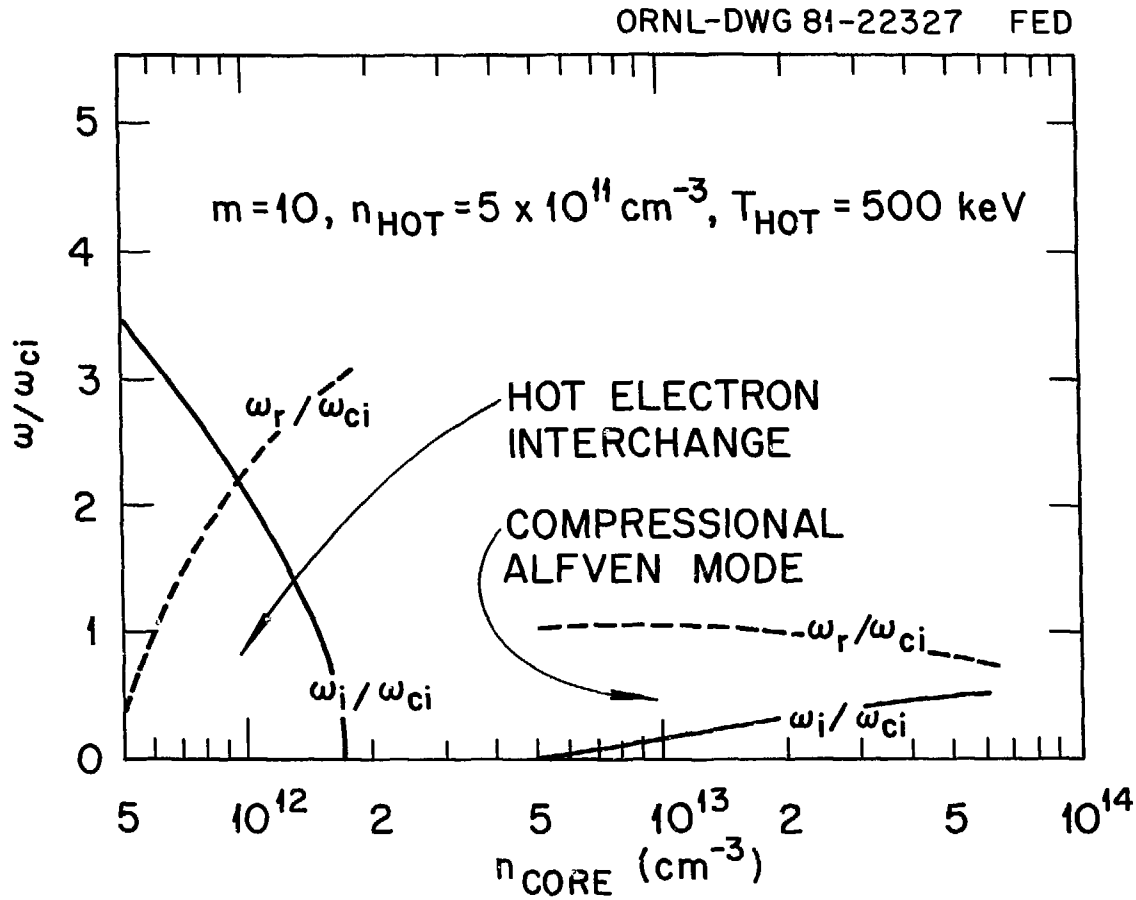
ORNL-DWG 81-22327 FED
m = 10, $n_{HOT} = 5 \times 10^{11}$ cm^{-3}, T_{HOT} = 500 keV
ω/ω_{ci}
ω_r/ω_{ci}
ω_i/ω_{ci}
HOT ELECTRON INTERCHANGE
COMPRESSIONAL ALFVEN MODE
ω_r/ω_{ci}
ω_i/ω_{ci}
0
1
2
3
4
5
5
10^{12}
2
5
10^{13}
2
5
10^{14}
n_{CORE} (cm^{-3})

Fig. 2

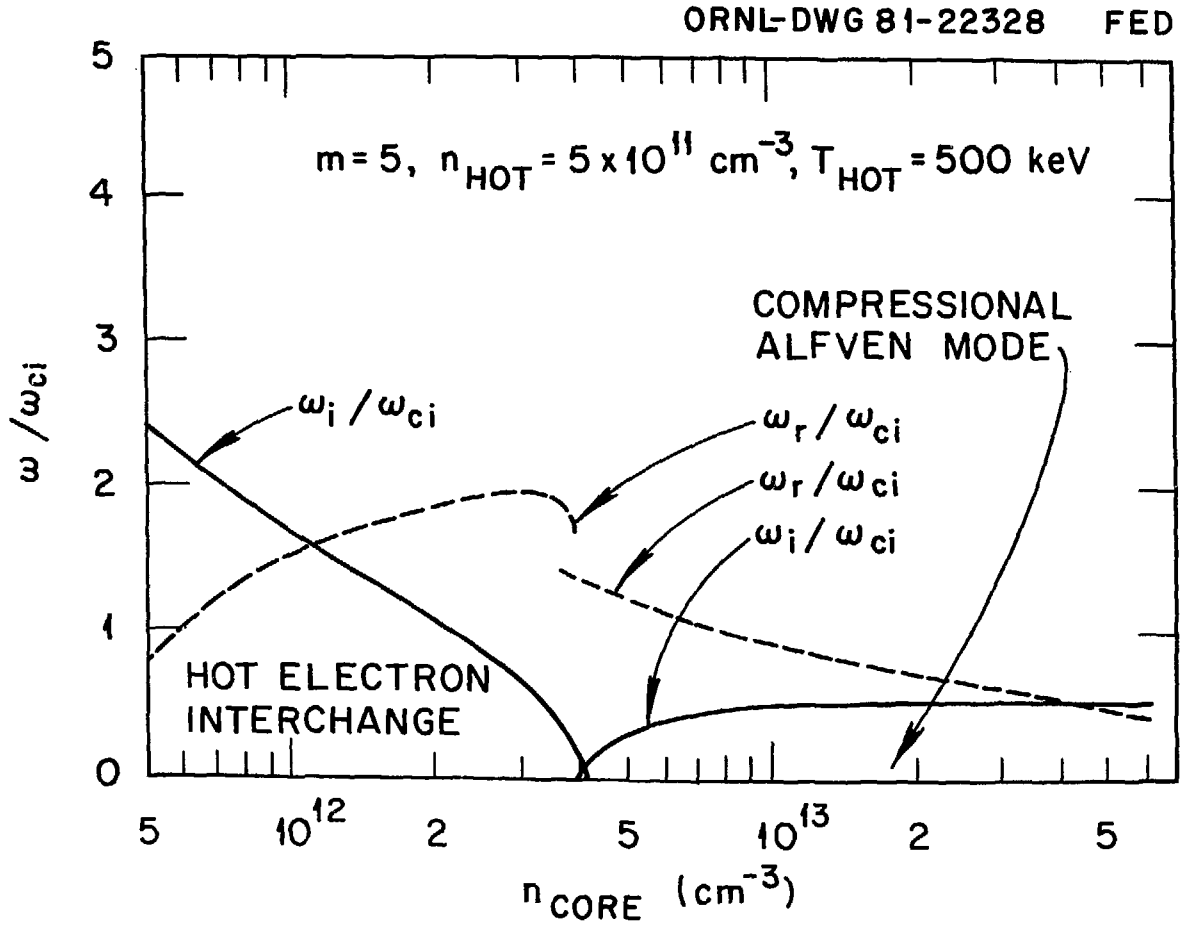
ORNL-DWG 81-22328 FED
m = 5, $n_{HOT} = 5 \times 10^{11}$ cm^{-3}, T_{HOT} = 500 keV
COMPRESSIONAL ALFVEN MODE
ω_i / ω_{ci}
ω_r / ω_{ci}
ω_r / ω_{ci}
ω_i / ω_{ci}
HOT ELECTRON INTERCHANGE
ω / ω_{ci}
0
1
2
3
4
5
5
10^{12}
2
5
10^{13}
2
5
n_{CORE} (cm^{-3})

Fig. 3

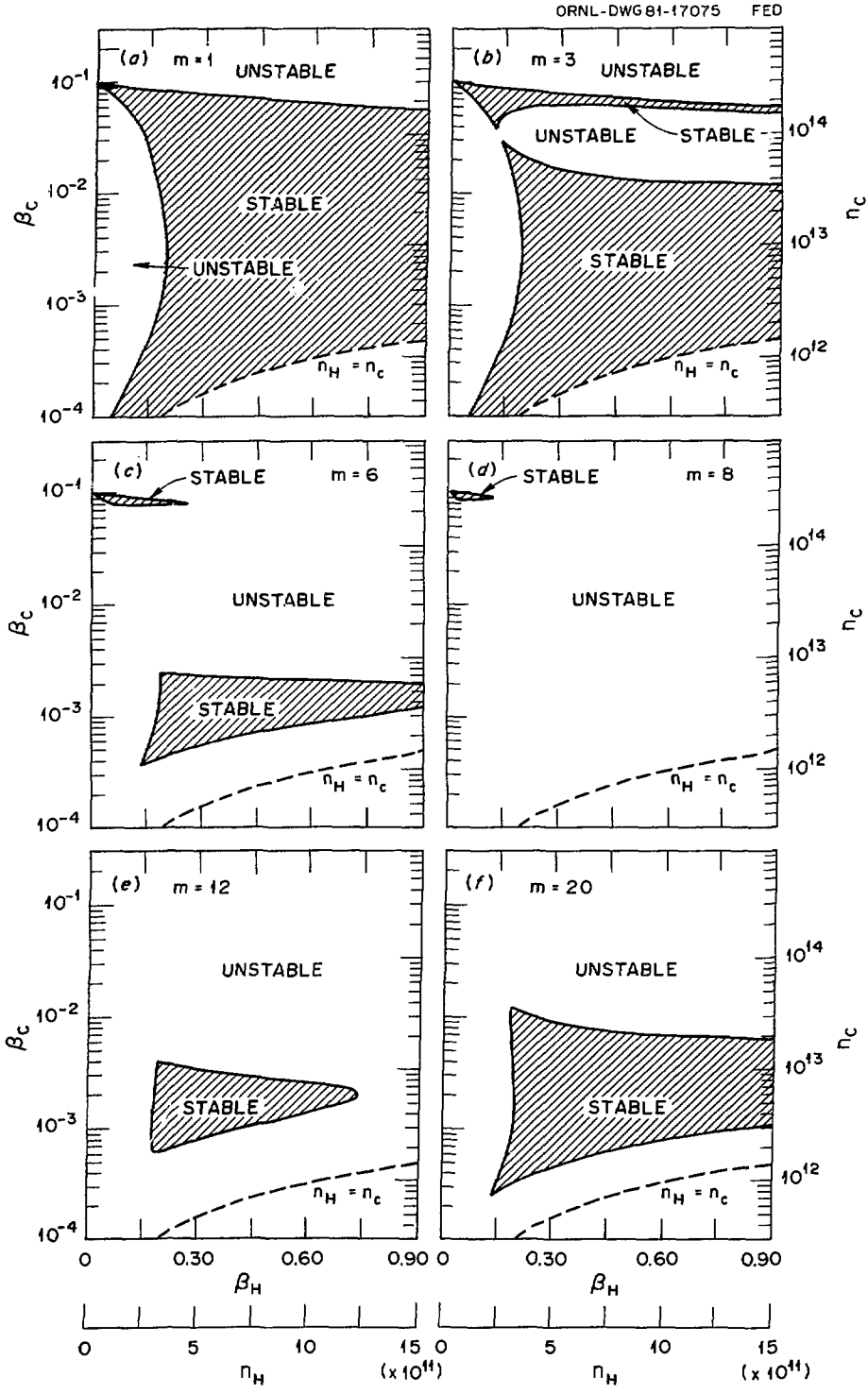
ORNL-DWG 81-17075 FED
(a) m = 1
UNSTABLE
STABLE
UNSTABLE
$n_H = n_c$
(b) m = 3
UNSTABLE
UNSTABLE
STABLE
STABLE
$n_H = n_c$
(c) STABLE m = 6
UNSTABLE
STABLE
$n_H = n_c$
(d) STABLE m = 8
UNSTABLE
$n_H = n_c$
(e) m = 12
UNSTABLE
STABLE
$n_H = n_c$
(f) m = 20
UNSTABLE
STABLE
$n_H = n_c$
β_c
10^{-1}
10^{-2}
10^{-3}
10^{-4}
n_c
10^{14}
10^{13}
10^{12}
0
0.30
0.60
0.90
β_H
0
5
10
15
n_H
$(\times 10^{11})$

Fig. 4

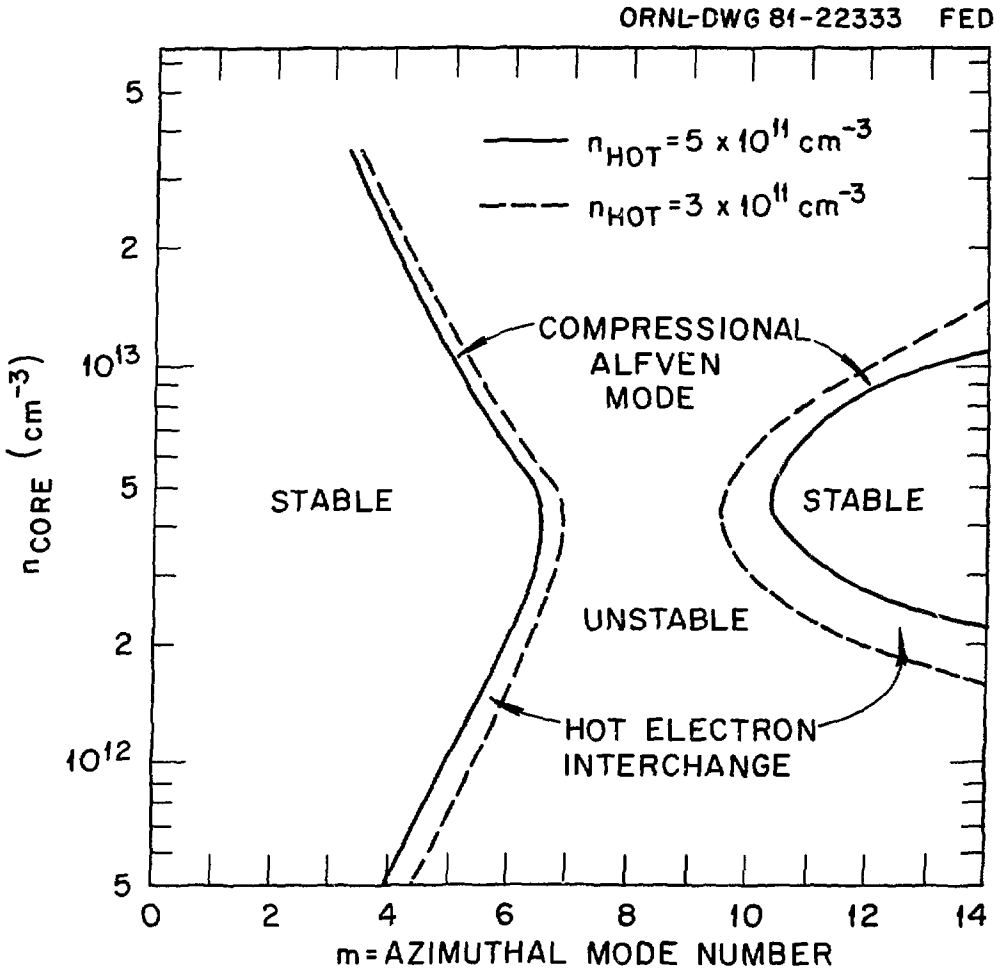
ORNL-DWG 81-22333 FED
$n_{HOT} = 5 \times 10^{11}$ cm^{-3}
$n_{HOT} = 3 \times 10^{11}$ cm^{-3}
COMPRESSIONAL ALFVEN MODE
STABLE
STABLE
UNSTABLE
HOT ELECTRON INTERCHANGE
n_{CORE} (cm^{-3})
5
2
10^{13}
5
2
10^{12}
5
0
2
4
6
8
10
12
14
m = AZIMUTHAL MODE NUMBER

Fig. 5

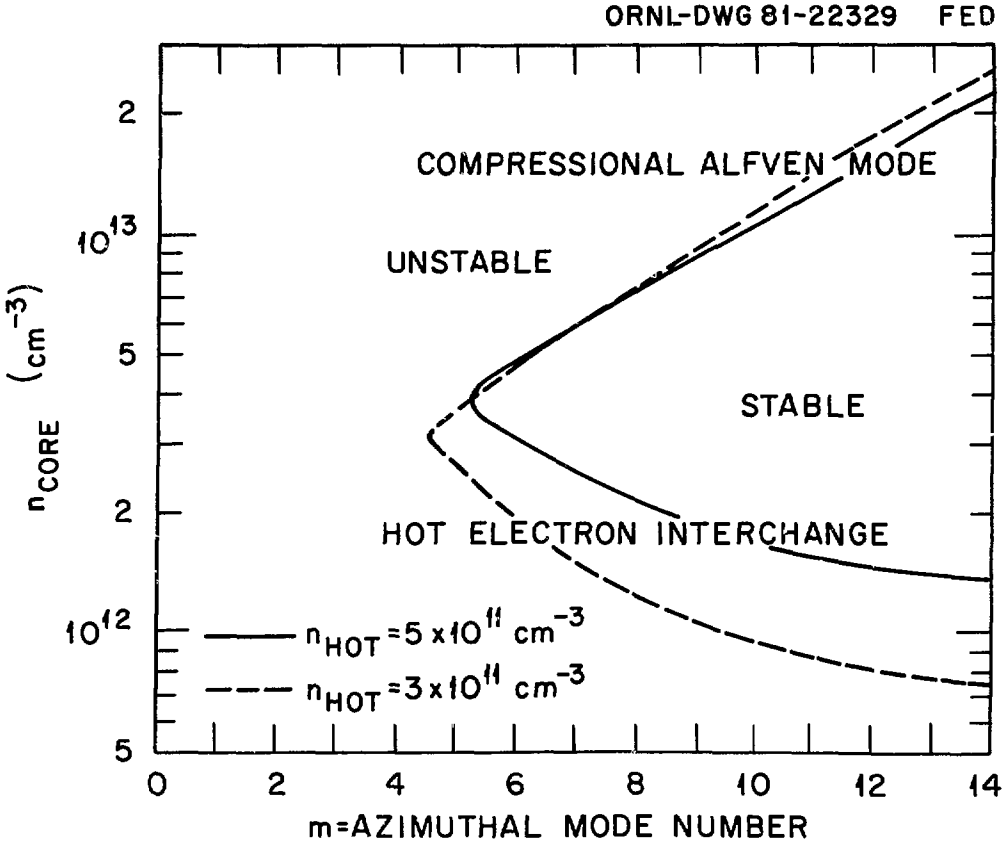
ORNL-DWG 81-22329 FED
COMPRESSIONAL ALFVEN MODE
UNSTABLE
STABLE
HOT ELECTRON INTERCHANGE
$n_{HOT} = 5 \times 10^{11}$ cm^{-3}
$n_{HOT} = 3 \times 10^{11}$ cm^{-3}
n_{CORE} (cm^{-3})
2
10^{13}
5
2
10^{12}
5
0
2
4
6
8
10
12
14
m=AZIMUTHAL MODE NUMBER

Fig. 6

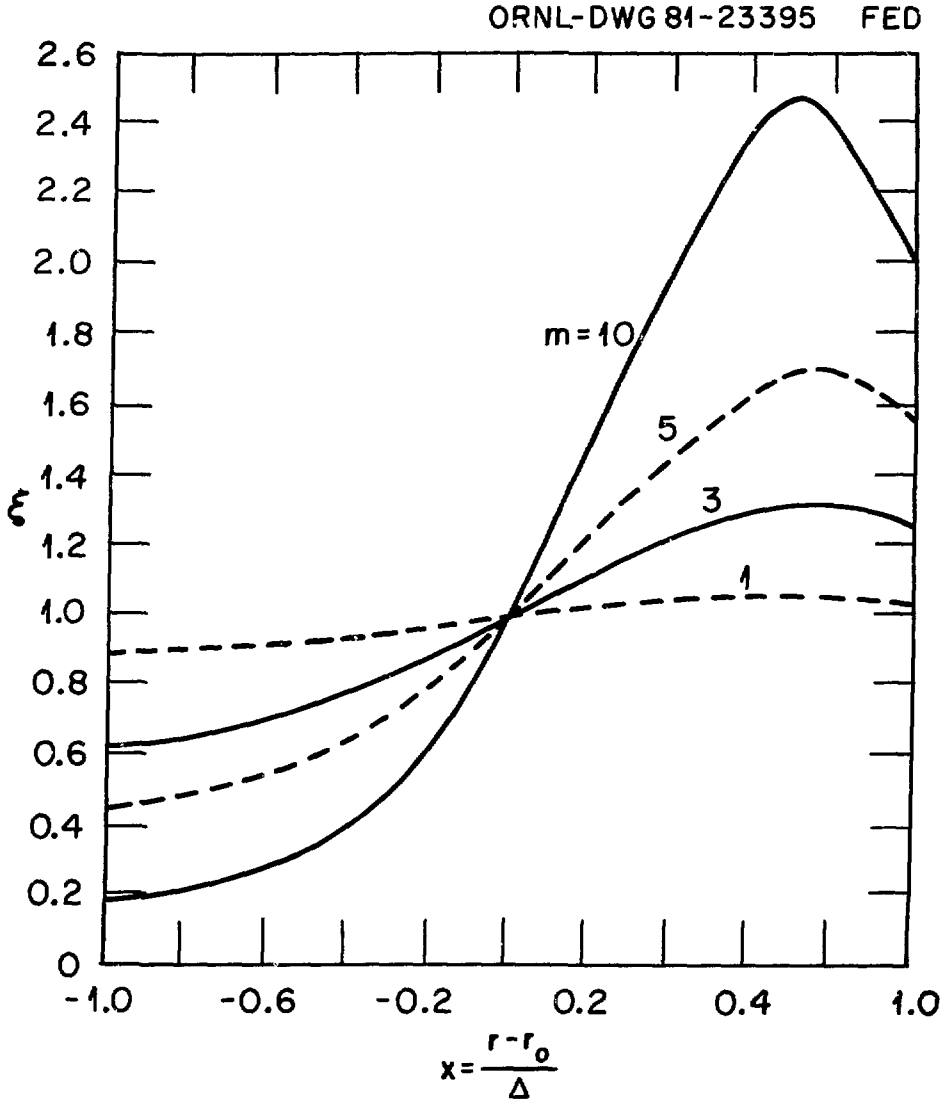
ORNL-DWG 81-23395 FED
2.6
2.4
2.2
2.0
1.8
1.6
1.4
1.2
1.0
0.8
0.6
0.4
0.2
0
ξ
m = 10
5
3
1
-1.0
-0.6
-0.2
0.2
0.4
1.0
x = (r - r_o)/Δ

Fig. 7

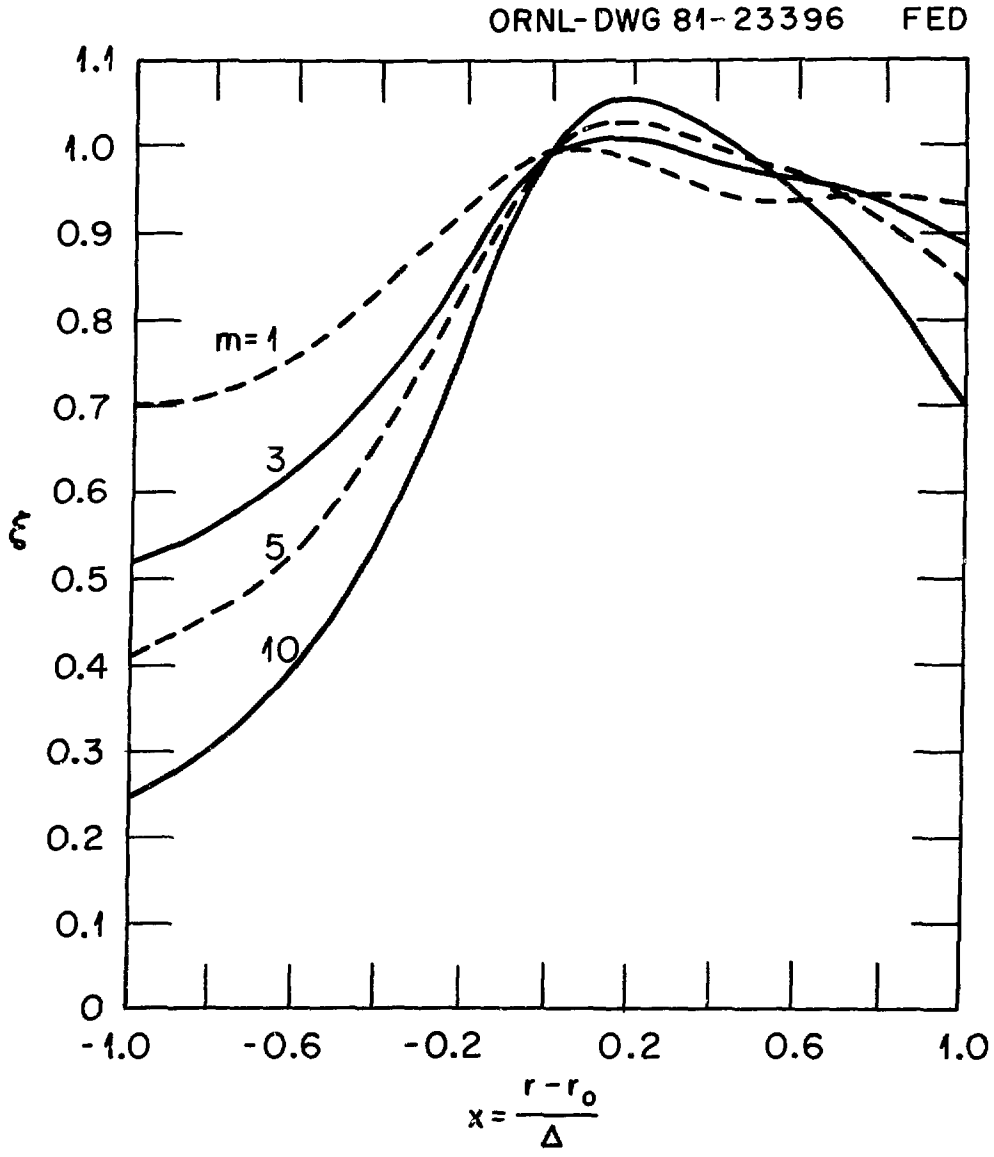
ORNL-DWG 81-23396 FED
1.1
1.0
0.9
0.8
0.7
0.6
0.5
0.4
0.3
0.2
0.1
0
ξ
m=1
3
5
10
-1.0
-0.6
-0.2
0.2
0.6
1.0
x = (r - r₀)/Δ

Fig. 8

STABILITY OF LOW FREQUENCY MODES IN A HOT ELECTRON BUMPY TORUS

K. T. Tsang and P. J. Catto
Science Applications, Inc.
Plasma Research Institute
934 Pearl Street
Boulder, Colorado 80302

ABSTRACT

The system of equations appropriate for describing low frequency modes ($\omega < \Omega_i$) in general geometry for a three-species plasma is derived. The derivation employs an eikonal ansatz and for simplicity assumes Maxwellian unperturbed distribution functions, but permits arbitrary beta and asymmetry. The full system of equations includes ballooning, interchange and compressional Alfvén modes. As examples, two limits of the general results are employed to study EBT stability. The first example, a local analysis of the high phase velocity ring model, leads to analytic estimates of stability boundaries due to interchange and compressional Alfvén modes, which agree with numerical solutions. In the second example, the hot electrons are treated as a trapped species and, in the limit of pure magnetic perturbations, the magnetic trapped particle mode is recovered.

1. INTRODUCTION

The stability studies[1-5] of the ring-core plasma system in the ELMO Bumpy Torus have thus far been limited to local or radial analyses. The ballooning nature of the eigenmodes along the field line (that is, the coupling to the shear Alfvén wave) are ignored due to shortcomings of the slab geometry and/or the cold ion fluid model used in these studies.

In this work, a set of coupled eigenmode equations retaining the ballooning-interchange and the compressional Alfvén modes is derived using the gyrokinetic technique of Catto, Tang and Baldwin.[6] The advantages of this approach are that general geometry can be handled easily, and the final equations are applicable to devices other than EBT's (e.g., tandem mirrors). The set of coupled eigenmode equations presented here are also complementary to the kinetic energy principles of Antonsen, et al.[7] and Van Dam, et al.[8] but with the advantage that the results need not be restricted by assuming the conservation of the longitudinal and flux invariants.

In the following, we first sketch the derivation of the eigenmode equations from the gyro-averaged Vlasov equation. The details of this derivation are presented elsewhere.[9] This set of eigenvalue equations is then analysed in the local limit. The interchange and compressional Alfvén mode dispersion relation is then reduced to a quartic equation which can be solved analytically in the most interesting limits. The Nelson-Van Dam-Lee result[1,2] is recovered in the appropriate limit. However, the resulting beta limit is not compatible with the beta limit imposed by the compressional Alfvén mode unless the finite frequency

shift due to the rings is retained. Finally the ballooning nature of the mode is retained and the hot electrons are treated as a trapped species. A magnetic trapped particle instability is then possible as was first pointed out by Rosenbluth.[10] However, the finite frequency shift and the coupling to the ballooning-interchange retained here are expected to change the stability limits of this mode significantly.

2. BASIC MODEL

To simplify the derivation we assume the equilibrium distribution functions for the three species (ions, background electrons and hot electrons) are Maxwellians, denoted by $F_j = N_j(m_j/2\pi T_j)^{3/2} \exp(-m_j v^2/2T_j)$, where j is the subscript distinguishing different species (i, e, and h) and m, N, T are the species mass, density and temperature, respectively. The perturbed field quantities are the electrostatic potential $\tilde{\Phi}$ and vector potential $\tilde{\underset{\sim}{A}}$. For any perturbed quantity Q, we employ the eikonal ansatz

$$Q(\underset{\sim}{r}) = \tilde{Q}(\underset{\sim}{r}) \exp[iS(\underset{\sim}{r}) - i\omega t] \quad , \tag{1}$$

with $\hat{\underset{\sim}{n}}\cdot\underset{\sim}{\nabla}S = 0$, $\underset{\sim}{k}_\perp \equiv \underset{\sim}{\nabla}S$, and $\tilde{Q}$ satisfying $k_\perp \equiv |\underset{\sim}{k}_\perp| >> k_\parallel \equiv |\hat{\underset{\sim}{n}}\cdot\underset{\sim}{\nabla}\ln\tilde{Q}|$ and $k_\perp >> |\underset{\sim}{\nabla}_\perp \ln\tilde{Q}|$, where $\hat{\underset{\sim}{n}} = \underset{\sim}{B}/B$ is the unit vector along the unperturbed magnetic field $\underset{\sim}{B}$ and $B \equiv |\underset{\sim}{B}|$.

Defining a displacement $\tilde{\underset{\sim}{\xi}}$ via $\tilde{\underset{\sim}{\xi}} = (c\tilde{\Phi}/\omega B)\underset{\sim}{k}_\perp \times \hat{\underset{\sim}{n}}$, the perturbed distribution function f_j can be written as[6,11]

$$\tilde{f}_j = -\frac{Z_j e}{T_j}\tilde{\Phi} F_j[1 - J_0 \exp(-iL_j)]$$

$$- J_0 \underset{\sim}{\tilde{\xi}} \cdot \underset{\sim}{\nabla} F_j \exp(-iL_j) + (\tilde{h}_j + \tilde{g}_j) \exp(-iL_j) , \qquad (2)$$

where $\tilde{h}_j$ satisfies the gyrokinetic equation

$$v_{\parallel} \underset{\sim}{\hat{n}} \cdot \underset{\sim}{\nabla} \tilde{h}_j - i(\omega - \omega_{dj})\tilde{h}_j = -\frac{Z_j e}{T_j} F_j \left[1 - (\omega_{*j}^T/\omega)\right] \times$$

$$\left[i(\omega_d \tilde{\Phi} J_0 + \frac{\omega v_\perp}{k_\perp c}\tilde{B}_{\parallel} J_1) + J_0 v_{\parallel}(\underset{\sim}{\hat{n}} \cdot \underset{\sim}{\nabla}\tilde{\Phi} - \frac{i\omega}{c}\tilde{A}_{\parallel}) + v_{\parallel}\tilde{\Phi}\underset{\sim}{\hat{n}} \cdot \underset{\sim}{\nabla} J_0\right] , \qquad (3)$$

with $\tilde{B}_{\parallel} = i\underset{\sim}{\hat{n}} \times \underset{\sim}{k}_\perp \cdot \underset{\sim}{\tilde{A}}$. The quantity $\tilde{g}_j$ is the gyrophase dependent correction to $\tilde{h}_j$ and therefore higher order in ω/Ω_j so that $\exp(-iL_j) \approx 1$ may be employed. We need only retain the ion contribution $\tilde{g}_i$ in the following because $|\Omega_e|$ is much larger than Ω_i. The exact solution for $\tilde{g}_i$ is quite complicated; and the interested reader is referred to Ref. 9. For the moment, all we need to know is that $\int d^3v\, \tilde{g}\, \underset{\sim}{v}_\perp \neq 0$ and

$$\int d^3v\, \tilde{g} \approx 0 \approx \int d^3v\, \tilde{g}\, v_{\parallel} \quad . \qquad (4)$$

In the preceding expressions, we have adopted the following notations: Z_j is the charge in units of e (the magnitude of the charge on an electron), $L_j \equiv \Omega_j^{-1} \underset{\sim}{k}_\perp \times \underset{\sim}{\hat{n}} \cdot \underset{\sim}{v}$, $\Omega_j = Z_j eB/m_j c$, J_0 and J_1 are the usual Bessel functions with argument $k_\perp v_\perp/\Omega_j$, and

$$\omega_{dj} \equiv (v_\perp^2/v_j^2)\omega_{bj} + 2(v_{\parallel}^2/v_j^2)\omega_{\kappa j} \quad ,$$

$$\omega_{bj} \equiv (T_j c/Z_j eB)\underset{\sim}{k}_\perp \times \underset{\sim}{\hat{n}} \cdot \underset{\sim}{\nabla} \ell n B \quad ,$$

$$\omega_{\kappa j} \equiv (T_j c/Z_j eB)\underset{\sim}{k}_\perp \times \underset{\sim}{\hat{n}}\cdot(\underset{\sim}{\hat{n}}\cdot\underset{\sim}{\nabla}\underset{\sim}{\hat{n}}) \quad ,$$

$$\omega_{*j}^T \equiv \omega_{*j}\left[1 + \eta_j(v^2/v_j^2 - 3/2)\right] \quad ,$$

$$\omega_{*j} \equiv (T_j c/Z_j eB)\underset{\sim}{k}_\perp \times \underset{\sim}{\hat{n}}\cdot\underset{\sim}{\nabla}\ell n N_j \quad ,$$

with $\eta_j \equiv \partial\ell n T_j/\partial\ell n N_j$ and $v_j^2 = 2T_j/m_j$.

From Eqs. (2) and (4) we can evaluate the perturbed density for each species, in the limit of small L_j ,

$$\int d^3v\ \tilde{f}_j = -\frac{Z_j e\tilde{\Phi}}{T_j} b_j N_j + b_j N_j \underset{\sim}{\tilde{\xi}}\cdot(\underset{\sim}{\nabla}\ell n N_j + \underset{\sim}{\nabla}\ell n T_j)$$
$$- \underset{\sim}{\tilde{\xi}}\cdot\underset{\sim}{\nabla} N_j + \int d^3v\ h_j J_o \ , \tag{5}$$

where $b_j = (k_\perp \rho_j)^2$, and $\rho_j^2 = T_j m_j c^2/(Z_j eB)^2$. We are interested in the limit $b_i \sim b_h < 1$ and $b_e << b_i, b_n$. Consequently, neglecting $N_h m_e/N_i m_i$ corrections the quasi-neutrality condition can be written as

$$\sum_j Z_j e \int d^3v\ \tilde{h}_j J_o = (N_i b_i Z_i^2 e^2/T_i)[1 - (\omega_{*i}/\omega)(1 + \eta_i)]\tilde{\Phi} \quad . \tag{6}$$

Equation (6) serves as an identity to be used later. Notice that $\tilde{g}_i$ does not contribute to Eq. (6) because of Eq. (4).

Finally, we require that the equilibrium quantities satisfy not only quasi-neutrality,

$$\sum_j Z_j N_j = 0 \quad , \tag{7}$$

but also pressure balance,

$$\underset{\sim}{\nabla}(4\pi p + \tfrac{1}{2}B^2) = \underset{\sim}{B}\cdot\underset{\sim}{\nabla}\underset{\sim}{B} \quad , \tag{8}$$

where $p = \sum_j N_j T_j$ is the total pressure, while $N_j T_j \equiv p_j$ is the species pressure.

3. EIGENMODE EQUATIONS

The perturbed perpendicular Ampere's law can be evaluated with the help of Eq. (2) to obtain

$$(1 - C)\tilde{B}_{\parallel} - (4\pi/B)\tilde{\underset{\sim}{\xi}}\cdot\underset{\sim}{\nabla}p = \tfrac{1}{2}B \sum_j \beta_j \left\{ \frac{3}{2} b_j \left[(Z_j e\tilde{\Phi}/T_j) - \tilde{\underset{\sim}{\xi}}\cdot\underset{\sim}{\nabla}\ln(N_j T_j^2) \right] - N_j^{-1} \int d^3v\, \tilde{h}_j (v_\perp^2/v_j^2) \frac{2\Omega_j}{k_\perp v_\perp} J_1 \right\} , \qquad (9)$$

where $\beta_j \equiv 8\pi N_j T_j/B^2$ and

$$C \equiv (4\pi Z_j e/ick_\perp^2 \tilde{B}_{\parallel}) \int d^3v\, \underset{\sim}{k}_\perp \times \hat{\underset{\sim}{n}}\cdot\underset{\sim}{v}_\perp \tilde{g}_j \quad .$$

As will be shown later, the perturbed perpendicular current due to $\tilde{g}_j$ gives rise to the compressional Alfvén mode.

The perturbed parallel Ampere's law, together with the lowest moment of Eq. (3) and Eqs. (6) and (9), give

$$\frac{v_A^2}{k_\perp^2} \underset{\sim}{B}\cdot\underset{\sim}{\nabla}\left(\frac{k_\perp^2 i\omega}{Bc}\tilde{A}_{\parallel}\right) + \Big\{ \omega[\omega - \omega_{*j}(i + \eta_j)]$$

$$+ (\omega_{\kappa j} - \omega_{bj})[\omega - \omega_{*j}(1 + 2\eta_j) - (b_h\delta/b_j)(\omega - \omega_{*h} - 2\eta_h\omega_{*h})]$$

$$+ (\omega_{\kappa j}\omega_{*p}/b_j) - 2\omega_{bj}(\omega_{\kappa j} - C\omega_{bj})/(b_j\beta_j) \Big\} \tilde{\Phi}$$

$$+ \Big\{ 2\omega(\omega_{\kappa j} - C\omega_{bj})/(b_j\beta_j) + (3\omega/2)[\omega - \omega_{*j}(1 + 2\eta_j)$$

$$- (b_h\delta/b_i)(\omega - \omega_{*h} - 2\eta_h\omega_{*h})]\Big\}(T_i/Z_i eB)(\tilde{B}_{\parallel} + \tilde{\underset{\sim}{\xi}}\cdot\nabla B)$$

$$-\left(\frac{2\omega T_i}{Z_i^2 eN_i b_i}\right)\sum_j Z_j\left[\omega_{\kappa j}\int d^3v\ \tilde{h}_j(v_{\parallel}^2/v_j^2)J_0 - \frac{1}{4}b_j\omega_{bj}\int d^3v\ \tilde{h}_j(v_{\perp}^4/v_j^4)\right] = 0 \quad (10)$$

where $\delta \equiv N_h/Z_i N_i$, $v_A^2 \equiv B^2/4\pi N_i m_i$, and $\omega_{*p} \equiv (c/Z_i eN_i B)\underset{\sim}{k}_{\perp}\times\hat{\underset{\sim}{n}}\cdot\underset{\sim}{\nabla}p$.

Equations (9) and (10) still contain moments of $\tilde{h}$, which in principle can be expressed in terms of $\tilde{B}_{\parallel}$, $\tilde{A}_{\parallel}$ and $\tilde{\Phi}$ by solving Eq. (3) for $\tilde{h}$. The perpendicular velocity moment of $\tilde{g}_i$, or C , is evaluated in Ref. 9. In the cold ion limit, it reduces to

$$C = (\omega/k_{\perp}v_A)^2 \quad (11)$$

Consequently, we have two equations, Eqs. (9) and (10), relating the three perturbed field quantities.

For simplicity we assume the perturbed parallel electric field vanishes, so that

$$\hat{\underset{\sim}{n}}\cdot\underset{\sim}{\nabla}\tilde{\Phi} = i\omega\tilde{A}_{\parallel}/c \quad (12)$$

This relationship can be derived from the parallel Ohm's law under certain conditions.[9] However, we caution the reader that its validity should be verified in each specific case.

Equations (9) - (12) provide us with a complete set of eigenmode equations along the magnetic field line with $\tilde{h}_j$ given by solution of Eq. (3).

4. HIGH PHASE VELOCITY RING MODEL

In the high phase velocity limit, Eq. (3) yields

$$\tilde{h}_j = F_j\left(\frac{\omega - \omega_{*j}^T}{\omega - \omega_{dj}}\right)\left\{\left[(v_\perp^2/v_j^2B)\left(\frac{2\Omega_j}{k_\perp v_\perp}J_1\tilde{B}_\parallel + J_0\tilde{\underset{\sim}{\xi}}\cdot\underset{\sim}{\nabla}B\right) + (2v_\parallel^2/v_j^2)J_0\tilde{\underset{\sim}{\xi}}\cdot(\hat{\underset{\sim}{n}}\cdot\underset{\sim}{\nabla}\hat{\underset{\sim}{n}})\right]\right.$$

$$\left. - \frac{iZ_j e v_\parallel J_0}{T_j\omega}\left(\hat{\underset{\sim}{n}}\cdot\underset{\sim}{\nabla}\tilde{\Phi} - \frac{i\omega}{c}\tilde{A}_\parallel\right)\right\} \quad , \tag{13}$$

where we have also neglected $\hat{\underset{\sim}{n}}\cdot\underset{\sim}{\nabla}J_0$ corrections as small.

Employing Eq (13) for $b_j \ll 1$, the perpendicular Ampere's law Eq. (9) reduces to

$$(Z_i e\tilde{\Phi}/\omega T_i)D_2 = D_3\tilde{\Psi} \tag{14}$$

where $\tilde{\Psi} \equiv (\tilde{B}_\parallel/B) + \tilde{\underset{\sim}{\xi}}\cdot\underset{\sim}{\nabla}\ell nB$,

$$D_2 \equiv \omega_{\kappa i}(1 - \sum_j \beta_j I_{2j}) - \omega_{bi}(C - \frac{1}{8}\sum_j \beta_j b_j I_{5j})$$
$$+(3b_i\beta_i/4)\left[\omega - \omega_{*i}(1 + 2\eta_i) - (b_h\delta/b_i)(\omega - \omega_{*h} - 2\eta_h\omega_{*h})\right] ,$$

$$D_3 \equiv 1 - C + \tfrac{1}{2}\sum_j \beta_j(I_{3j} - \tfrac{1}{2}b_j I_{5j}) \quad ,$$

and

$$(I_{ij}, I_{2j}, I_{3j}, I_{4j}, I_{5j})$$
$$\equiv \int \frac{d^3v\ F_j}{N_j}\left(\frac{\omega - \omega_{*j}^T}{\omega - \omega_{dj}}\right)\left[\left(\frac{v_\parallel}{v_j}\right)^4, \left(\frac{v_\parallel v_\perp}{v_j^2}\right)^2, \left(\frac{v_\perp}{v_j}\right)^4, \frac{v_\parallel^2 v_\perp^4}{v_j^6}, \left(\frac{v_\perp}{v_j}\right)^6\right]$$

Similarly, the parallel Ampere's law, Eq. (10) becomes

$$\frac{v_A^2}{k_\perp^2}\underset{\sim}{B}\cdot\underset{\sim}{\nabla}\left(\frac{k_\perp^2}{B}\hat{\underset{\sim}{n}}\cdot\underset{\sim}{\nabla}\tilde{\Phi}\right) + D_1\tilde{\Phi} + (2D_2\omega T_i/Z_i e b_i\beta_i)\tilde{\Psi} = 0 \quad , \tag{15}$$

where

$$D_1 \equiv \omega[\omega - \omega_{*i}(1 + \eta_i)] + \tfrac{1}{2}\beta_i\omega_{*p}[\omega - \omega_{*i}(1 + 2\eta_i)$$
$$- (b_h\delta/b_i)(\omega - \omega_{*h} - 2\eta_h\omega_{*h})]$$
$$+ b_i^{-1}\Big\{\omega_{\kappa i}\omega_{*p} + (2\omega_{bi}/\beta_i)\Big[C\omega_{bi} - \omega_{\kappa i}(1 - \tfrac{1}{2}\sum_j \beta_j b_j I_{4j})\Big]$$
$$- (4\omega_{\kappa i}^2/\beta_i)\sum_j \beta_j I_{1j}\Big\}$$

and $\tfrac{1}{2}\beta_i\omega_{*p} = \omega_{\kappa i} - \omega_{bi}$ from equilibrium pressure balance. Combining Eqs. (14) and (15), we get the eigenvalue equation for ballooning-interchange/compressional Alfvén modes, when a hot electron population is present, namely,

$$\frac{v_A^2}{k_\perp^2}\underset{\sim}{B}\cdot\underset{\sim}{\nabla}\left(\frac{k_\perp^2}{B}\underset{\sim}{\hat{n}}\cdot\underset{\sim}{\nabla}\tilde{\Phi}\right) + D\tilde{\Phi} = 0 \quad , \tag{16}$$

with $D \equiv D_1 + (2D_2^2/D_3 b_i\beta_i)$. Note that in the absence of hot electrons, $C \approx 1$ corresponds to a compressional Alfvén wave.

In the limit when $\underset{\sim}{\hat{n}}\cdot\underset{\sim}{\nabla} \approx 0$, an assumption used in all previous ring stability analyses, the high phase velocity ansatz becomes trivial. The perturbed parallel vector potential, $\tilde{A}_\parallel$, is decoupled from $\tilde{B}_\parallel$ and $\tilde{\Phi}$, and the parallel Ohm's law is then not required. The dispersion relation then reduces to

$$D = 0 \quad , \tag{17}$$

which contains the coupling of interchange and compressional Alfvén modes.

5. LOCAL STABILITY ANALYSIS

In order to obtain explicit illustrative results, it is convenient to examine the local limit $D = 0$. For the ions and background electrons we assume $|\omega| >> |\omega_{*j}^T|$, $|\omega| >> |\omega_{dj}|$, and $\beta_j << 1$ so that $I_{1j} \approx 3/4$, $I_{2j} \approx 1/2$, $I_{3j} \approx 2$, $I_{4j} \approx 1$, and $I_{5j} \approx 6$. Neglecting order $b_i\beta_i$ terms compared to unity the D's may be reduced to

$$
\begin{aligned}
D_1 &= \omega^2 + (2\omega_{\kappa i}^2/b_i\beta_i)(1 - \tfrac{3}{2}\beta_c - 2\beta_h I_{1h}) \\
&\quad + (2\omega_{bi}/b_i\beta_i)\Big[C\omega_{bi} - 2\omega_{\kappa i} + \tfrac{1}{2}\omega_{\kappa i}\beta_h b_h I_{4h} \\
&\quad + (\omega_{bi} - \omega_{\kappa i})b_h\beta_h \frac{\omega_{*h}(1 + 2\eta_h)}{2\omega_{bh}}\Big] \\
D_2 &= \omega_{\kappa i}(1 - \tfrac{1}{2}\beta_c - \beta_h I_{2h}) - \omega_{bi}\Big[C - \tfrac{1}{8}b_h\beta_h I_{5h} \\
&\quad + \tfrac{3}{4}b_h\beta_h \frac{\omega_{*h}(1 + 2\eta_h)}{\omega_{bh}}\Big] + \tfrac{3}{4}b_i\beta_i\omega \\
D_3 &= 1 - C + \beta_c + \tfrac{1}{2}\beta_h(I_{3h} - \tfrac{1}{2}b_h I_{5h})
\end{aligned}
\tag{18}
$$

where $\beta_c \equiv \beta_i + \beta_e$.

We next note that the ring electrons are far hotter than the ions and background electrons so that $|\omega_{*h}^T| \sim |\omega_{bh}| >> |\omega| \sim |\omega_{\kappa h}|$ may be employed to find

$$I_{2h} \approx \omega_{*h}(1 + \eta_h)/2\omega_{bh}$$

and

$$I_{3h} \quad \frac{\omega_{*h}(1 + \eta_h)}{\omega_{bh}}(1 - \varepsilon) + \frac{\omega(\omega_{*h} - \omega_{bh})}{\omega_{bh}^2} ,$$

where $\varepsilon = \omega_{\kappa i}/\omega_{bj}$ and we restrict our attention to the outer side of the well dug by the ring so that $\varepsilon < 0$ and $|\varepsilon| << 1$. In evaluating

I_{3h} it is necessary to retain the higher order terms indicated because when Eq. (8) is employed in D_3 cancellation occurs.

Defining

$$w \equiv 2\omega_{bi}^2/b_i\beta_i k_\perp^2 v_A^2 > 0$$

and

$$q \equiv -\beta_h(\omega_{*h} - \omega_{bh})k_\perp v_A/2\omega_{bh}^2 \quad ,$$

Eqs. (18) become

$$\begin{aligned} D_1 &\approx k_\perp^2 v_A^2[C - w(\varepsilon_1 - C)] \quad , \\ D_2 &\approx \omega_{bi}(\varepsilon_1 - C) \quad , \\ D_3 &\approx (\varepsilon_1 - C) + \beta_c + \Delta_c - (q\omega/k_\perp v_A) \quad , \end{aligned} \tag{19}$$

where $\beta_c << 1$ is employed, $\varepsilon_1 \equiv 2\varepsilon + b$, and $b \equiv b_h(1 + 2\eta_h)/(1 + \eta_h)$. On the outside of the ring we assume all species have the same density and temperature scale lengths and we define $\lambda \equiv \beta_c + \Delta_c \approx \beta_c(1 + 1/\beta_h)$. Inserting these expressions into $D = 0$ yields a quadratic equation for the quantity $C - \varepsilon_1$,

$$(C - \varepsilon_1)^2 - (C - \varepsilon_1)\left\{(1 + w)[\lambda - (q\omega/k_\perp v_A)] - \varepsilon_1\right\} - \varepsilon_1[\lambda - (q\omega/k_\perp v_A)] = 0 \tag{20}$$

which because $w \sim (k_\perp^{-1}|\nabla_\perp \ell n B|)^2 << 1$ yields the two roots

$$C[\lambda + \varepsilon_1 - (q\omega/k_\perp v_A)] \approx \varepsilon_1 w[\lambda - (q\omega/k_\perp v_A)] \quad , \tag{21}$$

and

$$C + (q\omega/k_\perp v_A) \approx \lambda + \varepsilon_1 + \frac{w[\lambda - (q\omega/k_\perp v_A)]^2}{[\lambda + \varepsilon_1 - (q\omega/k_\perp v_A)]} \quad . \tag{22}$$

Equations (21) and (22) are the dispersion relations describing the interchange and compressional Alfvén modes, respectively. The $q \to 0$, $b \to 0$ limit of Eq. (21) yields the usual Nelson[1]-Van Dam and Lee[2] result; that is, the interchange stability of the ring requires $\varepsilon\lambda/(\lambda + 2\varepsilon) > 0$. However, for $q \to 0$ and $b \to 0$ the compressional Alfvén mode requires $(\lambda + 2\varepsilon) + w\lambda^2/(\lambda + 2\varepsilon) > 0$ for stability. On the outside of the ring $\varepsilon < 0$ and $\lambda > 0$, so that both conditions cannot be satisfied. This incompatibility of the interchange and compressional Alfvén windows was noted in the energy principle treatment of Ref. 3 and 12. As a result, finite q modifications must be retained in order to obtain a stability window. The finite q modifications are referred to as "frequency shift" effects in Ref. 3.

Noting that for $|q|$ large, Eq. (21) requires $\varepsilon_1 > 0$ for stability we continue to employ the small $|q|$ form which gives the generalized Nelson-Van Dam-Lee ring stability condition

$$\varepsilon_1(\lambda + \varepsilon_1) \geq 0 \ . \tag{23}$$

However, in Eq. (22) we employ $w << 1$ to obtain the quadratic $C + (q\omega/k_\perp v_A) \approx \lambda + \varepsilon_1$, which requires

$$\lambda + \varepsilon_1 + \frac{1}{4}q^2 \geq 0 \tag{24}$$

for stability of the ring to compressional Alfvén modes. When $\varepsilon_1 < 0$ Eqs. (23) - (24) yield

$$0 \geq \lambda - |\varepsilon_1| \geq -\frac{1}{4}q^2 \tag{25}$$

so that a stability window exists that is largest when

$$q^2 \geq 4|\varepsilon_1| \ . \tag{26}$$

When q^2 gets larger than the value given by Eq. (26), the finite q corrections to Eq. (21) must be retained. In particular, by solving this cubic equation we find that

$$wq^2 \lesssim \frac{1}{2}|\varepsilon_1| \tag{27}$$

is required in order not to significantly decrease the size of the stability window from that given by the generalized Nelson-Van Dam-Lee value: $\lambda \leq |\varepsilon_1|$.

When $\varepsilon_1 = 2\varepsilon + b \geq 0$, both Eqs. (23) and (24) are satisfied. Defining $|\nabla \ell n N| = \Delta^{-1}$ and $|\hat{\underset{\sim}{n}}\cdot\underset{\sim}{\nabla}\hat{\underset{\sim}{n}}| = R_c^{-1}$, we note that this condition implies $\beta_h \geq 4\Delta/bR_c$. This important stabilizing effect for large b_h seems not to have been recognized in previous work because the finite hot electron gyroradius effects were ignored.

To verify these analytic results, we solve the quartic equation given by Eq. (20) numerically. When the finite b_h effects are ignored, Eq. (20) is characterized by the parameters $k_\perp\Delta$, Δ/R_c and $\bar{q}^2 = 8T_i\delta\Delta^2/Z_iT_h\rho_i^2$. The results shown in Figs. (1) are obtained by taking $k_\perp\Delta = 10$, $\Delta/R_c = 0.05$ and $\bar{q} = 0.2$, 1 and 3 . The Nelson-Van Dam-Lee stability boundary given by Eq. (23) and the compressional Alfvén stability boundary given by Eq. (24) are shown by the broken lines. The actual stability boundaries in each case obtained by solving Eq. (20) numerically are shown by the solid lines. In Fig. (1a) we have $\bar{q} = 0.2$ and the inequality (26) not satisfied, in which case the stability boundaries given by Eq. (25) qualitatively agree with the numerical result. In Figs. (1b) and (1c), the parameter $\bar{q}$ is chosen such that $\frac{1}{4}q^2$ and $2wq^2$ are larger than $|\varepsilon|$, respectively, to show the stability

window is indeed closing. These results agree with our analytic estimate given by Eqs. (26) and (27).

When the finite b_h effects are retained, we again employ

$$q^2 = \bar{q}^2(1 + \tfrac{1}{2}\beta_h)^2/\beta_h^3$$

but rewrite $\bar{q}^2 = 8\delta k_\perp \Delta m_e/b_h M_i$. For each fixed value of $\bar{q}$ as in Figs. (1), δ can be varied (so that b_h is changed proportionally) to illustrate the effect of finite b_h. Figures (2a) and (2b) are obtained in this manner from Figs. (1a) and (1b). For small values of b_h such that ε_1 is still negative, the stability boundaries move downward in β_c as b_h increases in accordance with the prediction of Eq. (25). To highlight the dramatic stabilizing effect due to sufficiently large b_h we take $\bar{q} = 0.1$ and increase δ from 0 ($b_h = 0$) to 0.01 ($b_h = 0.43$) as shown in Fig. (2c). The stable region moves downward in β_c as δ increase, similar to Figs. (2a) and (2b). However, when $\delta = 0.01$ for $\bar{q} = 0.1$, a new stability region appears with a boundary roughly given by $\beta_h \simeq 4\Delta/bR_c$. This result confirms our analytic expressions in Eqs. (23) and (24).

6. MAGNETIC TRAPPED PARTICLE MODE

The high phase velocity assumption used to solve Eq. (3) in Section 4 is in general valid for the background ion and electrons. However, this assumption need not be satisfied by the hot electrons for typical EBT parameters. In this section, we solve Eq. (3) in the opposite limit for the hot electrons.

When $|v_{\parallel}\hat{\underset{\sim}{n}}\cdot\underset{\sim}{\nabla}\ell n\tilde{h}| >> |\omega|$, $|\omega_d| \sim |\omega_*|$, we can bounce average Eq. (3) and apply appropriate trapped particle boundary condition at the turning points to yield

$$\tilde{h}_j \simeq \frac{Z_j e}{T_j} F_j \left(1 - \frac{\omega_{*j}^T}{\omega}\right)\left[-(\tilde{\Phi} - \tilde{\chi})J_o + \frac{\langle(\omega - \omega_{dj})(\tilde{\Phi} - \tilde{\chi})J_o\rangle}{\omega - \langle\omega_d\rangle}\right.$$

$$\left.\frac{\langle\omega_{dj}\tilde{\Phi}J_o + (\omega v_\perp/k_\perp c)\tilde{B}_{\parallel}J_1\rangle}{\omega - \langle\omega_d\rangle}\right] , \tag{28}$$

where $\tilde{\chi}$ is defined through $\hat{\underset{\sim}{n}}\cdot\underset{\sim}{\nabla}\tilde{\chi} = i\omega\tilde{A}_{\parallel}/c$, $\langle X\rangle \equiv (\oint d\ell X/|v_{\parallel}|)/(\oint d\ell/|v_{\parallel}|)$, and $\oint d\ell$ is the line integral along the bounce orbit.

For a pure magnetic mode[10] we can study perturbations with $\tilde{\Phi} = \tilde{A}_{\parallel} = 0$ and $\tilde{B}_{\parallel} \neq 0$. Inserting Eq. (28) into the perpendicular Ampere's law we obtain

$$(1 - C)\tilde{B}_{\parallel}/B + 2\beta_h \int d^3v \frac{\mu^2 B}{v_h^4} \frac{F_h}{N_h} \frac{\omega - \omega_{*h}^T}{(\omega - \langle\omega_{dh}\rangle)} \langle\tilde{B}_{\parallel}\rangle = 0 . \tag{29}$$

A variational principle can be obtained from Eq. (29) in the low frequency limit $|\omega| << |\omega_{*h}|$, $|\omega_{dh}|$ by multiplying it with $\tilde{B}_{\parallel}$ and integrating along magnetic field line. This procedure yields

$$\left(\frac{\omega}{k_\perp}\right)^2 \int d\ell \frac{\tilde{B}_{\parallel}^2}{Bv_A^2} = \int \frac{\tilde{B}_{\parallel}^2}{B} d\ell$$

$$+ \frac{16\pi^{\frac{1}{2}}}{v_h^5} \hat{\underset{\sim}{n}} \times \underset{\sim}{k}_\perp \cdot \underset{\sim}{\nabla} p_h \int d\mu\, dE \frac{\mu^2 (\oint d\ell\, \tilde{B}_{\parallel}/|v_{\parallel}|)^2 \exp(-mE/T_h)}{\oint \frac{d\ell}{|v_{\parallel}|} \hat{\underset{\sim}{n}} \times \underset{\sim}{k}_\perp \cdot [\mu\underset{\sim}{\nabla}B + v_{\parallel}^2(\hat{\underset{\sim}{n}}\cdot\underset{\sim}{\nabla}\hat{\underset{\sim}{n}})]} .$$

The righthand side of Eq. (30) is the energy principle used by Rosenbluth.[10] When the righthand side of Eq. (30) is negative, instability is possible. Comparing Eq. (30) with Eq. (22) earlier, it is not difficult to imagine that additional effects that destabilize the compressional Alfvén mode in the local analysis may further

destabilize the magnetic trapped particle mode. The stability boundary of this mode depends on the details of the magnetic field line geometry in addition to the parameters involved in the last section. Furthermore, coupling of this mode to the ballooning-interchange mode will complicate the analysis considerably. This coupling and other effects like the finite frequency shift and finite b_h should be an important part of the continuing effort of EBT stability study.

7. CONCLUSION

We have derived the system of eigenvalue equations which retain ballooning-interchange, and compressional Alfvén modes. In the most general case, this is a system of equations derived from the perpendicular and parallel Ampere's law, and the parallel Ohm's law, in which the moments of a portion of the perturbed distribution function, $\tilde{h}$, must be expressed in terms of the field variables $\tilde{B}_{\parallel}$, $\tilde{A}_{\parallel}$, $\tilde{\Phi}$ by solving Eq. (3). Under some circumstances the parallel Ohm's law can be reduced to the ideal MHD result $i\omega\tilde{A}_{\parallel}/c \approx \hat{\underset{\sim}{n}}\cdot\underset{\sim}{\nabla}\tilde{\Phi}$ so that only the two variables $\tilde{\Phi}$ and $\tilde{B}_{\parallel}$ remain. The resulting eigenvalue equation is valid for all frequencies less than the ion gyrofrequency. It extends the result of Lee and Catto[11] to include the potentially important stabilizing effect of magnetic compressibility for the special case of Maxwellian electrons and ions. When the hot electron population is retained, Eq. (3) must be solved for $\tilde{h}$ in order to obtain a closed set of equations.

As an example, we first consider the high phase velocity limit for all species. The final eigen equation is given by Eq. (16). In the flute limit, i.e., $\underset{\sim}{n}\cdot\underset{\sim}{\nabla} \approx 0$, the parallel Ohm's law is not required and Eq. (16) agrees with earlier results of local stability analysis[1-5] in the appropriate limits. In the flute limit, we investigate stability from the resulting local dispersion relation. In addition to the usual interchange stability condition, we find that the compressional Alfvén mode can be driven unstable. In fact, its stability can become incompatible with that of the usual interchange branch unless "frequency shift" effects are retained.[3] When finite hot electron gyroradius effects, i.e., b_h , are retained, both the interchange and the compressional Alfvén mode are stabilized if $\beta_h > 4\Delta/bR_c$ where $b = b_h(1 + 2\eta_h)/(1 + \eta_h)$. This suggests that high mode number or T_h is stabilizing. While the model treated is idealized, it nonetheless allows us to estimate the parameters necessary for the largest window of ring stability. Because of the simplicity of the model, more precise estimates are needed. In this regard, our principle results Eqs. (3), (9), (10), and an appropriate parallel Ohm's law would seem to be a logical starting place whenever $|\omega^2| << \Omega_i^2$.

In the second example, the hot electrons are treated as a trapped species and variations along the magnetic field line are retained. For idealized pure magnetic perturbations ($\tilde{\Phi} = \tilde{A}_{\parallel} = 0$, $\tilde{B}_{\parallel} \neq 0$), the magnetic trapped particle mode[10] is recovered.

ACKNOWLEDGMENTS

The authors have benefited from discussion with X. S. Lee, D. A. D'Ippolito and J. R. Myra, and are particularly grateful to X. S. Lee who made his unpublished notes available to the authors and noted the importance of retaining the finite gyroradius corrections to $\tilde{h}$ terms. In addition, the authors have profited from important conversations with H. L. Berk, C. Z. Cheng, D. A. Spong, and J. W. Van Dam.

This work was supported by the U. S. Department of Energy under Contract No. DE-AC03-76-ET-53057 with Science Applications, Inc.

REFERENCES

1. D. B. Nelson, Phys. Fluids 23, 1850 (1980).

2. J. W. Van Dam and Y. C. Lee, in Proceedings of the Workshop on EBT Ring Physics (Oak Ridge National Laboratory, Oak Ridge, Tenn. 1979), p. 471.

3. J. W. Van Dam, H. L. Berk, M. N. Rosenbluth and D. A. Spong, in Proceedings of the Workshop on EBT Stability Theory (Oak Ridge National Laboratory, Oak Ridge, Tenn. 1981), p. 97.

4. K. T. Tsang and C. Z. Cheng, ibid., p. 141.

5. A. M. El Nadi, Bull. of Am. Phys. Soc. 26, 995 (1981).

6. P. J. Catto, W. M. Tang and D. E. Baldwin, Plasma Phys. 23, 639 (1981).

7. T. M. Antonsen, B. Lane and J. Ramos, Phys. Fluids 24, 1465 (1981).

8. J. W. Van Dam, M. N. Rosenbluth and Y. C. Lee, Univ. of Texas Report IFSR #12 (March, 1981).

9. K. T. Tsang and P. J. Catto, Science Applications, Inc. Report No. SAI-254-81-386-LJ/PRI-34 (November, 1981).

10. M. N. Rosenbluth, Phys. Rev. Lett. 46, 1525 (1981).

11. X. S. Lee and P. J. Catto, Phys. Fluids 24, 2010 (1981).

12. K. T. Tsang and C. Z. Cheng, Bull. of Am. Phys. Soc. 26, 996 (1981).

FIGURE CAPTIONS

Figs. 1. Plots of the core beta, β_c, versus the hot electron ring beta, β_h, for three different values of the parameter $\bar{q}^2 = 16T_i\delta\Delta^2/Z_iT_h\rho_i^2$: (a) $\bar{q} = 0.2$, (b) $\bar{q} = 1.0$, and (c) $\bar{q} = 3.0$. The solid curves are obtained by solving Eq. (20) numerically for $\Delta/R_c = 0.05$, $\eta_h = b = 0$ and $k_\perp\Delta = 10$. The dashed curves are the $w \ll 1$ analytic results obtained from the Nelson-Van Dam-Lee (NVL) criterion $\beta_c(1 + \beta_h) = 4\Delta/R_c$ and the compressional Alfvén (C) stability boundary $\beta_c(1 + \beta_h) = (4\Delta/R_c)[1 - \bar{q}^2R_c(1 + \frac{1}{2}\beta_h)^2/16\beta_h^2\Delta]$. Note that in (b) and (c) the lower curve does not appear. The results are not valid for $\beta_h \lesssim 0.1$ since $|\varepsilon| \ll 1$ and $\beta_c \ll \beta_h$ are employed.

Figs. 2. Plots of the core beta, β_c, versus the hot electron ring beta, β_h, for three different values of $\bar{q}^2 = 8\delta k_\perp\Delta m_e/b_hM_i$: (a) $\bar{q} = 0.2$, (b) $\bar{q} = 1.0$, and (c) $\bar{q} = 0.1$. For each $\bar{q}$, δ is varied so that the effect of b_h is clearly exhibited. All curves are obtained by solving Eq. (20) numerically for $\Delta/R_c = 0.05$, $\eta_h = 0$ and $k_\perp\Delta = 10$.

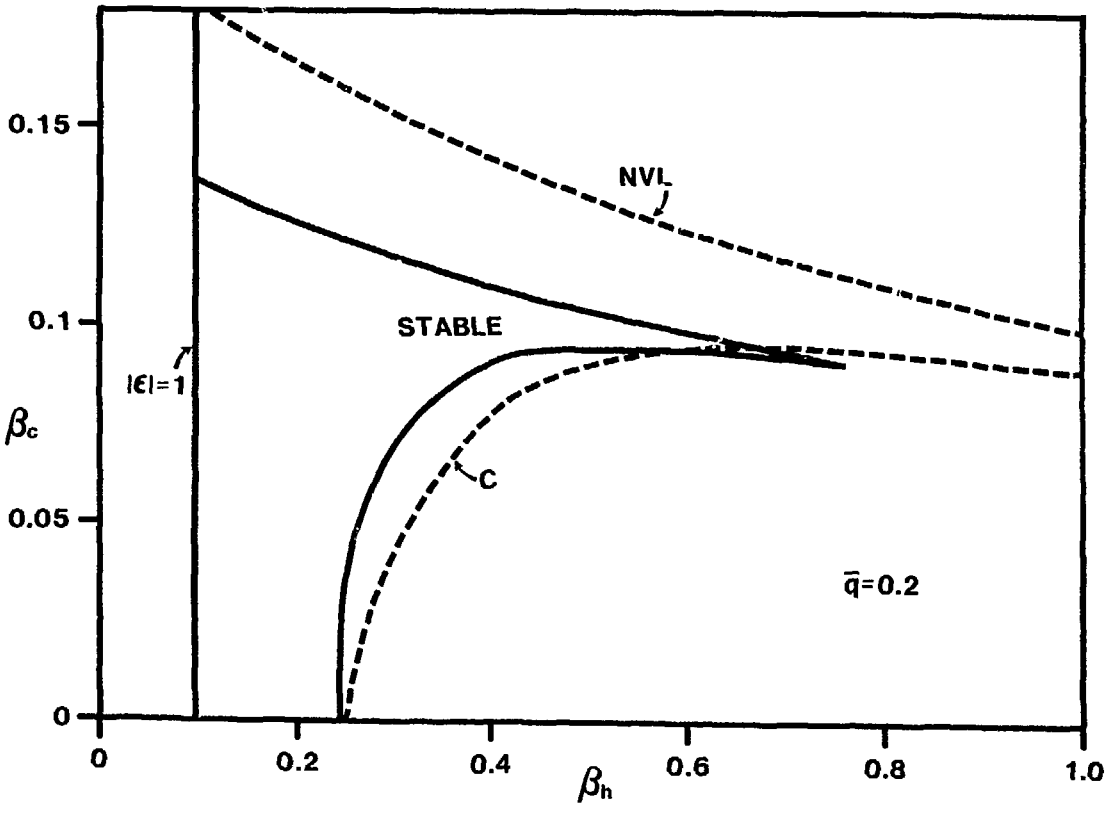
0.15
0.1
0.05
0
β_c
NVL
STABLE
$|\epsilon|=1$
C
$\bar{q}=0.2$
0
0.2
0.4
0.6
0.8
1.0
β_h

Fig. 1(a)

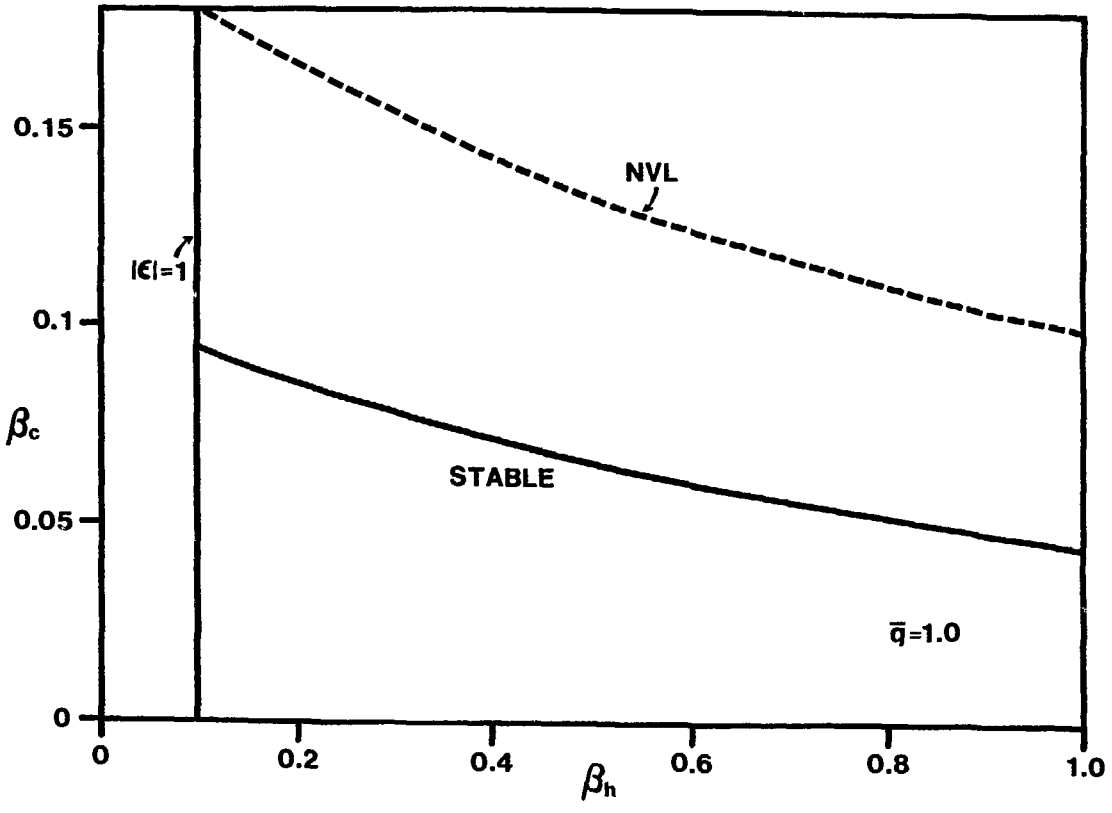

Fig. 1(b)

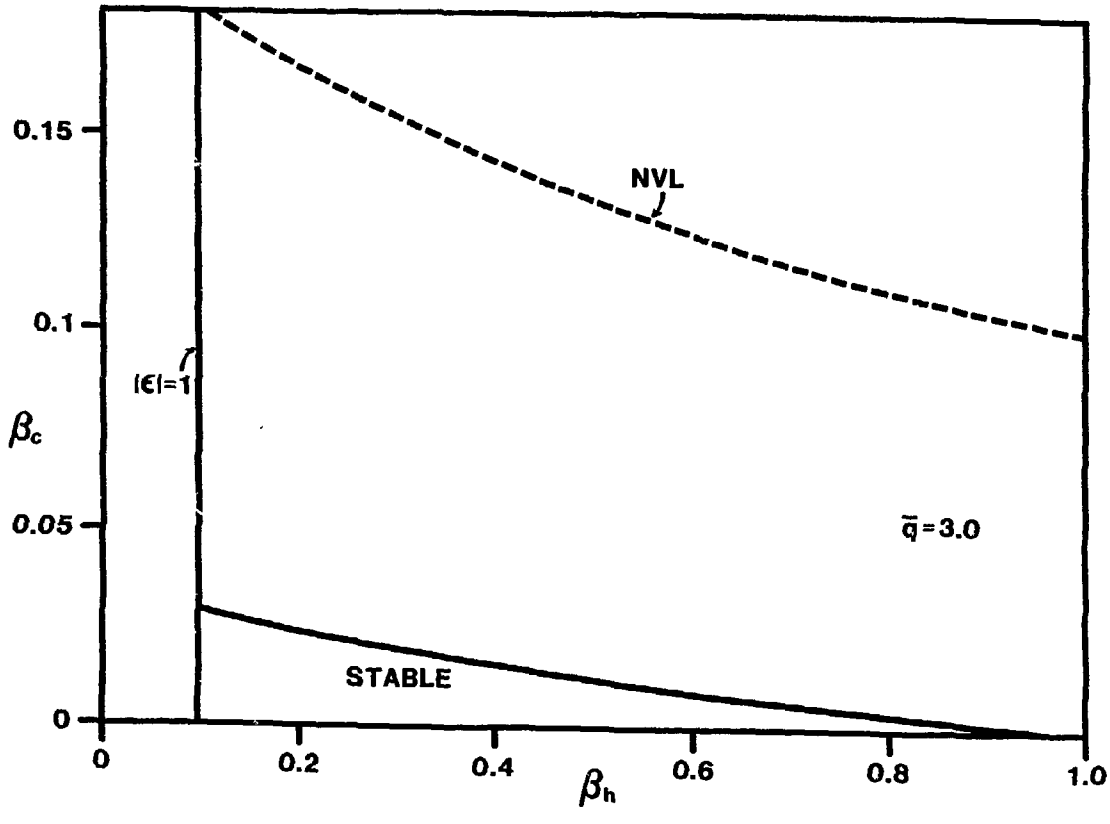
0.15
0.1
0.05
0
β_c
NVL
$|\epsilon|=1$
$\bar{q}=3.0$
STABLE
0
0.2
0.4
0.6
0.8
1.0
β_h

Fig. 1(c)

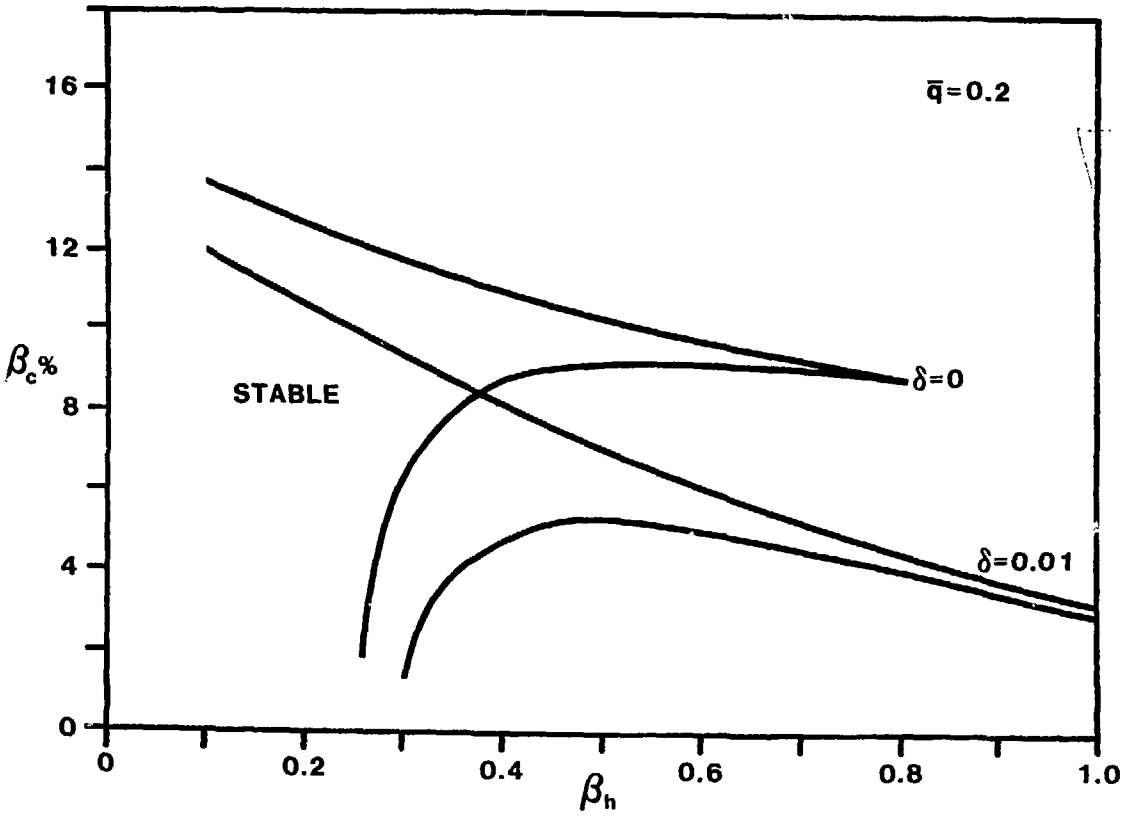

Fig. 2(a)

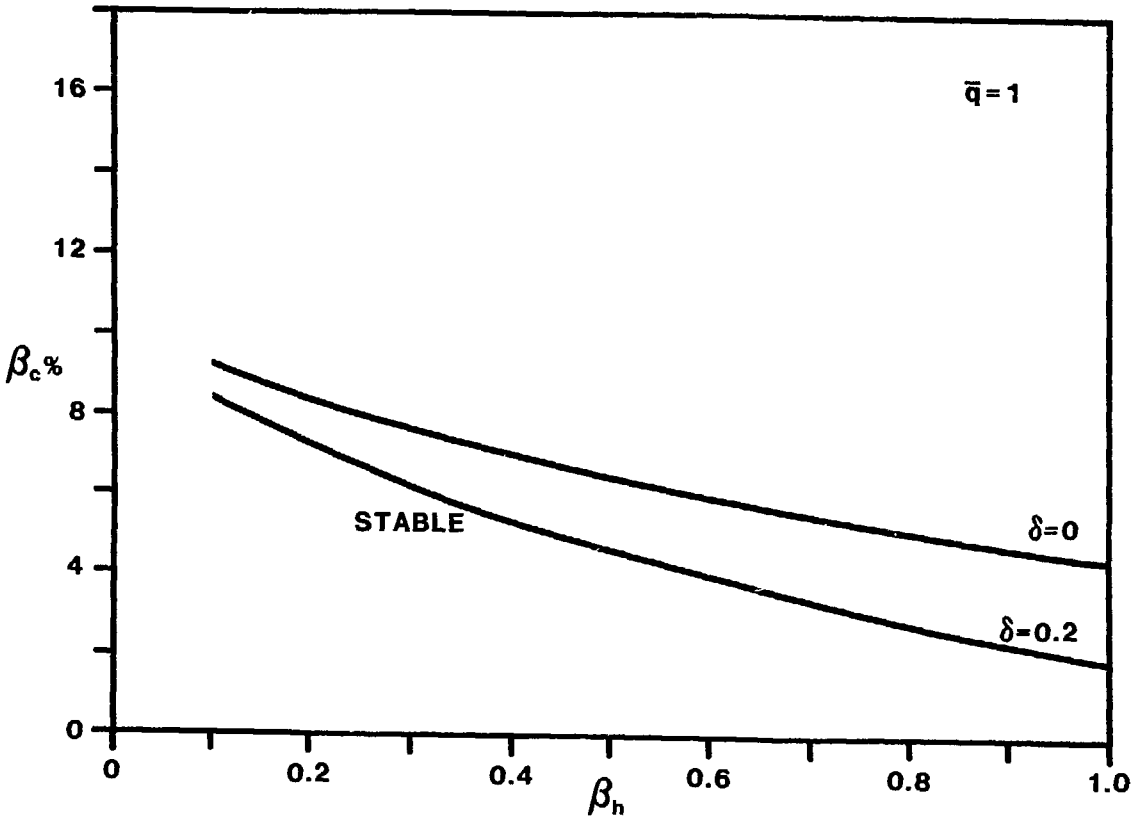
$\bar{q}=1$
16
12
8
4
0
β_c%
STABLE
$\delta=0$
$\delta=0.2$
0
0.2
0.4
0.6
0.8
1.0
β_h

Fig. 2(b)

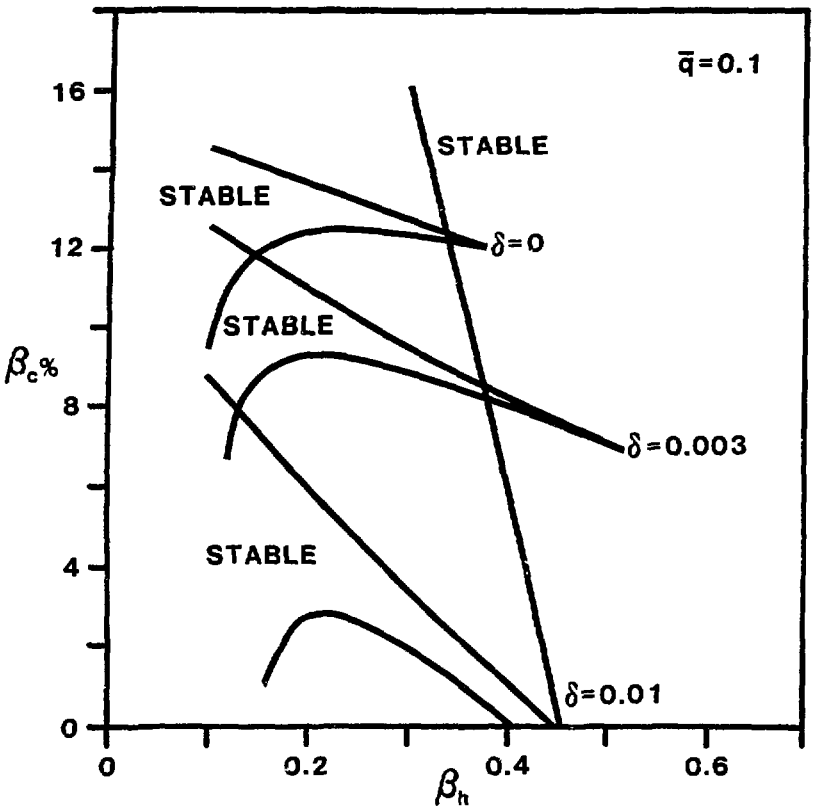
$\bar{q}$=0.1
STABLE
STABLE
STABLE
STABLE
δ=0
δ=0.003
δ=0.01
β_c%
β_h
0
4
8
12
16
0
0.2
0.4
0.6

Fig. 2(c)

KINETIC THEORY OF EBT STABILITY

C. Z. Cheng*
Institute for Fusion Studies
University of Texas
Austin, Texas 78712

T. L.

Eigenmode equations describing interchange, ballooning and compressional Alfvén instabilities of axisymmetric bumpy cylindrical plasmas with anisotropic pressures and ambipolar potential have been derived in four different frequency regimes: (a) high frequency regime with $\omega/k_{\parallel} > v_{h,e,i}$, (b) trapped hot electron regime with $v_h > \omega/k_{\parallel} > v_{e,i}$, (c) trapped electron regime with $v_{h,e} > \omega/k_{\parallel} > v_i$, and (d) trapped ion regime with $v_{h,e,i} > \omega/k_{\parallel}$. In the formulation, ω is assumed to be less than ω_{ce}, but can be greater than ω_{ci}. Our kinetic analysis allows for gyroradius effects, wave-particle resonances, and trapped particles. In particular, the stability conditions will be presented for the high frequency regime and the trapped hot electron regime.

*Permanent address is Princeton Plasma Physics Laboratory, Princeton University, Princeton, NJ.

STABILIZATION OF HIGH BETA PLASMA INSTABILIY WITH ECH HOT ELECTRON ANNULUS IN THE SYMMETRIC MIRROR

S. Hiroe
Oak Ridge National Laboratory*
Oak Ridge, Tennessee 37830

T. Kunibe, H. Akiyama and M. Inutake
Institute of Plasma Physics

Nagoya University, Nagoya 464, Japan

ABSTRACT

A hot electron annulus has been observed to decrease the fluctuation level for a high beta plasma in a symmetric mirror. The fluctuation is identified as the resistive drift wave, which is enhanced by the unfavorable curvature at the plasma edge. When the annulus is present, not only is the drift mode suppressed, but also the amplitude of the disruption caused by the drift mode decreases. The amplitudes of the drift mode and the disruption both decrease as the microwave power is increased.

---

*Operated by Union Carbide Corporation for the U. S. Department of Energy under contract W-7405-eng-26.

1. INTRODUCTION

If an axisymmetric mirror could be MHD stable it would be attractive as a reactor because the symmetric mirror is easily constructed as a module and because the cross-field diffusion is governed by classical, rather than by neoclassical,[1] processes. However, the parallel confinement along a field line is poor. To improve this confinement some end plugging scheme, either by rf[2] or by a dc potential plug,[3] is required.

It is very important to stabilize the instabilities in the symmetric mirror, such as flute modes or ballooning modes. One technique to provide this stabilization uses a hot electron annulus to produce a local magnetic well. This concept is basic to a bumpy torus.[4]

The plasma is created by high power microwaves in a mirror in which there are both fundamental and second harmonic resonance regions. The plasma is formed by interactions in the fundamental region, the high energy annulus by interactions in the second harmonic region. The location of the annulus is thus at the second harmonic position.[5] The width of the annulus is of the order of the electron Larmor radius, but the length is different for various machines since it depends on the curvature of the magnetic field lines. The geometry of the hot electron annulus has been determined for the SM device[6] in which the hot electron beta is about 50%.

In general, each of the (canted) mirror cells of a bumpy torus is unstable for the vacuum magnetic fields. However, the magnetic well formed by the hot electron annulus modifies the vacuum field so as to produce a stable plasma. The operating mode with the magnetic well is known as the T-mode.[7]

The preceding discussion pertains to the toroidal plasma stability but not to the stability of the annulus itself. In practice, for high microwave power levels or low ambient neutral densities the annulus is unstable.[7] The stability of the combined annulus and core plasmas has been presented in the proceedings of the previous workshop.[8] In EBT,

although the annulus beta exceeds 10%, the toroidal plasma beta is less than 1%.

The purpose of this paper is to present the experimental results for stabilization of the high beta plasma instability by the hot electron annulus in a symmetric mirror. In Sect. 2 the experimental setup is presented and the hot electron annulus is discussed. The instabilities observed in this machine are described in Sect. 3. In Sect. 4, the stabilization of the instabilities by the hot electron annulus is discussed.

2. EXPERIMENTAL SETUP

Figure 1 shows the experimental arrangement. The magnetic field is produced by two independent motor-generator sets. One set drives the four central coils, the other the outer six coils. In this way the mirror ratio can be varied. The typical mirror ratio is 2. In the central region the magnetic field is almost constant over 100 cm as shown by the dotted line.

The magnetic field can be deformed by iron rings that are placed inside the vacuum vessel. The deformed field is shown by the solid line in Fig. 1. There are small bumps at $z = \pm 31$ cm due to access through the iron rings for diagnostics and microwave power. The microwave frequency is 6.4 GHz and the maximum power is 6 kW.

A high density plasma is created in the region beyond the mirror in helium gas by a Magneto-Plasma Dynamic (MPD) arc jet. The electrodes in the MPD source float with respect the vacuum chamber.

The density of this plasma is measured by a 75-GHz microwave interferometer and with double probes. The density is higher than the 75-GHz cutoff, so it is estimated by extrapolating the measurement of the ion saturation current from the time when the interferometer cuts off. Typical densities, determined in this way, are about 2×10^{14} cm^{-3}. The density is not uniform in Z; at Z = -31 cm, it is several times higher than at Z = +31 cm.

The electron temperature is estimated from the characteristics of the double probe and is typically about 5 eV. The energy confinement time is assumed to be limited by the electron time-of-flight. The ion temperature is not measured. It is assumed that the energy input to the ions comes from coulomb collisions. The calculated ion temperature is then almost equal to the electron temperature.

The hard x-ray spectrum is measured by pulse height analysis of a NaI scintillation detector. The detector is collimated by three tapered baffles to reduce the scattered photon contribution. The lead shielding thickness is 9 cm. To reduce the thick-target bremsstrahlung from the wall opposite the collimator, a hole is placed in the wall. This hole is 5 cm deep, is surrounded by lead, and is 3.2 cm in diameter, which is larger than the collimated diameter.

The hot electron temperature is determined from the x-ray spectrum. In the deformed field it is 50 keV, but in the uniform field it is 210 keV.

The radial dimensions of the hot electrons are determined with a moving tungsten chip. The tungsten has a diameter of 1 mm and a length of 5 mm and is held in a low-Z ceramic. Characteristic (K_α) x-rays are produced when high energy electrons strike the tungsten. The 58.1-keV x-rays are monitored by a single-channel analyzer that covers the range 53-63 keV. The output of the analyzer is connected to a rate meter. Since bremsstrahlung emission is proportional to the Z of the target,[9] the emission from tungsten is three times that from the ceramic. Also, since the single-channel analyzer is restricted to the energy region near the tungsten K_α line, its output is representative of the rate at which hot electrons strike the tungsten tip and thus shows the location of the hot electrons.

The annulus location is shown in Fig. 2. As the magnetic field is increased the annulus location moves outward. The width of the annulus does not vary systematically with the magnetic field strength, for reasons that are not clear.

In general the annulus is destroyed when a probe is inserted. However, in this device, the gaps in the iron rings are such that secondary mirrors are created, as shown in Fig. 1. The hot electrons are heated and trapped in these four ripple mirrors independently. Thus, the probe can be used to measure the fluctuation levels and the hot electron profiles without destroying all the rings.

The hot electron annulus beta value cannot be determined experimentally. It is estimated on the basis of the following parameters: $B = 1140$ gauss, $T_h = 50$ keV, and $n = 4 \times 10^{10}$ cm^{-3}. (This density is only one-twelfth the cutoff density at 6.4 GHz.) These parameters lead to a beta of 6%, so the beta is assumed to be in the range of 4-8%.

As the microwave power increases, the bremsstrahlung also increases. Since the photon number, integrated over the spectrum, is proportional to $n_e^2 T_e^{1/2}$, the hot electron beta increases with microwave power as well.

The density fluctuation is measured with a current probe (Tektronix P6032) connected to the double probes which are at Z = -70 cm, -31 cm, 0 cm, 31 cm, and 164 cm, as shown in the figure. To measure the azimuthal phase a set of probes at Z = -31 cm is arranged as shown in Fig. 1. To determine the parallel wavelength a pair of probes is used at z = -31 cm with a Z separation of 2.15 cm.

The fluctuation data is Fourier analyzed by digitizing the output of the current with a data processor (IWATSU and SM1330) and then storing the results in memory (DM901).

The diamagnetic activity is measured with a probe at Z = 0 cm. The details of this probe are presented elsewhere.[10]

3. INSTABILITIES IN THE HIGH DENSITY PLASMA

When the high density plasma is injected into the symmetric mirror a disruption is observed, caused by the resistive drift mode that is enhanced by the bad magnetic curvature at the edge of the plasma. A typical example is shown in Fig. 3. At the plasma center the density increases gradually and then suddenly decreases, which we call a disruption. Just before the disruption the high frequency oscillation can be observed to grow rapidly at the plasma edge [Fig. 3(b)]. When the probe is far away from the plasma column, at r = 4 cm, only a burst is observed to accompany the disruption [Fig. 3(c)]. The density at the end of the vacuum vessel increases after the plasma at the center abruptly disrupts, as shown in Fig. 3(d). More details of this behavior are presented elsewhere.[10]

The characteristics of the high frequency oscillation (resistive drift mode enhanced by bad magnetic curvature) are as follows:

(1) The instability is located near the edge of the plasma, where the amplitude is large.

(2) The real frequency is about $\frac{H}{2\Pi} \sim 100$ kHz. The growth rate is $\gamma_H^{-1} \sim 30$ μs.

(3) The ratio of the imaginary to the real frequency is $\frac{\gamma_H}{\omega_H} \sim 0.05$

(4) The instability rotates azimuthally in the direction of the electron diamagnetic drift.

(5) The azimuthal mode numbers are m = 1, 2, 3, and 4.

(6) The parallel wave length is 26 cm and is much shorter than the machine length but is the same as the length of the pair of iron rings.

(7) The instability cannot be clearly observed at Z = −70 cm.

(8) The instability is stabilized when the plasma density is increased or when a metal plate is placed at Z = 0 cm.

(9) It is not certain that the instability is an electromagnetic mode.

The experimental results for the disruption can be summarized as follows:

(1) When the instabilities occur, the plasma escapes abruptly along and across the magnetic field line.
(2) The growth rate is $\gamma_D^{-1} \sim 2\text{-}5\ \mu s$.
(3) The amplitude is large at the plasma center.
(4) The azimuthal mode number is $m = 0$.
(5) The parallel phase is constant along the plasma inside the center cell despite the fact that the density is not uniform.
(6) The parallel wave number $k_{\parallel}$ is larger than $0.015\ cm^{-1}$.
(7) The escape speed along the magnetic field lines is 10^7 cm/s, which is almost equal to the Alfven speed for $n = 2 \times 10^{14}$ cm^{-3} and $B = 2$ kG.
(8) The disruption cannot be observed when the high frequency instability is stabilized.

The Fourier analysis of the instabilities is shown in Fig. 4. The frequency of the disruption is about 10 kHz. The frequency of the resistive drift mode is about 100 kHz.

4. STABILIZATION WITH HOT ELECTRON RINGS

To investigate the stabilizing effects of the hot electron annulus the high density plasma is injected along the field lines into the region with the annulus. The buildup of the annulus is shown in Fig. 5. The ordinate is the integrated count rate, over the energy interval up to 500 keV; the abscissa is time, in 1-ms intervals. The time starts when the microwave power is turned on. The hot electron density increases gradually and then reaches a steady state. When the steady state is reached the high density plasma is injected.

The lifetime of the high density plasma is 1.5 ms. It is clear from the figure that the annulus is present during the lifetime of the injected plasma. The neutral gas that is fed to MPD source flies to an experimental region with a sound velocity. Then, the hot electron density decreases as shown in the photograph.

Typical results from this experiment are shown in Fig. 6. In contrast to Fig. 4, both the low frequency and the high frequency oscillations are suppressed. It should be noted that the density is lower (by 10-20%) when the annulus is present. The amplitude of the instabilities is decreased by up to 50%. The density reduction with the annulus cannot explain this stabilization, since the disruptions can still be observed without the annulus when the plasma source is adjusted to give an 80% reduction in density.

The instabilities at the plasma edge, where the drift mode is observed, are Fourier analyzed and shown in Fig. 7. In the absence of the annulus there is an oscillation near 70 kHz that is clearly suppressed when microwaves are applied.

In Fig. 8 the radial profile of the fluctuations is shown. The fluctuations are averaged over five shots. The open circles show the fluctuations when the high density plasma is injected into a vacuum field. The solid circles show what happens when it is injected into the field with the annulus. The high frequency component of the fluctuation is shown in the lower graph in Fig. 8. This component is identified as the drift mode, which is enhanced by the bad magnetic curvature. When the annulus is present this component is decreased, the disruption is suppressed, and the loss of density in the burst becomes small.

This experiment has been carried out for central magnetic field values from 1.4 to 2.0 kG. For fields below 1.4 kG, and above 2.0 kG, the stabilizing effect is not apparent. As can be seen from Fig. 2, when the field is larger than 1.8 kG, the annulus diameter becomes larger than the plasma diameter. However, even in this situation the annulus is able to reduce the instability.

The fluctuation level for the disruption is shown in Fig. 9 as a function of the microwave power. As the microwave power is increased the instability level is decreased. Also, as the power is increased the x-ray count rate increases, which indicates that the hot electron beta increases.

When a stainless steel disk is inserted at Z = 0 cm, the drift mode disappears entirely,[10] so the disruption cannot be observed. A comparison of the stabilizing effect of the annulus and of line-tying shows that line-tying seems to be more effective.

The microwave power is not utilized efficiently in this experiment because there is a large hole in the chamber that leads to the vacuum pump. The diameter of this hole is of the same order as the wavelength. If the microwave power were used more efficiently the hot electron beta would perhaps increase, and the stabilizing effect could then be seen more clearly.

REFERENCES

1. D. D. Ryutov and G. V. Stupakov, Sov. Phys. JETP 26, 177 (1977); M. E. Kishinevskii, et al., in Plasma Physics and Controlled Nuclear Fusion Research (Proc. 7th Int. Conf., Innsbruck, 1978) Vol. II, p. 411.
2. S. Hiroe, et al., Phys. Fluids 21, 676 (1978); T. Watari et al., Phys. Fluids 21, 2076 (1978).
3. G. I. Dimov, V. V. Zakajdakon and M. E. Kishinevskii, in Plasma Physics and Controlled Nuclear Fusion Research (Proc. 6th Int. Conf., Berchtesgaden, 1976; T. K. Fowler and B. G. Logan, Comments Plasma Physics Controlled Fusion 11 167 (1976); Vol. III, p. 177. B. G. Logan, et al., in Plasma Physics and Controlled Nuclear Fusion Research (Proc. 7th Int. Conf. Innsbruck, 1978).
4. R. A. Dandl et al., Oak Ridge National Laboratory ORNL/TM-3694, Oak Ridge, Tennessee.
5. H. Ikegami, et al., Phys. Fluids 11, 1061 (1968). R. A. Dandl et al., in Plasma Physics and Controlled Nuclear Fusion Research (Proc. 3rd Int. Conf., Novosibirsk, 1968).
6. B. H. Quon et al., Bull. Am. Phys. Soc. 25(B),994 (1980).
7. R. A. Dandl et al., Oak Ridge National Laboratory ORNL/TM-6457 (1978).
8. EBT Ring Physics: (Proc. Workshop), ed. by N. A. Uckan, Oak Ridge National Laboratory, CONF-791228, 59 (1980).
9. H. W. Koch and J. W. Motz, Rev. Mod. Phys. 31, 920 (1959).
10. S. Hiroe, T. Kunibe and H. Akiyama, Institute of Plasma Physics IPPJ-538, Nagoya, Japan (1981).

FIGURE CAPTIONS

Fig. 1. Schematic view of ASMIC-1 device.

Fig. 2. Radial position of the hot electron annulus.

Fig. 3. Typical plasma density behavior at various probe positions.

Fig. 4. Fast Fourier analysis of the instabilities without a hot electron annulus. A horizontal axis of an upper photograph and a lower photograph corresponds to 5 kHz/div and 50 kHz/div, respectively.

Fig. 5. The hot electron behavior along an experimental time sequence from a microwave power on to a power off through a MPD injection.

Fig. 6. Fast Fourier analysis of the instabilities with a hot electron annulus. The scale of the vertical axis which corresponds to 5 kHz/div and 50 kHz/div is the same as that of Fig. 4.

Fig. 7. Fast Fourier analysis of the drift type instabilities near the plasma edge (r = 1.5 cm). The horizontal axis is 50 kHz/div and the vertical axis is the same to each other.

Fig. 8. Fluctuation levels of the instabilities are plotted against the radial position with and without an annulus. The microwave power of 5 kW is irradiated into the mirror.

Fig. 9. Fluctuation level of the disruption is plotted against the microwave power. The hot electron beta value is an increasing function of the microwave power.

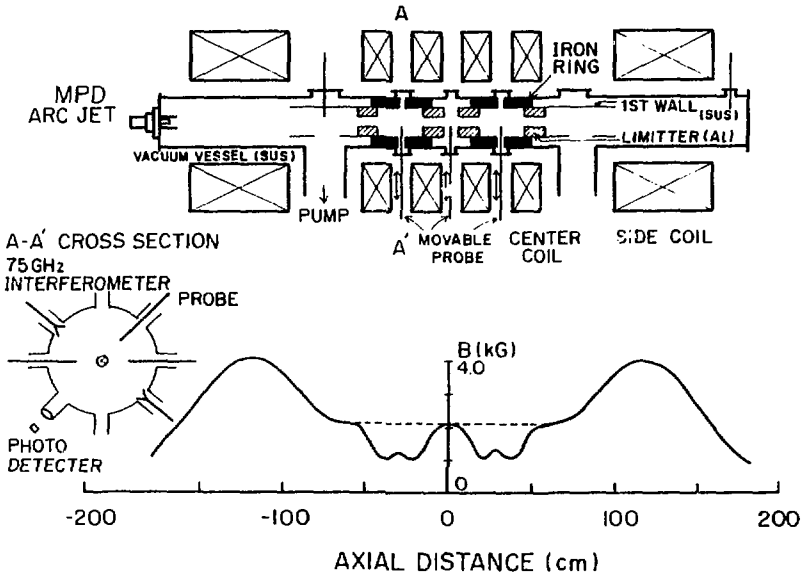
A
IRON RING
MPD ARC JET
1ST WALL (SUS)
LIMITTER (AL)
VACUUM VESSEL (SUS)
PUMP
A'
MOVABLE PROBE
CENTER COIL
SIDE COIL
A-A' CROSS SECTION
75GHz INTERFEROMETER
PROBE
PHOTO DETECTER
B (kG)
4.0
0
-200
-100
0
100
200
AXIAL DISTANCE (cm)

Fig. 1

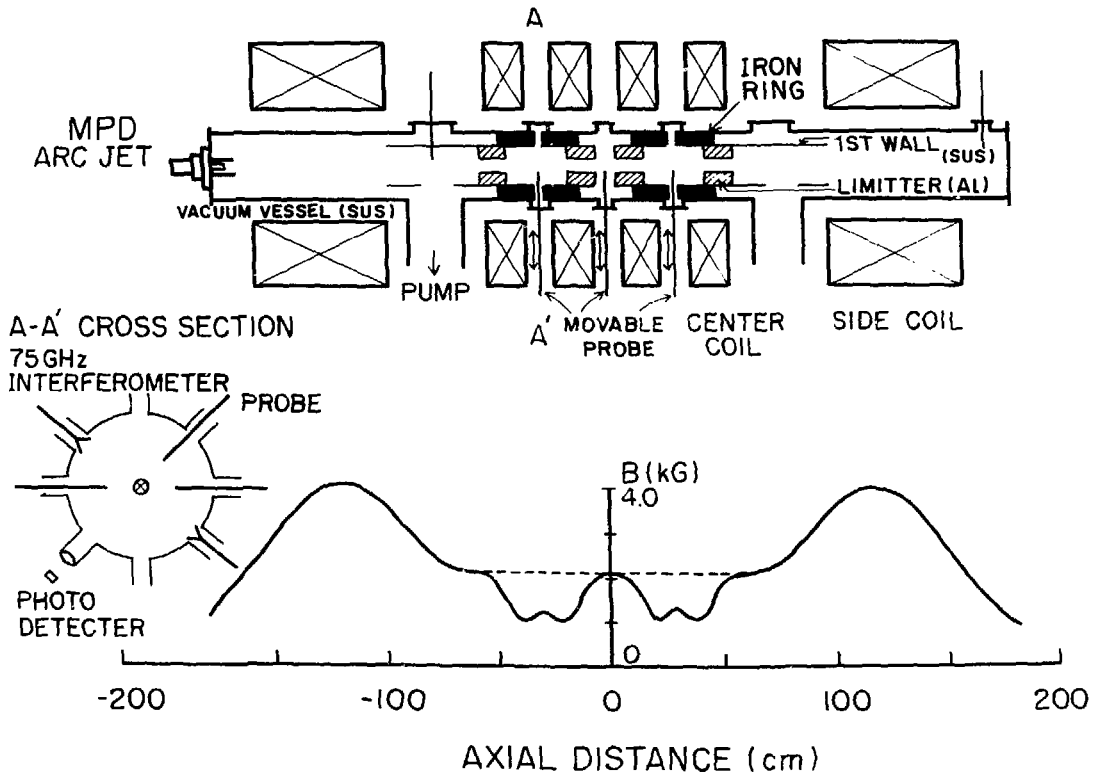
A
IRON RING
MPD ARC JET
1ST WALL (SUS)
LIMITTER (AL)
VACUUM VESSEL (SUS)
PUMP
A-A′ CROSS SECTION
A′ MOVABLE PROBE
CENTER COIL
SIDE COIL
75GHz INTERFEROMETER
PROBE
PHOTO DETECTER
B (kG)
4.0
0
-200
-100
0
100
200
AXIAL DISTANCE (cm)

Fig. 1

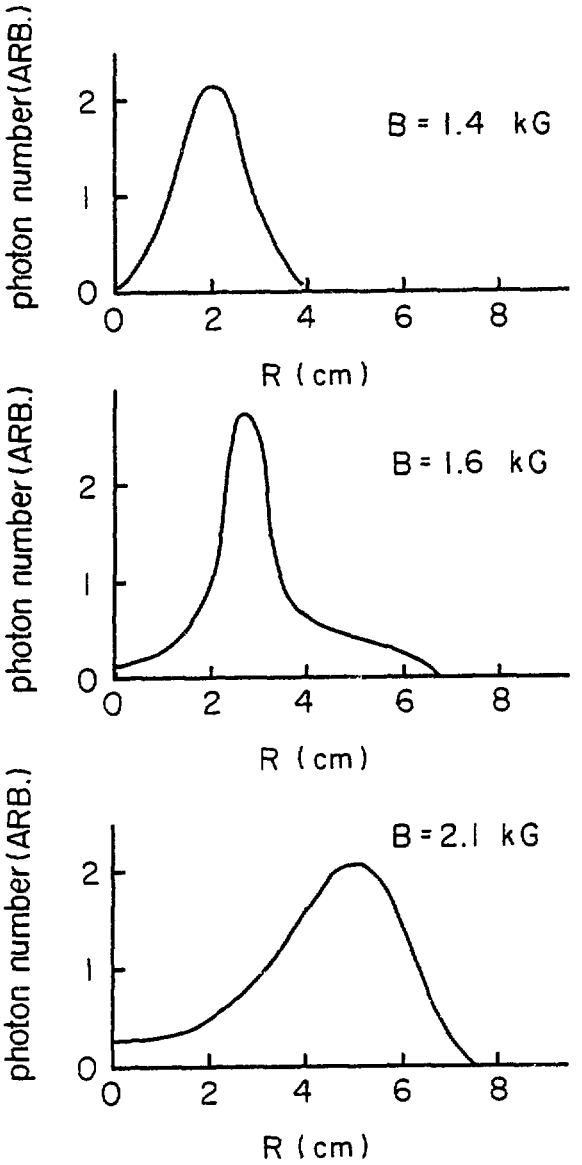
photon number (ARB.)
B = 1.4 kG
R (cm)
photon number (ARB.)
B = 1.6 kG
R (cm)
photon number (ARB.)
B = 2.1 kG
R (cm)

Fig. 2

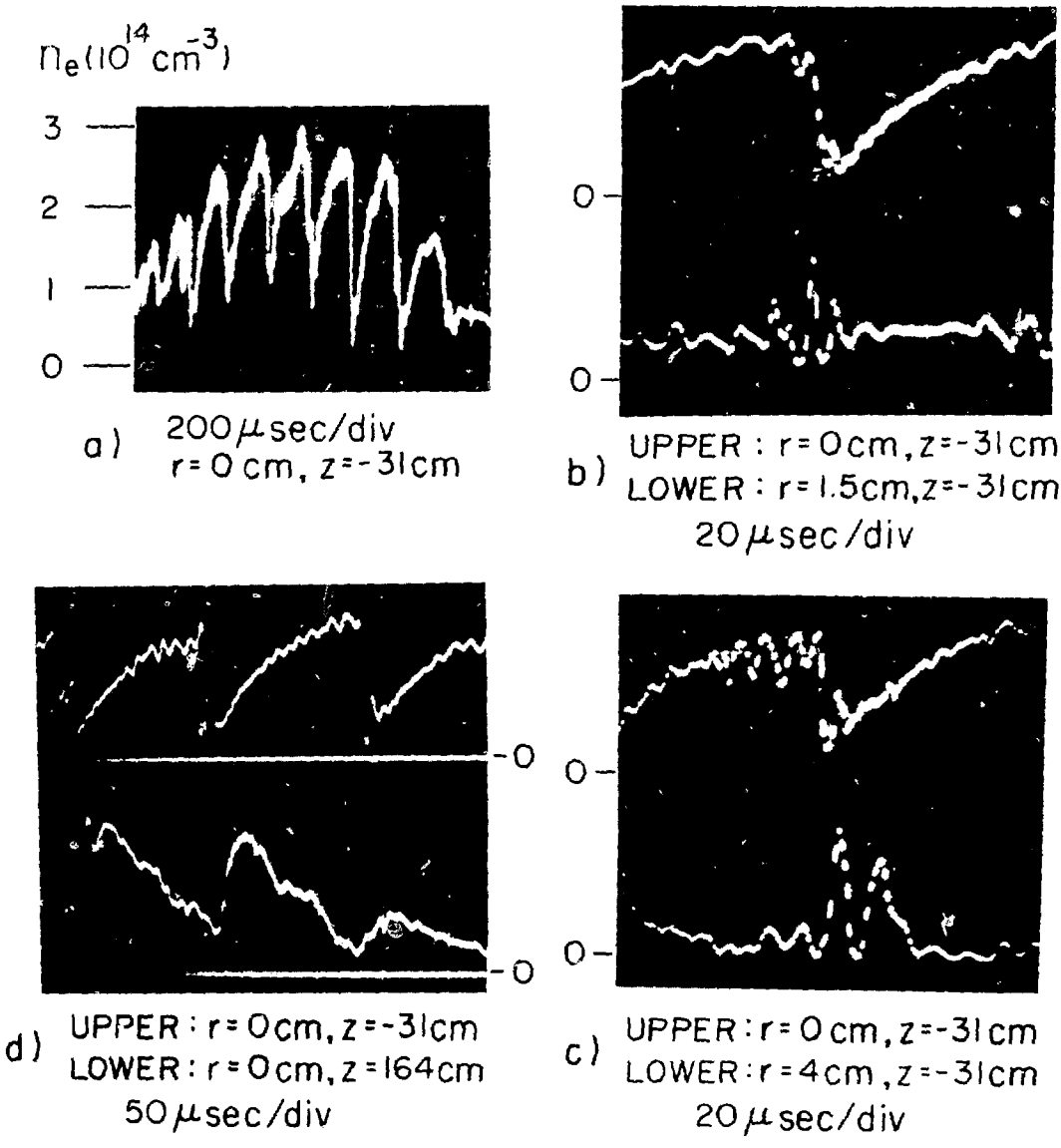
$n_e(10^{14} cm^{-3})$
3
2
1
0
a) 200μsec/div
r=0 cm, z=-31cm
0
0
b) UPPER : r=0cm, z=-31cm
LOWER : r=1.5cm, z=-31cm
20μsec/div
0
0
d) UPPER : r=0cm, z=-31cm
LOWER : r=0cm, z=164cm
50μsec/div
0
0
c) UPPER : r=0cm, z=-31cm
LOWER : r=4cm, z=-31cm
20μsec/div

Fig. 3

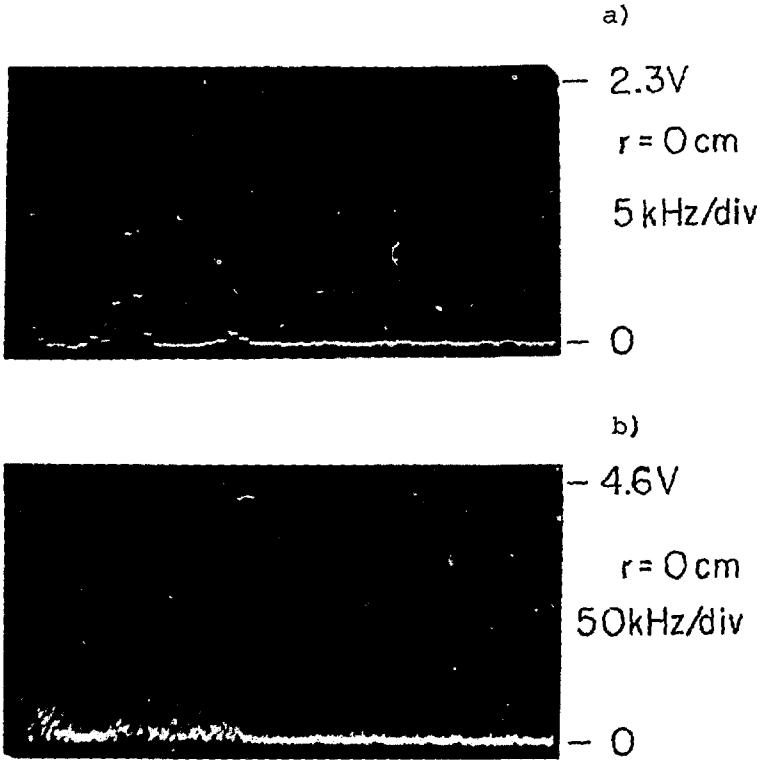

Fig. 4

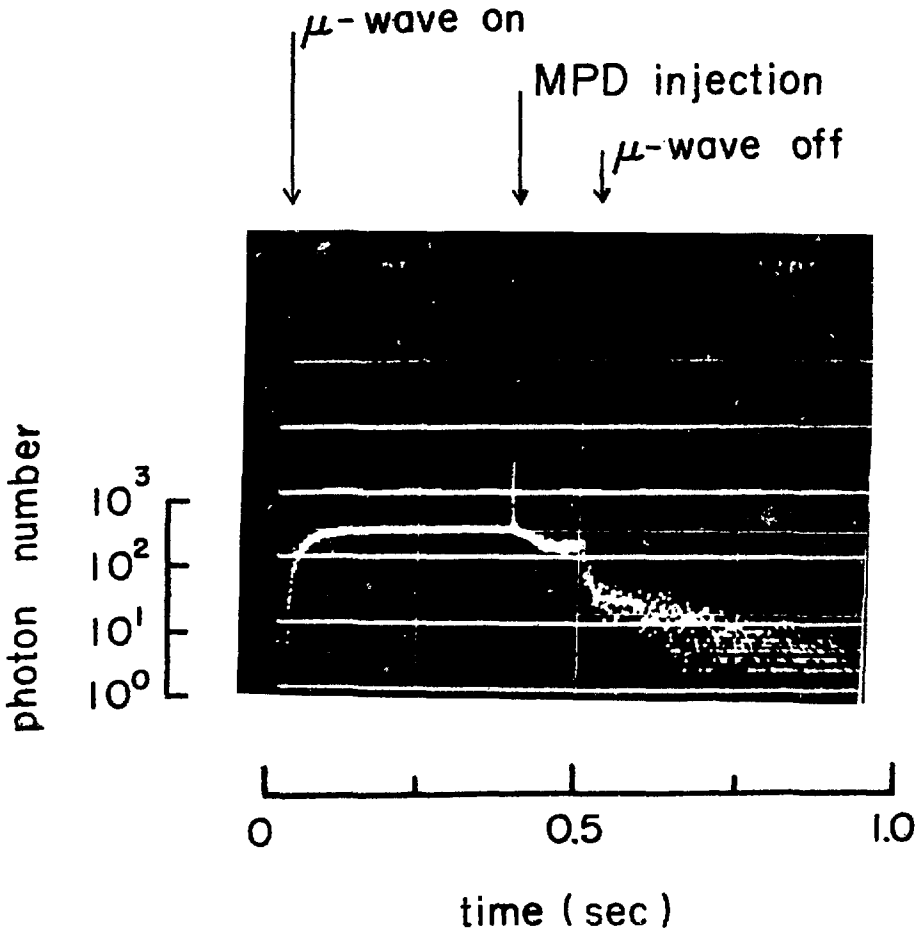
μ-wave on
MPD injection
μ-wave off
photon number
10^3
10^2
10^1
10^0
0
0.5
1.0
time (sec)

Fig. 5

5 kHz/div

r = 0

50 kHz/div

r = 0

Fig. 6

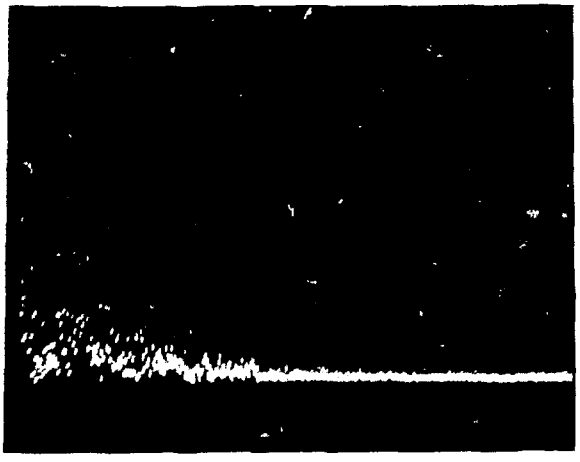

WITHOUT ANNULUS

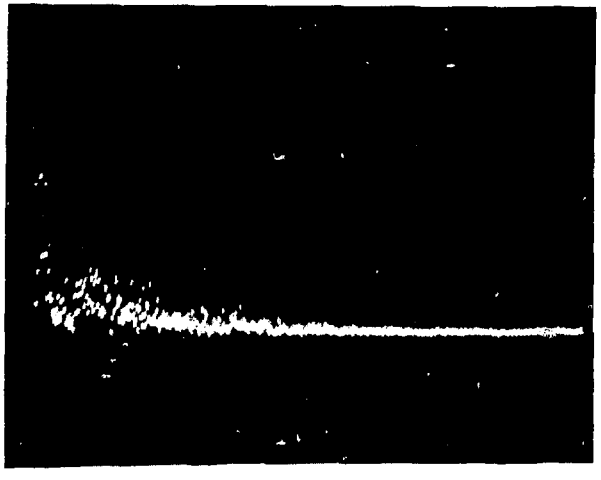

WITH ANNULUS

Fig. 7

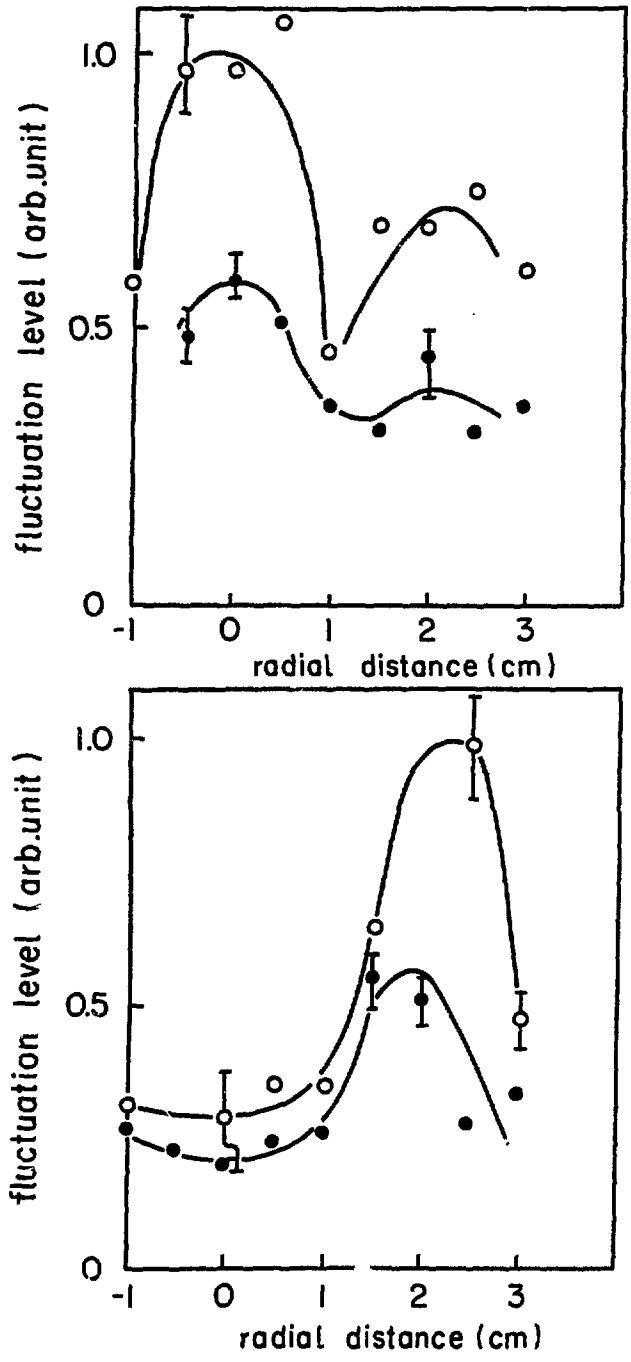
1.0
0.5
0
fluctuation level (arb.unit)
-1
0
1
2
3
radial distance (cm)
1.0
0.5
0
fluctuation level (arb.unit)
-1
0
1
2
3
radial distance (cm)

Fig. 8

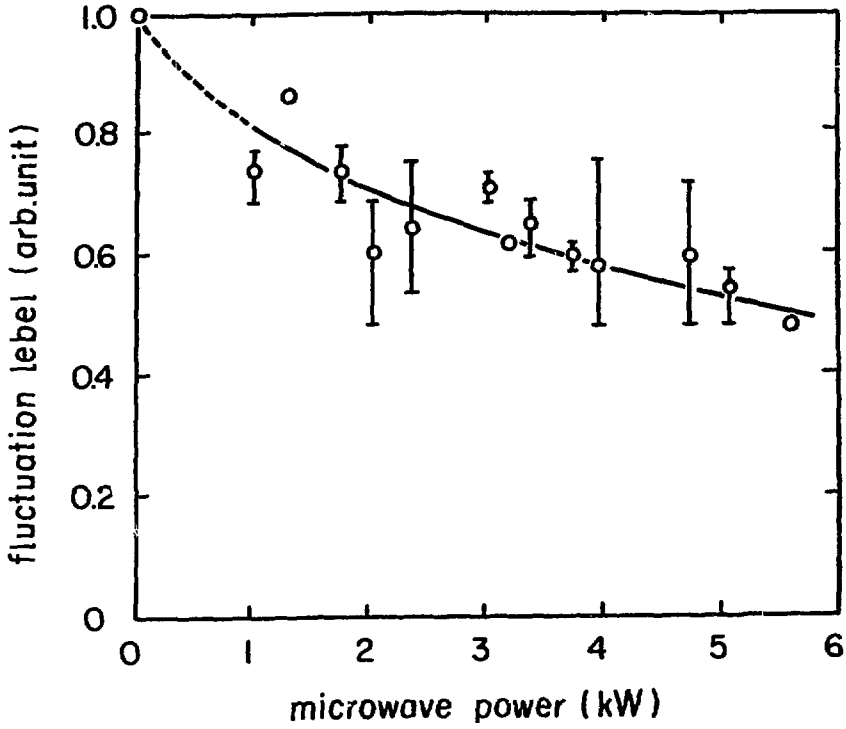
1.0
0.8
0.6
0.4
0.2
0
fluctuation lebel (arb.unit)
0
1
2
3
4
5
6
microwave power (kW)

Fig. 9

EXPERIMENTAL HOT-TO-WARM ELECTRON DENSITY RATIO FOR INSTABILITY THRESHOLD IN THE ELMO BUMPY TORUS*

S. Hiroe, L. A. Berry, R. J. Colchin, J. C. Glowienka,
G. R. Haste, D. L. Hillis and T. Uckan

Oak Ridge National Laboratory
Oak Ridge, TN 37830

ABSTRACT

The hot-to-warm electron density ratio is determined for the onset of instabilities that spontaneously grow in the region of large stored energy in the ELMO Bumpy Torus (EBT). When this ratio exceeds ~ 0.5, the instability becomes conspicuous as an oscillation on the microwave interferometer signal. When the microwave power and ambient pressure are varied, the ratio remains constant in spite of changes in the density, temperature, and beta value. The stable region in a β diagram increases when the microwave power increases.

*Research sponsored by the Office of Fusion Energy, U.S. Department of Energy, under contract W-7405-eng-26 with the Union Carbide Corporation.

The ELMO Bumpy Torus[1] (EBT) is designed to circumvent the MHD stability problem due to the unfavorable magnetic curvature by using the diamagnetism of energetic electron annuli produced by electron cyclotron heating (ECH). Since 1972, continuing efforts have been made to obtain stable toroidal plasmas in EBT. Recently, steady-state operation at 200 kW of 28-GHz gyrotron power has been achieved.[2] The parameters of the toroidal plasma are: an electron density n_e of $1\text{-}2 \times 10^{12}$ cm^{-3}, an electron temperature T_e of 1 keV, an ion temperature T_i of 20-40 eV, and an energy confinement time τ_E of 2-4 ms. The beta value β_h of the annuli that modify the unfavorable magnetic curvature reaches $\sim$30%.

The experiments[3] have been carried out by changing the ambient pressure p_o while keeping the microwave power P_μ constant. When the ambient pressure decreases from high pressure (several times 10^{-5} torr) to low pressure (several times 10^{-6} torr), the line integral density seen by a 75-GHz interferometer decreases, but the electron temperature increases. Plasma changes with pressure have been classified into three operational modes.

The C-mode is characterized by a high pressure, a large line integral density, a low electron temperature, and a noisy plasma of low frequency oscillations. As the ambient pressure is reduced, the amplitude of the low frequency oscillations becomes small and the plasma merges continuously into the T-mode. This transition region is called the T-C transition.

The T-mode is present at moderate ambient pressures. The plasma is quiescent, and the line integral density is almost constant in this mode. On approaching the M-mode at lower pressure, the line integral density decreases but the electron temperature continues to increase. A

the same time, the fluctuation level increases steeply. We define this as the T-M transition. At still lower pressure we reach the M-mode, where the plasma disrupts.

At higher power operation, the above-mentioned tendencies do not change but move to a higher ambient pressure. The relation between the ambient pressure p_o and the microwave power P_μ, which defines the T-M transition and the T-C transition, is obtained[4] empirically as

$$p_o \text{ (torr)} \simeq 4.5 \times 10^{-7} \sqrt{P_\mu \text{ (kW)}} \text{ , at the T-M transition,} \qquad (1)$$

and

$$p_o \text{ (torr)} \simeq 1.25 \times 10^{-6} \sqrt{P_\mu \text{ (kW)}} \text{ , at the T-C transition.} \qquad (2)$$

The diagnostics used in these experiments are a 9-channel, 75-GHz microwave interferometer system for density profile measurements, a diamagnetic pickup loop for hot electron stored energy determinations, and x-ray detectors for observation of electron temperature and density. The hot electron temperature and density are measured by means of a sodium-iodide scintillation detector whereas the warm electron temperature and density are measured with a windowless lithium-drifted silicon barrier detector. Both detectors measure free-free bremsstrahlung radiation. The spectrum from a plasma with a Maxwellian electron distribution is given by

$$I(\varepsilon)d\varepsilon = Gn_e n_i T^{-1/2} \exp(-\varepsilon/T) d\varepsilon \text{ ,} \qquad (3)$$

where ε is an x-ray energy, G is a geometrical factor, n_e and n_i are the electron and ion densities respectively, and T is the electron temperature of an energy unit. The details of the measurement are given in Ref. 5.

The hot electron density and temperature are verified by diamagnetic loop measurements. The warm plasma density measurements are corroborated by the multichannel microwave interferometer.

In Fig. 1, the hot electron density and the cold electron density are plotted as a function of the ambient pressure in the T- and M-modes. Upon decreasing the ambient pressure, the core density measured by both the microwave interferometer n_c (center) and the soft x-ray $\bar{n}_c$ (s.x) detector first increases and then decreases as the operational pressure is reduced beyond the T-M transition. On the other hand, the hot electron density n_h monotonically increases as the ambient pressure decreases.

The average density $\bar{n}_c(\mu)$ measured with the microwave interferometer is a slowly decreasing function as the ambient pressure is reduced. Near the T-M transition, the average density changes to a more steeply decreasing function with pressure. This dependence does not change with microwave power.

The value of n_c (center), which is obtained from Abel-inverted multichannel interferometer data, is within a factor of 2 of $\bar{n}_c$ (s.x) as measured by the soft x-ray detector. The soft x-ray detector is most sensitive to the warmest of the core electrons. In the following, we adopt the Abel-inverted density profile of the multichannel interferometer.

The difference between n_c (center) and $\bar{n}_c(\mu)$ can be explained by a reduction in the plasma radius as the ambient pressure is decreased.[2] The surface plasma located outside of the annulus decreases as p_o decreases. At the T-M transition, the contribution of the surface plasma to the interferometer output ($n_e\ell$) is small, so n_c (center) and $n_c(\mu)$ are the same value.

The operating conditions at the T-M transition are determined from Eq. 1. Fig. 2 shows these transitions as open circles. The core density first increases as the ambient pressure decreases and then decreases when the ambient pressure is lowered beyond the T-M transition. On the other hand, the hot density monotonically increases when the pressure decreases beyond the T-M transition, as shown in Fig. 1.

The hot-to-cold electron density ratio (n_h/n_c) is also shown as an insert in Fig. 1. It is clear that the ratio n_h/n_c increases steeply near the T-M transition. The hot electron density measured by the hard x-ray detector is the local density at the annulus. However, the densities measured by the microwave interferometer $\bar{n}_c(\mu)$ and the soft x-ray $\bar{n}_c$ (s.x) are average values along a chord through the plasma.

The effective plasma radius is almost constant[2] when EBT-S is operated under the condition of $p_o/\sqrt{P_\mu} \sim$ constant, which is the same parametric dependence as that of Eq. 1. Thus, at the T-M transition, the plasma diameter is almost constant (20 cm). The ratio n_h/n_c can be normalized by the local density obtained from the Abel-inverted interferometer output (density profile). The density at the annulus is approximately half the density at the center.

Figure 3 shows the line average density, the hot electron density, the hot electron beta value and the density ratio n_h/n_c at the T-M transition as a function of the microwave power. The first three parameters increase with the microwave power, but the density ratio is almost constant. The closed circles in the bottom of Fig. 3 represent the density ratio obtained using soft x-ray values normalized to the position of the rings. On the other hand, the open circles in the bottom of Fig. 3 are calculated using the microwave interferometer line

average density and assuming a chord length of 20 cm, again normalized to the ring position. The soft x-ray and microwave interferometer data have to be set equal at 100-kW applied ECH power. The data point at 50 kW obtained from the interferometer density deviates from all the other points and is the result of a somewhat low experimental value of the line average density.

At the T-M transition, we have measured the electron temperature, the core stored energy n_c, etc. Except for the density ratio (n_h/n_c), the plasma parameters (n_h, n_c, T_c, β_c, and β_h) are an increasing function of the microwave power.

In the experiments, a pair of the beta values for the core plasma and the hot electron annulus can be determined for each value of p_o and P_μ. The experimental relation between β_c and β_h under T-mode conditions is plotted in Fig. 4. In general, these experiments were carried out by changing the ambient pressure while keeping the microwave power constant. In the 100-kW case (open circles), upon decreasing the ambient pressure from the T-C transition to the T-M transition, both of the beta values began increasing, illustrating the fact that in EBT one cannot independently choose β_c and β_h.

The beta values at the T-C transition do not vary much, but the beta values at the T-M transition change with applied ECH power. With increasing microwave power, the stable operation range becomes wider as does the toroidal beta value.

The instability at the T-M transition has been tentatively[6] identified as an interchange instability. The theoretical density ratio n_h/n_c[7] for the high frequency interchange mode does not strongly depend on the beta value of the hot electron annulus. From the results of several

theories,[8] stable regions may be mapped on the beta diagram. These theoretical predictions are not in good agreement with the experimental results shown in Fig. 4.

It would be very interesting to stabilize the plasma at the T-M transition since stable low pressure operation would offer the possibility of higher density plasmas in a regime of high electron temperature and would minimize the gyrotron power. In oreder to stabilize the plasma at the T-M transition, the results of this analysis suggest to either increase the core plasma density or decrease the hot electron density. It may be possible to increase core density, by neutral gas puffing and/or by increasing the mirror ratio. To decrease the hot electron density, it is necessary to control the surface plasma just outside the annulus. One method for such control is to eliminate the fundamental resonance zone outside the magnetic lines which are connected to the hot electron annulus by using a skimmer probe.

ACKNOWLEDGMENT

The authors would like to thank D. A. Spong, A. M. El Nadi and B. H. Quon for many helpful discussions.

REFERENCES

1. R. A. Dandl, H. O. Eason, A. C. England, G. E. Guest, C. L. Hedrick, and J. C. Sprott, ORNL/TM-3694, Oak Ridge, TN (November 1971).
2. R. J. Colchin Bull. Am. Phys. Soc., 26, (1981) 845.
   R. A. Dandl, et al., Plasma Physics and Controlled Nuclear Fusion Research (Proc. 5th Int. Conf., Tokyo, Japan, 1974) Vol. II, p. 141 (1975).
3. R. A. Dandl, et al., ORNL/TM-6457, Oak Ridge, TN (1978).
   M. Fujiwara et al., Plasma Physics and Controlled Nuclear Fusion Research (Proc. 8th Int. Conf., Brussels, 1980) Vol. 1, p. 845.
4. L. A. Berry, private communication.
5. S. Hiroe, G. R. Haste, and R. A. Dandl, ORNL/TM-6820, Oak Ridge, TN, (1979).
6. A. Komori, ORNL/TM-7530, Oak Ridge, TN, (1981).
7. A. El Nadi, private communication.
8. D. A. Spong, J. W. Van Dam, H. L. Berk, and M. N. Rosenbluth, EBT Stability Theory, (Proc. Workshop), Oak Ridge, TN, p. 115 (1981); K. T. Tsang and C. B. Cheng, EBT Stability Theory, Proc. Workshop), Oak Ridge, TN, p. 141 (1981); C. B. Cheng and K. T. Tsang, EBT Stability Theory, Proc. Workshop), Oak Ridge, TN, p. 161, (1981).
   R. R. Dominquez, H. L. Berk, Phys. Fluids 21 (1978) 827.

FIGURE CAPTIONS

Fig. 1. Various densities are plotted against ambient pressure at an applied microwave power of 100 kW. The hot electron density is symbolized by n_h, the density at the plasma center by n_c (center), the average density from an interferometer by $\bar{n}_c(\mu)$, and the average density from a soft x-ray detector by $\bar{n}_c(s.x)$. The plasma radius is 20 cm. The density ratio is also plotted as a function of the ambient pressure in an insert.

Fig. 2. The core plasma density measured by the soft x-ray detector is displayed as a function of the ambient pressure. The open circles indicate the T-M transition as calculated using Eq. (1).

Fig. 3. The line average density, the hot electron density, the hot electron beta, and the hot-to-cold electron density ratio at the T-M transition are plotted against the microwave power.

Fig. 4. The beta diagram for EBT-S operation; β_c is calculated at a magnetic field strength of 1 T. Thresholds for instability onset are shown by arrows.

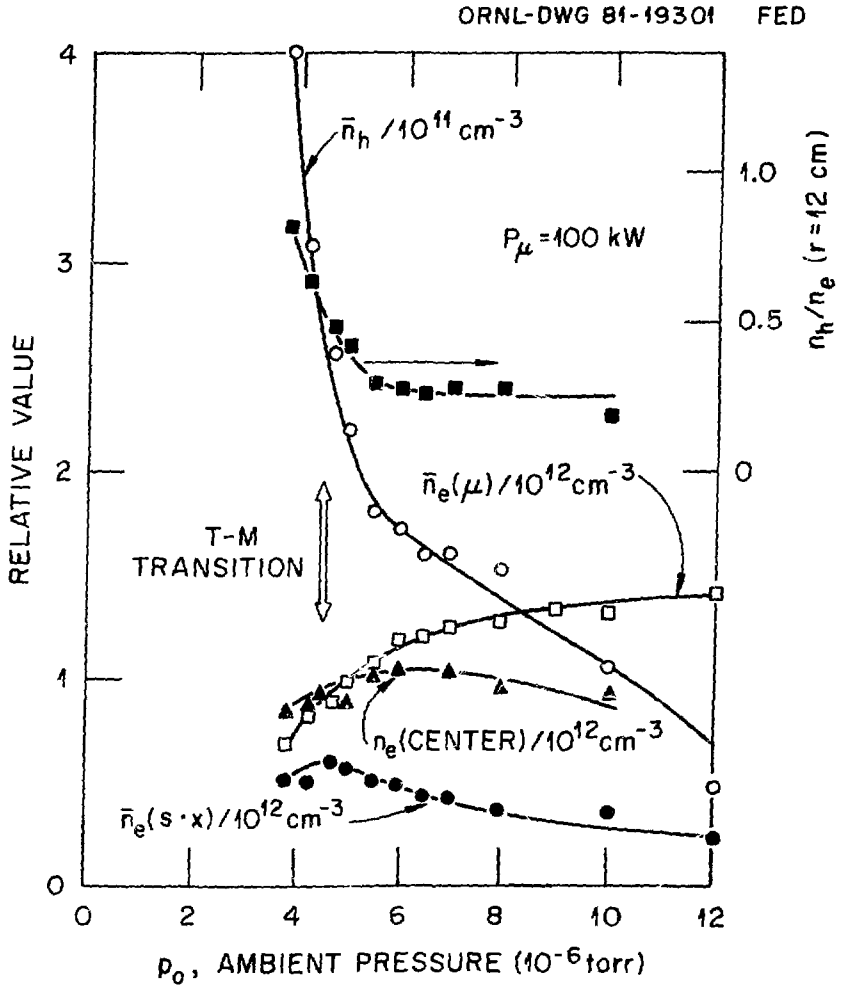
ORNL-DWG 81-19301 FED
$\bar{n}_h$ /10^{11} cm^{-3}
P_μ =100 kW
$\bar{n}_e(\mu)$/10^{12}cm^{-3}
T-M
TRANSITION
n_e(CENTER)/10^{12}cm^{-3}
$\bar{n}_e(s \cdot x)$/10^{12}cm^{-3}
RELATIVE VALUE
n_h/n_e (r=12 cm)
p_o, AMBIENT PRESSURE (10^{-6}torr)
0
1
2
3
4
0
2
4
6
8
10
12
0
0.5
1.0

Fig. 1

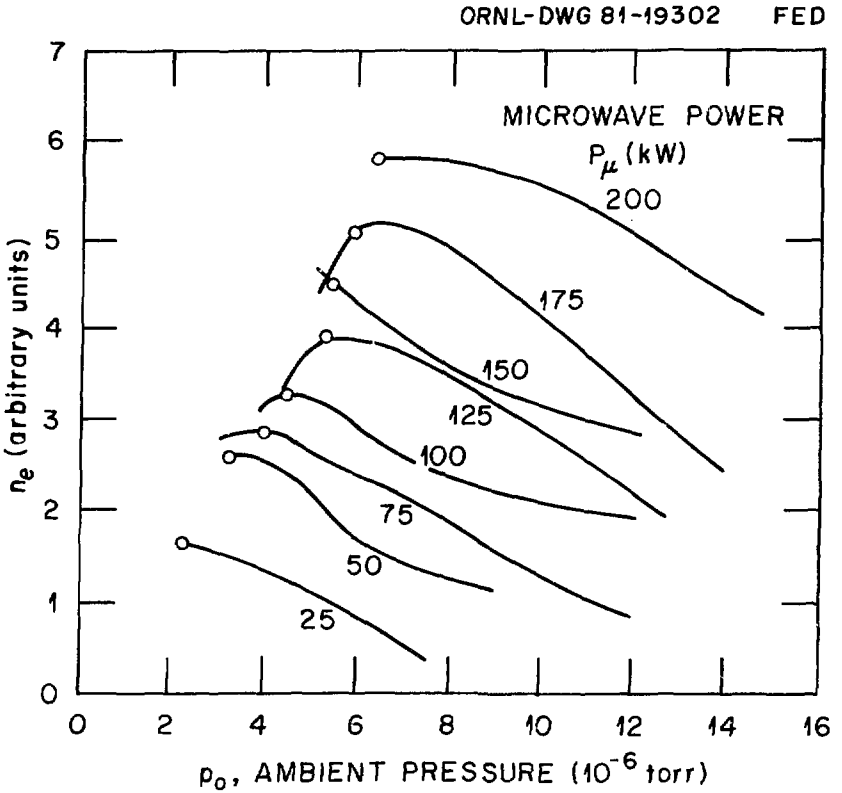
ORNL-DWG 81-19302 FED
MICROWAVE POWER
P_μ (kW)
200
175
150
125
100
75
50
25
n_e (arbitrary units)
p_o, AMBIENT PRESSURE (10^{-6} torr)
0
1
2
3
4
5
6
7
0
2
4
6
8
10
12
14
16

Fig. 2

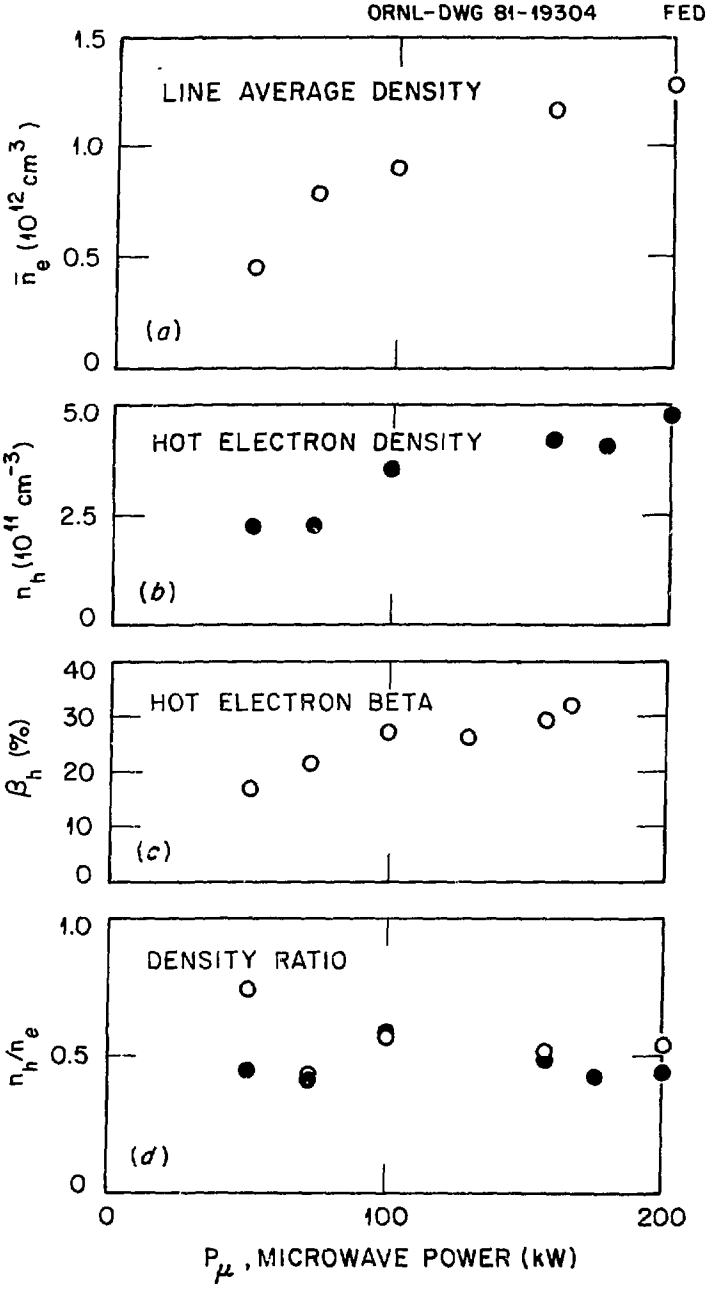
ORNL-DWG 81-19304 FED
LINE AVERAGE DENSITY
$\bar{n}_e$ (10^{12} cm^{-3})
1.5
1.0
0.5
0
(a)
HOT ELECTRON DENSITY
n_h (10^{11} cm^{-3})
5.0
2.5
0
(b)
HOT ELECTRON BETA
β_h (%)
40
30
20
10
0
(c)
DENSITY RATIO
n_h/n_e
1.0
0.5
0
(d)
0
100
200
P_μ, MICROWAVE POWER (kW)

Fig. 3

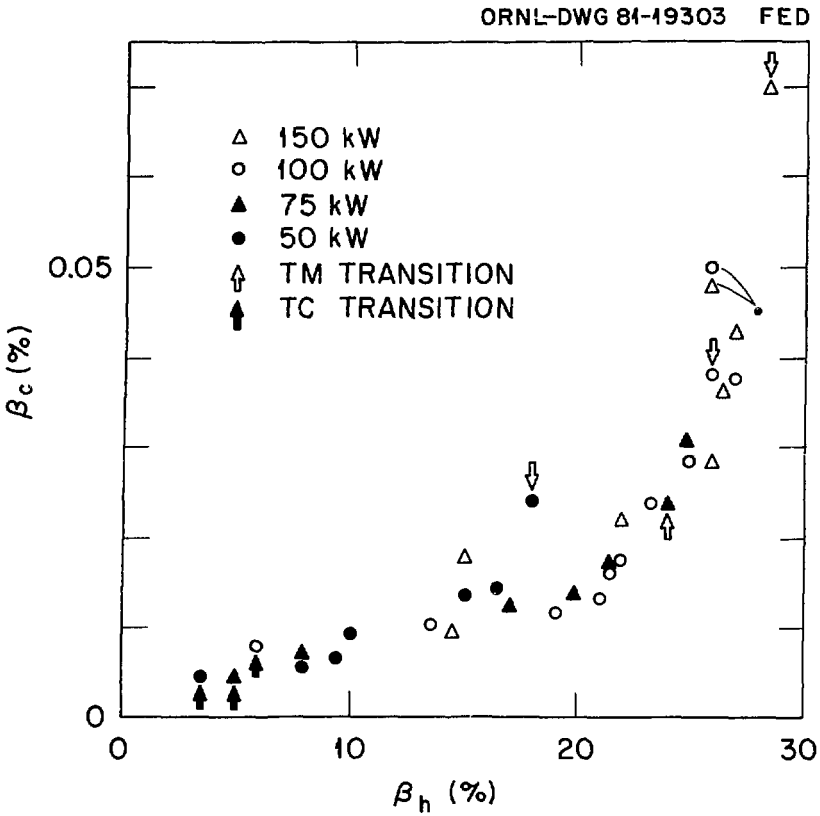
ORNL-DWG 81-19303 FED
150 kW
100 kW
75 kW
50 kW
TM TRANSITION
TC TRANSITION
0.05
0
β_c (%)
0
10
20
30
β_h (%)

Fig. 4

STABILIZATION OF THE FLUTE INSTABILITY BY A D.C. ELECTRIC FIELD IN TOROIDAL PLASMAS*

Igor Alexeff
University of Tennessee
Knoxville, Tennessee 37996-2100

ABSTRACT

The absence of the flute instability in the NASA Lewis Bumpy Torus and the Elmo Bumpy Torus at Oak Ridge is investigated by classical incompressible MHD. We find that radial electric fields produce rapid $\vec{E}\times\vec{B}$ precession about the minor perimeter. This precessional velocity is sheared with respect to distance along the Z-direction of the torus. We demonstrate by means of a simple model that this shear velocity reduces the flute growth rate to a value consistent with that of classical resistive drift, or in plasma terminology, classical diffusion.

*Supported in part by U.S. National Science Foundation Grant No. ENG-78-03400.

The basic observation is that both the NASA Lewis Bumpy torus and the Elmo Bumpy Torus at Oak Ridge are stable against the flute instability. We also note that both devices contain strong radial electric fields. In the case of the NASA Lewis Bumpy Torus, the fields are imposed by an external power supply by means of external electrodes. In the case of the Elmo Bumpy Torus, the fields arise as an artifact of the high-power, electron-heating via microwaves.

We also note that in the case of the NASA Lewis Bumpy Torus, the electric field points inward in some parts of the torus, and outward in others. This is made obvious when we note that the radial field points outward when an electrode is made positive, so it must have pointed inward beneath the electrode. Making the electrode negative causes the field to point inward, showing that it is <u>not</u> due to ambi-polar (non-reversible) effects. See Fig. 1.

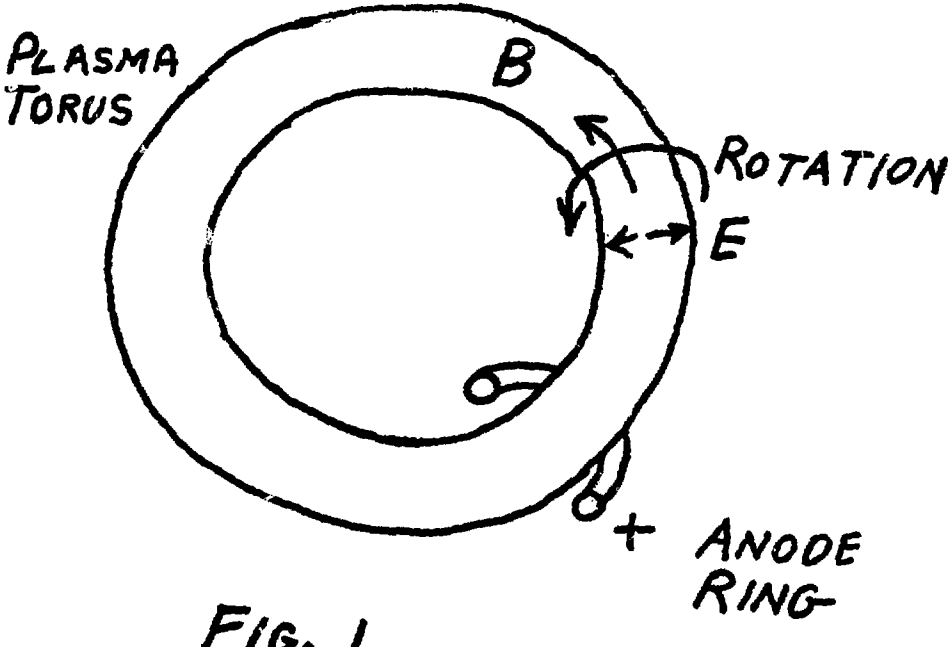

FIG. 1

The presence of the radially-inward electric field has been inferred[1] in the derivation of the "Geometric Mean Frequency". In the case of the Elmo Bumpy Torus at Oak Ridge, the electric field is ambipolar, but we expect that the bumpiness of the plasma causes variation in both the local electric and magnetic fields, causing both a rotation and a shear in rotation. Thus both plasma devices may be examined by the same model.

In Fig. 2, we demonstrate the basic feature of the model - a magnetically supported plasma column in rapid <u>sheared</u> rotation.

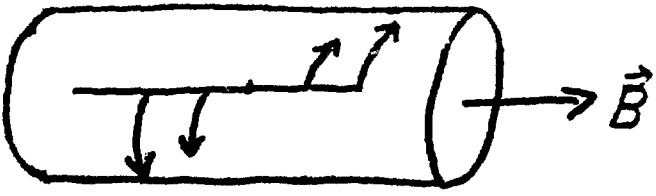

Figure 2

We neglect (for simplicity) the possible instabilities due to the shear, and concentrate on the effects of the shear on the flute instability.

For simplicity, we go to the classical model of a conducting, incompressible fluid supported by a magnetic field against gravity, as shown in Figure 3.

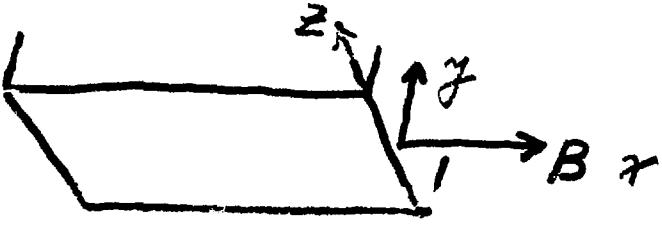

Figure 3

We ignore viscosity and consider simply momentum, pressure, magnetic viscosity, and gravity. The momentum equation is linearized, $\rho \frac{d\vec{v}}{dt} \simeq \rho \frac{\partial \vec{v}}{\partial t}$, as occurs at early times for small velocities. Our basic equations are,

$$\rho \frac{\partial \vec{v}}{\partial t} = - \sigma B^2 \vec{v} - \nabla p - \rho \vec{g} \ . \tag{1a}$$

for $\vec{v} \perp \vec{B}$

$$\rho \frac{\partial \vec{v}}{\partial t} = - \nabla p - \rho \vec{g} \tag{1b}$$

for $\vec{v} \parallel \vec{B}$

$$\nabla \cdot \vec{v} = 0 \tag{2}$$

Here ρ is the fluid mass density in kg meter^{-3}, σ is the conductivity in mho meter^{-1}, B is in Tesla, p in newtons meter^{-2}, and g is in meters (+) second^{-2}. Equation 1a and 1b are simply the equations for momentum balance, and equation 2 is the consequence of fluid incompressibility.

We assume a Fourier decomposition of modes at the bottom surface. The characteristic solution for ripples perpendicular to the magnetic field ($\vec{k}_x \parallel \vec{B}$) in the absence of shear is,

$$y = y_0 \ e^{+ \frac{\rho g \ k_x}{\sigma B^2} t} \cos k_x \ x \ .$$

Thus, the magnetic field dramatically reduces the growth rate for $k_x \parallel B$. The reason for this is that $\nabla x \vec{E} = \nabla x (\vec{v} x \vec{B}) \neq 0$ in the liquid metal, and eddy currents can flow. In the above derivation, we have noted that the magnetic term dominates, and have ignored the momentum term in Eq. 1a.

For the case of ripples parallel to the magnetic field, $\vec{k} \perp \vec{B}$, the magnetic field has no effect. The dispersion relation is,

$$y = y_0 \ e^{+ \sqrt{k_z g} \ t} \cos k_z \ z,$$

The reason that the magnetic field has no effect is that for this case, $\nabla \times (\vec{v} \times \vec{B}) = 0$, and no eddy currents can flow.

In the case of the SHEARED FLOW, we find that the direction of the $\vec{k}$ vector is continually changing relative to the direction of the magnetic field. As shown in Fig. 4, although $\vec{k}$ may initially be perpendicular to $\vec{B}$ (no stabilization), a short time later, this is no longer true!

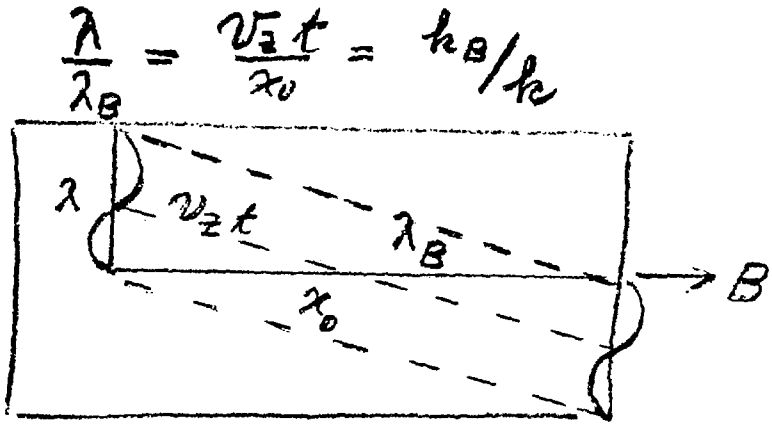

Figure 4

Bottom view of slab

Thus, in a sheared fluid, $\vec{k}$ is perpendicular to $\vec{B}$ only for an instant.

Since the projection of $\vec{k}$ on $\vec{B}$ is what can provide stability we note that the projection of $\vec{k}$ on $\vec{B}$ is

$$k_0 \left(\frac{v_z t}{x_0}\right) ,$$

where $\left(\frac{v_z}{x_0}\right)$ is the rate of shear flow in the fluid slab.

The spatial part of the fluid flow is as before. Only the time dependence changes. We neglect the momentum term in Eq. 1a, and obtain the following result (see appendix),

$$y = y_0 \left(\frac{t}{t_0}\right)^{\left(\frac{\rho g\ k_z}{\sigma B^2}\right)\left(\frac{x_0}{v_z}\right)}$$

The effect of the magnetic field reappears in the equation, which is no longer an exponential, but a power law. The constant t_0 is merely required to dimensionally correct the new equation. As long as the shear parameter $\frac{v_z}{x_0}$ is non-zero, conventional flutes cannot appear, and a dramatic decrease in cross-field transport occurs. In our equation, if the shear parameter goes to zero, the equation for v_y diverges. This divergence is due to our neglecting the momentum term in the derivation - in reality the equation reverts to the case for $\vec{k} \perp \vec{B}$. Also, the equation is not valid for t near zero, for the same reason. We also note that the equation is only valid for $\frac{v_z t}{x_0} \sim 1$, since for highly sheared fluids, the actual waves are being folded back on themselves ($\vec{k}$ is increasing) so a more detailed treatment is required.

CONCLUSIONS

For an MHD incompressible fluid supported on a magnetic field, the normal flute instability cannot occur if a velocity shear parallel to the surface is present. Instead, a much slower, magnetic-field-dependent, non-exponential growth occurs, with a coefficient resembling that of classical diffusion $\left(\frac{\sigma g\ k_z}{\sigma B^2}\right)$ modified by a shear parameter.

NOTE ADDED IN PROOF

A more detailed treatment keeping the inertial term removes the divergence in velocity at t = 0, and shows a rapid, inertial expansion followed by the above slower, MHD growth.

APPENDIX

Let $\sigma B^2 \vec{v} = - \nabla p - \rho \vec{g}$

$$\nabla \cdot \vec{v} = 0$$

Let $v_y = v_o \, e^{-\alpha y} \cos kx \; f(t)$

Use $\nabla \cdot \vec{v} = 0$

$$\frac{\partial v_x}{\partial x} + \frac{\partial v_y}{\partial y} = 0$$

$$\frac{\partial v_x}{\partial x} = - \left(-\alpha \, v_o \, e^{-\alpha y} \cos kx \; f(t)\right)$$

$$v_x = \frac{\alpha v_o}{k} e^{-\alpha y} \sin kx \; f(t)$$

Next go to the MHD equations. If the fluid is of constant density, the effect of gravity does not show up in the bulk. We obtain,

$$+\sigma B^2 \vec{v} = - \nabla p$$

For v_x,

$$+\sigma B^2 v_x = - \frac{\partial p}{\partial x}$$

$$\sigma B^2 \frac{\alpha v_o}{k} \; e^{-\alpha y} \sin kx \; f(t) = - \frac{\partial p}{\partial x}$$

$$- \frac{\sigma B^2 \alpha v_o}{k^2} e^{-\alpha y} \cos kx \; f(t) = -p.$$

For v_y,

$$\sigma B^2 v_y = - \frac{\partial p}{\partial y}$$

$$\sigma B^2 \; v_o \; e^{-\alpha y} \cos kx \; f(t) = - \frac{\partial p}{\partial y}$$

$$- \frac{\sigma B^2 v_o}{\alpha} e^{-\alpha y} \cos kx \; f(t) = -p.$$

If the two expressions are identical (as they must be!) we must have $\alpha = k$.

$$\text{So } p = + \frac{\sigma B^2 v_o}{k} e^{-ky} \cos kx \, f(t)$$

Now for the boundary condition. The pressure is driven by gravity. At $y = 0$, we find,

$$F = + y_o \rho g \cos kx \, G(t)$$

But $p = F$ at $y = 0$,

$$+ \frac{\sigma B^2 v_o}{k} \cos kx \, f(t) = + y_o \rho g \cos kx \, G(t),$$

or

$$\frac{\sigma B^2 v_o}{k} f(t) = + y_o \rho g \, G(t).$$

But the velocity is the derivative of the displacement,

$$v_o \cos kx \, f(t) = \frac{d}{dt} y_o \cos kx \, G(t),$$

$$\text{so } f(t) = \frac{y_o}{v_o} \frac{\partial G(t)}{\partial t} .$$

We get,

$$\frac{\sigma B^2 v_o}{k} \frac{y_o}{v_o} \frac{\partial G(t)}{\partial t} = + y_o \rho g \, G(t).$$

$$\frac{dG}{G} = \frac{\rho g k}{\sigma B^2} dt .$$

Now we note that $\vec{k}$ along the magnetic field is the projection of $\vec{k}$ in the plasma onto $\vec{B}$

$$k = k_o \frac{x_o}{v_z t} ,$$

$$\frac{dG}{G} = \frac{\rho g \, k_o}{\sigma B^2} \frac{x_o}{v_z} \frac{dt}{t} ,$$

$$\ln \quad G = \frac{\rho g \; k_o}{\sigma B^2} \frac{x_o}{v_z} \; \ln_e \; t + C \; ,$$

$$G = C_1 t^{\left(\frac{\rho g \; k_o \; x_o}{\sigma B^2 \; v_z}\right)} \; ,$$

$$= \left(\frac{t}{t_o}\right)^{\frac{\rho g \; k_o}{\sigma B^2} \; \frac{x_o}{v_z}} \; ,$$

Thus for the displacement at the boundary, we find,

$$y = y_o \cos kx \left(\frac{t}{t_o}\right)^{\left(\frac{\rho g \; k_o}{\sigma B^2} \; \frac{x_o}{v_z}\right)} \; .$$

q.e.d.

1. Igor Alexeff, J. Reece Roth and J. Douglas Birdwell, Phys. Fluids 23, 1348 (1981).

NECESSARY AND SUFFICIENT CRITERIA FOR THE STABILITY OF A HOT PARTICLE RING - PLASMA SYSTEM

T. M. Antonsen, Jr. and Y. C. Lee
Laboratory for Plasma and Fusion Energy Studies
University of Maryland
College Park, Maryland 20742

The stability of a collisionless plasma with a population of energetic particles is analysed. All species are assumed to obey the guiding center equations of motion, and thus, finite gyroradius and finite cyclotron frequency effects are not considered. The equilibrium magnetic field configuration is allowed to be arbitrary, and both equilibrium and perturbed electrostatic fields are included. A quadratic form is derived from the equations of motion and stability criteria are deduced from this form with the aid of Nyquist's technique. No apriori assumption concerning the constancy of the third adiabatic invariant is made. Nevertheless, in the case in which the drifts of the energetic particles are favorable (i.e. $\partial F/\partial \varepsilon|_J < 0$) marginal stability occurs at zero frequency and the quadratic form gives necessary and sufficient conditions for stability. The relationship of the instability thresholds predicted by the variational principle to those predicted by a modal analysis will be examined, and possible discrepancies between the two theories will be clarified.

I. INTRODUCTION

The stability of hot particle ring-plasma systems is relevant to the study of EBT[1-7] and tandem mirror configurations.[8] A major theoretical problem that exists is to understand the influence of the energetic particle rings on the stability of modes that grow on the Alfvén time scale. In particular, if one uses the low frequency energy

principle[9,10] one finds that in the presence of unfavorable curvature instability is always possible[4,7,10]. It has been argued that the energy principle is overly pessimistic, and that a modal analysis[7] reveals a window of stability. On the other hand a recent analysis of low frequency perturbations of a guiding center plasma[11] indicates that in the presence of favorable drifts the energy principle is necessary and sufficient for stability.

The purpose of this paper is to examine in detail the stability problem for an energetic particle ring - plasma system, and to resolve any discrepancies between the energy principle and modal analyses. We find that if one includes in the analysis the collisionless dissipation that results from drift resonances for the ring particles and bounce resonances for the bulk particles, and if the drifts of the energetic particles are favorable, then the relevant kinetic energy principle gives necessary and sufficient conditions for stability. If these dissipative effects are not included then neutrally stable oscillations are predicted to occur for cases in which ΔW can be made negative. These oscillations are shown to be negative energy modes and, therefore, it is reasonable to expect them to be unstable in the presence of dissipation.

The outline of the remainder of this paper is as follows. In Sec. II we present our model of the ring-plasma system, in Sec. III we linearize the governing equations, in Sec. IV we apply Nyquist's technique to quadratic forms derived from the linear equations and derive a variational energy principle. In Sec. V we address the problem of resonantly unstable modes and demonstrate the existence of negative energy modes.

II. MULTISPECIES GUIDING CENTER PLASMA

We consider the stability of a hot particle ring - plasma system to modes with frequencies characteristic of Alfvén waves. The plasma is composed of three species of particles: bulk electrons, bulk ions, and

energetic ring particles. All three species are assumed to obey the guiding center equations of motion. The bulk particles and ring particles are distinguished by the ordering of their drift frequency with respect to the frequency of the wave. In particular, if v_a is a typical Alfvén velocity and L is a typical scale length of the configuration, we look for modes with complex wave frequency satisfying,

$$\omega \sim v_a/L.$$

For the bulk particles the wave frequency will greatly exceed the particle drift frequency

$$\omega \gg v_d/L,$$

where

$$\underline{v}_d = \frac{c}{q}\frac{\underline{b}}{B} \times (mv_\parallel^2\underline{\kappa} + \mu\nabla B + q\nabla\Phi)$$

is the drift velocity of particles across field lines.

We consider the wave frequency to be comparable to the drift frequency of the ring particles which, in turn, is much less than the bounce frequency of the ring particles,

$$\omega \sim v_d/L \ll v_t/L,$$

where v_t is the mean speed of the ring particles. Given these orderings, we expect the behavior of the bulk particles and ring particles to be qualitatively different.

The starting point of our derivation is the drift kinetic equation,

$$f_t + (v_\parallel\underline{b} + \underline{v}_d + \underline{u}) \cdot \nabla f + [\mu B_t + q\Phi_t - \frac{q}{c}(v_\parallel\underline{b} + \underline{v}_d)\cdot A_t]f_\varepsilon = 0, \quad (1)$$

where $f(\varepsilon,\mu,\underline{x},t)$ is the distribution function for guiding centers, ε is

the total energy

$$\varepsilon = \frac{1}{2} mv^2 + q\Phi(\underline{x},t) \tag{2}$$

m is the particle mass, $\underline{v}$ is the particle velocity, and q is the particle charge. The quantity $\Phi(\underline{x})$ is the electrostatic potential and the quantity $\underline{A}(\underline{x},t)$ is the vector potential, which give the electromagnetic fields,

$$\underline{E} = -\nabla\Phi - \frac{1}{c}\underline{A}_t, \tag{3}$$

and

$$\underline{B} = \nabla \times \underline{A}. \tag{4}$$

The velocity of a field line, $\underline{u}$ is defined by $\underline{u} = B^{-1}\underline{b} \times \underline{A}_t$.[11,12]

The quantity $\mu = \frac{1}{2} mv_\perp^2/B$ is the conserved magnetic moment, and $v_\parallel = \pm[2(\varepsilon-\mu B-q\Phi)/m]^{1/2}$ is the parallel velocity. Subscripted variables indicate partial differentiation with respect to the subscript.

We consider first the case of the ring particles. Given the largeness of the bounce frequency of the ring particles compared with the wave frequency we conclude that the dominant term in Eq. (1) is $v_\parallel \underline{b}\cdot\nabla f = 0$. Thus, to lowest order f is constant along a field line,

$$f = f(\varepsilon,\mu,\alpha,\beta,t), \tag{5}$$

where $\underline{B} = \nabla\alpha \times \nabla\beta$. The evolution equation for f is then obtained by bounce averaging Eq. (1),

$$J_\varepsilon f_t - J_t f_\varepsilon + \frac{c}{q}(J_\alpha f_\beta - J_\beta f_\alpha) = 0, \tag{6}$$

where

$$J(\varepsilon,\mu,\alpha,\beta,t) = \int d\ell m|v_\parallel| \tag{7}$$

is the longitudinal invariant. Thus, the problem of determining the distribution function of the ring particles is reduced to solving the bounce averaged drift kinetic equation (6).

In the case of the bulk particles a different procedure is followed. The smallness of the drift freqeuncy in comparison with the wave frequency allows us to drop the $\underline{v}_d \cdot \nabla f$ term in Eq. (1). Thus, the particles are "frozen" to field lines. We make no assumption concerning the relative sizes of the terms f_t and $v_\parallel \underline{b} \cdot \nabla f$. Therefore, our formulation is capable of analysing bounce resonances of the bulk particles. The drift kinetic equation describing both species of bulk particle can be written,

$$f_t + (v_\parallel \underline{b} + \underline{u}) \cdot \nabla f + [\mu B_t + q\Phi_t - \frac{q}{c}(v_\parallel \underline{b} + \underline{v}_d) \cdot A_t] f_\varepsilon = 0. \qquad (8)$$

The system of equations is completed by considering the momentum balance equations and the quasineutrality condition. Information describing momentum balance along the field lines is already contained in the drift kinetic equations. Thus, we consider only the perpendicular part of the momentum balance equation,

$$\rho_m \frac{d\underline{v}}{dt} = - \nabla \cdot \underline{\underline{P}} + \frac{1}{4\pi} (\nabla \times \underline{B}) \times \underline{B} \ , \qquad (9)$$

where ρ_m is the mass density (due mainly to the bulk ions) $\underline{v}$ is bulk ion velocity, and $\underline{\underline{P}}$ is the total pressure tensor (summed over all three species)

$$\underline{\underline{P}} = p_\perp \underline{\underline{I}} + (p_\parallel - p_\perp) \underline{b}\ \underline{b}$$

where

$$p_\perp = \sum_q \int d\Gamma\ \mu B f \qquad (10a)$$

$$p_\parallel = \sum_q \int d\Gamma\ m v_\parallel^2 f \qquad (10b)$$

and

$$\int d\Gamma = \frac{2\pi B}{m^2} \int \frac{d\varepsilon\, d\mu}{|v_\parallel|} = \int d^3v$$

is the integral over all velocity. The quasineutrality condition is written

$$\rho(\underline{x}) = \sum_q q \int d\Gamma f = 0 \quad . \tag{11}$$

Finally, we recall that the frequencies of interest greatly exceed the bulk ion drift frequency, and that bulk particles are frozen to field lines. Consequently, bulk ion velocity must satisfy the frozen in law,

$$\underline{v} = \underline{u} \quad . \tag{12}$$

This completes our model of the plasma. In subsequent sections this model will be used to determine the stability of a ring-plasma configuration.

III. LINEAR STABILITY ANALYSIS

In this section we linearize the equations presented in the previous section about a time independent equilibrium. We now label the equilibrium field $\underline{B}(\underline{x})$ where $\underline{B}(\underline{x}) = \nabla\alpha \times \nabla\beta$ and we label the perturbed magnetic field $\underline{Q}$. We consider the perturbed vector potential, $\tilde{\underline{A}}$, in a gauge where $\underline{B}\cdot\tilde{\underline{A}} = 0$. Consequently we can write,

$$\tilde{\underline{A}} = \underline{\xi} \times \underline{B} \tag{13}$$

and

$$\underline{Q} = \nabla \times (\underline{\xi} \times \underline{B}) \tag{14}$$

The implications of this representation have been discussed

previously[11]. Using the expression for the velocity of a field line we find,

$$\underline{u} = \underline{\xi}_t, \tag{15}$$

indicating that $\underline{\xi}$ is the displacement of a field line. The equilibrium electric field is given by

$$\underline{E} = -\nabla\Phi \ , \tag{16}$$

and the perturbed electric field is given by

$$\underline{\tilde{E}} = -\nabla\phi - \frac{\underline{\xi}_t \times \underline{B}}{c} \ . \tag{17}$$

With the given form of the equilibrium and perturbed fields we consider the solution of the linerarized drift kinetic equations. In equilibrium the distribution functions depend on the constants of motion in the equilibrium fields,

$$f = \hat{f}^o(\varepsilon,\mu,J(\varepsilon,\mu,\alpha,\beta)) \tag{17a}$$

which can also be written,

$$f = f^o(\varepsilon,\mu,\alpha,\beta), \tag{17b}$$

where in the case of Eq. (17b) the dependence of f on its arguments must be consistent with Eq. (17a).

The linearization of the bounce averaged drift kinetic equation, Eq. (6) was performed in Ref. 11. We will not repeat it here, but we quote the result, $f = f^1 + \hat{f}^o$ where

$$f^1 = f^1_L - \underline{\xi}\cdot\nabla\hat{f}^o \tag{18}$$

and

$$f_L^1 = -H^1 J_\varepsilon \hat{f}_J^o - \hat{f}_\varepsilon^o \sum_{n=-\infty}^{\infty} \exp(in\theta) \frac{\omega}{\omega - n\Omega} \langle \exp(-in\theta) H^1 \rangle_\theta . \tag{19}$$

In Eqs. (18) and (19) the following quantities have been defined: f^1 is the perturbed Eulerian distribution function, f_L^1 is the perturbed distribution function as seen in a frame moving with the field lines, H^1 is the perturbed energy of a particle,

$$H^1 = \langle m v_\parallel^2 \underline{\xi} \cdot \underline{\kappa} + \mu Q_L + q\phi_L \rangle_\ell \tag{20}$$

where $\langle\rangle_\ell$ denotes averaging over the bounce motion,

$$\langle \cdot \rangle_\ell = J_\varepsilon^{-1} \int \frac{d\ell}{|v_\parallel|} (\cdot),$$

Q_L and ϕ_L are the perturbed parallel component of the magnetic field and the perturbed electrostatic potential as seen in a frame moving with the field lines,

$$Q_L = Q_\parallel + \underline{\xi} \cdot \nabla B, \tag{21a}$$

$$\phi_L = \phi + \underline{\xi} \cdot \nabla \Phi \ . \tag{21b}$$

The infinite sum in Eq. (19) represents a Fourier decomposition of the perturbed distribution function in harmonics of the drift orbit. Here, θ is an angle like variable that measures the drift orbit phase,

$$\theta(\beta, \varepsilon, J, \mu) = \Omega(\varepsilon, J, \mu) \frac{q}{c} \int^{\beta} d\beta' J_\varepsilon / J_\alpha \tag{22a}$$

and

$$2\pi/\Omega = \frac{q}{c} \int d\beta' J_\varepsilon / J_\alpha \tag{22b}$$

is the time required for a particle to complete its drift orbit. The integrals in Eqs. (22a) and (22b) are carried out along a curve of

constant ε, μ, and J in the α-β plane. Finally, we note that $\langle\rangle_\theta$ denotes averaging over the drift orbit

$$\langle\cdot\rangle_\theta = \int \frac{d\theta}{2\pi}(\cdot) \quad .$$

An important feature of Eq. (19) is the appearance of resonant demoninators in the infinite sum. The vanishing of these denominators allows for a collisions energy exchange between the mode and the ring particles. This collisionless dissipation can give rise to resonant instability as will be seen subsequently.

The linearization of Eq. (8) for the bulk particles will be presented in more detail. Writing again $f = f^1 + f^o$, we find,

$$-i\omega f^1 + v_\parallel \underline{b}\cdot\nabla f^1 + (v_\parallel \frac{\underline{Q}}{B} - i\omega\underline{\xi})\cdot\nabla f^o$$
$$= i\omega(\mu Q_\parallel + q\phi - \frac{\underline{b}\times(mv_\parallel^2\underline{\kappa} + \mu\nabla B + q\nabla\Phi)}{B}\cdot\underline{\xi}\times\underline{B})\, f_\varepsilon^o \quad . \tag{23}$$

Using Eq. (14) for $\underline{Q}$, the third term in Eq. (23) becomes

$$(v_\parallel \frac{\underline{Q}}{B} - i\omega\underline{\xi})\cdot\nabla f^o = v_\parallel \underline{b}\cdot\nabla(\underline{\xi}\cdot\nabla f^o) - i\omega\underline{\xi}\cdot\nabla f^o \quad .$$

Thus, we write $f^1 = f_L^1 - \underline{\xi}\cdot\nabla f^o$ where f_L^1 satisfies

$$(\omega + iv_\parallel \underline{b}\cdot\nabla)f_L^1 = -\omega f_\varepsilon^o \;\tilde{H} \tag{24}$$

and

$$\tilde{H} = mv_\parallel^2\underline{\xi}\cdot\underline{\kappa} + \mu Q_L + q\phi_L \quad .$$

Equation (24) may be solved by expansion in bounce harmonics. In particular, we define the bounce frequency $\nu(\varepsilon,\mu,\alpha,\beta)$

$$2\pi\nu^{-1} = \int \frac{d\ell}{|v_\parallel|} = J_\varepsilon$$

and the bounce angle ζ

$$\zeta(\ell,\varepsilon,\mu,\alpha,\beta) = \nu \int^{\ell} \frac{d\ell'}{|v_{\parallel}|} ,$$

and expand the quantities in Eq. (24) in a Fourier series in ζ. The result is

$$f_L^1 = -f_\varepsilon^o \sum_m \exp(im\zeta) \frac{\omega}{\omega - m\nu} \langle \exp(-im\zeta) \tilde{H} \rangle_\ell . \tag{25}$$

Finally, we linearize the momentum balance equation and the quasineutrality condition. In equilibrium Eq. (9) yields[11]

$$\hat{\nabla} p_\perp + B\rho_B(-\rho_\Phi)^{-1}\hat{\nabla}\rho + \frac{\tau_* B}{4\pi} \nabla_\perp B = \sigma \frac{B^2}{4\pi} \underline{\kappa}$$

where $p_\perp(\alpha,\beta,B,\Phi)$ is the equilibrium perpendicular pressure, $\rho(\alpha,\beta,B,\Phi)$ is the equilibrium charge density functional, $\hat{\nabla} = \nabla\alpha\partial/\partial\alpha + \nabla\beta\partial/\partial\beta$,

$$\tau_* = 1 + \frac{4\pi}{B} p_{\perp B} + 4\pi\rho_B^2(-\rho_\Phi)^{-1} ,$$

is the quantity associated with the stability of mirror modes, and

$$\sigma = 1 + \frac{4\pi(p_\perp - p_\parallel)}{B^2} ,$$

is the quantity asociated with the stability of fire hose modes.

The linearization of Eq. (9) yields

$$-\omega^2 \rho_m \underline{\xi} = -\nabla \cdot \underline{\underline{P}}^1 + \frac{1}{4\pi} [(\nabla \times \underline{B}) \times \underline{Q} + (\nabla \times \underline{Q}) \times B] \tag{26}$$

where $\underline{\underline{P}}$ is the perturbed stress tensor,

$$\underline{\underline{P}}^1 = \sum_q \int d\Gamma\, f^1 [\mu B \underline{\underline{I}} + (mv_\parallel^2 - \mu B)\underline{b}\underline{b}] + (\underline{Q}_\perp \underline{b} + \underline{b}\underline{Q}_\perp) B^{-1}(p_\parallel - p_\perp)$$

$$+ \left[Q_{\parallel} \frac{\partial}{\partial B} + \phi \frac{\partial}{\partial \Phi}\right] \left[p_{\perp} \underline{\underline{I}} + (p_{\parallel} - p_{\perp}) \underline{b}\underline{b}\right] \quad .$$

The linearized quasineutrality constraint is written,

$$\sum_q q \int d\Gamma f^1 + (Q_{\parallel} \frac{\partial}{\partial B} + \phi \frac{\partial}{\partial \Phi})\rho = 0 \quad . \tag{27}$$

Our linearized system contains three unknown functions that determine the electromagnetic field: ϕ and two components of $\underline{\xi}$, expressions for the perturbed distribution functions: Eq. (19) and Eq. (25), and three field equations: two components of Eq. (26), and Eq. (27).

IV. QUADRATIC FORMS

The system of equations derived in the preceeding section describes perturbations of a coupled ring-plasma system. It is unlikely that these equations will be solved except in very restrictive cases. Therefore, it is instructive to examine quadratic forms derived from these equations. We dot the momentum balance equation, Eq. (26), with the complex conjugate of the field line displacement, $\underline{\xi}^*$, and integrate over all volume. After many manipulations, the details of which are given in Ref. 12, we obtain the following quadratic form,

$$\omega^2 \int d^3x\, \rho_m |\underline{\xi}|^2 = \Delta W(\omega) = \Delta W_f + \Delta W_k(\omega), \tag{28}$$

where

$$\Delta W_f = \frac{1}{2} \int d^3x \left\{ \frac{\sigma |\underline{Q}_{\perp}|^2 + \tau_* |\hat{Q}_L|^2}{4\pi} + \frac{\sigma J_{\parallel} \underline{b} \cdot \underline{\xi}^* \times \underline{Q}}{c} \right.$$

$$\left. - \underline{\xi}^* \cdot \underline{\kappa} \left[\frac{\sigma}{\tau_*} (\underline{\xi} \cdot \hat{\nabla} p_{\perp} + B\rho_B (-\rho_{\Phi})^{-1} \underline{\xi} \cdot \hat{\nabla} \rho) + \underline{\xi} \cdot \hat{\nabla} p_{\parallel}\right]\right\} \tag{29}$$

is the fluid contribution to ΔW, and

$$\Delta W_k(\omega) = \frac{1}{2} \int d^3x \sum_q d\Gamma f_L^1 \, (\tilde{H}^* - q\hat{\phi}^*) \tag{30}$$

is the kinetic contribution to ΔW. The new quantities $\hat{\phi}_L$ and $\hat{Q}_L$ are defined by

$$\hat{\phi}_L = \phi_L + \rho_B(-p_\Phi)^{-1} Q_L$$

and,

$$\hat{Q}_L = Q_L - B\sigma\tau_*^{-1}\, \underline{\xi}\cdot\underline{\kappa} \quad .$$

The perturbed electrostatic potential is determined by the quasi-neutrality constraint,

$$0 = \rho_\Phi \hat{\phi}_L + \sum_q q \int d\Gamma f_L^1 \ . \tag{31}$$

Determination of the eigenvalue ω, the mode frequency, is made difficult because ΔW_k depends in a very complicated way on ω. In particular, the expressions for f_L^1 are complicated functions involving ω and nonlocal averages of field variables. To simplify the situation we introduce the artificial eigenvalue λ by adding $-\rho_m \lambda \underline{\xi}$ to the left-hand side of the linearized momentum balance equation, Eq. (26), and we consider ω to be a known parameter. Solution of the linearized equations subject to appropriate boundary conditions will then yield the complex, analytic function, $\lambda(\omega)$. Clearly, those values of ω satisfying $\lambda(\omega) = 0$ will be true eigenvalues of the original system of equations. Stability can then be determined by finding the number of solutions of $\lambda(\omega) = 0$ with ω in the upper half plane. To do this we derive a quadratic expression for $\lambda(\omega)$, to which we apply Nyquist's technique. Following the procedure used to construct ΔW we obtain the quadratic form,

$$\frac{1}{2}\,(\lambda(\omega) + \omega^2) \int d^3x\, \rho_m |\underline{\xi}|^2 = \Delta W_f + \Delta W_k(\omega) \ . \tag{32}$$

In order to determine the number of unstable modes we evaluate $\lambda(\omega)$ along a contour that completely encircles the upper half ω-plane.

For $|\omega| \to \infty$ we note that the expressions for f_L^1 remain finite, and consequently $\Delta W_k(\omega)$ remains finite as well. Thus, for $|\omega| \to \infty$ $\lambda(\omega) \sim -\omega^2$. For ω on the real axis we see that $\lambda(\omega)$ will have an imaginary part due to the bounce and drift resonance contributions to $\Delta W_k(\omega)$. We may determine the sign of the imaginary part of $\lambda(\omega)$ by multiplying the quasineutrality constraint, Eq. (31), by $\hat{\phi}_L^*$, integrating over all volume, and combining with the expression for $\Delta W_k(\omega)$. In particular,

$$\Delta W_k(\omega) = \frac{1}{2} \int d^3x \left(\sum_q \int d\Gamma f_L^1 \tilde{H}^* + \rho_\Phi |\hat{\phi}_L|^2 \right) \quad . \tag{33}$$

We then use Eq. (19) and Eq. (25) to express f_L^1 in Eq. (33), and we separate the imaginary part of $\Delta W_k(\omega)$ by replacing the resonant demoninators with delta functions. We find,

$$\mathrm{Im}\{\Delta W_k(\omega)\} = \frac{\pi\omega}{2} \int d^3x \left\{ \sum_{\text{bulk}} \int d\Gamma f_\varepsilon^o \sum_m \delta(\omega - m\upsilon) \, |\langle \exp(-im\zeta)\tilde{H}\rangle_\ell|^2 \right.$$
$$\left. + \sum_{\text{ring}} d\Gamma \hat{f}_\varepsilon^o \sum_n \delta(\omega - n\Omega) |\langle \exp(-in\theta) H^1\rangle_\theta|^2 \right\} \quad . \tag{34}$$

If $f^o(\varepsilon,\mu,\alpha,\beta)$ and $\hat{f}^o(\varepsilon,\mu,J)$ are monotonically decreasing functions of energy, i.e. $f_\varepsilon^o < 0$ and $\hat{f}_\varepsilon^o < 0$ then the imaginary part of $\Delta W_k(\omega)$ and $\lambda(\omega)$ will be positive for real $\omega < 0$ and will be negative for real $\omega > 0$. Therefore, the contour of $\lambda(\omega)$ in the λ-plane can only cross the real λ axis when $\omega = 0$. This is illustrated in Fig. 1 where two possible λ contours are shown. In Fig. 1a the real part of $\lambda(\omega = 0)$ is negative, and the origin in the λ-plane is encircled. This indicates instability. In Fig. 1b the real part of $\lambda(\omega = 0)$ is positive, and the origin in the λ-plane is not encircled. This indicates stability. Thus, a <u>necessary</u> and <u>sufficient</u> condition for stability is $\lambda(0) = \Delta W(0) > 0$.

There remains one more step in our procedure that must be made before we have a useful stability criteria. That is to find a convenient way of determining $\lambda(0)$. The expression obtained

for $\lambda(\omega)$ for arbitrary ω is only a quadratic form; it is not in general variational due to the complex operators in $\Delta W(\omega)$. However, we are only interested in $\lambda(0)$, and for the special value $\omega = 0$ the expression for λ is variational. Thus, if trial functions $\underline{\xi}^t$ are found (with $\hat{\phi}_L$ determined as a functional of $\underline{\xi}^t$ from the quasineutrality constraint) which render ΔW negative, then the system is unstable. If no such trial functions can be found then the system is stable.

For $\omega = 0$ the expression for ΔW_k simplifies greatly

$$\Delta W_k(o) = -\frac{1}{2}\int d^3x \sum_q \int d\Gamma f_\varepsilon^o(|H^1|^2 - H^1\langle q\hat{\phi}_L\rangle_\ell^*)$$

$$+\frac{1}{2}\int d^3x \int_{\text{ring}} d\Gamma\, \hat{f}_\varepsilon^o\, [|H^1|^2 - H^1\langle q\hat{\phi}_L\rangle_\ell^* - |\langle H^1\rangle_\theta|^2 + \langle H^1\rangle_\theta\, \langle\langle q\hat{\phi}_L\rangle_\ell\rangle_\theta^*] \quad (35)$$

The first term in Eq. (35) contains a sum over all species. The contribution from the bulk particles is given by the Kruskal-Oberman[13], Rosenbluth-Rostoker[14] expression including the perturbed electrostatic field[11]. This term is positive definite and therefore stabilizing. The contribution to the first term from the ring particles togther with the second term represent the low frequency expression for ΔW_k[9,10] including the perturbed electrostatic field[11]. This term is destabilizing and in fact is responsible for the unstable compressional mode.

Finally, we show that the expression $\Delta W(o)$ is the energy required to make a zero frequency perturbation. We imagine that the system is brought to its perturbed state by a small divergence free test current, $\underline{J}^t$. The work that is done on the test current is given by

$$\Delta W^t = \int d^3x \int_{-\infty}^{t} dt'\, \underline{J}^t \cdot \underline{E} \quad .$$

Using the expression for the electric field we find that ΔW^t can be expressed,

$$\Delta W^t = \int d^3x \int_{-\infty}^{t} dt'\, \underline{\xi}_{t'} \cdot \frac{\underline{J}^t \times \underline{B}}{c} \qquad (36)$$

The presence of the test current modifies the linearized equation of momentum balance,

$$\rho_m \underline{\xi}_{tt} = -\nabla\cdot\underline{\underline{P}}^1 + \frac{1}{4\pi}[(\nabla\times\underline{B})\times\underline{Q} + (\nabla\times\underline{Q})\times\underline{B}] - \frac{1}{c}\underline{J}^t\times\underline{B}\ , \quad (37)$$

which follows from the fact that $(c/4\pi)\nabla\times\underline{Q}$ is the total perturbed current including the plasma current and the test current. We assume that the test current has the time dependence $\exp(\gamma t)$ and that it is turned on adiabatically. Thus, we evaluate Eq. (36) in the limit $\gamma \to 0$ which yields,

$$\Delta W^t = \frac{1}{2}\int d^3x\, \underline{\xi}^*\cdot\{-\nabla\underline{\underline{P}}^1 + \frac{1}{4\pi}[(\nabla\times\underline{B})\times\underline{Q} + (\nabla\times\underline{Q})\times\underline{B}]\} \quad (38)$$

Therefore, the energy required to perturb the plasma is $-\Delta W^t$ which according to Eq. (36) and Eq. (28) is simply $\Delta W(\omega = o)$.

V. RESONANT INSTABILITY - NEGATIVE ENERGY WAVES

The energy principle we have derived gives necessary and sufficient conditions for stability. It does not, however, give information on the magnitude of the growth rate or frequency. Determining these requires a modal analysis[7]. In this regard it is instructive to examine the predictions of a modal theory obtained by making certain approximations and to compare these predictions with those of the energy principle. The simplifyng approximations we will make concern the relative sizes of the ring particle drift frequency, Ω, the mode frequency, the bulk ion bounce frequency, and the bulk electron bounce frequency. In particular, we assume $\omega < \Omega$ and thus, for the ring particles,

$$f_L^1 \cong -H^1 J_\varepsilon \hat{f}_J^o - \hat{f}_\varepsilon^o \langle H^1\rangle_\theta - \sum_{n\neq o}\frac{\omega}{n\Omega}\exp(in\theta)\,\langle H^1\exp(-in\theta)\rangle_\theta$$

For the bulk particles we assume for illustrative purposes that the mode frequency is much less than the bounce frequency, $\omega \ll \nu$, which yields,

$$f_L^1 = -f_\varepsilon^o \langle \tilde{H} \rangle_\ell \quad .$$

(A more appropriate assumption might be $\omega << \nu$ for electrons and $\omega >> \nu$ for ions.)

With these approximations we can construct a quadratic form,

$$\omega^2 K = \Delta W(o) + \omega \Delta W_\omega + R(\omega), \tag{39}$$

where $\Delta W(o)$ is given by Eq. (35), $K = 1/2 \int d^3x \, \rho_m |\underset{\sim}{\xi}|^2$,

$$\Delta W_\omega = \frac{1}{2} \int d^3x \int_{ring} d\Gamma \hat{f}_\varepsilon^o \sum_{n \neq o} (n\Omega)^{-1} \, |\langle H^1 ex(-in\theta) \rangle_\theta|^2 \ ,$$

and $R(\omega)$ represents the terms we have dropped in our approximations, i.e. $R(\omega) = \Delta W(\omega) - \omega \Delta W_\omega - \Delta W(o)$. If our approximations are valid then $R(\omega)$ can be regarded as being small, and the quadratic form predicts oscillations with frequency $\omega \simeq \omega_o$ where,

$$\omega_o = \frac{\Delta W_\omega \pm [(\Delta W_\omega)^2 + 4K\Delta W(o))]^{1/2}}{2K} \tag{40}$$

Thus, we find neutrally stable oscillations when

$$(\Delta W_\omega)^2 > -4K\Delta W(o). \tag{41}$$

Equation 40 indicates the stabilization of modes by a finite frequency shift[7], which is in apparent contradiction to the assertion that $\Delta W(o) > 0$ is necessary and sufficient for stability. This discrepancy is resolved by examining the next order correction to the mode frequency due to the neglected terms. In particular, we write $\omega = \omega_o + \delta\omega$, where $\delta\omega$ is the correction,

$$\delta\omega(2\omega_o K - \Delta W_\omega) = \pm\delta\omega[(\Delta W_\omega)^2 + 4K\Delta W(o)]^{1/2} = R(\omega_o). \tag{42}$$

Recalling Eq. (34) we see that the imaginary part of $R(\omega_o)$ is positive

(negative) for negative (positive) ω_o. If $\Delta W(o) > 0$ then the solution for ω_o associated with the + sign in Eq. (40) is positive and the solution associated with the negative sign is negative. Thus, the imaginary part of $\delta\omega$ for both cases is negative indicating stability. On the other hand, if $\Delta W(0) < 0$ then the solutions for ω_o given by Eq. (38) are either both positive or both negative depending on the sign of ΔW_ω. Using Eq. (42) we see that at least one of these solutions will be unstable (in general the solution with the smallest value of $|\omega_o|$). This confirms that in the presence of dissipation $\Delta W(o) > 0$ is both necessary and sufficient for stability under the stated conditions $f_\varepsilon^o < 0$ and $\hat{f}_\varepsilon^o < 0$.

In the preceeding discussion we saw that the marginally stable oscillations predicted by an approximate modal theory become unstable when the effects of drift and bounce resonances are included. This occurence has two possible explanations. The first is that the marginally stable oscillations are positive energy waves which extract energy from the particles and grow due to the resonances. The second explanation is that the oscillations are negative energy waves which feed energy to the particles and grow. The latter case can be expected to be more dangerous than the former case because in the latter case the instability is tapping the macroscopic free energy of the configuration with the dissipation mechanism only serving as a catalyst for the instability. In fact if one includes nonlinear effects, explosive growth may be possible[15-17]. In contrast, in the former case the instability may be saturated by a small modification to the equilibrium distribution function.

We now show that in the present case the resonantly unstable oscillations are in fact negative energy modes. To do this we recall the expression for the work done on a test current in creating a perturbation given in Eq. (36). We consider the test current to have a time dependence $\exp(-i\omega_o t + \gamma t)$ with $0 < \gamma << |\omega_o|$, where ω_o is the frequency of a marginally stable mode in the absence of dissipation. The field line displacement can be written

$$\underline{\xi} = (\underline{\xi}^o + \underline{\xi}^1)\exp(-i\omega_o t + \gamma t) + c.c. \tag{43}$$

where $\underline{\xi}^o \exp(-i\omega_o t)$ satisfies the homogeneous equations with $\omega = \omega_o$. Inserting the given form of the displacement in Eq. (37), expanding for $\gamma \ll \omega_o$ and $\underline{\xi}^1 \ll \underline{\xi}^o$, and using the fact that the operators in Eq. (37) are self adjoint in the absence of resonances we find,

$$\Delta W^t = \frac{\partial}{\partial \omega_o} \omega_o \lambda(\omega_o) \frac{1}{2} \int d^3x \, \rho_m |\underline{\xi}|^2 \quad . \tag{44}$$

Thus, if $\omega_o \, \partial\lambda/\partial\omega_o$ is positive, work is done on the test current in building up the oscillation, and the oscillation is therefore a negative energy mode.

The sign of $\lambda(\omega)$ can be determined by a reconsideration of the Nyquist plots in the absence of dissipation. Figure 2 shows Nyquist plots for two cases in which $\Delta W(o) < 0$. In the first case the maximum value of $\lambda(\omega)$ for real ω is negative and the origin is completely encircled indicating instability. This corresponds to the case in which the finite frequency shift terms[7] are not strong enough to produce marginally stable oscillations. In the second case $\lambda(\omega)$ has a positive maximum. Recalling that in the absence of dissipation λ is real we see that there will be two solutions for ω_o satisfying $\lambda(\omega_o) = 0$. If we indent the contour in the ω-plane to exclude these solutions we obtain the Nyquist plot of Fig. 2b. Here the arrows indicate the direction of increasing ω. In this case the origin is not encircled indicating stability. However, it is clear that the value of $\omega\partial\lambda/\partial\omega$ near the root ω_{02} is positive. This indicates the mode with frequency ω_{02} is negative energy mode.

VI. CONCLUSIONS

In this paper we have derived necessary and sufficient conditions for the stability of an energetic ring-plasma system. The stability criterion is in the form of an energy principle in which the bulk particles are treated in the high frequency limit[13,14] and the ring particles are treated in the low frequency limit[9,10,11]. Our analysis shows that inclusion of dissipation is essential to the derivation of the energy

principle. In the absence of dissipation stable negative energy modes can be present when $\Delta W < 0$, due to finite frequency shift[7]. The fact that these modes are negative energy mode points out the need to examine possible dissipation mechanisms, both linear and nonlinear, that will allow them to grow. It may be true that a sufficient amount of dissipation is always present in which case the observed stability of the modes must be due to effects not contained in the guiding center model.

ACKNOWLEDGMENT

This work was supported by the U. S. Department of Energy.

REFERENCES

1. N. A. Krall, Phys. Fluids 9, 820 (1966).
2. R. R. Dominguez and H. L. Berk, Phys. Fluids 21, 827 (1978).
3. D. B. Nelson and C. L. Hedrick, Nucl. Fusion 19, 283 (1979).
4. J. W. Van Dam and Y. C. Lee, in EBT Ring Physics (Proc. of the Workshop, Oak Ridge, Dec. 1979), Oak Ridge National Laboratory CONF-791228 (1980), 471.
5. D. B. Nelson, Phys. Fluids 23, 1850 (1980).
6. D. A. Spong and A. M. El-Nadi, Bull. Am. Phys. Soc. 25, 964 (1980).
7. J. W. Van Dam, H. L. Berk, M. N. Rosenbluth and D. A. Spong. Institute for Fusion Studies Report, IFSR #34 (1981).
8. J. Kesner, Bull. Am. Phys. Soc. 26, 1021 (1981).
9. T. M. Antonsen Jr., B. Lane and J. J. Ramos, Phys. Fluids. 24, 1465 (1981).
10. J. W. Van Dam, M. N. Rosenbluth, and Y. C. Lee, Phys. Fluids, to be published.
11. T. M. Antonsen, Jr., and Y. C. Lee, Phys. Fluids, to be published.
12. H. Grad, Phys. Fluids 9, 251 (1965).
13. M. D. Kruskal and C. R. Oberman, Phys. Fluids 1, 275 (1958).
14. M. N. Rosenbluth and N. Rostoker, Phys. Fluids 2, 23 (1959).

15. B. Coppi, M. N. Rosenbluth, and R. N. Sudan, Ann. of Phys. 55, 207 (1969).

16. M. N. Rosenbluth, B. Coppi, and R. N. Sudan, Ann. of Phys. 55, 248 (1969).

17. C. T. Dum and E. Ott, Plasma Phys. 13, 177 (1971).

FIGURE CAPTIONS

Fig. 1. Nyquist contours of $\lambda(\omega)$ given by Eq. (32) for the case a) $\Delta W(o) < 0$ and b) $\Delta W(o) > 0$.

Fig. 2 Nyquist contours of $\lambda(\omega)$ in the absence of dissipation for the case a) $\Delta W(o) < 0$ and one unstable mode and b) $\Delta W(o) < 0$ and two marginally stable modes with frequencies ω_{01} and ω_{02}.

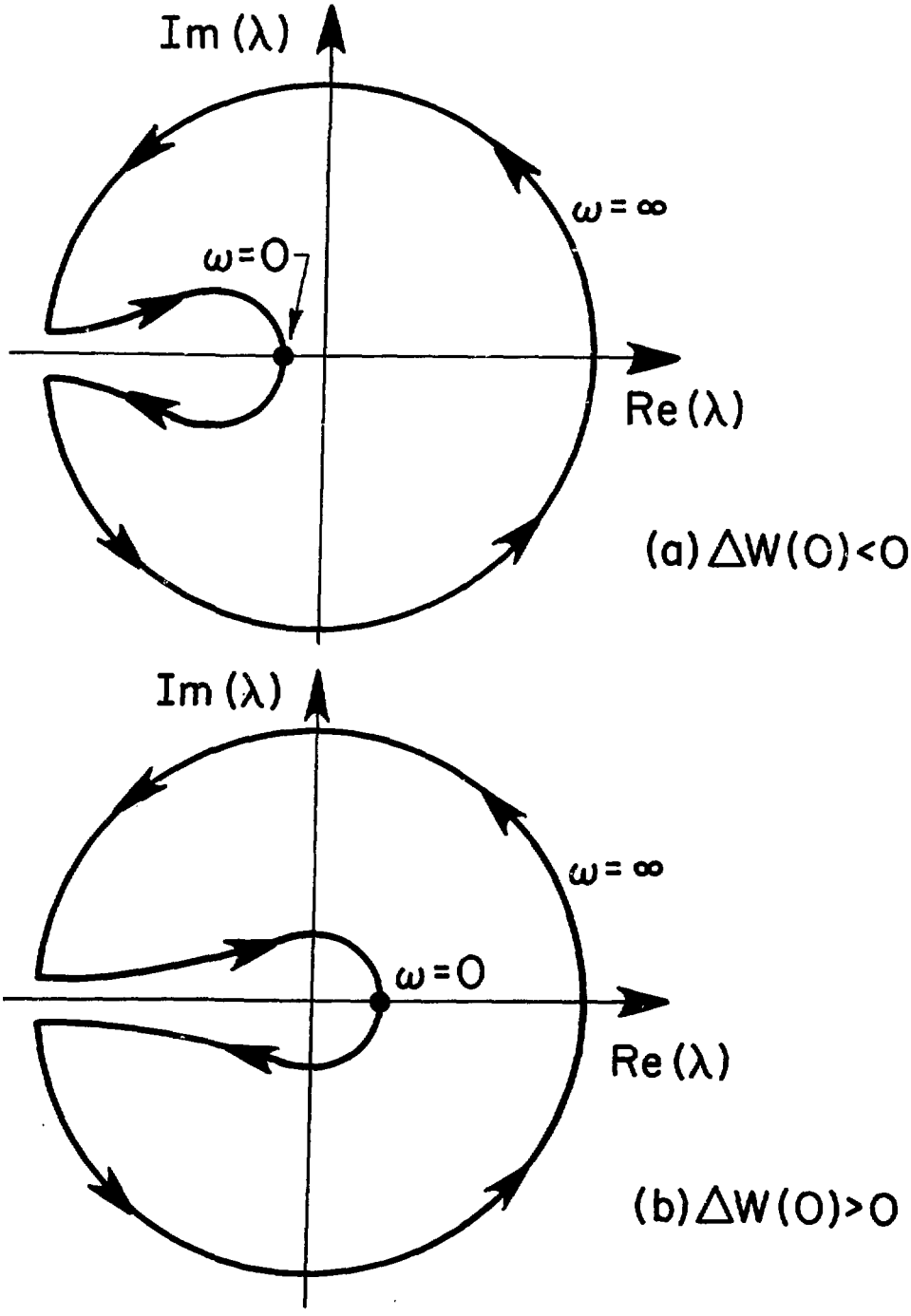

Figure 1

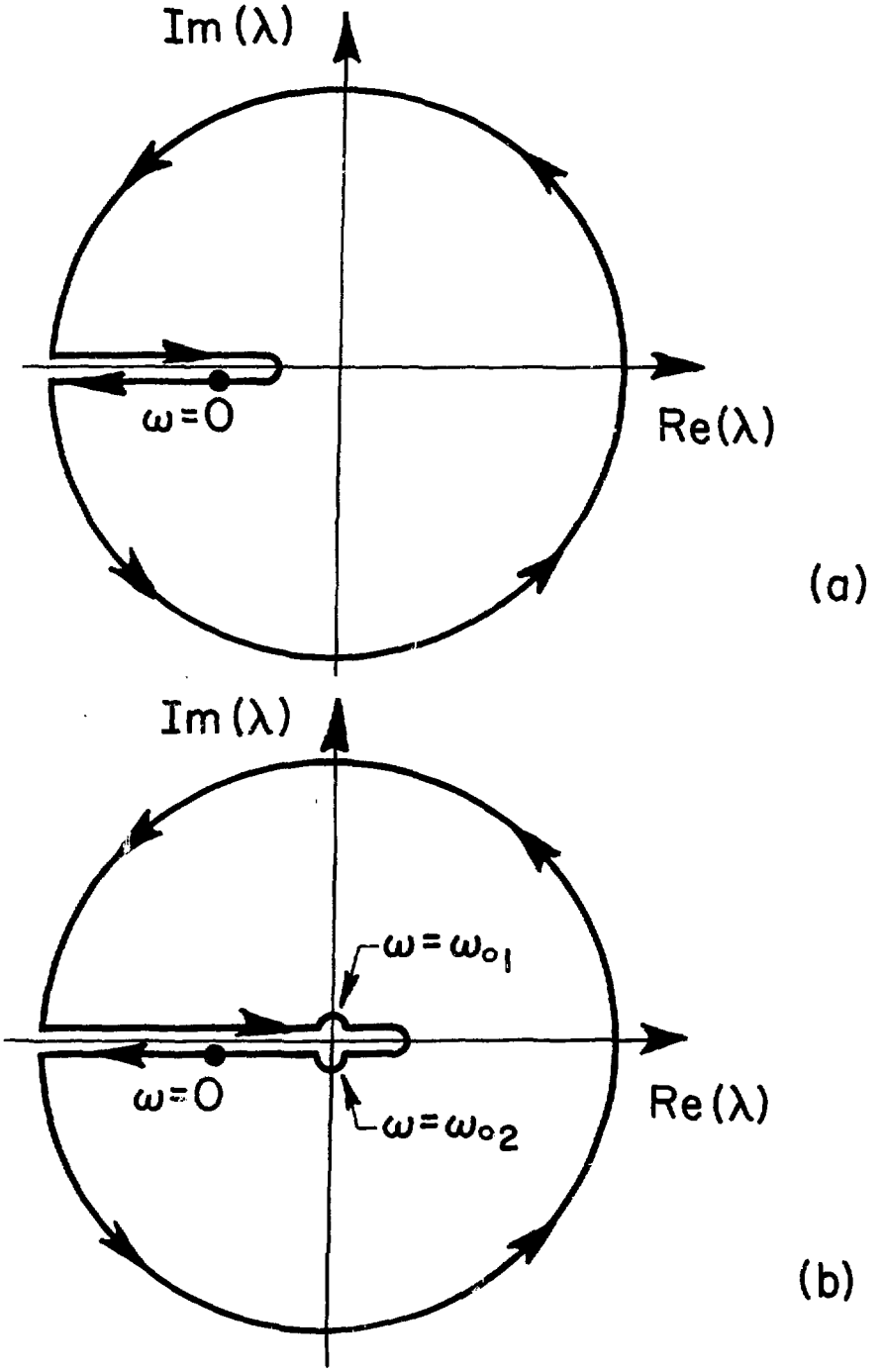

Figure 2

Simulation Studies on Stability and β Limits of EBT

Y. Ohsawa* and J. M. Dawson

Department of Physics

University of California, Los Angeles

Los Angeles, California 90024

ABSTRACT

Stability and β limits of a slab model for an EBT-like configuration is studied by using a 2-1/2 dimensional fully electromagnetic code. When there are no hot electrons in our simulation, the low frequency interchange mode grows; its growth rate agrees well with MHD theory. When we put in a hot electron layer with appropriate conditions, the growth of the interchange mode can be suppressed. However, the results are sensitive to the position of hot electrons, scale lengths for the magnetic field and density gradients and β-values of the bulk plasma and hot electrons. No evidence for excitation of magnetc acoustic instabilities has been seen.

*On leave from the Institute of Plasma Physics, Nagoya University, Nagoya, Japan.

I. Introduction and Model

In the ELMO BUMPY torus, the hot electron ring plays an essential role for the stability of a plasma. In its simplest conception the ring produces a minimum B field which confines the plasma stably while its stiffness due to relativistic effects keep the ring stable. Nelson et al. derived a beta limit of the core plasma, β_c, on the basis of a rigid ring model; the hot electron annulus being treated as a rigid noninteracting current ring.[1,2] According to their theory the maximum can be of the order of the beta value of the hot electrons β_h, i.e., $\beta_c \lesssim \beta_h$, if β_h is larger than a certain critical value. Van Dam et. al have calculated attainable core plasma beta taking into account of the response of the hot electrons.[3,4] Their calculation gives a core plasma beta limit substantially lower than β_h.

The purpose of our work is to use computer simulation to study the stability and beta limits of EBT including effects of finite Larmor radii, ring thickness, pressure and magnetic scale lengths and other effects difficult to include in analytic treatments.

In order to study instabilities in EBT, we use a 2-1/2 dimensional fully electromagnetic particle code.[5] Simulation particles move in the (x,y) plane, and the z-axis is an ignorable coordinate. The system is periodic in the y direction and bounded (finite plasma) in the x direction. The grid size is 128 x 64.

The initial ion density profile $n_i(x)$ is constant for $10 \leq x \leq 36$, and decreases with x for $x > 36$; $n_i/|dn_i/dx| \sim 50$. The external magnetic field points to the z-direction and its intensity varies as $1/(x + R_o)$, where the constant R_o is a measure of the gradient of the external magnetic field. The initial ion and cold electron temperatures are constant. The hot electron ring (layer) is localed in the region of steep pressure gradient in a slab

parallel to the y-axis.

Typical simulation parameters are as follows. $M_i/M_e = 9.0$, $\omega_{ce}/\omega_{pe} \sim 1.0$, the light velocity $c = 8.0$, thermal velocity of cold electrons $v_e \equiv \sqrt{T_e/m_e}$ ranged between $0.8 \sim 2.4$ depending on the core β, the thermal velocity of hot electrons was $v_h = 4.3$ (in one direction), giving a relativistic γ_h of $\gamma_h \equiv (1 - 3V_h^2/c^2)^{-1/2} = 2.84$, the Alfvén velocity was $V_A \sim 2.7$, the system length in x $L_x = 128$, in y it was $L_y = 64$, $\rho_i \sim 8.0$, $\rho_e \sim 2.8$, $\rho_h \sim 12.3$, and β-value of core plasma β_c ranged from $0.01 \sim 0.1$, $\beta_e \sim \beta_i$, where the subscripts i, e, and h denote the ion, the cold electron, and the hot electron, respectively. The hot ring had β_h in the range $\beta_h \sim 0.2$, 0.3. The number of ion particles is 16384.

The rest mass of the hot electrons is smaller than that of cold electrons ($m_e/m_h = 2$ or 4, $m_e/e_e = m_h/e_h$) in our simulation. Therefore the ratio of the kinetic energy between the hot electron and the cold electron is given by $m_n(\gamma_h - 1)/m_e(\gamma_e - 1)$.

II. Flute Instability

In our simulation, when there is no hot electron ring, both the plasma density and the external magnetic field decrease with x for $x \gtrsim 36$. Hence the flute instability is expected to occur. This is demonstrated in Figs. 1a to 1c, where contour maps of the electric potential are plotted. The β-value of the core plasma, β_c, is 10% in this case. The scale length of the gradient of the magnetic field, R_o, is 64. The long-wavelength perturbation with m = 1 ($m \equiv L_y/(2\pi/k_y)$) grows. The phase velocity of the perturbation is almost zero. From Figs. 1 and the density profile in Fig. 2a, we see that the instability grows in the region of steep density gradient. Figures 3a and b show time variation of $|B_z(m = 1, x)|^2$, where $B_z(m = 1, z)$ is the Fourier transform of $B_z(x,y)$ in the y direction with m = 1. At x = 35, the amplitude does not grow with time, while at x = 70, perturbation grows linearly until $\omega_{pe}t \sim 220$. From these data we can estimate the growth rate of the instability with m = 1 as a function of x, which is shown in Fig. 4. The growth rate agrees well with the estimation $\gamma = (k_y g)^{1/2}$, where g is given by $|(K_\perp/M_i)|\nabla B_z/B_z|$ with $K_\perp$ being the perpendicular kinetic energy of a plasma.

III. Stabilization by a Hot Electron Layer

In Figs. 5a to d, we demonstrate the stabilization of the flute instability by a hot electron layer. Here, $\beta_c \sim 10\%$, $\beta_h \sim 30\%$, $R_o = 640$ and the width of the hot electron ring ~ 50. The temperature of the cold electrons is equal to the ion temperature at $\omega_{pe}t = 0$. Potential contour maps in Figs. 5 and the density profiles in Figs. 6 indicate that no instability grows in the plasma except in the outer region beyond the hot electron layer. Here there is a weak instability with phase velocity relative to the plasma almost zero. (The plasma moves very slowly in the y direction by $\vec{E} \times \vec{B}$ drift. E_x is generated because of the difference of the Larmor radii of ions, cold electrons, and hot electrons.) The growth rate γ of the longitudinal electric field $|E_L(m = 1, x)|$ is plotted as a function of x in Fig. 7. The growth rate is almost zero in the inner part of the plasma. In the outer region the m = 2 mode has the larger growth rate than the m = 1 mode. These are consistent with the contour maps in Fig. 5. Even in the outer region the growth rate is not large.

IV. Sensitivity of Stability to Ring Position

The stability of a plasma is sensitive to the position and the width of the hot electron layer. Figures 8 and 9 show the sensitivity of the stability to the position of the hot electron layer. The center of the hot electron layer is at $x \sim 60$ for Fig. 8, while for Fig. 9 it is at $x \sim 80$. Other parameters in Figs. 8 and 9 are the same; $\beta_c \sim 10\%$, $\beta_h \sim 20\%$, $R_o = 64$, and the width of the hot electron layer ~ 30. In both cases, the ion density falls from $x \sim 50$. In the case of Fig. 8, an instability develops in the region $x \sim 70$. On the other hand, in Fig. 9 an instability grows just inside the hot electron layer. The growth rates as a function of x are plotted in Figs. 8e and 9e. The growth rate in Fig. 8e is about the same as that without the hot electrons. The growth rate in Fig. 9e is greatly reduced in comparison with the case without hot electrons. However, we see the instability inside the hot electron layer.

The reason why the instability occurs inside the hot electron layer in the case of Figs. 9 is that, in the region of positive gradient of the hot electron density, both the ion density and the magnetic field intensity have steep negative gradient. That is, the plasma tries to fall into the magnetic well created by the hot electron layer.

It is thus expected that if we make the hot electron ring as wide as the ion density scale length, and if we put the center of the hot electron ring at the position where the ion density begins to fall, the plasma could be stabilized. This has been demonstrated already in Figs. 5 to 7, where the β_c is 10%, a wide ring was used and the plasma is stable. If we decrease the width of the hot electron ring to 1/2 of the value in Figs. 5 to 7 (i.e., the same width with those in Figs. 8 and 9), the plasma is no longer stable.

V. Conclusions

In conclusion we have constructed a 2-1/2 dimensional, fully electromagnetic fully relativistic particle model suitable for investigating many questions of stability and critical β's for EBT type geometries. First results show that stability can be achieved with a hot ring for plasmas β's up to 10%; the stability is sensitive to the position and width of the hot layer. High frequency instabilities have never been observed in our observation.

Acknowledgements

This work was supported by U.S.D.O.E.

References

1. D. B. Nelson and C. L. Hedrick, Nucl. Fusion 19 283 (1979).

2. D. B. Nelson, Phys. Fluids 23, 1850 (1980).

3. J. W. Van Dam and Y. C. Lee, in "EBT Ring Physics" (Proc. of the Workshop, Oak Ridge, TN, Dec. 1979), Oak Ridge National Laboratory CONF-791228, 471 (1980).

4. J. W. Van Dam, H. L. Berk, M. N. Rosenbluth, and D. A. Spong, IFS Report #34 (1981).

5. A. B. Langdon and B. Lasinski, in "Methods in Computational Physics," (B. Adler, S. Fernbach, and M. Rotenburg, eds.) vol. 16, p. 339, Academic Press, New York.

Figure Captions

Fig. 1 Equi-potential lines. Solid lines indicate positive value, dotted lines show negative value. $\beta_c \sim 10\%$. $R_o = 64$. There is no hot electron ring, and flute instability grows.

Fig. 2 (a) Ion density profile $n_i(x)$, and (b) magnetic field profile $B_z(x)$ at $\omega_{pe}t = 120$. They are averaged over y direction.

Fig. 3 Time variation of $|B_z(m = 1, X)|^2$. (a) at x = 35, and (b) at x = 70.

Fig. 4 Growth rate γ of $|B_z(m=1)|$ versus x. Dotted line indicates theoretical estimation $\gamma = (k_y g)^{1/2}$.

Fig. 5 Equi-potential lines. $\beta_c \sim 10\%$, $\beta_h \sim 30\%$, and $R_o = 640$. Flute instability is stabilized by hot electron layer.

Fig. 6 (a) Ion density profile $n_i(x)$, (b) cold electron density profile $n_e(x)$, (c) hot electron density profile $n_h(x)$, and (d) magnetic field profile $B_z(x)$ at $\omega_{pe}t = 180$.

Fig. 7 Growth rate γ versus x.

Fig. 8 (a) Equi-potential lines, (b) ion density profile $n_i(x)$, (c) hot electron density profile $n_h(x)$, (d) magnetic field profile $B_z(x)$, and (e) growth rate γ versus x. $\beta_c \sim 10\%$, $\beta_h \sim 20\%$, $R_o = 64$. Center of hot electron layer is at $x \sim 60$.

Fig. 9 (a) Equi-potential lines, (b) ion density profile $n_i(x)$, (c) hot electron density profile $n_h(x)$, (d) magnetic field profile $B_z(x)$, and (e) growth rate γ as a function of x. Center of hot electron layer is at $x \sim 80$. Other parameters are the same as those in Fig. 8.

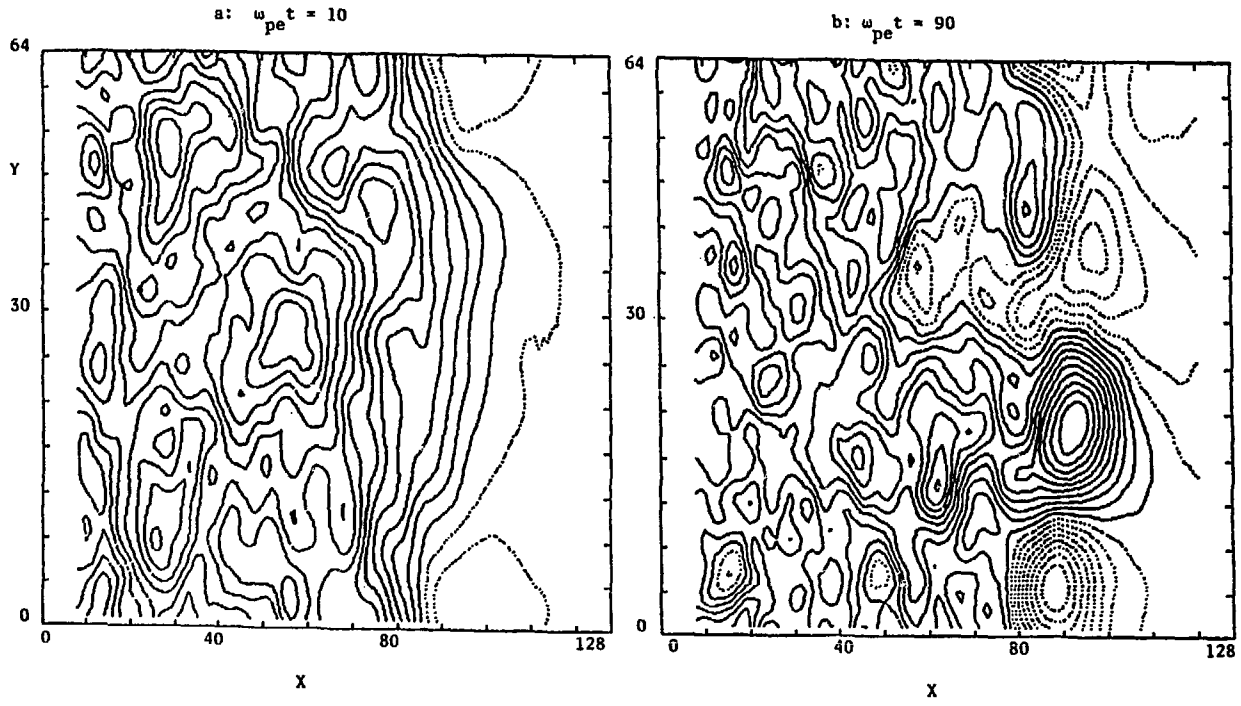

Fig. 1a, b

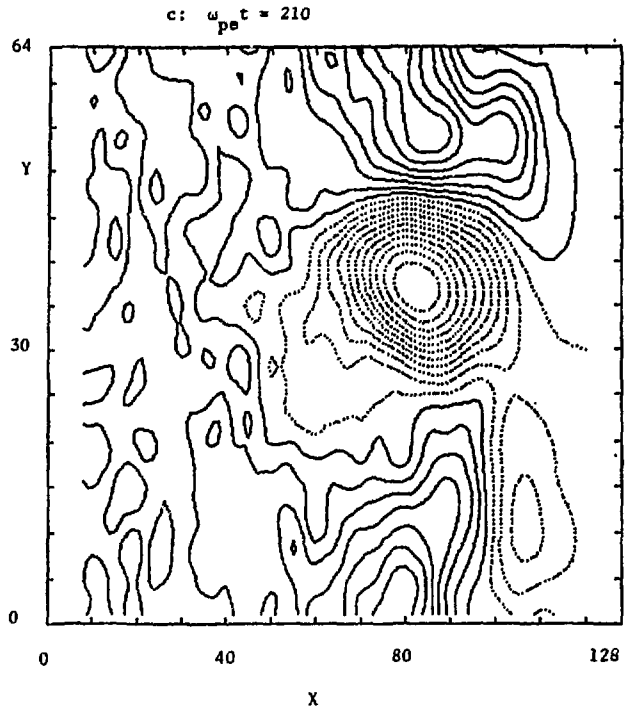

Fig. 1c

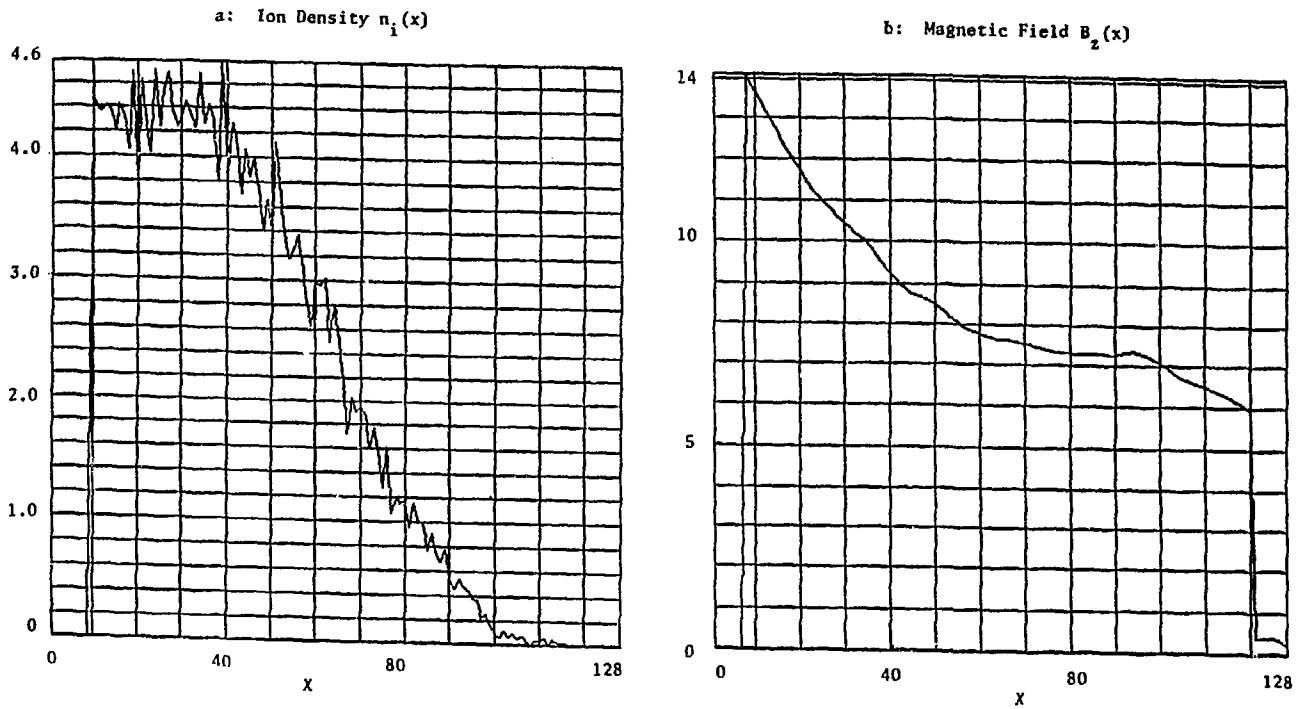
a: Ion Density $n_i(x)$
4.6
4.0
3.0
2.0
1.0
0
0
40
80
128
X
b: Magnetic Field $B_z(x)$
14
10
5
0
0
40
80
128
X

Fig. 2

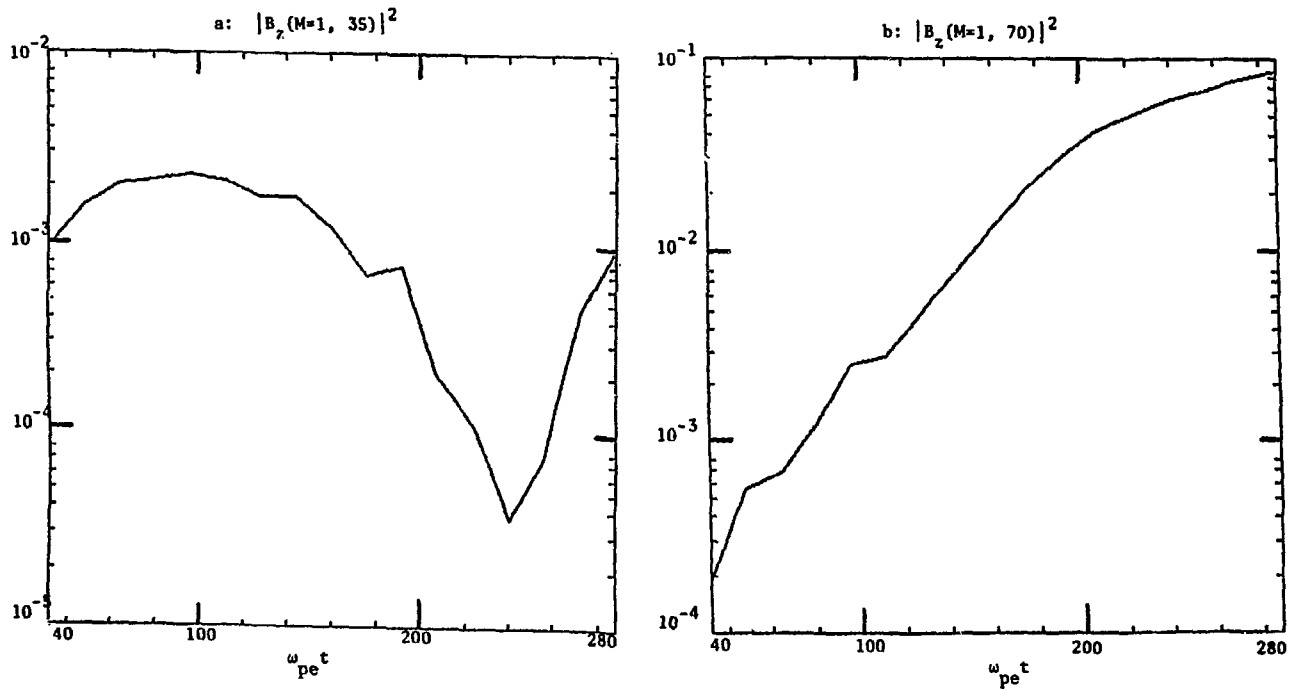
a: $|B_z(M=1, 35)|^2$
10^{-2}
10^{-3}
10^{-4}
10^{-5}
40
100
200
280
$\omega_{pe}t$
b: $|B_z(M=1, 70)|^2$
10^{-1}
10^{-2}
10^{-3}
10^{-4}
40
100
200
280
$\omega_{pe}t$

Fig. 3

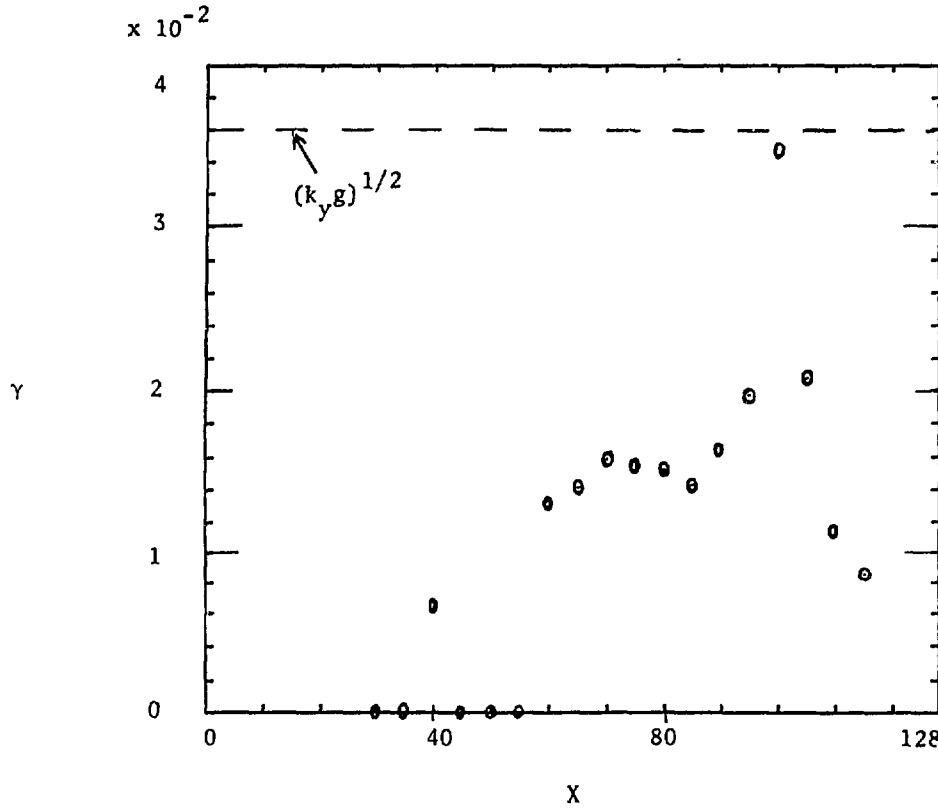

Fig. 4

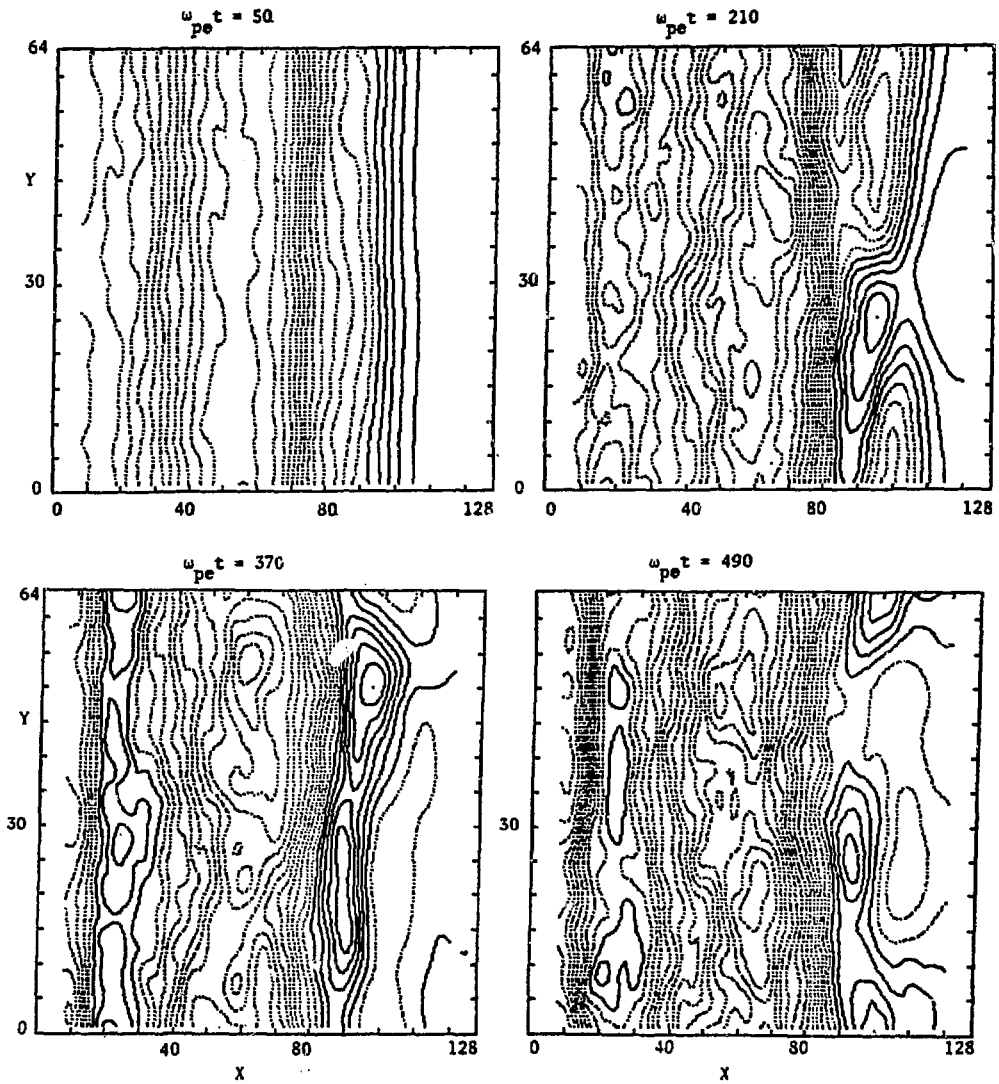
$\omega_{pe}t$ = 50
$\omega_{pe}t$ = 210
$\omega_{pe}t$ = 370
$\omega_{pe}t$ = 490
64
Y
30
0
0
40
80
128
X

Fig. 5

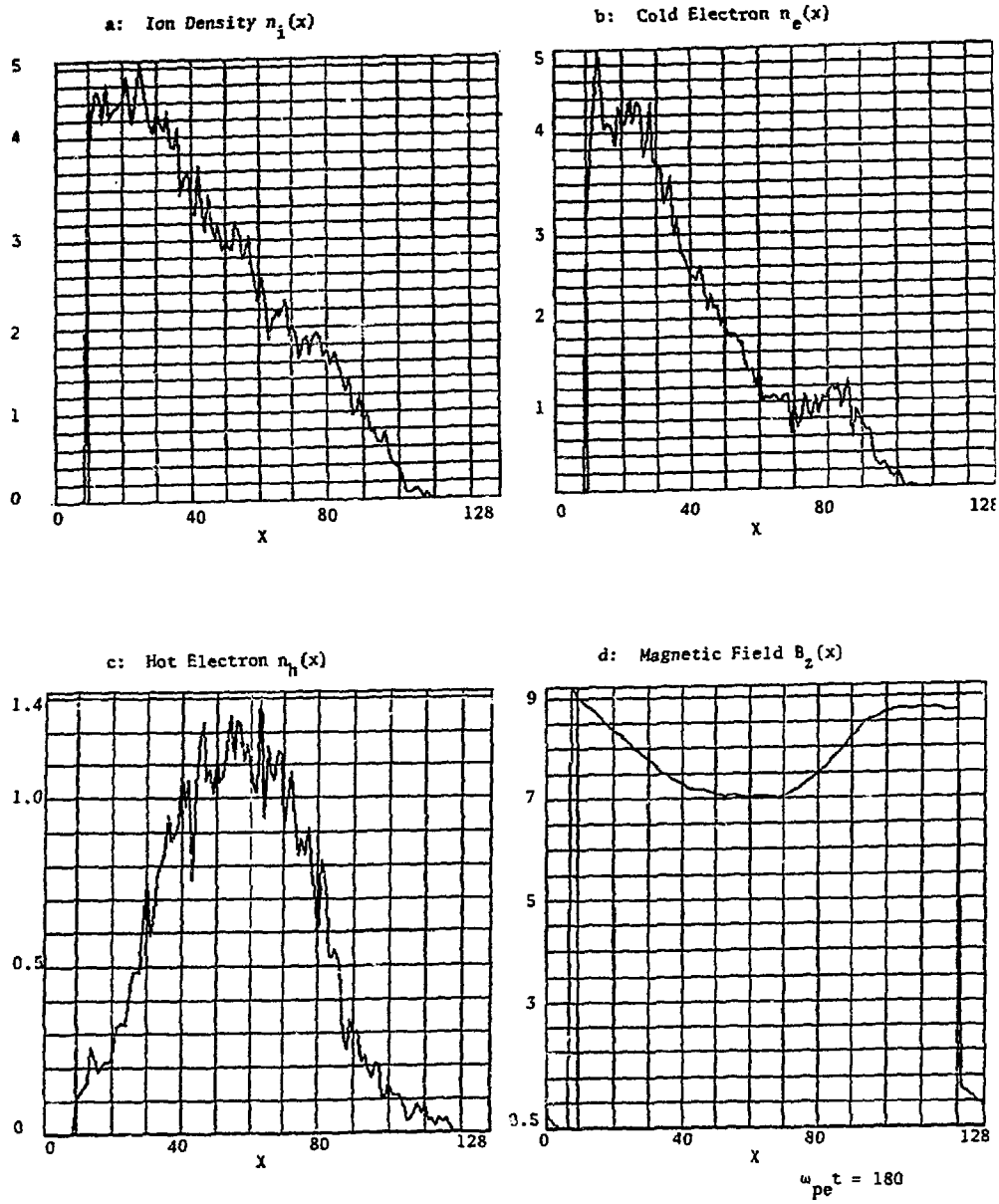
a: Ion Density $n_i(x)$
b: Cold Electron $n_e(x)$
c: Hot Electron $n_h(x)$
d: Magnetic Field $B_z(x)$
X
$\omega_{pe}t = 180$

Fig. 6

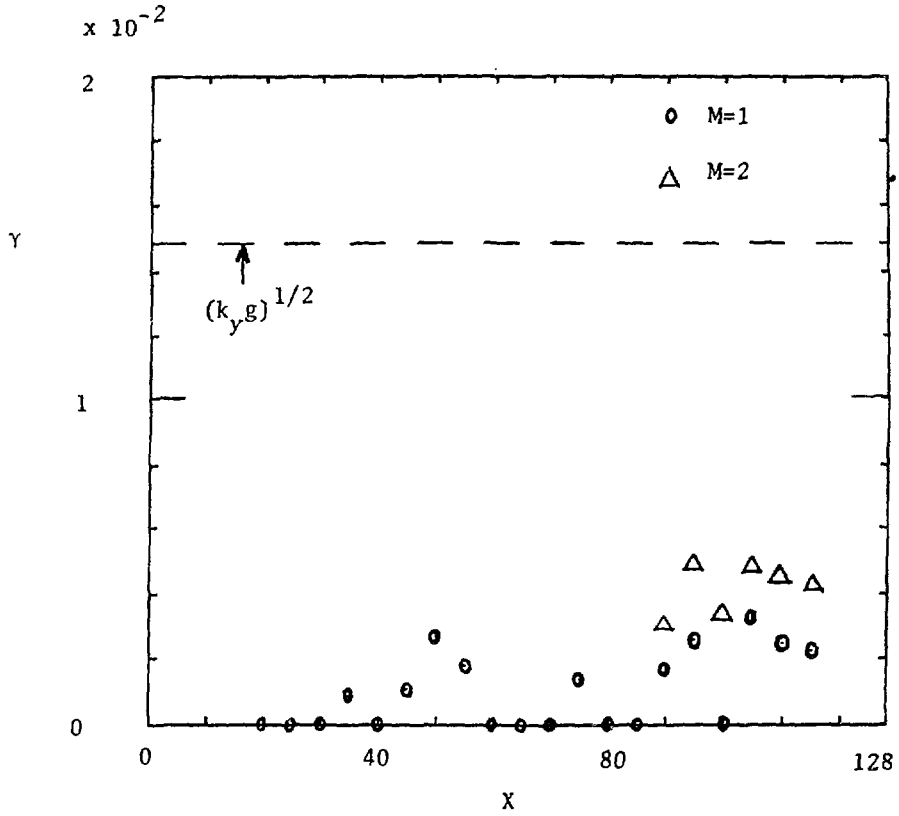

Fig. 7

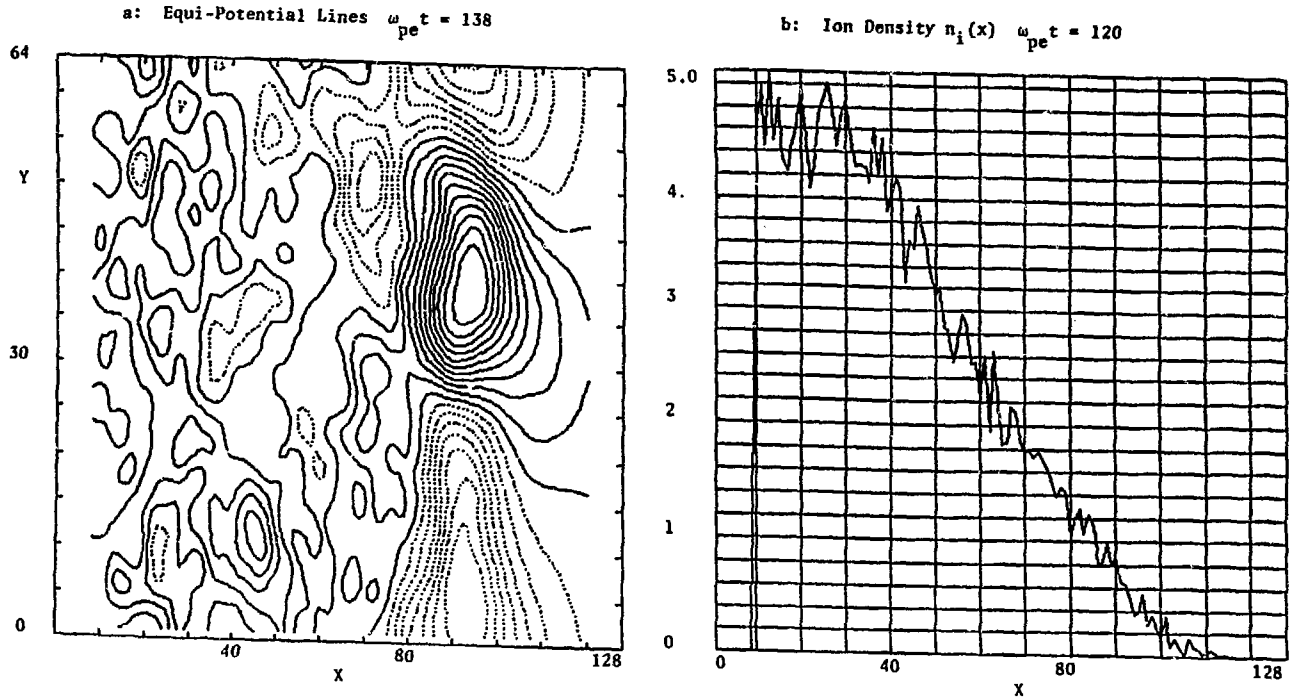
a: Equi-Potential Lines $\omega_{pe}t = 138$
64
Y
30
0
40
80
128
X
b: Ion Density $n_i(x)$ $\omega_{pe}t = 120$
5.0
4.
3
2
1
0
0
40
80
128
X

Fig. 8a, b

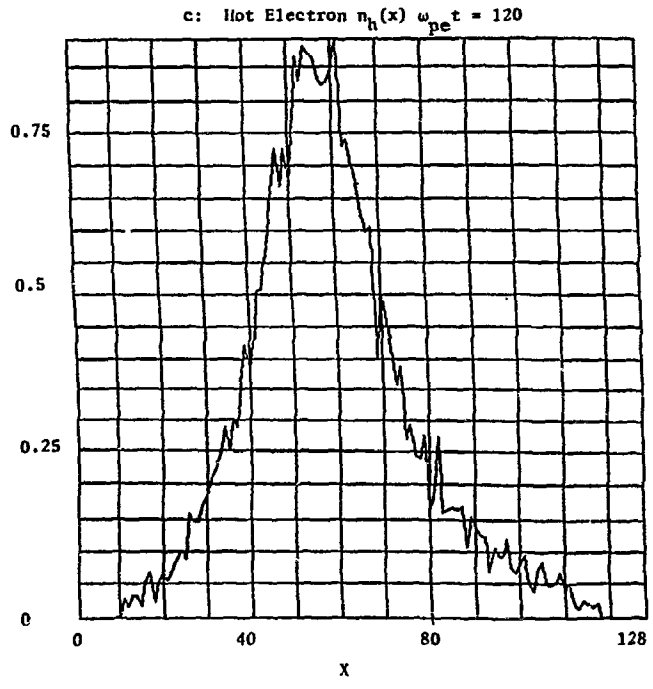
c: Hot Electron $n_h(x)$ $\omega_{pe}t$ = 120
0.75
0.5
0.25
0
0
40
80
128
X

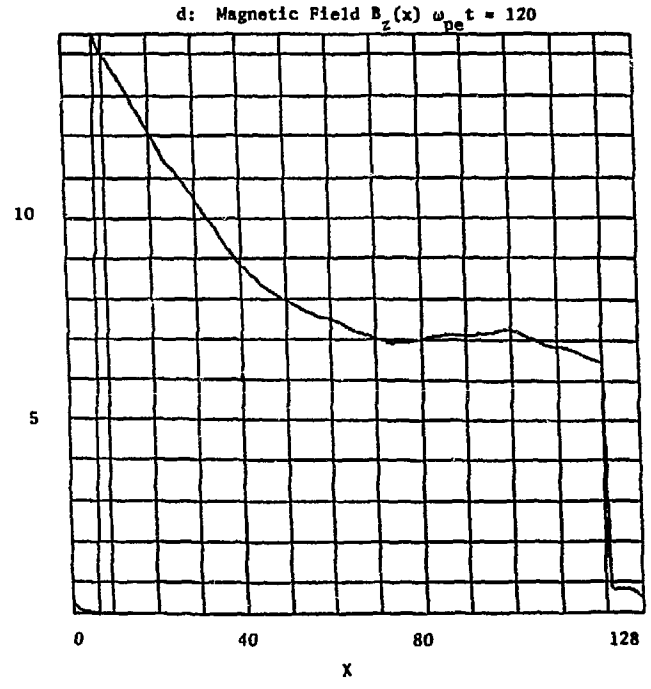
d: Magnetic Field $B_z(x)$ $\omega_{pe}t$ = 120
10
5
0
40
80
128
X

Fig. 8c, d

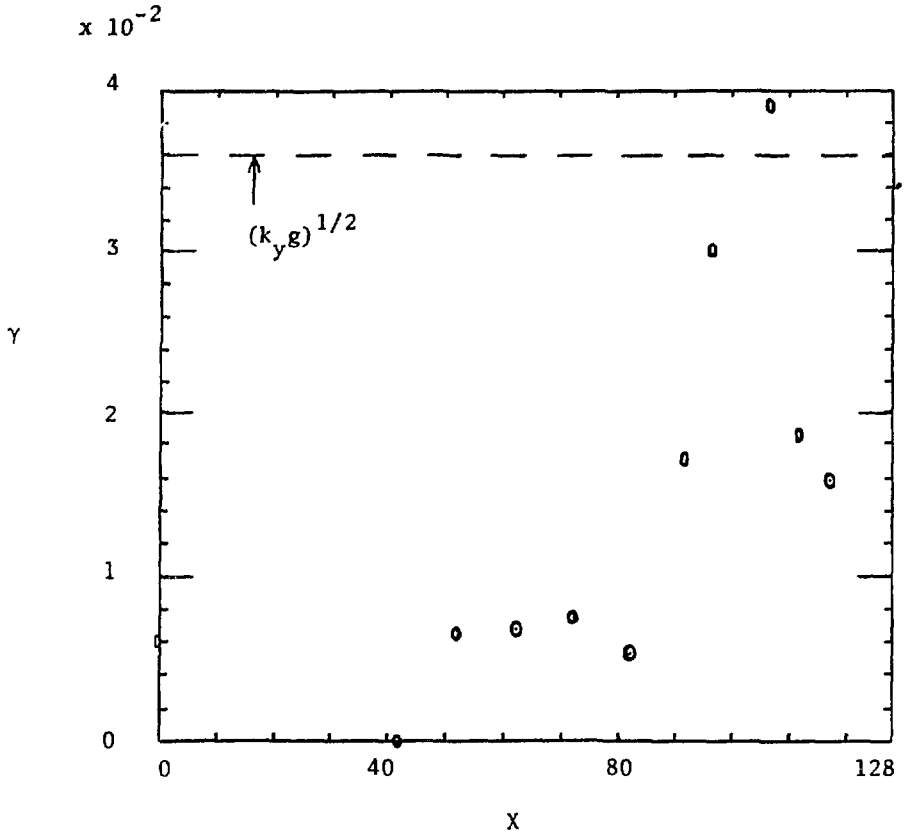

Fig. 8e

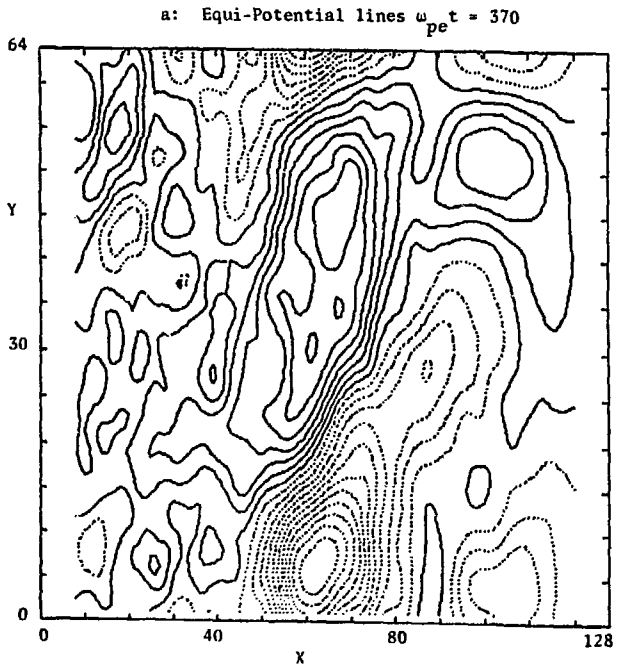
a: Equi-Potential lines $\omega_{pe}t$ = 370
64
Y
30
0
0
40
80
128
X

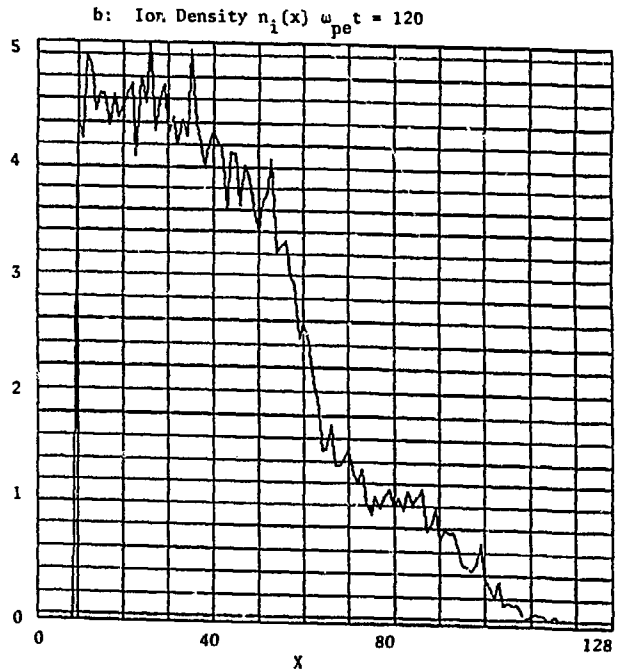
b: Ion Density $n_i(x)$ $\omega_{pe}t$ = 120
5
4
3
2
1
0
0
40
80
128
X

Fig. 9a, b

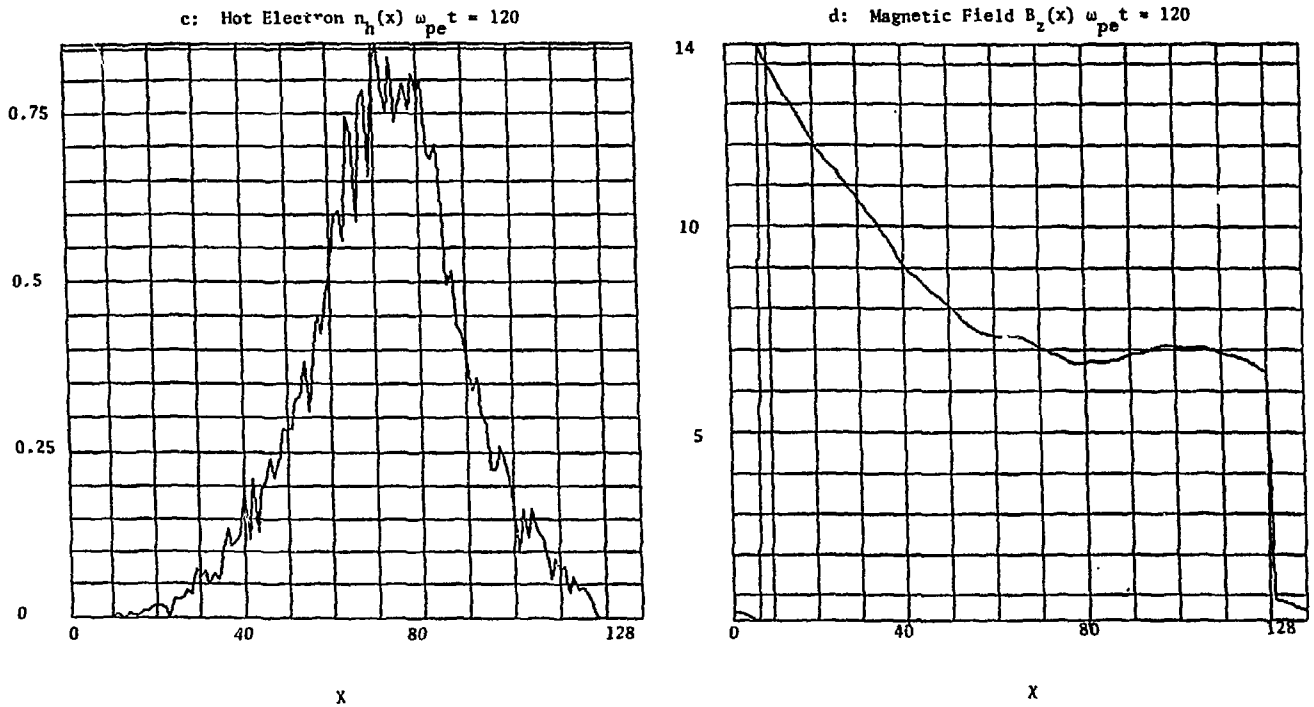
c: Hot Electron $n_h(x)$ $\omega_{pe}t$ = 120
0.75
0.5
0.25
0
0
40
80
128
X
d: Magnetic Field $B_z(x)$ $\omega_{pe}t$ = 120
14
10
5
0
40
80
128
X

Fig. 9c, d

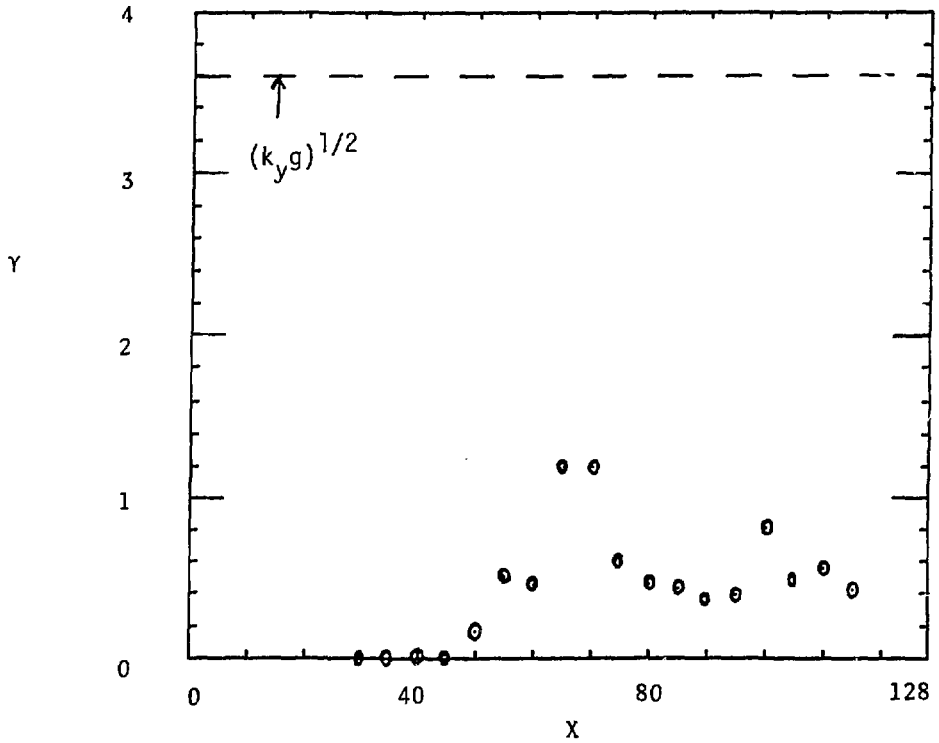

Fig. 9e

PARAMETRIC DECAY INSTABILITIES IN ECR HEATED PLASMAS*

M. Porkolab
Lawrence Livermore National Laboratory
Livermore, California 94550
and
Massachusetts Institute of Technology
Cambridge, Massachusetts 02139

ABSTRACT

The possibility of parametric excitation of electron Bernstein waves and low frequency ion oscillations during ECR heating at $\omega_0 \simeq \ell\omega_{ce}$, $\ell = 1,2$ is examined. In particular, the thresholds for such instabilities are calculated. It is found that Bernstein waves and lower hybrid quasi-modes have relatively low homogeneous and convective thresholds at $\omega_0 \simeq \omega_{UH}$ and $\omega_0 \gtrsim 2\omega_{ce}$, even in plasmas where $T_e \simeq T_i$. Thus, these processes may lead to nonlinear absorption and/or scattering of the incident pump wave. The resulting Bernstein waves may lead to either more effective heating (especially during the start-up phase) or to loss of microwave energy if the decay waves propagate out of the system before their energy is absorbed by particles. While at $\omega_0 = \omega_{UH}$ the threshold is reduced due to the WKB enhancement of the pump wave, (and this instability may be important in tokamaks) in EBT's and tandem mirrors the instability at $\omega_0 \gtrsim 2\omega_{ce}$ may be more important. The instability may persist even if $\omega > 2\omega_{ce}$ and this may be the case during finite beta depression of the magnetic field in which case the decay waves may be trapped in the local magnetic well so that convective losses are minimized. The excited fluctuations may lead to additional scattering of the ring electrons and the incident microwave fields. Application of these calculations to ECR heating of tokamaks, tandem mirrors, and EBT's will be examined.

---

*Work supported by the US Department of Energy.

1. INTRODUCTION

We wish to consider parametric decay processes near the upper hybrid frequency and near the harmonic of the electron cyclotron frequency. The parametric decay conditions require that the following selection rules be satisfied:[1]

$$\omega_0 (\vec{k}_0) = \omega_1 (\vec{k}_1) + \omega_2 (\vec{k}_2)$$
$$\vec{k}_0 = \vec{k}_1 + \vec{k}_2 \, . \tag{1}$$

Here $\omega_0 (\vec{k}_0)$ is the incident electromagnetic pump wave frequency, $\omega_1 (\vec{k}_1)$ is a low frequency ion mode such that $\omega_1 \lesssim 2\omega_{LH}$ (where ω_{LH} is the lower hybrid frequency), and $\omega_2 (\vec{k}_2)$ is an electrostatic upper hybrid (Berstein) wave. While it is necessary that the high frequency sideband, $\omega_2 (\vec{k}_2)$ be a normal mode of the system, (i.e., $\varepsilon_R (\omega_2, \vec{k}_2) = 0$, so that in a Maxwellian plasma instability may occur in regions where $\omega_0 > \omega_{ce}$) for the low frequency mode it is not essential. In particular, when for the low frequency mode $\varepsilon_R (\omega_1, \vec{k}_1) \neq 0$, we talk about decay into quasi-modes. In general, when $T_e \simeq T_i$, decay into heavily Landau-damped quasi-modes dominates. Landau (cyclotron) damping on both electrons and ions may occur.

Parametric decay near the upper hybrid frequency and the first few cyclotron harmonics has been observed and studied in some detail in past experiments.[2-4] In these experiments coupling to both high frequency electron Bernstein waves and low frequency ion-acoustic and/or lower hybrid modes has been observed. These experiments were performed at modest power levels ($P \simeq 10$ W - 2 kW) in low temperature ($T_i \lesssim T_e \lesssim 10$ eV) and low density ($n_e \lesssim 10^{12}$ cm^{-3}) plasmas. Usually plasma heating was observed concurrently with the excited instabilities. More recently, parametric excitation has also been observed in the MIT Versator II tokamak during ECR heating experiments using the NRL 35 GHz gyrotron at the 40 - 100 kW level.[5] Parametric excitation has also been studied in

recent numerical simulations,[6] as well as in analytical works[7,8] at $\omega_o \simeq \omega_{UH}$. In this paper we wish to study in greater detail the growth rates and thresholds for parametric excitation of Bernstein waves and low frequency lower hybrid quasi-modes in plasmas characterized by $T_e \gtrsim T_i$, $\omega_o \simeq \omega_{UH}$, or $\omega_o \simeq 2\omega_{ce}$. Of particular interest is the threshold for excitation of these modes in an inhomogeneous plasma. The plan of this paper is as follows: In Sec. 2 we study parametric processes at $\omega_o \simeq \omega_{UH}$, in Sec. 3 we study the regime $\omega_o \simeq 2\omega_{ce}$, and in Sec. 4 the conclusions are given.

2. PARAMETRIC DECAY AT $\omega_o = \omega_{UH}$

First we examine the selection rules, Eq. (1), for decay into Bernstein waves propagating at an angle to the magnetic field, and into lower hybrid waves. The dispersion relationships of these modes in a Maxwellian plasma are given by the following expressions:

$$\omega_1^2 = \omega_{LH}^2 \left[1 + \frac{k_\parallel^2}{k^2} \frac{m_i}{m_e} + 3b_e \frac{T_i}{T_e} \frac{\omega_{ce}\,\omega_{ci}}{\omega_1^2} \right] \tag{2}$$

$$\omega_2^2 = \omega_{UH}^2 - \omega_{pe}^2 \left[b_e + \frac{k_\parallel^2}{k^2} \frac{\omega_{ce}^2}{\omega_{UH}^2} \right] \tag{3}$$

where $b_e = k_\perp^2 r_{ce}^2$, $\omega_{UH}^2 = \omega_{pe}^2 + \omega_{ce}^2$, $\omega_{LH}^2 = \omega_{pi}^2 / (1 + \omega_{pe}^2 / \omega_{ce}^2)$ and where we assumed $\omega_{pe}^2 \lesssim \omega_{ce}^2$, $b_e << 1$, $k_\parallel^2 / k^2 << 1$. For simplicity, we shall assume in Eq. (1) that $|\vec{k}_o| << |\vec{k}_1|$, and thus $\vec{k}_1 \simeq \vec{k}_2$ (the introduction of finite $\vec{k}_o$ does not significantly modify the following results). In Eq. (3) we also assumed that $\omega_{pe}^2 < \omega_{ce}^2$ so that $\omega_{UH} < 2\omega_{ce}$. We can now distinguish between three limiting cases:

A. $k_\parallel \simeq 0$.

In this case the selection rules (1) yield

$$b_e \simeq 2 \frac{\omega_{ce}^2}{\omega_{pe}^2} \frac{\omega_{LH}}{\omega_{ce}} \left[1 + \frac{3T_i}{T_e} \frac{\omega_{ce}\,\omega_{ci}}{\omega_{LH}^2} b_e \right]^{1/2} \tag{4}$$

For $T_e \simeq T_i$ we find that $b_e \simeq 0.2$, $\omega_1 \simeq (1.4 - 2)\ \omega_{LH}$ and $\omega_2 \simeq \omega_{UH} - 0.1\ (\omega_{pe}^2 / \omega_{UH}^2)$ for typical plasma parameters of interest. Thus we have

$$\frac{\omega_1}{k_\perp v_{ti}} \simeq \left(\frac{T_e}{T_i}\right)^{1/2} \frac{\omega_{pe}}{\omega_{ce}} \frac{1}{b_e^{1/2}} \simeq 1$$

for $\omega_{pe} / \omega_{ce} \simeq 0.4$ and $T_e \simeq T_i$. Thus the low frequency lower hybrid "wave" is expected to be a heavily ion-Landau damped "quasi-mode", which should produce perpendicular ion heating. On the other hand, the high frequency Bernstein wave should propagate to the cyclotron resonance layer and be absorbed there by collisions and/or electron cyclotron damping if $k_\parallel \neq 0$.

B. $0 < (k_\parallel^2 / k^2)\ (\omega_{ce}^2 / \omega_{UH}^2) < b_e < 1$.
In this case we find $b_e \simeq 0.1 - 0.2$, $(k_\parallel^2 / k_\perp^2)\ (m_i / m_e) \simeq 1$, and in addition to $\omega_1 / k_\perp v_{ti} \simeq 1$ we also have $\omega_1 / k_\parallel v_{te} \simeq 1$. Thus, the low frequency "quasi-mode" will experience both "perpendicular" ion Landau damping, and "parallel" electron Landau damping.

C. $0 < b_e < (k_\parallel^2 / k^2)\ (\omega_{ce}^2 / \omega_{UH}^2)$.
In this case $\omega_1 \to \omega_{pe}$, $\chi_i\ (\omega) \to 0$, and parametric coupling diminishes to an uninterestingly low level.

In the dipole limit ($\vec{k}_o = 0$) the growth rate and threshold for decaying into a resonant sideband and a low frequency quasi-mode is given by:[9]

$$\gamma + \Gamma_2 = \frac{\mu^2}{4} \frac{\chi_{eI}\ (\omega_1)\ |\ \chi_i\ (\omega_1)\ |^2 + \chi_{iI}\ (\omega_1)\ |\ 1 + \chi_e\ (\omega_1)\ |^2}{|\varepsilon\ (\omega_1)\ |^2\ (\partial\varepsilon_R / \partial\omega_2)} \tag{5}$$

where

$$\mu^2 = \frac{e^2 E_{ox}^2 k_x^2}{m_e^2(\omega_o^2 - \omega_{ce}^2)^2} \left[1 + (E_{oy}^2 / E_{ox}^2)(\omega_{ce}^2 / \omega_o^2) \right] \tag{6}$$

is the parametric coupling coefficient, k_x is the decay wave number, χ_e (χ_i) is the electron (ion) susceptibility, $\varepsilon = 1 + \chi_e + \chi_i$ is the dielectric constant, sub-I designates the imaginary part, sub-R designates the real part, $|\varepsilon|^2 = \varepsilon_R^2 + \varepsilon_I^2$, and the collisional (cyclotron) damping rate at the sideband is designated by Γ_2. Here we assumed that E_{ox} is the electrostatic component of the pump wave which is significant only in the region of the upper hybrid mode conversion layer, and E_{oy} is the incident electromagnetic wave field (i.e., the pump wave is assumed to propagate in the x-direction). After some algebra, Eq. (5) reduces to

$$\frac{\gamma + \Gamma_2}{\omega_{ce}} = \frac{\theta_M E_{ox}^2 b_e}{32\pi n_o T_e} \left(1 + \frac{E_{oy}^2}{E_{ox}^2} \frac{\omega_{ce}^2}{\omega_o^2} \right) , \tag{7}$$

where the maximum value of θ is near $\theta_M \simeq 1$, and it includes both electron and ion Landau damping terms (which we shall not bother writing down here). Thus, the uniform plasma threshold is obtained by taking $\gamma = 0$. Taking typical tokamak parameters near the plasma edge, namely $n_e \simeq 2 \times 10^{12}$ cm^{-3}, B = 1.1 T, $T_e = T_i \simeq 120$ eV, we obtain $E_{ox} \simeq$ 100 volt/cm, or if we assume a WKB enhancement factor of 5, for the incident wave field we obtain $E_{oy} \simeq 20$ volt/cm, or approximately P/A $\simeq$ 50 watts/cm^2, which is easily exceeded in the Versator II experiment.[5] (Note that for $n_e \simeq 5 \times 10^{11}$ cm^{-3}, $T_e \simeq 10$ eV we would get $E_{ox} \simeq 47$ volt/cm and $E_{oy} \simeq 10$ volt/cm.) Similar thresholds would be expected in TMX-U during the plasma build-up phase[10] and in the ISX-B pre-ionization experiments.[11] In EBT-S[12] we may consider similar density and magnetic field, but higher electron temperature so that the collision frequency would be lower, by a factor of $1/T_e^{3/2}$ and thus the threshold E would be down by a factor of $1/T_e^{1/4}$. For example, at

a temperature of $T_e \simeq 500$ eV and $n_e \simeq 2 \times 10^{12} cm^{-3}$ the collisional threshold would be reduced to $E_{ox} \simeq 70$ volt/cm, (or $E_{oy} \simeq 14$ volt/cm) a relatively low value. However, we note that in both EBT and TMX-U the magnetic field is parallel-stratified, and hence the incident electromagnetic wave should be completely absorbed during incidence from the high magnetic field side at the electron cyclotron resonance layer, before arrival to the upper hybrid layer.

Let us now examine the convective threshold due to the finite length of the distance between the ω_{ce} layer and the ω_{UH} layer (for decay due to E_{oy}), or more importantly, the x-distance of the WKB enhanced E_{ox}. We take the amplification distance to be comparable to the free space wavelength of the incident electromagnetic wave, namely $\Delta X \simeq 1$ cm. The convective threshold for an exp (2π) amplification of $|E_2|^2$ is given by

$$\frac{\gamma \Delta X}{V_{gx}} \gtrsim \pi \tag{8}$$

which in the present case reduces to

$$\frac{E_{ox}^2}{32\pi\ n_e T_e} \geq \frac{\omega_{pe}^2}{\omega_{ce}^2} \frac{\pi}{\theta_M\ k_x\ \Delta X} \quad . \tag{9}$$

For parameters $\Delta X \simeq 1$ cm, $\theta_M \simeq 1$, $n_e \simeq 10^{12}$ cm^{-3}, $T_e \simeq T_i \simeq 100$ eV, Eq. (9) gives $E_{ox} \simeq 1800$ volt/cm, or $E_{oy} \simeq 360$ volt/cm and $P_o/A \simeq 525$ watts/cm^2. For the Versator II tokamak taking $A \simeq 50 cm^2$ (corresponding to a 10° antenna half-width angle) we obtain $P_o \simeq 26$ kW total incident power. Had we considered a lower temperature near the plasma surface, namely, $T_e \simeq T_i \simeq 20$ eV, we would obtain $P_o \simeq 5$ kW. Both of these power levels are less than those used in the experiment[5]

($P_0 \simeq 100$ kW). These power levels should also be typical in the TMX-U experiments. On the other hand, in EBT-S at the higher temperatures, and non-focused microwave injection geometry (cavity excitation), it is unlikely that such instabilities would be excited.

3. PARAMETRIC DECAY AT $\omega_0 = 2\omega_{ce}$

This regime is relevant to the ring formation region in EBT[12], the thermal barrier formation in TMX-U[10], and certain tokamak experiments (TM-3, T-10, etc.). In this case we are interested in the regime $1/3 \lesssim \omega_{pe} / \omega_{ce} \lesssim 1$, $b_e \simeq 1$ and we find that $\omega_1 / k_\perp v_{ti} \lesssim 2$ if $1 \lesssim T_e / T_i \lesssim 20$, and if $20 \lesssim T_e / T_i$, $\omega_1 / k_\parallel v_{te} \simeq 1$. Thus, again the low frequency wave is a Landau-damped quasi-mode (if we take the stochastic straight-line orbit for ions). We also note that the second harmonic layer is accessible from both low and high magnetic field injection if $\omega_{pe} \lesssim \omega_{ce}$. The Bernstein wave may be described by the expression

$$\omega_2 \simeq 2\omega_{ce} \quad [1 + \delta_1 + \delta_2] \tag{10}$$

where

$$\delta_1 \simeq (\omega_{pe}^2/\omega_{ce}^2)\ (I_2\ (b_e)\ e^{-b_e} / b_e)$$

$$\delta_2 \simeq \delta_1 (I_1\ (b_e) - I_2\ (b_e) / 2 - 18\ I_3(b_e)/3)/I_2(b_e)$$

Typically $\delta_2 < \delta_1$, and since $\delta_2 << 1$, we shall neglect δ_2. The growth rate for instability in a uniform plasma is

$$\frac{\gamma + \Gamma_2}{2\omega_{ce}} = \frac{E_{oy}^2\ \tilde{\theta}}{144\pi\ n_e T_e} \left(\frac{\omega_{ce}}{\omega_2}\right)\left(\frac{\omega_{pe}^4}{\omega_{ce}^4}\right) \frac{I_2(b_e)\ e^{-b_e}}{(1 + 8\delta_1/3)^2} \tag{11}$$

where again the maximum value of $\tilde{\theta}$ is $\tilde{\theta}_M \simeq 1$. Introducing the collisional damping rate at the sideband via the collision frequency ν_e in a uniform plasma, we obtain the following threshold electric field for parametric excitation:

$$E_{oy} = (144\pi\, n_e T_e)^{1/2} \left(\frac{\omega_{c\epsilon}^2}{\omega_{pe}^2}\right)\left(\frac{\nu_e}{\omega_{ce}}\right)^{1/2} \frac{(1 + 8\delta_1/3)(1 + \delta_1)^{1/2}}{(\tilde{\theta}\, I_2(b_e)e^{-b_e})^{1/2}} \quad (12)$$

For $n_e \simeq 4 \times 10^{12}$ cm^{-3}, $T_e \simeq 200$ eV, $f_o \simeq 28$ GHz, we obtain $E_{oy} \simeq 150$ volt/cm. We note that as T_e increases, E_{oy} decreases as $T_e^{1/4}$ (since $\nu_e \propto T_e^{-3/2}$ and we may assume that b_e remains constant). For example, if $T_e \simeq 6$ keV, $n_e \simeq 4 \times 10^{12}$ cm^{-3}, $\nu_e \simeq 10^3$ sec^{-1}, $E_{oy} \simeq 60$ volt/cm. Again, we expect that in TMX-U such threshold would be exceeded (where the applied electric field may approach 1 kV/cm). In EBT typical electric fields are expected to be less due to the larger plasma volume and the spatially more evenly distributed microwave power. Thus, unless resonant cavity modes were set up we would not expect that such instabilities would play a significant role in EBT-S.

The convective threshold can be estimated as previously, except in the present case the direction of wave propagation is the y-direction (along the incident electric field, perpendicular to the direction of the pump wave propagation):

$$\gamma L_y \,/\, v_{gy} \;\geq\; \pi \quad (13)$$

where L_y is the spatial extent of the region of microwave illumination. For example, in TMX-U we expect 4 horns to radiate power onto the fan in the y-direction, each having an illumination width of $L_y = 10$ cm, for a total width of 40 cm.[10] Evaluating Eq.(13) at $\omega_o \simeq 2\omega_{ce}(1 + \delta_1)$ we obtain

$$E_{oy} \geq \frac{(16\, n_e T_e)^{1/2}\, 6\pi\, (1 + 8\delta_1/3)(1 + \delta_1)^{1/2}\, \xi^{1/2}}{b_e^{1/2}\, L_y\, \tilde{\theta}^{1/2}\, (\omega_{pe} / \omega_{ce})} \tag{14}$$

where

$$\xi = (1/2\, \frac{b_e^{1/2}}{I_2(b_e)e^{-b_e}}\, \frac{\partial(I_2(b_e)e^{-b_e})}{\partial b_e} - 1)\ .$$

We note that near the peak of the Bernstein wave dispersion relationship $\xi \to 0$ (i.e., $v_{gy} \to 0$) and the convective losses disappear. For such wavelengths the uniform threshold, Eq. (12) prevails. Also, if the plasma is nearly uniform in the y-direction (which is the case in TMX-U in the direction of the plasma fan) there is no additional threshold due to the density gradient. For example, for $L_y \simeq 10$ cm, $E_{oy} \gtrsim (8\pi\, n_e T_e\, \xi/9)^{1/2}$ and we recover the collisional threshold if $\xi \lesssim 10^{-4}$ which corresponds to $k_{IM} / k_{Re} < 10^{-2}$, in which case the weakly damped Bernstein wave concept still holds (i.e., Eq. (13)). This corresponds to the case of $\omega_{pe}^2 / \omega_{ce}^2 \simeq 1$, $\delta_1 \simeq 0.2$. Thus this instability would occur before the $2\omega_{ce}$ layer in a Maxwellian plasma when the wave is launched from the low magnetic field side, or from the high field side if finite β significantly depressed the magnetic field. If single pass absorption is not complete, the instability is excited for launching from either low or high magnetic field side.

4. CONCLUSIONS

We have examined the thresholds for parametric decay into Bernstein waves and lower hybrid electron and ion quasi-modes in ECR heated plasmas when $\omega_o \simeq \omega_{UH}$ or $\omega_o \simeq 2\ _{ce}$. Such instabilities should produce enhanced absorption. It was found that near $\omega \simeq \omega_{UH}$, the threshold electric field is a few hundred volts per cm in present day gyrotron heating experiments. The threshold, which is dominated by convective losses, should

be exceeded in tokamak and tandem mirror experiments, especially during start-up phase. It should also be important in future large tokamak experiments during pre-ionization and start-up phase, but not during the heating phase. In EBT-type plasmas the instability is not excited due to the low electric fields. At $\omega_0 \simeq 2\omega_{ce}$ the convective threshold may disappear near critical layers where $v_g \simeq 0$ at $\omega_0 \simeq 2\omega_{ce}$ $(1 + \delta_{crit})$. The collisional threshold decreases from a few hundred volt/cm at $T_e \simeq 200$ eV to $E_0 \simeq 60$ volt/cm at $T_e \simeq 6$ keV (for example). Such instabilities may be excited in TMX-U, tokamaks, and even EBT if cavity modes were set up. We note that the excitation of these instabilities should produce enhanced heating, and due to the short wavelengths, very little enhanced radial diffusion. On the other hand, undesirable enhanced particle scattering into the loss-cone may also result for both ring electrons in EBT and thermal barrier electrons in TMX-U.

REFERENCES

1. M. Porkolab, Nuclear Fusion 18, 367 (1978).
2. B. Grek and M. Porkolab, Phys. Rev. Lett. 30, 836 (1973).
3. M. Okabayashi, Chen and M. Porkolab, Phys. Rev. Lett. 31, 1113 (1973).
4. M. Porkolab, V. Arunasalam, N. C. Luhmann Jr., and J. P. M. Schmitt, Nuclear Fusion 16, 269 (1976).
5. F. S. McDermott, K. E. Hackett, A. S. Fisher, G. Bekefi, M. Porkolab, J. S. Levine and M. E. Read, Bull. Am. Phys. Soc. 26, 1034 (1981).
6. A. T. Lin and C. C. Lin, Phys. Rev. Lett. 47, 98 (1981).
7. M. Porkolab, Nuclear Fusion 12, 329 (1972).
8. E. Ott, B. Hui, and K. R. Chu, Phys. Fluids 23, 1031 (1980).
9. M. Porkolab, Phys. Fluids 20, 2058 (1977).
10. T. C. Simonen, T. J. Orzechowski, M. Porkolab, and B. W. Stallard, Lawrence Livermore Laboratory, Report UCRL 85827 (1981).
11. R. M. Gilgenbach et al, Nuclear Fusion 21, 319 (1981).
12. N. A. Uckan et al, 8th Int. Conf. on Plasma Phys. and Contr. Nucl. Fusion Res., Brussels, 1980 IAEA-CN-38/BB-3-2, (Nucl. Fusion Suppl. 1, 831 (1981)).

THE WHISTLER INSTABILITY AT RELATIVISTIC ENERGIES*

N. T. Gladd
JAYCOR, P. O. Box 85154, San Diego, California 92138

ABSTRACT

The whistler instability, driven by the temperature anisotropy $T_\perp > T_\parallel$, represents a potentially serious drain on the energy content of hot electron rings. While indirect measurements suggest that scattering losses in EBT are classical,[1] this instability has been directly observed in other ECH heated plasmas.[2] The traditional reason given for the absence of dramatic effects in EBT due to this instability is that the relativistic broadening of the whistler wave resonance with ring electrons stabilizes the instability.[3] While this idea is very plausible, its firm establishment requires the accurate solution of a formidable dispersion equation. We report here the results of a detailed numerical analysis of the dispersion equation for the relativistic whistler. In brief, we find that the relativistic broadening acts to reduce the growth rate of the whistler but does not completely suppress the mode. Although the whistler is not stabilized, the relativistic reduction of the growth rate can readily result in situations where the effects of parallel electron dynamics (bounce motion) are significant over times of interest. Parameterizing the ring by its pressure ($\beta_\perp$), its anisotropy ($T_\perp/T_\parallel$) and the relative fraction of ring electrons (Δ), we calculate how relativistic ($T_\perp/mc^2$) the ring must be in order that the whistler growth rate be reduced to a value on the order of the bounce frequency.

*This work is supported by the U.S. Department of Energy.

1. INTRODUCTION

The electron cyclotron resonance heating process used in Elmo Bumpy Torus results in hot electron rings which are characterized by an anisotropic velocity distribution, $\langle v_\perp^2 \rangle > \langle v_\parallel^2 \rangle$. In addition, the magnetic geometry results in other anisotropies which take the form of a generalized loss cone. Such a hot electron velocity distribution, far from thermodynamic equilibrium, is subject to a variety of micro-instabilities. In this paper we study the whistler instability, an electromagnetic instability driven by the temperature anisotropy. In particular, we carefully and systematically examine the consequences of relativistic effects, important at the high temperatures of the EBT ring electrons, on the whistler instability.

In a typical EBT environment, the whistler instability is not important in terms of the limitations that it places on the global stability of the confinement geometry but rather from the fact that it can enhance particle losses (and hence energy losses) from the rings. These anomalous losses, in conjunction with such classical loss processes as Coulomb scattering, electron drag, and synchrotron radiation, impose limitations on achievable steady-state ring properties. Although there exists experimental evidence that the present losses in EBT rings are predominantly classical,[1] the whistler mode has actually been observed in a hot electron, ECH produced plasma.[2] Although the whistler is obviously not dominating energy loss in current experiments, the question of the relative importance of this anomalous loss process when compared with classical processes is an open question which should be examined as steps are taken toward the new parameter environments implied by EBT-P.

One of the reasons put forward for the weakness of the whistler instability in current experiments is that the relativistic energies of the ring will lead to a broadening of the unstable resonance between whistler waves and the ring electrons. This broadening has the consequence that very high energy particles actually absorb energy

from the waves and act as a stabilizing effect on the mode. When there are sufficient hot electrons, it is argued that this process will actually suppress the whistler instability.[3] This idea is certainly plausible but the broadening of the wave-particle resonance is not the only relativistic effect occurring and it is necessary to undertake a careful analysis of the formidable dispersion equation describing the relativistic whistler in order to ascertain the extent to which relativistic resonance broadening affects the mode. The published literature dealing with relativistic effects on the whistler is meager and is restricted to analyses where the electrons are only mildly relativistic[4] or where the Plemelj approximation for the resonant integral may be invoked.[5] Neither approximation is well satisfied in a typical EBT plasma environment.

In this paper we shall carefully examine the effects of relativistic electrons on the whistler mode in a plasma environment typical of EBT. Because of the complexity of the dispersion equation, we shall depend primarily on numerical analysis. Specifically, we shall numerically evaluate the two-dimensional resonant integral describing the interaction of hot electrons with whistler waves.

The organization of this paper is as follows. In Section 2, we review some basic properties of the whistler instability. In Section 3, we qualitatively discuss relativistic effects on the whistler and examine the parametric dependence of the whistler growth rate at relativistic energies. In Section 4, we apply the results of our analysis to EBT plasmas. Finally, in Section 5, we summarize our results and draw some conclusions.

2. SOME BASIC PROPERTIES OF THE WHISTLER INSTABILITY

Whistler waves are right-hand, circularly-polarized, electromagnetic waves propagating parallel to the ambient magnetic field in a magnetoplasma. The waves exist even if the field is unidirectional and the plasma is uniform. This situation is illustrated in Figure 1. The waves rotate in the same sense as the electron gyromotion and resonant interactions between waves and electrons are possible. Such interactions can lead to instability if the velocity distribution of the electrons is such that $\langle v_\perp^2 \rangle > \langle v_\parallel^2 \rangle$.

The dispersion equation for whistler waves may be written as

$$n^2 - \epsilon_R = 0 \tag{1}$$

where $n = (kc/\omega)$ and

$$\epsilon_R = \epsilon_{xx} - i\epsilon_{xy} \tag{2}$$

is the right-hand, circularly-polarized construct of the dielectric tensor. From kinetic theory

$$\epsilon_R = 1 - 2\pi \frac{\omega_p^2}{\omega} \int_0^\infty v_\perp dv_\perp \int_0^\infty dv_\parallel \frac{v_\perp^2 \left[\frac{\partial f_o}{\partial v_\perp^2} \left(1 - \frac{kv_\parallel}{\omega}\right) + \frac{\partial f_o}{\partial v_\parallel^2} \left(\frac{kv_\parallel}{\omega}\right) \right]}{(kv_\parallel - \omega \pm \omega_c)} . \tag{3}$$

The summation over plasma specie is implied and the sign choice ($+/-\omega_c$; $\omega_c > 0$ refers to electrons/ions, respectively). Standard analyses are usually based on the biMaxwellian distribution

$$f_o(v_\perp, v_\parallel) = \left(\frac{m}{2\pi T}\right)^{3/2} \left(\frac{T_\perp}{T_\parallel}\right)^{\frac{1}{2}} \exp\left\{ - \frac{mv_\perp^2}{2T_\perp} - \frac{mv_\parallel^2}{2T_\parallel} \right\} , \tag{4}$$

in which case

$$\epsilon_R = 1 - \omega_p^2 \left(1 - \frac{T_\perp}{T_\parallel}\right) - \omega_p^2 \left[\frac{\pm\,\omega_c}{k\bar{v}_\parallel} - \left(\frac{T_\perp}{T_\parallel}\right)\left(\frac{\omega \pm \omega_c}{k\bar{v}_\parallel}\right)\right] Z\left(\frac{\omega \pm \omega_c}{k\bar{v}_\parallel}\right) \quad . \quad (5)$$

The whistler instability was first analyzed by Sudan[6] and an extensive literature has evolved because of the relevance of this instability to both magnetic confinement fusion physics and astrophysics. An excellent review and guide to the literature has recently been presented by Cuperman.[7] We shall establish only a few, very basic, properties of the whistler here and refer the reader to the literature for details.

The whistler instability is a high frequency ($\omega_{ci} < \omega < \omega_{ce}$), short wavelength ($kc/\omega > 1$) mode. Ions participate only weakly in whistler physics and the assumption $m_e/m_i \to 0$ is usually invoked. Under these approximations the dispersion equation (5) is simplified to

$$\frac{K^2}{\beta_\parallel} + (1 - \eta) - \frac{1}{K}\left[1 + \eta(\Omega - 1)\right] Z\left(\frac{\Omega - 1}{K}\right) = 0 \quad , \qquad (6)$$

where $K = k\bar{v}_\parallel/\omega_c$, $\Omega = \omega/\omega_c$, $\eta = T_\perp/T_\parallel$, and $\beta_\parallel = 8\pi n T_\parallel/B^2$. In writing (6) we have also assumed, for purposes of illustration, only one population of electrons. In applications to EBT we will have to consider two populations with very different temperatures.

Under the approximations, $(\Omega - 1)/K \ll 1$ and $\Omega_I \ll \Omega_R$, we may readily solve (6) and obtain

$$\Omega_R = (\eta - 1)/\eta \qquad (7a)$$

$$\Omega_I = \frac{K}{2\sqrt{\pi}\beta_\parallel \eta}\left[(\eta - 1)\beta_\parallel - K^2\right] \quad . \qquad (7b)$$

Maximum growth in this weakly resonant regime occurs when $K = [(\eta - 1)\beta_\parallel/3]^{\frac{1}{2}}$ and is given by

$$\Omega_I^{MAX} = \frac{2}{3}\left(\frac{1}{3\pi}\right)^{\frac{1}{2}} \frac{(\eta - 1)^{2/3}}{\eta} \beta_{\parallel}^{\frac{1}{2}} \quad . \tag{8}$$

Note in particular that maximum growth scales with $\beta_{\parallel}^{\frac{1}{2}}$. The self-consistency of these solutions requires that the degree of anisotropy is small, $(\eta - 1)/\eta << 1$.

The resonant regime just considered is not the only possibility for instability: the whistler can also exist as a reactive instability. This is seen by making the opposite approximation, $(\Omega - 1)/K >> 1$. This occurs when the anisotropy is strong, $\eta >> 1$. If we formally introduce a small parameter, through the substitution $\tilde{\eta} \to \eta/\epsilon$, then (6) becomes a singular perturbation problem of the form

$$\tilde{\Omega}^3(2\beta_{\parallel}\epsilon + 2K^2\epsilon) + \tilde{\Omega}^2(2\beta_{\parallel}\epsilon) + \tilde{\Omega}(\beta_{\parallel}K^2\tilde{\eta}) + (\beta_{\parallel}K^2\epsilon) = 0 \quad , \tag{9}$$

where $\tilde{\Omega} = \Omega - 1$. The dominant self-consistent balance occurs between the first and third terms and we have

$$\Omega \approx 1 + \frac{i(\beta_{\parallel}\eta)^{\frac{1}{2}} K}{\sqrt{2}(\beta_{\parallel} + K^2)^{\frac{1}{2}}} \quad . \tag{10}$$

We again see $\Omega_I \sim \beta_{\parallel}^{\frac{1}{2}}$, even though the detailed physics is quite different in this reactive regime.

Except for indicating the scaling $\Omega_I \sim \beta_{\parallel}^{\frac{1}{2}}$, the formulae (8) and (10) are of limited utility. For general parameters, the whistler typically has maximum for $(\Omega - 1)/K \sim 1$, and neither the large or small argument expansions of $Z[(\Omega - 1)/K]$ are accurate. To illustrate the principle parametric dependencies of the whistler, we numerically solve the dispersion equation,

$$\frac{K^2\Delta}{\beta_{\parallel}} + \left\{(1 - \Delta)\left(\frac{\Omega}{\Omega - 1}\right)\right\}$$

$$+ \Delta \left\{(1 - \eta) - \frac{1}{K}\left[1 + \eta(\Omega - 1)\right] Z\left(\frac{\Omega - 1}{K}\right)\right\} \quad , \qquad (11)$$

where $\Delta = n_h/(n_c + n_h)$ is the relative fraction of hot, anisotropically distributed electrons. The dispersive properties are depicted in Figure 2 where the frequency (a) and growth rate (b) are shown as a function of wavenumber. Three values of anisotropy are illustrated for a completely hot ($\Delta = 1$) electron plasma with perpendicular pressure $\beta_{\perp} = \eta\beta_{\parallel} = 0.3$. It should be noted that the frequencies all lie in the range $\omega_{ci} < \omega < \omega_{ce}$, that a range of unstable wavenumbers exist for a given value of η, and that maximum growth in all three cases occurs for $|(\Omega - 1)/K| \sim 1$.

As mentioned previously, we saw an indication in formulae (8) and (10) that the whistler growth was proportional to the square root of the plasma pressure, as measured by β. This tendency is bourn out, in general, as shown in Figure 3. Here the growth rate, maximized with respect to k is log-log plotted as a function of $\beta_{\perp}$. The scaling $\gamma_{max} \sim \beta_{\perp}^{\frac{1}{2}}$ is clearly indicated unless the plasma pressure is quite low.

Another important parameter in determining whistler properties is the relative fraction of hot electrons. In Figure 4 we show the maximum growth rate as a function of $\Delta = n_h/(n_c + n_h)$. Here the plasma pressure is chosen to satisfy $\beta_{\perp} = 0.2$ and two values of anisotropy are illustrated. Note that the growth rate increases linearly with Δ for low concentrations of hot plasma but, for the lower anisotropy $\eta = 3$, the growth rate is maximized for a fraction of hot electrons of order 25 percent. This phenomenon is well known to the space physics community and it has been suggested[8] that increases in cold plasma density, and concomitant increases in whistler activity, could explain in the observed dumping (in early morning hours) of energetic electrons from the earth's outer radiation belt. In the context of EBT, we are presented with another instance where the relative fraction of hot to cold electrons may have an important consequence for plasma stability.

3. RELATIVISTIC EFFECTS ON THE WHISTLER INSTABILITY

As we discussed in the previous section, the whistler instability grows because of wave-particle resonances by which the waves access the free energy resident in the anisotropic electron distribution function. Quite often, such resonant instabilities can be accurately described by the "$i\pi$" or Plemelj approximation of the resonant integral. In the case of the whistler, this approximation is not quantitatively accurate for most parameters of physical interest. It is possible, however, to understand some qualitative properties of the whistler by examining certain features of the wave-particle resonance. We illustrate this in Figure 5, where we show the growth rate as a function of the cyclotron shifted phase velocity of the wave and draw a correspondence between growth and the relative position of the wave within the velocity distribution. We first note that the growth rate is small (exponentially) when the phase velocity falls outside the bulk of the distribution. Maximum growth obtains when $v_{ph}/\bar{v}_{\parallel} \sim -1$. For lower phase velocities, the sign of the energy exchange between waves and particles reverses and the whistler is actually cyclotron damped. It is on this last fact that the heuristic arguments for the relativistic stabilization of the whistler is based.

To generalize the expression (3) for ϵ_R to include relativistic effects, we must change to momentum coordinates and introduce the relativistically corrected electron mass. Explicitly, we have

$$\epsilon_R = 1 - 2\pi\omega_p^2 \int_0^\infty P_\perp \, dP_\perp \int_{-\infty}^{\infty} dP_\parallel \frac{\left[P_\perp^2 \frac{\partial f_o}{\partial P_\perp^2}(\Omega\bar{\gamma} - \tilde{K}P_\parallel) + \frac{\partial f_o}{\partial P_\parallel^2}(\tilde{K}P_\parallel) \right]}{[\tilde{K}P_\parallel - \Omega\bar{\gamma} + 1]} \quad , \quad (12)$$

where $\Omega = \omega/\omega_{co}$, $\tilde{K} = kc/\omega_{co}$, $P = p/m_o c$, $\omega_{co} = eB/m_o c$, and $\bar{\gamma} = [1 + P_\perp^2 + P_\parallel^2]^{\frac{1}{2}}$. Note in particular that the resonant denominator is complicated by the appearance of $\bar{\gamma}(P_\perp, P_\parallel)$. In the nonrelativistic limit, the

resonance occurs at $P_{\parallel}^{res} = (\Omega - 1)/K$. Relativistically, if $P_{\perp}^{2} << P_{\parallel}^{2} < 1$, it is shifted to the right

$$P_{\parallel}^{res} \cong \left(\frac{\Omega - 1}{K}\right)\left[1 + \frac{1}{2}\left(\frac{\Omega}{K}\right)\left(\frac{\Omega - 1}{K}\right)\right] \; ; \; P_{\perp}^{2} << P_{\parallel}^{2} \quad . \tag{13}$$

If $P_{\perp}^{2} >> P_{\parallel}^{2}$, we have an increasing distortion of the resonance

$$P_{\parallel}^{res} = \frac{\Omega[1 + P_{\perp}^{2}]^{\frac{1}{2}} - 1}{K} \quad ; \quad P_{\perp}^{2} >> P_{\parallel}^{2} \quad . \tag{14}$$

In general, we see in Figure 6 that the resonance is warped (perhaps a better term than broadened) to the right.

We have seen in Figure 5 that any displacement of the resonance to the right of the point corresponding to maximum growth implies that the resonance energy exchanged to the wave is lessened. In fact, if the displacement is sufficiently large, the sign of the energy exchange is actually reversed. For relativistic energies, we would, therefore, anticipate that the high energy particles (particularly those with $P_{\perp}^{2} >> P_{\parallel}^{2}$) would absorb energy from the whistler and, at some level of relativistic energy, would stabilize the mode. What really happens is more complicated.

The analysis of the relativistic dispersion equation is complicated by the fact the integrand of the resonant integral is not generally separable—the presence of $\overline{\gamma}(P_{\perp}, P_{\parallel})$ producing algebraic difficulties. Separation can be affected if the Plemelj approximation is made.[9] In this case, one of the integrals may be performed and the general solution takes the form of an infinite series of such integrals. This procedure is of limited utility, however, since we have seen in the nonrelativistic limit that the validity of the Plemelj approximation is quite limited when describing maximal growing modes. Our procedure, which we will detail in the Appendix, is to evaluate the double resonance integral in a straightforward, essentially brute force,

manner. In the numerical computations, we choose the equilibrium distribution function to be

$$f_0(P_\perp, P_\parallel) = \left[\frac{\eta^{\frac{1}{2}}}{4\pi\epsilon_\perp K_2(1/\epsilon_\perp)}\right] \exp\left\{-\frac{1}{\epsilon_\perp}\left[1 + P_\perp^{\,2} + \eta P_\parallel^{\,2}\right]^{\frac{1}{2}}\right\} , \qquad (15)$$

where $\epsilon_\perp = T_\perp/m_0c^2$ and K_2 is the second order Bessel function of imaginary argument. This distribution has two desirable features: it reduces to the usual biMaxwellian (4) if $\epsilon_\perp << 1$, and it spreads faster than a Gaussian at relativistic energies [$\sim \exp(-P)$].

The particular dispersion equation we solve is Eq. (11), but we replace the hot electron component (the term proportional to Δ) with expression (12) and use the distribution (15). We still typically invoke the approximation $kc/\omega >> 1$: tests indicate that its relaxation induces only small corrections, even at relativistic energies.

In Figure 7, we illustrate how the unstable spectrum of the whistler is modified as the energy of the hot electrons becomes relativistic. We also show corresponding changes in the structure of the resonance. We see that the maximum growth rate is reduced as the energy ($T_\perp/m_0c^2$) is increased. To isolate this effect, we hold $\beta_\perp$ constant as we increase $T_\perp$. The warping of the resonance is clear as the distribution becomes more relativistic and the reduction of growth rate is due to the resonant absorption of the high energy electrons. We also notice that maximum growth is being shifted to longer wavelengths and hence the resonance shifted to larger phase velocities. On first thought, we would expect this to also be a strongly stabilizing effect since the number of particles which can give energy to the waves is diminishing rapidly. However, the relativistic spreading of the distribution (compare contour lines between the $T_\perp/m_0c^2 = 0.01$ and $T_\perp/m_0c^2 = 0.2$ case) provides more particles at high $|P_\parallel|$ to drive the instability. For the distribution function (15), the stabilizing effect associated with the relativistic warping of the resonance can never

overcome the destabilizing effect associated with the relativistic spreading of the distribution and the whistler remains unstable at relativistic energies.

In Figure 8, we show how the maximum whistler growth rate changes at relativistic energies for different values of $\beta_\perp$ and one specific value, $T_\perp/T_\parallel = 3$. Alternatively, in Figure 9, we show the maximum growth for different $T_\perp/T_\parallel$ and the specific value, $\beta_\perp = 0.3$. In both cases, we see that there is a substantial reduction in whistler growth but complete stabilization does not occur.

In both Figures 8 and 9, all the electrons were taken to be hot. The important case from the standpoint of EBT is when only a small fraction of the electrons are hot. This is illustrated in Figure 10, where the maximum growth rate is traced to relativistic energies for different fractions of hot electrons. We see that the relativistic reduction of growth is much less pronounced when the relative fraction of hot electrons is small. Physically, this is because the location of the resonance is also being influenced by the cold electrons.

4. APPLICATION TO EBT

The theory which we have developed in the previous sections is highly idealized. In any real ECH heated plasma and in EBT in particular, there are numerous factors which could alter the results of such an idealized theory. For example, the field in EBT is neither uniform in direction or magnitude and the plasma itself is inhomogeneous, especially in the sense that the spatial extent of the hot electrons along the field is limited. In addition, the actual velocity distribution of the hot electrons in EBT is probably much more complicated than the simple model distributions chosen in this analysis. We should not be deterred by these complications, however, for the procedure here, as is always the case in the analysis of complex physical systems, is to start with a firm understanding of simple models and to systematically add additional effects.

In this spirit, we can immediately make one simple modification to this theory. The relativistic effects acted to reduce the growth rate of the whistler but not to suppress it completely. If the reduction of the growth rate is such that a growth time (γ^{-1}) is less than the bounce time of a thermal electron in the nonuniform axial field, then at the very least we would expect a substantial modification of the theoretical results. Simple intuition would lead us to believe that the bounce motion would be a stabilizing effect in the sense that it places limitations on the amount of time a hot electron can stay in resonance with the waves. Therefore, we might expect that a meaningful threshold for existence of the whistler would be that $\gamma^{-1} > \omega^{-1}_{\text{bounce}}$ It should be pointed out that whistler-like instabilities which depend on bounce resonances can exist,[10] but they require multiple resonances of passing particles from cell to cell.

Roughly approximating the bounce and cyclotron frequencies in EBT, we note that

$$\frac{f_{\text{bounce}}}{f_{\text{cyc}}} \simeq \frac{c/(2 \times 30 \text{ cm})}{1.9 \text{ GHz}} \simeq 0.03 \quad . \tag{16}$$

We shall be conservative and take as our criterion of marginal stability (or, at least, marginal "validity"), the requirement γ/ω_{ce} = 0.01 and show the parametric dependence of the curves described by

$$\frac{\gamma}{\omega_{ce}}(\eta, \beta, \Delta, \epsilon_\perp) = 0.01 \quad . \tag{17}$$

In Figure 11, we show variation of the curve defined by Eq. (17) as a function of pressure ($\beta_\perp$) and anisotropy (η) for different energies ($\epsilon_\perp = T_\perp/m_0c^2$). The plasma is taken to be completely hot. One interpretation of this graph is as follows. If a hot electron plasma in a mirror field has a pressure corresponding to $\beta_\perp = 0.2$ and an anisotropy of $\eta = 3$, then it would be whistler unstable if the temperature were so low that the plasma were nonrelativistic. On the other hand, if the plasma temperature was $T_\perp \sim 250$ keV ($\epsilon_\perp = T_\perp/m_0c^2 \sim 0.5$), then the relativistic effects would reduce to growth rate to less than one percent of the cyclotron frequency. At such a low rate of growth, the parallel bounce motion would probably suppress the mode.

From the standpoint of EBT, the electron plasma usually contains only a small fraction of hot electrons (10 to 20 percent). It is, therefore, interesting to consider the marginal stability curves as a function of the fraction of hot electrons. In Figure 12, we show the variation of the curve defined by Eq. (17) as a function of anisotrophy and fraction of hot electrons. The plasma pressure corresponds to $\beta_\perp = 0.4$. In this figure, we see that it is relatively easier to excite the whistler if the fraction of hot electrons is of order 10 to 20 percent. This is consistent with the variation of whistler growth with the fraction of hot electrons which we illustrated in Figure 4. Furthermore, the relativistic modification of the marginal stability curve is less pronounced if only a small fraction of electrons are hot. This could have been anticipated from Figure 10.

5. SUMMARY AND CONCLUSIONS

We have presented a systematic analysis of the linear stability properties of the whistler instability in a plasma environment typical of EBT. Our primary focus has been on understanding what the effect of relativistic hot electron energies would be. In brief, we have found a competition between two effects: the relativistic warping of the whistler resonance in the hot electrons--a stabilizing effect, and the relativistic spreading of the distribution function--a destabilizing effect. The net consequence of this competition of effects is a substantial reduction of the maximum growth rate of the whistler. However, the mode remains weakly unstable, even at high energies. We have also pointed out that there is a strong dependency of the whistler growth on the relative fractions of hot electrons. Unfortunately, the relative fraction of hot electrons in EBT plasmas (10 to 20 percent) is in a range where the whistler growth rate is enhanced.

We have argued that if the relativistic reduction of the growth rate is sufficient to bring the growth rate to a value on the order of the parallel bounce frequency of the hot electrons, then we would expect that bounce effects would stabilize the instability. In this sense we constructed marginal stability curves as a function of plasma pressure, $\beta_\perp$, anisotropy, $\eta = T_\perp/T_\parallel$, fraction of hot electrons, $\Delta = n_h/(n_c + n_h)$, and the extent to which the energy is relativistic, $\epsilon_\perp = T_\perp/mc^2$. Although the combination of relativistic effects and bounce effects tend to increase the volume of parameter space in which stable whistler operation could be expected, they were not generally sufficient to stabilize the mode in the parametric volume thought to be typical of EBT experiments. Thus, on the basis of this idealized theory, it is still possible for whistlers to be operative in EBT and to be potentially responsible for anomalous energy losses from the rings.

The results of this analysis may help in the explanation of some of the results of observations of whistler activity in the TPM mirror by Hosokawa and Ikegami.[2] In Figure 10 of Reference 2, it is

observed that the electrons scattered from the ring by whistler activity tend to be concentrated at lower energies. We pointed out in Figure 6 and the accompanying discussion that we would expect unstable whistler activity to be concentrated in the lower energy levels of the hot electron distribution function: higher energy exchanges of particles with waves tend to stabilize the whistler. This expected unevenness of whistler activity in velocity space is consistent with Hosokawa and Ikegami's observations.

In the past year there have been detailed studies of the scattering losses from hot electron rings in EBT.[1] Specifically, measurements of the Bremsstrahlung radiation produced when energetic electrons hit the cavity walls, are used to infer the nature of the scattering process in the rings. A simple, heuristic argument that the scattering is due to Coulomb scattering leads to a prediction for the scaling of the observed X-ray power,

$$P_{BREM} \sim n_r n_c T_r^{\frac{1}{2}} \quad , \tag{18}$$

and this scaling seems to be bourn out empirically. This agreement of experimental measurement and simple theory argues strongly that the scattering losses are indeed classical. However, we would like to emphasize here that the empirical scaling is not inconsistent with the possibility of anomalous scattering losses due to the whistler instability. The first point to make is that the temperature scaling of (18) has not been tested over a very extensive range of temperature: (a factor of 2 to 3) - the dominant empirical scaling is associated with the density variation. This is important because the temperature dependencies of loss processes associated with anomalous whistler and classical Coulomb scattering would be expected to be very different; the density dependencies of these processes would be similar.

If the whistler activity is small, we might expect the scattering rate to roughly scale as

$$\dot{N} \sim (n_r)\gamma^{whist} \quad . \tag{19}$$

Since we saw that the whistler growth rate scales as the relative fraction of hot electrons if that fraction is small (Figure 4), we would expect

$$P_{brem}^{whist} \sim \dot{N} \sim n_r \left(\frac{n_r}{n_c}\right) \quad . \tag{20}$$

It would be interesting to know if the observations of P_{brem} are sufficiently detailed to distinguish between the crude classical prediction (18) and the crude anomalous prediction (20). Our purpose here is not to argue that anomalous scattering associated with the whistler mode is the dominant scattering loss mechanism in the ring, but rather to argue that the observed empirical scaling of P_{brem} is not sufficient, by itself, to preclude anomalous scattering processes. Detailed analyses of ring energy balance, to be reported in this workshop,[11] find that a number of energy loss processes, including classical scattering losses, anomalous whistler losses, and energy losses due to the loss of adiabaticity are required to accurately model experimental results.

The sensitivity of whistler growth to the relative fraction of hot electrons suggests an experiment which might shed light on the nature of scattering losses from the EBT rings. From Hosokawa and Ikegami,[2] we know that whistler particle losses tend to occur in high frequency bursts. On the other hand, we would expect classical losses to be much more constant in time. In the current experiments in EBT in which microwave power is turned off to one of the mirror cells and the ring decay properties are studied, it would be interesting to see whether the time behavior of P_{brem} was relatively constant or showed a bursting character. In addition, the puffing of gas into the mirror cell as the ring was decaying would be expected to affect the relative fraction of hot electrons and hence might affect whistler activity in a way which could be observed in the time variation of P_{brem}.

REFERENCES

1. G. R. Haste, Bull. Am. Phys. Soc. 26, 979 (1981).
2. H. Ikegami and M. Hosokawa, Proceedings of the Workshop on EBT Ring Physics, 59, Oak Ridge (1979).
3. L. Hedrick, private communication.
4. J. Jacquinot and C. Lelour, Phys. Fluids 14, 2440 (1971).
5. F. V. Coroniti, Astrophysical Journal Supplement Series No. 244, 27, 261 (1974).
6. R. N. Sudan, Phys. Fluids 6, 57 (1963).
7. S. Cuperman, Reviews of Geophysics and Space Physics 19, 307 (1981).
8. N. M. Brice and C. Lucas, J. Geo. Res. 76, 900 (1971).
9. K. R. Chu and B. Hui, Naval Research Laboratory Memorandum Report 4634 (1981).
10. P. N. Guzdar and R. Marchand, University of Maryland Laboratory for Plasma and Fusion Energy Studies, Report 80-046.
11. S. Hamasaki, N. A. Krall, and J. L. Sperling, Proceedings of the 2nd EBT Ring Workshop, San Diego (1981) (Paper D.4).

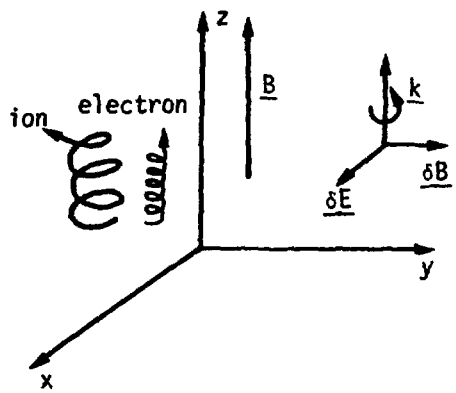

Figure 1. Geometry of the whistler.

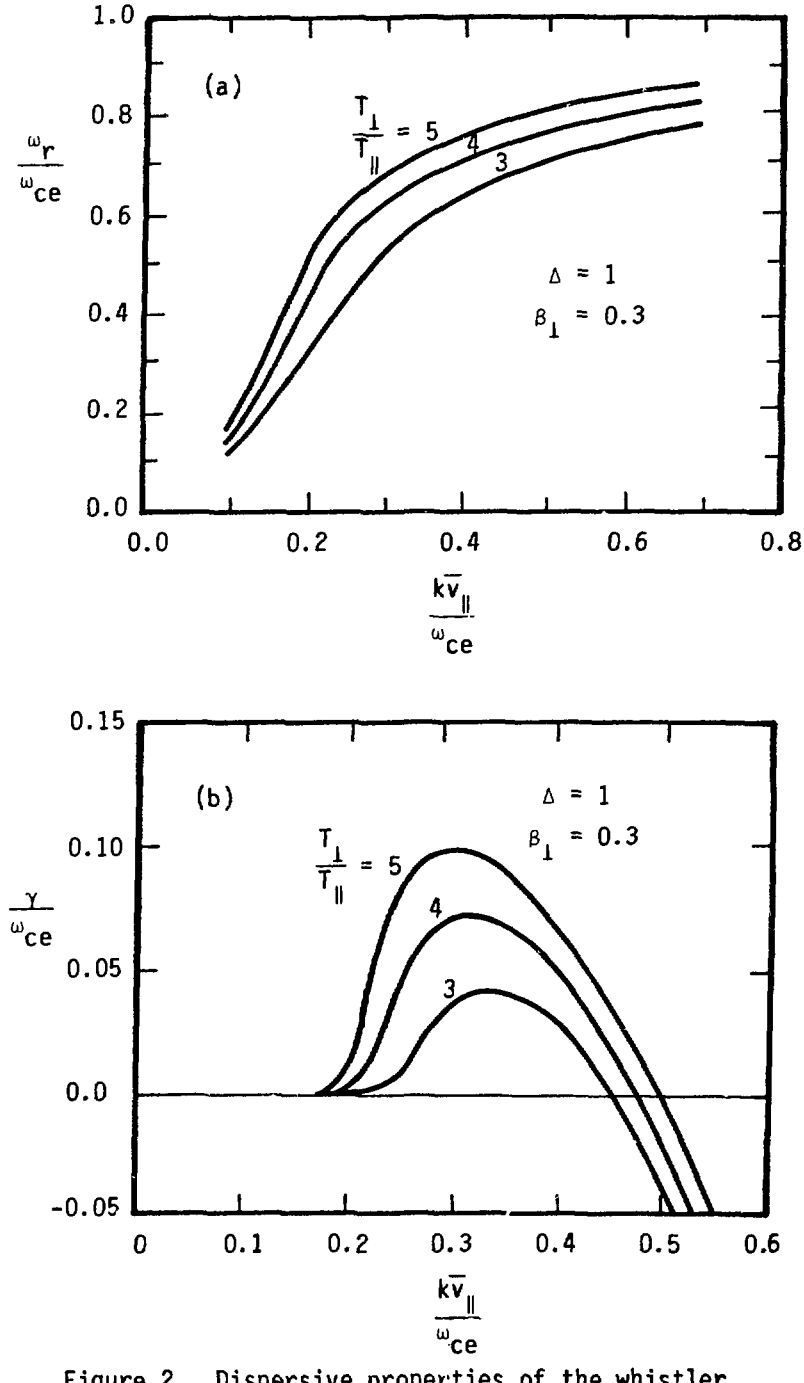

Figure 2. Dispersive properties of the whistler mode in a hot electron plasma.

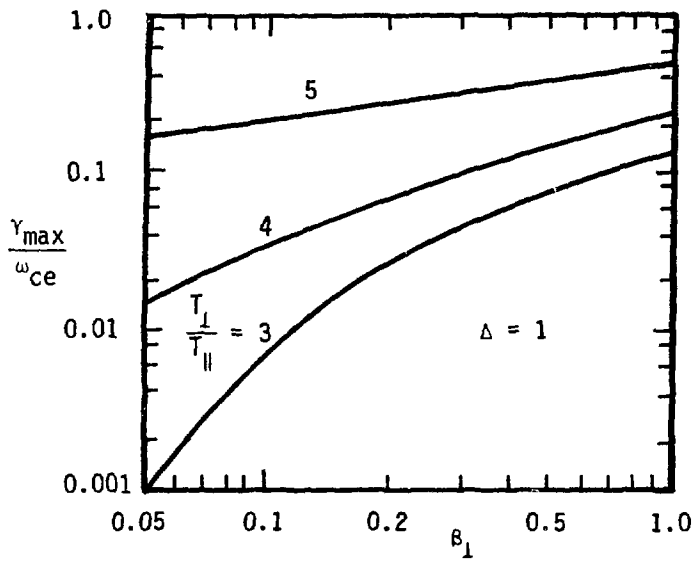

Figure 3. Dependence of whistler growth on plasma pressure.

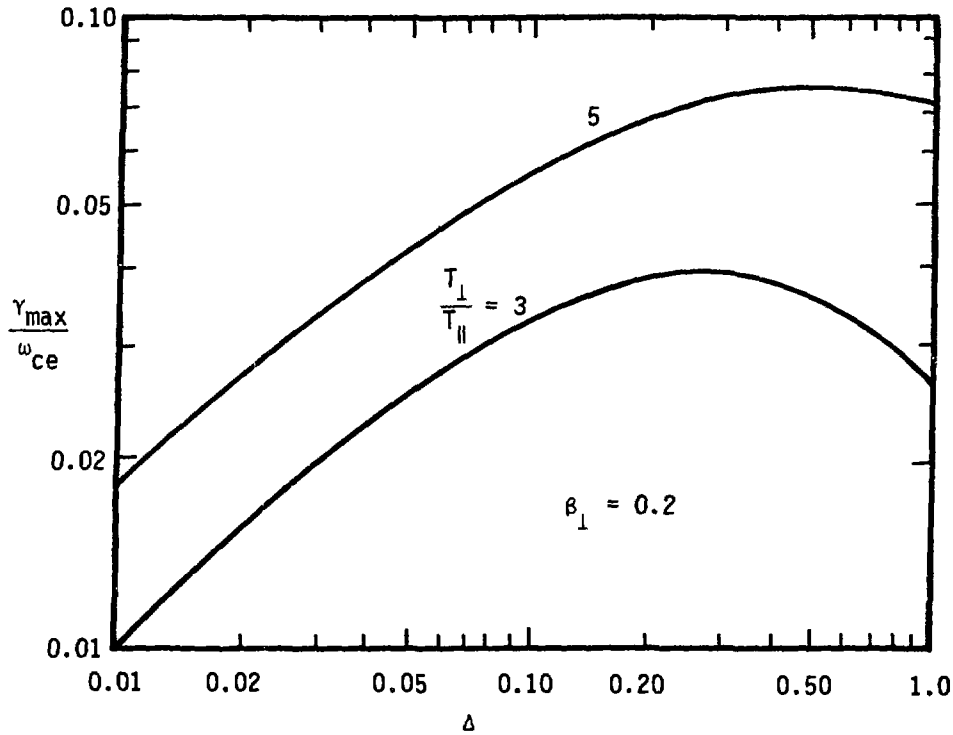

Figure 4. Dependence of whistler growth on the relative fraction of hot electrons.

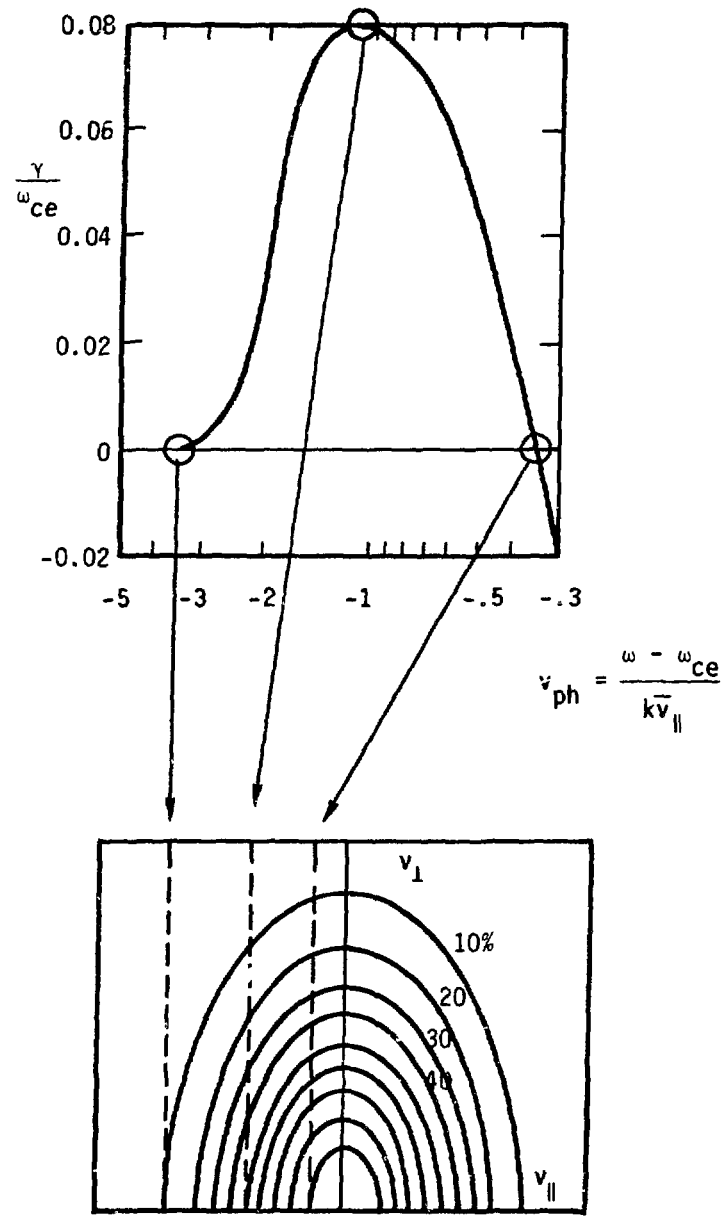

Figure 5. Resonant character of the whistler instability.

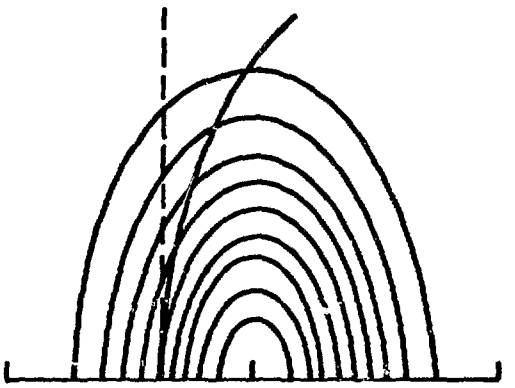

Figure 6. Relativistic warping of the whistler resonance.

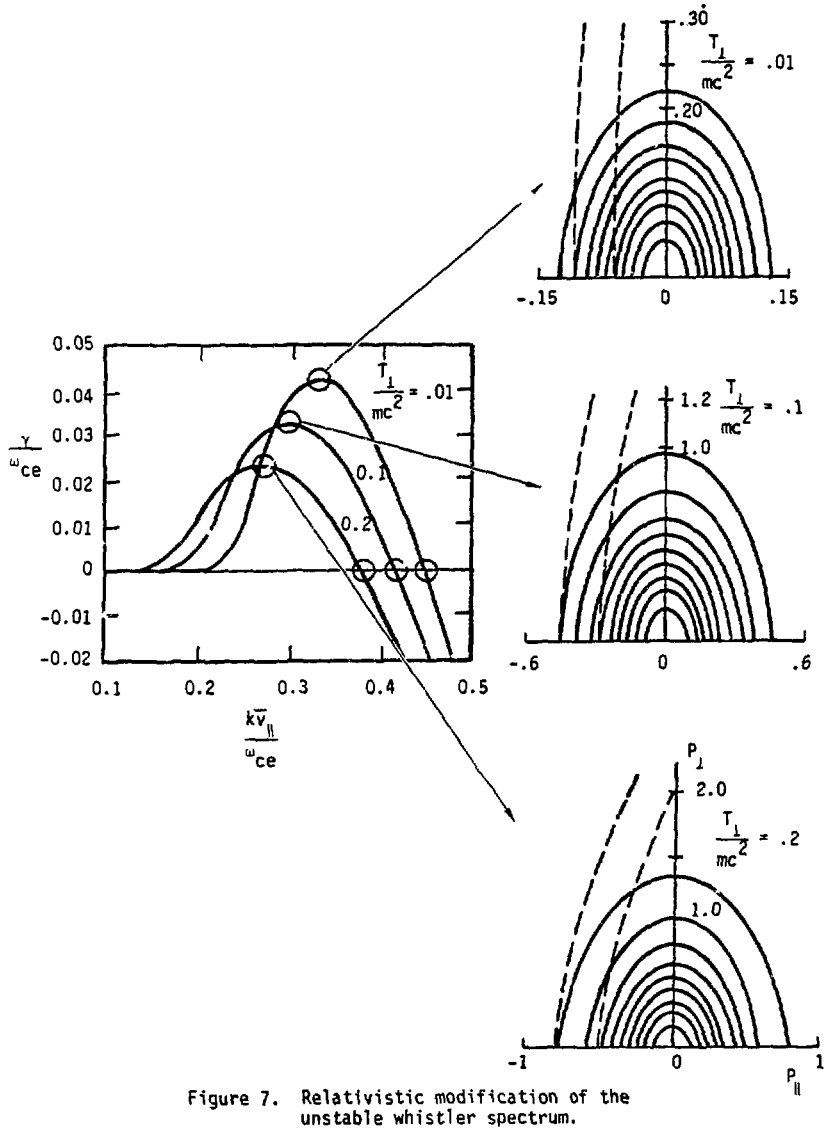

Figure 7. Relativistic modification of the unstable whistler spectrum.

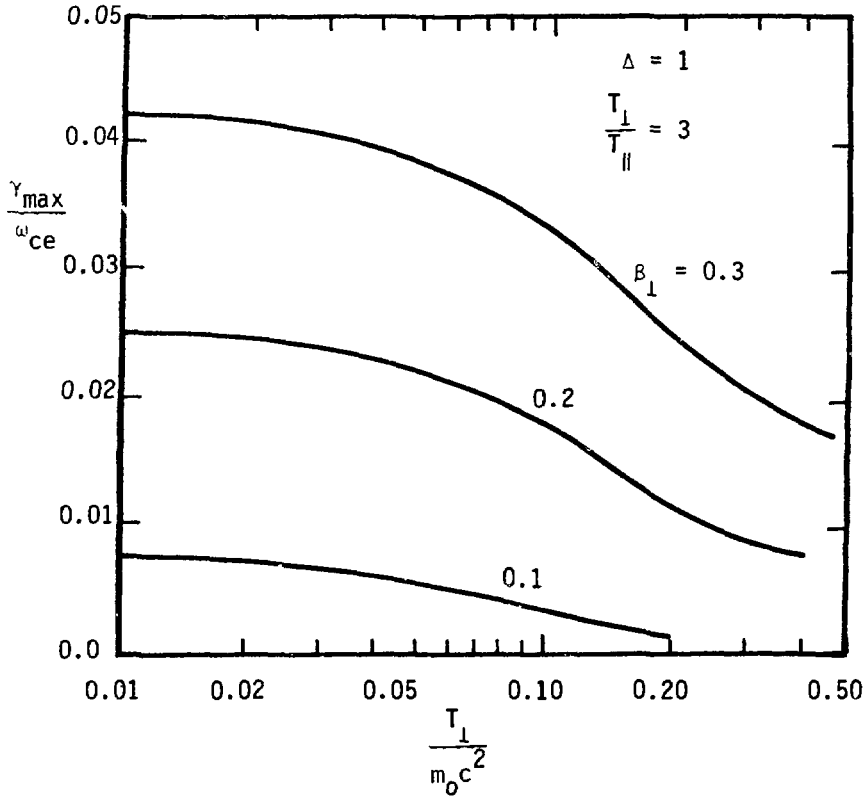

Figure 8. Maximum growth rate at relativistic energies for different plasma pressure.

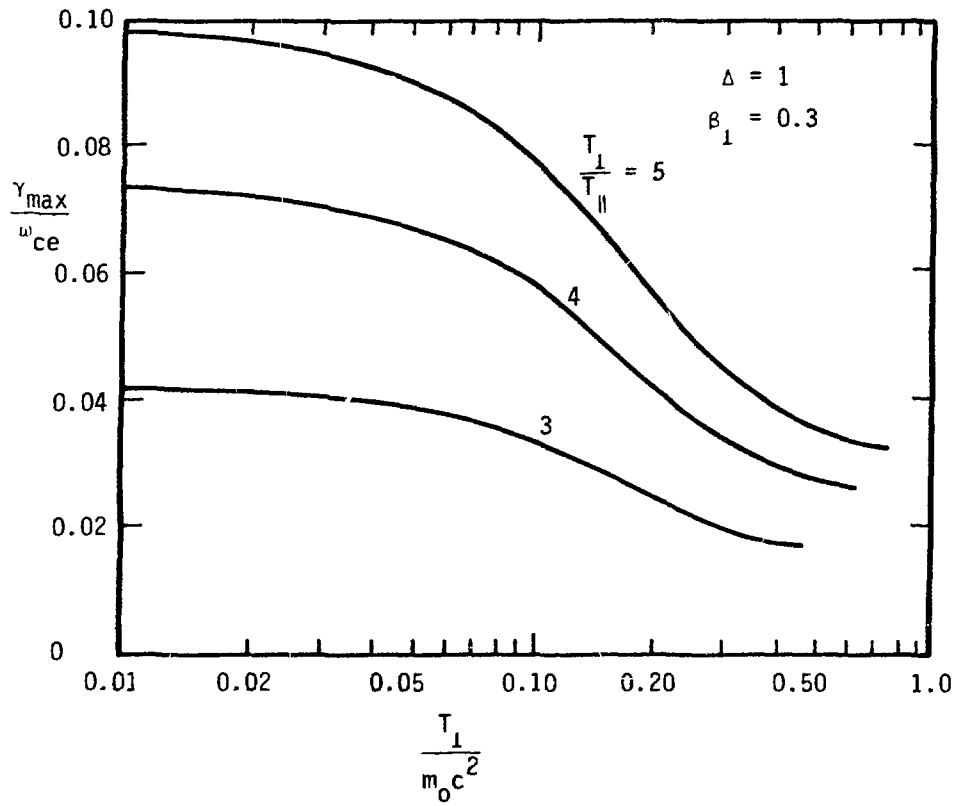

Figure 9. Maximum growth rate at relativistic energies for different anisotropies.

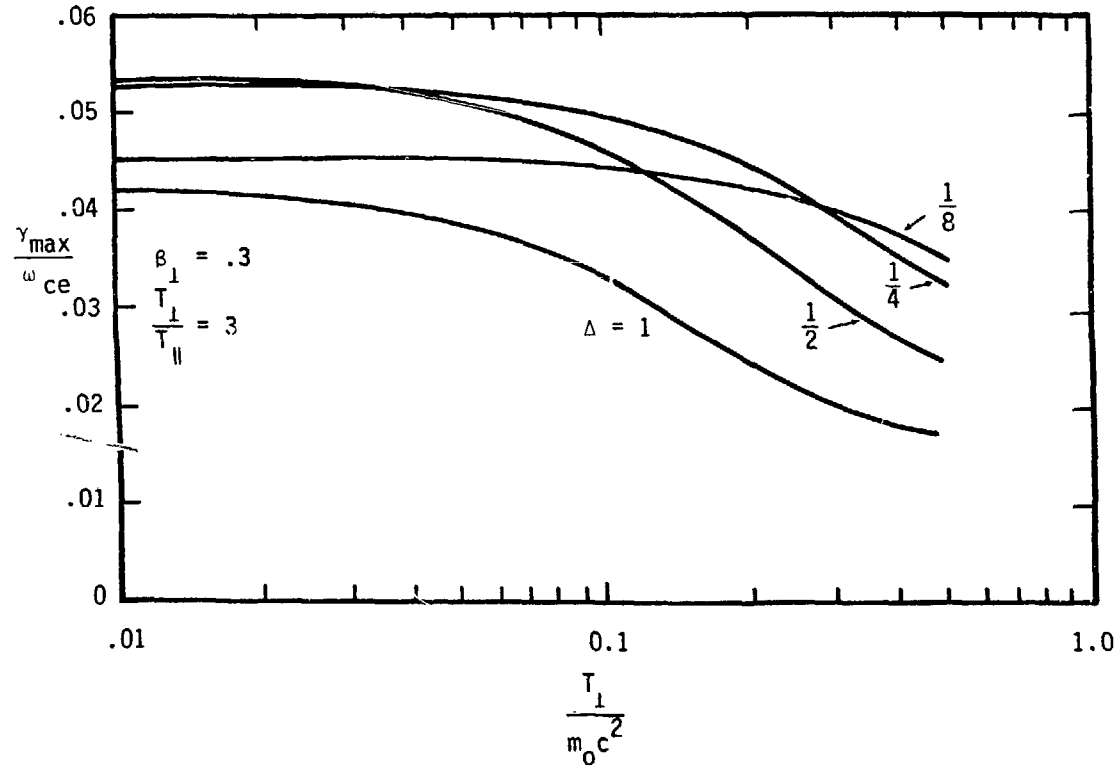

Figure 10. Maximum growth rate at relativistic energies for different fractions of hot electrons.

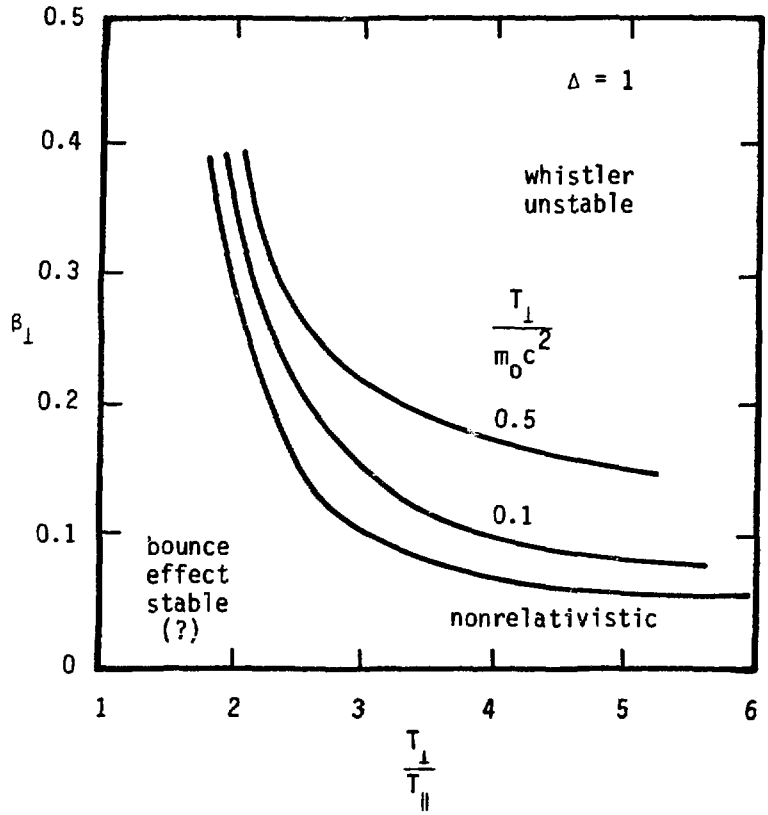

Figure 11. Marginal stability curves for the whistler in EBT as a function of pressure and anisotropy.

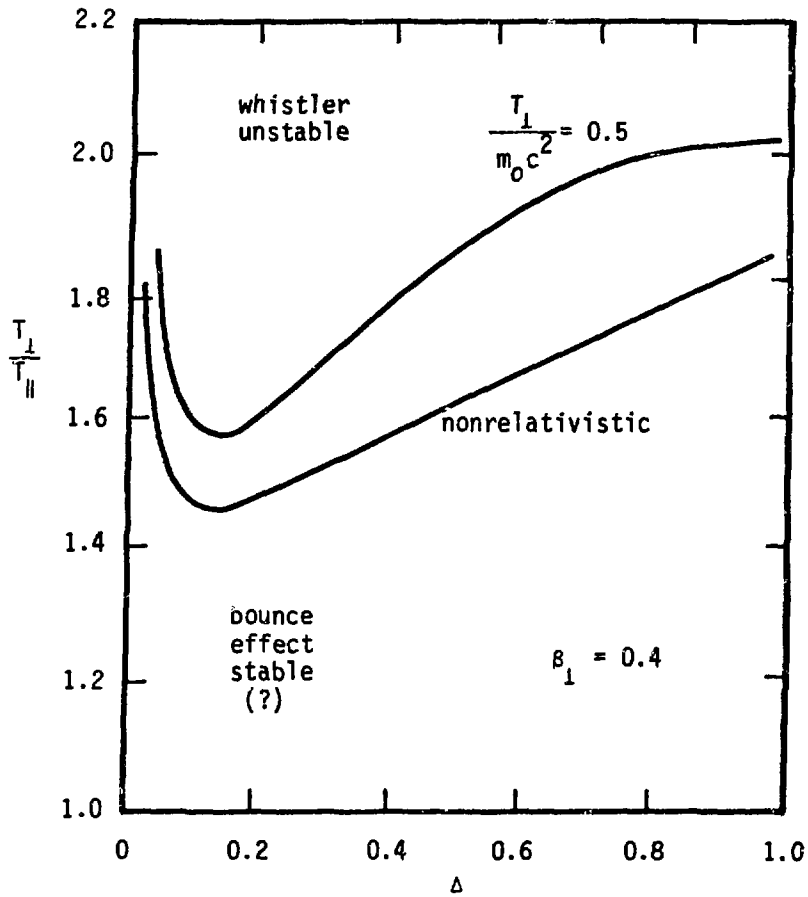

Figure 12. Marginal stability curves for the whistler in EBT as a function of anisotropy and fraction of hot electrons.

APPENDIX A. NUMERICAL EVALUATION OF THE RESONANT INTEGRAL

In calculating relativistic corrections to the whistler instability, we encountered a double resonant integral of the form

$$I = \int_0^\infty P_\perp dP_\perp \int_{-\infty}^\infty dP_\parallel \frac{P_\perp^2 \left[\frac{\partial f_o}{\partial P_\perp^2} (\Omega\bar{\gamma} - \tilde{K}P_\parallel) + \frac{\partial f_o}{\partial P_\parallel^2} (\tilde{K}P_\parallel) \right]}{[\tilde{K}P_\parallel - \Omega\bar{\gamma} + 1]} \quad , \tag{A.1}$$

where $\bar{\gamma} = [1 + P_\perp^2 + P_\parallel^2]^{\frac{1}{2}}$, $\tilde{K}$ is a real constant of order unity, and Ω is a complex constant of order unity. In general, the presence of $\bar{\gamma}$ makes the integrand nonseparable for physically reasonable distributions. If the Plemelj approximation is invoked, requiring

$$|\mathrm{Im}\Omega| << |\mathrm{Re}\Omega - 1| \quad , \tag{A.2}$$

then it is possible to affect a separation of variables and one of the integrals may be performed.[9] However, this approximation is not very accurate in the parameter regimes of interest in this paper.

Our procedure for evaluating this integral is straightforward and essentially utilizes brute force. We construct a grid in $P_\perp - P_\parallel$ space. The maximum grid point in $P_\perp$ is determined by the requirement

$$P_\perp^3 f_o(P_\perp, P_\parallel = 0) = \epsilon \quad , \tag{A.3}$$

and the minimum and maximum grid points in $P_\parallel$ are determined by the requirement

$$P_\parallel f_o(P_\perp = 0, P_\parallel) = \epsilon \quad , \tag{A.4}$$

where $\epsilon << 1$ is a specified parameter. The number of grid points in the $P_\perp$ and $P_\parallel$ and specified by the parameters $N_\perp$ and $N_\parallel$. In order to

avoid accuracy problems associated with the singular curve defined by the physical branch of

$$\tilde{K}P_{\parallel} - \Omega[1 + P_{\perp}^{2} + P_{\parallel}^{2}]^{\frac{1}{2}} + 1 = 0 \quad , \tag{A.5}$$

we deform the $P_{\parallel}$ contour of integration into the lower half-plane

$$(P_{\parallel},0) \rightarrow (\mathrm{Re}P_{\parallel}, -d) \quad . \tag{A.6}$$

In practice this is only required if $|\mathrm{Im}\Omega| \lesssim |\mathrm{Re}\Omega - 1|$. A Simpson's rule algorithm is then used to calculate the complex $P_{\parallel}$ integral for each value of $P_{\perp}$. These integrals are then summed over $P_{\perp}$, again using Simpson's rule. In terms of our numerical parameter, we then have

$$I(\epsilon, N_{\perp}, N_{\parallel}, d) \tag{A.7}$$

We may readily test the accuracy of this procedure at nonrelativistic energies in which case the integral can be evaluated in terms of the plasma dispersion function, Eq. (5). At relativistic energies, we rely on empirical tests of the sensitivity of $I(\epsilon, N_{\perp}, N_{\parallel}, d)$. In almost all calculations performed in this paper, the parameter values,

$$\begin{aligned} \epsilon &= .005 \\ N_{\perp} &= 41 \\ N_{\parallel} &= 21 \\ d &= 0.1 \end{aligned} \quad , \tag{A.8}$$

were found to be sufficient for our purposes. Other independent tests of accuracy would be desirable, but we have not undertaken them at this time.

HIGH-FREQUENCY MICROINSTABILITIES IN HOT-ELECTRON PLASMAS

Yu-Jiuan Chen, William M. Nevins, and Gary R. Smith
Lawrence Livermore National Laboratory, University of California
Livermore, California 94550

Instabilities with frequencies in the neighborhood of the electron cyclotron frequency are of interest in determining stable operating regimes of hot-electron plasmas in EBT devices and in tandem mirrors. Previous work used model distributions significantly different than those suggested by recent Fokker-Planck studies. We use much more realistic model distributions in a computer code that solves the full electromagnetic dispersion relation governing longitudinal and transverse waves in a uniform plasma. We allow for an arbitrary direction of wave propagation. Results for the whistler and upper-hybrid loss-cone instabilities are presented.

1. INTRODUCTION

The hot-electron plasmas in EBT devices and in tandem mirrors may be unstable at frequencies comparable to the electron cyclotron frequency Ω. By studying these instabilities we hope to prevent deleterious effects by learning how to operate experiments without strong instabilities.

An early review of microinstabilities of ECRH plasmas was provided by Guest and Sigmar.[1] The instabilities that led to the most stringent constraints on plasma parameters were the electromagnetic whistler instability and the electrostatic "upper-hybrid loss-cone" (UHLC) instability. Later work on the whistler instability has shown that relativistic effects are significantly stabilizing even for mean electron energies much less than the rest energy.[2-4] The UHLC instability was the subject of a detailed study for plasma parameters appropriate to the earth's magnetosphere.[5]

In this previous work[1-5] it is found that the wavelengths associated with these high-frequency electron modes are short in comparison to typical macroscopic scale lengths of the plasma. Hence, requiring stability to these modes tends to constrain the electron distribution function rather than the configuration of an experimental plasma.

In this paper we describe our present numerical study of instabilities of ECRH plasmas. Our work improves on earlier work by modeling more

accurately the electron distribution functions suggested by recent Fokker-Planck studies of electron-cyclotron-resonance heating in a magnetic-mirror field.[6,7]

2. MODELING OF THE ELECTRON DISTRIBUTION

Fokker-Planck studies[7] have found distributions like the one shown in Fig. 1. From the contour plot (Fig. 1a) we see, first, that the anisotropy (disparity between mean perpendicular and parallel energies) is moderate. Therefore, instabilities requiring extreme anisotropy are not expected; the whistler and UHLC instabilities may occur, however, in a plasma with such a distribution. Also, we notice that the distribution is not separable in $v_\perp$ and $v_\parallel$, i.e.,

$$f(\underline{v}) \neq f_\perp(v_\perp)\, f_\parallel(v_\parallel) \quad .$$

Separable distributions, like those used in Ref. 1, have constant-density contours in velocity space that are generally elliptical with the major and minor axes aligned with the $v_\perp$ and $v_\parallel$ axes. It is clear from Fig. 1a that the Fokker-Planck distribution is not separable. Separable distributions have been used in most previous studies; exceptions are the whistler-instability studies of Scharer[8] and Jacquinot and Leloup.[2]

Modeling our Fokker-Planck distribution by a separable distribution would lead to erroneous conclusions about microstability. This is apparent when we compare Figs. 1b and 1c with Fig. 1a. If $f_\perp(v_\perp)$ is chosen to approximate the distribution shown in Fig. 1b and $f_\parallel(v_\parallel)$ is chosen to model the distribution of Fig. 1c, then the separable model distribution, $\tilde{f}(\underline{v}) = f_\perp(v_\perp)\, f_\parallel(v_\parallel)$ would not have a loss cone. Hence, only anisotropy-driven modes, like the whistler, would appear with positive growth rates in our stability analysis. Clearly such a model would greatly overestimate the stability of the actual electron distribution to modes, like the UHLC mode, that are driven by the loss cone.

The Fokker-Planck distribution in Fig. 1a clearly has a loss cone. Since the average of $f(\underline{v})$ over parallel velocity is a monotonically decreasing function of perpendicular energy, $W_\perp$, this loss cone cannot drive modes with $k_\parallel = 0$. However, modes with finite $k_\parallel$ can be driven by this loss cone since

the resonant particles [i.e. those particles with $v_{\parallel} = (\omega - n\Omega)/k_{\parallel}$] can be localized at a parallel velocity where there is an inverted distribution in distribution in perpendicular velocity. Hence, we expect that distribution functions like the Fokker-Planck distribution shown in Fig. 1a can drive the UHLC mode.

We model Fokker-Planck distributions like that in Fig. 1 by superposing a number N of electron "species" with various parameters:

$$f(\underline{v}) = \sum_{s=1}^{N} f_s(\underline{v}) \quad . \tag{1}$$

Each species has a separable distribution

$$f_s(\underline{v}) = \frac{n_s}{\pi^{3/2}\ \alpha_{\perp,s}^2\ \ell_s!\ \alpha_{\parallel,s}} \left(\frac{v_\perp}{\alpha_{\perp,s}}\right)^{2\ell_s} \exp\left(-\frac{v_\perp^{\ 2}}{\alpha_{\perp,s}^{\ 2}} - \frac{v_\parallel^{\ 2}}{\alpha_{\parallel,s}^{\ 2}}\right) \quad . \tag{2}$$

By appropriate choices of the densities n_s, thermal speeds $\alpha_{\perp,s}$ and $\alpha_{\parallel,s}$, and indices ℓ_s, we achieve a good reproduction of Fig. 1, as shown in Fig. 2.

Superposing separable distributions to model a nonseparable distribution allows us to avoid numerical velocity-space integrations, a considerable computational advantage. Distribution (2) is precisely that used by Callen and Guest,[9] who provided all the formulae necessary for numerical calculation of the dielectric function $D(\omega,\underline{k}) = \det\,[\underset{\sim}{D}(\omega,\underline{k})]$, whose roots describe the small amplitude waves of a collisionless plasma in a uniform magnetic field, $\underline{B}_0$.

We have written a code which solves this dispersion relation numerically. We allow for an electron distribution function in the form of Eq. (1), i.e., an arbitrary superposition of separable distributions as given by Eq. (2). Currently the index ℓ is limited to the values 0 (a bi-Maxwellian) and 1 (a "loss-cone" distribution). We solve the full electromagnetic dispersion relation for waves that propagate in an arbitrary direction with respect to $\underline{B}_0$ in a uniform, non-relativistic plasma. Some results from this code are described in Sec. 3.

3. INSTABILITY GROWTH RATES

For the model distribution shown in Fig. 2 we have plotted contours in the $\underline{k}$ plane of the temporal growth rates, Im ω, of the whistler and UHLC instabilities. For the whistler (Fig. 3) the maximum growth rate occurs at $k_\perp = 0$ and $k_\parallel c/\Omega = 1.18$, where $\omega/\Omega = 0.57 + i\ 0.013$. Doubling the total electron density without changing the shape of the distribution (Fig. 2) shifts the maximum growth rate to $k_\parallel c/\Omega = 1.45$, where $\omega/\Omega = 0.55 + i\ 0.027$. This increase in $k_\parallel$ is not unexpected since, in the $T_\parallel = 0$ approximation, the whistler dispersion relation depends on $k_\parallel$ only through the combination $k_\parallel c/\omega_{pe}$.

The temporal growth rates of the UHLC mode are shown in Fig. 4. We find that the maximum growth rate occurs at $k_\perp c/\Omega = 9.2$ and $k_\parallel/k_\perp = 0.048$, where $\omega/\Omega = 1.09 + i\ 0.0046$. These values of $k_\parallel$ and $k_\perp$ for the most unstable mode are in line with estimates presented by Guest and Sigmar.[1] Note that the growth rate of the UHLC mode goes to zero as $k_\parallel$ goes to zero. This behavior follows from our discussion of the Fokker-Planck distribution in Sec. 2.

When we double the total electron density, we find that the wave vector that maximizes the growth rate shifts to $k_\perp c/\Omega = 10.04$ and $k_\parallel/k_\perp = 0.072$, where the frequency is given by $\omega/\Omega = 1.16 + i\ 0.0066$.

4. SUMMARY

We are currently studying high-frequency instabilities in hot-electron plasmas. We have chosen model electron distribution functions that are numerically efficient and resemble the electron distributions obtained from Fokker-Planck studies[6,7] of electron-cyclotron resonance heating. Both UHLC and whistler instabilities occur with low growth rates.

ACKNOWLEDGMENTS

This work was performed under the auspices of the U.S. Department of Energy under Contract No. W-7405-ENG-48.

REFERENCES

1. G. E. Guest and D. J. Sigmar, Nucl. Fusion 11, 151 (1971).
2. J. Jacquinot and C. Leloup, Phys. Fluids 14, 2440 (1971).
3. N. T. Gladd, et al., "Microstability of the EBT Boundary," Sec. IV, in Proc. Workshop on EBT Stability Theory, ed. N. A. Uckan, Oak Ridge, TN, May 1981.
4. N. T. Gladd, "The Whistler Instability at Relativistic Energies," in Proc. 2nd EBT Ring Physics Workshop, ed. N. A. Uckan, San Diego, CA, Dec. 1981.
5. M. Ashour-Abdalla and C. F. Kennel, J. Geophys. Res. 83, 1531 (1978).
6. Y. Matsuda, W. M. Nevins, and R. H. Cohen, "Electron-Cyclotron Resonant Heated Electron Distribution Functions," in Proc. Workshop on EBT Stability Theory, ed. N. A. Uckan, Oak Ridge, TN, May 1981.
7. B. W. Stallard, Y. Matsuda, and W. M. Nevins, "Fokker-Planck Calculations of Electron Cyclotron Resonant Heating (ECRH) in Mirror Geometry," in Proc. 2nd EBT Ring Physics Workshop, ed. N. A. Uckan, San Diego, CA, Dec. 1981.
8. J. E. Scharer, Phys. Fluids 10, 652 (1967).
9. J. D. Callen and G. E. Guest, Nucl. Fusion 13, 87 (1973).

FIGURE CAPTIONS

Fig. 1 Electron distribution found in Fokker-Planck studies of the ECRH plasma in the TMX-Upgrade Experiment. The total electron density is given by $\omega_p^2/\Omega^2 = 1.55$. (a) Contours of constant distribution function. Contours are logarithmically spaced with a factor of two separating adjacent contours. (b) and (c) Distributions integrated over parallel and perpendicular velocity, respectively. The vertical scale is logarithmic, covering five decades.

Fig. 2 Model electron distribution formed by superposing five separable distributions (2). The plasma frequencies ω_p, perpendicular temperatures $T_\perp \equiv \frac{1}{2} m\alpha_\perp^2 (\ell+1)$, parallel temperatures $T_\parallel \equiv \frac{1}{2} m\alpha_\parallel^2$, and indices ℓ are given by $\omega_p^2/\Omega^2 = 0.35$, 0.5, -0.02, 0.025, and -0.01, $T_\perp = 3$, 40, 12, 12, and 4 keV, $T_\parallel/T_\perp = 0.3$, 0.35, 4, 2, and 6, and $\ell = 0$, 1, 1, 1, and 1. Dotted contours give unphysical negative values of the distribution function. The spacing between adjacent contours is also a factor of 2, and the most negative value of the distribution function has magnitude < 1/2000 of the most positive value.

Fig. 3 Temporal growth rate of the whistler instability for the electron distribution shown in Fig. 2. The interval between adjacent contours is 0.00063 Ω.

Fig. 4 Temporal growth rate of the upper-hybrid loss-cone instability for the electron distribution shown in Fig. 2. Solid contours give $\mathrm{Im}\,\omega \geq 0$, dotted contours give $\mathrm{Im}\,\omega < 0$. The interval between adjacent contours is 0.00058 Ω.

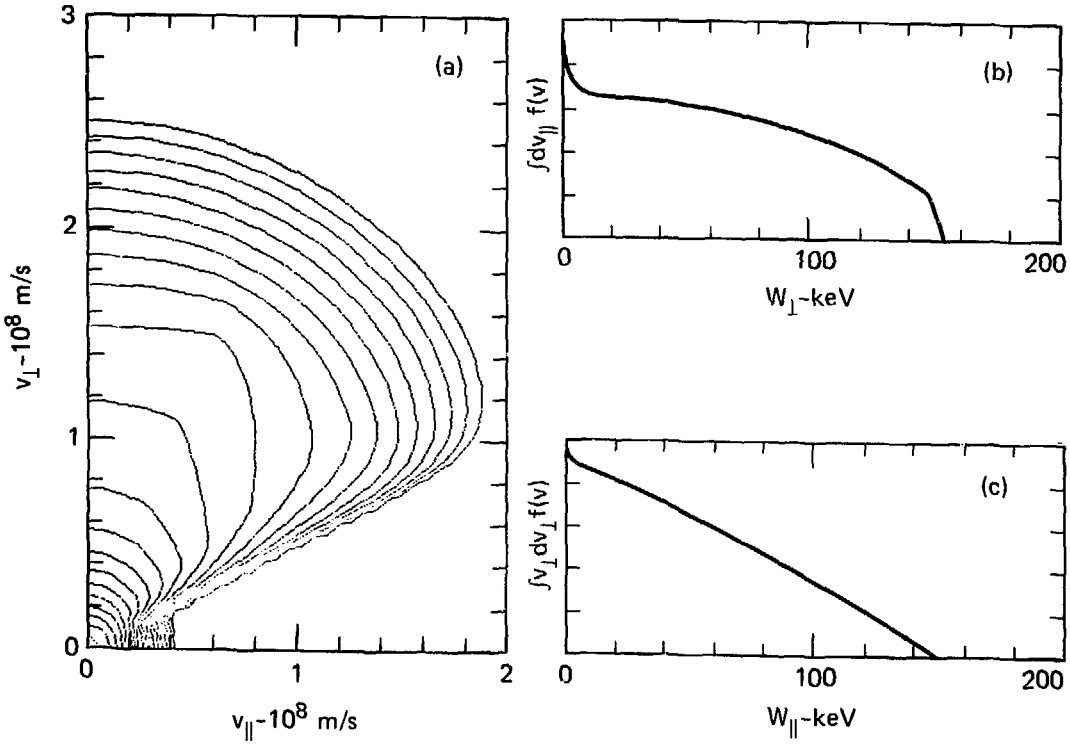
(a)
(b)
(c)
$v_\perp$-10^8 m/s
$v_\parallel$-10^8 m/s
$\int dv_\parallel f(v)$
$W_\perp$-keV
$\int v_\perp dv_\perp f(v)$
$W_\parallel$-keV
0
1
2
3
100
200

Fig. 1

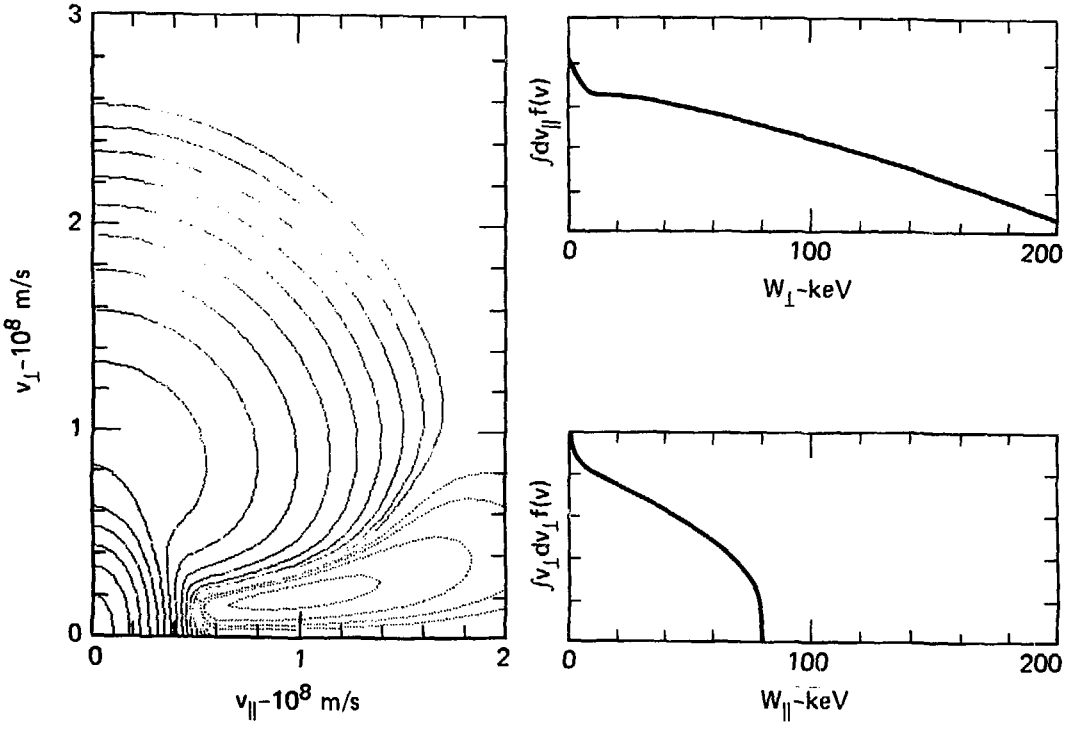
3
2
1
0
0
1
2
$v_\perp$-10^8 m/s
$v_\parallel$-10^8 m/s
$\int dv_\parallel f(v)$
0
100
200
$W_\perp$-keV
$\int v_\perp dv_\perp f(v)$
0
100
200
$W_\parallel$-keV

Fig. 2

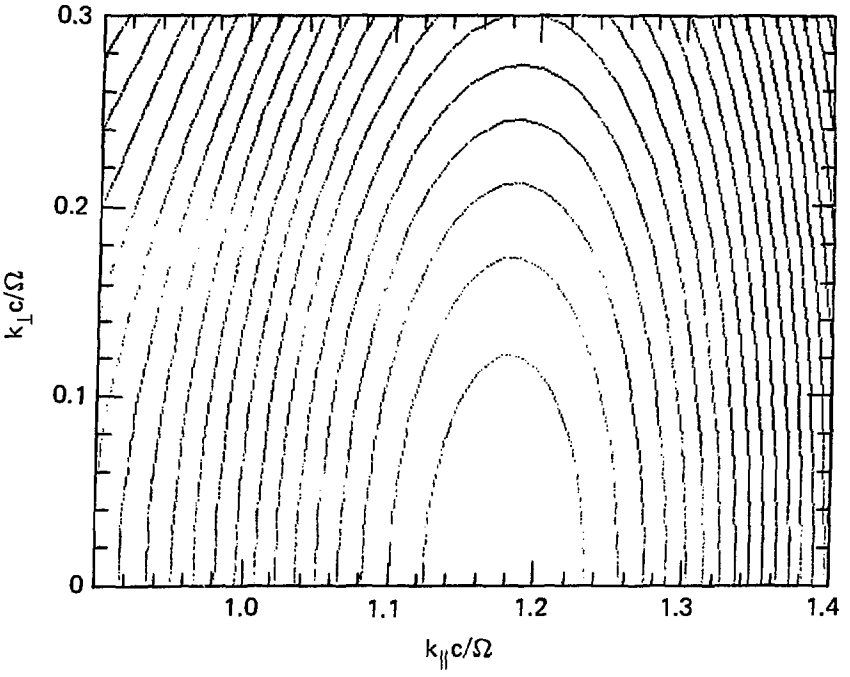

Fig. 3

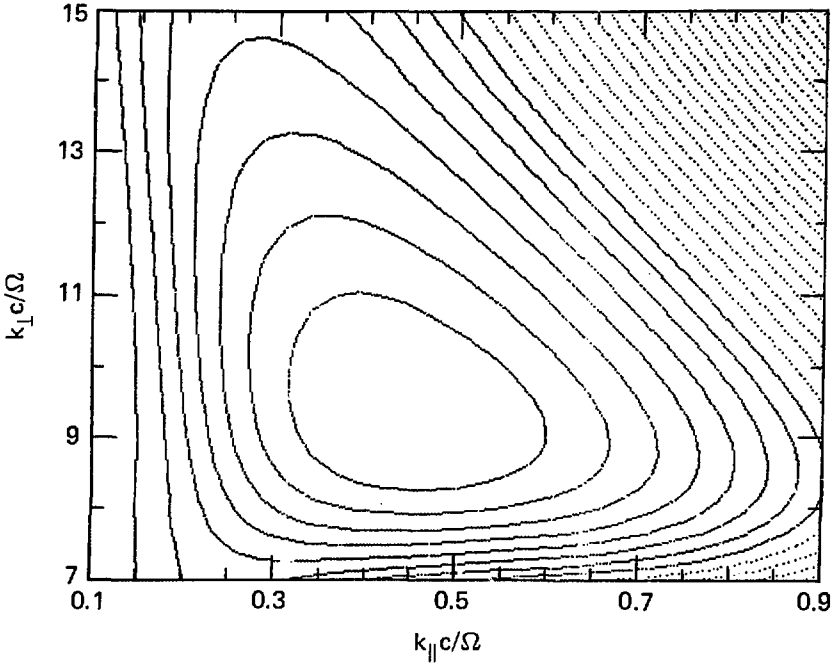

Fig. 4

Stability of Anisotropic Relativistic Hot Electron Plasma in The Elmo Bumpy Torus*

K. T. Nguyen and T. Kammash
University of Michigan, Ann Arbor, MI 48109

R. J. Kashuba
McDonnell Douglas Corp., St. Louis, MO 63116

Abstract

The stability of an EBT plasma with an anisotropic, relativistic hot electron component is examined using the kinetic approach in a slab geometry model. An anisotropic equilibrium distribution function is constructed for the hot electrons by assuming that $\langle p_z^2 \rangle \ll \langle p_\perp^2 \rangle, mc^2$ where p_z and $p_\perp$ are respectively the parallel and perpendicular momenta, and mc^2 is the rest mass energy. We find that a significant enhancement in the stability of the flute interchange mode occurs as a result of relativity. For typical EBT parameters the ion beta, β_i, increases by about 50% as a result of increasing the hot electron energy from about 5 keV to about 5 MeV. For energies beyond the rest mass energy the increase in β_i is not as dramatic. We also find that ρ_i / L_n where ρ_i is the ion gyroradius, and L_n is the density gradient scale length, is a critical parameter for instabilities arising from coupling between the interchange mode, the hot electron drift mode and the compressional Alfven mode. For these modes a window in the hot electron beta, β_h, defines a channel of stable region in

*Work supported by DOE

which more than one critical value of β_i exists. Finally, when the hot electrons are assumed to have a delta function in their perpendicular energy we find that the system is more (by a factor of about 2 in β_i) stable than the Maxwellian counterpart but that the coupled mode instability occurs at a higher β_h.

Introduction

The Elmo Bumpy Torus (EBT) device has been advanced as an alternative (to the mainline devices) concept due to several advantages that result from its unique combination of toroidal and open-ended magnetic configurations. As with all other approaches, its potential as a fusion reactor, however, depends critically on the beta value that can be achieved[1] since that represents the maximum power density attainable by the system. In EBT, this limitation is determined mainly by the stability of the hot electron component which is utilized to provide the gross stability of the system. A very promising value for the core plasma beta ($\sim$ 50%) was predicted by Nelson and Hedrick[2] in an early investigation in which a modified magnetohydrodynamic approach was used to examine the stability of a plasma equilibrium in which the hot electrons were treated as a current carrying, non-interacting rigid annulus. This optimistic value was significantly altered, however, when subsequent analyses by Nelson[3] and VanDam and Lee[4], using the kinetic approach, took into account the stability of the hot electron annulus itself. They showed that the stability

boundary in this case can be approximately characterized by $\beta_i \lesssim 4 \frac{L_n}{R_c} (1+\beta_h)^{-1}$ where β_i and β_h are the beta values for the core ions and hot electrons respectively, and L_n and R_c are the density gradient scale length and the radius of curvature of the magnetic field respectively. For typical EBT parameters the above stability condition predicts $\beta_i \sim 0.2$.

The results of these investigations were also limited because they were restricted to low (compared to the ion gyro) frequency flute interchange modes. It has been pointed out[5] that for typical EBT parameters the diamagnetic drift, and the magnetic gradient and curvature drifts of the hot electrons - which are the sources of free energy for these instabilities - have frequencies greater than or comparable to the ion cyclotron frequency.

Extending the above-mentioned analyses into the high frequency regime, Spong and El-Nadi[6] and Tsang and Cheng[7] showed that new instabilities arise as a result of coupling between the high frequency compressional Alfven wave ($\omega \sim \Omega_i$) and the flute interchange mode ($\omega < \Omega_i$) when the hot electron beta, β_h , becomes sufficiently large. In fact both of these studies reveal that the stability boundaries obtained earlier are greatly changed resulting in a substantially reduced core beta value in one case and an increase in the other.

All of the investigations described thus far have treated the hot electrons as non-relativistic species represented, in equilibrium, by the usual Maxwellian distribution. In this

paper we reexamine the same problem treating the hot electrons as a relativistic species. More explicitly, we study, in the slab model, the stability of an inhomogeneous EBT plasma with a relativistic component in a non-uniform magnetic field, and focus attention on drift modes with frequencies near the ion cyclotron frequency. Since most of the energy of the hot electrons is in a direction perpendicular to the magnetic field we construct an anisotropic relativistic equilibrium distribution function for these particles by assuming that $\langle p_z^2 \rangle \ll \langle p_\perp^2 \rangle , mc^2$ where p_z and $p_\perp$ are the momenta parallel and normal to the field respectively, and mc^2 is the electron rest mass energy. We derive a dispersion equation that reduces to that of Ref. 3 in the non-relativistic limit which we then numerically investigate for stability. We find that a significant enhancement in the stability of the interchange mode occurs when the hot electrons are made relativistic. We also observe a substantial improvement in the stability of the interchange mode when the temperature of the ions is increased relative to that of the cold electrons. This analysis further reveals that one of the most critical parameters affecting the stability of the system is ρ_i / L_n where ρ_i is the ion gyroradius and L_n is the density gradient scale length mentioned earlier. Below a critical value of this parameter, β_i achieves a maximum value at a certain value of β_h below and above which β_i decreases indicating an optimum value of β_h for the stabilization of the interchange mode. Above that critical value of ρ_i / L_n the stability boundary

is dictated by the coupling between the interchange and the compressional alfven modes and in this case β_i increases with β_h until a critical β_h (~ 0.35) is reached beyond which the stability boundary turns around forming a cusp. A second critical β_h (~ 0.2) is arrived at as one moves further along the stability boundary reflecting a region in which there are more than one critical value of β_i and a channel of stable region. When a delta function distribution is used we find that the maximum achievable β_i is almost twice that for a Maxwellian but the coupling between the modes occurs at a higher β_h value.

The Dispersion Equation

As pointed out earlier, we consider a three component inhomogeneous plasma situated in a non-uniform magnetic field. Using a slab geometry we take the variations in the density (∇n) and the magnetic field (∇B) to be along the X direction, while the magnetic field itself is assumed to be along the z - axis. The hot electron component of the plasma is taken to be relativistic for which we write the Hamiltonian:

$$H = (m^2c^4 + p^2c^2)^{1/2} + f_g x \tag{1}$$

where m is the rest mass of the electron, p is the momentum, c is the speed of light and f_g is the gravitational force associated with the magnetic curvature. Since, by virtue of their heating, these electrons are highly anisotropic with most of their energy perpendicular to the magnetic field, we simulate this effect in eq (1) by letting $\langle p_z^2 \rangle \ll \langle p_\perp^2 \rangle$, mc^2

where p_z and $p_\perp$ are respectively the momentum parallel and normal to the field, and mc^2 is the rest mass energy. With this modification, eq (1) becomes

$$H \simeq (m^2c^4 + p_\perp^2 c^2)^{1/2} + f_g x = \gamma m c^2 + f_g x \tag{2}$$

having let the relativistic parameter γ be given by

$$\gamma = \left(1 + \frac{p_\perp^2}{m^2c^2}\right)^{1/2} \tag{3}$$

For a magnetic field represented by $\vec{B} = B_0(1 + \epsilon x)\hat{z}$ the constants of motion are the above Hamiltonian and a canonical angular momentum which together allow us to write for the hot electron equilibrium distribution the expression

$$f_0(p_z, p_\perp^2, x_g) = N_0(1 + \epsilon' x_g)\, F(p_z)\, f_B(\gamma m c^2)\, e^{-\frac{f_g x}{T_\perp}} \tag{4}$$

where $x_g = \frac{c p_y}{e B_0} + x$ and

$$\int_{-\infty}^{+\infty} F(p_z)\, dp_z = 1 \quad ; \quad T_\perp = \frac{1}{2}\int_0^\infty \gamma m v_\perp^2 f_B\, p_\perp\, dp_\perp \tag{5}$$

If we now write

$$f_B(\gamma m c^2) = A\, e^{-\beta\gamma} \tag{6}$$

where A is a normalization factor and $\beta = mc^2/T_\perp$, then one can easily show that eq (6) can be put in the form

$$f_B(\gamma m c^2) = \left(\frac{\pi\beta}{2}\right)^{1/2} \frac{e^{-\beta\gamma}}{m^2c^2 K_{3/2}(\beta)} = A e^{-\beta\gamma} \tag{7}$$

where $K_{3/2}(\beta)$ is the modified Bessel function. Using the above expression, the gravitational force simply becomes

$$\begin{aligned} f_g &= \int_0^\infty \frac{\gamma m v_\perp^2}{R_c} f_B\, p_\perp\, dp_\perp \\ &= \frac{2mc^2}{R_c\beta} = \frac{2T_\perp}{R_c} \end{aligned} \tag{8}$$

With these results the equilibrium distribution function for the hot electrons can be written as

$$f_0(p_z, p_\perp^2, x_g) = N_0(1+\epsilon' x_g) F(p_z) \left(\frac{\pi\beta}{2}\right)^{1/2} \frac{e^{-(\beta\gamma + \frac{2x}{R_c})}}{m^2c^2 K_{3/2}(\beta)} \tag{9}$$

with R_c being the radius of curvature of the magnetic field. Following the standard procedure[5] it can be shown that

$$\begin{aligned} \epsilon' &= \frac{1}{L_n} + \frac{2}{R_c} \\ \epsilon &= -\frac{\beta_t}{2}\epsilon' = \frac{1}{B}\left(\frac{dB}{dx}\right) \end{aligned} \tag{10}$$

where $L_n = N\left(\frac{dN}{dx}\right)^{-1}$ is the density gradient scale length and β_t is the total ($\beta_e + \beta_i + \beta_h$) beta of the system.

We trun now to the solution of the linearized Vlasov equation for the relativistic species. The perturbed distribution function can be put in the form

$$f_1 = e \int_{-\infty}^{t} dt' \left[\vec{E} + \frac{\vec{v} \times \vec{B}}{c} \right] \cdot \frac{\partial f_0}{\partial \vec{p}'} \tag{11}$$

where the integral is over the unperturbed particle orbits. These orbits are directly obtained from the equation of motion, namely

$$\frac{d\vec{p}}{dt} = \frac{e}{c} \vec{v} \times \hat{z} B_0 (1 + \epsilon x) - f_g \hat{x} \tag{12}$$

where the gravitational force f_g is given by eq (8). The solutions can be readily obtained to yield in the slab model

$$\begin{aligned} v_x &= v_\perp \sin\left(\theta - \frac{\Omega}{\gamma} t\right) \\ v_y &= -v_\perp \cos\left(\theta - \frac{\Omega}{\gamma} t\right) + \frac{\epsilon v_\perp^2 \gamma}{2\Omega} + \frac{f_g}{m\Omega} \\ x &= \frac{\gamma v_\perp}{\Omega} \cos\left(\theta - \frac{\Omega}{\gamma} t\right) - \frac{\gamma v_\perp}{\Omega} \cos\theta \\ y &= -\frac{\gamma v_\perp}{\Omega} \sin\left(\theta - \frac{\Omega}{\gamma} t\right) + \frac{\epsilon v_\perp^2 \gamma t}{2\Omega} + \frac{f_g t}{m\Omega} + \frac{\gamma v_\perp}{\Omega} \sin\theta \end{aligned} \tag{13}$$

where the gyrofrequency $\Omega = \gamma B_0/mc$ is defined in terms of the rest mass. Noting that

$$\frac{\partial f_0}{\partial \vec{p}} = \frac{\partial f_0}{\partial(\gamma m c^2 + f_g x)} \vec{v}_\perp + \frac{\partial f_0}{\partial p_z} \hat{z} + \frac{c}{eB} \frac{\partial f_0}{\partial x_g} \hat{y} \tag{14}$$

and introducing the scalar and vector potentials φ , $\vec{A} = A_x \hat{x}$ (thereby ignoring shear waves) we can write

$$\vec{E} + \frac{\vec{v} \times \vec{B}}{c} = -i\vec{k}\varphi + \frac{i\omega\vec{A}}{c} + \frac{i\vec{k}(\vec{v}\cdot\vec{A})}{c} - \frac{i(\vec{k}\cdot\vec{v})}{c}\vec{A} \tag{15}$$

In obtaining the above result we have assumed that the perturbed fields vary as exp($\exp(i\vec{k}\cdot\vec{r} + i\omega t)$), and since we are interested in local ($k_x = 0$) flute - like ($k_z = 0$) modes we shall assume that $\vec{k} = k_y \hat{y}$ i.e., in the y-direction only. Substituting these results in eq (11) we obtain

$$f_1 = -e \frac{\partial f_0}{\partial(\gamma m c^2 + f_g x)} \varphi - ie\omega D \int_{-\infty}^{t} \left(\varphi - \frac{v_x A_x}{c}\right) dt' \tag{16}$$

where

$$D = \frac{\partial f_0}{\partial(\gamma m c^2 + f_g x)} - \frac{k_y c}{e B_0 \omega} \frac{\partial f_0}{\partial x_g} = -\frac{1}{T_\perp}\left(1 + \frac{k_y c T_\perp \epsilon'}{e B_0 \omega}\right) f_0 \tag{17}$$

$$= -\frac{1}{T_\perp}\left(1 - \frac{\omega_*}{\omega}\right) f_0$$

having introduced the diamagnetic drift frequency as $\omega_* = \epsilon' k_y T_\perp / m\Omega$. If we now insert (13) into (16), carry out the needed integrations and combine the result with (9) we find that the perturbed distribution function assumes the form

$$f_1 = \frac{+eN_0 F(p_z)}{T_\perp} f_B \left(1 - \frac{\epsilon' p_\perp \cos\theta}{m\Omega} + \epsilon' \frac{v_d}{\Omega}\right) \Bigg\{ \varphi$$
$$+ (\omega - \omega_*)\varphi \sum_\ell \sum_n \frac{J_\ell J_n e^{i(\ell - n)\theta}}{\omega_d - \omega - \ell\Omega/\gamma} \tag{18}$$
$$+ \frac{i}{c} v_\perp A_x (\omega - \omega_*) \sum_\ell \sum_n \frac{J_\ell' J_n e^{i(\ell - n)\theta}}{\omega_d - \omega - \ell\Omega/\gamma} \Bigg\}$$

In the above expression $J_\ell = J_\ell(k_y p_\perp / m\Omega)$ is the ordinary Bessel function and prime denotes differentiation with respect to the argument. In addition the drift frequency

$$\omega_d = k_y v_d = k_y \left(\frac{\epsilon p_\perp^2}{2m^2\gamma\Omega} + \frac{f_g}{m\Omega} \right) \tag{19}$$

contains the contributions from the field gradient as well as the field curvature. When the perturbed charge and current densities are computed by taking appropriate moments of the perturbed distrbution function, and the results are inserted in Maxwells equations the components of the dielectric tensor for the hot electrons can be obtained. Following the steps outlined in reference 3 the results may be expressed as

$$\epsilon_{11} = \frac{m\omega_p^2}{k^2 T_\perp} \int_0^\infty p_\perp \, dp_\perp \, f_B \left[1 + \frac{\omega - \omega_*}{\tilde{\omega}} \left(\frac{k^2 p_\perp^2}{2m^2\Omega^2} - 1 \right) \right] \tag{20}$$

$$\epsilon_{12} = \epsilon_{21} = \frac{m\omega_p^2}{2kcT_\perp} \int_0^\infty p_\perp \, dp_\perp \, f_B \frac{p_\perp^2}{m^2\gamma\Omega} \left(\frac{\omega - \omega_*}{\tilde{\omega}} \right) \tag{21}$$

$$\epsilon_{22} = -\frac{m\omega_p^2}{k^2c^2T_\perp}\int_0^\infty p_\perp\, dp_\perp\, f_B(\omega-\omega_*)\left[\frac{k^2p_\perp^4}{4m^4\Omega^2\gamma^2\tilde{\omega}}\right] \tag{22}$$

In the above expressions we have let

$$\tilde{\omega} = \omega - \omega_B\frac{p_\perp^2}{2m\gamma T_\perp} - \omega_g \tag{23}$$

where $\omega_B = \epsilon k T_\perp / m\Omega$ is the drift frquency associated with the magnetic field gradient, and $\omega_g = k f_g / m\Omega$ is the drift frequency associated with the magnetic field curvature. We now introduce the parameters

$$a = \frac{2(\omega-\omega_{gh})}{\beta\,\omega_{Bh}}\ ;\quad \alpha = \frac{a}{2} - \frac{1}{2}(a^2+4)^{1/2}$$

$$\Delta = \frac{a}{2} + \frac{1}{2}(a^2+4)^{1/2};\quad G = \beta(\alpha-1) \tag{24}$$

$$Q = \beta(\Delta-1)\ ;\quad \beta = \frac{mc^2}{T_{\perp h}}$$

and if we let $x = \gamma$, and $p_\perp^2 = m^2c^2(x^2-1)$ we find that the integrals in eqs (20-22) can be expressed in terms of the exponential integral given by

$$E_i(z) = \begin{cases} -\displaystyle\int_{-z}^{\infty}\frac{e^{-t}}{t}\,dt & z<0 \\ -P\displaystyle\int_{-z}^{\infty}\frac{e^{-t}}{t}\,dt & z>0 \end{cases} \tag{25}$$

where $\mathcal{P}$ denotes the principal value. In terms of this function the dielectric tensor components for the hot electrons become

$$\epsilon_{11}^{h} = (k\lambda_{Di})^{-2}\frac{\delta}{\tau_h}\left[1+\frac{2(\omega-\omega_{*h})}{\omega_{Bh}}\frac{\beta}{1+\beta}\left\{\frac{1}{\beta}+\frac{1}{\Delta-\alpha}\left(e^{-G}(a\alpha+1)E_i(G)-e^{-Q}(a\Delta+1)E_i(Q)\right)\right\}\right]+\frac{\delta}{\tau_h}(k\lambda_{Di})^{-2}\times FLR \tag{26}$$

where the finite Larmor redius term, FLR, is represented by

$$FLR = -\frac{(k\rho_{eh})^2}{2}\frac{(\omega-\omega_{*h})}{\omega_{Bh}}\frac{\beta^2}{1+\beta}\left\{\frac{1+a}{\beta}+\frac{1}{\beta^2}+\frac{1}{\Delta-\alpha}\left[e^{-G}(a^2\alpha+a)E_i(G)-e^{-Q}(a^2\Delta+a)E_i(Q)\right]\right\} \tag{27}$$

In addition we have

$$\epsilon_{22}^{h} = \frac{\beta_h}{4}\left(\frac{\omega-\omega_{*h}}{\omega_{Bh}}\right)\frac{\beta^3}{1+\beta}\left\{\frac{(1+a)a}{\beta}+\frac{2+a}{\beta^2}+\frac{2}{\beta^3}+\frac{1}{\Delta-\alpha}\left[e^{-G}(a^3\alpha+a^2)E_i(G)-e^{-Q}(a^3\Delta+a^2)E_i(Q)\right]\right\} \tag{28}$$

$$\epsilon_{12}^{h} = (k\lambda_{Di})^{-1}\left(\frac{\beta_i}{2}\right)^{1/2}\frac{\delta\beta^2}{(1+\beta)}\left\{\frac{1+a}{\beta}+\frac{1}{\beta^2}+\frac{1}{\Delta-\alpha}\left[e^{-G}(a^2\alpha+a)E_i(G)-e^{-Q}(a^2\Delta+a)E_i(Q)\right]\right\}\times\left(\frac{\omega-\omega_{*h}}{\omega_{Bh}}\right) \tag{29}$$

In the above relations we have used

$$\tau_h = \frac{T_{\perp h}}{T_{ci}} \quad ; \quad \delta = \frac{N_h}{N_i} = \frac{\beta_h}{\tau_h \beta_i}$$

$$\lambda_{Di}^2 = \frac{T_{ci}}{4\pi N_i e^2} \tag{30}$$

The corresponding terms for the background electrons and ions are obtained in the manner described in references 3 and 5. That includes the assumption that the frequency of oscillation is larger than the drift frequencies of both species, namely $\omega > \omega_{*i,e}$, $\omega_{di,e}$ and that both components have Maxwellian distrubutions. In addition we have incorporated ion cyclotron harmonics terms in order to examine the high reequency modes alluded to earlier. The results can then be written as

$$\epsilon_{11}^i + \epsilon_{11}^e = (k\lambda_{Di})^{-2}\left[\frac{\omega_{di}(\omega_{*i}-\omega_{di})(1+\tau_e)}{\tilde{\omega}_i\,\tilde{\omega}_e} - \frac{\delta}{\tau_e}\left(\frac{\omega_{*e}-\omega_{de}}{\tilde{\omega}_e}\right)\right.$$

$$\left. -\frac{1}{2}(k\rho_i)^2 \frac{\Omega_i^2}{(\tilde{\omega}_i-\omega_{Bi})^2-\Omega_i^2}\left(\frac{\omega-\omega_{*i}}{\tilde{\omega}_i-\omega_{Bi}}\right)\right] \tag{31}$$

$$\epsilon_{22}^i + \epsilon_{22}^e = -\beta_i(\omega-\omega_{*i})\left[\frac{1}{\tilde{\omega}_i-2\omega_{Bi}} + \frac{1}{(k\rho_i)^2}\left\{\frac{\tilde{\omega}_i-\omega_{Bi}}{(\tilde{\omega}_i-\omega_{Bi})^2-\Omega_i^2}\right\}\right] - \beta_i\tau_e(1-\delta)\left(\frac{\omega-\omega_{*e}}{\tilde{\omega}_e-2\omega_{Be}}\right) \tag{32}$$

$$\epsilon_{12}^{i} + \epsilon_{12}^{e} = -(k\lambda_{Di})^{-1}\left(\frac{\beta_i}{2}\right)^{1/2}\left[\frac{\Omega_i^2}{(\tilde{\omega}_i - \omega_{Bi})^2 - \Omega_i^2}\left\{\frac{\omega - \omega_{*i}}{\tilde{\omega}_i - \omega_{Bi}}\right\} + (1-\delta)\left(\frac{\omega - \omega_{*e}}{\tilde{\omega}_e - \omega_{Be}}\right)\right] \tag{33}$$

where we have let $\tau_e = T_{ee} / T_{ei}$. Upon combining these results with those for the hot electrons we obtain the dispersion equation which we can write in a condensed form as[15]

$$D_{es} D_{em} + (CT)^2 = 0 \tag{34}$$

where

$$D_{es} = 1 + \epsilon_{\parallel}^{i} + \epsilon_{\parallel}^{e} + \epsilon_{\parallel}^{h} \simeq \epsilon_{\parallel}^{i} + \epsilon_{\parallel}^{e} + \epsilon_{\parallel}^{h}$$

$$D_{em} = 1 - \left(\epsilon_{22}^{i} + \epsilon_{22}^{e} + \epsilon_{22}^{h}\right) \tag{35}$$

$$CT = \epsilon_{12}^{i} + \epsilon_{12}^{e} + \epsilon_{12}^{h}$$

In writing the electromagnetic portion of the dispersing eq, i.e. Dem, we have ignored w/ck on the premise that the phase velocity of the waves under consideration is much smaller than the speed of light. Although algebraic, equation (34) is investigated numerically for its roots due to the multiplicity of the free parameters that characterize the system. They are β, β_h, β_i, ρ_i/L_n, $k\rho_i$, $\frac{L_n}{R_c}$, τ_h, and τ_e .

Results

The use of relativistic hot electrons seems to enhance the stability of the system considerably. As shown in figs. 1 and 2 the value of the ion beta (β_i) increases by about 50% as the energy of the hot electrons is increased from about 7 kev to about 5 Mev. These figures also show that, although tangible, the improvement in the value of β_i is not as dramatic when the hot electron energy goes past the rest mass energy. Moreover these results indicate that stabilization due to relativistic effects is primarily associated with the interchange mode and the coupled mode since the pure compressional Alfven mode (seen at the lower right corner of these plots) appears to be unaffected. Another result that emerges from a comparison of figs. 1 and 2 is the appreciable stabilizing effect of increasing the ion temperature relative to that of the background electrons as manifested in the ratio (T_{ce} / T_{ci}). The resulting increase in the value of β_i is quite dramatic even though this represented practically no change in the value of the core beta, $\beta_c \left(= \beta_e + \beta_i\right)$. Furthermore, figs. 1 and 2 reveal that a critical parameter for coupling between the interchange and Alfven modes is the ratio of the ion gyroradius to the density gradient scale length i.e. (ρ_i / L_n). For the parameters shown in fig. 2 it is seen that the two modes do not couple for $\left| \rho_i / L_n \right| \lesssim 0.045$. This is further illustrated in fig. 3 where we note the stabilizing effect of β_h on the interchange mode up to $\beta_h \simeq 0.3$ beyond which the effect is seen to be a destabilizing one.

The same behavior also persists in the case of the coupled interchange and Alfven modes as illustrated in fig. 4. We observe in this case that the outer boundary represents the interchange mode while the inner one represents the Alfven wave. Once again we see the stabilizing effect of β_h up to about $\beta_h \simeq 0.3$, a destabilizing effect between 0.3 and $\sim$ 0.6 where coupling between the modes takes place, and a further decline in the stability when β_h exceeds 0.6 at which point decoupling between the modes reoccurs. This is vividly demonstrated in fig. 5 where β_i is plotted against ω/Ω_i.

Figures 6 and 7 further demonstrate the sensitivity of the stability boundary to the parameter (ρ_i/L_n). When compared with fig. 6, fig. 7 reveals the shrinking of the stable region with increasing values of (ρ_i/L_n). Moreover, both figures show that for the coupled modes there exists a window in the hot electron beta (β_h) which defines a channel of stable region in which more than one critical β_i value may exist. Such a window becomes narrower as (ρ_i/L_n) becomes larger.

In the non-relativistic limit (see fig. 1) the maximum attainable β_i ($\sim$ 3.5%) agrees with those of references 3 and 5. In an attempt to assess the dependence of the results on the hot electron model we have repeated the analysis using a delta function distribution for this component. The results are illustrated in fig. 8 for the interchange mode. We note readily that the maximum β_i for the delta function is about twice that for the Maxwellian in disagreement with the results of ref. 7 where the opposite is true. These results are however, in

agreement with those of Nelson[3] who gives as the upper limit for the core beta, β_c , the expressions:

I) Delta function

$$\beta_c \leq \frac{4\, L_n / R_c}{1 + \beta_h}$$

II) Maxwellian

$$\beta_c \leq \frac{2\, L_n / R_c}{1 + 6\, L_n / R_c}$$

For $\frac{L_n}{R_c}$ = 0.05 which characterizes the results in fig. 8 the above expressions yield $\beta_c \leq 0.2$ and $\beta_c \leq 0.076$ for the delta function and Maxwellian respectively. We see from fig. 8 that the present analysis yields $\beta_c \leq$ 0.165 and $\beta_c \leq$ 0.065 respectively which agree quite well with the above results. Finally, we observe from the same figure that the coupling to the Alfven wave occurs at a higher β_h value for the delta function than it does for the Maxwellian distribution.

Acknowledgement

We are grateful to D. A. Spong for many useful discussions.

References

1. N. A. Uckan, D. A. Spong, and D. B. Nelson, Oak Ridge National Laboratory Report, ORNL/TM - 7857 (1981)

2. D. B. Nelson and C. L. Hedrick, Nuclear Fusion, 19, 283 (1979)

3. D. B. Nelson, phys. fluids 23, 1850 (1980)

4. J. W. VanDam, and Y. C. Lee, Proc. Workshop on EBT Ring Physics, Oak Ridge, CONF - 791228, Dec. 1979, p. 471.

5. D. A. Spong, Oak Ridge Report ORNL/TM - 8021, October 1981.

6. D. A. Spong and A. El-Nadi, Bull. Am. Phys. Soc. 25, 964 (1980)

7. K. T. Tsang, and C Z. Cheng, proc Workshop on EBT Stability Theory, Oak Ridge, CONF- 81052, May 1981, p. 141.

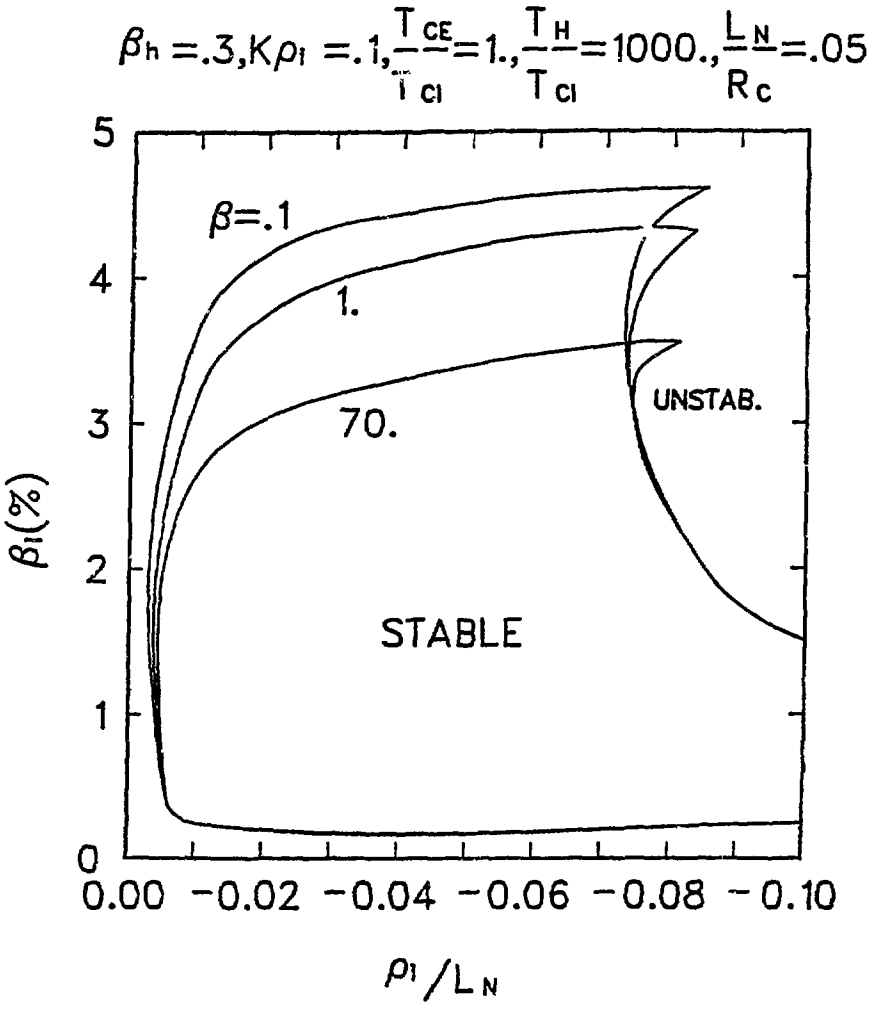

Fig. 1 Effects of Relativity on β_i for $\beta = \frac{mc^2}{T_{\perp h}} = 70$, 1, and 0.1

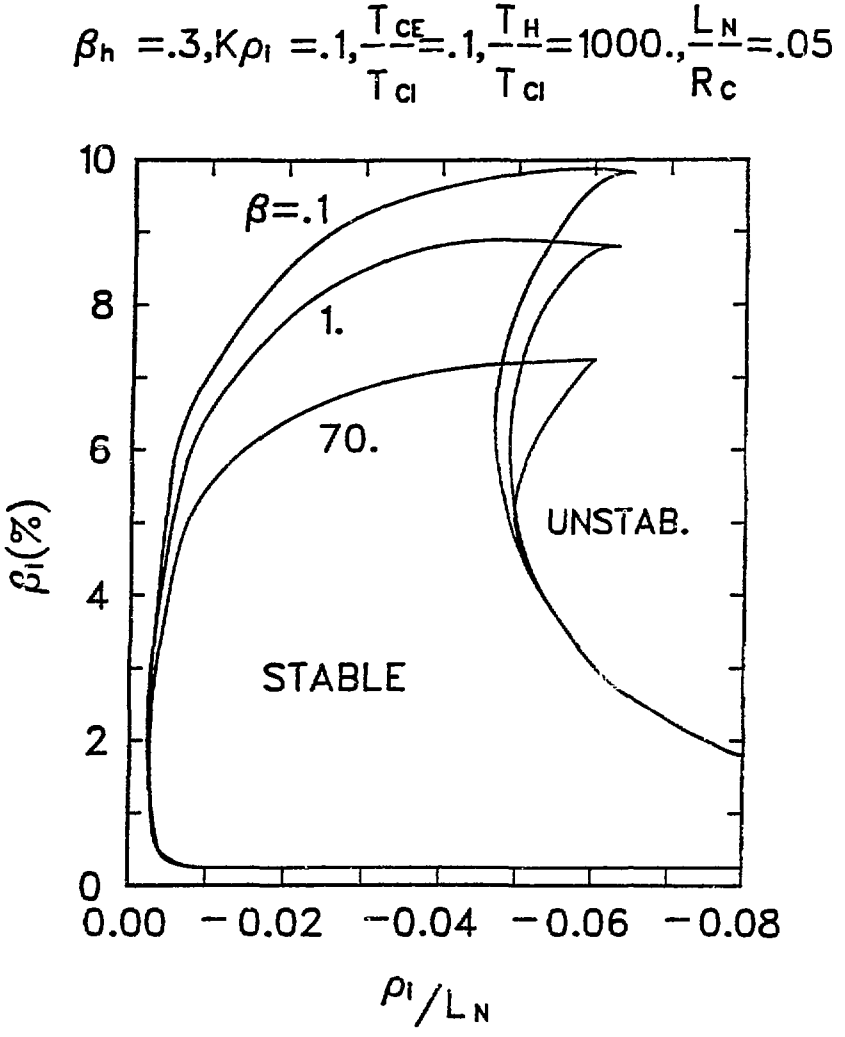

Fig. 2 Enhancement in β_i due to relativistic effects and $T_{ce}/T_{ci} < 1$

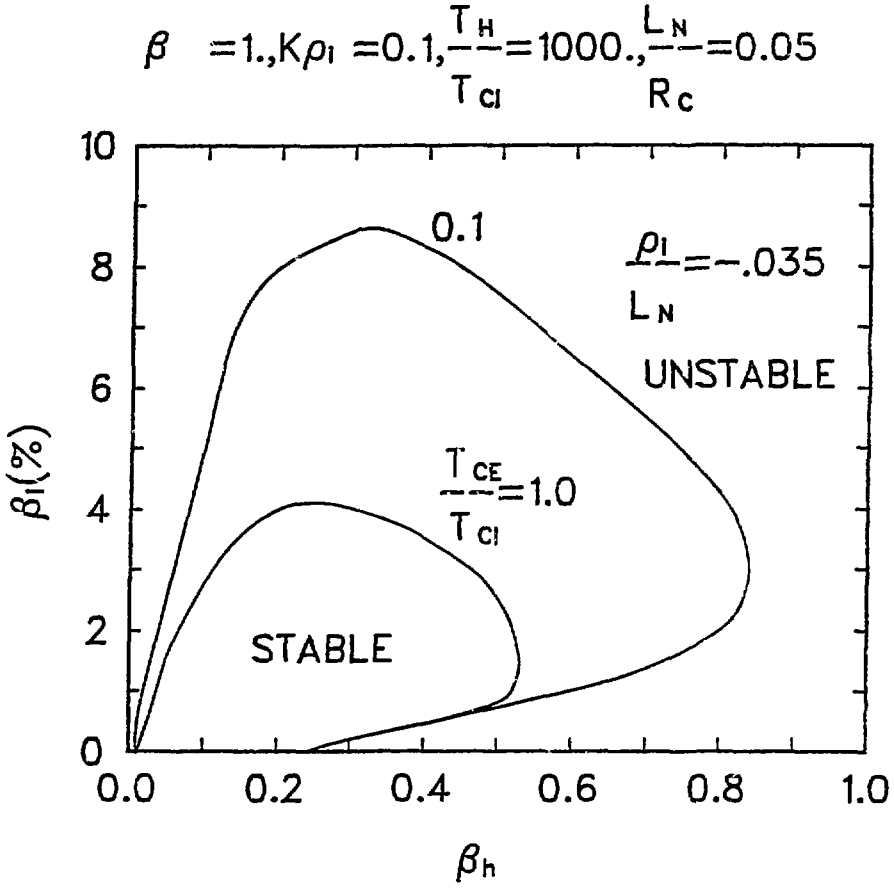

Fig. 3 Enhancement of stability of interchange mode by lowering T_{ce}/T_{ci}.

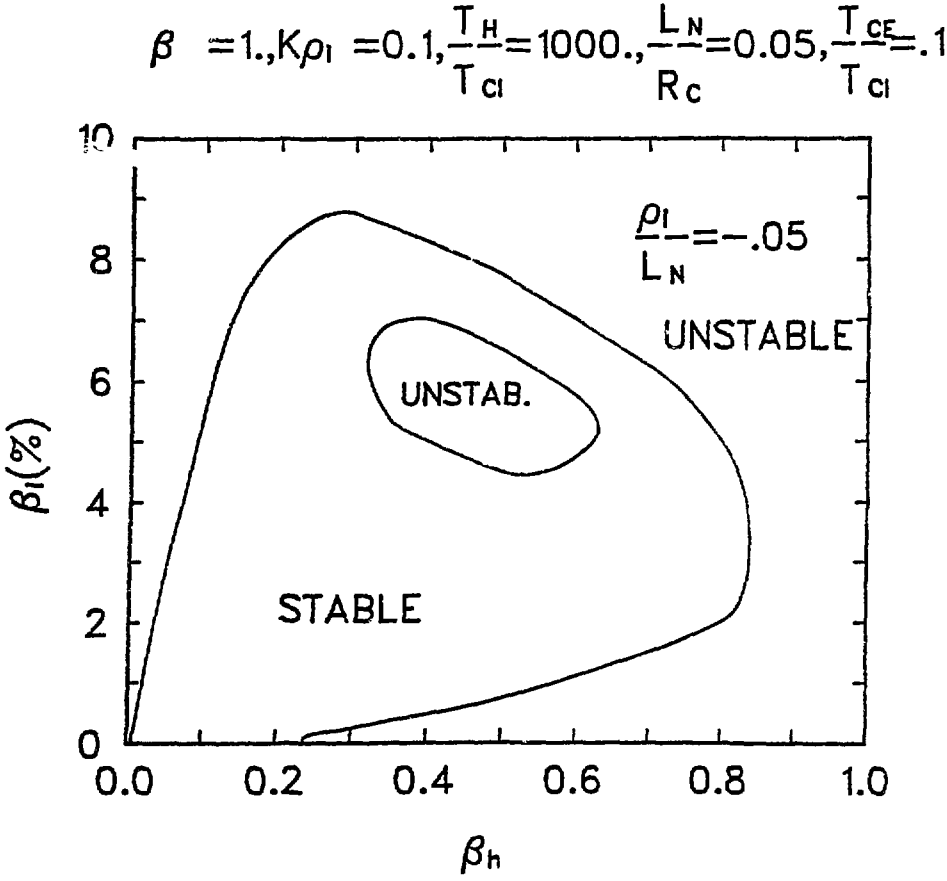

Fig. 4 Dependence of coupling of interchange and Alfven modes on hot electron beta, β_h

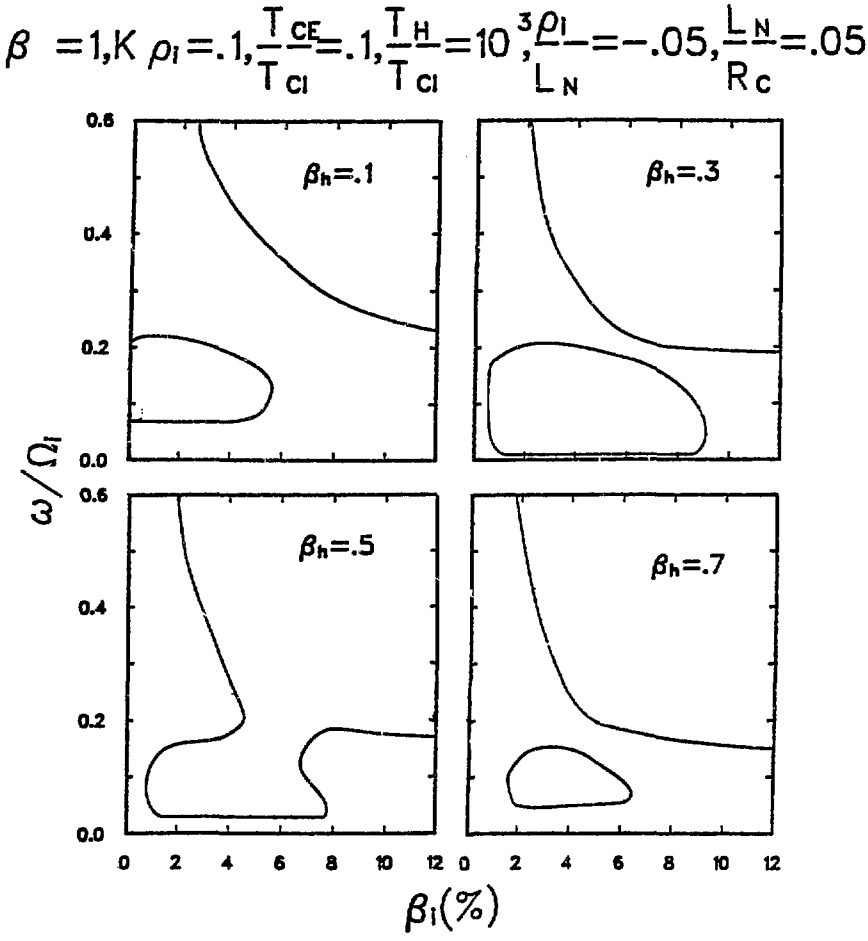

Fig. 5 Coupling of interchange and Alfven modes in frequency domain

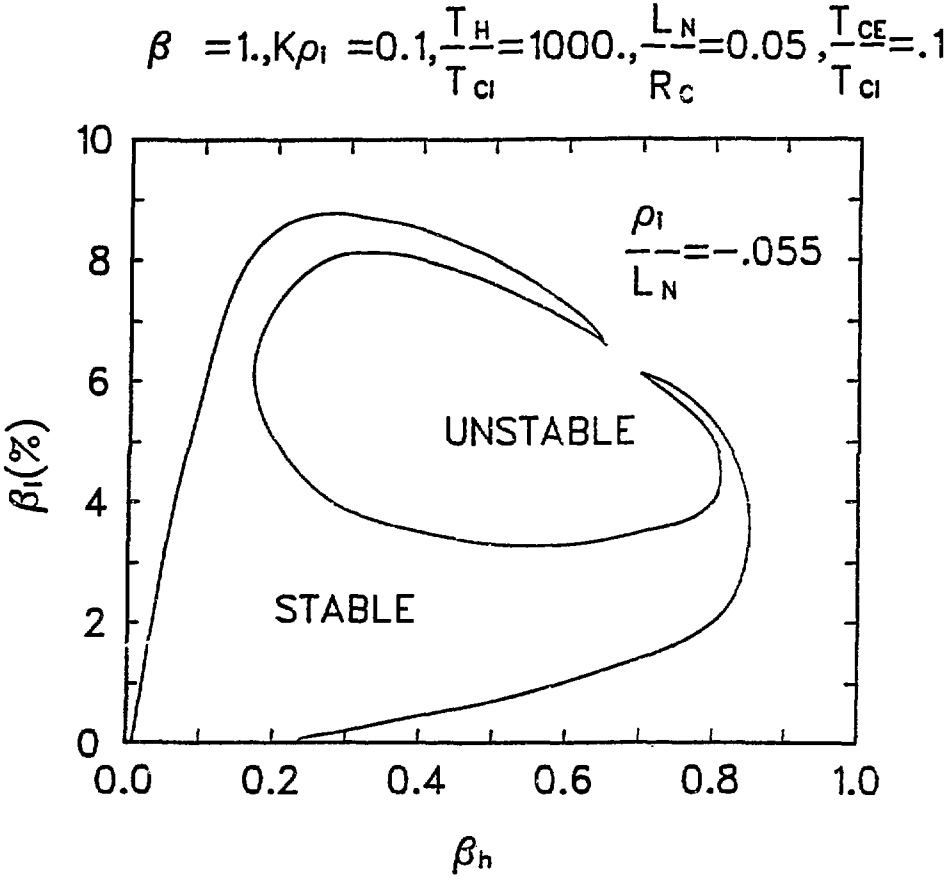

Fig. 6 Channel of stable region with multiple β_i values

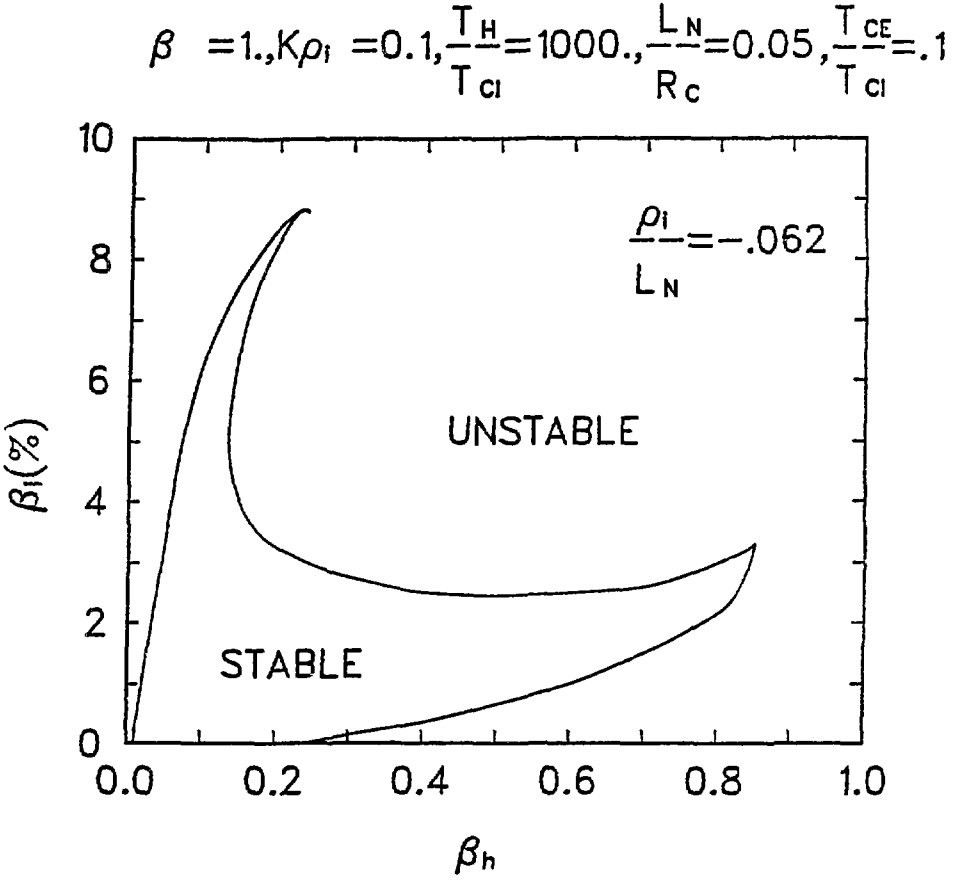

Fig. 7 Shrinking of stable region at large ρ_i / L_n

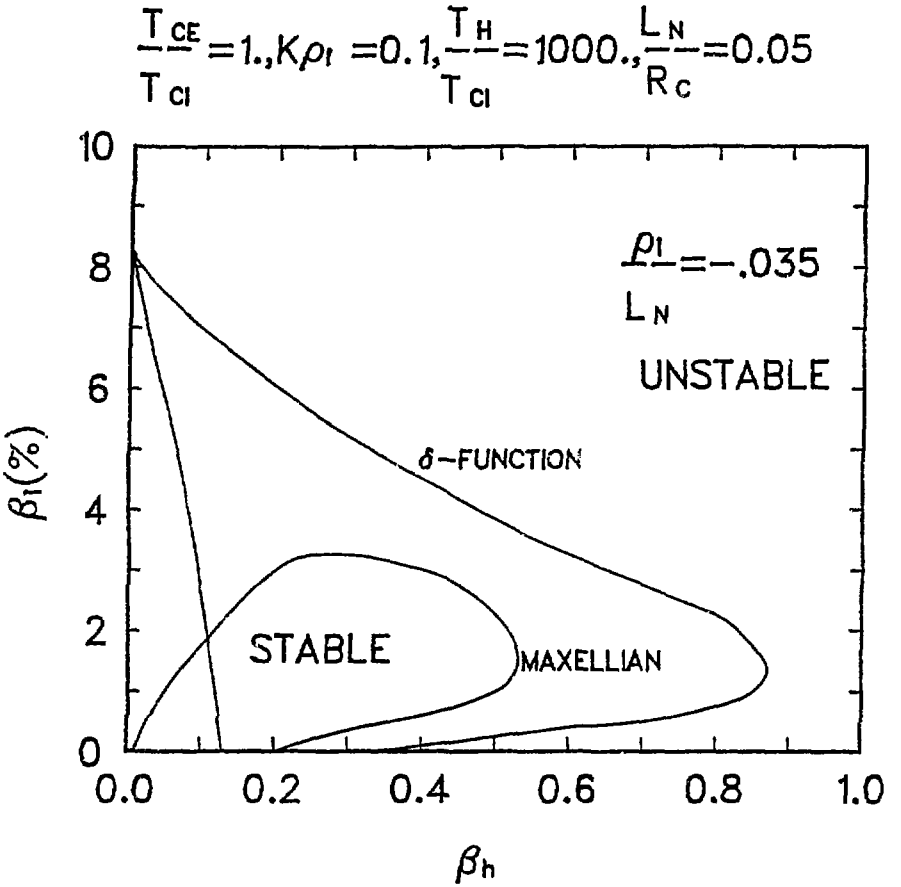

Fig. 8 Interchange stability boundary for delta function and Maxwellian distributions

4. RING PROPERITES AND SCALING

HARD X-RAY MEASUREMENTS OF THE HOT ELECTRON RINGS IN EBT-S*

D. L. Hillis
Oak Ridge National Laboratory
Oak Ridge, Tennessee 37830

ABSTRACT

A thorough understanding of the hot electron rings in ELMO Bumpy Torus-Scale (EBT-S) is essential to the bumpy torus concept of plasma production, since the rings provide bulk plasma stability. The hot electrons are produced via electron cyclotron resonant heating using a 28-GHz cw gyrotron, which has operated up to power levels of 200 kW. The parameters of the energetic electron rings are studied via hard x-ray measurement techniques and with diamagnetic "pickup" coils. The hard x-ray measurements have used collimated NaI(Tl) detectors to determine the electron temperature T_e and electron density n_e for the hot electron annulus. Typical values of T_e are 400-500 keV and of n_e 2-5 $\times 10^{11}$ cm^{-3}. The total stored energy of a single energetic electron ring as measured by diamagnetic pickup loops approaches $\sim$40 J and is in good agreement with that deduced from hard x-ray measurements. By combining the experimental measurements from hard x-rays and the diamagnetic loops, an estimate can be obtained for the volume of a single hot electron ring. The ring volume is determined to be $\sim$2.2 litres, and this volume remains approximately constant over the T-mode operating regime. Finally, the power in the electrons scattered out of the ring is measured indirectly by measuring the x-ray radiation produced when those electrons strike the chamber walls. The variation of this radiation with increasing microwave power levels is found to be consistent with classical scattering estimates.

*Research sponsored by the Office of Fusion Energy, U.S. Department of Energy, under contract W-7405-eng-26 with the Union Carbide Corporation.

1. INTRODUCTION

An essential feature of the ELMO Bumpy Torus (EBT)[1,2] is the presence of an energetic electron annulus in each of the 24 mirror sectors. These high-beta ($\beta \sim 25\%$) annuli are formed and sustained solely by steady-state microwaves resonant at the electron cyclotron frequency. The presence of the hot electron annulus[3,4] modifies the unfavorable vacuum field and acts to stabilize the toroidally confined core plasma against interchange modes.

The magnetic field configuration in EBT-I ($B_{res} \cong 0.64$ T) utilizes klystrons that deliver up to 60 kW for primary electron cyclotron resonance heating (ECRH) near the mirror throats and 30 kW of 10.6-GHz microwave power mainly for profile heating near the outer radial boundary of the plasma. Recently, additional ECRH was added to EBT using a 28-GHz cw gyrotron that was operated at power levels of up to 200 kW. This upgraded EBT, which distributes the 200 kW of 28-GHz microwave power and provides the higher resonant magnetic field ($B_{res} \cong 1$ T), is called EBT-S. Typical machine characteristics and physical dimensions for EBT can be found in Refs. 1 and 2.

The overall behavior of the EBT toroidal streaming plasma is dependent upon the microwave power P_μ and the background neutral pressure ρ_o. (1) The C-mode occurs at high ambient pressure and/or low microwave power and is characterized by a cold, dense, and noisy plasma. No energetic electrons are present. (2) The T-mode occurs at lower pressure when hot electron rings form and produce a quiescent toroidally streaming plasma that is macrostable. Electron temperatures approaching 1 keV have been observed for this toroidally streaming bulk plasma during T-mode operation with 200 kW of 28-GHz microwave power. (3) Finally, the M-mode occurs at still lower pressures, the plasma begins to exhibit instabilities, and the torus begins to appear as disconnected mirror segments.

The purpose of this paper is to investigate the properties of the hot electron rings of EBT-S. The x-ray energy distribution of free-free bremsstrahlung (continuum radiation) in the hard x-ray regime has been

measured to determine the electron temperature T_e and density n_e of the hot electron annuli of EBT-S. The x-ray analysis system utilizes a calibrated NaI(Tl) detector for these measurements. First, the experimental results are presented for EBT-S as a function of the controllable parameters microwave power P_μ and ambient pressure p_o. The first results on ring parameters from EBT-S when operated at cw microwave powers of up to 200 kW at 28 GHz are reported herein. Hard x-ray results indicate that the energetic electron rings have electron temperatures of $\sim$450 keV and that densities of about 3.0×10^{11} cm^{-3} are obtainable. Additional information is obtained about the ring stored energy from diamagnetic pickup loops. Finally, our conclusions about the properties of hot electron rings on EBT-S are presented.

2. EXPERIMENTAL DETAILS

The x-ray energy distribution of free-free bremsstrahlung in the hard x-ray regime (50 keV-2.5 MeV) is measured with a calibrated (12.7 cm × 12.7 cm) NaI(Tl) detector. The hard x-ray detection system used on EBT-S is shown in Fig. 1. The NaI detector is collimated to view a single chord in the midplane region of a single EBT-S cavity. The energetic electron ring is located midway between two of the toroidal field coils, has a radius of 12.5 cm as measured from the plasma center and is located at the second harmonic resonance of the applied microwave frequency. Incoming x-rays that strike the NaI detector produce voltage pulses whose pulse height is proportional to the photon energy E. The resultant pulses are sorted according to their energies and counted by a Nuclear Data ND6600 computer based pulse height analysis system to yield an x-ray energy spectrum. A series of Pb collimators is used to ensure that the detector sees only a small, well-defined single chord of the ring plasma. To reduce the hard x-ray attenuation (due to the thick aluminum vacuum vessel of EBT), a thin aluminum x-ray window of 0.025 cm is used along the detector line of sight. The NaI detector's energy calibration, as well as its detection efficiency, was obtained by using a set of nine calibrated gamma ray sources.

Figure 2(a) shows a typical hard x-ray spectrum obtained for an EBT-S plasma with an applied microwave power P_μ = 50 kW at 28 GHz and a filling pressure of 6.0×10^{-6} torr. The spectrum has been corrected for detector efficiency, attenuation of x-rays due to air, and the thin aluminum x-ray window. The most notable feature of the spectrum of Fig. 2(a) is its lack of structure. The hard x-ray energy distribution arising from the rings appears to be a continuum of radiation that can be represented by a single exponential.

The x-ray bremsstrahlung from a hydrogenic plasma has been treated extensively in the literature.[5-7] For a Maxwellian plasma the free-free bremsstrahlung emission is given by

$$\frac{dW}{dE} = 3.2 \times 10^{-15}\, n_e \ell n_i Z_i^2 T_e^{-1/2} g_{ff} \exp^{(-E/T_e)}\, A \frac{\Omega}{4\pi}\,, \qquad (1)$$

where dW is the radiated power per second into the photon energy interval dE, n_e and n_i are the electron and ion density, respectively, Z_i is the ion charge of the scattering center, g_{ff} is the temperature average gaunt factor, T_e is the electron temperature, E is the x-ray photon energy, A is the plasma area viewed by the NaI detector whose solid angle is Ω, and ℓ is the effective chord length of plasma seen by the detector. For typical operating regimes present on EBT-S we are justified in assuming that (1) all electron scattering is due to hydrogen ions ($Z_i^2 \approx 1$) and (2) the energetic electrons of the rings scatter from the bulk ion population n_i, which exists at the ring location. The electron temperature can then be extracted from the measured photon energy distribution by calculating the inverse slope of the data in a semilogarithmic plot of intensity dW/dE versus x-ray energy. The line averaged electron density $n_e \ell$ can also be found by evaluating Eq. (1) after T_e is determined.

The determination of n_i is taken from an independant measurement of the electron density for the bulk plasma using a multichord microwave interferometer. The bulk plasma electron density at the ring location is assumed to be equal to n_i.

3. EXPERIMENTAL RESULTS

Shown in Fig. 2 are three typical spectra obtained for EBT plasmas under three different operating conditions. Three separate microwave systems of 10.6, 18, and 28 GHz are available on EBT. Steady-state klystrons deliver up to 30 kW of 10.6-GHz microwaves and up to 60 kW of 18-GHz microwaves on EBT. The most recent addition to EBT is a cw gyrotron that delivers up to 200 kW of 28-GHz microwaves. Each of the three hard x-ray spectra shown in Fig. 2 corresponds to single-frequency ECRH. The magnetic field on EBT is adjusted for each microwave frequency such that the energetic electron rings are produced at the second harmonic of the electron cyclotron frequency and at the same location within the EBT cavity.

The three spectra, shown in Figs. 2(a)-2(c), are clearly quite different. By utilizing the techniques outlined in Section 2, the electron temperature T_e and density n_e are determined from a least-squares fit to the experimental data. Clearly, both the ring temperature and ring density increase with microwave frequency. Ring temperatures of $\sim$450 keV were obtained for the 28-GHz microwave frequency.

Following the general analysis procedure outlined in Section 2, T_e and n_e for the hot electron rings were measured for a variety of different operating conditions on EBT-S. Both the applied microwave power out of the 28-GHz gyrotron P_μ and the ambient gas pressure ρ_o were varied with hard x-ray spectra being measured at each new condition. To illustrate the microwave power dependence of T_e and $n_e\ell$, Figs. 3 and 4 show T_e and $n_e\ell$ plotted as functions of P_μ at constant pressure. The values of T_e do not have a strong variation with either microwave power or ambient pressure. The values of $n_e\ell$, however, do vary appreciably with both P_μ and ρ_o, with the highest densities being achieved at the highest values of P_μ or the lowest values of ρ_o. The thickness of the hot electron ring has been measured using a skimmer probe and found to be 2.5 cm. The hard x-ray measurement sees an effective chord length of 5.0 cm and therefore indicates that the ring densities n_e are $\sim 4.2 \times 10^{11}$ cm^{-3} at the highest ECRH power levels. The three pressures are chosen to span most of the T-mode operating regime, where rings are

present. Even though a slight decrease in T_e for the ring is observed with increasing P_μ, the ring temperature does not change markedly from its average value of $T_e \approx 450$ keV. Figure 4 shows that the major change in the ring occurs in $n_e\ell$, where the ring density is observed to increase with increased microwave power and/or neutral pressure.

As was pointed out earlier, EBT has three microwave frequencies (10.6, 18, and 28 GHz) with which to form the energetic electron rings. The magnetic field is varied such that the hot electron rings are formed at the second harmonic resonance of the applied ECRH and at the same radial location within the EBT cavity. The same variations of T_e and $n_e\ell$ with respect to P_μ and ρ_o are observed with the 18- and 10.6-GHz microwave sources, as shown in Figs. 3 and 4. However, major changes in the absolute values of T_e and n_e do occur with the applied microwave frequency. Figure 5 shows the range of values for T_e and n_e observed for the rings when the rings are heated via single-frequency microwaves. The various data points shown at each microwave frequency are points acquired over a range of different values of P_μ and ρ_o where the rings are present. Even though T_e varies only slightly with P_μ and ρ_o for 28-GHz microwave heating (see Fig. 3), dramatic changes in T_e occur as the microwave heating frequency is varied. This is also indicated in the three hard x-ray spectra shown in Fig. 2. The values of both T_e and n_e are shown in Fig. 5 to increase dramatically with the applied microwave frequency. It should be noted that the frequency axis could equally well be replaced by the magnetic field at the ring location that is needed to produce the necessary electron resonance at the second harmonic of the applied microwave frequency.

As a separate ring diagnostic, each of the EBT cavities is surrounded by diamagnetic pickup loops. By measuring the induced currents in these pickup coils due to the energetic electron rings, the stored energy can be determined for an individual electron ring. Figure 6 shows the stored energy of a single EBT-S ring as deduced from these diamagnetic loops as a function of ρ_o at a variety of values of P_μ. At the lowest pressures and highest P_μ, rings are produced with up to 40 J of stored energy.

4. PROPERTIES OF THE HOT ELECTRON RINGS

The rings of EBT must form with sufficient stored energy $W_\perp$ to modify the magnetic field gradients and to provide an average minimum-B stabilization of the toroidally streaming core plasma. Experimentally, stabilization of the core plasma is characterized by a reduction in density fluctuations and by the formation of a symmetric ambipolar potential well.[8] This is known as the C-T transition region and is the point at which the ring just forms. Experimentally, the ring stored energy at the C-T transition is just a few joules and is approximately constant for large changes in microwave power and pressure. This is illustrated by the crosshatched region of Fig. 6.

At the lowest pressure and the very highest ring stored energies at each value of P_μ, another operating boundary is encountered — i.e., the T-M transition. This is also shown in Fig. 6. At the T-M transition the EBT rings begin to exhibit instabilities and finally disappear at still lower pressures. The region of interest for normal EBT operation is the T-mode regime, as this is the region where all of the basic EBT concepts are at work. Another important feature shown in Fig. 6 is the wider operating regime (pressure window) for the T-mode, which occurs at the higher values of P_μ.

From the hard x-ray measurements of the ring T_e and n_e, the average ring beta β can be calculated according to

$$\beta = \frac{8\pi n_e T_e}{B_r^2} , \qquad (2)$$

where B_r is the magnetic field at the ring location (B_r = 0.5 T for EBT-S). The values for both n_e and T_e are the result of chord integrated measurements and therefore represent average values for these parameters. Figure 7 shows ring beta plotted as a function of microwave power for constant ambient gas pressures. Ring betas approaching 25% are obtained for the highest values of applied microwave power. It is encouraging that ring beta, as well as ring stored energy, continues to increase as the applied microwave power is increased.

By combining the information obtained from the rings by the hard x-ray diagnostic and the diamagnetic loops, information can be obtained

about the volume of the hot electron ring plasma. The energy density of the hot electron ring is obtained from the hard x-ray measurements of T_e and n_e, since

$$\text{energy density} = \frac{W_\perp}{V_A} = n_e T_e \ , \tag{3}$$

where V_A is the ring plasma volume. The diamagnetic loop diagnostic, however, measures the ring stored energy $W_\perp$ directly. By plotting $W_\perp$ (diamagnetic loop)/$n_e T_e$ (hard x-ray) versus $W_\perp$ from the diamagnetic loops, the volume of the hot electron ring can be determined as a function of stored energy. This is shown in Fig. 8 for a variety of microwave power levels and ambient pressures. Over the entire range of conditions studied the annulus volume appears to be constant at an average value of about 2.2 litres.

From skimmer probe measurements the hot electron ring is known to have a radius $a_p \sim 12.5$ cm and a thickness $\delta_A \sim 2.5$ cm. The axial extent of the ring, L_A, is less well known but can be inferred from these measurements. For simplicity we take the annulus volume to be

$$V_A = 2\pi a_p \delta_A L_A \ , \tag{4}$$

which infers an axial extent for the ring $L_A \sim 10$ cm. Since we have observed that large changes in the ring volume are not apparent over our data set, the ring dimensions are also not expected to change dramatically over the T-mode operating regime.

Another area of importance for EBT-type devices is the overall radiation level produced by the energetic electrons that are scattered out of the ring and strike the vacuum chamber wall, producing thick target bremsstrahlung. These electron scattering losses from the rings are measured indirectly by measuring the overall x-ray level (R/h) observed within the EBT lead enclosure with a calibrated Reuter-Stokes nitrogen-filled ionization chamber. The ionization chamber is centrally

located near the center of EBT. On the basis of classical scattering the thick target bremsstrahlung observed in this detector is given by[9]

$$P_b \propto Z_W n_e n_i T_e^{1/2} V_A \ , \tag{5}$$

where P_b is the radiated power in the form of x-rays generated when energetic electrons scatter from the ring and strike the vacuum vessel wall of atomic number Z_W. Figure 9 shows the radiation level observed inside the EBT lead enclosure as the stored energy of each individual EBT ring is increased. Clearly, as more energetic rings are produced in EBT at the higher microwave powers, the radiation level becomes greater within the lead enclosure. With 200 kW of ECRH power more than 3000 R/h is produced within the enclosure.

Utilizing the relation of Eq. (5), the enclosure radiation is plotted against $n_e n_i T_e^{1/2}$ in Fig. 10. The values of n_e and T_e are determined from our hard x-ray measurements, whereas n_i is determined from microwave interferometer results described earlier herein. Figure 10 illustrates that the variation of the enclosure radiation is consistent with classical scattering.

High-beta, hot electron plasmas have been produced with ECRH in several experiments other than EBT. Details of these experiments can be found in Ref. 4. A wide variety of conditions was present in these experiments, where (a) magnetic fields varied from 1 to 10 kg, (b) microwave heating frequencies varied from 6 to 55 GHz, and (c) hot electrons were produced with temperatures from 50 to 1200 keV. An analysis of these other ECRH experiments[8] is shown in Fig. 11, where the temperature of the hot electron annulus is plotted for each experiment as a function of the resonance magnetic field at the ring location. These data are all for single-frequency ECRH and indicate that the hot electron temperatures increase with magnetic field strength or equivalently with the microwave frequency. These data are then compared with the results obtained from EBT, which were presented earlier in Fig. 5. The ring temperature, microwave frequency, and magnetic field are all important in determining the hot electron gyroradius. The solid curves show that

the data from the various ECH experiments, as well as EBT, can be understood on the basis of a constant relativistic gyroradius ρ_e between 0.5 and 0.6 cm. The data from the STM and Interem devices, however, require a larger ρ_e of 1.2 cm. These two devices are much larger in physical dimensions than the other devices. By using an appropriate magnetic scale length L for each device, the values of ρ_e/L are displayed within the insert of Fig. 11. For all of the devices investigated, the dimensionless constant ρ_e/L appears to be a constant and lies between 0.05 and 0.06.[8] The observation that $\rho_e/L \approx$ constant on the devices discussed herein may be an important quantity to be addressed on newly proposed ECRH devices.

REFERENCES

1. R. A. Dandl et al., ORNL/TM-3694 (1971); R. A. Dandl et al., Plasma Physics and Controlled Nuclear Fusion Research 1974, Vol. II, 141 (1975).
2. J. C. Glowienka, J. Vac. Sci. Technol. 18(3), 1088 (1981).
3. R. A. Dandl et al., Plasma Physics and Controlled Nuclear Fusion Research 1968, Vol. II, 435 (1975); R. A. Dandl et al., Plasma Physics and Controlled Nuclear Fusion Research 1971, Vol. II, 607 (1972).
4. N. A. Uckan, ed., EBT Ring Physics: Proceedings of Workshop, Conf.-791228, Oak Ridge, Tennessee (1979).
5. T. F. Stratton, Plasma Diagnostic Techniques (Academic Press, New York, 1965) 362.
6. S. von Goeler, Diagnostics for Fusion Experiments, edited by E. Sindoni and C. Wharton (Pergamon Press, Oxford and New York, 1979) 79.
7. R. J. Gould, Astrophys. J. 238, 1026 (1980).
8. N. A. Uckan, ORNL/TM-8006 (1981) and Proceedings of 10th European Conference on Controlled Fusion and Plasma Physics (to be published).
9. H. Knoepfel, Diagnostics for Fusion Experiments, edited by E. Sindoni and C. Wharton (Pergamon Press, Oxford and New York, 1979) 111.

ORNL-DWG 80-2632R FED

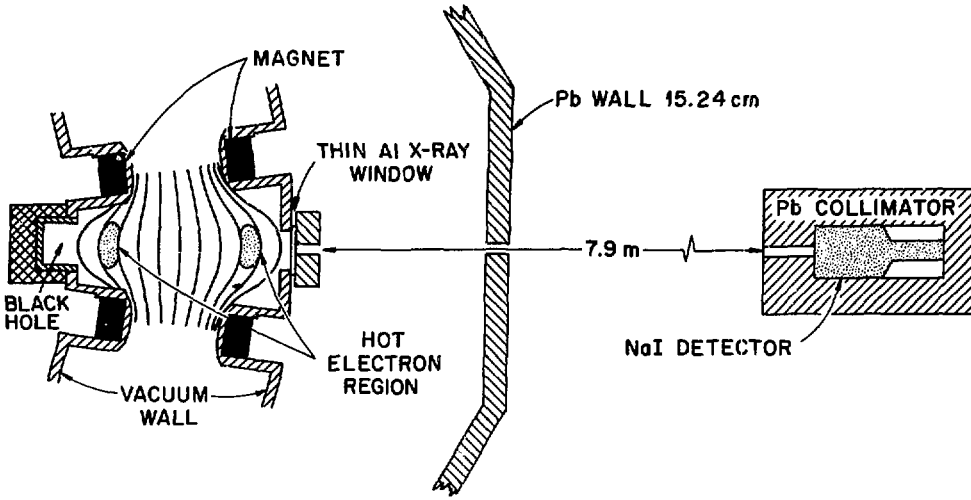

HARD X-RAY DETECTION SYSTEM

Fig. 1. The NaI detection system used on EBT for hard x-ray measurements.

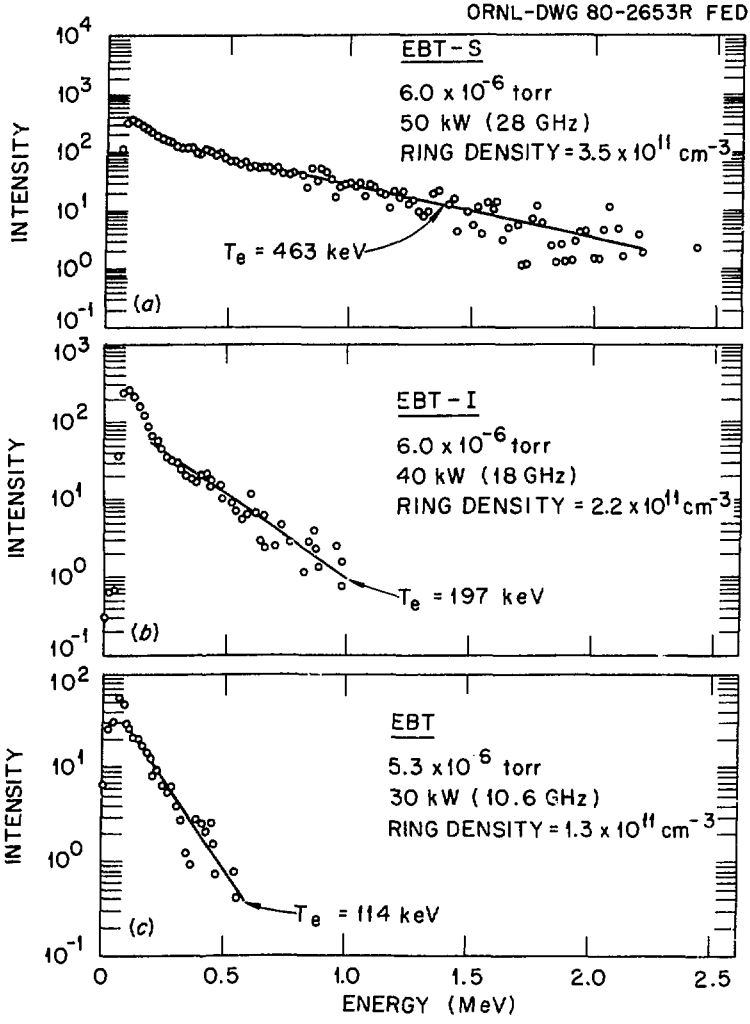

Fig. 2. Typical hard x-ray bremsstrahlung spectra observed during EBT operation when single-frequency microwave heating was used to form the energetic electron rings; (a), (b), and (c) show x-ray spectra generated when 28-, 18-, and 10.6-GHz microwave heating frequencies, respectively, were used. The spectra were obtained with a calibrated NaI detector.

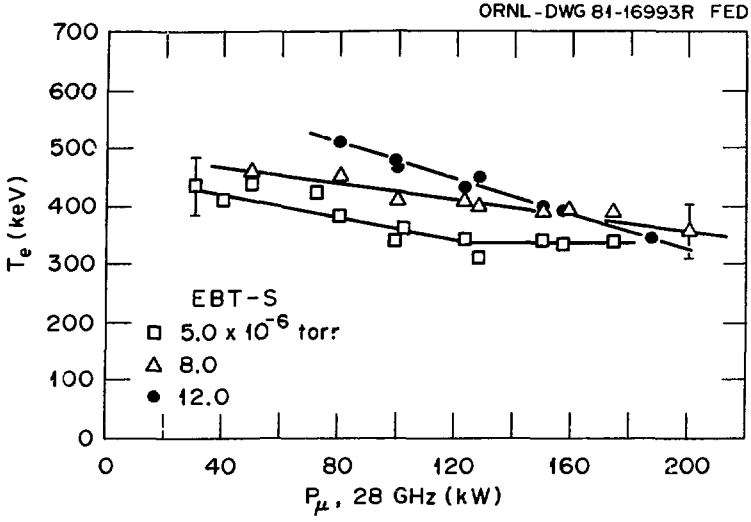

Fig. 3. The electron temperature, as measured by the hard x-ray detection system, is plotted against microwave power out of the 28-GHz gyrotron for several values of ambient pressure (5×10^{-6}, 8×10^{-6}, and 12×10^{-6} torr).

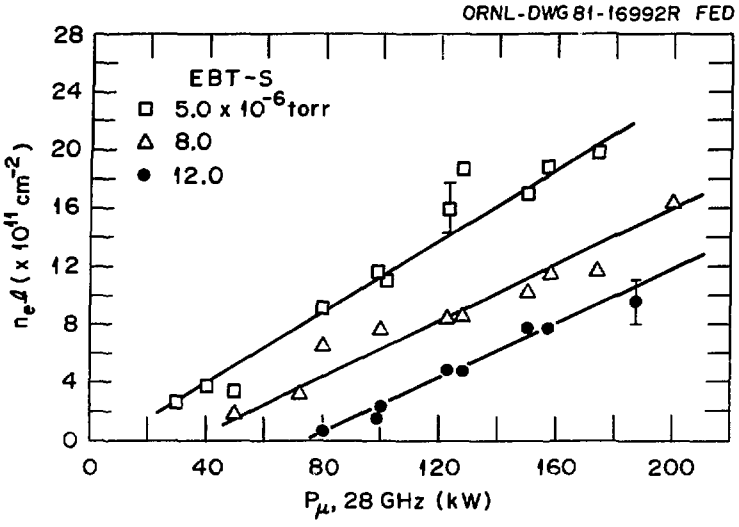

Fig. 4. The line averaged electron density $n_e \ell$, as measured by the hard x-ray detection system, is plotted against microwave power out of the 28-GHz gyrotron for several values of ambient pressure (5×10^{-6}, 8×10^{-6}, and 12×10^{-6} torr).

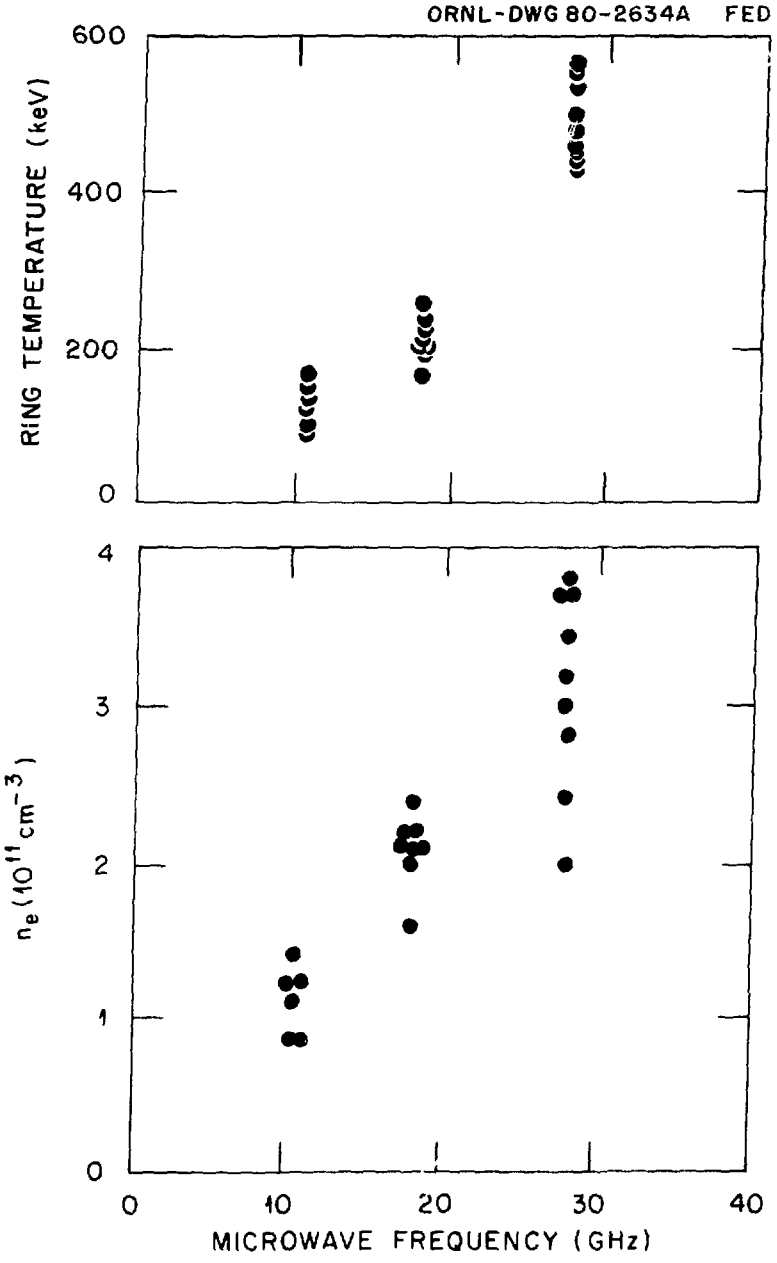

Fig. 5. Ring temperature and ring density variations with the applied microwave frequency. The range of data points at each frequency corresponds to a wide range of experimental conditions for P_μ and ρ_o.

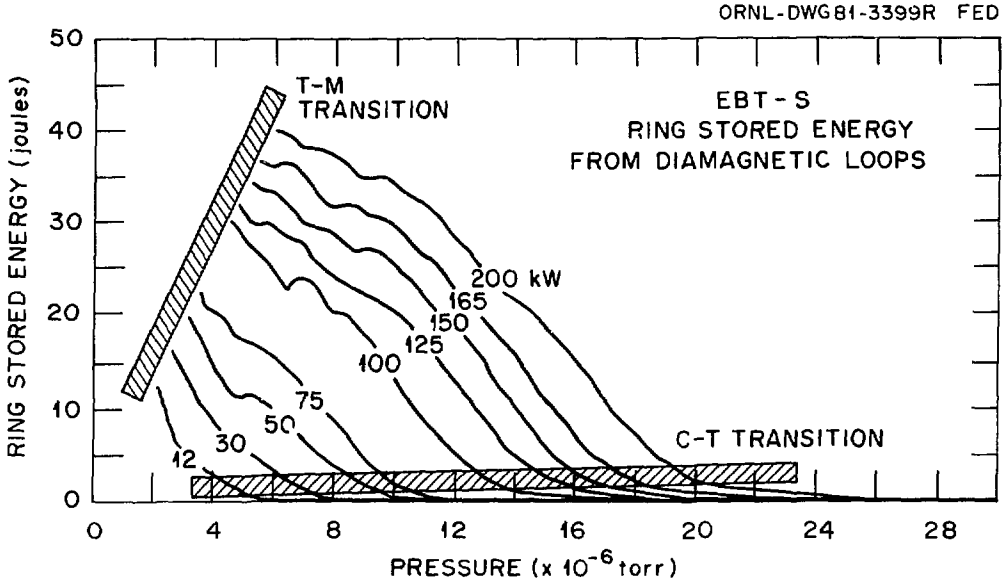

Fig. 6. Experimental measurements of the stored energy of a single EBT-S hot electron ring as a function of operating pressure for various amounts of applied 28-GHz microwave power. The locations of the C-T and T-M operating boundaries are indicated by the crosshatched regions.

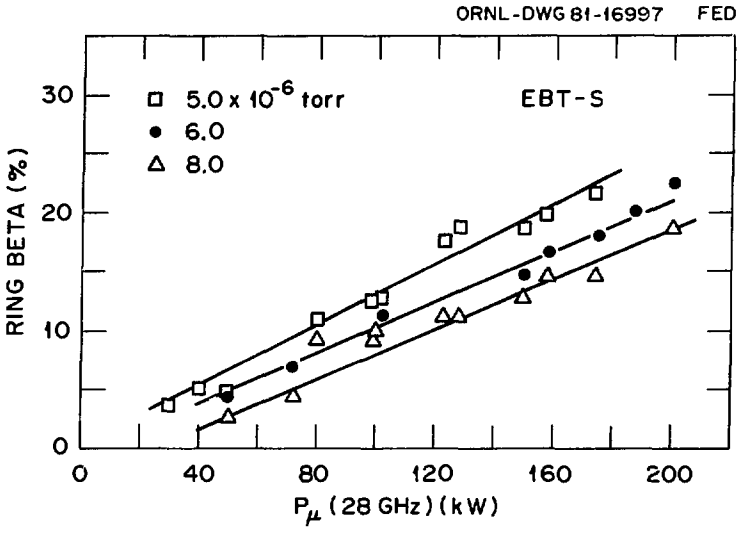

Fig. 7. The hot electron ring beta is plotted as a function of applied 28-GHz microwave power for several values of ambient pressure (5×10^{-6}, 8×10^{-6}, and 12×10^{-6} torr). The ring beta is deduced from the hard x-ray measurements of T_e and n_e.

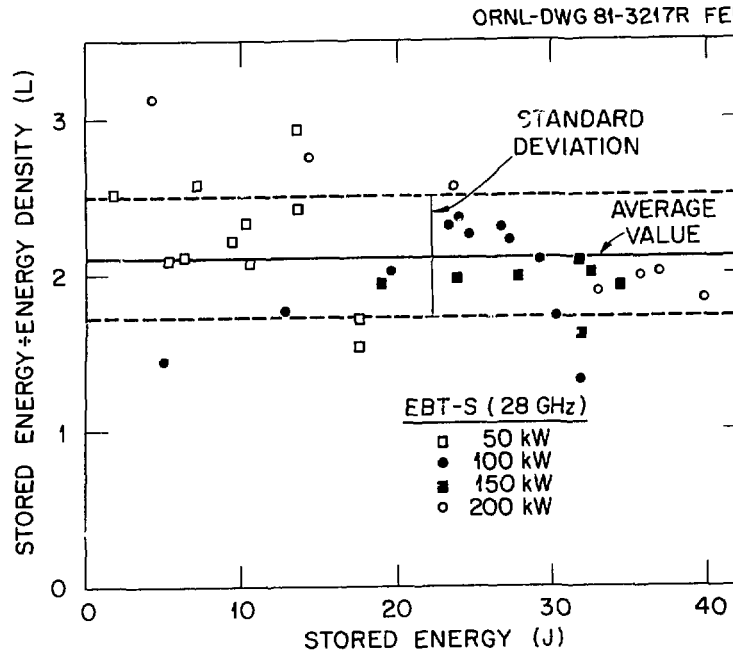

Fig. 8. The volume of a single hot electron ring for EBT-S is plotted against the ring stored energy. The various data points correspond to a variety of conditions for P_μ and ρ_o. (See text for detailed explanation.) A ring volume of ∿2.2 liters is found using this experimental technique.

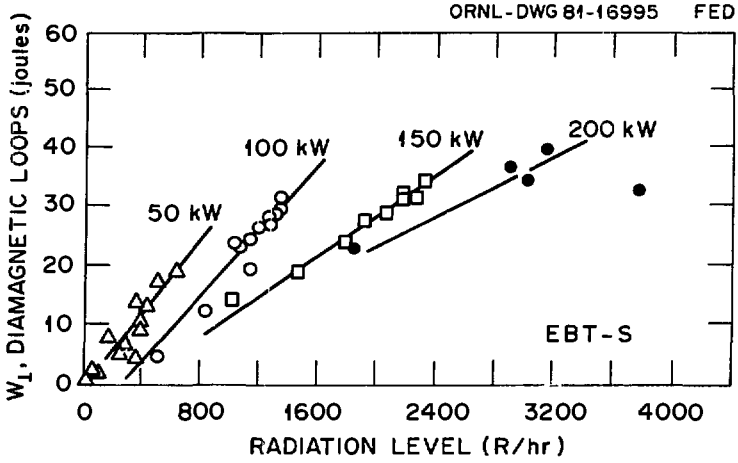

Fig. 9. The stored energy of a single hot electron ring is plotted against the overall enclosure radiation observed for EBT-S. The various data points correspond to a variety of operating conditions due to changes in P_μ and ρ_o. (See text for discussion.)

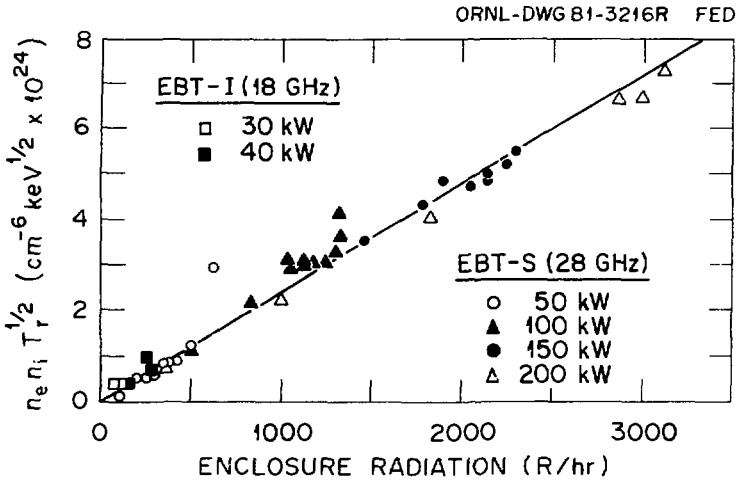

Fig. 10. The quantity $n_e n_i T_r^{1/2}$ is plotted against the enclosure radiation found for EBT-S. The various data points correspond to a variety of operating conditions due to changes in P_μ and ρ_o. This variation of the enclosure radiation is consistent with classical scattering estimates.

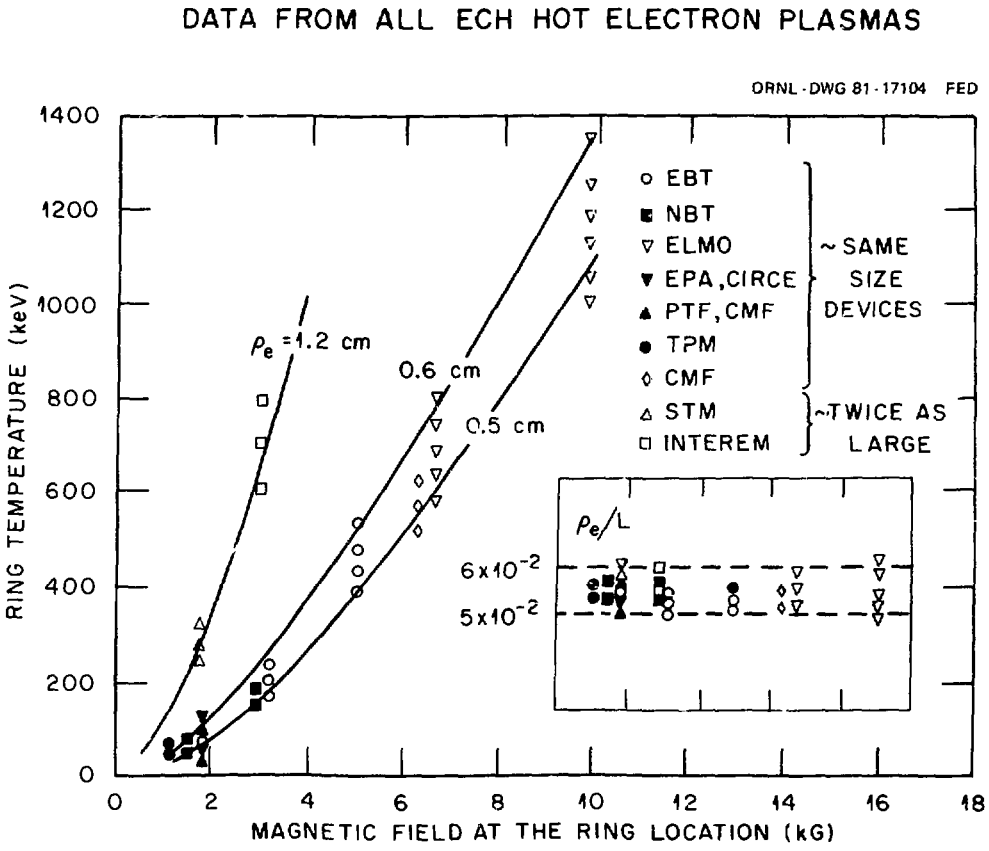

Fig. 11. Ring temperature is plotted as a function of magnetic field at the ring location for a variety of microwave heated hot electron plasmas. The data are compared to the EBT-S results. The solid lines are for constant hot electron gyroradii ρ_e, as shown. Data from all of the above hot electron plasmas can be represented by a value of $\rho_e/L \approx$ 0.05-0.06, where L is a magnetic field scale length (see insert). Data from all of these hot electron plasmas indicate that the ring temperatures obey a simple ρ_e/L scaling.

INTERACTION OF MICROWAVE WITH HOT ELECTRON RING IN NAGOYA BUMPY TORUS

M. Tanaka, M. Hosokawa, M. Fujiwara and H. Ikegami
Institute of Plasma Physics, Nagoya University,
Nagoya 464, Japan

ABSTRACT

Decay of hot electron rings is experimentally studied on Nagoya Bumpy Torus (NBT) plasmas with the hot electron temperature of 100 keV and density of 10^{11} cm^{-3} in the background cold plasma density of 5 x 10^{11} cm^{-3}. With hydrogen plasmas the decay of the ring is observed to be governed by the Coulomb drag, if we take the contribution from electrons in the neutral atomic shell, as well as plasma electrons. It is also observed that the ring intensity levels off as the microwave power increases. The saturation in the ring beta can be attributed to a decrease in the cyclotron damping when the hot electron density increases beyond a critical value, which may determine the maximum ring β.

1. INTRODUCTION

Characteristics of hot electron rings are well studied on mirror plasmas[1-4] with ELMO series of mirror machine at ORNL and TPM series of mirror machine at IPP, Nagoya. The ring formation is a result of complicated and mutually related several processes. Electrons gain their perpendicular energy through stochastic process traversing the cyclotron resonance zone. They tend to be squeezed into the central mirror region and lose the interaction at the fundamental cyclotron resonance near the throat. The electrons now confined in the midplane have a larger energy and will start interacting with microwave field in the second cyclotron harmonic resonance region which exists in a belt zone in the midplane. They further gain perpendicular energies,

generating a so-called hot electron ring.

In most cases, their kinetic energy saturates at a few 100 keV, which corresponds to an energy that produces a minimum energy loss in terms of Coulomb drag and synchrotron radiation. A few mechanisms are considered to be responsible to keep the hot electrons in the energy range of minimum loss: firstly, the relativistic mass effect associated with the large kinetic energy will reduce the energy gain by shifting a resonance condition, secondly the ring beta itself will change the local magnetic field intensity resulting in a less energy gain like the relativistic mass effect, and thirdly adiabatic holes in the phase space will bar the generation of higher energy particles in the stochastic process[5-12] unless multifrequencies[3] are employed to change the adiabatic condition.

In Section 2 of the present paper, the ring location in the midplane is studied with the use of a skimmer probe. The hot electron ring in a bumpy torus has a crucial difference from that in a linear mirror, that is, the ring electrons in the bumpy torus decay as they change their radial orbits sweeping the whole cross section in the midplane and are lost to the inner wall of the mirror throat through a rather narrow loss channel, while in a linear mirror the ring electrons decay out to the end wall along the magnetic lines of force that connect to the ring in the midplane.

As to the ring energy, corresponding to three models for the energy saturation previously mentioned, the present paper will propose the fourth mechanism in Section 3. From the dispersion relation with hot electrons present, it is found that the cyclotron damping decreases as the density of the hot electrons increases, which can cause the saturation.

Loss of the ring energy that balances the microwave power is estimated by using various gas plasmas in Section 4. Electrons in the atomic shell are observed to play as much role as plasma electrons. The effect of atomic electrons has never been paid much attention on the energy loss of hot electrons.

2. PROFILE OF HOT ELECTRONS

Previously the location of the hot electron ring measured by an ionization chamber[13] was reported, which was very sensitive to the toroidal hot electrons. In the present paper, the change of synchrotron radiation from the ring is measured by decomposing it with a skimmer probe. The skimmer probe is made of stainless steel and movable perpendicularly to the magnetic field, as shown in Fig.1. When the tip of the probe is located at position x scraping off the ring electrons from the wall, the received microwave radiation, which is mostly composed of synchrotron emission from the hot electron ring, is proportional to the number of the hot electrons left, that is,

$$I(x) \propto \int_0^x f(d)dx \ , \qquad (1)$$

where the origin is taken at the plasma axis, the quantity I(x) is the received power of radiation when the tip of the skimmer locates at x, and f(x) is the spatial density distribution of the ring electrons. Differentiating I(x) with x, the spatial density distribution is obtained.

Figure 2 shows the location and shape of the ring for various magnetic field intensity at the midplane. The peak and the width of the ring is plotted in Fig.3, where the horizontal bar corresponds to the half-width of the hot electron distribution. The solid curve indicates the fundamental and the second harmonic cyclotron resonance zone with the electron rest mass. As shown in Fig.3, the ring position is not always coincides with the cyclotron resonance zone, but locates somewhere between the resonance zones.

Three mechanisms are considered to account for the observation. A series of peaks in the lower magnetic field corresponds to the second cyclotron harmonic resonance zone with the relativistic mass effect. The second series in the higher magnetic field may correspond to the region of a long confinement time around the toroidal plasma axis. The electrons in that region can have ten times longer confinement time than the electrons in the other region. The ring location is

determined by the largest product of heating rate and confinement time. As observed in Fig.2, these two sources of the ring coexist being separated in space.

3. SATURATION IN THE RING ENERGY

The criterion for the magnetic well formation by the hot electron ring may be estimated by

$$\beta \sim \frac{2\Delta}{a} \quad , \tag{2}$$

where Δ is the ring width and a is the characteristic length of the field gradient. It has been experimentally realized that the hot electron temperature is almost independent of the microwave power, but the hot electron density may increase to produce a higher ring β.

Microwaves in the ordinary mode at 8.5 GHz with a 200 msec pulse width was irradiated into one sector of the device up to 10 kW which is equivalent to 240 kW operation with the full torus. Synchrotron radiation from the ring electron was measured by a radiometer with an assumption that the radiation intensity is proportional to the hot ring energy.

Figure 4 shows the radiation received as a function of the input microwave power (kW/cavity). The target plasma has been produced by a 30 kW microwave power, that is, 1.25 kW per cavity. The radiation power is observed to saturate with the input of 5 kW per cavity associated with a saturation in the ring beta. Hard X-rays from the ring revealed that the ring temperautre is almost constant as shown in Fig.5, while the hot electron density is observed to increase linearly with the microwave power. The fact is understood as follows: the radiometer receives mostly radiations from gyrating electrons in the extraordinary mode, while hard X-rays are almost independent of the direction of motion of electrons, so that the linear increase of the X-ray signal may be due to the increase of the toroidal hot electrons which circulate the torus along the toroidal plasma axis. Three mechanisms of saturation have been discussed in the introduction, which are all related to the relativistic energy effect in some sense. Here the

fourth saturation mechanism can be considered to be due to either reduction of heating efficiency or enhanced scattering loss of the hot electrons, or both. Experimentally the latter is observed to be a slightly increasing function of the input microwave power (see Fig.11).

The power absorption rate is found to decrease as the hot electron density increases. The dispersion equation for the ordinary mode is solved for the plasma with cold electrons and hot electrons (Appendix I). As shown in Fig.6, the absorption rate, which is given by Im(n), increases first as the hot electron density increases. It reaches a maximum with $n_h = (4\text{-}5) \times 10^{11}$ cm^{-3}, which is little sensitive to the cold plasma density, and then decreases. It will be important to note that an increase in the cold plasma density also reduces the absorption rate. The effect is due to the change of wavelength in the plasma. In the calculation, it is assumed that the cold electron density in the ring region is as much as the hot electron density.

With the use of two frequencies, heating was examined to study the effect on the saturation. Microwave power of 10.5 GHz was applied to the plasma produced by 8.5 GHz power. Figure 7 shows the hot electron temperature as a function of 10.5 GHz power, where the result for the single frequency heating is also shown for comparison. As seen in Fig.7, the hot electron temperature increases by applying 10.5 GHz power. It should be noted that the temperature saturates already with a low power level of 1 kW per cavity, beyond which it increases only slightly with increasing microwave power. The additional increase in the hot electron temperature with the two frequencies may be considered to be due to the disintegration of adiabatic holes in the stochastic heating process, or in the present case more likely to be due to the broadening of the ring width with the additional resonance zone.

4. ENERGY LOSS OF HOT ELECTRONS

In order to study energy loss mechanisms of the hot electrons, additional microwave pulse was applied to one sector of the NBT device and the decay time of the radiation intensity from the ring electrons

was measured with heating power system shown in Fig.8. The driver power through the TWT amplifier is fed to the klystron amplifier. The output microwave power is a pulse of 400 msec duration with a maximum of 10 kW and is irradiated into the test cavity from the top side port with the ordinary mode polarization.

The upper trace in Fig.9 indicates radiation signals received in the extraordinary mode,and the input power in the bottom trace. After the turn off of the pulse,the increment in radiation is observed to decay with a time constant of approximately 100-200 msec. The decay of hard X-rays is consisted of two time constants as shown in Fig.10, and the slow component is observed to be in good agreement with the decay of the synchrotron radiation which is shown in Fig.11.

The dominant energy loss mechanism[13-15] of the ring electron in the present experiment is estimated from Coulomb drag by surrounding cold electrons. Then the cooling rate is given by[17]

$$\frac{dE}{dt} = \frac{4\pi e^4 n_e}{mv^2}\left[\ln\Lambda - \frac{v^2}{2c^2}\right] , \tag{3}$$

where n_e is the cold electron density and $\ln\Lambda$ is Coulomb logarithm. The ring decay time is obtained as

$$\tau_h = \left(\frac{1}{E}\frac{dE}{dt}\right)^{-1} \tag{4}$$

$$= 1.6 \times 10^{18} \frac{(\gamma - 1)^{3/2}(\gamma + 1)^{1/2}}{n_e\gamma} \quad [\mathrm{sec}]$$

where $\gamma = (1 - v^2/c^2)^{-1/2}$. As shown in Fig.12, the next large loss is due to scattering of the hot electrons. The scattering loss in the bumpy torus is rather difficult to estimate but still negligibly small, that is, in the present bumpy torus, NBT and EBT, those ring electrons produced in the higher magnetic field (in Fig.2) have by a value of aspect-ratio times better confinement time than the ring electrons produced in the lower magnetic field regime, or in a simple mirror.

Figure 13 shows the observed decay time of microwave radiation as a function of the number density of target electrons including the electrons in the neutral atoms. Solid lines show the decay time given

by eq.(4) with the typical hot electron temperature observed in the experiments, indicating a good agreement with the experimental results. It should be noted that the decay time in an afterglow plasma, where much less plasma electrons are present, agrees with the calculation. The fact means that the electrons in neutral atoms must be considered to compose a cooling electron media with approximately a half value of Coulomb logarithm compared with that for plasma electrons, owing to the maximum impact parameter taken as Bohr radius rather than Debye length. The result with different gas species (He and Ne) also supports the conclusion. From Fig.13 we can also confirm that the energy loss mechanism of hot electrons in the present NBT is the Coulomb drag loss.

One can estimate the microwave power delivered to the hot electron ring,

$$P = P_{drag} = \frac{n_h T_h}{\tau_h} N_h V_h \ , \qquad (5)$$

where N_h is the number of the rings and V_h is the ring volume. Substituting experimental values, $n_h = 10^{11}$ cm^{-3}, $T_h = 100$ keV, $\tau_h = 100$ msec and $V_h = 8 \times 10^3$ cm^3, one obtains P = 3 kW which may be the minimum microwave power required to sustain 24 rings in NBT. The estimated microwave power could sustain the rings, if they have been already produced. However, if core plasmas were produced by some methods other than ECH, much more power would be required to produce the rings. In other words, the same rings in NBT cannot be generated by the estimated microwave power of 3 kW, if the core plasma is produced by ICH, for example. Most of the microwave power is dissipated in generating warm electrons with a proper pitch angle distribution before they can interact in the second harmonic resonance zone with microwaves to form the ring. Estimation of the microwave power to generate the hot electron ring has a crucial importance in the design of a bumpy torus reactor, where the main recirculating power is for the ring formation and sustain.

APPENDIX I

The dispersion relation for the ordinary mode wave is given by

$$n^2 = \varepsilon_{33} \ , \tag{A-1}$$

where n is the refractive index, and ε_{33} is the dielectric tensor. When the plasma consists of relativistic electrons and cold electrons, ε_{33} is given by

$$\varepsilon_{33} = 1 - \frac{\omega_{pe}^2}{\omega^2} + \varepsilon_{hot} \ , \tag{A-2}$$

where ω_{pe} is the electron plasma frequency of the cold electron, and ε_{hot} is the term due to the relativistic electron component given by[18,19]

$$\varepsilon_{hot} = i \frac{\omega_{pe(h)}^2}{\omega x \omega_{ce}} \frac{c^4}{v_t^4 K_2(c^2/v_t^2)} \int_0^\infty d\xi \frac{K_2(\sqrt{R})}{R} \ , \tag{A-3}$$

$$R = \left(\frac{c^2}{v_t^2} - i\xi \frac{\omega}{\omega_{ce}}\right)^2 + 2\left(\frac{kc}{\omega_{ce}}\right)(1 - \cos\xi) \ ,$$

$$v_t = \sqrt{\frac{T}{m_e}} \ , \qquad \omega_{ce} = \left|\frac{eB}{m_e}\right| ,$$

$$\omega_{pe(h)} = \frac{n_h e^2}{\varepsilon_o m_e} \ ,$$

$K_2(x)$: modified Bessel function of the second order,

T : temperature of the relativistic electron,

m_e : electron rest mass,

B : magnetic field intensity,

n_h : density of the relativistic electron,

The cold electron term does not contribute to the imaginary part of

eq.(A-1), so that the absorption is entirely due to the relativistic electrons. The dispersion relation of the ordinary wave mode is produced by inserting the numerical solution of eq.(A-3) into eq.(A-2).

REFERENCES

1. R. A. Dandl, A. C. England, W. B. Ard, H. O. Eason, M. C. Becker, G. M. Haas, Nucl. Fusion 4 (1964) 344.
2. H. Ikegami, S. Tanaka, H. Ikezi, M. Hosokawa, Phys. Rev. Lett. 19 (1967) 779.
3. R. A. Dandl, H. O. Eason, P. H. Edmonds, A. C. England, Nucl. Fusion 11 (1971) 411.
4. H. Ikegami, S. Aihara, M. Hosokawa, H. Aikawa, Nucl. Fusion 13 (1973) 351.
5. M. Seidal, Plasma Phys. 6 (1964) 597.
6. A. D. Piliya, V. Ya. Frenkel, Sov. Phys. Tech. Phys. 9 (1965) 1356.
7. A. F. Kuckes, Plasma Phys. 10 (1968) 367.
8. H. Grave, Plasma Phys. 11 (1969) 151.
9. A. J. Lichtenberg, M. J. Schwartz, D. T. Tuma, Plasma Phys. 11 (1969) 101.
10. E. Canobbio, Nucl. Fusion 9 (1969) 27.
11. T. Kawamura, H. Momota, C. Namba, Y. Terashima, Nucl. Fusion 11 (1971) 339.
12. M. A. Lieberman, A. J. Lichtenberg, Phys. Rev. 5 (1972) 1852.
13. M. Fujiwara, M. Hosokawa, H. Iguchi, T. Shoji, M. Tanaka, H. Sanuki, H. Ikegami, Proc. Workshop on Ring Physics (Oak Ridge, 1979) 123.
14. R. J. Kashuba, W. B. Ard, ibid., 333.
15. A. Andrade, R. A. Krakowski, C. G. Bathke, ibid., 363.
16. S. K. Borowski, N. A. Uckan, E. F. Jaeger, T. Kammash, Nucl. Fusion 20 (1980) 177.
17. J. D. Jackson, *Classical Electrodynamics* (2nd ed., John Wiley, 1975) Chap.13.
18. B. A. Trubnikov, *Plasma Phyiscs and the Problem of Controlled Thermonuclear Reactions* (Pergamon Press, 1959) Vol.3, 122.
19. I. P. Shkarofsky, Phys. Fluids 9 (1966) 561.

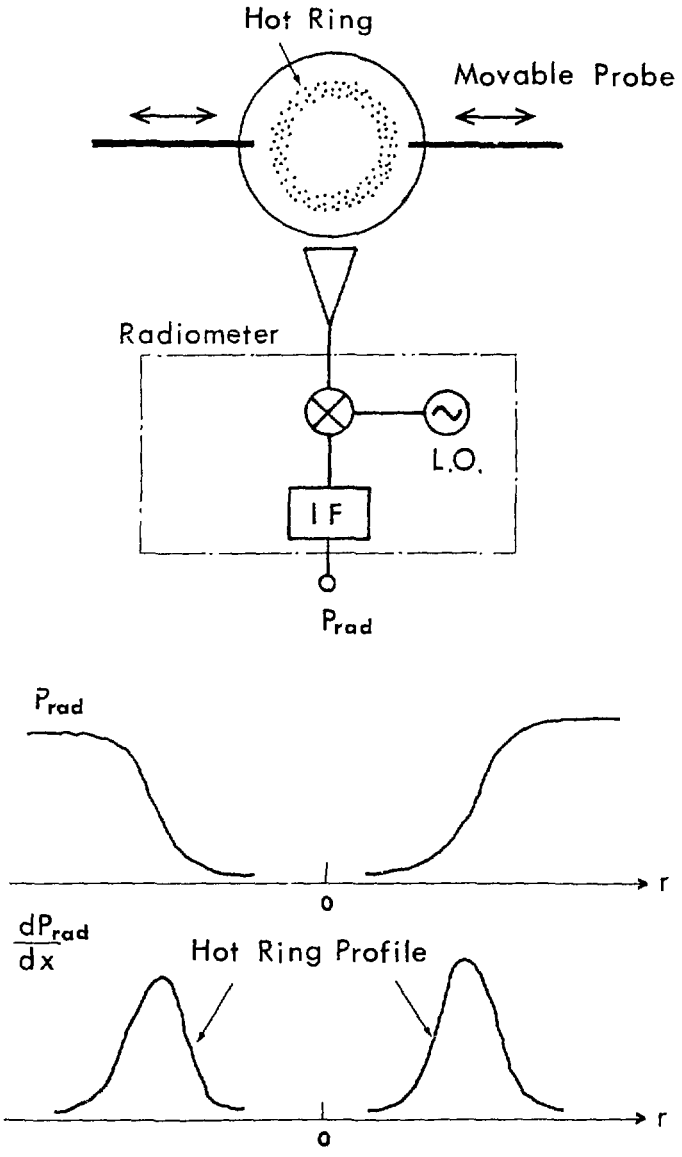

Fig.1 Schematic illustration of a skimmer probe system.

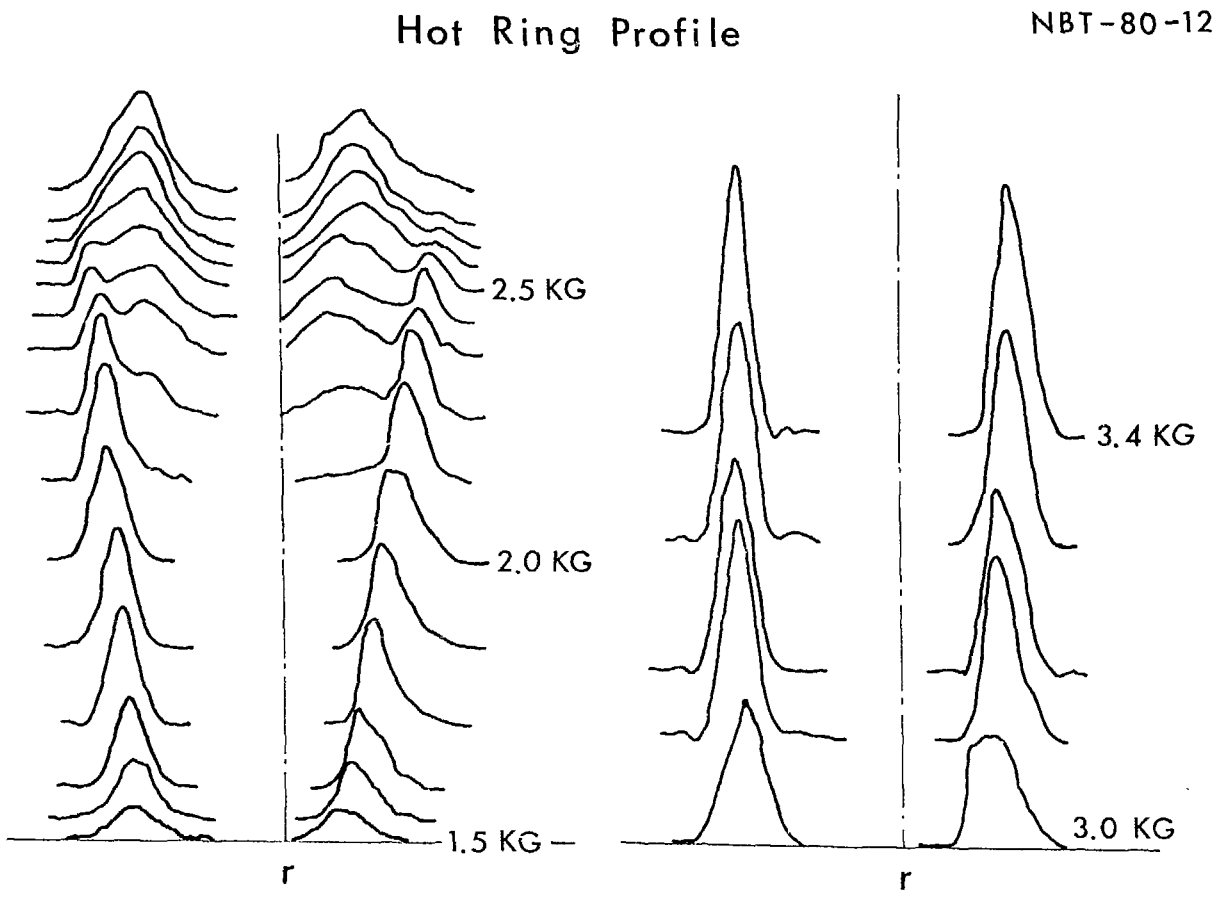

Fig.2 Profile of hot electrons measured by the skimmer probe.

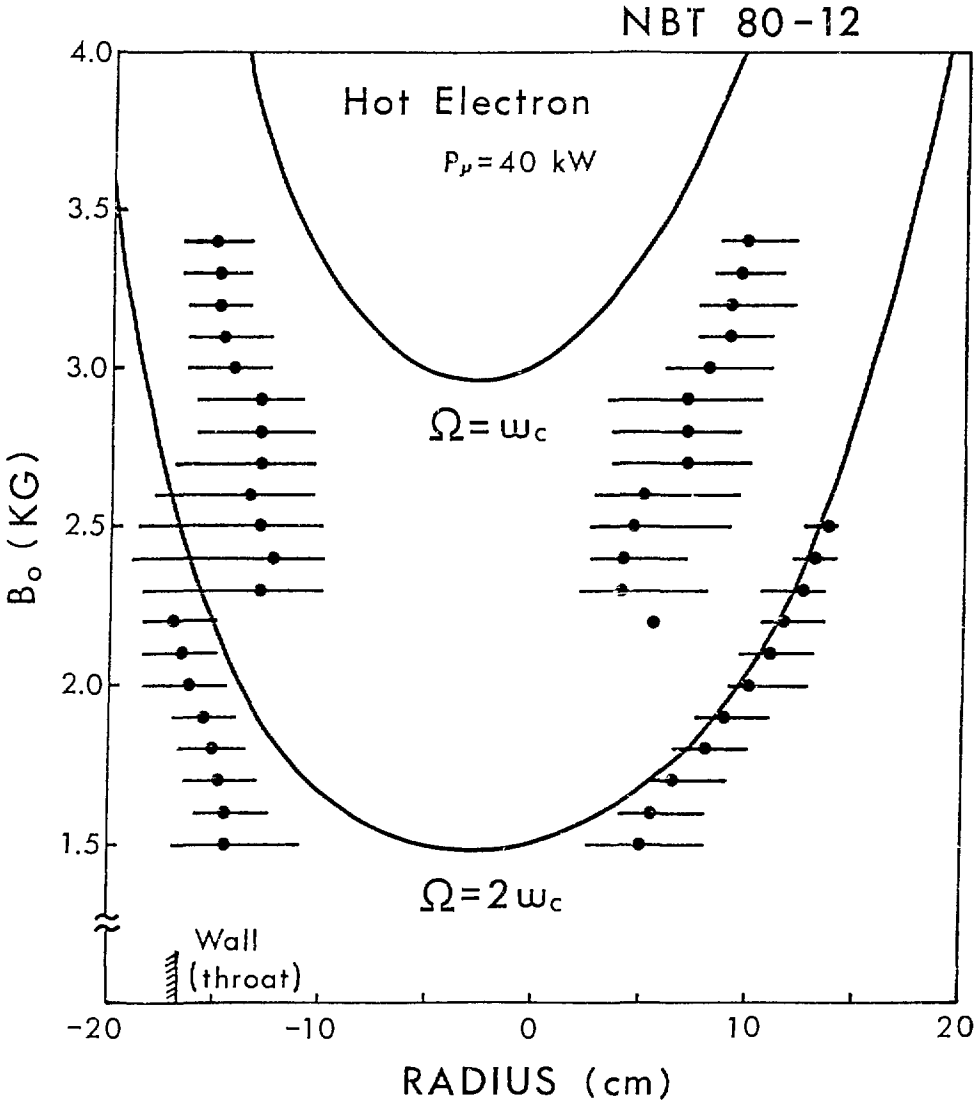

Fig.3 Ring position as a function of magnetic field intensity. Fundamental and second harmonic cyclotron resonance points at the midplane are shown in the figure.

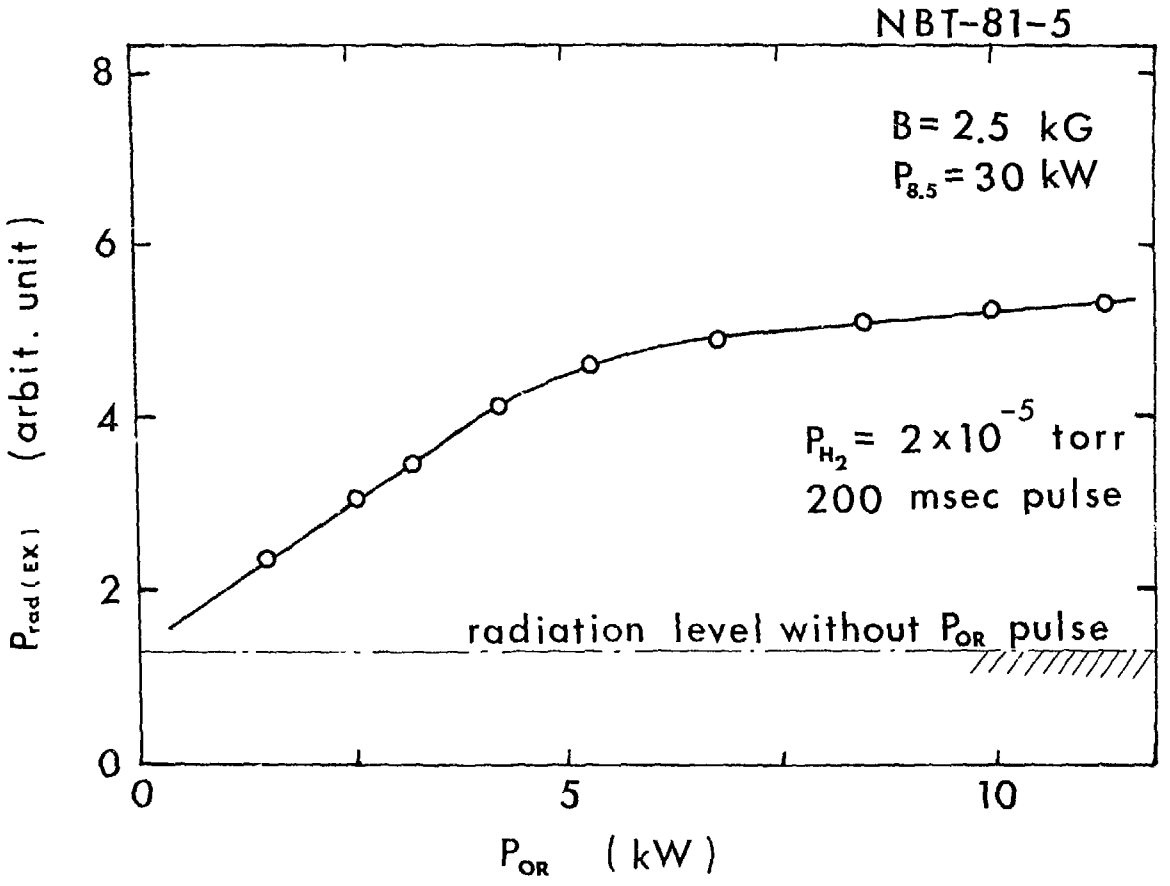

Fig.4 Radiation intensity as a function of input microwave power (per cavity).

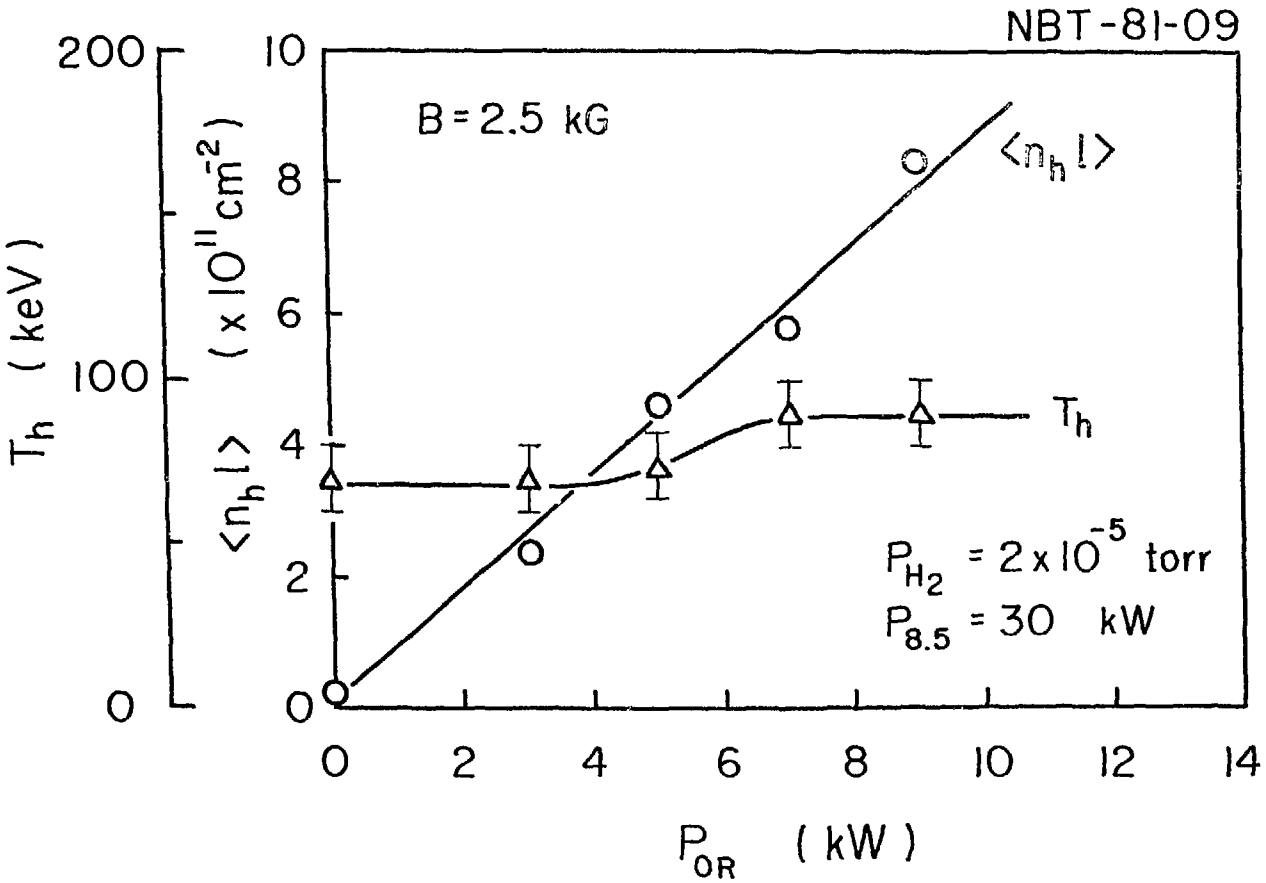

Fig.5 Hot electron temperature and density determined by the hard X-ray measurement.

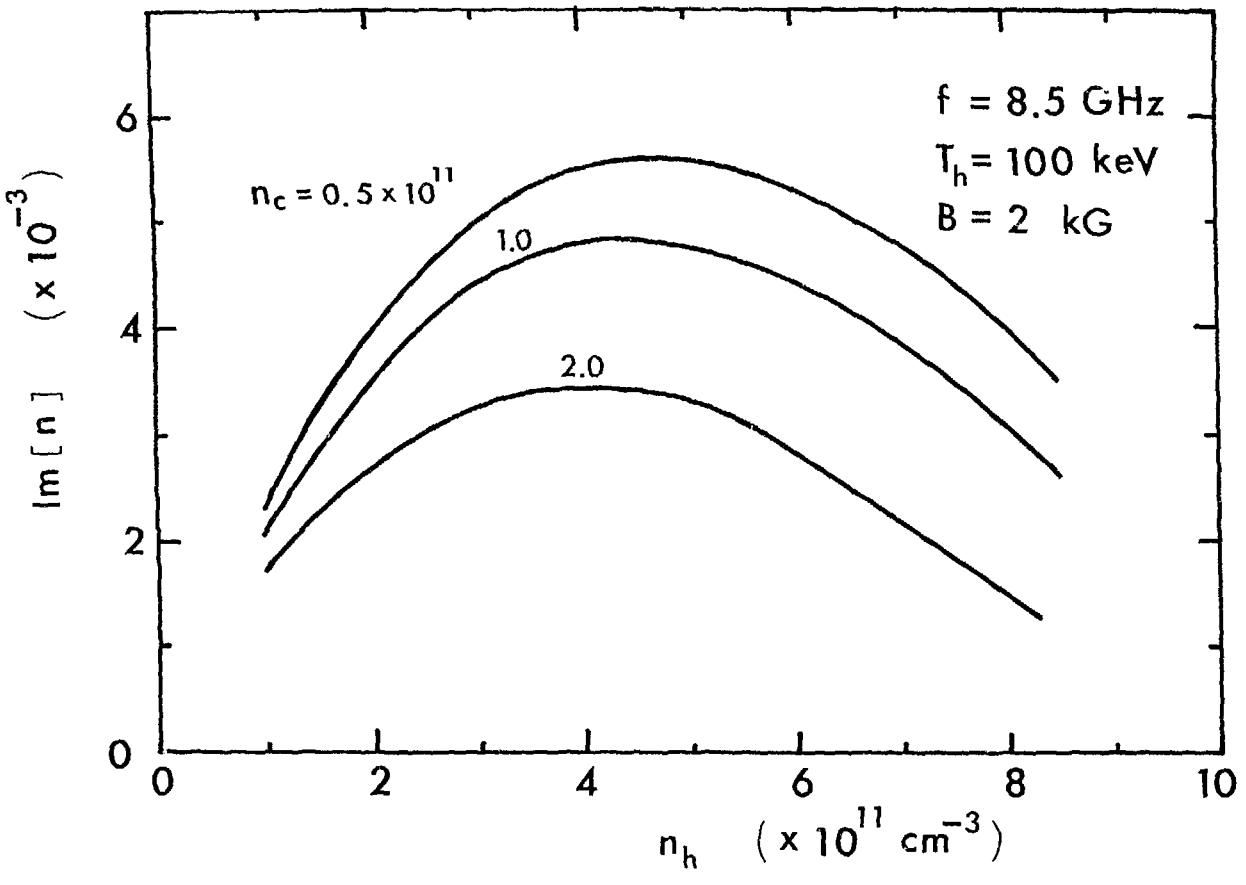

Fig.6 Imaginary part of refractive index as a function of hot electron density for various density of cold electrons.

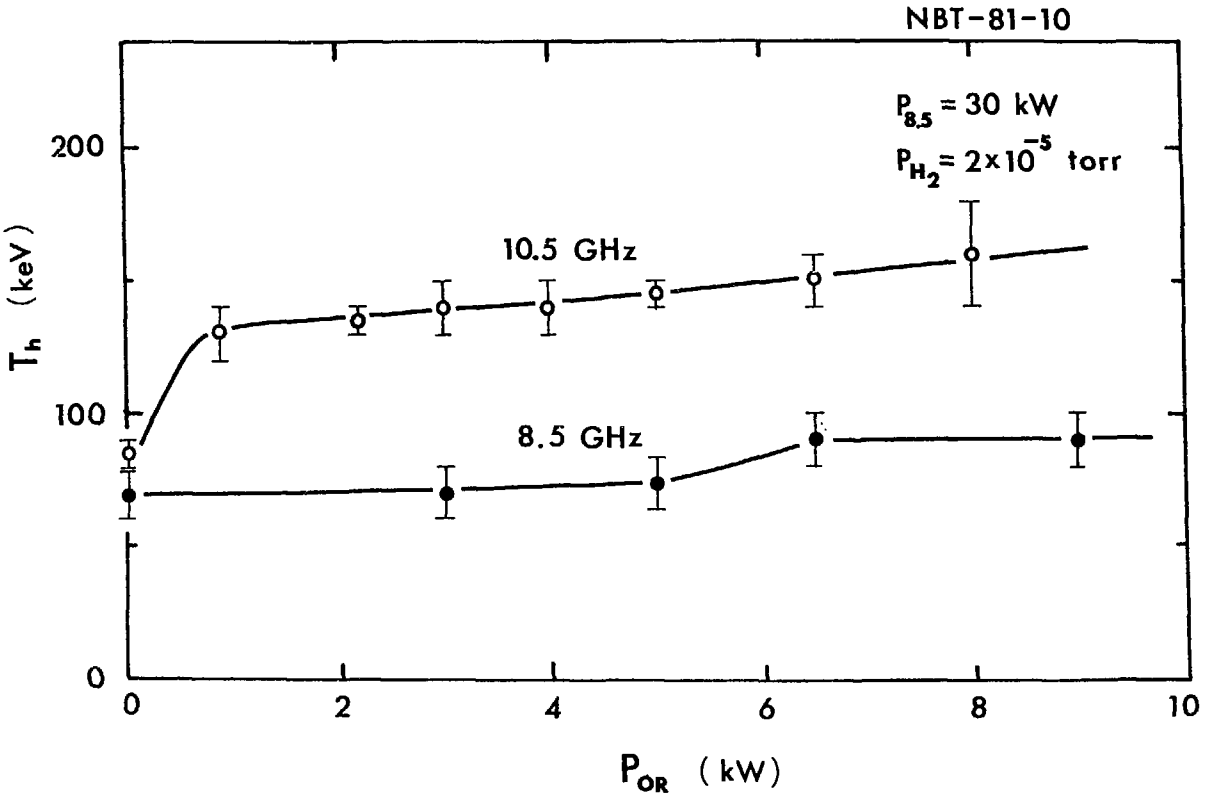

Fig.7 Effect of multifrequency heating on the hot electron temperature as a function of input microwave power (per cavity). Base microwave power of 30 kW (1.25 kW/cavity) at a frequency 8.5 GHz is fed to the plasma.

BLOCK DIAGRAM OF MICROWAVE CIRCUIT

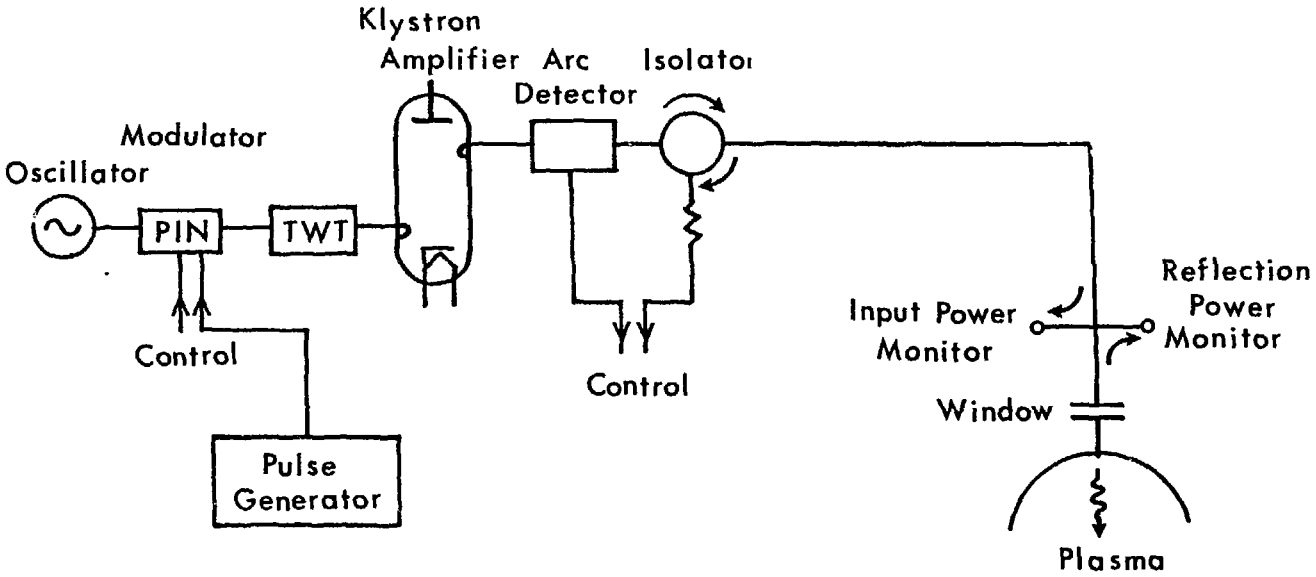

Fig.8 Block diagram of microwave circuit used in the hot ring decay measurement.

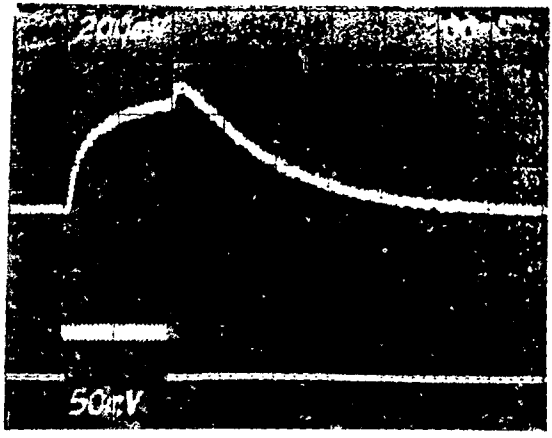

Fig.9 Decay of radiation intensity (upper trace) with 400 msec microwave pulse (bottom trace). Input microwave pulse is 4.5 kW.

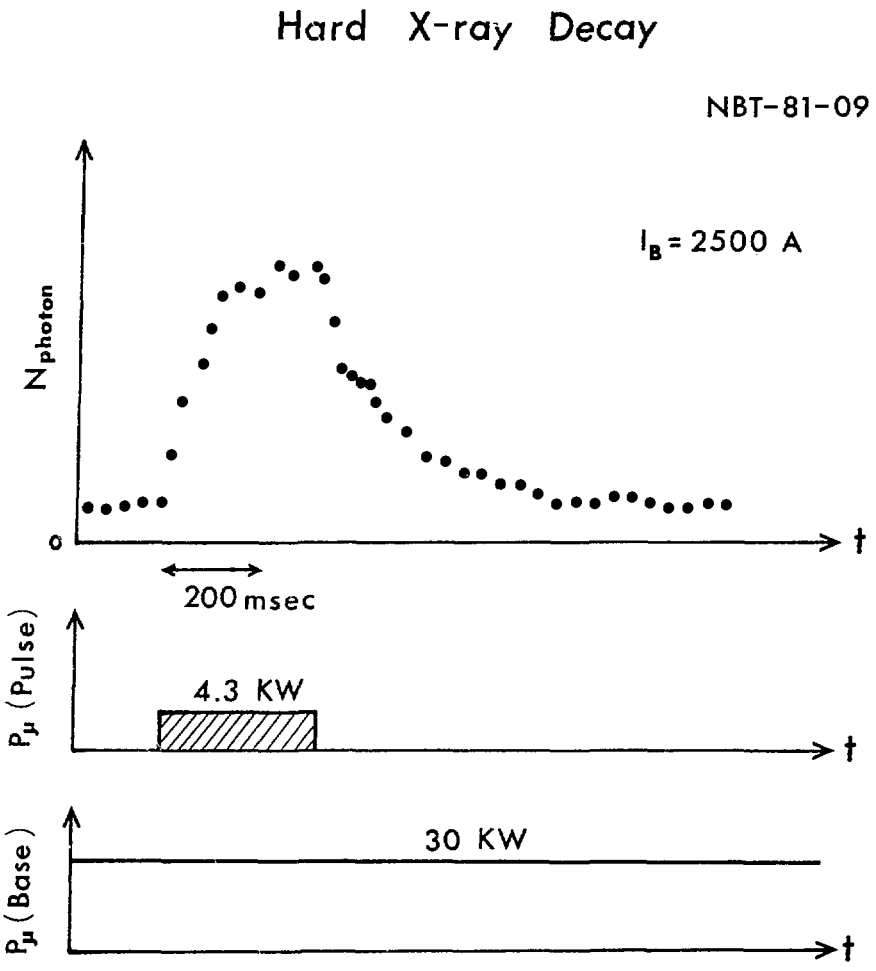

Fig.10 Time development of hard X-ray bremsstrahlung with 4.3 kW microwave pulse.

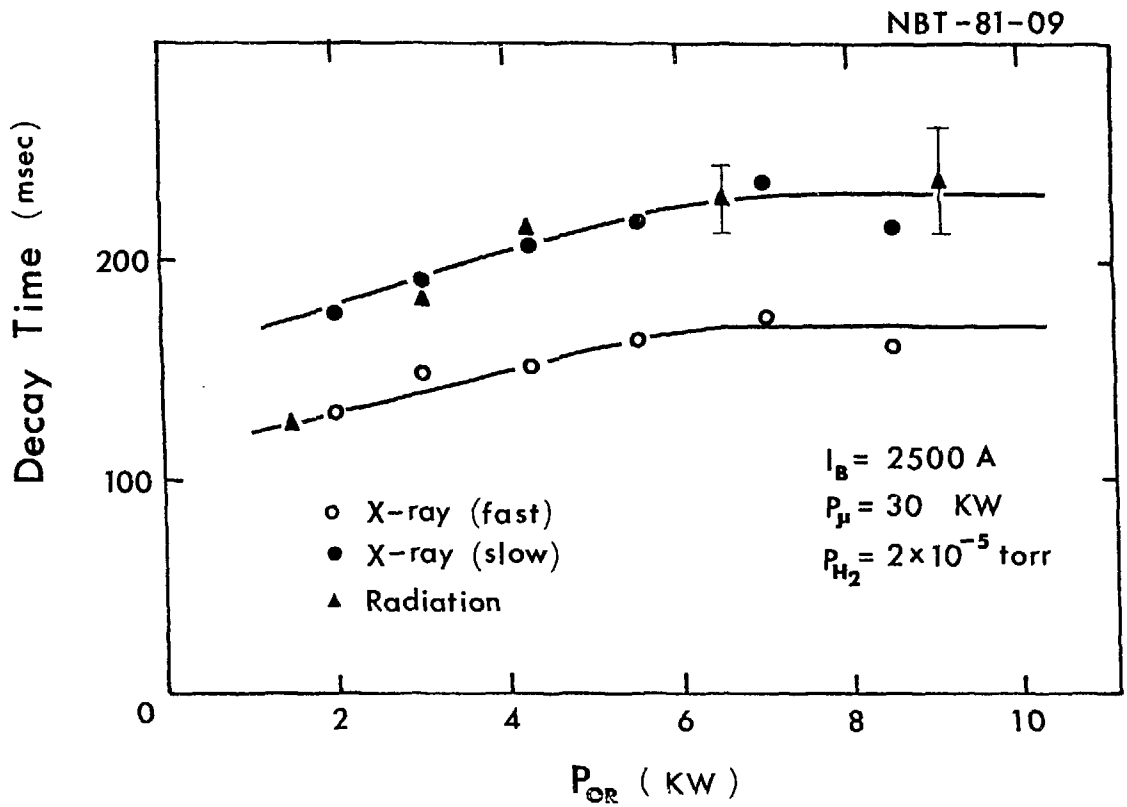

Fig.11 Hard X-ray and synchrotron radiation decay time as a function of input microwave power (per cavity).

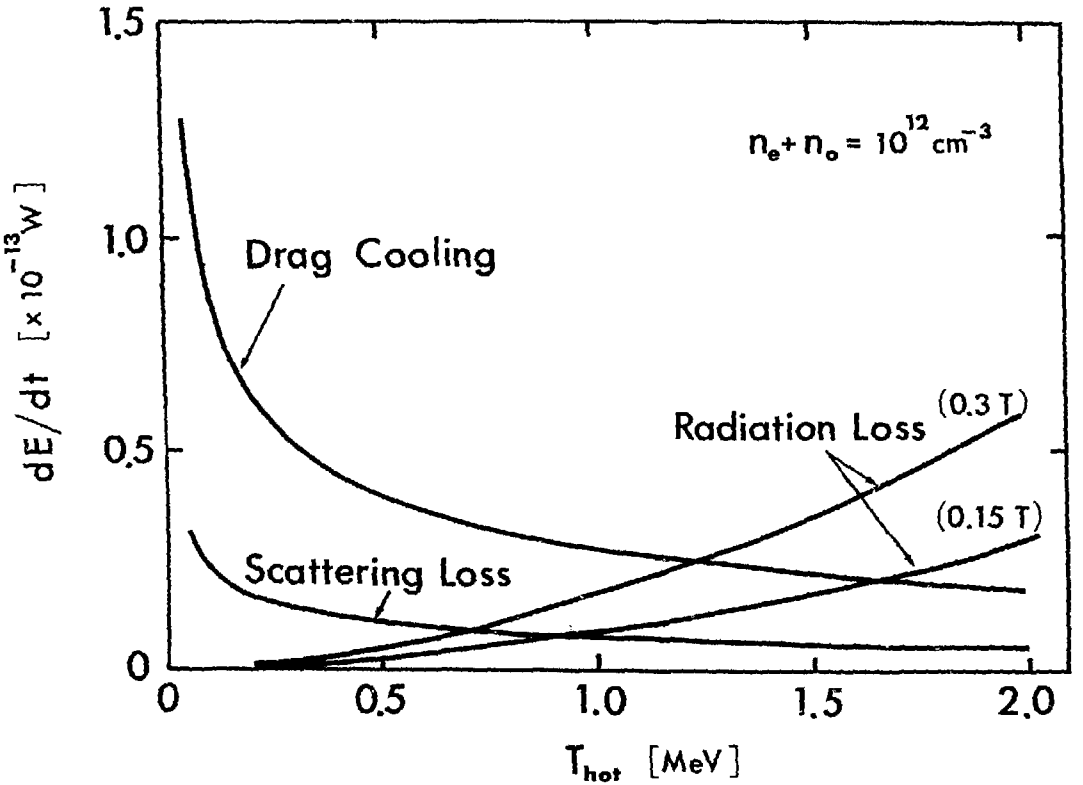

Fig.12 Energy loss rate of hot electron as a function of hot electron energy. Total target electrons are assumed to be 1×10^{12} cm^{-3}.

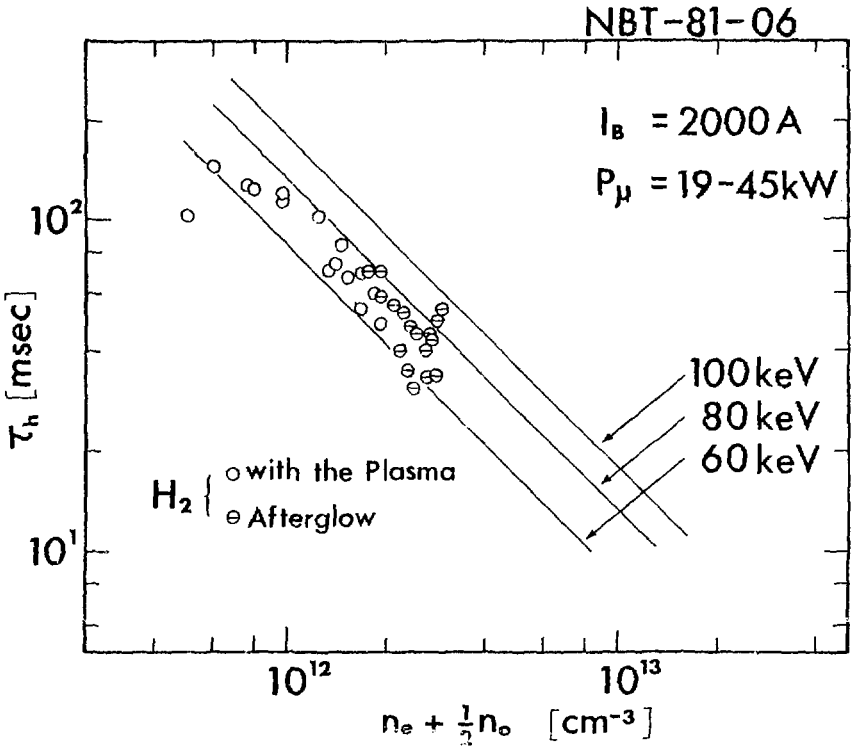

Fig.13 Hot ring decay time as a function of number density of target cold electrons. Calculated values with typical hot ring temperature are shown for comparison (solid lines).

RING TEMPERATURE SCALING*

N. A. Uckan
Oak Ridge National Laboratory
Oak Ridge, Tennessee 37830

ABSTRACT

During the last two decades the production of high-beta, hot electron plasmas with electron cyclotron heating (ECH) has been amply demonstrated in open and closed geometries. A wide variety of conditions was present in these experiments with a factor of 2 change in device dimensions and more than an order of magnitude change in magnetic fields ($\sim$1-10 kG), ECH frequencies ($\sim$6-55 GHz), and hot electron temperatures ($\sim$50-1200 keV). An analysis of the data from all the experiments that used single ECH frequency indicates that the hot electron temperatures do increase with magnetic field strength (or, equivalently, ECH frequency) and scale length. In particular, they all obey $\rho/L \approx$ constant ($\sim 5\text{-}6 \times 10^{-2}$) scaling, where ρ and L are the hot electron gyroradius (relativistic) and the magnetic field scale length, respectively. This is roughly the value at which conservation of the adiabatic invariant μ begins to break down and suggests that the hot electron temperatures are probably limited by nonadiabatic particle behavior. Results, primarily from hot electron ring experiments (ELMO, EBT, NBT, etc.), are discussed, and projections for future experiments are given. It is shown that although in all previous experiments the ring temperature is determined by the ρ/L criterion EBT-P will be the first experiment unconstrained by this limit.

*Research sponsored by the Office of Fusion Energy, U.S. Department of Energy, under contract W-7405-eng-26 with the Union Carbide Corporation.

I. INTRODUCTION

Nearly two decades of experimental investigations exist on energetic electron plasmas in open (simple and minimum-B mirrors) and closed (bumpy tori) geometries.[1-24] The high-beta, hot electron plasmas in these experiments are produced by electron cyclotron heating (ECH). A wide variety of conditions was present in these devices along with a variety of purposes and goals in the conduct of the experiments. For example, some of the experiments in minimum-B mirrors[6,12-13] (IMP, INTEREM, etc.) were directed toward providing a target plasma for effective neutral injection, whereas some of the simple mirror experiments[1-11] (PTF, ELMO, TPM, etc.) were directed toward gaining a general understanding of heating, equilibrium, and stability of hot electron plasmas. It was first observed in ELMO[5-8] that the high-beta, hot electron plasmas have the maximum plasma energy density located around the magnetic axis in the form of an annulus (ring). These rings were macroscopically stable, and the diamagnetic currents produced were strong enough to create a local magnetic well. If the ring beta is sufficiently high, the local magnetic wells produced by these rings stabilize the toroidally confined plasma (an average minimum-B stabilization[25]) in the bumpy torus, as was first demonstrated in the ELMO Bumpy Torus[1,16] (EBT) and then in the Nagoya Bumpy Torus[1,19] (NBT). In tandem mirror experiments the use of ECH hot electron plasmas (discs) are also considered to form thermal barriers and potential plugs in the end cells.[26-28]

In recent years, the high-beta, hot electron rings (or discs) have become of great interest because of the key role they play in the EBT concept and in thermal barriers for mirror machines. The existence of stable equilibrium for these hot electrons and the ability to maintain them with sufficiently low amounts of ECH power are central to the successful operation of present and planned experiments and to the viability of reactors. Routine production of the hot electron rings has been amply demonstrated in both simple mirror and EBT experiments, and their formation and stability will not be discussed here. The temperature of these hot electrons is important both in stability[29] and

in power balance,[30-31] and it is the purpose of this paper to deduce the temperature scaling of these hot electrons from the experimental data.

Compilation of data from more than a dozen experiments is given in Sec. II. In these experiments the hot electron plasma was normally generated with a single frequency microwave power though in some cases multiple ECH frequencies were also used. An analysis of data from all these experiments shows that the limiting hot electron (ring) temperature scales such that ρ/L = constant, where ρ is the relativistic hot electron gyroradius and L is the characteristic magnetic field scale length. Projection of this scaling to future experiments is discussed in Sec. III.

II. COMPILATION OF EXPERIMENTAL DATA

There is a wealth of information on hot electron ECH plasmas from more than a dozen experiments, as indicated in Table I. Listed in Table I, in chronological order, are only those devices that have some relevance or similarity to EBT (or the tandem mirror). These devices include simple (PTF,[2-4] EPA,[4] ELMO,[5-8] TPM,[10-11]) and minimum-B (INTEREM,[6,12-13] CIRCE[14]) mirrors, a canted mirror (CMF[5,13,18]), a symmetric tandem mirror (STM[23-24]), and bumpy tori (EBT-I,[1,16-18] EBT-S,[18,20-22] NBT[1,19]). The common feature of the experiments is that they were all performed to produce hot electron plasmas (though for different purposes) and were relatively free of gross macro- or microinstabilities. Most of these experiments have had a similar device size and comparable mirror ratios (~2 ∓ 0.2) with the exception of INTEREM and STM, which were twice as large, and ELMO, which had a variable mirror ratio (~1.6-2.6). In addition, as can be seen from Table I, a wide variety of conditions was present in these experiments with more than an order of magnitude change in magnetic fields (~1-10 kG), ECH frequencies (~2.4-55 GHz), and hot electron temperatures (~10-1300 keV).

Figure 1 represents the experimental data graphically, in that the hot electron (ring) temperatures are shown for each of the experiments listed in Table I as functions of the magnetic field. The values of the magnetic field in Fig. 1 are the magnetic field strengths near where the population of the hot electrons or rings is observed. In the case of hot electron ring experiments (ELMO, CMF, EBT-I/S, NBT, STM, etc.), rings were observed to form at the location of the second harmonic ($\omega \sim 2\omega_{ce}$) resonance in the midplane. However, it was also possible to form the rings with first harmonic heating.[19] Most of the data shown in Fig. 1 are for a single frequency heating. In terms of the hot electron temperature and its variation with operating conditions, results from several experiments (EBT-I/S, NBT, STM, etc.) were not any different for multiple ECH frequencies than for a single frequency if the magnetic field strengths were kept the same.

An analysis of the data (listed in Table I and shown in Fig. 1) from all these ECH hot electron plasma experiments indicates that the hot electron temperatures do increase with magnetic field strength (or, equivalently, ECH frequency, $B \sim f$) and scale length ($\sim$ device dimension) and that temperatures are nearly independent of operating conditions (i.e., power levels, etc.). As can be seen from Fig. 1, the hot electron gyroradius ρ_e ($= 1.7 \times 10^{-3}\sqrt{\gamma^2-1}/B$, in mks units) is nearly constant for similar size devices (i.e., $\rho_e \simeq 0.5$-0.6 cm for EBT, NBT, ELMO, etc., and $\rho_e \simeq 1.2$ cm for STM, INTEREM, etc.). By defining a dimensionless quantity ρ/L (where L is the magnetic field scale length), one can eliminate the size dependence and find that in all cases the hot electron (ring) temperature scales with a simple "scaling law:"

$$\rho/L = \text{constant} \simeq 5\text{-}6 \times 10^{-2} \quad .$$

This is roughly the value at which conservation of adiabatic invariant μ begins to break down and suggests[32] that the hot electron temperatures are probably limited by nonadiabatic particle behavior.

III. EXTRAPOLATION OF ρ/L SCALING TO FUTURE EXPERIMENTS

The ring temperatures, as discussed in the previous section, in past (ELMO, CMF, EBT-I, etc.) and present (EBT-S, NBT, STM, etc.) experiments are all determined by the ρ/L criterion; only a small variation is observed (<20%). The projection of this limit to future experiments (such as EBT-P,[33] reactor,[34] etc.), however, requires more than just straightforward extrapolation of ρ/L; it requires some knowledge of ring properties and characteristics of ring losses.

The ring power losses in EBT experiments are observed to scale classically,[1,18,31] and the dominant ring losses are identified[1,30] as drag cooling, scattering, and synchrotron radiation. For hot electron temperatures characteristic of past and present experiments ($T < 1$ MeV), drag losses dominate (decreasing as $T^{-1/2}$). At high energies ($T \gtrsim 2$ MeV) accelerated ring cooling occurs due to synchrotron radiation. Hence, the resulting loss rate has a broad minimum (near $T \sim 1$ MeV) that is bounded by these loss mechanisms. Assuming classical losses, Fig. 2 shows the energy loss rate as a function of hot electron (ring) temperature indicating this minimum. Also shown in the hatched region are the limits of ρ/L scaling (adiabatic energy limit) for some of the ring experiments (ELMO, EBT-I, and EBT-S); the limit for EBT-P is indicated with a vertical line.

All of the ECH experiments to date have been operated to the left of the minimum in the energy loss curve shown in Fig. 2 where drag losses dominate (only in the ELMO experiment did synchrotron radiation have a significant contribution), and ring energies are limited by the ρ/L scaling given in Fig. 1. However, if the same limit is to apply to EBT-P (or to the EBT reactor), one finds the ring temperature to be in excess of 3 MeV (or 30 MeV), which is above the temperature corresponding to the minimum in the energy loss curve where radiation losses dominate. Thus, one should expect that the temperature in these future large devices should be close to the minimum in the energy loss curve and should not be determined by the adiabatic limit. On the other hand if enough power is available to overcome the synchrotron losses, it may be possible to vary the ring temperature and observe scaling characteristics in this regime as well.

IV. CONCLUSIONS

From the compilation of data of many ECH hot electron plasma experiments in mirrors and bumpy tori, it is found that a temperature limit exists and that in all cases the limiting hot electron temperature obeys ρ/L = constant scaling. It is also observed that although the temperatures increase with magnetic field and with scale length they are nearly independent of other operating parameters (such as power, etc.). These results cover a factor of 2 in device dimensions and an order of magnitude in operating magnetic field strength.

ACKNOWLEDGMENTS

The author gratefully acknowledges numerous discussions with R. A. Dandl during the initial phases of this study in 1979. Thanks are also due to W. B. Ard, L. A. Berry, G. E. Guest, G. R. Haste, C. L. Hedrick, and N. A. Krall for comments and criticisms as well as for careful review of the findings of the study. Although the original work was completed in 1980, it was necessary to await for the results from EBT-S and STM (which were operated and obtained results in 1980-1981) to verify the validity of the ρ/L scaling.

REFERENCES

1. N. A. Uckan, ed., EBT Ring Physics Proceedings of Workshop, (Oak Ridge National Laboratory, Oak Ridge, 1980), and papers published therein.

2. W. B. Ard and R. A. Dandl, Proceedings of 6th International Conference on Ionization Phenomena in Gases, Vol. 4, 75 (1963).

3. W. B. Ard et al., Phys. Fluids 9, 1498 (1966).

4. R. A. Dandl et al., Nucl. Fusion 4, 344 (1964).

5. R. A. Dandl et al., in Relativistic Plasmas, edited by O. Buneman and W. B. Pardo, (Benjamin, New York, 1968), p. 181.

6. R. A. Dandl et al., in Plasma Physics and Controlled Nuclear Fusion Research (IAEA, Vienna, 1969) Vol. 2, p. 435.

7. R. A. Dandl et al., Nucl. Fusion 11, 411 (1971).

8. R. A. Dandl et al., in Plasma Physics and Controlled Nuclear Fusion Research (IAEA, Vienna, 1972), Vol. 2, p. 607.

9. H. Ikegami et al., Phys. Rev. Lett. 19, 778 (1967).

10. H. Ikegami et al., Phys. Fluids 11, 1061 (1968).

11. H. Ikegami et al., Nucl. Fusion 13, 351 (1973).

12. G. R. Haste, in Feedback and Control of Plasma edited by T. K. Chu and W. W. Hendel (American Institute of Physics, New York, 1970).

13. W. B. Ard et al., in Plasma Physics and Controlled Nuclear Fusion Research (IAEA, Vienna, 1972) Vol. 2, p. 619.

14. R. A. Dandl et al., Nucl. Fusion 13, 693 (1973).

15. R. Bardet et al., Nucl. Fusion 15, 865 (1975).

16. R. A. Dandl et al., in Plasma Physics and Controlled Nuclear Fusion Research (IAEA, Vienna, 1975), Vol. 2, p. 141; (1977) Vol. 2, p. 145; (1979) Vol. 2, p. 365.

17. R. A. Dandl et al., Oak Ridge National Laboratory Report ORNL/TM-6457, 1978.

18. N. A. Uckan et al., in Plasma Physics and Controlled Nuclear Fusion Research (IAEA, Vienna, 1981), Vol. 1, p. 831.

19. M. Fujiwara et al., in Plasma Physics and Controlled Nuclear Fusion Research (IAEA, Vienna, 1981), Vol. 1, p. 845.

20. G. R. Haste, Bull. Am. Phys. Soc. 25, 921 (1980).

21. D. L. Hillis and G. R. Haste, Bull. Am. Phys. Soc. 26, 979 (1981).

22. N. A. Uckan, Proceedings 10th Conference on Controlled Fusion and Plasma Physics (Moscow, 1982), Vol. 2; Oak Ridge National Laboratory Report ORNL/TM-8006, 1982).

23. B. H. Quon et al., Bull. Am. Phys. Soc. 25, 994 (1980); Bull. Am. Phys. Soc. 26, 893 (1981).

24. N. H. Lazar et al., Bull. Am. Phys. Soc. 25, 993 (1980).

25. D. B. Nelson and C. L. Hedrick, Nucl. Fusion 19, 283 (1979); G. E. Guest, C. L. Hedrick, and D. B. Nelson, Phys. Fluids 18, 871 (1975).

26. D. E. Baldwin and B. G. Logan, Phys. Rev. Lett. 43, 1318 (1979).

27. G. A. Carlson et al., Lawrence Livermore Laboratory Report UCRL-52836, 1979.

28. B. W. Stallard et al., Lawrence Livermore National Laboratory Report UCRL-86826, 1981.

29. N. A. Uckan, ed., EBT Stability Theory, Proceedings of Workshop (Oak Ridge National Laboratory, Oak Ridge, 1981), and papers published therein.

30. S. K. Borowski et al., Nucl. Fusion 20, 177 (1980).

31. G. R. Haste, Bull. Am. Phys. Soc. 26, 979 (1981).

32. R. H. Cohen, G. Rowlands, and J. H. Foote, Phys. Fluids 21, 627 (1978).

33. "EBT-P Proposed Reference Design," Oak Ridge National Laboratory Report ORNL/TM-7191, 1980.

34. N. A. Uckan, Nucl. Eng. Des. 63, 271 (1981).

TABLE I. Hot electron ECH plasma experiments.

Chronology	Device	Reference(s)	Pulsed or steady state (cw)	ECH frequency (GHz)	Magnetic field[a] (kG)	Hot electron temperature (keV)
Early 60's	PTF	[2-4]	cw	2.4	~0.4	~10
				10.6	~1.5	~50-100
	EPA	[4]	cw	10.6	~1.9	~80-120
Mid 60's	ELMO	[5-8]	cw	35.7	~6.4	~600-800
				55.0	~9.5	~1000-1300
	TPM	[9-11]	pulsed	6.4	~1.1	~50
Late 60's	INTEREM	[6,12-13]	cw	10.6	~3.8	~600-800
Early 70's	CMF	[5,8,14]	cw	10.6	~1.9	~100
				35.7	~6.4	~500-700
	CIRCE	[15]	pulsed	8.0	~1.4	~100
Mid 70's	EBT-I	[16-18]	cw	18.0	~3.2	~180-230
Late 70's	NBT	[19]	pulsed	8.5	~1.5	~80
Early 80's				(8.5)[b]	~3.0	(~160)[b]
	EBT-S	[18,20-22]	cw	28.0	~5.0	~450-550
	STM	[23-24]	pulsed/cw	8.3-10.2[c]	~1.5-1.7	~250-350

[a]Magnetic field strength near where the population of hot electrons (or rings) are observed.

[b]Rings are formed with fundamental resonance heating.

[c]Multiple ECH frequencies are used (8.3, 9.2, 9.5, and 10.2 GHz).

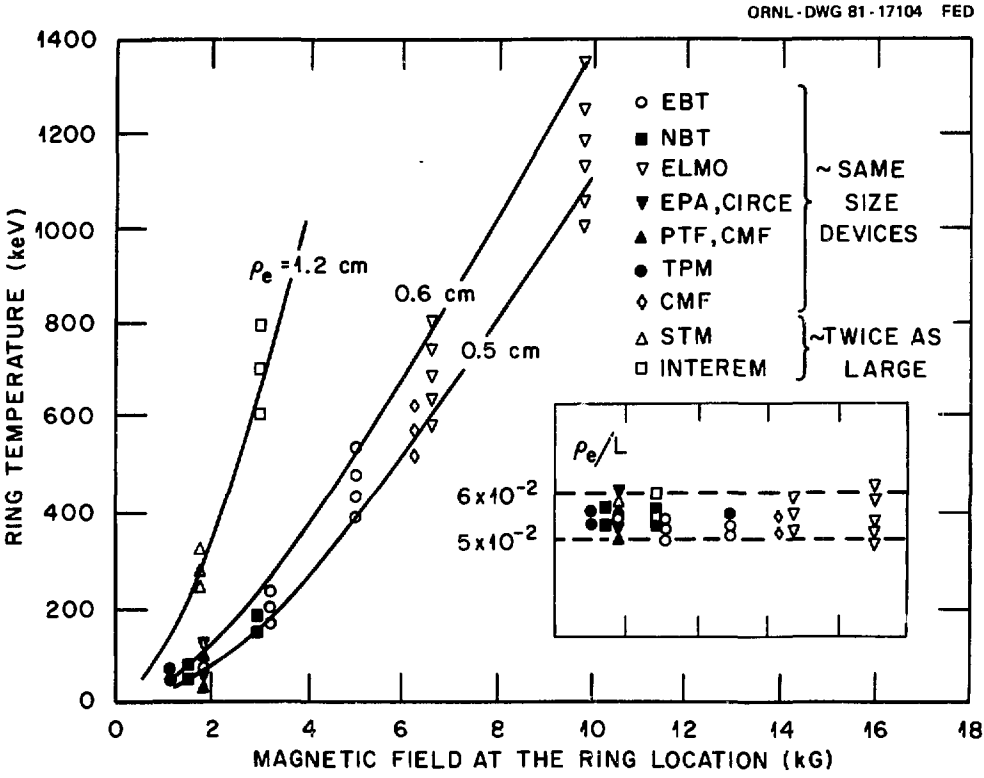

FIG. 1. Compilation of data from all ECH hot electron (ring) plasma experiments; hot electron (ring) temperature vs magnetic field at the location of the hot electrons (rings). Solid lines are for constant hot electron gyroradius ρ_e. Data from these experiments indicate that the hot electron (ring) temperatures obey a simple scaling law: ρ_e/L = constant (≈ 5–6×10^{-2}), where L is the magnetic field scale length. Insert in lower right-hand corner (ρ_e/L vs magnetic field) shows this scaling.

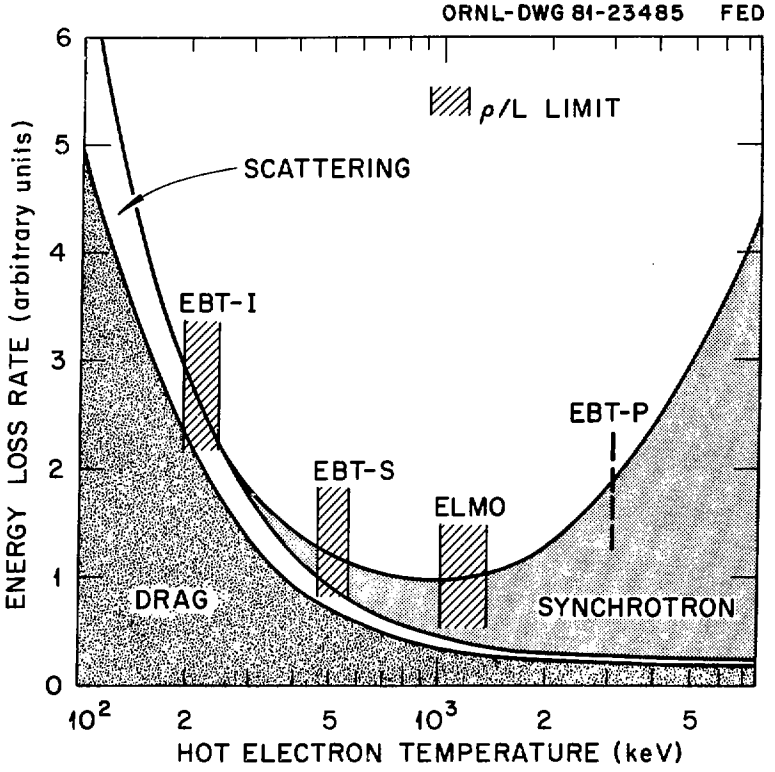

FIG. 2. Energy loss rate (in arbitrary units) as a function of hot electron temperature. Normalization constant is $\sim V\beta B^{1/2}$, where V and β are the volume and beta of the hot electrons and B is the magnetic field. Shown (hatched) are the limits of ρ/L scaling for EBT-I, EBT-S, and ELMO. (The vertical line is the limit for EBT-P.)

PARAMETRIC STUDY OF THE RELATIVISTIC ELECTRON RING

S. Hamasaki, N. A. Krall, and J. L. Sperling
JAYCOR, P. O. Box 85154, San Diego, California 92138

ABSTRACT

In the JAYCOR relativistic ring model, appropriate moments of the relativistic electron kinetic equation are used to determine the steady-state ring parameters by equating the microwave heating and the losses associated with various processes including collisions, synchrotron radiation, loss of adiabaticity, and microinstabilities. The model has the flexibility to permit the evaluation of the role that various combinations of loss processes play on steady-state ring parameters and the energy balance. For example, it is demonstrated that collisions and synchrotron radiation alone cannot account for the experimental ring temperatures in present bumpy tori, but the combination of collisions, synchrotron radiation, nonadiabaticity, and whistler turbulence provides a better comparison with present experiments. The ring model has been applied to larger projected bumpy tori (e.g., EBT-P and EBT-R). Collisions and synchrotron radiation are shown to play a relatively more significant role in the ring dynamics in these larger bumpy tori than in present-day smaller devices.

1. ELECTRON RING MODEL

1.1 INTRODUCTION

The bumpy torus is a fusion-oriented device which consists of a toroidally linked set of simple mirror sections.[1-6] A central feature of the bumpy torus concept is the formation in each mirror section of an annulus of relativistic electrons through irradiation of the plasma with microwaves. The significance of the annuli is their diamagnetic modification of the bumpy torus magnetic fields and the consequent stability of the bulk toroidal plasma.[2-9] Without the relativistic annuli the bumpy torus could not contain a stable plasma. The success of the bumpy torus concept as a reactor depends critically on the ability to minimize the energy required to form and sustain relativistic electron annuli sufficient to provide the magnetohydrodynamic stability of the core plasma.

In this paper we calculate the balance between microwave heating and loss processes consistent with an assumed form for the relativistic electron distribution function which permits consideration of anisotropy and loss-cone effects. In doing so, we have adopted our own unique approach.[10,11] Here, we indicate the advantages of our ring model relative to ray-tracing and Fokker-Planck calculations and also outline the methodology of the model. The interested reader is referred to Appendix A and Refs. 10 and 11 for additional details and explicit formulation.

In ray-tracing, the spatial deposition of wave energy is determined by following the ray self-consistently,[12] but the temperature of the electron ring is assumed rather than being calculated self-consistently. On the other hand, the Fokker-Planck approach addresses how the electron ring distribution can be heated by microwaves locally,[13] but it is quite out of the scope of this approach to investigate how the electron annuli behave as a whole, in a nonlocal way, as the relativistic electrons travel along magnetic field

lines and undergo acceleration and deceleration forces which are a function of spatial position. Our analysis of the electron rings addresses the questions relating to self-consistent calculation of temperature and nonlocal effects. Our approach to the question of the electron ring energetics can be summarized in the following way. We approximate the EBT-geometry as a straight bumpy cylinder, and so ring electrons drift around the mirror axis concentrically as they travel back and forth along field lines between their mirroring points. The electrons confined to a concentric drift surface form a single basic unit which is described by a distribution function with two temperature parameters, $T_\perp$ and $T_\parallel$. Most of the electrons of this basic unit are trapped, and as a consequence, the fraction of the electrons which reach a specific location along a field line decreases as the distance increases from the midplane in the EBT geometry. At each location along a field line, some fraction of the ring electrons can either gain or lose energy. By comparing the total microwave heating with the total losses on a specific drift surface, we obtain the "net" energy gain or loss for each unit of the ring. The steady-state ring distribution function for the unit is obtained by balancing the energy gain with the energy loss. At this steady-state point we have a self-consistent estimate of the ring parameters with the associated microwave heating and energy loss rates at specific radial points (drift surfaces).

A variety of different loss mechanisms can be included within the framework of the ring model. Our early calculations, which included only classical processes, i.e., collisions and synchrotron radiation, showed a clear discrepancy with experimental measurement of electron rings.[11] Without a loss cone, the combination of microwave heating and assumed loss processes resulted in a relativistic electron distribution function with much larger parallel than perpendicular pressure. The model results compared favorably with the observation of relativistic passing electrons but not with diamagnetic electron rings.[6] With a loss cone, the perpendicular pressure

is automatically larger than parallel pressure in agreement with ring measurements, but collisions and synchrotron radiation still do not account for the observed scaling of ring temperature for two reasons.[11] First, the classical model suggests that the perpendicular temperature in EBT-1 is larger than in EBT-S because of the larger synchrotron losses in the higher magnetic field environment of EBT-S. This contrasts with observations which indicate higher perpendicular temperature in EBT-S than in EBT-1.[14,15] Second, the model gives perpendicular electron temperatures which tend to be larger (i.e., $\lesssim$ 1 MeV) and more sensitive to microwave power than actually observed. Experiments show an insensitivity to microwave power for perpendicular temperatures above $\sim$200 keV and $\sim$500 keV in EBT-1 and EBT-S, respectively.[14,15]

The ring model demonstrates that additional processes, besides collisions and synchrotron radiation, contribute to ring dynamics. The loss of adiabaticity for very high energy electrons[15] and electromagnetic turbulence (i.e., whistlers)[11,16] have been proposed as additional mechanisms influencing ring performance. To assess their impact, nonadiabaticity and whistler turbulence have been included in the ring model.

1.2 NONADIABATICITY MODEL

Numerical studies of nonadiabatic electron motion[17-19] show that a rather sharp transition occurs from adiabatic to nonadiabatic behavior as the parameter $\lambda = \rho/L$ is increased. Here, $\rho = v/\Omega$ is the electron gyroradius for speed, v, and L is the radius of curvatures. The magnetic moment of an electron, μ, undergoes jumps usually when the particle passes through the point of minimum (maximum) magnetic field strength on its guiding-center trajectory. The sign of the jump, $\Delta\mu$, depends on the gyrophase of the electron at the minimum- (maximum-) point. The mean square quantity, $\langle\Delta\mu\rangle^2$, averaged over gyroradius, can be expressed as[17-19]

$$\frac{\langle\Delta\mu\rangle^2}{\mu^2} = A\,\frac{v^2}{v_{\perp o}^{\;2}}\;\exp\left[-2\;K(v^2/v_{\perp o}^{\;2})\;\frac{L}{\rho}\right] \tag{1}$$

where v, $v_{\perp o}$ is the electron speed and its perpendicular component at the minimum (maximum) point of magnetic field strength. The coefficient A is roughly constant, $A \approx 4$. The value of $K(v^2/v_{\perp o}^{\;2})$ is a strong function of electron pitch angle, especially for trapped electrons, $v^2/v_\perp^{\;2} < 2$. The value of $K(v^2/v_{\perp o}^{\;2})$ increases with the pitch angle, i.e., $K(v^2/v_{\perp o}^{\;2}) \gg 1$ for $(v/v_{\perp o})^2 \to 1$. $K(v^2/v_{\perp o}^{\;2})$ is roughly constant (of the order of 1) for the regime $(v/v_{\perp o})^2 > 4$. The magnetic moment jumps are quite important in the analysis of the electron ring. As the ring temperature increases, the originally trapped hot electrons can be pushed into loss cones as a result of the nonadiabatic magnetic moment jumps.

A velocity space diffusion operator has previously been developed for the nonrelativistic limit using a Fokker-Planck formalism.[17] This operator is readily extrapolatable to relativistic energies because particle energy is unchanged by the nonadiabatic changes in magnetic moment. Specifically, for present purposes, we need only replace the nonrelativistic mass, m_0, by the relativistic mass, $m_0\gamma$, in the diffusion operation. The parameter γ is defined by

$$\gamma = (1 - v^2/c^2)^{-\frac{1}{2}}$$

for particle speed, v, and speed of light, c. According to Ref. 17, the diffusion operator describing nonadiabaticity effects, N, has the following form,

$$N(\mu,\varepsilon)f = \frac{\partial}{\partial\mu}\left(\frac{\langle(\Delta\mu)^2\rangle}{2\Delta t}\;\frac{\partial f}{\partial\mu}\right) \quad . \tag{2}$$

with f the velocity distribution function and Δt the bounce period.

For application to the ring model, it proved useful to rewrite Eq. (2) in terms of electron momentum components at the midplane. In particular,

$$N(p_\perp, p_\parallel)f = \left(\frac{p_{\parallel o}}{p_{\perp o}}\frac{\partial}{\partial p_{\perp o}} - \frac{\partial}{\partial p_{\parallel o}}\right)\frac{<(\Delta\mu)^2>}{2\Delta t}\;\frac{\gamma^2 m^2 B_o^{\,2}}{p_{\parallel o}^{\,2}}$$

$$\left(\frac{p_{\parallel o}}{p_{\perp o}}\frac{\partial}{\partial p_{\perp o}} - \frac{\partial}{\partial p_{\parallel o}}\right) f(p_{\perp o}, p_{\parallel o}) \quad , \tag{3}$$

with

$$p_{\perp o} = m\gamma v_{\perp o} \quad , \qquad p_{\parallel o} = m\gamma v_{\parallel o} \quad , \tag{4}$$

and the parallel midplane velocity, $v_{\parallel o}$.

1.3 WHISTLER MODEL

Electromagnetic whistler turbulence can be driven linearly unstable in plasmas where the perpendicular pressure is larger than the parallel pressure. The anisotropic relativistic electron ring can cause the whistler instability with a cold, isotropic, plasma background.[20] Relativistic effects reduce the growth rate but do not entirely stabilize the instability.[20] The whistler mode interacts with the electron ring by reducing the ring temperature anisotropy. This temperature relaxation is significant not only because it leads to direct particle loss into the loss cone, but also because it reduces electron pitch angle. High energy ring electrons whose pitch angles are not too large are preferentially affected by nonadiabatic scattering.

The whistler contribution to the ring model is constructed in the following way. The whistler real frequency, ω', which

corresponds to maximum growth is approximately determined by the relativistic generalization of Eq. (11) of Ref. 21,

$$\omega' = \frac{eB_o}{m_o c} \left(1 - \frac{T_\parallel}{T_\perp}\right) / \bar{\gamma} \quad , \tag{5}$$

with

$$\bar{\gamma} = \left[1 + 3 \frac{(T_\perp + T_\parallel)}{m_o c^2}\right] \quad . \tag{6}$$

Here, $T_\parallel$ and $T_\perp$ are the parallel and perpendicular temperatures, respectively. Although Eqs. (5) and (6) are somewhat ad hoc, the final results with respect to the ring model are not substantially changed by a somewhat different choice of frequency. Next, substitution of Eq. (5) into the cold plasma dispersion relation for exact parallel propagation, permits evaluation of the parallel wavenumber.[10-12] Only modes with parallel wavelengths smaller than the axial length of the magnetic field lines in one mirror section are permitted. Substitution of the frequency and wavenumber for constant wave amplitude into the relativistic quasilinear operator provides us with an explicit way of including whistler effects into the ring model which is finally analogous to our treatment of microwave heating.[10,11]

2. NUMERICAL CALCULATION

2.1 RING CALCULATIONS WITH NONADIABATICITY AND WHISTLER

The steady-state electron ring temperatures are calculated by balancing the microwave heating rate with the various energy loss processes. As we include more relevant loss mechanisms into our model, the calculation should give more accurate estimates of ring

energy balance. As previously mentioned, if collisions and synchrotron radiation alone are considered, the model does not reproduce the experimentally obtained temperature scaling laws. Results of our numerical calculations, which include the nonadiabaticity plus the whistler turbulence effects, in addition to collision and synchrotron radiation, are shown here to give better comparison with experiment.

Figure 1 is a plot of steady-state perpendicular and parallel ring temperatures (i.e., $T_\perp$ and $T_\parallel$ in eV) versus whistler mode electric field amplitude squared, $|E_w|^2$ (10^{-4} ergs/cm^3), for the EBT-1 and EBT-S parameters given in Table I. For the quantitative calculations we consider the following dependences for $\langle\Delta\mu\rangle^2$, A = 4, L = 12 cm, and

$$K\left(\frac{v_{\perp o}^2}{v^2}\right) = \frac{0.80 + 0.0264\ (v_{\perp o}^2/v^2)}{1 - 0.983\ (v_{\perp o}^2/v^2)} \quad , \quad \Delta t = L/v \quad . \quad (7)$$

The function $K(v_\perp^2/v^2)$ is chosen so that K is monotonically increasing with the pitch angle, or $v_{\perp o}^2/v^2$, i.e., K(0) = 0.8, K($\frac{1}{2}$) = 1.6, and K(1) = 50.

The figure shows that with no whistler turbulence (i.e., $|E_w| = 0$), EBT-1 and EBT-S have comparable perpendicular temperatures and much smaller parallel temperatures, with the parallel temperature in EBT-1 being smaller than in EBT-S. These results can be explained in the following way. Electrons with very large pitch angles are very weakly affected by nonadiabatic changes in pitch angle. Their energy is limited, in the absence of whistler turbulence, primarily by collisions, a process which depends on particle energy but not magnetic field strength. Therefore, the perpendicular temperature comes out to be roughly equal in EBT-1 and EBT-S. On the other hand, since the overall energy balance is determined primarily by nonadiabatic particle leakage into the loss cone, the exponent in the

expression for $(\Delta\mu)^2$ in Eq. (1) must be roughly the same for EBT-1 and EBT-S, i.e.,

$$KL/\rho \approx \text{constant} \quad . \tag{8}$$

Since L and v are roughly the same in both devices, without whistler turbulence, then

$$KB_0 \approx \text{constant} \quad , \tag{9}$$

and $T_\perp/T_\parallel$ must be larger in EBT-1 than in EBT-S. This interpretation of the results has been verified by additional numerical studies with varying KL. The result is that $T_\perp$ remains constant but $T_\parallel$ changes. Collisions, synchrotron radiation, and nonadiabaticity alone cannot account for the empirical[14,15]

$$\rho \approx \text{constant} \tag{10}$$

scaling attributed to present ring experiments in bumpy tori. Without whistler turbulence, temperature ratio, but not absolute temperature, scales with the magnetic field in accordance with Eq. (9).

With a finite whistler electric field amplitude (i.e., $|E_w|^2 \gtrsim 1 \times 10^{-4}$ erg/cm^3), which can be much smaller than the applied extraordinary wave electric field amplitude (i.e., $|E|^2 \approx .02$ ergs/cm^3), the distribution functions for both EBT-1 and EBT-S become more isotropic because of pitch angle scattering by the whistler wave. Since very high energy electrons with oblique pitch angles are very rapidly lost because of nonadiabatic leakage, the overall perpendicular temperature must decrease and so reasonable power balance can be achieved. Figure 1 shows that the parallel temperature is not a strong function of whistler amplitude. The whistler relaxation process imposes an approximately,

$$\rho \approx \text{constant} \tag{11}$$

scaling for the perpendicular temperature of the ring. This is still consistent with the nonadiabaticity scaling given by Eq. (8) since the ratio of perpendicular to parallel temperature deduced from Figure 1 becomes more comparable for EBT-1 and EBT-S as the level of whistler turbulence increases. Hence, whereas the combination of collisions, synchrotron radiation, and nonadiabaticity alone cannot account for the gyroradius constant scaling empirically attributed to perpendicular ring temperature, the combination of nonadiabaticity, whistler turbulence, collisions, and synchrotron radiation does provide a very much better fit to the empirical scaling. Further numerical studies demonstrate that this result is not very sensitive to the choice of A, K, and L in Eq. (1).

2.2 ENERGY BALANCE FOR DIFFERENT BUMPY TORI

To estimate expected ring parameters and the relative significance of various loss processes on ring parameters, the ring model has been evaluated for different bumpy tori devices using the nominal set of parameters given by Table I.[1-6,22,23] The results, which are tabulated in Table II, illustrate two significant points. First, in previous or presently operating bumpy tori (e.g., NBT, EBT-0, EBT-1, and EBT-S), the power balance is determined primarily by the leakage associated with whistler turbulence and nonadiabaticity. Also, collisional damping, although somewhat less important than electron leakage, is still much more significant than synchrotron radiation damping. By contrast, collisional damping and synchrotron radiation clearly dominate the power loss rate in larger projected bumpy tori like EBT-P and EBT-R. Hence, ring dynamics are likely to be very different in EBT-P and EBT-R than in earlier and smaller bumpy tori. For example, ring temperature is likely to be more sensitive to microwave power in the projected relative to present bumpy tori.[11] Second, the power per unit volume required to sustain annuli is much more substantial in the dense projected bumpy tori than in present devices.

This is also reflected by the values of $|E|^2$ given in Table I required to give the temperatures in Table II.

In summary, the classical loss processes, collisions, and synchrotron radiation alone cannot account for the ring temperature scaling observed in small bumpy tori like NBT, EBT-0, EBT-1, and EBT-S. The addition of only nonadiabaticity effects to the ring model does not correct this discrepancy with experiment, but the combination of collisions, synchrotron radiation, nonadiabaticity, and low-level whistler turbulence does result in good agreement between the ring model and experiment. It is noteworthy that the necessary electric fields of the whistler modes can be much smaller than those associated with the microwaves. In larger, projected bumpy tori, like EBT-P and EBT-R, ring losses are likely to be dominated by the drag resulting from collisions and synchrotron radiation. Nonadiabaticity and whistler turbulence play a secondary role in the power balance of large bumpy tori.

ACKNOWLEDGEMENT

This work is supported by the U.S. Department of Energy.

REFERENCES

1. Dandl, R. A., et al., The ELMO Bumpy Torus Experiment, Oak Ridge National Laboratory Report ORNL/TM-3694 (November 1971).
2. Dandl, R. A., et al., Research Program for Plasma Confinement and Heating in ELMO Bumpy Torus Devices, Oak Ridge National Laboratory Report ORNL/TM-4641 (June 1975).
3. Dandl, R. A., et al., in Plasma Physics and Controlled Nuclear Fusion Research (Proc. 5th Int. Conf., Tokyo, 1974) Vol. 2, IAEA, Vienna (1975) 141.
4. EBT Experimental Group, Summary of EBT-1 Experimental Results, Oak Ridge National Laboratory Report ORNL/TM-6457 (1978).
5. Dandl, R. A., et al., The EBT-II Conceptual Design Study, Oak Ridge National Laboratory Report ORNL/TM-5955 (September 1978).
6. Fujiwara, M., et al., in EBT Ring Physics, Proceedings of the Workshop (Oak Ridge, Tennessee, December 3-5, 1979) 123.
7. Guest, G. E., Hedrick, C. L., Nelson, D. B., Phys. Fluids 18 (1975) 871.
8. Dominguez, R. R., Berk, H. L., Phys. Fluids 21 (1978) 827.
9. Nelson, D. B., Hedrick, C. L., Macroscopic Stability and β Limits in the ELMO Bumpy Torus, Oak Ridge National Laboratory Report ORNL/TM-5697 (December 1977).
10. Hamasaki, S., Klein, H. H., Krall, N. A., McBride, J. B., Sperling, J. L., Phys. Fluids 24 (1981) 1706.
11. Hamasaki, S., Krall, N. A., Sperling, J. L., The Classical Theory of the Bumpy Torus Relativistic Annulus, JAYCOR Report J510-81-048 (1981).
12. Batchelor, D. B., Goldfinger, R. C., Nuclear Fusion 20 (1980) 403.
13. McCoy, M. G., Mirin, A. A., Killeen, J., FPPAC - A Two-Dimensional Multispecies Nonlinear Fokker-Planck Package, Lawrence Livermore Laboratory Report UCRL-85666 (March 1981).
14. Haste, G. R., Hillis, D. L., Bull. Am. Phys. Soc. 25 (1980) 831.

15. Uckan, N. A., Bull. Am. Phys. Soc. 26 (1981) 994.
16. Hamasaki, S., Krall, N. A., Sperling, J. L., Bull. Am. Phys. Soc. 26 (1981) 995.
17. Bernstein, I. B., Rowlands, G., Phys. Fluids 19 (1976) 1546.
18. Howard, J. E., Phys. Fluids 14 (1971) 2378.
19. Cohen, R. H., Rowlands, G., Foote, J. H., Phys. Fluids 21 (1978) 627.
20. Gladd, N. T., in 2nd EBT Ring Physics Workshop (San Diego, California, December 1-3, 1981) paper C.6.
21. Hamasaki, S., Krall, N. A., Phys. Fluids 16 (1973) 145.
22. Elmo Bumpy Torus Proof of Principle, Phase II - Proposal Alternate Site, Volume I - Device and General Project, McDonnell Douglas Astronautics Co. Report MDC-E2229.
23. Klein, H. H., Hamasaki, S., Bathke, C. G., A Multi-Dimensional Model of the EBT Reactor, JAYCOR Report J510-81-001 (1981).

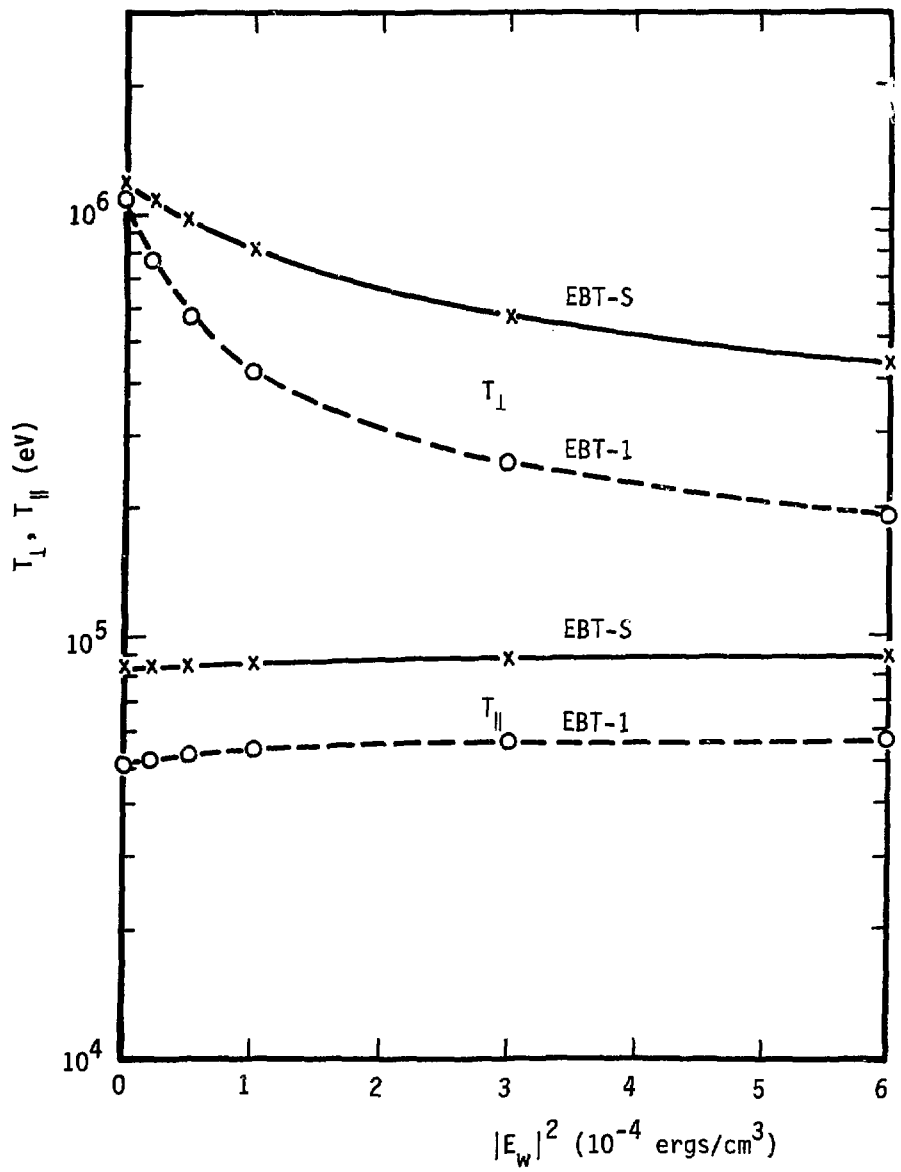

Figure 1: Plot of $T_\perp$, $T_\parallel$ (keV) versus $|E_w|^2$ (ergs/cm^3) for EBT-1 (- - -) and EBT-S (———). Relevant parameters are found in Table I.

Table I. Nominal Plasma and Wave Parameters for Various Bumpy Tori. B_0 (magnetic field strength on axis at the midplane, R_T (major radius), a (minor radius), N (mirror sectors), f (microwave frequency), n_e (background electron density), n_a (annulus density), $|E|^2$ (8π x electric field energy density assumed for both extraordinary and ordinary waves), and $|E_w|^2$ (8π x electric field energy density of whistlers).

	B_0 (kg)	R_T (cm)	a (cm)	N	f (GHz)	n_e ($10^{12}/cm^3$)	n_a ($10^{11}/cm^3$)	$\|E\|^2$ ($ergs/cm^3$)	$\|E_w\|^2$ (10^{-4} $ergs/cm^3$)
NBT	2.13	150	14.~7.	24	8.5	0.35	0.35	0.02	3.
EBT-0	2.63	150	14.~7.	24	10.6	0.6	0.5	0.02	3.
EBT-1	4.5	150	14.~7.	24	18.0	1.0	1.0	0.02	3.
EBT-S	7.0	150	14.~7.	24	28.0	1.0	2.0	0.02	3.
EBT-P	14.0	450	24.~14.	36	60.0	10.0	5.0	0.4	3.
EBT-R	22.5	3500	130.~80.	36	90.0	100.0	10.0	10.0	3.

Table II. For the Nominal Parameters of Table I, the Calculated Annulus Perpendicular Temperature ($T_\perp$) and Parallel Temperature ($T_\parallel$). The steady-state microwave heating rate per unit volume is given as well as the percentage of the microwave power which is lost due to various processes (i.e., collisions, synchrotron radiation, and leakage into the loss cone). Classical leakage is associated with microwave heating, collisions, and synchrotron radiation.

	$T_\perp$ (keV)	$T_\parallel$ (keV)	Heating (w/cm^3)	Collision	Synchrotron	Leakage		
						Classical	Whistler	Nonadiabaticity
NBT	87	23	7.2×10^{-3}	8.8%	0.03%	1.1%	20.4%	69.7%
EBT-0	120	29	9.8×10^{-3}	10.1%	0.07%	0.82%	21.8%	67.2%
EBT-1	263	55	1.6×10^{-2}	16.1%	0.5%	1.3%	20.0%	62.0%
EBT-S	578	89	2.2×10^{-2}	13.8%	4.6%	1.5%	15.1%	65.0%
EBT-P	697	340	2.4×10^{-1}	53.4%	31.0%	2.8%	12.4%	0.4%
EBT-R	786	260	4.22	69.4%	21.3%	4.6%	4.7%	-

APPENDIX A. SUMMARY OF METHODOLOGY

The central feature of the model is a kinetic equation which permits the determination of distribution functions consistent with wave heating and loss processes. In particular, microwave heating, collisions, and synchrotron radiation are considered here in a quasi-linear formalism. Bremsstrahlung has not been included because it has been shown to be of negligible importance to the annulus energy balance.[10,11] The kinetic equation for a given spatial point in EBT-geometry is

$$\frac{\partial f(p_\perp, p_\parallel)}{\partial t} = \Big[Q(p_\perp, p_\parallel) + C(p_\perp, p_\parallel) + S(p_\perp, p_\parallel) + (P(p_\perp, p_\parallel) + N(p_\perp, p_\parallel) + W(p_\perp, p_\parallel)\Big] \; f(p_\perp, p_\parallel) \quad , \qquad (A.1)$$

where Q, C, and S are relativistic generalizations of well known quasilinear wave heating, collisional drag, and synchrotron radiation loss formulas. The nonadiabatic, N, and whistler, W, terms are described in the main text. The explicit form of the other terms is given elsewhere.[11] Here, $p_\perp$ and $p_\parallel$ are the relativistic perpendicular and parallel momentum, respectively.

The source term, $P(p_\perp, p_\parallel)$, is introduced in order to conserve the total number of relativistic electrons in the steady-state distribution function and has the sole purpose of exactly compensating for the loss of electrons, if any, into loss cones. It is presumed that the energy of source electrons is much smaller than the mean energy of the relativistic electrons. Therefore, this term does not contribute net momentum or energy to the relativistic electron distribution function.

Using Eq. (A.1), we calculate the contributions from the various heating and loss processes at each point along magnetic field

lines on a drift surface assuming that the electron trajectories along magnetic field lines are determined by the adiabatic invariants. The electron distribution functions are constructed in such a manner that the adiabatic electron motion is automatically included.

As electrons travel along magnetic field lines, the relative magnitude of perpendicular and parallel momentum satisfies

$$p_{\perp o}^{\ 2} = p_{\perp}^{\ 2}\, B_o/B(z) \tag{A.2a}$$

$$p_{\parallel o}^{\ 2} = p_{\parallel}^{\ 2} + p_{\perp}^{\ 2} - p_{\perp o}^{\ 2} \quad , \tag{A.2b}$$

where subscript zero denotes evaluation at the intersection between a field line and the midplane of a mirror section (i.e., $z = 0$). The symbol $B(z)$ is the magnetic field strength at a distance z on the specific magnetic field lines as measured from the midplane.

In general, the exact time-dependent solution of a kinetic equation like Eq. (A.1) is prohibitive. To assess the effect of wave heating and loss processes on the anisotropy of the relativistic distribution function, it is sufficient to constrain it to a specified form and take appropriate moments of the kinetic equation. The relativistically correct distribution function which has been chosen for the present calculation is at $z = 0$,

$$f(p_{\perp},p_{\parallel},0) = \frac{n_o}{A} \exp\left[-\frac{1}{m_o(\gamma + 1)}\left(\frac{p_{\parallel}^{\ 2}}{T_{\parallel}} + \frac{p_{\perp}^{\ 2}}{T_{\perp}}\right)\right]$$

$$H(a_o p_{\perp}^{\ 2} - p_{\parallel}^{\ 2}) \quad , \tag{A.3a}$$

and therefore for arbitrary z,

$$f(p_\perp, p_\parallel, z) = f(p_{\perp o}, p_{\parallel o}, 0) \quad , \tag{A.3b}$$

where $p_{\perp o}$ and $p_{\parallel o}$ are given by Eq. (A.2) and A is the normalization constant which permits density at z = 0 to be given by

$$n_o = \int d^3 p \; f(p_\perp, p_\parallel, 0) \quad .$$

In Eq. (A.3a) a Heavyside function, $H(a_o p_\perp^2 - p_\parallel^2)$, is added to account for a loss cone corresponding to a magnetic field line intersecting the wall. No electrons are permitted in the loss cone within our model. The value of a_o is determined by the mirror ratio

$$a_o = \sqrt{[B(z_w)/B_o] - 1} \quad , \tag{A.4}$$

where z_w is the intersection point with the wall along the field line.

Note that the distribution function approaches a non-loss-cone limit as $a_o \to \infty$. Note also that f reduces to a two temperature maxwellian form in the limit of the parameters $T_\perp$ and $T_\parallel$, much smaller than $m_o c^2$. Hence, the parameters, $T_\perp$ and $T_\parallel$, can be interpreted as perpendicular and parallel temperatures, but only in the nonrelativistic limit. Also, for the case when $T_\perp = T_\parallel$, Eq. (A.3) reduces to the relativistic maxwellian. Finally, for the general case of $T_\perp \neq T_\parallel$, the density is a function of the coordinate z. This is most easily seen by taking the zero moment of Eq. (A.3),

$$n(z) = \int d^3 p \; f(p_\perp, p_\parallel, z) = \frac{n_o}{\left[\frac{B_o}{B(z)}\left(1 - \frac{T_\perp}{T_\parallel}\right) + \frac{T_\perp}{T_\parallel}\right]} \quad . \tag{A.5}$$

The relativistic electron distribution function of Eq. (A.3) is determined through parameters n_o, $T_\perp$, and $T_\parallel$. The particular

moments of the kinetic equation used to determine these parameters are zero, $p_{\perp o}^2/(\gamma + 1)$, and $p_{\parallel o}^2/(\gamma + 1)$.[11] The momentum moment, $\vec{p}$, of Eq. (A.1) is trivial and need not be considered.

As electrons travel along the magnetic field lines they are heated by the various appropriate electron-cyclotron resonances and so the electron distribution function at steady state is influenced by the magnetic field geometry. The particular magnetic field geometry chosen for the present analysis is appropriate to a straight cylinder with dimensions comparable to EBT-1 and EBT-S,

$$B_z(r,z) = 0.5\, B_o \left[3 - I_0\left(\frac{\pi}{L_o} r\right) \cos\left(\frac{\pi}{L_o} z\right)\right] \quad , \qquad \text{(A.6a)}$$

$$B_r(r,z) = -0.5\, B_o\, I_1\left(\frac{\pi}{L_o} r\right) \sin\left(\frac{\pi}{L_o} z\right) \quad . \qquad \text{(A.6b)}$$

Here L_o = 19.64 cm. The field B_o has ranged from 2600 to 7000 gauss in various EBT experiments. The symbols, r and z, are the radial and axial coordinates of the straight cylinder, respectively. The functions, I_0 and I_1, are the modified Bessel functions of the first kind and of order zero and one, respectively. The form for the fields assumes that only vacuum magnetic fields are present and neglects plasma diamagnetism.

Ring electrons confined on a specific concentric drift surface are represented by the distribution function specified in Eq. (A.3). The heating rate and energy loss rate, calculated by the moments of the above kinetic equation, are integrated along a field line on a drift surface to give the total heating rate and the total energy loss rate. The steady state for ring electrons (confined on a specific drift surface) is obtained by balancing the total heating rate with the total energy loss.

PROSPECTS FOR CONTROL OF ELMO RINGS

G.E. Guest and R.A. Dandl
AMPC, Inc.
Encinitas, California

In this note, we consider a conceptual approach to controlling some important properties of hot-electron plasmas created by electron cyclotron heating, particularly the high-beta ELMO Rings. The approach to be considered is based on the anticipation that a significant number of collisionless, "warm" electrons can be accumulated in limit cycles arising from one of several possible coherent interactions with the ECH fields. If stochastic behavior is restored to these electrons, they can be heated to the relativistic energies characteristic of ELMO Rings. The number of "warm" electrons that can be manipulated for control purposes can also be affected by choice of system parameters. As we will discuss here, this approach may already have been illustrated in the multiple-frequency ECH experiments on SM-1 [1], but more general implementations can also be envisioned.

An immediate objective in manipulating the warm electrons of an ECH plasma is to increase the overall efficiency with which microwave power is converted into stored plasma energy. This is of considerable

practical importance in EBT where formation of macrostable equilibria depends on achieving hot-electron pressures above a certain threshold value, while cost and technical complexity increase with the level of microwave power required. For other applications, such as maintaining thermal barriers or enhancing plug potentials in tandem mirrors, efficiency may be less important than reducing the level of microturbulence or controlling the radial and/or axial distributions of hot-electron pressure. In this note, we discuss some of the fundamental processes underlying ELMO Ring formation that might be utilized to control these aspects of the equilibrium.

Broadly speaking, the fundamental processes of interest are those involved in heating, confining, and providing the source of ion-electron pairs. It is in the details of these elemental processes that we seek ways of controlling the ELMO Rings.

The heating processes have two broad aspects in the case of ECH: wave propagation, conversion, absorption, etc, and the interaction of individual electrons with the RF electric field. The first aspect governs the amplitude of the right-hand circularly-polarized wave incident on the resonant surface. We will not discuss this aspect here, although the details of the wave launching and resonant surface irradiation can obviously be exploited for control purposes. Here we will focus our attention on the interaction of individual electrons with an assumed

RF field and show that the existence of certain types of coherent phenomena offer an attractive approach to enhanced efficiencies and other types of control functions.

The confinement and the particle sources and sinks can vary widely with different applications so, for definiteness, we will use simple magnetic-mirror confinement to illustrate the possibility of control arising from the interplay between heating and confinement. We consider an electron cyclotron heated plasma created by ionization of ambient gas and identify some of the important details of heating and confinement in the schematic picture shown in Fig. 1.

In this picture, the arrows represent fluxes of electrons, both in an energy dimension (associated with heating) and a spatial dimension (associated with loss of confinement). The equilibrium distribution function of electrons is determined by the competition between the two fluxes. Note that the energy dimension is increasing upward in the drawing, starting at 10 eV for the newly created ion-electron pairs and ending somewhere above 100 keV where non-adiabatic losses may be dominant in typical simple-mirror experiments. The energy scale has been set rather arbitrarily, and any particular process might be important at lower or higher energies. The ordering is, however, representative of typical ELMO Ring plasmas.

SCHEMATIC ECH MODEL

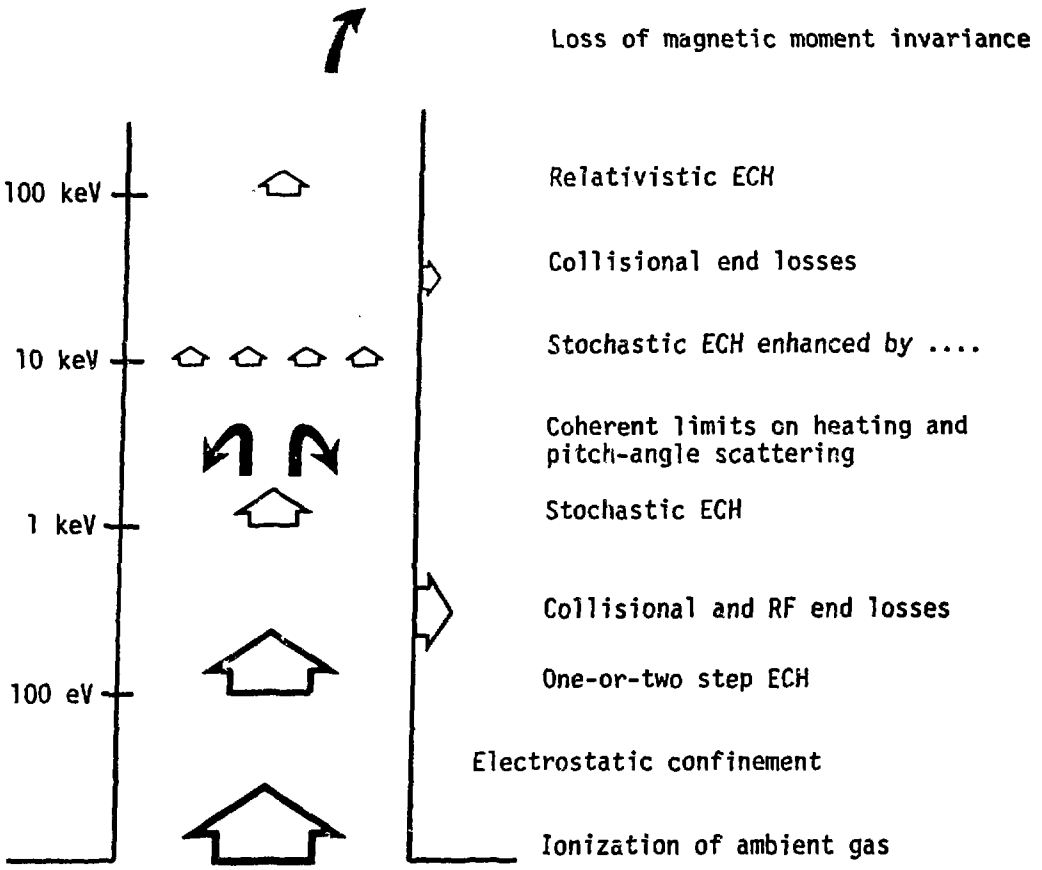

Fig. 1. A schematic model of ECH processes in a magnetic mirror.

We now discuss each of the elements of heating and confinement called out in Fig. 1 that can be used for control of the ELMO Rings.

In the first energy decade shown in Fig. 1, between 10 eV and 100 eV, electrons are confined in an ambipolar electrostatic field whose magnitude is governed by conditions for quasi-neutrality. Typically, ions escape by flowing freely along magnetic lines of force at their thermal speed. The much faster electrons first escape more rapidly, leaving a positive electric space charge which retards their further loss. The steady-state value of this retarding field is such that the total electron flux out of the plasma just balances the ion flux out of the mirror. Notice that the electrons make a number of transits (bounce orbits) before escaping and therefore encounter ECH resonance a number of times. Under typical ECH conditions, only a few transits through resonance are required to heat electrons to energies above the ambipolar potential. We have indicated this process as "One-or-two step ECH" in Fig. 1.

Electrons heated to energies above the ambipolar potential can escape directly, if they are in the mirror loss cone, or by scattering into the loss cone if they are initially outside of it. The rate of scattering into the loss cone is governed by the electron energy, and therefore by the magnitude of the ambipolar potential. Clearly, this loss of electrons will be reduced if the potential is large since collisional scattering decreases with the cube of electron speed.

Thus, a possible approach to increased efficiency would be to raise the ambipolar potential, for example, by inhibiting the outward flux of ions by anisotropic ion heating or by replacing some of the cold ions by well-confined hot ions. Notice that any parameter changes that reduce the ambipolar potential or, particularly, that cause it to change sign are likely to cause a reduction in efficiency or a loss of the hot-electron equilibrium althogether unless additional steps are taken to prevent large losses of electrons in this first energy interval.

The second energy decade identified in Fig. 1, 10^2-10^3 eV, is typically characterized by a high enough collision frequency to ensure that an electron (in this energy range) will encounter successive resonances with random values of its gyrophase (relative to the phase of the ECH electric field, for example). Electrons in this energy range will therefore be heated stochastically by the ECH and diffuse in energy and pitch angle. The pitch-angle diffusion is related to the energy diffusion by virtue of the local character of the resonant interaction. In fact, the change in the turning point, B_t, resulting from a given resonance, is related to the change in energy, $\delta W_\perp$, by

$$\frac{\delta B_t}{B_t} = \left(1 - \frac{B_t}{B_\mu}\right)\frac{\delta W_\perp}{W_\perp} \quad .$$

Here, B_μ is the resonant magnetic field, so that electrons turning beyond resonance and heated ($\delta W_\perp > 0$) by that ECH resonance will subsequently turn at a smaller magnetic field, $\delta B_t < 0$. Electrons that loose energy ($\delta W_\perp < 0$) may increase their turning points sufficiently to escape from the magnetic mirror. These RF associated end losses can be affected by choosing B_μ relative to the maximum magnetic fields, i.e., heating nearer the midplane or the mirror throat. The stochastic heating rates depend quadratically on the amplitude of the right-hand, circularly-polarized component of the ECH electric field at the resonant surface, but only rather weakly on other parameters.

In the third energy interval identified in Fig. 1, from 10^3-10^4 eV, electrons typically achieve or approach so low a Coulomb scattering rate that phase randomization between successive resonances may no longer obtain. Stochastic heating will then cease for electrons experiencing coherent interactions with the ECH electric field, and these electrons will accumulate around stable fixed points in energy and pitch angle. We identify two particular types of coherent phenomena, as indicated in Figs. 2 and 3.

Figure 2 is a schematic representation of an electron bounce orbit (in a symmetric simple magnetic mirror) that intersects the ECH resonant surfaces at $z = \pm z_\mu$. If the electrons are coherent with the RF fields

COHERENT PHENOMENA THAT MAY AFFECT STOCHASTIC ECH - SUPER ADIABATICITY

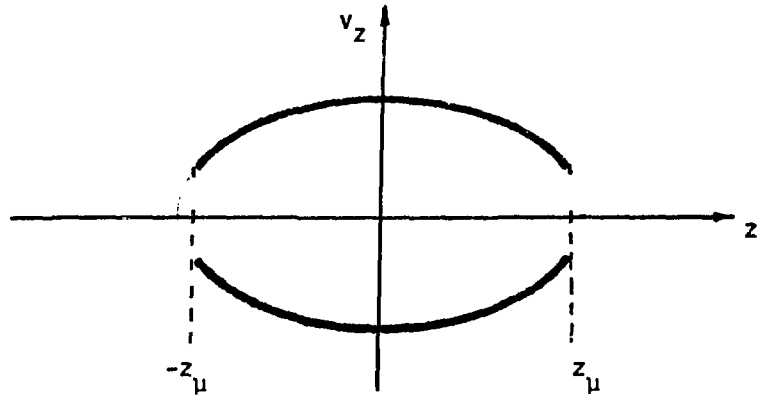

- Superadiabaticity requires wave-particle coherence for $\tau_b/2$ over distances equal to the separation of resonant surfaces

- Critical energy for superadiabaticity

$$eE_\mu \cdot 2L \lesssim \frac{8}{3} W_\perp \sqrt{\frac{M-1}{R_\mu}} \left(\frac{3\pi}{2} \frac{\omega_b}{\omega_\mu} \frac{R_\mu}{R_\mu - 1} \right)^{2/3}$$

- Typical SM-1 values

$$E_\mu \sim (5\text{-}10)\ \text{V/cm} \rightarrow W_{\perp,\ crit} \sim 1\text{-}3\ \text{keV}$$

Fig. 2. Some characteristics of superadiabatic behavior.

COHERENT PHENOMENA THAT MAY AFFECT STOCHASTIC ECH - NULL-HEATING SURFACES

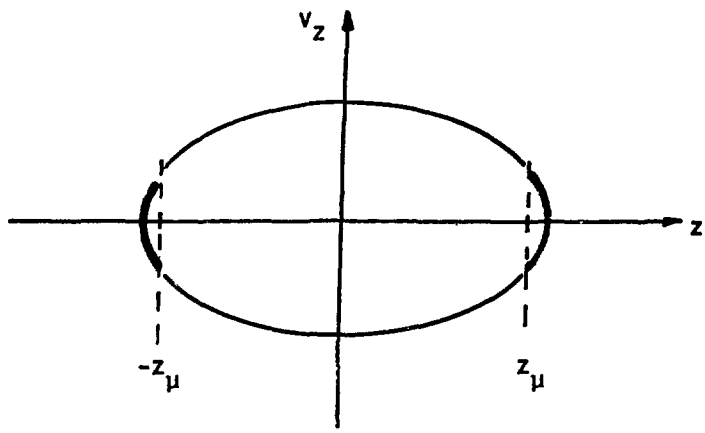

- Null-heating surfaces require coherence over a small fraction of a bounce period and distances smaller than a wavelength

- Two closely-spaced resonances interfere if

$$\delta z_n \equiv \frac{z_{t,n}^2}{z_\mu^2} - 1 \cong \left[\frac{3\pi}{4}(2n+1)\frac{\omega_b}{\omega_\mu}\frac{R_\mu}{R_\mu - 1}\right]^{2/3}$$

- The corresponding pitch angles are given by

$$\tan\theta_n = \sqrt{(R_\mu - 1)(1 + \delta z_n)}$$

Fig. 3. Coherent behavior leading to null-heating surfaces.

between successive resonances, they may exhibit superadiabatic behavior [2] in which their energy and pitch angle undergo slow oscillation about fixed points. The limiting energy, $W_\perp$, is related to the RF electric field strength, E_μ, roughly as follows:

$$eE_\mu \cdot 2L \lesssim \frac{8}{3} W_\perp \sqrt{\frac{M-1}{R_\mu}} \left(\frac{3\pi}{2} \frac{\omega_b}{\omega_\mu} \frac{R_\mu}{R_\mu - 1} \right)^{2/3}$$

Here, 2L is the separation of the mirrors, M is the (axial) mirror ratio, R_μ is the ratio of the resonant magnetic field strength to the midplane (axial) magnetic field strength, $R_\mu = B_\mu/B_o(0)$, and ω_b and ω_μ are the bounce and resonant frequencies respectively.

Figure 3 indicates a second coherent interaction that also leads to limit cycles for the electron energy and pitch angle. Here, the coherence is between closely-spaced successive resonances of electrons turning just beyond the resonant surface. These closely-spaced resonances can interfere destructively if the gyrophase changes (between resonances) by an odd integral multiple of pi. This can be expressed in terms of the turning points as follows:

$$\delta z_n \equiv \frac{z_{t,n}^2}{z_\mu^2} - 1 \cong \left[\frac{3\pi}{4} (2n + 1) \frac{\omega_b}{\omega_\mu} \frac{R_\mu}{R_\mu - 1} \right]^{2/3}$$

or, in terms of the electron pitch angle,

$$\tan \theta_n = \sqrt{(R_\mu - 1)(1 + \delta z_n)} \quad .$$

Samec [3] has evaluated these conditions numerically for the SM-1 device and displayed these "null-heating surfaces" as shown in Fig. 4. Electrons will tend to accumulate around these surfaces unless some mechanism destroys the coherence between electron gyration and ECH electric field.

From the point-of-view of controlling the source of energetic electrons that form ELMO Rings, it appears that electrons trapped in these limit cycles can provide a useful mechanism. These electrons are nearly collisionless and are therefore well-confined by the magnetic mirror. Moreover, the pitch angles of these electrons are restricted to relatively narrow ranges by the combined action of the ECH power and the static, inhomogeneous magnetic field of the mirror. Thus, the limit cycles can be broken selectively, and the associated electrons can be stochastically heated with high efficiency, if suitable, perturbing forces are applied.

Multiple frequency ECH is well suited to this purpose. MFECH has been shown by Rognlien [4] to destroy superadiabaticity provided the frequency separation is near the bounce frequency of the coherent electrons. Similarly, MFECH seems very likely to restore stochastic behavior

MIRROR RATIO AT TURNING POINTS
FOR NULL-HEATING SURFACES
IN SM-1 (SAMEC)

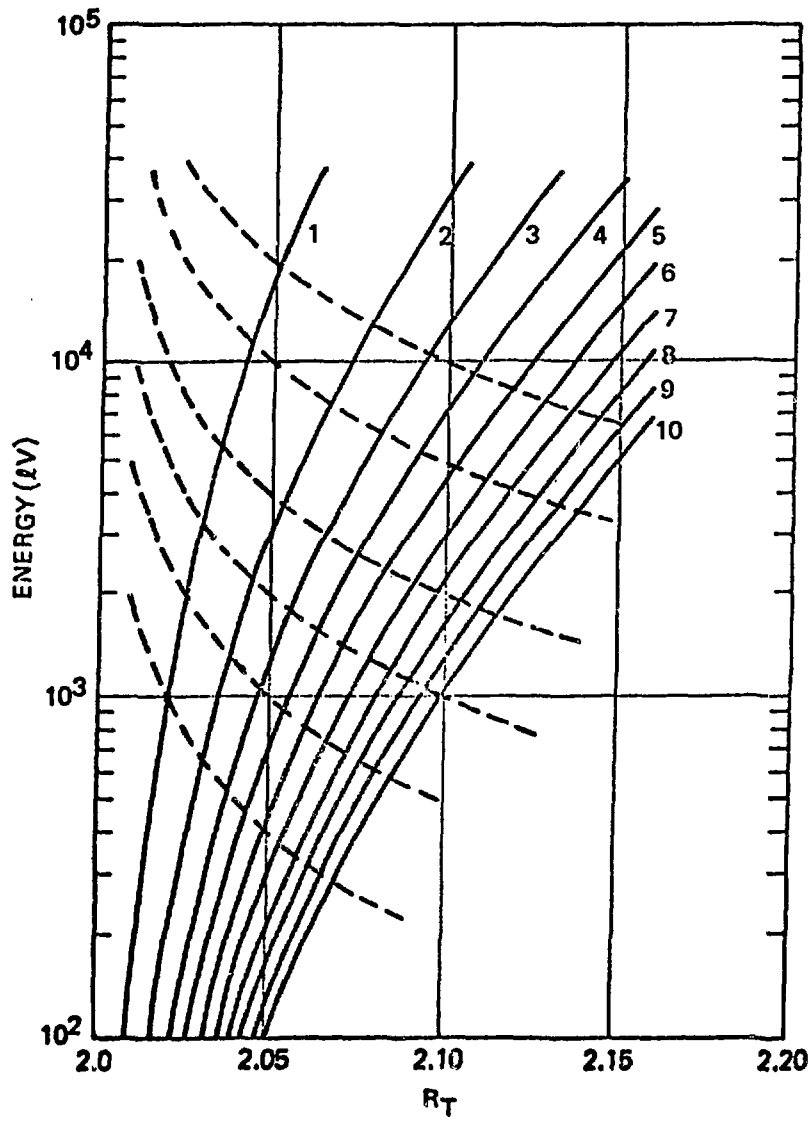

Fig. 4. (after Samec) - Mirror ratios of the first ten null-heating surfaces in SM-1.

to electrons trapped near null-heating surfaces if the secondary gyroresonance occurs between the primary gyroresonance and the null-heating surface.

Other interactions may also be used to destroy the coherence underlying these limit cycles, such as the "automatic" second-harmonic heating that occurs if the associated resonance surfaces intersect the magnetic flux surfaces on which the limit cycles obtain. But our primary interest here is the use of MFECH. To make this approach more concrete, we estimate the conditions under which stochastic ECH can be restored to electrons trapped on null-heating surfaces. We require that an auxiliary ECH source change the electron pitch angle by an amount comparable to half the spacing of the null-heating surfaces:

$$\Delta(\delta z)_{out} \sim (\delta z_{n+1} - \delta z_n)/2 \quad ,$$

where

$$\delta z \equiv (z_t/z_\mu)^2 - 1 \cong \left(\frac{\varepsilon}{\mu B_o} - R_\mu\right)/(R_\mu - 1) \quad .$$

The auxiliary ECH source must change the electron perpendicular energy by

$$\Delta W_{\perp,crit} \cong \frac{\Delta(\delta z)_{crit}\, W_{\perp\mu a}}{\delta z + \dfrac{R_\mu - R_{\mu a}}{R_\mu - 1}} \quad .$$

A numerical evaluation of this rough condition is shown in Fig. 5 for the case of SM-1.

CRITICAL ENERGY INCREMENT FOR BREAKUP OF NULL-HEATING SURFACES

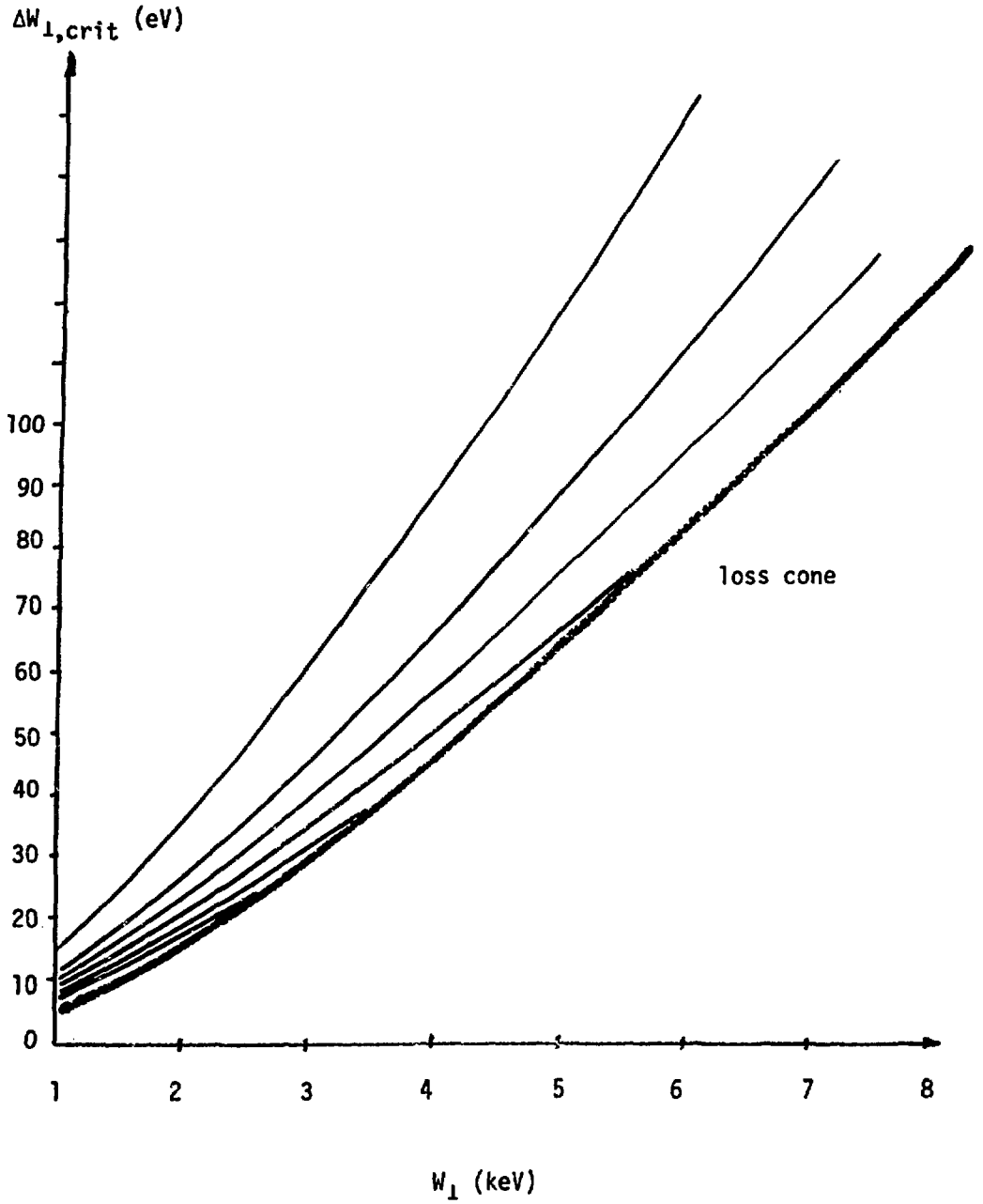

Fig. 5. Critical values of the increment in perpendicular energy required for break-up of the null-heating surfaces in SM-1 (approximate).

More generally, it seems likely that electrons in limit cycles can be heated stochastically by suitable auxiliary ECH sources, either MFECH, second-harmonic ECH, upper-off-resonant ECH or others. And by restoring stochastic behavior to such electrons, one can control such aspects of ELMO Ring formation as the efficiency, the anisotropy (and hence the micro turbulence) and the spatial distribution of hot-electron pressure.

Returning to Fig. 1, we identify the fourth energy decade, 10^4-10^5 ev, with renewed stochastic heating, since finite values of the relativistic electron gyroradius lead to significant heating at the second (and higher) gyroharmonics. In fact, the conventional quasilinear theory of ECH [5] should give a reasonable model of the dominant heating processes in this interval, and recent Fokker-Planck studies based on this theory [6] should provide a reliable guide to the resulting form of the hot-electron distribution.

The final process shown in Fig. 1 is the onset of losses due to the breakdown of the invariance of the magnetic moment of relativistic electrons, generally expected to occur when $\rho_e/R_B \gtrsim 0.05$ [7]. Here, ρ_e is the electron gyroradius and R_B is the characteristic scale length of the inhomogeneous magnetic field. Recent refinements in the effect of non-adiabatic behavior on the temperature of the relativistic electrons are just now being reported.

To conclude, we suggest that the framework introduced in Fig. 1 serves to identify promising control mechanisms, particularly the selective destruction of limit cycles that hold collisionless electrons in stable orbits around fixed points in energy and pitch angle, and manipulation of the ambipolar potential that confines cold electrons.

REFERENCES

[1] QUON, B.H., DANDL, R.A., DIVERGILIO, W., GUEST, G.E., LAO, L.L., LAZAR, N.H., SAMEC, T.K. and WUERKER, R.F., "Impace of Multiple Frequency Heating on ELMO Ring Formation and Control in the SM-1 Axisymmetric Mirror," to be published.

[2] AAMODT, R.E., Phys. Rev. Lett. 27, 135 (1971).

[3] SAMEC, T.K., private communication, see paper E4 of this conference.

[4] ROGNLIEN, T.D., paper E5 of this conference.

[5] BERNSTEIN, I.B. and BAXTER, D.C., Phys. Fluids 24, 108 (1981).

[6] See, for example, paper E2 of this conference, STALLARD, B.W., MATSUDA, Y and NEVINS, W.M., "Fokker-Planck Calculations of Electron Cyclotron Resonant Heating (ECRH) in Mirror Geometry."

[7] See, for example, COHEN, R.H., ROWLANDS, G. and FOOTE, J.H., Phys. Fluids 21, 627 (1978) and references cited there.

NONADIABATICITY AND HIGH ENERGY PARTICLE ORBITS IN EBT*

L. W. Owen and L. E. Deleanu
UCCND Computer Sciences Division
Oak Ridge National Laboratory
Oak Ridge, Tennessee 37830

and

C. L. Hedrick
Oak Ridge National Laboratory
Oak Ridge, Tennessee 37830

The scaling of hot electron ring temperatures in ELMO Bumpy Torus (EBT) and mirror experiments and results of recent ICH experiments on EBT-S suggest the scaling law $\rho/L \approx 0.05$, where ρ is the gyroradius and L is the magnetic scale length. This is roughly the value at which conservation of the adiabatic invariant μ begins to break down. The behavior of $\mu(t)$ and particle drift orbits are obtained by numerical integration of the equations of motion. In the absence of electric fields it is shown that nonconservation of μ for $\rho/L \approx 0.05$ is so weak that it has little effect on drift orbits and affects particle losses only through enhanced pitch angle scattering. Only for particle energies of about five times the temperature do rapid direct losses, due to magnetic moment jumps, start to become important.

*Research sponsored by the Office of Fusion Energy, U. S. Department of Energy, under contract W-7405-eng-26 with the Union Carbide Corporation.

Here, we discuss some preliminary calculations associated with the fundamental physics of the rings in EBT. The motivation for these calculations is provided by the experimental observation that the ring temperature in both mirror and EBT experiments usually follows the scaling law $\rho/L \simeq 0.05$. This is roughly the value at which one expects the adiabatic invariant μ to begin to break down. The first part of this paper is devoted to an examination of single particle orbits over rather long time scales (comparable to a poloidal drift period). The second part of the paper is devoted to a simplified Fokker-Planck model that investigates the effects of boundary conditions on ring temperature.

The orbits here discussed were computed using a magnetic field produced by the Oak Ridge National Laboratory (ORNL) three-dimensional (3-D), finite-beta, tensor ring pressure equilibrium code. Figure 1 (a) shows the magnitude of beta as a function of major radius at the intersection of a midplane and the equatorial plane. Notice that the pressure of the hot electron rings has produced substantial radial gradients in beta. From the contours of constant B shown in Fig. 1 (b) it is observed that the axial gradients in the vicinity of the ring are not nearly as steep as the radial gradients. The effect on the drift motion produced by the sharp radial gradients in B is, of course, significant. However, the effect on μ-fluctuation seems to be rather minimal as would be expected from analytic calculation [1], where the dominant scale lengths are found to be the axial gradients of B and the radius of curvature. (The latter is relatively unchanged for $\beta \simeq 30\%$). This comparison of numerical results with analytic work is not yet quantitative; we hope to carry out a more quantitative comparison in the near future.

The numerical calculations to date have been exploratory. We have not as yet attempted to accumulate a massive statistical base; rather, we have examined a representative sample of initial conditions in phase space. From these calculations we have noted a number of features that are persistent and have drawn some tentative conclusions. Figures 2-7

represent a subset of the calculations and illustrate most of the features that have been observed to be more or less universal.

Figures 2 and 3 represent particles that have the same initial position and velocity direction but differ in energy. Figure 2 is for a 500-keV electron (0.5-cm gyroradius) whereas Fig. 3 is for a 3-MeV electron that has a larger gyroradius (2 cm). It will be observed that the fluctuations in μ are, as expected, substantially larger for the larger gyroradius, 3-MeV electron. The fluctuations in μ occur on several time scales. The most rapid fluctuations occur on a gyroperiod time scale and are associated with the fact that μ has been calculated at the position of the particle (rather than the guiding center). The (generally larger) jumps in μ occur when the particle crosses a midplane. Although we have not illustrated it here, we have followed a few particles for several poloidal drift periods and observed a still longer periodic behavior on the drift time scale.

In Fig. 3 it will be noted that μ undergoes sufficiently large fluctuations such that, over a fraction of a drift period, it ceases to be trapped (large μ) and becomes passing (small μ). The short discontinuity in the "drift surface" that occurs in the upper left hand portion is associated with this "passing" phase. This qualitative behavior is further illustrated in Fig. 4.

A significant point to note is that the passing portion of the orbit would be lost in a single mirror cell (because the particle would follow a field line to an "end-wall"), whereas in EBT it must drift radially to strike a material wall. For the case illustrated in Figs. 3 and 4 this does not happen because the particle again becomes trapped (by a μ fluctuation) and approximately follows a well-confined drift orbit.

The orbits of Fig. 3 also illustrate a point that may have quantitative importance. The time that the electron is a passing particle is small compared to the time that it is trapped. This would be expected on analytic grounds because $\Delta\mu/\mu$ rises rapidly with $V_{\parallel}/V$. Thus, there is more likelihood that a particle will be changed from passing to trapped than vice versa. This is potentially important

because the trapped particle drift orbits are better confined than the passing drift orbits.

Figures 5, 6, and 7 illustrate a similar behavior to that seen in Figs. 2 and 3. Figures 5 and 6 correspond to initially less deeply trapped electrons that are near the trapped/passing interface (even at low energy). Figure 7 corresponds to an initially passing particle of high energy that becomes trapped over a portion of its orbit because of μ-fluctuation.

For energies somewhat in excess of those shown (e.g., gyrodiameter comparable to the radial extent of the ring), the particles cease to follow (approximately) drift surfaces based on ε, μ, and J and become more chaotic or "pathological."

Figure 8 represents a simplified picture of the behavior of electrons based on these single particle calculations as well as earlier guiding center calculations. For low energies (comparable to core electron temperature), particles are confined by the ambipolar electric field. At somewhat higher energies (where μ is still a good invariant), passing and transitional electrons tend to drift out of the system because their orbits are not well-centered in the device. (The shift of the orbit center for these modest energy electrons is qualitatively represented by the orbit shown in Fig. 7, which is for much higher energy.) At still higher energies, μ begins to fluctuate significantly, and particles can be driven into the passing region (with its poorly confined orbits) by these fluctuations. For sufficiently large fluctuations in μ, particles arriving in this region have a significant probability of leaving this loss region (because of μ-fluctuation) before they drift to the wall, and this probability is generally higher than the probability that they "scatter" into this region in the first place. Finally, at very high energies, electrons become "pathological"; i.e., their orbit bears no resemblance to a drift surface and they rapidly wander out of the device.

From the foregoing it seems likely that μ-fluctuations play a strong role in determining the behavior of the hot electron rings. However, the energy losses due to μ-fluctuations alone are not clearly dominant because when the fluctuations become large enough to be the clearly dominant microscopic effect the electrons have a higher probability of "scattering" off unconfined drift orbits than they have of scattering onto such orbits in the first place. In any event, a complete description of the ring behavior will involve the effects of both sources and sinks and "scattering" in both pitch angle (or μ) and energy. Mathematically this will most likely take the form of a Fokker-Planck equation whose coefficients represent the various processes involved: microwave heating, Coulomb collisions, synchrotron radiation, μ-fluctuation due to "large" gyroradius, whistlers, etc.

It seems germane to us that the existing expressions for most of the Fokker-Planck coefficients have not included μ-fluctuations in their derivations. For example, existing expressions for the Fokker-Planck coefficients due to microwave heating are derived assuming μ is constant in the absence of the microwave field, whereas even in the presence of a microwave field the dominant microscopic feature can easily be changes in velocity produced by μ-fluctuations. It seems likely that the existing formulas are inadequate for describing ring physics and that new expressions for the Fokker-Planck coefficients must be derived which take into account μ-fluctuations produced by "large" gyroradius.

Because this is a complicated and probably time-consuming mathematical problem, it is useful to examine a simplified Fokker-Planck equation to gain insight into the possible interplay of energy and pitch angle scattering as well as boundary conditions. The simplest equation one can write down for this purpose is

$$\frac{\partial f}{\partial t} = 0 = A\frac{\partial^2 f}{\partial \varepsilon^2} + B\frac{\partial^2 f}{\partial \left\langle \frac{v_\parallel}{v} \right\rangle^2} \quad . \tag{1}$$

Here, the Fokker-Planck coefficients A and B will be treated as constants and represent the previously mentioned physical processes (microwave heating, Coulomb collisions, etc.). The region of assumed applicability for this equation is indicated in Fig. 8. Notice in Fig. 8 that the boundaries occur at high values of energy and the pitch angle-like variable, $\langle v_{\parallel}/v \rangle$, and that the distribution function is assumed to be zero on and beyond these boundaries.

To treat the boundary condition at $\langle v_{\parallel}/v \rangle = a$, we write

$$f = F(\varepsilon)\cos\left(k\left\langle\frac{v_{\parallel}}{v}\right\rangle\right) \qquad k \equiv \frac{\pi}{a} . \tag{2}$$

When this is inserted into Eq. (1) we obtain

$$A\frac{\partial^2 F}{\partial \varepsilon^2} - k^2 BF(\varepsilon) = 0$$

or

$$\frac{\partial^2 F}{\partial \varepsilon^2} - \frac{1}{T^2}F(\varepsilon) = 0 , \tag{3}$$

where

$$T = \frac{1}{k}\sqrt{\frac{A}{B}} . \tag{4}$$

Equation (3) has two linearly independent solutions: $\exp(\pm\varepsilon/T)$. To satisfy the boundary condition at

$$\varepsilon = \varepsilon_{max} \equiv bT \ , \tag{5}$$

F must have the form

$$F(\varepsilon) = \text{constant } x\left(\varepsilon^{-\varepsilon/T} - \varepsilon^{\varepsilon/T-2b}\right) \ . \tag{6}$$

Figure 9 shows the shape of F (or ln F) for various values of b. Notice that the shape of these curves closely follows $\exp(-\varepsilon/T)$ except near $\varepsilon = bT = \varepsilon_{max}$. Thus, the slope of the curve is primarily determined by Eq. (4) rather than by behavior at high energy. For known values of A and B we would say that for $b > 3$ the boundary condition at $\langle v_{\parallel}/v\rangle = \varepsilon$ determines the "temperature" (slope of the curve) and that the boundary condition at $\varepsilon = \varepsilon_{max}$ has little effect.

On the other hand, the value of a [and hence k from Eq. (2)] is reasonably well-known. This simple calculation suggests that we should expect that the temperature of the ring is determined by the ratio of scattering in energy and pitch angle (of all the mechanisms involved) and hence provides some guidance for developing improved expressions for the coefficients in the Fokker-Planck equation.

Finally, we should mention the constant of proportionality in Eq. (6), which corresponds to the ring number density. Within the present simplified mathematical model, it is determined by a boundary condition at relatively low energy (tens of keV). The physical processes that determine this boundary condition are associated with the "feed" or heating of core electrons of relatively low energy (~1 keV) to tens of keV.

References

[1] R. H. Cohen, G. Rowlands, and J. H. Foote, Nonadiabaticity in Mirror Machines, Phys. Fluids 21(4), 627 (April 1978).

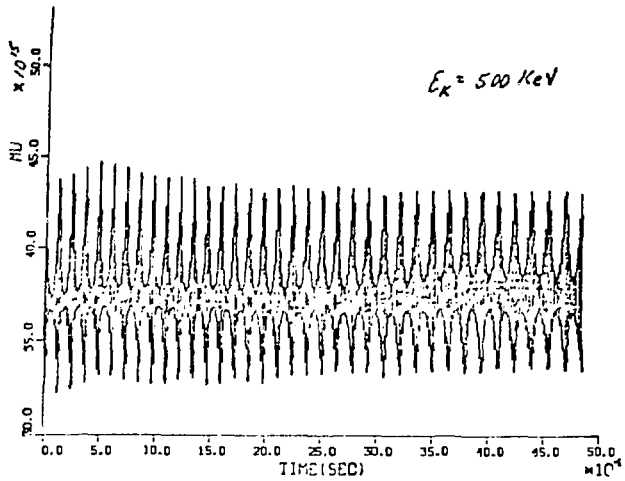

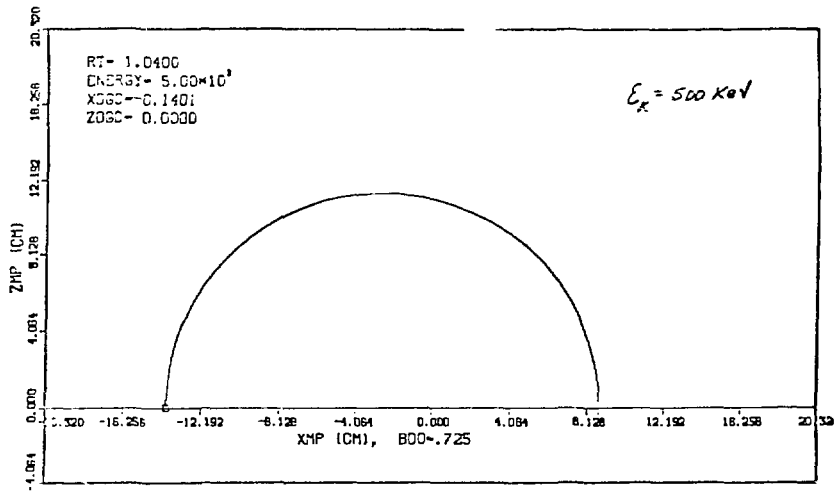

Figure 2. Magnetic moment μ as a function of time (a) and drift surface in the midplane (b) for a trapped electron with energy of 500 keV.

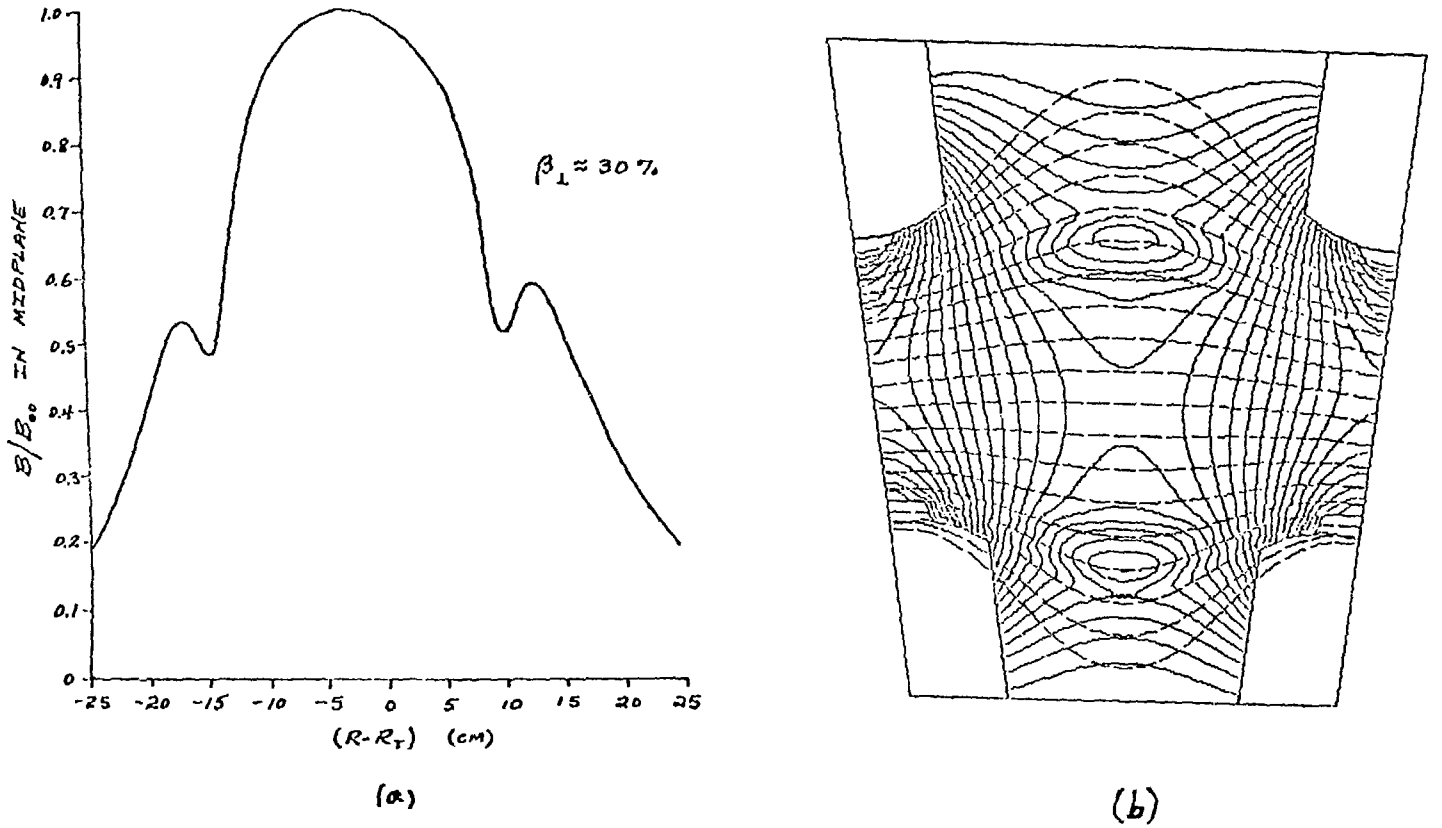

Figure 1. Equilibrium magnetic field with $\beta_\perp \approx 30\%$ for the hot electron rings is displayed (A) in the midplane and (B) in the equational plane (mod B contours are solid and flux lines are dashed) of EBT-I/S.

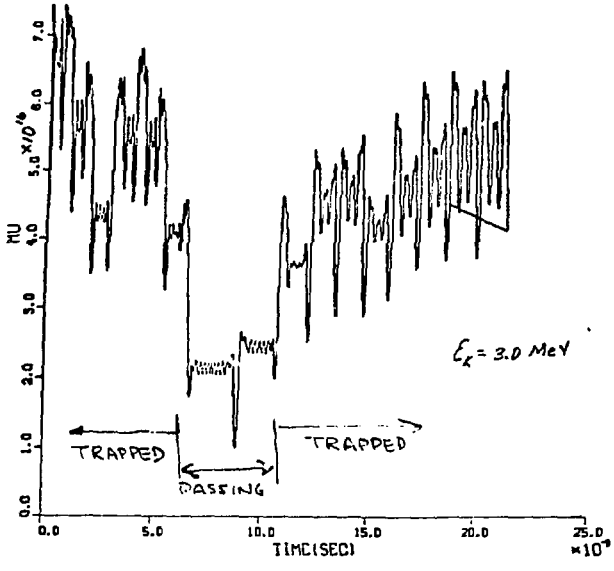

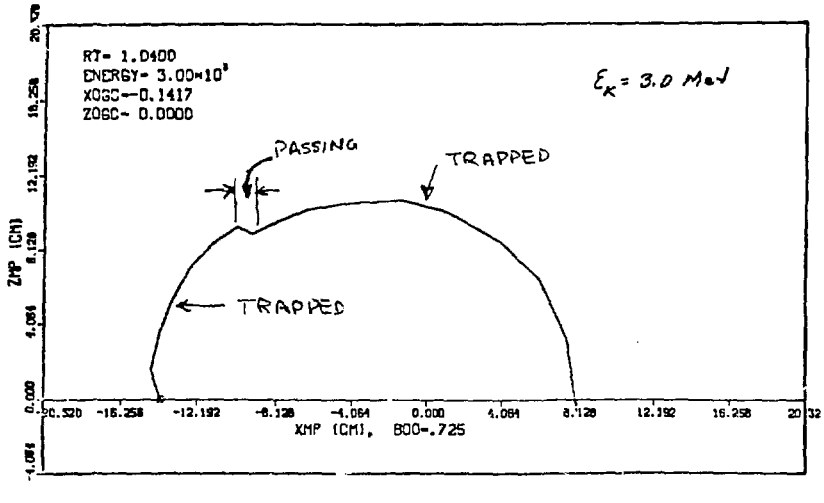

Figure 3. Magnetic moment μ as a function of time (a) and drift surface (b) for an initially trapped electron with energy of 3 MeV. The initial position, gyrophase, and ε/μ are the same as in Fig. 2. The larger fluctuations in μ permit the particle to become passing over a small portion of its orbit.

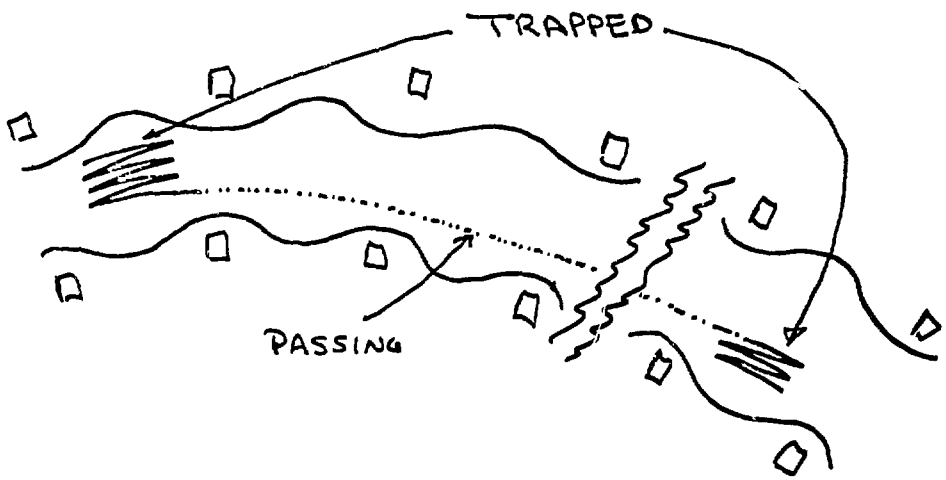

Figure 4. Top view (sketch) of the guiding center associated with Fig. 3 to further illustrate the trapped/passing character caused by μ-fluctuation.

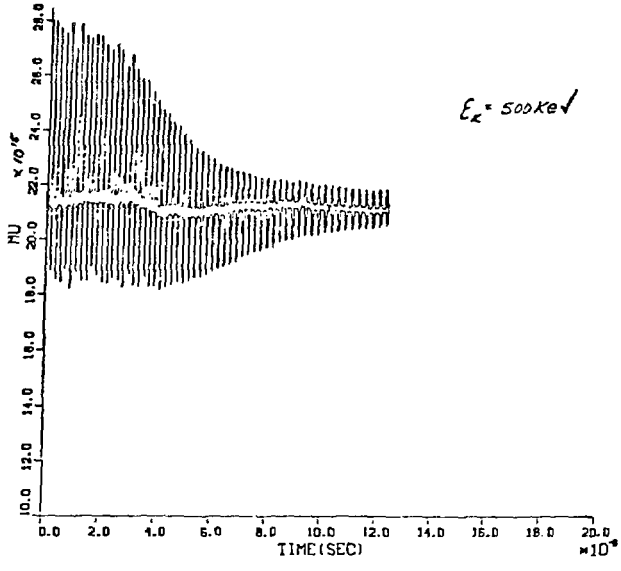

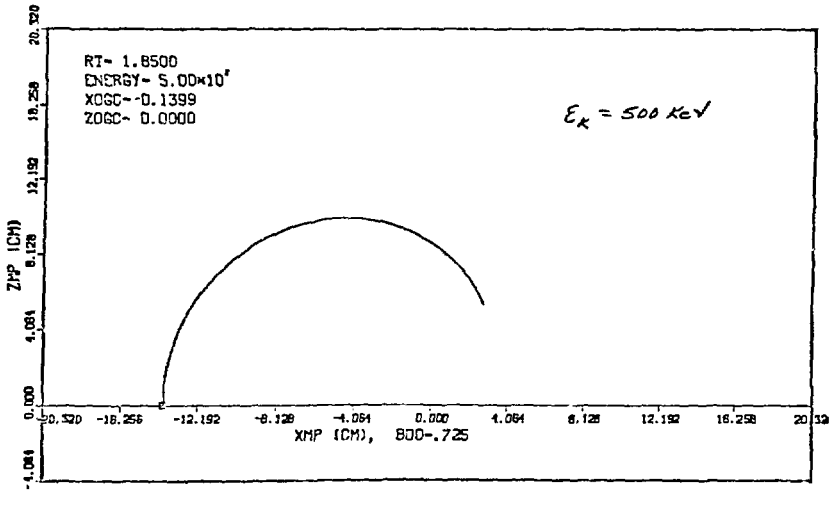

Figure 5. Magnetic moment μ as a function of time (a) and drift surface (b) for a barely trapped electron with energy of 500 keV.

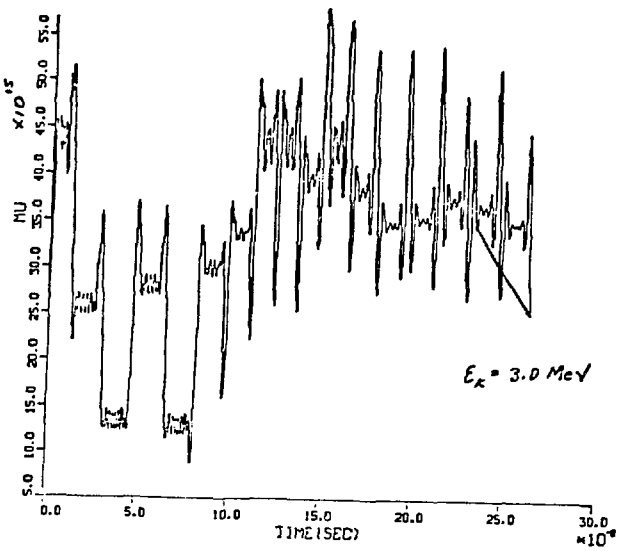

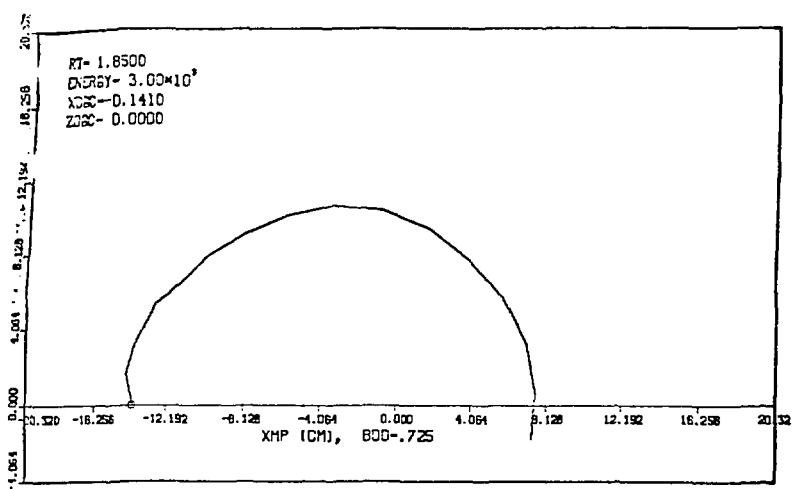

Figure 6. Magnetic moment μ as a function of time (a) and drift surface (b) for an initially barely trapped electron of energy 3 MeV. (Compare with Fig. 5).

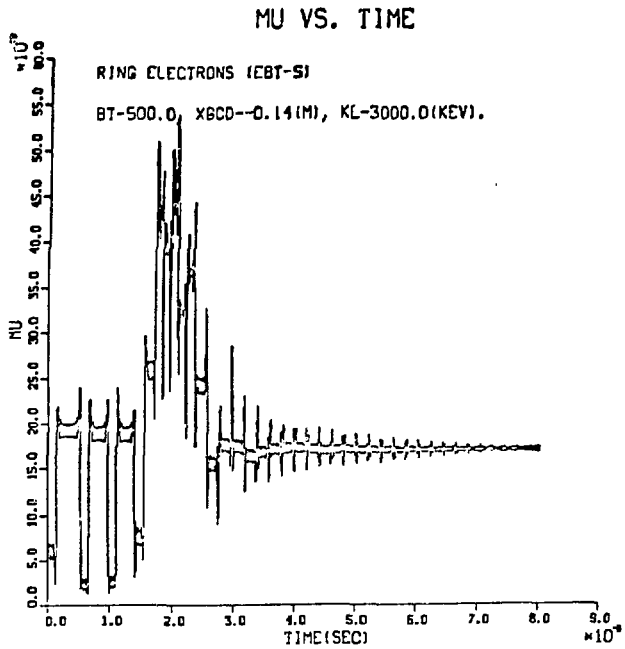

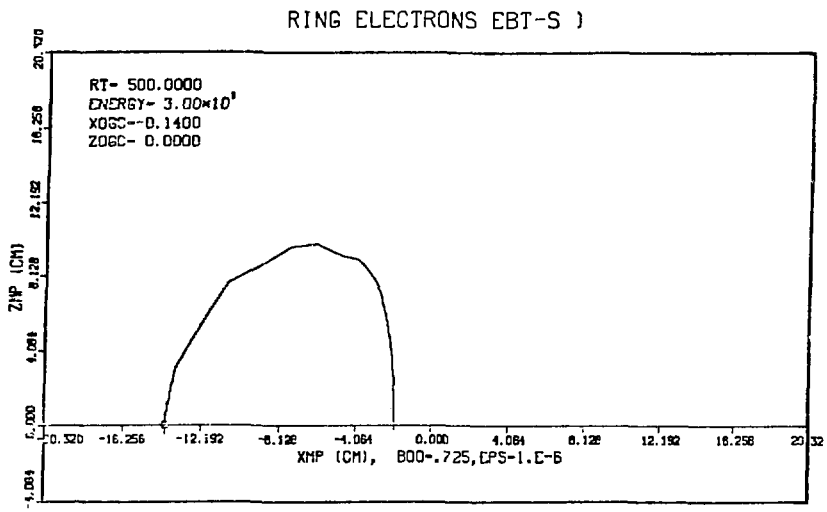

Figure 7. Magnetic moment μ as a function of time (a) and drift surface (b) for an initially passing electron of energy 3 MeV. As in Figs. 3 and 6, the μ-fluctuations are sufficiently large that it changes from passing to trapped and vice versa.

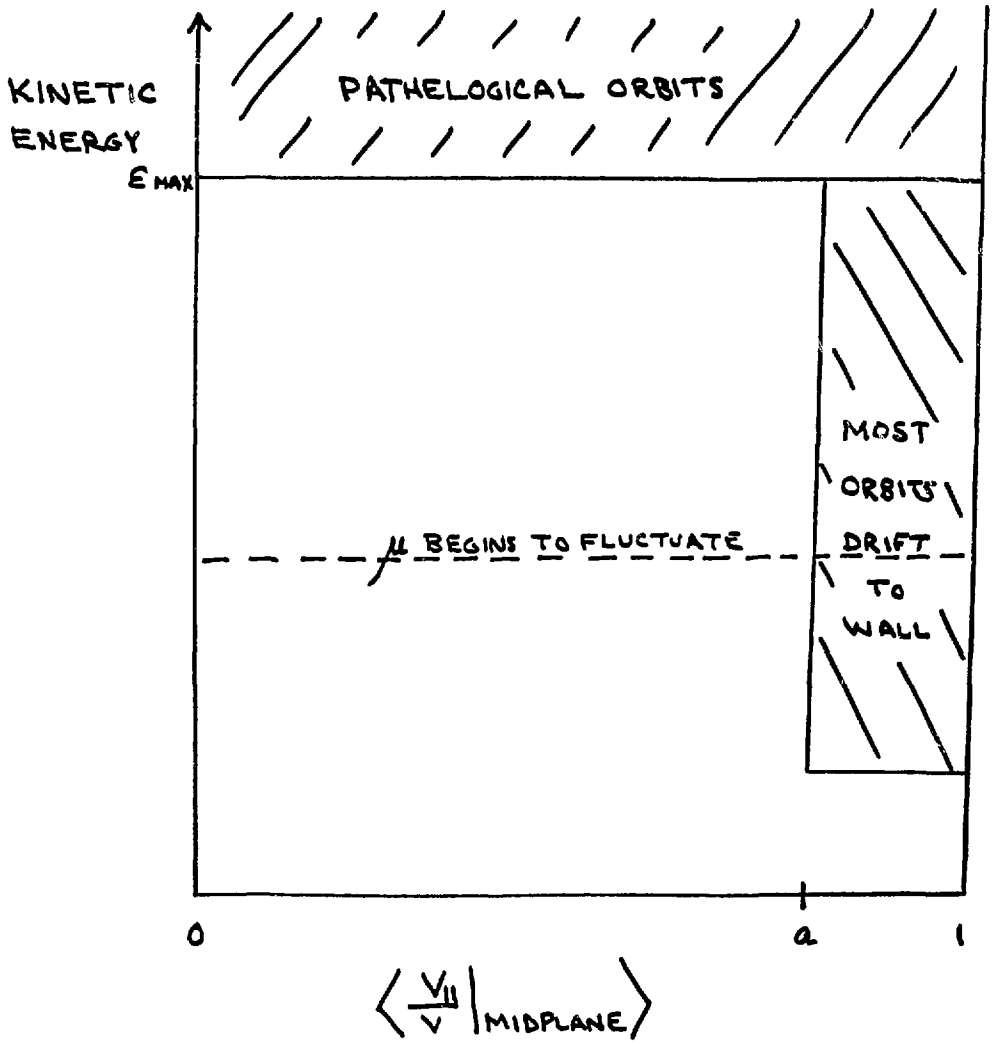

Figure 8. Schematic of orbit behavior. For $\langle v_{\parallel}/v \rangle > a$ (and modest energy) most drift orbits strike the wall and to a first approximation the distribution of electrons is zero. Similarly, for $\varepsilon > \varepsilon_{max}$ to a first approximation, the distribution is zero.

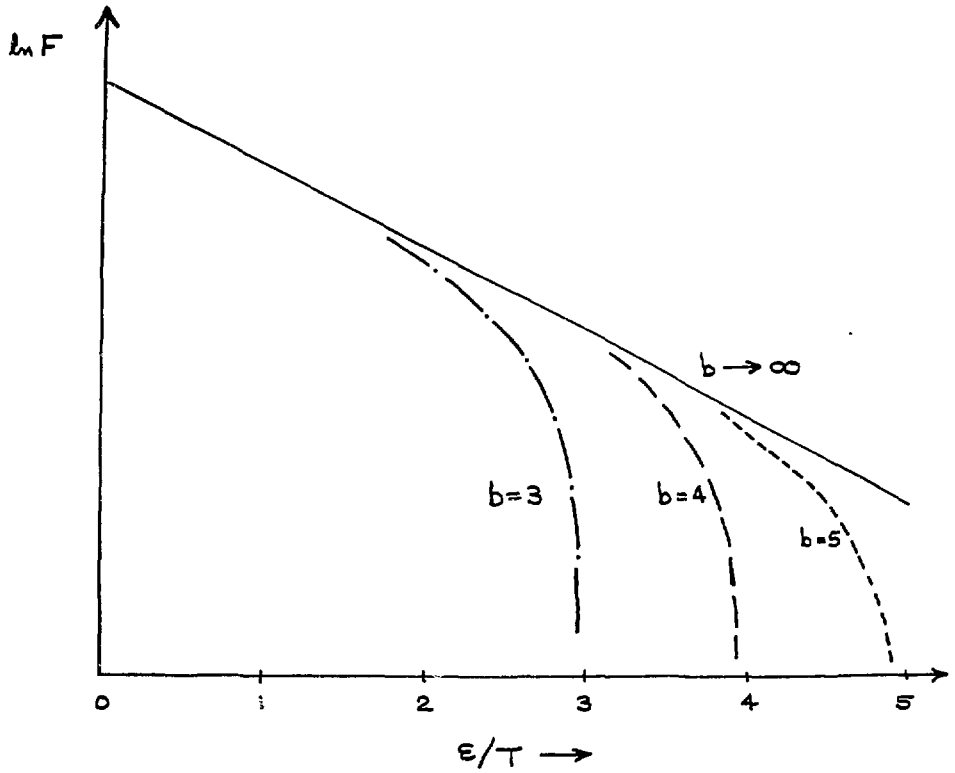

Figure 9. Logarithm of the electron distribution versus scaled energy for various values of $b \equiv \varepsilon_{max}/T$. Note that $b_{T\infty}$ corresponds to the pure Maxwellian, $\exp(-\varepsilon/T)$.

THE NONADIABATIC MOTION OF HOT ANNULUS ELECTRONS IN EBT-I AND EBT-P

R. E. Juhala
McDonnell Douglas Astronautics Company, St. Louis, MO 63166
and
M. A. Prelas and C. B. Wallace
University of Missouri, Columbia, MO 65211

Single particle motion in a magnetically confined plasma is usually taken to be adiabatic, i.e., $\rho_L \frac{\nabla B}{B} \ll 1$, where ρ_L is the gyroradius. In this case the magnetic moment ($\gamma\mu = P_\perp^2/2mB$) is a constant of the motion. Experimental and theoretical studies have shown that adiabatic motion is obtained for $\rho_L/L_m \lesssim 0.4$ (where L_m denotes the magnetic scale length). In an EBT device the electron annulus diamagnetism can be expected to modify the magnetic scale lengths, and it appears that the ring temperature may be limited by non-adiabatic losses of electrons from the mirror trap in the present EBT-I experiment. This phenomenon has been studied by tracking single particles in an axisymmetric mirror with rigid ring magnetic fields derived from an ad hoc vector potential so that $\nabla \cdot B = 0$ is satisfied. The lack of toroidal curvature is of no consequence since the poloidal magnetic scale length is greater than either the axial or radial scale lengths. The ring field width and thickness are set to be consistent with measured values on EBT-I, approximately 10 cm and 3 cm, respectively. The strength of the diamagnetism is appropriate for a ring beta of 25-30%. For these nominal values a comparison of $\Delta\mu/\mu$ is made with and without the annulus field present. The results indicate the onset of non-adiabatic behavior occurs at about the measured ring temperature and an energy cutoff roughly in the 2-3 MeV range. It is noted that the hot toroidal electron component in EBT-I appears to be narrowly confined to a region around 2 MeV. This seems consistent with nonadiabatic behavior. Using the same model for the ring field the EBT-P configuration was modeled, again assuming axisymmetry. The results of a comparison of single particle motion in the vacuum and annulus fields are presented.

INTRODUCTION

Particle confinement on closed surfaces in EBT depends on preserving the first and second adiabatic invariants, namely, $\gamma\mu = P_\perp^2/2m_oB$ and $J = \int P_\parallel d\ell$. These will be preserved provided $\rho_L|\vec{\nabla}B|/B<<1$, i.e. the motion can be described as adiabatic. Previous experimental and theoretical work[1,2,3] has shown that adiabatic motion will be obtained when $\rho_L/L_m \lesssim 0.04$. (L_m is the magnetic scale length.) In one experiment[1] involving an axisymmetric mirror the influence of two of the three scale lengths were studied which in this case were those due to the poloidal and axial field gradients (a poloidal gradient was obtained by biasing the field with an iron plate). The results indicated that the shortest scale length dominated the nonadiabatic losses whether axial or poloidal. In this experiment the lifetime τ of particles in the nonadiabatic regime was shown to vary according to $\tau = A\exp(B/(\rho_L/L_m))$ where $A \sim 10^{-8}$ sec and $B \sim 1$, and that otherwise the lifetime was limited by scattering as expected. A further inference from this experiment was that the change in the magnetic moment $\Delta\mu/\mu$ in the nonadiabatic region is proportional to $\sqrt{N}$, where N is the number of reflexions, thus implying that the particle escape is stochastic.

It has been suggested[4] that only the axial scale length in a mirror trap is effective in producing the nonadiabatic scattering loss. This becomes an especially important issue for the EBT concept because of the steep radial gradients produced by the hot electron (or hot ion) diamagnetism. Therefore, a study was initiated to determine the relative importance of the axial and radial magnetic scale lengths in the EBT magnetic field configuration. Although the approach to addressing this problem is still evolving, partial results are given for the magnetic configurations of EBT-I and EBT-P.

EBT CONFIGURATION:

The physical parameters of the present and planned EBT devices are given in Table I along with current and predicted plasma parameters. The electron gyroradii are determined for the ring temperature in the vacuum field. The Debye length at the ring is seen to be comparable to

the ring width and the ratio is about the same in all three configurations. Hence the ring electrons are not shielded from each other.

The EBT-I magnetic field consists of a steady state bumpy toroidal field modified locally in the midplane by an energetic ring of electrons. The radial and axial scale lengths in the vacuum field (at the ring radius) are approximately 10 cm and 16 cm, respectively. Since the poloidal magnetic scale length is considerably larger than either of these, and only the trapped ring electrons are of interest here, an axisymmetric mirror can be used to represent a single EBT sector. The local mirror ratio at the annulus radius and field strength are of course aligned with the respective toroidal values. A half cell of the axisymmetric field is shown in Figure 1. A single pair of current loops is used to generate the magnetic field.

The electron annulus magnetic fields are generated from an ad hoc vector potential[5] which yields field characteristics that seem reasonable based on the current experimental results from EBT-I.

From this the magnetic field in cylindrical coordinates is given by:

$$B_x = \frac{C_1 Z^3 \cos\phi}{\rho} \quad \mathrm{ERF}\left(\frac{\rho - \rho_o}{\Delta\rho}\right) e^{-\frac{Z}{\Delta Z}^4}$$

$$B_y = \frac{\sin\phi}{\cos\phi} B_x$$

$$B_z = \frac{C_2}{\rho} \exp\left(-(Z/\Delta Z)^4 - ((\rho - \rho_o//\Delta\rho)^2\right)$$

where the toroidal effect has been eliminated for the axisymmetric mirror.

The annulus location used to represent the EBT-1 magnetic field is shown in Figure 1. In this work a rectangular annulus was used. Physically this may be somewhat reasonable since the resonant heating zone might tend to reduce the curvature in the annulus. It would be better, however, to utilize a curved annulus in order to separate the axial and radial effects (this is easily done by including a Z dependence in ρ_o). The mirror field radial profiles with and without the annulus are shown

in Figure 2. In the same figure the axial dependence is given with the particle turning points noted for various pitch angles. The dip in magnetic field is $0.3B_v$ at the annulus radius of 16 cm. This corresponds[6] roughly to a ring beta of 30% which is considered a typical value for EBT-I.

METHOD OF ANALYSIS:

Using a computer code[7] the relativistic Lorentz force equation of motion is solved for single particles in the magnetic fields described earlier. The ambipolar electric field which has not been included should only have a minor perturbation on the motion in the nearly axisymmetric EBT magnetic field. The algorithm used to track the particles is known as the "Leapfrog Particle Pusher." This technique steps the coordinates and velocities with half an interval step in between. The gyro-orbit is divided into 32 sectors which has maintained energy conservation to a high degree of accuracy.

Particles covering a range of pitch angles, energy, and radial positions spanning the annulus region are followed and the average magnetic moment determined as well as the minimum and maximum excursions. In most instances particles were tracked for $\sim 10^{-8}$ sec of real time resulting in only a few bounces (usually less than 10). Consequently the phenomena of "prompt" nonadiabatic particle losses will be observed in these results.

Three areas of interest are explored here, 1) onset of nonadiabatic behavior, 2) maximum energy cutoff, and 3) relative importance of the radial and axial scale lengths. With regard to EBT-I these questions have been studied for only a single choice of annulus parameters at the present time. The EBT-P configuration having no experimental data base is studied using different ring widths and field depressions.

RESULTS:

EBT-I - A typical operational mode for EBT-I includes 18 and 10.6 GHz microwave power with the ring established by second harmonic heating from the bulk ECRH supplemented by the 10.6 GHz profile heating. The ring was located as shown in Figure 2 with a full length of 10 cm and full width of 3 cm, and at a radius of 16 cm. The vacuum field mirror ratio at this radius is 4.6. Therefore, particles with $v_{\parallel}/v \gtrsim 0.88$ will be lost from the mirror trap. As can be seen from Figure 2, the diamagnetism due to the ring is minimal beyond Z = 6 cm.

A comparison of the effect the ring has on the magnetic moment relative to the vacuum field can be seen in Figures 3 and 4. In these figures the relative change in magnetic moment $\Delta\mu/\mu$ is shown as a function of $P_{\perp}$. The magnetic moment is averaged over approximately 300 gyro-periods, and $\Delta\mu$ is the standard deviation. In this case $P_{\perp}$ is the initial value at the midplane and is approximately equal to the electron gyro-radius in centimeters since the vacuum field at the ring is $\sim$0.33 tesla. The four radii were chosen to include regions of maximum and minimum radial field gradients. The vacuum field results, Figure 3, show a slight increase in $\Delta\mu/\mu$ as $V_{\parallel}/V$ increases from 0.1 to 0.5. At smaller pitch angles ($V_{\parallel}/V > 0.5$). $\Delta\mu/\mu$ increases rapidly beyond $P_{\perp} = 1.0$ MeV/c. With the annulus added the dependence of $\Delta\mu/\mu$ in P is virtually identical for $V_{\parallel}/V = 0.1$ to 0.3 where the radial gradient is mainly responsible for the deviation in μ (Figures 4a and b). At $V_{\parallel}/V = 0.5$, however, where the axial scale length as modified by the electron ring is sampled by the electrons the spread in μ rises sharply (Figure 4c).

The spread in $\Delta\mu/\mu$ at the different radii is of course due to large variations in radial field gradients over the annulus region. A comparison of $\Delta\mu/\mu$ and ρ_L/L_r is given in Figure 5 for the vacuum and annulus fields. In this figure ρ_L/L_r is simply determined at the center of gyration in the midplane, whereas $\Delta\mu/\mu$ is averaged as usual over a 10-15 μsec time period.

The variation in $\Delta\mu/\mu$ is not shown for $P_{\perp} \gtrsim 2.0$ MeV/c because of the steep increase in particle loss rate. In this case it is more appropriate to determine the prompt loss fraction. The fraction of particles lost within $\sim$10 nsec is given in Figure 6 with and without the electron annulus.

These data are integrated over pitch angle and radius. From these data it is evident that electrons with energies above 4 MeV cannot remain trapped in the rings regardless of pitch angle. The effect of the annulus fields is to enhance the loss at lower energies. This ring enhanced prompt loss occurs only at the smaller pitch angles ($V_{\parallel}/V > 0.5$). The dashed line shows the prompt loss fraction for $V_{\parallel}/V < 0.5$ with or without the annulus.

The EBT-I plasma has been observed to contain a component of hot toroidal electrons narrowly confined on the inside of the torus. Measurements of hard x-ray emission from this component are consistent with those produced by a monoenergetic beam of electrons around 2 MeV[6]. This seems consistent with ring losses expected from the sharp energy cutoff shown in Figure 6 which indicates a mean energy between 2 and 3 MeV for the upper energy cutoff.

EBT-P - The EBT-P magnetic configuration has been modeled with an axisymmetric mirror in the same manner described above for EBT-I. The magnetic field profile is shown in Figure 7. The annulus diamagnetic effect is shown for ring half widths of 1.5 and 2.0 cm, and field depressions, $B_A/B_V = 0.5$ and 0.67. The axial width is again set at 10 cm as in the case of EBT-I. The axial length scaling of the ring is not known. A short ring is preferred for this study in order to separate axial and radial scale length effects. An axially long ring without curvature is probably physically unrealistic. The axial profile at r = 20.5 cm is also shown in Figure 7 along with the turning points for various pitch angles. The loss cone for the vacuum field at the annulus location occurs for $V_{\parallel}/V > 0.85$. The vacuum field at the ring is 1.0 tesla as is appropriate for EBT-P baseline operation with 60 GHz bulk ECRH microwave power, and 28 GHz for ring heating.

In the vacuum field $\Delta\mu/\mu$ slowly increases out of approximately $P_{\perp} = 10$ MeV/c, beyond which a significant spread due to pitch angle dependence becomes evident (Figure 8, curves a and b). In this case the gryoradius is equal to $P_{\perp}/3$ since the vacuum field at the annulus is 1.0 tesla. The effects of adding the annulus are shown in curves c, d and e of Figure 8. In this case the data has been averaged over pitch angle and radial position. This was done in order to distinguish the net effects due to the different ring configurations.

From these data it can be stated that the onset of nonadiabaticity for this ring model occurs between a $P_\perp$ of 0.75 to 1.0 MeV/c, which for the vacuum field of 1 tesla is a gyroradius of 0.25 to 0.33 cm. From the $\rho/L_m \sim 0.04$ rule this yields a magnetic scale length of approximately 8 cm. The average of $\Delta\mu/\mu$ does not change appreciably from $P_\perp = 3.0$ to 16.0. This is due to the particles sampling weaker field gradients outside the ring as gyroradius grows with energy which cancel the growth in $\Delta\mu/\mu$ for $V_\parallel/V \gtrsim 0.5$. Beyond 16 MeV/c the growth rate in average $\Delta\mu/\mu$ increases and particle losses occur. The maximum energy cutoff has not been determined as yet, however, the data on hand so far point to an energy of approximately 24 MeV. Since synchrotron radiation damping is dominant above 2-3 MeV few particles will reach the cutoff in EBT-P. Therefore the available computer time was used instead to begin to look more closely at the region $P_\perp \leq 4.5$ MeV/c. In particular the tracking time was increased by a factor of 10 (~100 μsec) for a set of particles at $P_\perp = 3.0$ and 4.5 MeV/c. In this case ~60% of the particles with $V_\parallel/V \geq 0.5$ were lost, and none were lost for $V_\parallel/V < 0.5$ nor were any lost in the corresponding runs in the vacuum field. These runs were made for ring configuration (d) in Figure 8. No particles were lost during the first 10 μsec which was the tracking time for the data shown in Figure 8.

CONCLUSIONS:

Preliminary results of a nonadiabatic behavior of single particles in axisymmetric mirror geometry representing sectors of EBT-I and EBT-P indicate that the onset of nonadiabaticity occurs at about the ring temperature. In EBT-I an upper energy cutoff between 2 and 3 MeV is indicated. The hot toroidal electron component in EBT-I can be attributed to this upper energy cutoff. Nonadiabaticity, which makes the loss cone dependent on energy, increases the size of the loss cone. Adding the electron ring to the vacuum field does not appear to change the upper energy cutoff drastically, although further broadening of the loss cone can be observed. The cutoff is due predominantly to the vacuum field axial magnetic scale length. The electron ring reduces both axial and radial magnetic scale lengths but the axial scale length is mainly responsible for producing anisotropy in the hot electron distribution.

A monoenergetic hot electron component will not be caused by nonadiabaticity in EBT-P until energies around 24 MeV are reached. This is unlikely since synchrotron damping should prevent any sizable fraction of electrons

from exceeding a few MeV. As might be expected, increasing the ring width or diamagnetic field depression increases the deviation in magnetic moment at a given energy. Particles with average $\Delta\mu/\mu \gtrsim 0.4$ are going to be lost from the diamagnetic well within a few bounces. On the other hand sizable deviations in the instantaneous value of μ can occur such as those due to the radial field gradients in the diamagnetic well without inciting prompt losses.

Tracking single particles en masse is obviously impracticle for life times approaching a drift time, however, further exploration of the functional relationship between pitch angle and ρ_L/L_m may be useful in order to define a greatest lower bound on the particle loss fraction.

ACKNOWLEDGEMENT

This work was supported by the McDonnell Douglas Corporation Independent Research and Development Program.

REFERENCES

1. A. N. Dubinina, L. S. Krasitskaya, and Yu. N. Yudin, Motion of Charged Particles in a Magnetic Trap with a Mirror Configuration, Plasma Physics 11, 551 (1969)

2. J. H. Foote, Nonadiabatic Energy Limit versus Mirror Ratio in Magnetic-Well Geometry, Plasma Physics 14 543 (1972)

3. J. R. Roth, Experimental Investigation of Single Interaction Nonadiabatic Losses from Axisymmetric Magnetic Mirrors Phys. Fluids 9 2538 (1966)

4. Y. Matsuda, W. M. Nevins, and R. H. Cohen, A Theory of Hot Electron Plasmas, Annual Controlled Fusion Theory Conference, April 8-10, 1981 Austin, Texas

5. H. Berk and A. Clark, University of Texas, Austin, Private communication.

6. L. Owen, Oak Ridge National Laboratory, Private Communication.

7. D. E. Driemeyer, Ph.D Thesis, University of Illinois, Urbana, Illinois (1980).

8. G. Haste, Oak Ridge National Laboratory, Private Communication.

TABLE 1.

EXPERIMENTAL RING AND CORE PLASMA PARAMETERS IN EBT-I/S/P

	EBT-I	EBT-S	EBT-P
MAJOR RADIUS (m)	1.52	1.52	4.5
MEAN COIL RADIUS (m)	0.16	0.16	0.29
MIRROR RATIO	1.87	1.87	2.20
NUMBER OF COILS	24	24	36
PLASMA DENSITY (cm^{-3})	1×10^{12}	3×10^{12}	1×10^{13}
CORE ELECTRON TEMPERATURE	0.3	0.6	2.0
CORE ION TEMPERATURE (KeV)	0.05	0.05	0.4
FIELD AT ELECTRON RING (TESLA)	0.32	0.50	1.0
RING TEMPERATURE (MeV)	0.15	0.60	1.0
RING DENSITY (cm^{-3})	2×10^{11}	5×10^{11}	1×10^{12}
ELECTRON GYRO RADIUS (cm)	0.4	0.6	.46
DEBYE LENGTH AT RING (cm)	0.6	0.7	0.74

Figure 1: Field Lines in an Axisymmetric Mirror Approximating a Single Sector in EBT-I.

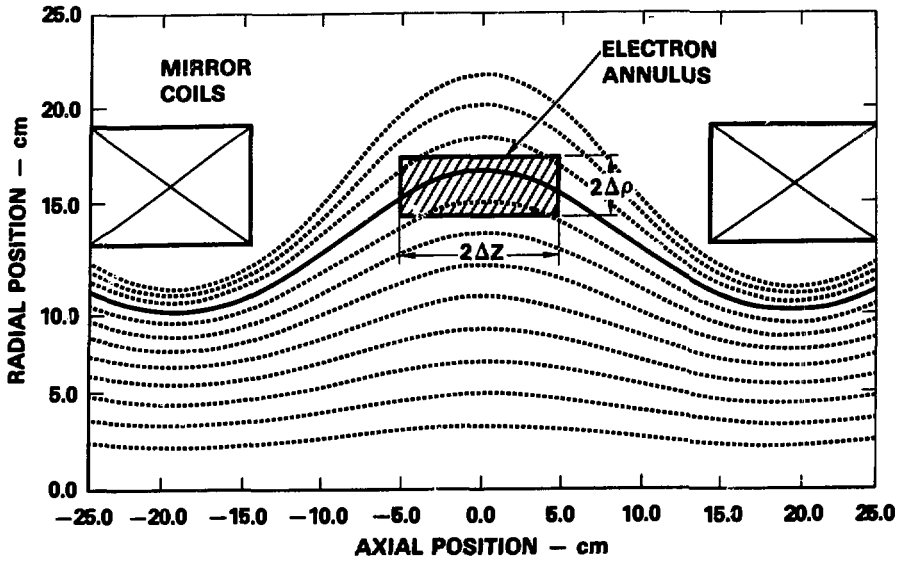

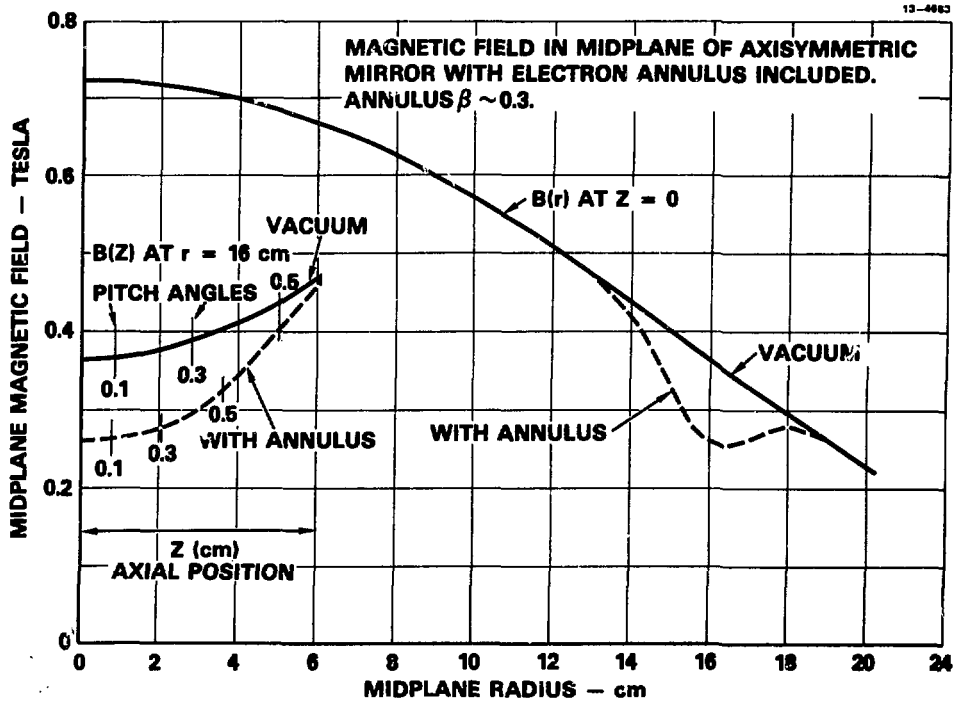

Figure 2: Radial Magnetic Field Profile of an EBT-I Axisymmetric Mirror Configuration.

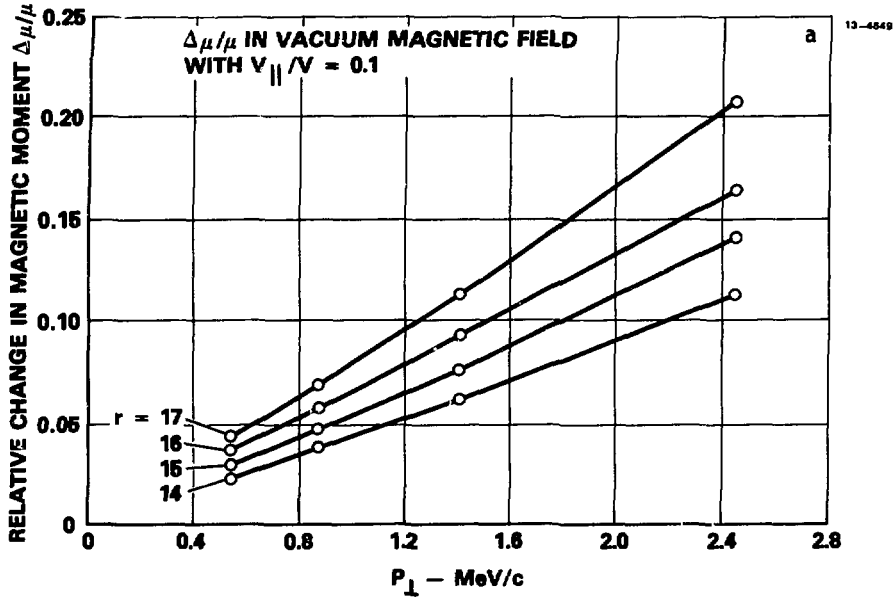

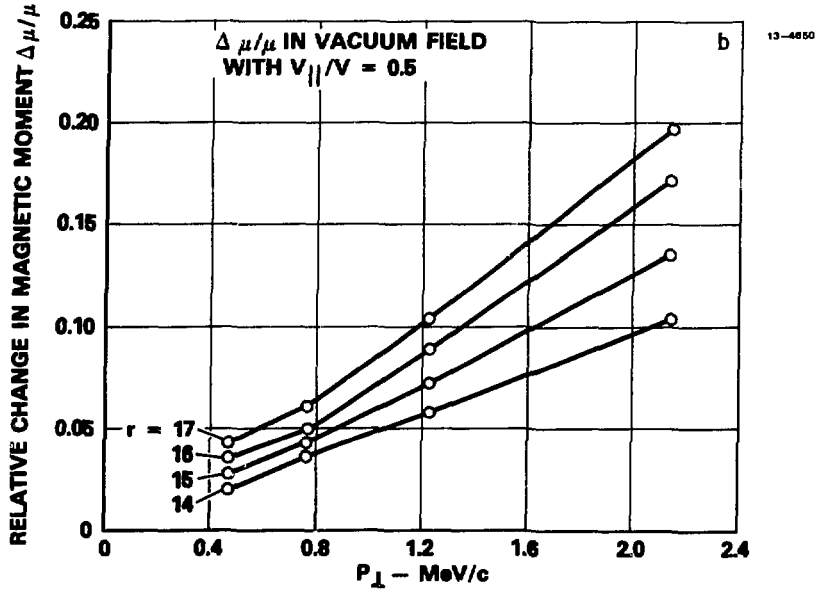

Figure 3: Average Magnetic Moment for Trapped Hot Annulus Electrons in an EBT-I Axisymmetric Mirror Configuration for the Vacuum Field.

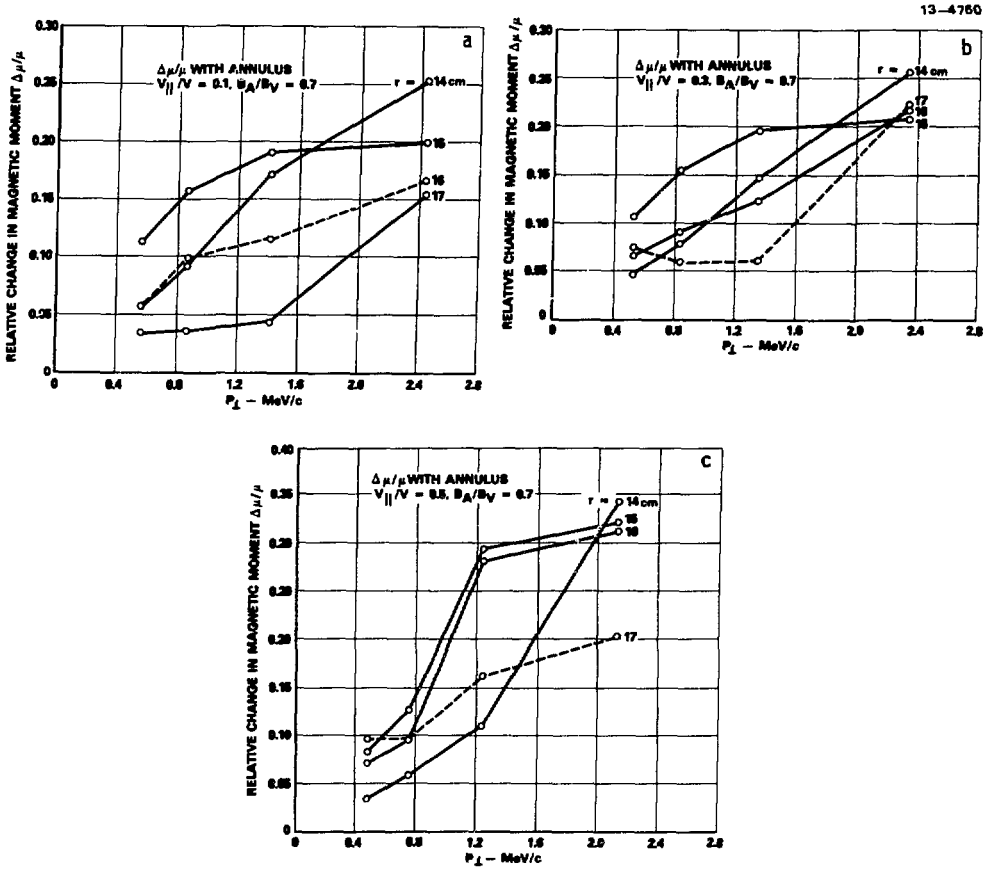

Figure 4: Average Magnetic Moment for Hot Annulus Electrons in an EBT-I Axisymmetric Mirror Configuration including Annulus Diamagnetism.

Figure 5: Comparison of $\Delta\mu/\mu$ and ρ_L/L_r for 0.5 MeV Annulus Electrons in an EBT-I Axisymmetric Mirror Configuration.

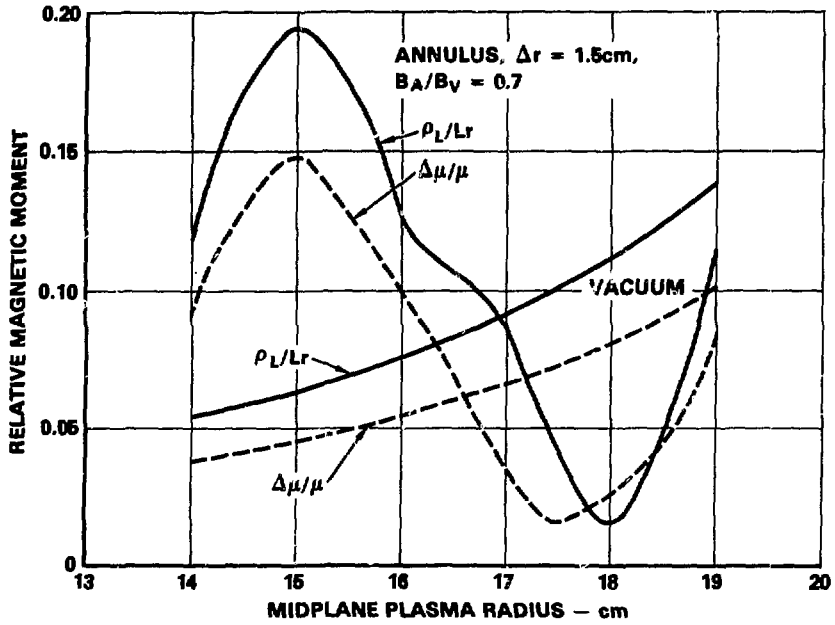

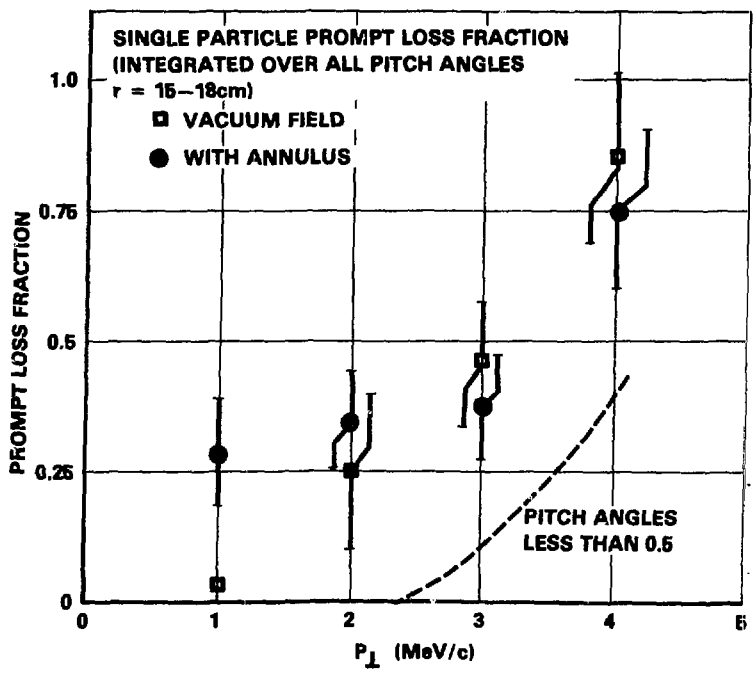

Figure 6: The Non-adiabatic Maximum Energy Cutoff for Annulus Electrons in an EBT-I Axisymmetric Mirror Configuration.

Figure 7: Radial Magnetic Field Profiles in an EBT-P Axisymmetric Mirror Configuration.

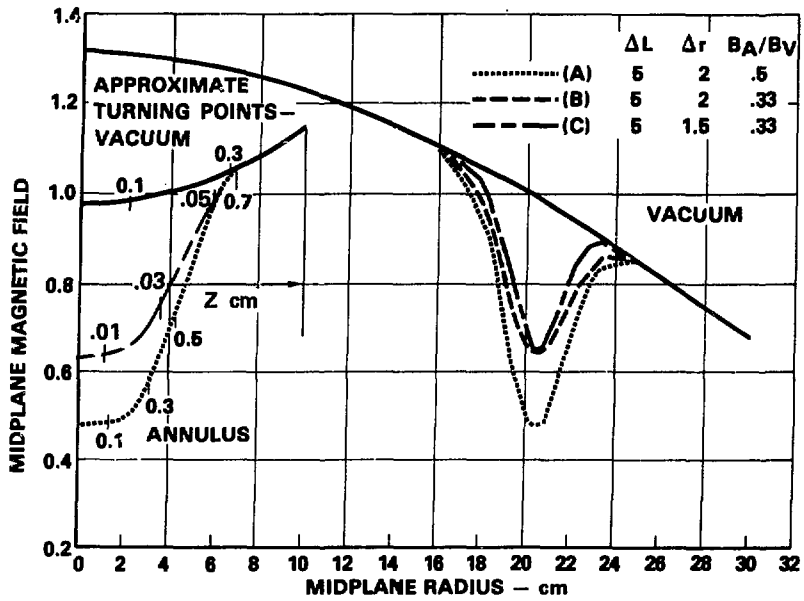

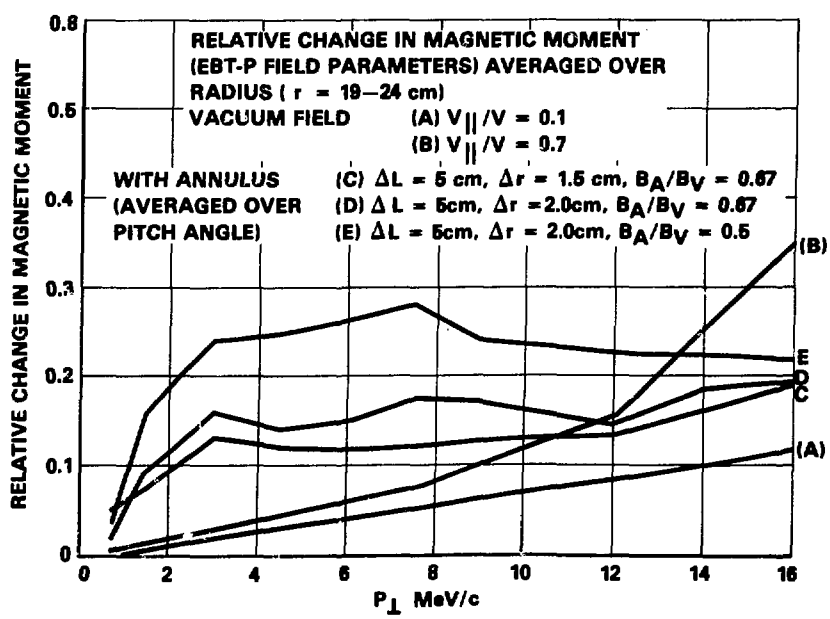

Figure 8: Average Magnetic Moment for Trapped Hot Annulus Electrons in an EBT-P Axisymmetric Mirror Configuration.

HEATING OF ENERGETIC ELECTRONS AND ELMO RING FORMATION IN SYMMETRIC MIRROR FACILITY

B. H. Quon, R. A. Dandl*, N. H. Lazar and R. F. Wuerker
TRW, Inc.
One Space Park, Redondo Beach, California 90278

ABSTRACT

The spatial structure of the high beta, hot-electron ECH plasma, (ELMO Ring), has been studied by using a Hall probe array diagnostic system which measures the diamagnetic field of the hot electron plasma in a large number of spatial locations. The steady state pressure profile obtained using a two-gaussian geometric model that best fits the measurements is found to peak at the mirror midplane near the vacuum field second harmonic resonant point. The radial width of the ring is typically 4-7 cm, and the axial length extends significantly beyond the second harmonic resonance zone of the total magnetic field. The radial thickness and the Ring beta are increased by multiple frequency ECH. The electron Ring is observed to evolve from a "sloshing"-like turning point distribution which was observed in the early times following a microwave turnon, demonstrating stochastic processes involved in ELMO Ring formation.

* AMPC, Inc., 2210 Encinitas Boulevard, Encinitas, California 92024
Work supported by the Department of Energy

1. INTRODUCTION

Here we report results on the formation and control of ELMO Rings in the Symmetric Mirror Facility (SM-1) at TRW. The plasmas produced in this facility are very similar to those studied previously in PTF and ELMO[1-5]. A significant amount of diamagnetic energy, $W_\perp \approx 25$ joules, is stored in a group of relativistic, mirror-confined electrons with energies in excess of several hundred kilo electron volts. The characteristic temperature of these electrons is estimated from the free-free bremsstrahlung X-ray intensity spectrum to be $T \approx 350 - 400$ keV. As demonstrated in previous experiments[1-5] the characteristic temperature does not depend strongly on the heating microwave power, P_μ, or the neutral gas pressure, p_0, in the operation ranges: $P_\mu = 500 - 1500$ watts; and $p_0 = 0.3 = 1 \times 10^{-5}$ torr. Instead, the hot-electron temperature appears to be limited by the breakdown of the invariance of the electron magnetic moment[6] for energies above a threshold roughly given by $\rho/R_c \gtrsim 0.05$, where ρ is the electron gyroradius $\rho = m_0c^2/eB\ (\gamma^2 - 1)^{1/2}$ and $\gamma = 1 + T/m_0c^2$. The total stored energy, $W_\perp$, does however depend on both the power, P_μ, and pressure, p_0. $W_\perp$ increases with P_μ up to a limiting value that depends on p_0. However, as was previously noted in our experiments[7], if a given amount of microwave power is distributed among several closely-space frequencies, $W_\perp$ can be substnatially increased over the level achieved with the same amount of power applied at a single frequency.

This observation has motivated a series measurements to clarify details of the ECH process that can influence strongly the overall efficiency of hot electron production. As part of these measurements, the spatial distribution of the hot electrons was studied in some detail using Hall probe arrays to measure the plasma diamagnetic field. The magnetic field configuration and the hot electron pressure profile, deduced from an equilibrium model, closely approximated the measurements, and demonstrated that heating at the nonrelativistic second harmonic resonances is important for the buildup of the energetic electron population. However, these heating zones shifted significantly away from the ring region for electrons at their steady state energies, $W \approx \kappa T$. The time-dependent measurements, furthermore, demonstrated that the heated electrons, having a "sloshing"-

like distribution initially, are "scattered" into the mirror midplane region, forming the bulk of the ring in a time much smaller than the coulomb collision time. These observations, together with the improved hot electron production using multiple frequency ECH, suggest the importance of the induced stochastic heating and trapping processes.

2. EXPERIMENTAL ARRANGEMENTS

A. The Symmetric Mirror (SM-1) Facility

A schematic diagram of the SM-1 facility is shown in Figure 1. The magnetic mirror configuration is created by energizing two magnetic field coils with a Nutek 100 kVA power supply. The mirror ratio on the machine axis is 2.2:1 and the maximum field is operated in the range of 3.5 - 4.5 kG. The mirror length, i.e., the distance between the mirror throats, is L = 71 cm. The large diameter of the field coils results in large magnetic field line curvatures R_c, r $R_c \simeq 600$ cm^2, where

$$R_c^{-1} = \left(\frac{1}{B}\frac{dB}{dr}\right)_{z = o}$$

The vacuum vessel between the two field coils is formed into a 40 cm cubic box cavity, which is bounded by two microwave cutoff screens at the mirror throats and is connected to the vacuum pumps by two 25 cm diameter cylinders.

Four Klystron amplifiers at frequencies of 8.3, 9.2, 9.4, and 10.1 GHz are used to supply microwave heating power. The microwave power is piped to the vacuum cavity in dominant mode waveguides and launched through hybrid junctions placed on the wall of the cavity center section. The coupling orientation emphasizes ordinary wave launch for all power sources used. The Klystron amplifiers can be driven by microwave signals at several frequencies within the tolerable bandwidth of 50 MHz. Fast pin-diodes are used either to modulate the microwave signal or provide simultaneous microwave turnoff for all sources as required by experiments.

The plasmas are produced in the ambient gas of hydrogen or helium in the pressure range 0.2 - 1 x 10^{-5} torr. The typical background plasma parameters are: electron temperature $T_e \sim 10 - 50$ eV, plasma density $n \sim 1 - 3 \times 10^{11}$ cm^{-3} and the plasma volume $V \sim 25 \times 10^3$ cm^3. The general properties of these plasmas have been investigated[8] and were found to be determined by the balance between microwave heating and ionization process, radiation and free-streaming ion losses. These parameters are quite independent of the heating frequency so long as ECH zones exist inside the vacuum cavity.

B. Basic Diagnostics

Figure 1 shows the basic diagnostics arrangement used in these experiments to study the properties of the energetic electrons. These included an axial and a radial array of Hall probes used to measure the diamagnetic field strength at appropriately selected spatial locations. The total perpendicular energy stored in the hot-electron population, $W_\perp$, is measured by the diamagnetic flux through a pick-up loop mounted at the mirror midplane. A compensation loop, installed near the magnetic field coil, is used to cancel spurious signals caused by small fluctuations in the vacuum magnetic fields. Other diagnostics used included a shielded axial current detector that was biased to only collect escaping electrons with energies above $\sim$1 keV and a large cross-section electron collector plate located just outside of the microwave cutoff screen used to study the plasma fluctuations. The X-ray energy was monitored in early experiments using a 3 x 3 inch NaI(Tl) scintillation spectrometer.

The spatial distribution of the hot electrons was determined from diamagnetic field measurements using arrays of Hall probes. Because of the long particle lifetime, the hot electron plasma can be easily disturbed by probes protruding into the plasma volume. To minimize such disturbances Hall probe measurements were performed well away from the bulk of the hot electrons. An axial Hall probe array, with 12 BH203 axial Hall elements spaced 2.5 cm was inserted into the mirror along the machine axis, and a radial Hall probe array, with 6 BH203 axial Hall elements and 5 BH700 transverse Hall elements alternativeliy spaced 1.25 cm apart, was inserted through a side vacuum port at z = 13.3 cm from the midplane. The

tip of the radial probe structure was only inserted to r = 18 cm to avoid disturbing the plasma configuration.

To achieve the necessary measurement accuracy (0.5 percent) the sensitivity and orientation of all the Hall probes were determined using a precisely wound long solenoid and a coil precisely oriented (45°) to the probe axis. A movable 1 mm magnetic gap was used to locate the relative probe centers to an accuracy of 0.1 mm. The Hall probe assembly was rigidly housed in double water-cooled probe jacket.

The block diagram of this diagnostic system is shown in Figure 2. The vacuum magnetic field sensed by each Hall probe is proportionally subtracted to within 1 percent of the common mode translator, which obtains its vacuum field information from a bucking field Hall element and flux concentrator monitoring the field coil current. The resultant diamagnetic field signals are then amplified by very low noise amplifiers with a constant gain of 10^4. A balance and hold circuit is used in each channel so that a nulled readout is generated before the plasma turnon. The readout signals from all channels are fed to the 32-input differential analog-digital converter and transferred into a PDP-11 based computer via a Camac Highway.

A diamagnetic profile is usually measured by microwave turnoff/turnon experiments. A data file for every turnoff consists of 50 measurements, separated by a time interval of 10-100 ms, with about 10 measurements taken before the turnoff, 30 measurements during the plasma decay and the last 10 measurements after the plasma has disappeared. For steady state information, we have averaged 5 to 10 measurements both before and after the plasma decay, thus minimizing the random experimental errors. Time dependent measurements are also taken during plasma turnon, with sufficient time space resolution to permit study of the ring formation.

3. SPATIAL STRUCTURE OF THE HOT ELECTRON PLASMA

A. The Pressure Profile Model

To facilitate the studies of the spatial distribution of the Ring structure during the formation phase, we have developed an approximate

pressure profile model which can be more sensitive to the change of the axial pressure profile variation than the comprehensive equilibrium model[9,10]. This model assumes the pressure profiles to be described by a two-gaussian geometric function

$$P_{\perp}(r,z) = P_0 \exp\left[-\left(\frac{r-R}{\Delta R}\right)^2\right] \cdot \exp\left[-\left(\frac{z-Z}{\Delta z}\right)^2\right] \tag{1}$$

and the diamagnetic current is required to satisfy

$$J_{\perp}(r,z) = \frac{1}{B(r,z)} \frac{\partial P_{\perp}}{\partial r} - \frac{P_{11} - P_{\perp}}{B(r,z)\, R_c} \tag{2}$$

where R_c is the radius of curvature for the magnetic field lines and P_{11} is assumed to have a similar form as $P_{\perp}$. Since the self-consistent field is not determined separately, we have approximated the current by

$$J_{\perp}(r,z) = \frac{1}{B(R,z)} \frac{\partial P_{\perp}}{\partial r} - \frac{AP_{\perp}}{B(R,z)} \tag{3}$$

where the radial field variation is neglected and a parameter A is introduced in Equation (3) to account for the difference thereby generated.

The ring parameters, R, Z, ΔR, Δz, p_0 and A are determined by the minima of the root-mean-square deviation (RMSD) between the measured diamagnetic fields and the values calculated using the diamagnetic current, i.e., Equation (3). An example of the field deviations are shown in Figure 3 for a typical case in which energetic electrons having a total stored energy of 20 joules were produced in SM-1 using four equally distributed power sources with a total power P_{μ} = 1000 watts. The RMSD was about $\sim$0.1 gauss out of a maximum diamagnetic field of 43.0 gauss.

B. Spatial Pressure Profiles of Energetic Electrons

Figure 4 shows the resultant radial profiles of the total magnetic field, the diamagnetic current and the electron density on the mirror midplane. Since the spatial electron-temperature variation has not yet been

measured, we have assumed a uniform temperature in the calculation. We see from Figure 4 that (1) a local magnetic well depth of $\delta B/B \sim 20\%$ was produced in the Ring region, (2) a sizable diamagnetic current was measured, and (3) the hot electrons are localized radially to have a total thickness of 2-3 inches. The local maximum of the Ring beta is, $\beta \simeq 43\%$.

The axial normalized density profile, $n(z)\ B(R,o)/B(R,z)$, where $R \simeq 9.7$ cm corresponds to the radial pressure peak position, is shown in Figure 5. One of the significant observations from this figure is that, to obtain an optimum fit to the measured field, the electron pressure must extend axially to the fundamental resonant locations $z \simeq 20$ cm. The length of the high pressure population, therefore, is considerably longer than previously thought. It remains true that the principal contributions to the stored energy come from particles close to the midplane. Nevertheless, the implication that the hot electrons must be present all the way to the fundamental resonance provides a connection between the fundamental and second harmonic heating of plasma which has heretofore been lacking.

The total magnetic field, i.e., the vacuum field plus the diamagnetic field, is shown in Figure 6(b), comparing with the vacuum field in Figure 6(a). The first region inside the one e-fold contour curve represents the principal Ring component which is surrounded by the second harmonic resonant surfaces. The second region between the one e-fold and the four e-fold contours represents the second component which is heated between the fundamental and the second harmonic resonances. Note that for relativistic electrons, the second region is the primary heating region. The bulk of the hot electrons in the first region is no longer heated by the relativistic second harmonic resonances.

C. Effects of Multiple Frequency Heating on Ring Parameters

Based on the contours of contant $|B|$ in the vacuum magnetic field, multiple frequency ECH should significantly spread the second harmonic resonant heating zones over a larger region, and would be expected to increase the Ring thickness as well as the total energy stored in the electrons. We have examined the Ring thickness and the Ring beta together as a function of the heating frequency spectrum. In Figure 7 we show the measured values of ΔR and β when one, two, three and four frequencies are applied using the same total microwave power at a constant ambient neutral

gas pressure. The Ring thickness increases systematically, demonstrating possible control over this important parameter. The increase is less evident when the plasma beta is high enough, $\beta \simeq 30\%$, as shown for the cases with three and four frequencies. This result is reasonable when one considers the magnetic field configuration shown in Figure 6, where the second harmonic resonant surfaces are closed in the neighborhood of the Ring by the plasma diamagnetism, thus counteracting, by heating effects, the tendency for thickness increase.

In Figure 7 we also note the strong increase of maximum Ring beta, using MFECH. For example, the Ring beta is about 30% using two frequency heating, as compared to 14% using single frequency heating, while the same total power is applied in both cases. The total stored energy in the Ring is estimated from

$$W_{\perp} \simeq \oint dV\ (N\ T)\ \alpha\ 2\pi R\ \Delta R\ L\ \beta \tag{4}$$

which is seen to increase by a factor of 3.0, indicating an improvement in the hot electron production efficiency, as reported previously[7] using the global diamagnetic loop measurements.

4. TIME-EVOLUTION OF THE ELECTRON TURNING POINT DISTRIBUTIONS

A. The Turning Point Distribution Function

In this subsection we are particularly interested in the qualitative changes of the pitch angle distribution during the buildup phase of the electron annulus. A description for the turning point distribution, h(A), which is equivalent to the pitch angle distribution in the parabolic magnetic well, is obtained from the pressure profile using the Abel inversion[11]:

$$\frac{n(z)}{B(z)} B(p) = \frac{1}{\sqrt{\pi}} \int_z^0 \frac{f(A)}{(Z^2 - A^2)^{1/2}} dA$$

$$f(A) = -\frac{2}{\sqrt{\pi}} \int_A^0 \frac{dz}{\sqrt{(\frac{z}{A})^2 - 1}} \frac{d}{dz} \left[\frac{n(z)}{B(z)} B(o)\right] \tag{5}$$

and

$$h(A) \equiv \int d\varepsilon\ \varepsilon^{1/2}\ f(\varepsilon\ \mu(A)) = \frac{f(A)\ 2LA}{\left(L^2 + A^2\right)^{3/2}} \tag{6}$$

Here the function $n(z)/B(z)\ B(o)$ is obtained by directly integrating the diamagnetic current, Equation (1), and assuming a uniform hot electron temperature T.

$$\frac{n(z)}{B(z)} B(o) = \int_0^\infty J(r,z)\ dr\ \frac{B(R,0)}{T} \tag{7}$$

B. Time-dependent Measurements

Assuming quasi-steady state, the turning point distributions are calculated for t = 0.2, 0.3, and 0.5 sec following turnon of the microwaves, as shown in Figure 8(b), together with the density profile, Figure 8(a). In these three time steps the local peak plasma betas are β = 0.04, 0.08, and 0.15, respectively. The pressure profile measured at t = 0.5 sec is essentially the same as that obtained in the steady state except the value of beta in the later case, $\beta \simeq 0.18$, is somewhat higher.

The main difference among the turning point distributions in Figure 8(b) can be easily recognized: at the earlier time, t = 0.2 sec, the energetic electrons appear to have a "sloshing"-like distribution with most of the electrons turning at z ≃ 5-6 cm, significantly far away from

the mirror midplane. At this location the value of magnetic field strength is about B = 1.8 kg. The magnetic field strength at the mirror minimum is reduced by ∿2% from the vacuum field value, B ≈ 1.7 kg, which corresponds to the (nonrelativistic) second harmonic resonant field for one of the frequency components (f ≈ 9.4 GHz). At t = 0.3 sec, these electrons turn in a smaller distance from the mirror midplane, z ≈ 2 cm. Because the increase in the plasma beta, the (nonrelativistic) second harmonic resonant point moves outward further to about z ≈ 3.5 cm, and the midplane field depresses by ≈ 4%. At time t = 0.5 sec, the turning point distribution is peaked at the midplane. The observed evolution of the Ring structure required about ∿0.3 sec, in which the turning point distribution changes from a partially trapped "sloshing"-like distribution to a well trapped Ring type of configuration. Note again that at t = 0.5 sec the second harmonic resonant field moves outward further to about Z ≈ 5 cm, while the magnetic field at the mirror minimum is reduced by ∿7.5%. The general tendency observed is that the second harmonic resonant zone moves away from the midplane, while more and more electrons become fully trapped in the mirror midplane region.

C. The Characteristic Parameters, $\tau(A)$ and $S(A)$

The characteristic lifetime, $\tau(A)$, for particles turning at distance A are calculated from the time-dependent turning point distributions h(A) shown in Figure 8(b). The results of these calculations are shown in Figure 8(c) together with the source function S(A) satisfying

$$\frac{\partial h(A)}{\partial t} = - \frac{h(A)}{\tau(A)} + S(A) \tag{8}$$

These results are sensitive to the detailed shape of the turning point distribution, which for small values of turning distance, A ≤ 2 cm, are likely to be inaccurate from the inversion technique. The space-averaged value of the plasma lifetime was about $< \tau > \sim 0.3$ sec, which is about 30% smaller than the overall plasma decay time $\tau_{decay} \sim 0.45$ sec measured during a microwave turnoff under the same plasma conditions. The shorter lifetime observed while heating with microwave power may be attributed to losses of those particles that are driven to the nonadiabatic energy limits by the heating field.

5. DISCUSSION AND CONCLUSION

The spatial structure of the ELMO Ring has been studied using Hall probe array measurements of the diamagnetic field. The steady state pressure profile obtained using a two-gaussian geometric model that best fits the measurements was found to peak at the mirror midplane near the second harmonic resonant point. The radial width of the ring is typically 4 to 7 cm, i.e., $\sim$3 to 5 electron gyroradia. The axial length extends significantly beyond the second harmonic resonance zone of the total field approaching the fundamental resonance location in the mirror throat. Controls of Ring parameters using combined variations in the vacuum magnetic field, the neutral gas pressure, and the microwave heating frequency and power spectrum have been demonstrated in a reasonable range.

The total magnetic field configuration is strongly modified by the hot electron diamagnetism. A local magnetic well depth, $\Delta B/B \sim 25\%$, has been produced in our experiments. The (nonrelativistic) second harmonic resonant surfaces are generally compressed to the neighborhood of the Ring by the return flux of the diamagnetism. This marked feature appears to enhance the heating of the nonrelativistic warm electrons, i.e., electrons with finite gyroradius but below about 50 keV. However, at their steady state energies, $W \sim \kappa T$ most of the ring electrons are no longer heated by the second harmonic heating because of the large relativistic mass shift. Higher harmonic ($n \geq 3$) or nonresonant heating[12] must be presumed to maintain the steady state temperature $T \approx 350$-400 keV of these electrons.

The time-dependent turning point distribution obtained during the plasma buildup demonstrated that a significant amount of pitch-angle "relaxation" is involved in the Ring formation. The time involved, $\Delta t \sim 0.3$ sec, appears to be much shorter than that of the corresponding small pitch-angle coulomb collisions, $t_c \geq 2$ sec. We suggest that this change may be related either to nonadiabatic jumps in the magnetic moment,[6] or induced stochasticity introduced by the heating process[13,14,15]. Note that the steady state hot electron temperature has been found to be a factor of $\sim$4 smaller than that calculated from the theoretical nonadiabatic

"energy Limit"[6], at which energy the nonadiabatic change in the magnetic moment, $\Delta\mu$, would "scatter" the electron itself into the mirror loss-cone as rapidly as collisional and radiational losses.

Finally, the authors are grateful to G.E. Guest, L.L. Lao, and T.K. Samec for useful discussions. This work was supported by the Department of Energy. Part of this work was also supported by Oak Ridge National Laboratory.

REFERENCES

(1) M.C. Becker, R.A. Dandl, H.O. Eason, A.C. England, R.J. Kerr, W.B. Ard, Nucl. Fusion: 1962 Supplement, Part 1 (1962) 345.

(2) R.A. Dandl, A.C. England, W.B. Ard, H.O. Eason, M.C. Becker and G.M. Haas, Nucl. Fusion 4 (1964) 344.

(3) R.A. Dandl, Bull. Amer. Phys. Soc. 12 (4), 461 (April 1967).

(4) H. Ikegami, H. Ikezi, M. Hosokawa, S. Tanaka and K. Takayam, Phys. Rev. Letts. 19 778 (1967).

(5) R.A. Dandl, H.O. Eason, G.E. Guest, C.L. Hedrick, H. Ikegami and D.B. Nelson, in Plasma Physics and Controlled Nuclear Fusion Research, Tokyo, Japan, 1974, IAEA Vol II, p. 141 (1975).

(6) Ronald H. Cohen, George Rowlands and James H. Foote, Phys. Fluids 21, (4), 627 (1978).

(7) N.H. Lazar, R.A. Dandl, W.F. Divergilio, B.H. Quon and R.F. Wuerker, Bull. Amer. Phys. Soc. 25, 993 (1980).

(8) R.F. Wuerker, Bull. Amer. Phys. Soc. 25, 994 (1980).

(9) L.L. Lao, B.H. Quon, R.A. Dandl and N.H. Lazar, "Spatial Structure of the SM-1 Symmetric Mirror Hot Electron Ring using Diamagnetic Measurements," Paper D9, this proceeding.

(10) E.F. Jaeger, L.L. Lao, L.W. Owen and C.L. Hedrick, to be published, Oak Ridge National Laboratory Report: ORNL/TM-7558 (1980)
D.B. Nelson and C.L. Hedrick, Nucl. Fusion 19, 283 (1979).

(11) G.R. Haste, N.H. Lazar, Phys. Fluids 16, (5), 683 (1973).

(12) D.B. Batchelor and R.C. Goldfinger, Nucl. Fusion 20, 403 (1980)
S. Hamasaki, H.H. Klein, N.A. Krall, John B. McBride and J.L. Sperling, Phys. Fluids 24, (9), 1076 (1981)
H. Grawe, Plasma Physics Vol. 11, 151 (1969).

(13) T.K. Samec, B.I. Hauss and G.E. Guest Bull. Amer. Physc. 26 (7), 928, (1981).
T.D. Rognlien, Bull. Amer. Phys. Soc. 26, (7), 1035 (1981).

(14) James E. Haward, M.A. Lieberman and A.J. Lichenberg, Bull. Amer. Phys. Soc. 26, (7), 1036 (1981).

(15) C.R. Menyuk, Y.C. Lee, Phys. Fluids 23, (11), 2225 (1980).

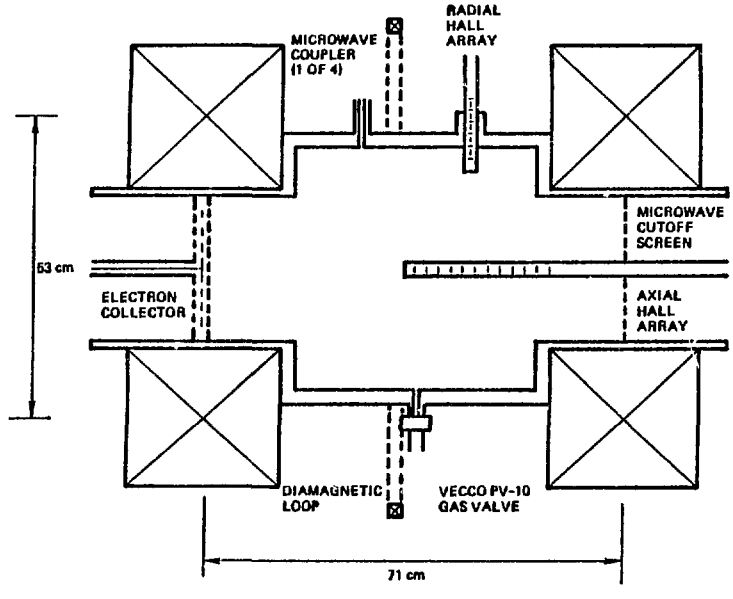

Fig. 1. Experimental arrangement of SM-1 facility at TRW.

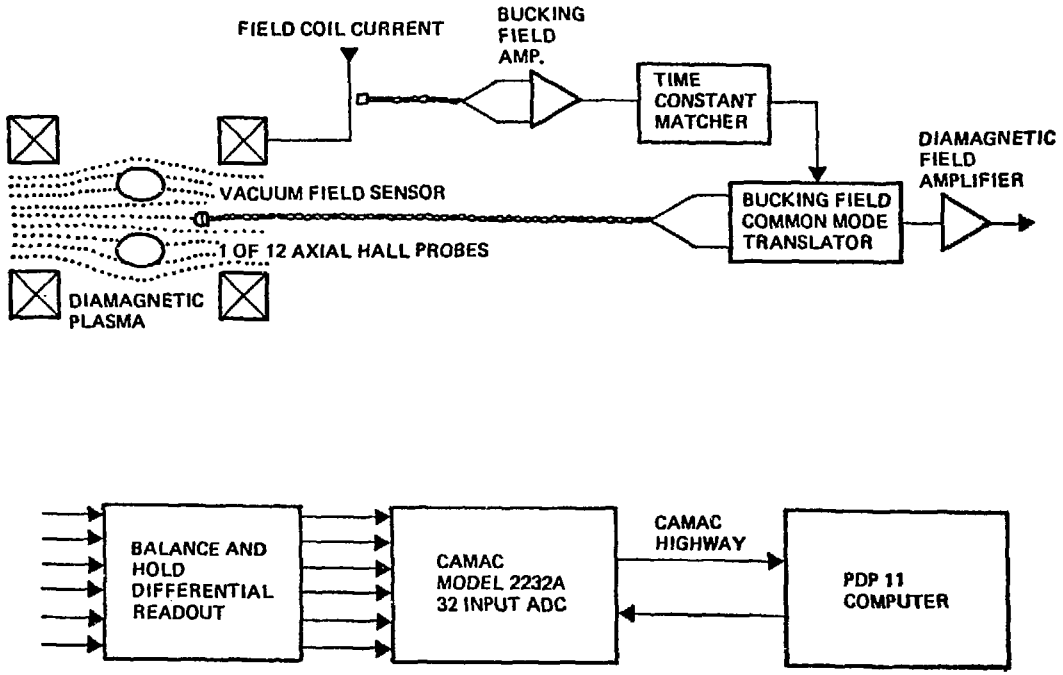

Fig. 2. Schematic diagram of Hall probe array diagnostic and data acquisition system.

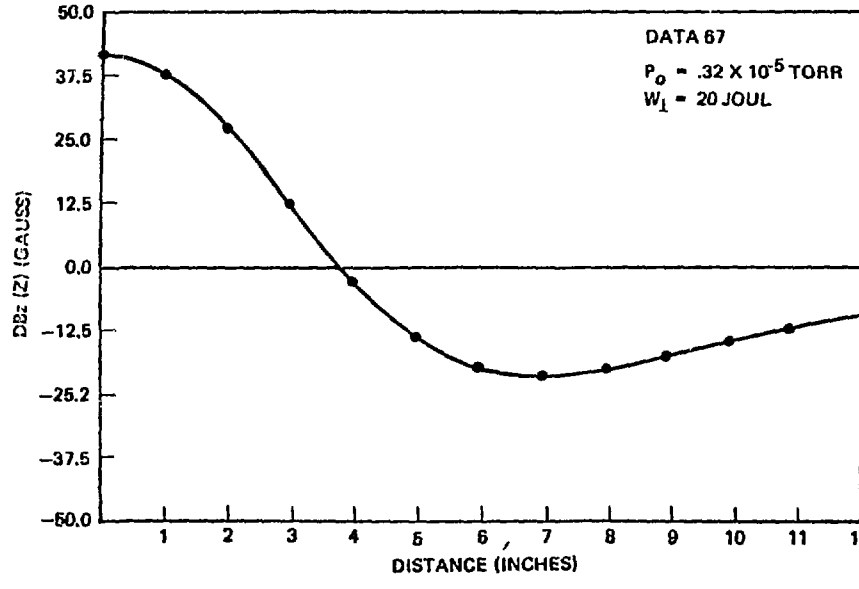

Fig. 3. Comparison of the reconstructed diamagnetic field and the measured data from the axial Hall probe array.

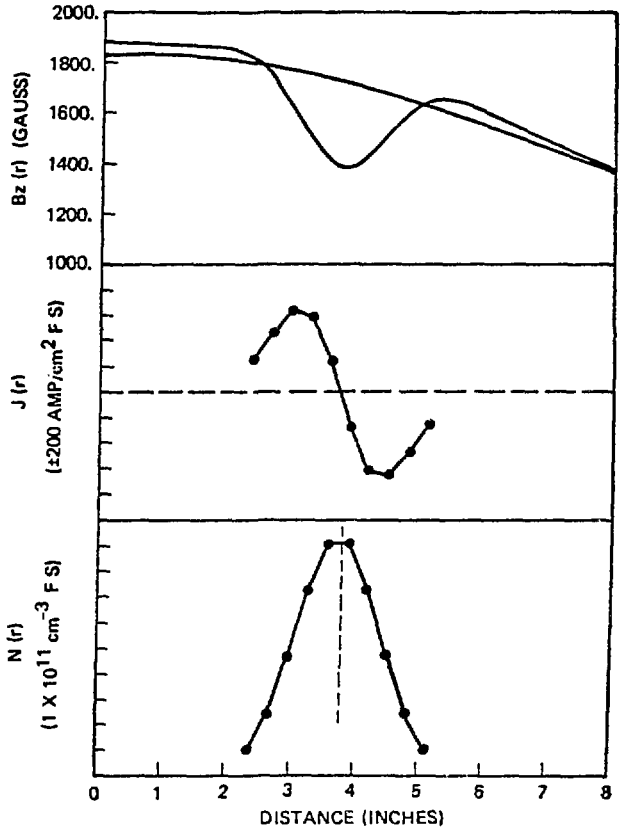

Fig. 4. Radial profile of the total magnetic field, the diamagnetic current and the hot electron pressure on the mirror midplane.

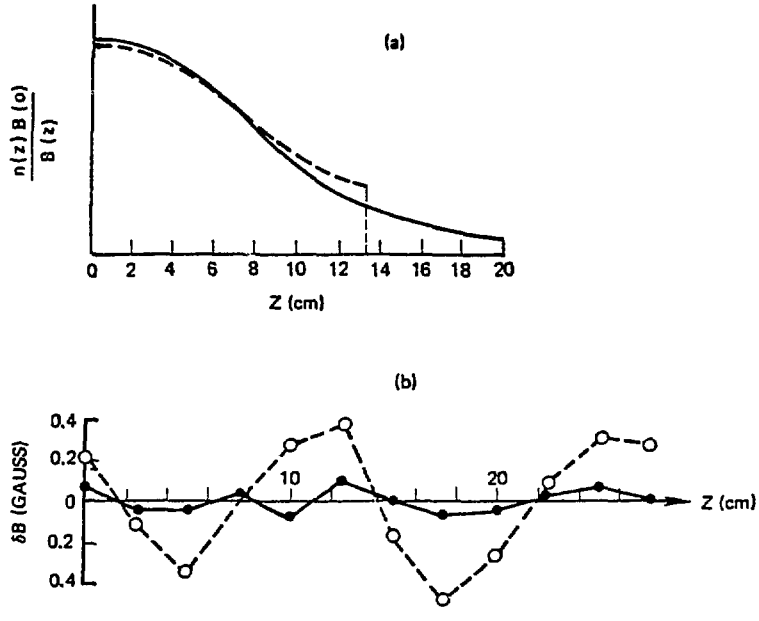

Fig. 5. Axial hot-electron pressure profiles and deviations between the model-generated and the measured diamagnetic field points.

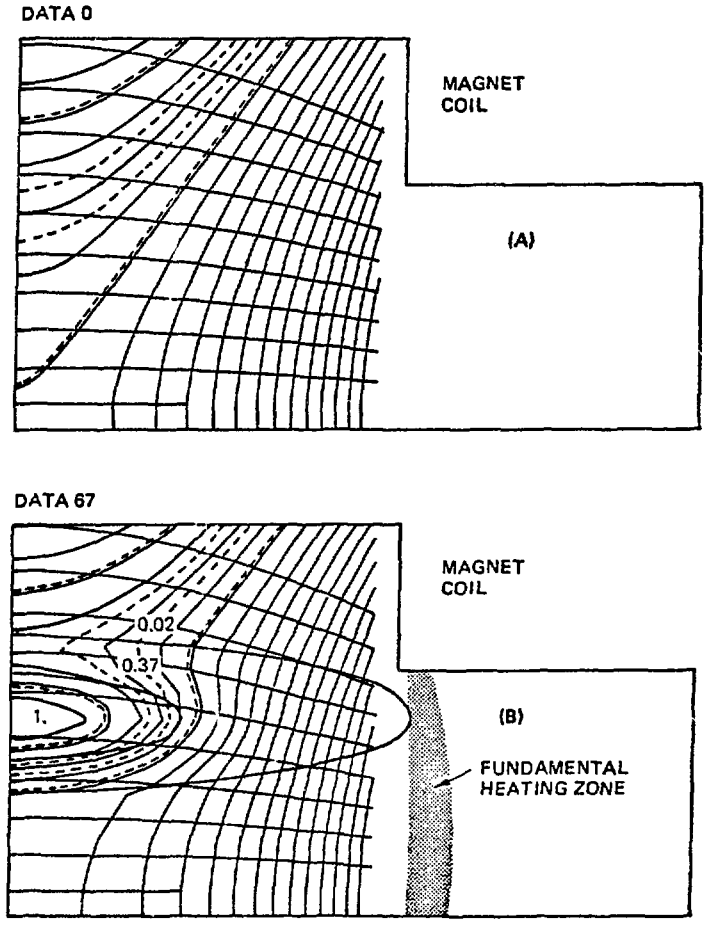

Fig. 6. An example of the resultant total magnetic field configuration (b) as compared to the vacuum field configuration (a).

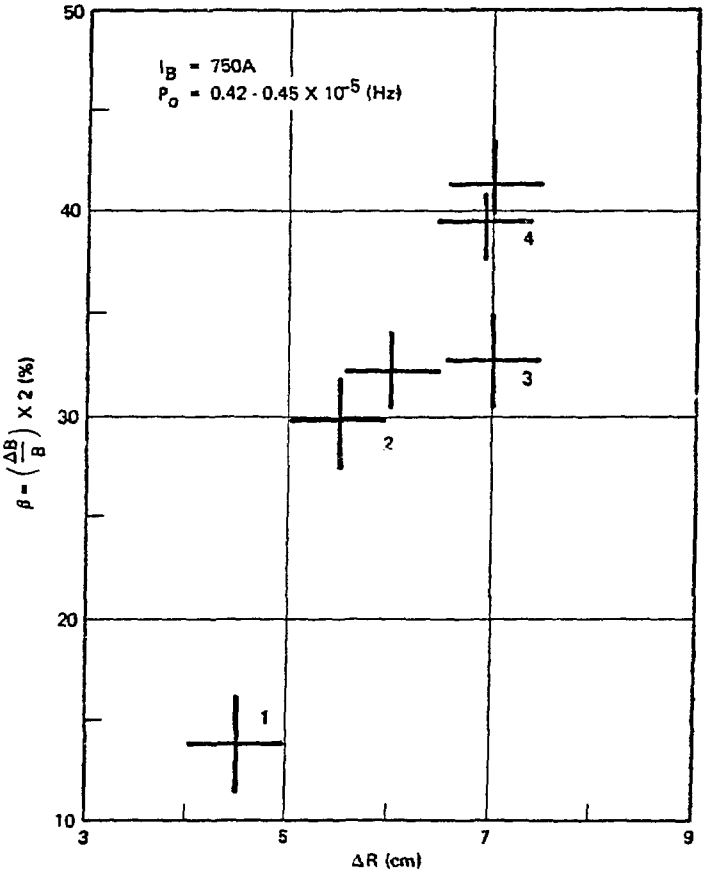

Fig. 7. Plasma betas and the radial Ring thickness vs number of frequencies used in the heating spectrum.

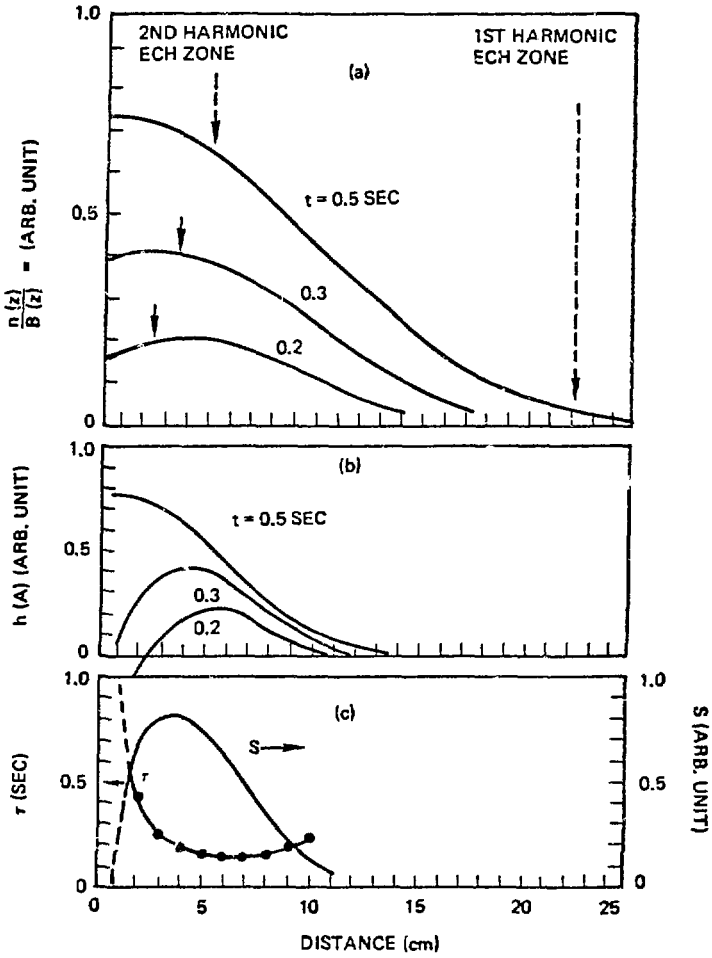

Fig. 8(a) Time-dependent axial electron pressure profile following the buildup of the ELMO Ring,

Fig. 8(b) The deduced time-dependent turning point distributions, and

Fig. 8(c) The characteristic lifetime $\tau(A)$ and the source function $S(A)$ obtained from time-dependent measurements.

Spatial Structure of the SM-1 Symmetric Mirror Hot Electron Ring Using Diamagnetic Measurements*

L. L. Lao, B. H. Quon, R. A. Dandl**, N. H. Lazar
TRW DSSG
Redondo Beach, California 90278

ABSTRACT

The spatial structure of the hot electron ring in the SM-1 symmetric mirror device is deduced by correlating the diamagnetic measurements with the values predicted using anisotropic, guiding-center multi-fluid equilibrium models. These models are defined by a small enough number of parameters to permit efficient fitting of empirical data using linear regression methods. The hot electrons are found to consist of two components. The first one has the usual Elmo ring structure in the vicinity of the second harmonic resonant surfaces and the second one extends up to the fundamental resonant surfaces and contains a sizeable fraction of the total stored energy.

*Work supported by TRW and U.S. DOE.
**AMPC, Inc., 2210 Encinitas Boulevard, Encinitas, CA

1. INTRODUCTION

A knowledge and an understanding of the spatial structure of the hot electron ring is essential to the optimization of the formation and control of the ring as well as to the stability theory of the hot electron ring stabilized mirror and bumpy torus. One method to infer the spatial structure of the ring is by correlating measurements of the diamagnetic field with the values predicted using anisotropic, guiding-center fluid equilibrium models.

2. EQUILIBRIUM MODEL

For an axisymmetric two-dimensional system, the equilibrium equations can be written as [1]

$$\Delta^{*}\Psi + 1/\sigma\, \overline{\nabla}\, \sigma \cdot \overline{\nabla}\, \Psi = - \frac{\mu_0\, r^2}{\sigma} \frac{\partial P_{\parallel}}{\partial \Psi} (\Psi, B) \tag{1}$$

$$\overline{B} \cdot \overline{\nabla}\, P_{\parallel} = \frac{P_{\parallel} - P_{\perp}}{B} \overline{B} \cdot \overline{\nabla}\, B$$

where $2\pi\Psi$ is the magnetic flux,

$$\Delta^{*} = \frac{\partial^2}{\partial r^2} - \frac{1}{r}\frac{\partial}{\partial r} + \frac{\partial^2}{\partial z^2} , \tag{2}$$

and σ is the anisotropy factor

$$\sigma = 1 + \frac{\mu_0 \, (P_{\perp} - P_{\parallel})}{B^2} . \tag{3}$$

To closely approximate the diamagnetic measurements, the pressure profiles are assumed to consist of two components

$$P_{\perp,\parallel}(\Psi, B) = g(\Psi) \left[\hat{P}_{\perp,\parallel}^{(1)}(B) + \hat{P}_{\perp,\parallel}^{(2)}(B) \right] . \tag{4}$$

The radial and the axial pressure functions $g(\Psi)$ and $\hat{P}_{\perp,}^{(n)}(B)$ are taken to have the forms

$$g(\Psi) = \begin{cases} 0 & \Psi < \Psi_1 \\ \dfrac{(\Psi - \Psi_1)^2 (\Psi - \Psi_a)^2}{(\Psi_2 - \Psi_1)^2 (\Psi_2 - \Psi_a)^2} & \Psi_1 \leq \Psi < \Psi_2 \\ \dfrac{(\Psi - \Psi_b)^2 (\Psi - \Psi_3)^2}{(\Psi_2 - \Psi_b)^2 (\Psi_2 - \Psi_3)^2} & \Psi_2 \leq \Psi \leq \Psi_3 \\ 0 & \Psi > \Psi_3 \end{cases} \tag{5}$$

$$\hat{P}_{\perp}^{(n)}(B) = P_{\perp 0}^{(n)} \left[1 - \left(\frac{B}{B_{cn}} \right)^2 \right] \qquad B \leq B_{cn} \tag{6}$$

$$\hat{P}_{\parallel}^{(n)}(B) = P_{\perp 0}^{(n)} \left(1 - \frac{B}{B_{cn}} \right)^2 \qquad B \leq B_{cn} \tag{7}$$

$$\hat{P}_{\perp}^{(n)}(B) = \hat{P}_{\parallel}^{(n)}(B) = 0 \qquad B > B_{cn} \tag{8}$$

where $\Psi_a = 2\Psi_2 - \Psi_1$ and $\Psi_b = 2\Psi_2 - \Psi_3$

3. RECONSTRUCTION

Assuming the ring has equal inner and outer thickness in the mid-plane, in this equilibrium model six parameters Ψ_1, Ψ_2, $P_{\perp 0}^{(1)}$, $P_{\perp 0}^{(2)}$, B_{c1}, and B_{c2} are used to describe the spatial properties of the rings. Ψ_2 and Ψ_1 describe the radial location and thickness of the ring. $P_{\perp 0}^{(1)}$ and $P_{\perp 0}^{(2)}$ describe the perpendicular energy stored in each of the components. B_{c1} and B_{c2} describe the axial thickness of each of the components. The parameters Ψ_1, Ψ_2, B_{c1}, B_{c2}, and $P_{\perp 0}^{(2)}$ are determined by minimizing the root-mean-square deviation (RMSD) between the measured diamagnetic fields and the values perdicted using the equilibrium model. The remaining parameter $P_{\perp 0}^{(1)}$ is determined by specifying the total perpendicular stored energy in the ring using the measured data from the diamagnetic loop.

An example of the reconstructed field configuration is shown in Fig. 1 obtained for a typical experimental case in which energetic electrons having a total stored energy of 20 Joules were produced in the TRW SM-1 Symmetric Mirror device using four equally distributed power sources with a total

power of 1000 Watts. The RMSD is about 0.3 Gauss out of a maximum diamagnetic field of 43 Gauss, closely compared with the experimentally measurement errors. The energetic electrons are found to localize in a narrow volume near the mid-radius, extending axially from the mirror mid-plane to about the mid-point between the mid-plane and the mirror throat. At the mid-plane, the ring has a thickness about 5.8 cm and the pressure peaked at a distance r = 10.4 cm from the magnetic field axis.
The major component has an axial thickness of about 10 cm. The minor component has an axial thickness of about 18 cm. The relative amplitude of the two components is $P_{\perp 0}^{(2)} / P_{\perp 0}^{(1)} \simeq 31\%$. The spatial dependence of the perpendicular pressure, the parallel pressure, and the self-consistent magnetic field strength are illustrated in Figs. 2, 3, and 4. The average pressure anisotropy is $\bar{\beta}_{\perp} / \bar{\beta}_{\parallel} \cong 4.3$. Note that the choice of the functional forms of $\hat{P}_{\perp}^{(n)}$ and $\hat{P}_{\parallel}^{(n)}$ satisfies the firehose stability criteria, $\sigma > 0$, immediately. Furthermore, from the reconstructed ring parameters it is seen that $-\frac{1}{B}\frac{\partial P_{\perp}}{\partial B} = 2\mu_0 \left(P_{\perp 0}^{(1)} / B_{c1} + P_{\perp 0}^{(2)} / B_{c2}^2\right) \cong 0.5 < 1$, as required by the ellipticity condition of Eq. 1 and the mirror stability criteria, $1 + \frac{1}{B}\frac{\partial P_{\perp}}{\partial B} > 0$. In the case shown, the average ring betas are $\bar{\beta}_{\perp} \cong 32\%$ and $\bar{\beta}_{\parallel} \cong 7.5\%$.

REFERENCE

1. D. B. Nelson and C. L. Hedrick, Nucl. Fusion 19, 283 (1979)

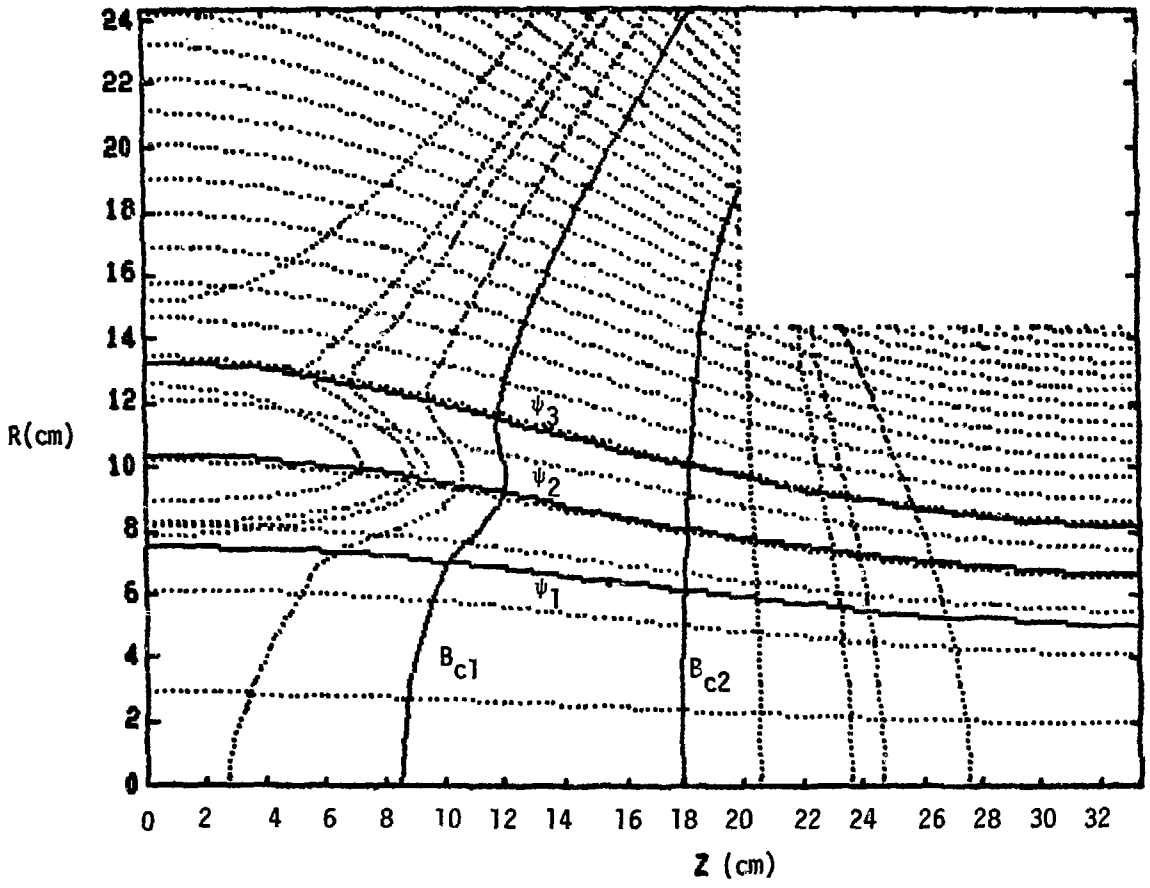

Figure 1. Radial and axial pressure cut-off surfaces and resonant surfaces.

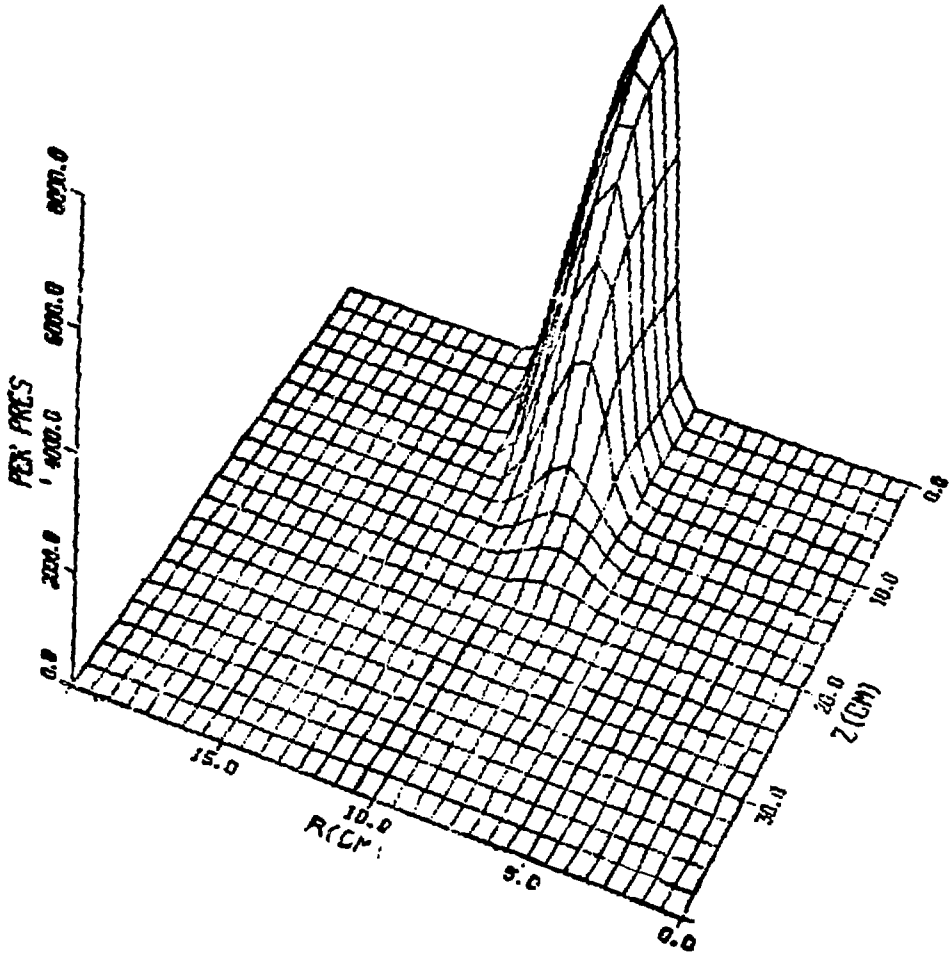

Figure 2. Perpendicular Pressure Distribution

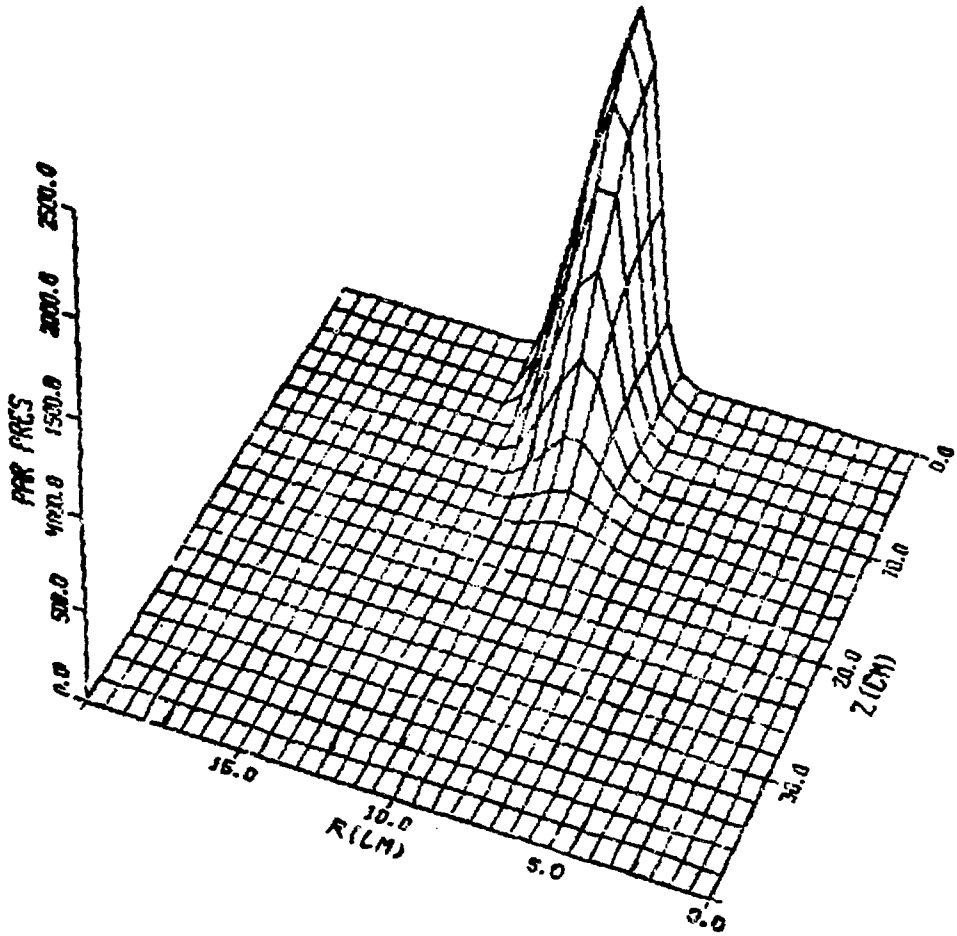

Figure 3. Parallel Pressure Distribution

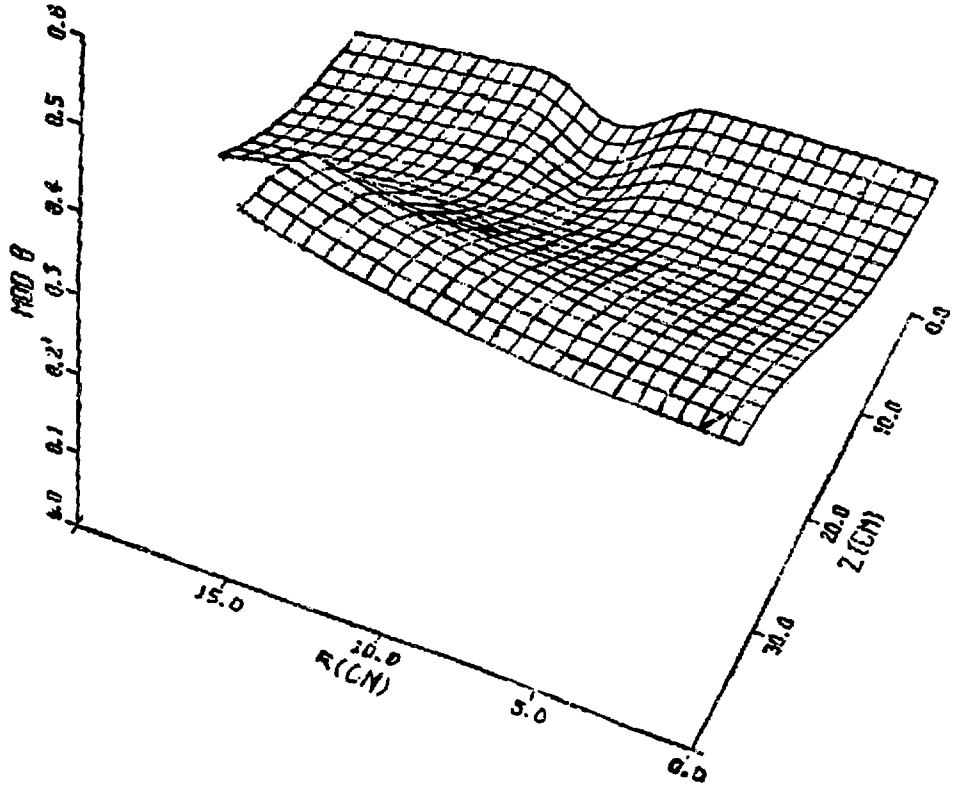

Figure 4. Magnetic Field Strength

BUMPY TORUS ANNULUS STARTUP

J. L. Sperling, S. Hamasaki, and N. A. Krall
JAYCOR, P. O. Box 85154, San Diego, California 92138

ABSTRACT

In order that a stable bumpy torus plasma configuration can be attained, it is first necessary to irradiate the plasma with sufficient external power to cause annulus formation. To estimate the power required to initiate annuli, it is assumed that quasilinear electron-cyclotron heating by microwaves is the dominant electron heating mechanism. A scaling law for required microwave power is derived which shows that annulus formation is assisted by smaller cross-section areas, lower density, lower microwave frequency, and higher C-mode temperature. The scaling law is quantitatively evaluated for NBT, EBT-1, EBT-S, EBT-P, and EBT-R parameters. The resulting power estimates are consistent with the available microwave power in previous and present experiments. In larger projected bumpy tori, like EBT-P and EBT-R, it may be necessary to initiate annulus formation at densities which are lower than in the stable T-mode so that the necessary microwave power can be reduced to reasonably modest levels. It is suggested that instabilities as well as rf heating can aid the formation of bumpy torus electron annuli. Rf experiments on NBT and EBT-S would be beneficial in determining the capability of rf power to assist annulus startup.

Relativistic electron annuli are the key elements permitting a stable plasma to be maintained within the bumpy torus plasma configuration, which consists of simple mirror cells connected in a torus.[1] The annuli are formed and sustained through the irradiation of the plasma by microwaves with frequencies approximating the second harmonic of the nonrelativistic electron-cyclotron frequency at a point radially outward from the axis at the midplane. The spatial location of the second harmonic heating zones are very close to the observed annuli location. In a previous paper, we showed that relativistic electrons have a sufficiently large cyclotron radii that second and higher electron-cyclotron harmonic heating adequate to sustain the annulus can occur through quasilinear mechanisms.[2] However, in the early stages of annulus formation, the electrons are cold, do not have appreciable cyclotron radii, and consequently are not strongly heated near the second and higher harmonic electron-cyclotron resonance zones.

In order to explain the early states of annulus formation it is necessary to invoke a process which permits electrons, during the early evolution of the annuli, to be heated to sufficiently high energies so that collisional drag can be overcome and appreciable second electron-cyclotron harmonic heating can occur.[2] In earlier work, annulus formation has been attributed to parametric decay into electrostatic electron Bernstein waves[3] and to the nonlinear interaction of electrons near the second harmonic heating zone.[4] The purpose of this paper is to derive a scaling law and to estimate power requirements for initial annulus startup in various bumpy tori with the assumption that first harmonic electron-cyclotron heating plays a dominant role. Instabilities and rf heating are indicated to be additional mechanisms which can assist annulus formation. Several features of first harmonic heating make it especially plausible. First, it is a linear process which takes place even for low wave amplitudes. Second, first harmonic heating occurs even for cold electrons with nearly zero electron gyroradius.

Third, the mode conversion of ordinary to extraordinary waves, as a result of reflection by conducting walls, readily occurs in the throat of each mirror cell.[2,5] The invoking of this mode conversion process is necessary because extraordinary waves launched near the midplane propagate to a cutoff layer before they can reach the fundamental resonance zones where they are strongly absorbed. Also, ordinary waves are ineffective at heating cold electrons through fundamental electron-cyclotron damping. Fourth, drift surfaces connecting the fundamental and second harmonic heating zones are present in bumpy tori.

The first harmonic electron-cyclotron interaction occurs for individual electrons when

$$\omega - \Omega_o = k_{\parallel} v_{\parallel} \quad , \tag{1}$$

where $v_{\parallel}$ is the parallel electron velocity. Because Eq. (1) is satisfied for a specific electron at a discrete location along a field line of length L_f, it can be anticipated that a single electron receives an impulse of energy upon crossing a resonance zone. Hence, a weak wave absorption model is appropriate for a single electron with the field line averaged rate of wave energy absorption by a single electron given by[5,7]

$$P_1 = 2\pi N \frac{L_1}{L_f} \frac{ec}{B_o} |E_-|^2 \quad , \tag{2}$$

where L_1 is the field aligned gradient of the magnetic field strength and $|E_-|$ is the right-hand electric field strength at the resonance location. This expression corresponds to two resonance zones per mirror section and N mirror sections.

The rate at which tail electrons lose energy due to collisions with background electrons is given by[8]

$$P_2 = \frac{4\pi ne^4}{mv} \ln \left[\left(\frac{T_e}{8\pi n} \right)^{\frac{1}{2}} \frac{mv^2}{2e^3} \right] \quad , \tag{3}$$

where the bulk electron temperature, background electron density, and tail electron speed are represented by T_e, n, and v, respectively.

For the subsequent analysis it is useful to average Eq. (3) over perpendicular velocities, $v_\perp$. In particular,

$$\langle P_2 \rangle = \left[\int_0^\infty dv_\perp \; v_\perp \; P_2 \exp(-v_\perp{}^2/2v_e{}^2) \right]$$

$$\times \left[\int_0^\infty dv_\perp \; v_\perp \; \exp(-v_\perp{}^2/2v_e{}^2) \right]^{-1} \quad , \tag{4}$$

with thermal velocity, $v_e = (T_e/m)^{\frac{1}{2}}$. Neglecting the weak dependence of the Coulomb logarithm on perpendicular velocity in the integration permits the explicit integration of Eq. (4). The result is,

$$\langle P_2 \rangle = F \frac{4\pi ne^2}{mv_\parallel} \ln (\Lambda) \tag{5}$$

with

$$F = (\pi)^{\frac{1}{2}} \; b \exp(b^2) \; \mathrm{erfc}(b) \quad ,$$

$$b = v_\parallel/(2)^{\frac{1}{2}} \; v_e \quad ,$$

$$\Lambda = \left[\left(\frac{T_e}{8\pi n} \right)^{\frac{1}{2}} \frac{mv_\parallel{}^2}{2e^3} \right] \quad , \tag{6}$$

and the complementary error function, erfc. The parameter, F, is always a positive number less than one and approaches one asymptotically for b going to infinity.

For tail electrons to overcome the effects of collisional drag as a result of fundamental electron-cyclotron heating, it is necessary that

$$\langle P_2 \rangle < P_1 \quad , \tag{7}$$

or

$$\frac{2F\, n\, e^3\, B_o}{m\, c\, v_{\parallel}} \ln(\Lambda) < \frac{NL_1}{L_f} |E_-|^2 \quad . \tag{8}$$

Noting that

$$\omega \approx \Omega_o \tag{9}$$

permits Eq. (8) to be rewritten as

$$\frac{L_f}{NL_1} \frac{2F\, n\, \omega\, e^2}{|E_-|^2} \ln(\Lambda) < v_{\parallel} \tag{10}$$

It follows that the capability to overcome drag is benefited by high electron kinetic energy, low frequency, low background density, large ratio of magnetic field line gradient scale length to magnetic field line length, and large values of the right-hand circularly polarized component of the wave electric field.

In a cold plasma, like the one expected during bumpy torus startup, cyclotron absorption by ordinary waves and second harmonic electron-cyclotron absorption by extraordinary waves is negligible. To establish whether fundamental cyclotron absorption by extraordinary

waves is appreciable, it is necessary to estimate the extraordinary wave electric field expected within the mirror throat where fundamental cyclotron heating occurs. Now electrons with parallel velocities ($v_{\parallel}$) greater than the electron thermal speed undergo cyclotron resonant absorption at spatial locations such that

$$\omega - \Omega_o = - (2)^{\frac{1}{2}} b \, |k_{\parallel}| \, v_e \quad . \tag{11}$$

For sufficiently large b, the local dispersion relation for extraordinary waves has the asymptotic cold plasma form[5,9]

$$\left(\frac{k_{\parallel} c}{\omega}\right)^2 = 1 + \frac{\omega_e^{\,2}}{\omega(\Omega_o - \omega)} \approx \frac{\omega_e^{\,2}}{\omega[(2)^{\frac{1}{2}} b \, |k_{\parallel}| \, v_e]} \quad , \tag{12}$$

with ω_e the electron plasma frequency. Equation (12) assumes wave propagation which is exactly parallel to the magnetic field and is a reasonable approximation for extraordinary waves beaching into fundamental electron-cyclotron resonance surfaces.[5] Equation (12) implies that for a specified value of b,

$$\frac{k_{\parallel} c}{\omega} = \left(\frac{\omega_e^{\,2}}{\omega^2} \, \frac{c}{v_e} \, \frac{1}{(2)^{\frac{1}{2}} b}\right)^{1/3} \quad . \tag{13}$$

The Poynting flux for the waves is[9]

$$S = \frac{c}{4\pi} \left(\frac{k_{\parallel} c}{\omega}\right) |E_-|^2 \quad , \tag{14}$$

and so the total flux of energy approaching a single resonant surface where bulk wave absorption occurs is

$$S_1 = SA = \frac{c}{4\pi} A \left(\frac{k_{\parallel} c}{\omega}\right) |E_-|^2 \quad , \tag{15}$$

where A is the area of the resonant surface.

For $b > 1$, S_1 can be reasonably assumed to be constant. The combination of Eqs. (13) and (15) permits replacement of $|E_-|^2$ in Eq. (10) in terms of plasma parameters and power flux into a resonance zone. In particular, for electrons of velocity $v_{\parallel}$ ($= b\sqrt{2}\, v_e$) to run away, the energy flux approaching a resonant surface must satisfy

$$S_1 > 4.0 \times 10^{-20} \frac{L_f}{NL_1} FA \left(\frac{n^4}{b^4} \frac{f}{T_e^2}\right)^{1/3} \ln(\Lambda) \text{ watts} \tag{16}$$

with units: $A(cm^2)$, $n(cm^{-3})$, $f(hz)$, and $T_e(eV)$. Equation (16) gives the total power requirement for runaway of electrons with speed greater than $b\, v_e \sqrt{2}$ in a bumpy torus device with 2N surfaces,

$$S_T = 2N\, S_1 \quad . \tag{17}$$

This scaling law shows that the critical velocity for runaway in bumpy tori is decreased by smaller field line to gradient scale length ratios, cross-section area, density and frequency, as well as by higher bulk electron temperatures.

If the critical runaway velocity is too high, the ring formed by the runaway will not be sufficiently dense (have insufficient β) to stabilize the bulk plasma. A formula for the critical runaway velocity ratio parameter, b_c, required to form an adequate ring, can be derived by first recognizing that the minimum annulus beta required for quiescent bulk plasmas is approximately 0.1.[10] Hence, the annulus density (n_A) for local annulus background

magnetic field strength (B_A) and steady-state annulus temperature (T_A) is determined from[11]

$$n_A = B_A^2/(4.03 \times 10^{-10}\ T_A) \tag{18}$$

for the units: $n_A(cm^{-3})$, B_A(gauss), and T_A(eV). The assumption that the annulus density is a consequence of the initial acceleration of a cold maxwellian tail implies an expression for b_c,

$$n_A/n = \mathrm{erfc}(b_c) \overset{b_c > 1}{\sim} \exp(-b_c^2)/[(\pi)^{\frac{1}{2}}\ b_c] \quad . \tag{19}$$

Equations (18) and (19) together determine b_c, and also give the required initial electron temperature necessary for annulus startup with a given power level.

To quantify the required power level, we first estimate the magnetic field gradient scale length, L_1, by approximating the magnetic field strength on axis

$$B(z) = a_1 + a_2 \cos(\pi N z/L_f) \quad , \tag{20}$$

where z is the coordinate along the magnetic field direction and a_1 and a_2 are constants determined from a specific magnetic field geometry. For example, for EBT-S,[10]

$$a_1 = 10.5 \times 10^3\ G \quad , \quad a_2 = 3.5 \times 10^3\ G \quad , \tag{21}$$

which corresponds to a magnetic field strength of 7000 G and 14000 G at the midplane and throat, respectively. For an applied microwave frequency in EBT-S of 28 GHz, fundamental electron-cyclotron resonance

occurs for $B(z) = 1 \times 10^4$ gauss. Equations (20)-(21) then suggest that

$$L_1 = B(z)/[dB(z)/dz] = .92\ L_f/N \tag{22}$$

The set of equations, (16)-(19) and (22), give the power necessary for annulus startup for a given electron temperature, T_e, and electron density, n. For quantitative evaluation we assume T_e = 30 eV, which is reasonable for the transition between the C-mode (without relativistic electron annuli) and the T-mode (with relativistic electron annuli).[10,12,13] This electron temperature is also consistent with the surface electron temperature of the "C-mode" like plasma exterior to the annulus during T-mode operation.[13]

Table I shows the values of b_c and S_T required for startup in various operating and projected bumpy tori. The table shows power requirements for present bumpy tori, NBT,[14] EBT-1,[13] and EBT-S,[10] which are very consistent with the applied microwave power. This result clearly supports the premise that electron-cyclotron heating at the first harmonic plays an important role in annulus startup. For larger projected bumpy tori, EBT-P[15] and EBT-R,[16] the approximation used for the analysis, $b > 1$, is better satisfied than in the present operating devices. More importantly, the startup power requirements are significantly larger for EBT-P and EBT-R than they are for NBT, EBT-1, and EBT-S. As a point of comparison, the alpha power output for the version of EBT-R considered is 300 MW.[16]

In EBT-P and EBT-R, the smallest power requirements for annulus startup might be achieved through initial operation at the lowest background densities consistent with the T-mode. Note from Eqs. (16) and (19) that a tenfold reduction in electron density, if possible, can result in an order of magnitude reduction in the requisite power for startup. Once an annulus with $\beta \gtrsim 0.1$ is formed, the desired electron density could be built-up. Also, a bulk temperature in excess of 30 eV in the C-mode could assist startup.

The key to the creation of relativistic annuli is a method of accelerating electrons at a rate which is more rapid than losses. Instabilities and rf waves represent two mechanisms, besides microwaves, which can heat electrons. Instabilities, like the universal[17] and lower-hybrid drift,[18] can transfer free energy into electron kinetic energy but with the possible price of decreased electron confinement. Furthermore, instabilities are often not easily controllable. Rf heating is probably a more viable way for externally assisting annulus formation. Specifically, rf heating can accelerate electrons along magnetic field lines.[19] Frequencies (e.g., first harmonic ion-cyclotron) which preferentially lead to heating of cold ions should be avoided. Microwaves can then pitch angle scatter and further heat the electrons. The advantages of the rf-assisted startup are twofold. First, rf power is cheaper and more easily obtained than microwave power. Second, rf heating has been successfully coupled to bumpy torus plasmas.[19]

In conclusion, a scaling law, Eq. (16), and quantitative power estimates for annulus startup in various bumpy tori have been presented under the assumption that the primary process responsible for initial annulus formation is fundamental electron-cyclotron heating by extraordinary waves. The quantitative estimates represent an upper bound because they only consider the cyclotron acceleration of electrons with parallel velocities larger than the electron thermal speed and do not explicitly include the possible contribution to the runaway electron tail formation from superthermal electrons whose parallel velocities are less than or comparable to the electron thermal speed. Wave properties for these electron velocities are not obvious and require detailed separate calculation. Nevertheless, the power requirements listed for NBT, EBT-1, and EBT-S are reasonable and support the premise that fundamental electron-cyclotron heating plays a significant role in annulus startup. They also indicate that substantially more microwave power is required for annulus startup in EBT-P and EBT-R than in present, operating, smaller bumpy tori. Rf

experiments on NBT and EBT-S would be beneficial in determining the capability of rf power (e.g., at higher harmonics of the ion-cyclotron frequency) to aid the formation of electron annuli and reduce microwave power requirements in startup.

ACKNOWLEDGEMENT

This work was supported in part by U.S. Department of Energy Contract No. DE-AC03-80ER53092.

Table I. Device Power Requirements for Annulus Startup

	N	$n(10^{12}\ cm^{-3})$	$A(cm^2)$	$f(10^9\ hz)$	$T_A(MeV)$	$n_A(10^{12}\ cm^{-3})$	b_c	$S_T(watts)$
NBT	24	0.5	350	8.5	0.1	0.057	1.1	5.8×10^3
EBT-I	24	1	350	18	0.2	0.13	1.1	1.9×10^4
EBT-S	24	1	350	28	0.5	0.12	1.1	2.2×10^4
EBT-P	36	10	620	60	1.0	0.29	1.6	1.1×10^6
EBT-R	36	100	7900	90	1.0	0.64	1.9	2.5×10^8

REFERENCES

1. Dandl, R. A., Eason, H. O., Guest, G. E., Hedrick, C. L., Ikegami, H., Nelson, D. B., in Plasma Physics and Controlled Nuclear Fusion Research (Proc. 5th Int. Conf., Tokyo, 1974), Vol. 2, IAEA, Vienna (1975) 141.
2. Hamasaki, S., Klein, H. H., Krall, N. A., McBride, J. B., Sperling, J. L., Phys. Fluids 24 (1981) 1706.
3. Tripathi, V. K., Ott, E., Liu, C. S., in Proceedings of the Workshop on EBT Ring Physics (Oak Ridge National Laboratory, Oak Ridge, Tennessee, 1979) 289.
4. Batchelor, D. B., in Proceedings of the Workshop on EBT Ring Physics (Oak Ridge National Laboratory, Oak Ridge, Tennessee, 1979) 261.
5. Batchelor, D. B., Goldfinger, R. C., Nucl. Fusion 20 (1980) 403.
6. Eldridge, O., Phys. Fluids 15 (1972) 676.
7. Sperling, J. L., Wave Heating Models for Ion-Cyclotron Heating in Elmo Bumpy Torus-Scale, JAYCOR Report J510-80-013 (1980).
8. Spitzer, L., Physics of Fully Ionized Gases, Wiley, New York (1962).
9. Stix, T. H., The Theory of Plasma Waves, McGraw-Hill, New York (1962).
10. Dandl, R. A., et al., The EBT-II Conceptual Design Study, Oak Ridge National Laboratory Report ORNL/TM-5955 (1978).
11. Book, D. L., NRL Plasma Formulary, Naval Research Laboratory, Washington, D.C. (1980) 28.
12. Dandl, R. A., et al., in Plasma Physics and Controlled Nuclear Fusion Research (Proc. 7th Int. Conf., Innsbruck, 1979), Vol. 2, IAEA, Vienna (1979) 365.
13. Dandl, R. A., et al., Summary of EBT-1 Experimental Results, Oak Ridge National Laboratory Report ORNL/TM-6457 (1978).
14. Fujiwara, M., et al., in Proceedings of the Workshop on EBT Ring Physics (Oak Ridge National Laboratory, Oak Ridge, Tennessee, 1979) 123.

15. Elmo Bumpy Torus Proof of Principle, Phase II - Proposal Alternate Site, Volume I - Device and General Project, McDonnell Douglas Astronautics Co. Report MDC-E2229.
16. Klein, H. H., Hamasaki, S., Bathke, C. G., A Multi-Dimensional Model of the EBT Reactor, JAYCOR Report J510-81-001 (1981).
17. Sagdeev, R. Z., Galeev, A. A., in Nonlinear Plasma Theory (O'Neill, T. M., Book, D. L., eds.), Benjamin, New York (1969) 73-87.
18. Gladd, N. T., Davidson, R. C., Phys. Fluids 18 (1975) 1327.
19. Owens, T. L., Mullen, J. H., Henderson, A. L., Baity, F. W., Eldridge, O. C., Bull. Am. Phys. Soc. 26 (1978) 1981.

☆U.S. GOVERNMENT PRINTING OFFICE: 1982-546-067/41